Conference Proceedings of the Society for Experimental Mechanics Series

Bo Song · Leslie Lamberson
Daniel Casem · Jamie Kimberley *Editors*

Dynamic Behavior of Materials, Volume 1

Proceedings of the 2015 Annual Conference on Experimental and Applied Mechanics

SEM

Springer

Conference Proceedings of the Society for Experimental Mechanics Series

Series Editor

Kristin B. Zimmerman, Ph.D.
Society for Experimental Mechanics, Inc.,
Bethel, CT, USA

More information about this series at http://www.springer.com/series/8922

Bo Song • Leslie Lamberson • Daniel Casem • Jamie Kimberley
Editors

Dynamic Behavior of Materials, Volume 1

Proceedings of the 2015 Annual Conference on Experimental and Applied Mechanics

Springer

Editors
Bo Song
Department of Mechanics of Material
Sandia National Laboratories
Livermore, California, USA

Daniel Casem
U.S. Army Research Laboratory
Aberdeen Proving Ground, USA

Leslie Lamberson
Drexel University
Philadelphia, Pennsylvania, USA

Jamie Kimberley
New Mexico Institute of Mining and Technology
Socorro, New Mexico, USA

ISSN 2191-5644 ISSN 2191-5652 (electronic)
Conference Proceedings of the Society for Experimental Mechanics Series
ISBN 978-3-319-22451-0 ISBN 978-3-319-22452-7 (eBook)
DOI 10.1007/978-3-319-22452-7

Library of Congress Control Number: 2015951226

Springer Cham Heidelberg New York Dordrecht London

Printed on acid-free paper

Springer International Publishing AG Switzerland is part of Springer Science+Business Media (www.springer.com)

Preface

Dynamic Behavior of Materials represents one of nine volumes of technical papers presented at the 2015 SEM Annual Conference & Exposition on Experimental and Applied Mechanics organized by the Society for Experimental Mechanics and held in Costa Mesa, CA, June 8–11, 2015. The complete Proceedings also includes volumes on the following: *Dynamic Behavior of Materials; Challenges in Mechanics of Time-Dependent Materials; Advancement of Optical Methods in Experimental Mechanics; Experimental and Applied Mechanics; MEMS and Nanotechnology; Mechanics of Biological Systems and Materials; Fracture, Fatigue, Failure and Damage Evolution; and Residual Stress, Thermomechanics and Infrared Imaging, Hybrid Techniques and Inverse Problems.*

Each collection presents early findings from experimental and computational investigations on an important area within Experimental Mechanics. Dynamic Behavior of Materials is one of these areas.

The Dynamic Behavior of Materials track was initiated in 2005 and reflects our efforts to bring together researchers interested in the dynamic behavior of materials and structures, and provide a forum to facilitate technical interaction and exchange. In the past years, this track has represented an ever growing area of broad interest to the SEM community, as evidenced by the increased number of papers and attendance.

The contributed papers span numerous technical divisions within SEM, which may be of interest not only to the dynamic behavior of materials community but also to the traditional mechanics of materials community.

The track organizers thank the authors, presenters, organizers, and session chairs for their participation, support, and contribution to this track. We are grateful to the SEM TD chairs for co-sponsoring and/or co-organizing the sessions in this track. They would also like to acknowledge the SEM support staff for their devoted efforts in accommodating the large number of paper submissions this year, making the 2015 Dynamic Behavior of Materials Track successful.

Livermore, California, USA — Bo Song
Philadelphia, Pennsylvania, USA — Leslie Lamberson
Aberdeen Proving Ground, USA — Daniel Casem
Socorro, New Mexico, USA — Jamie Kimberley

Contents

Chapter 1
Impact Response of Coquina

S.G. Subhash, P. Jannotti, and G. Subhash

Abstract The Castillo de San Marcos Fort in St. Augustine, FL was built over 330 years ago and has endured numerous wars between the Spanish and the British. During these wars, cannonballs were fired at the fort walls and became embedded in the walls. The walls did not shatter, nor did large cracks form. The fort was constructed from a native rock called coquina, found on the east coast of Florida and the west coast of Australia. Coquina is a highly porous sedimentary rock, consisting of crushed shells, fossils, limestone, sand, minerals, and clay. There are no scientific studies illustrating coquina's ability to withstand cannonball impacts. This research focused on testing coquina and a similar material (a commercial cellular foam) in uniaxial compression. The compression experiments revealed that coquina had two times the specific energy compared to a structural foam. The research revealed that the microstructure of coquina allows impact to be absorbed by progressive failure and hence possesses a high energy absorption capability.

Keywords Coquina • Rock • Energy absorption • Impact • Castillo de San Marcos

1.1 Introduction

The Castillo de San Marcos fort in St. Augustine, Florida, has been standing for 330 years [1–3]. It has endured numerous wars between the Spanish and British, and several hurricane. During the wars, cannon balls were fired and the impact impressions can still be seen in the fort walls. The fort is built from the native rock called coquina which is was quarried along the east coast of Florida. Coquina rock is mainly formed of crushed shell, fragmented fossils and coral, limestone, sand, minerals and clay [4, 5]. It contains many pores and is relatively soft when quarried and it hardens over the years from surface exposure [6].

Currently, little scientific information is available which details the mechanical response of coquina which can be used to rationalize its historical significance as a structural material. To the authors' knowledge, only one study by Knab and Clifton [7] has been conducted to examine the physical properties of coquina such as static compressive and flexural strength, dry density, and water absorption; however, beyond determining these properties there is a lack of experimental investigation of the energy absorbing capacity of the coquina. The current study seeks to identify the specific energy of coquina compared to a modern day structural foam which has a similar cellular structure (albeit man-made).

The Castillo de San Marcos Fort was built by Spanish and each wall of the fort is 12 ft thick and the wall facing the harbor is 19 ft thick. Seven years after the fort was built, the British attacked the fort [1]. However, when the cannon balls hit, the coquina absorbed the impact without causing large cracks in the wall. The cannon balls became stuck a few inches deep into the wall. The walls did not crack or fragments from the wall did not eject off. Surprisingly, to date, no systematic studies have been performed to understand this behavior. More than a million visitors and students visit each year but no detailed scientific explanation is available to these visitors. With this motivation, the current study was conducted to understand the behavior of Coquina under quasistatic compression (Figs. 1.1, 1.2, and 1.3).

S.G. Subhash (✉)
Buchholz High School, Gainesville, FL 32606, USA
e-mail: subhash@ufl.edu

P. Jannotti • G. Subhash
Mechanical and Aerospace Engineering, University of Florida, Gainesville, FL 32611, USA

B. Song et al. (eds.), *Dynamic Behavior of Materials, Volume 1*,
Conference Proceedings of the Society for Experimental Mechanics Series, DOI 10.1007/978-3-319-22452-7_1

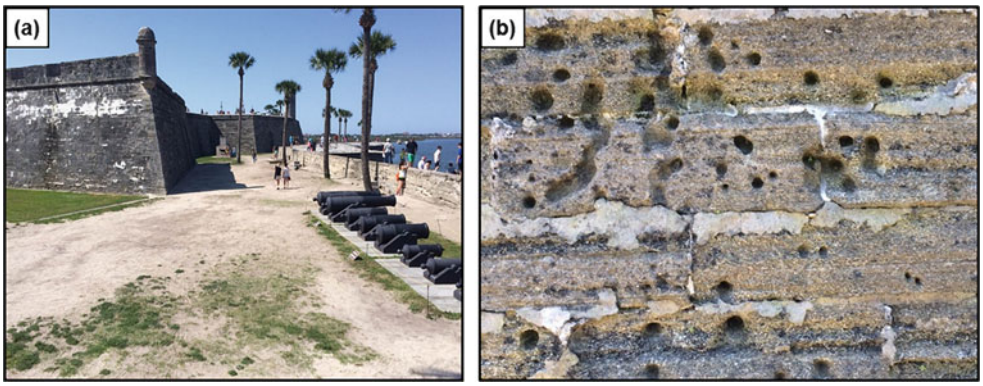

Fig. 1.1 Image of the Castillo de San Marcos fort in St. Augustine, FL and (**a**) residual impressions left in the fort walls due to projectile impacts. Notice in (**b**) that no significant cracking extends beyond the impact craters

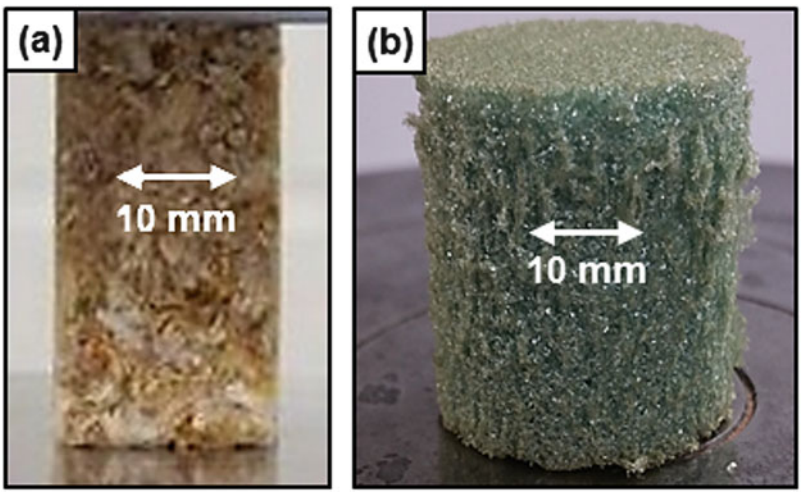

Fig. 1.2 Images of the (**a**) coquina and (**b**) foam samples used for testing

Fig. 1.3 Image of the servo-hydraulic testing machine used to perform quasi-static compression experiments

1.2 Materials

Coquina is a sedimentary rock made up primarily of small clam, oyster, and mollusk shells as well as fossils, sands, and calcite [4, 5]. Samples of approximately 100 mm × 100 mm × 25 mm were purchased from the Castillo de San Marcos Fort Gift Shop and cut into appropriate size and shape for various tests. This coquina was quarried from Summer Haven, FL. To gain better insight into its deformation behavior another material with similar microstructure, i.e., a commercial foam, was also obtained and cut into the appropriate size and shape for testing. The commercial foam, trade named Divinicell® H-60, was selected due to its uniformity in porosity and cellular structure. This material is expected to provide the response of an ideal cellular material with uniform porosity and will act as a reference to understand the response of natural materials (Table 1.1).

1.3 Experimental

Quasi-static uniaxial compression studies were conducted using a servo-hydraulic testing machine (MTS model 309.2, Eden Prairie, MN USA). The force-displacement data from quasistatic tests were plotted for each material and the area under the curves, which represents the energy absorbed during deformation, was calculated and compared. The surfaces in contact with the test specimens were lightly lubricated prior to experimentation to minimize friction between the loading surfaces and the specimens. Using displacement control, specimens were tested at a nominal strain rate of 10^{-4} s^{-1}.

1.4 Results and Discussion

The compression tests revealed interesting differences in the behaviors of coquina and foam. The force-displacement curves, shown in Fig. 1.4, revealed that for coquina, the applied force increased initially and reached a maximum. At this stage, the load dropped rapidly as is typical for brittle materials, but rather than experiencing catastrophic failure the load stabilized to around 20 % of the peak load. This behavior was marked by intermittent increase and decrease (load oscillation) until the

Table 1.1 Selected properties of coquina and foam

Material	Density(g/cc)	Compressive strength (MPa)
Coquina	1.4–1.6 [7]	1.0–1.9 [7]
Foam	0.06 [8]	0.9 [8]

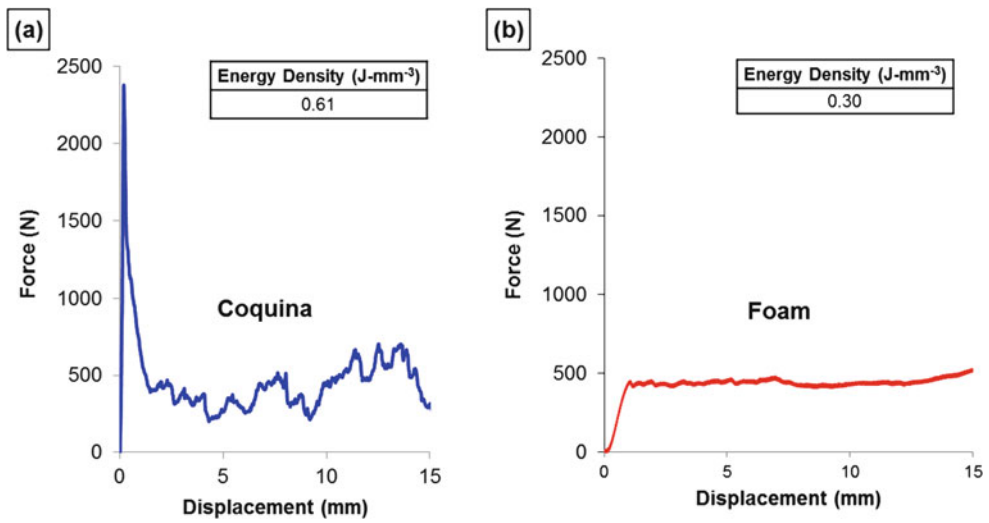

Fig. 1.4 Representative load-displacement curves for (**a**) coquina and (**b**) foam

coquina was fully crushed. In this way, coquina exhibits a progressive failure as it is crushed beyond is elastic limit. It can be inferred that such crushing in coquina occurs by particle debonding due to weak interparticle bonding. On the other hand, the commercial foam revealed an initial peak in applied load followed by continuous crushing behavior at the peak stress. Unlike the brittle coquina, the foam had a nearly constant load bearing capacity beyond its peak load. Here, crushing relates to the buckling of cell walls, resulting in pore closure and crushing.

The area under each force-displacement curve represents the energy consumed in the deformation process for that specimen. For the coquina and foam approximately 0.61 and 0.30 J-mm^{-3} was absorbed over ~15 mm of displacement. It is noted that coquina has around two times the energy absorption capability compared to foam. Despite being a brittle material, the coquina exhibits an ability to retain load after its initial load drop, which contributed to the excellent dissipation of energy due to the cannon ball impacts during the wars.

1.5 Conclusions

The energy absorbed per unit volume of coquina is significantly higher than that of the foam with similar cellular/porous structure. As the cannon ball impacted the coquina, these mechanisms came into play immediately and hence cracks did not propagate long distances and no large fragments ejected from the fort wall. The energy of the impact was absorbed locally. These mechanisms contributed to the ability of the fort to withstand the impacts of cannon balls and the effects of hurricanes.

References

1. National Park Service: Castillo de San Marcos. nps.gov/casa (2015)
2. Maynard, C.C.M.: Castillo de San Marcos. PowerKids Press, New York (2002)
3. National Park Service (NPS): Castillo de San Marcos: a guide to the Castillo de San Marcos National Monument, U.S. National Park Service, Division of Publications. U.S. Dept. of the Interior, Washington, DC (1993)
4. U.S. Bureau of Mines Staff: Dictionary of Mining, Mineral, & Related Terms. Report SP-96-1. U.S. Department of Interior, U.S. Bureau of Mines, Washington, DC (1996)
5. Neuendorf, K.K.E., Mehl Jr., J.P., Jackson, J.A.: Glossary of Geology, 5th edn. American Geological Institute, Alexandria (2005)
6. Flynn, B.: The Complete Guide to Building with Rocks and Stone: Stonework Projects and Techniques Explained Simply. Atlantic Publishing Group, Ocala (2011)
7. Knab, L.I., Clifton, J.R.: Mechanical and Physical Properties of Coquina Stone from the Castillo de San Marcos National Monument, NBSIR 88-3714.National Bureau of Standards, U.S. Dept. of Commerce, Gaithersburg (1988)
8. Matweb: Online materials information resource. matweb.com (2015)

Chapter 2
Experimental Investigation of the Dynamic Fragmentation Process in a Transparent Ceramic Under Impact Loading

P. Forquin

Abstract In the present project, edge-on impact (EOI) experiments have been conducted to improve the understanding and modelling of the dynamic fragmentation process in a transparent ceramic. In the EOI experiments a cylindrical projectile hits the edge of the target with an impact velocity ranging from 60 to 175 m/s. An ultra-high speed camera is used to visualize the fragmentation process with an interframe time set to 1 μs. An intense and complex cracking network develops in a ten of μs into the target composed of numerous "radial cracks", "Rayleigh cracks" and "release cracks". The intensity of damage increases with the impact velocity. In addition, numerical simulations of impact tests have been conducted considering the DFH (Denoual-Forquin-Hild) anisotropic damage model. Finally the numerical predictions of DFH model are compared to the experimental results in terms of cracking density and velocity of damage front.

Keywords Dynamic fragmentation • High speed imaging • ZnS ceramic • Impact loading • Anisotropic damage model

2.1 Introduction

The present project aims to investigate the fragmentation properties of a transparent ceramic in an Edge-On Impact configuration. During EOI experiments, a cylindrical projectile hits the edge of the brittle material tile inducing the propagation of a compressive wave in the sample. Radial motion of the material induces tensile hoop stresses being responsible of intense damage in the target. In open configuration, the fragmentation of the target in visualized with an ultra-high speed camera [1]. In the so-called 'sarcophagus configuration' a metal casing surrounds the tested target [2, 3] so the damage pattern is analyzed post-mortem. During the last decade, edge-on impact (EOI) experiments have been widely used to investigate the fragmentation properties of ceramics [4], microconcrete [5], rocks [6] and concrete [7] samples. In the present work, this technique has been employed with a (ZnS) transparent ceramic considering cylindrical projectile made of high-strength steel impacting the target with an impact velocity of 60, 100 and 175 m/s. The fragmentation patterns are compared to the results of numerical simulations conducted considering the DFH (Denoual-Forquin-Hild) anisotropic damage model (Denoual and Hild 2000; [8]). The experimental method is presented first. The DFH model is detailed in the second part. Comparisons between experimental and numerical data are given in the third part of the paper. The influence of impact velocity is discussed at the end of the paper.

2.1.1 Experimental Technique

The device used to perform the EOI experiments is described on the Fig. 2.1. The gas gun, of caliber 20 mm, is used to launch small cylindrical projectile at impact velocity ranging from 10 to 300 m/s. In the present work, the projectiles are made of high-strength steel. They are 10 mm in diameter and 15 mm in length. In addition their hemispherical end cap of large radius (100 mm) allows ensuring better contact conditions when impacting the target. The camera used to visualize the target is a Shimadzu HPV1 ultra-high speed camera. The resolution of the images is 312 × 260 pixels. The interframe time is set to 1 μs. The target is a transparent ZnS ceramic of size 60 × 30 × 4 mm^3. The impacted edge is 60 × 4 mm^2.

P. Forquin (✉)
3SR laboratory, Grenoble Alpes University, Grenoble 38041, France
e-mail: pascal.forquin@3sr-grenoble.fr

B. Song et al. (eds.), *Dynamic Behavior of Materials, Volume 1*,
Conference Proceedings of the Society for Experimental Mechanics Series, DOI 10.1007/978-3-319-22452-7_2

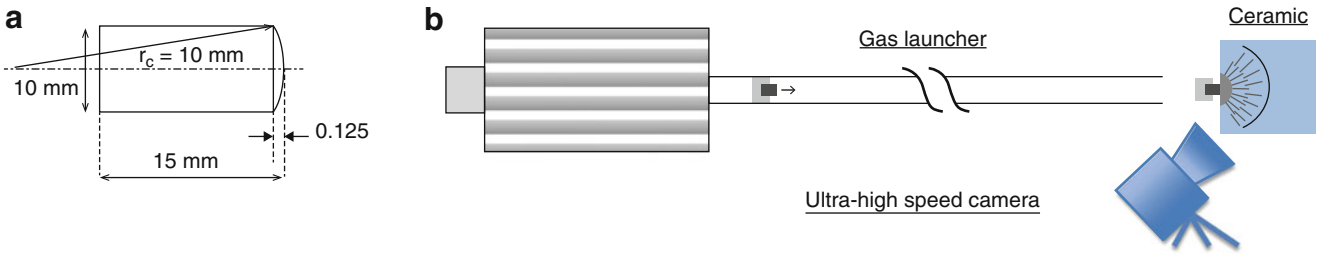

Fig. 2.1 Geometry of projectile and sketch of the experimental device

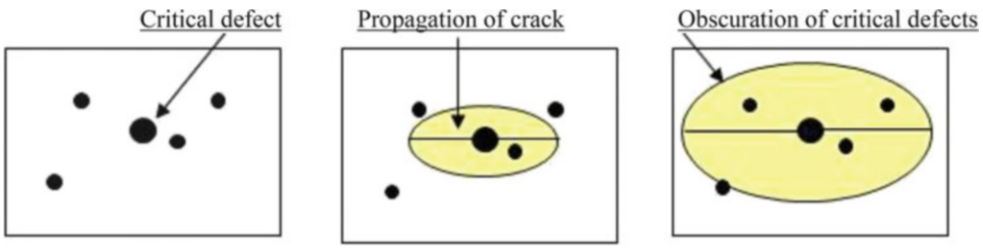

Fig. 2.2 Illustration of the obscuration mechanism in a dynamic fragmentation process

2.1.2 The DFH (Denoual-Forquin-Hild) Anisotropic Damage Model

Dynamic fragmentation in brittle solids is the consequence of the triggering and the propagation of cracks from defects such as sintering flaws in ceramics, pores in concrete and scratches in glass (Denoual and Hild 2000; [8]). The dynamic fragmentation process is driven by three types of parameters: parameters related to initiation of defects (Weibull parameters), parameters related to cracks propagation (crack speed) and parameters related to the loading rate (applied stress-rate). The dynamic fragmentation process corresponds to a competition between the initiation of cracks on critical defects and the obscuration of existing critical defects due to release wave in the vicinity of existing cracks. Obscuration is defined as a relaxation of stress ($\sigma^\circ < 0$) in a domain of size $Z_o(T-t)$ in the vicinity of a propagating crack, preventing activation of potential critical defects. $T-t$ corresponds to the time interval between the crack inception t and the current time T. One assumes that the zone of stress release is centered on the point of crack initiation and grows in a self-similar way with a diameter proportional to the size of the crack (Fig. 2.2).

$$Z_o(T-t) = S[kC\ (T-t)]^n \tag{2.1}$$

S is a shape parameter of the obscuration volume equal to $4\pi/3$ when assuming that obscuration volumes are similar to spheres in 3D ($n = 3$), k is a constant parameter assumed equal to 0.38 [9] and C is the 1D wave speed. The interaction law between critical defects of the material and cracks already created is given by the concept of probability of non-obscuration P_{no} or "local weakest link hypothesis" [8]:

$$P_{no} = \exp\left(-\iint_{Horizon(M,T)} \frac{d\lambda_t(m,t)}{dt} dVdt\right) \tag{2.2}$$

In a case of a multiple fragmentation process, the non-obscuration probability (Denoual and Hild 2000) reads:

$$P_{no} = \exp\left(\int_0^T \frac{d\lambda_t(t)}{dt} V_o[T-t]dt\right) \tag{2.3}$$

Where λ_t is the density of critical defects given by Eq. (2.4):

$$\lambda_t(\sigma) = \lambda_0 \left(\frac{\sigma}{\sigma_0} \right)^m \tag{2.4}$$

$\lambda_0/{\sigma_0}^m$ and m are the Weibull parameters identified through quasi-static bending test series. Furthermore, a damage variable D can be defined for each principle stress assuming that damage corresponds to the ratio of the obscured volume to the total volume:

$$D \approx \frac{V_0}{V_{total}} = 1 - P_{no} \tag{2.5}$$

The macroscopic stress can be calculated as function of the microscopic stress σ according to:

$$\Sigma = \sigma(1 - D) \tag{2.6}$$

If a constant stress-rate is assumed ($\sigma = \sigma^\circ t$) the growth of damage is given by the following close-form solution:

$$D(t) = 1 - \exp\left(- \frac{n!m!}{(n+m)!} \left(\frac{t}{t_c} \right)^{n+m} \right) \tag{2.7}$$

Where t_c corresponds to the characteristic time of fragmentation:

$$t_c = \left(\sigma_0 \lambda_0^{-\frac{1}{m}} \right)^{\frac{m}{m+n}} \left(\dot{\sigma} \right)^{-\frac{m}{m+n}} \left(kCS^{\frac{1}{n}} \right)^{\frac{n}{m+n}} \tag{2.8}$$

In addition, the cracking density can be calculated by considering that new cracks are only triggered in non-obscured zones [8]:

$$\frac{\partial \lambda_{cracks}}{\partial t} = P_{no} \frac{\partial \lambda_t}{\partial t} \tag{2.9}$$

This model was used to simulate the fragmentation process in dense or porous ceramics ([10, 11]), in ultra-high performance concretes [3], in microconcrete [5], in glass [12] and in limestone rock [6].

2.1.3 Experimental Results and Numerical Simulation of Edge-on Impact Tests

Three edge-on impact experiments have been conducted considering different impact velocities: 60, 100 and 175 m/s. The pictures of Shimadzu HPV1 ultra-high speed camera are given on the left side of each next figures considering three times after impact. The experiments have been simulated numerically with the finite-element code Abaqus-Explicit. The mesh of the target is composed of 230 400 C3D8R finite-elements (eight nodes, reduced integration). Three types of parameters are used for modelling the behavior of ZnS ceramic: the elastic parameters ($E = 87.6$ GPa et $\nu = 0.331$), the Weibull parameters identified in 3-point bending tests ($m = 11$, $\sigma_w = 68.2$ MPa, $V_{eff} = 86.7$ mm^3) and the parameters related to the growth of obscuration zones: the shape parameter ($S = 3.74$) and the crack speed ($k = 0.38$). The results of each numerical simulation are given on the right side of each figure in terms of damage isocontours.

The Fig. 2.3 presents the experimental and numerical results obtained with an impact velocity of 60 m/s. An intense damage composed of a large number of small radial cracks is observed at T = 4.5 µs. At T = 8.5 µs, many isolated (i.e. not connected to the main damage zone) radial cracks are noted. It demonstrates that cracks initiate on independent defects existing in the microstructure. Moreover, some cracks initiate on the rear face of the target and propagate orthogonally to the rear surface. This damage is due to "release wave" forming when the incident wave reflects on the free rear surface. In

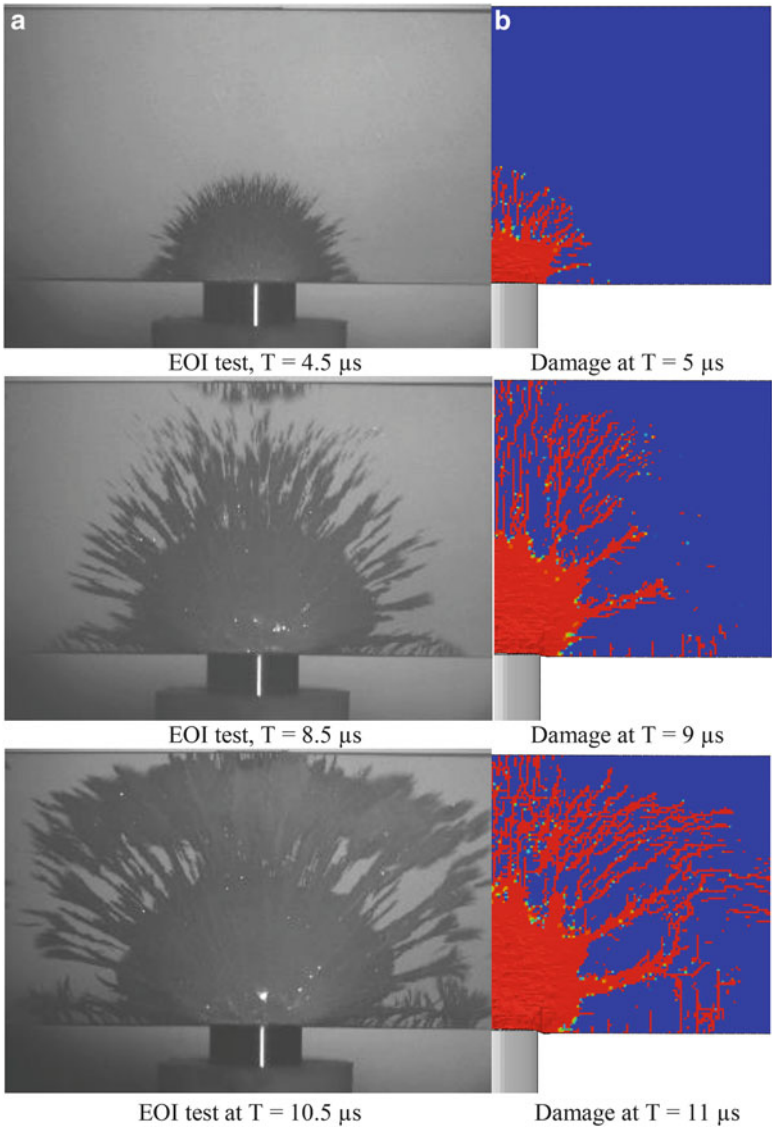

Fig. 2.3 Edge-on impact experiment performed at $V_{impact} = 60$ m/s. (**a**) Images of ultra-high speed camera. (**b**) Numerical simulation with DFH anisotropic damage model

addition "Rayleigh cracks" are initiated on the impacted edge ($T = 8.5$ µs) and propagate through the target with an inclined angle. The target is totally damage at $T = 10.5$ µs.

Numerical predictions of DFH (Denoual-Forquin-Hild) anisotropic damage model are given on the right hand-side of the Fig. 2.3. The calculation provides correct predictions of cracking density and crack extension at $T = 5$ µs and $T = 9$ µs. In particular the central zone corresponding to damage of high intensity is noted in the calculation. "Numerical cracks" (i.e. damage corridor) initiated on the impacted edge and on the rear edge are consistent with experimental observations. The final damage pattern ($T = 11$ µs) is also correctly predicted.

The next Figure (Fig. 2.4) concerns the EOI experiment performed with an impact velocity of 100 m/s. The damage front is composed of a large amount of radial cracks. The cracking density is significantly increased compared to the previous test (60 m/s). The target is totally damaged at $T = 9$ µs. The damage pattern is compared to numerical predictions on the same figure. A good agreement is noted in terms of cracking density, cracking orientation and velocity of damage front.

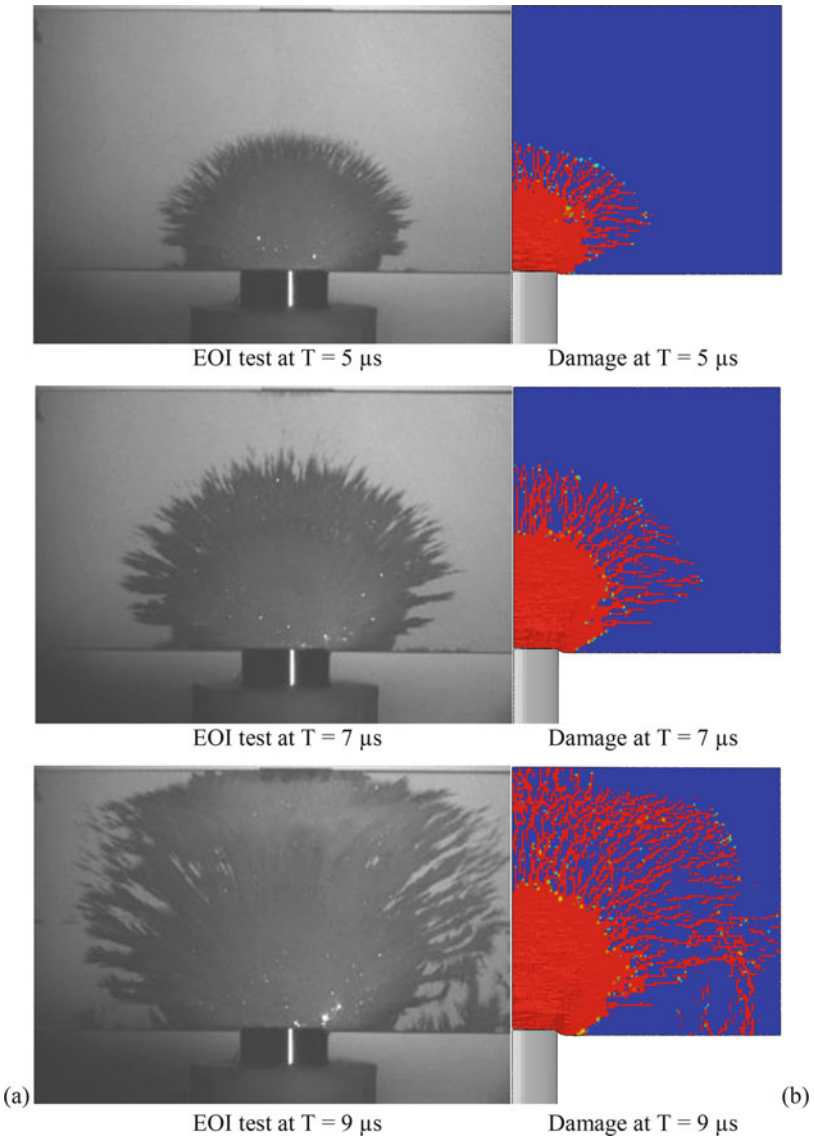

Fig. 2.4 Edge-on impact experiment performed at $V_{impact} = 100$ m/s. (**a**) Images of ultra-high speed camera. (**b**) Numerical simulation with DFH anisotropic damage model

The Fig. 2.5 presents the EOI experiment performed with an impact velocity of 175 m/s. The damage front is so strong that makes difficult to visualize each individual crack. Again cracking density is significantly increased compared to the tests conducted at lower impact velocities (60 and 100 m/s). The target is totally damaged at T = 9 µs. Again, the damage pattern is compared to numerical predictions on the same figure. Again a satisfactory agreement is noted in terms of damage front.

Influence of impact velocity on the intensity of damage is discussed in the last Figure. The Fig. 2.6 provides a comparison of damage pattern for three impact velocities (60, 100, 175 m/s). It is observed that DFH model enables to reproduce the increase of damage intensity with the increase of impact velocity.

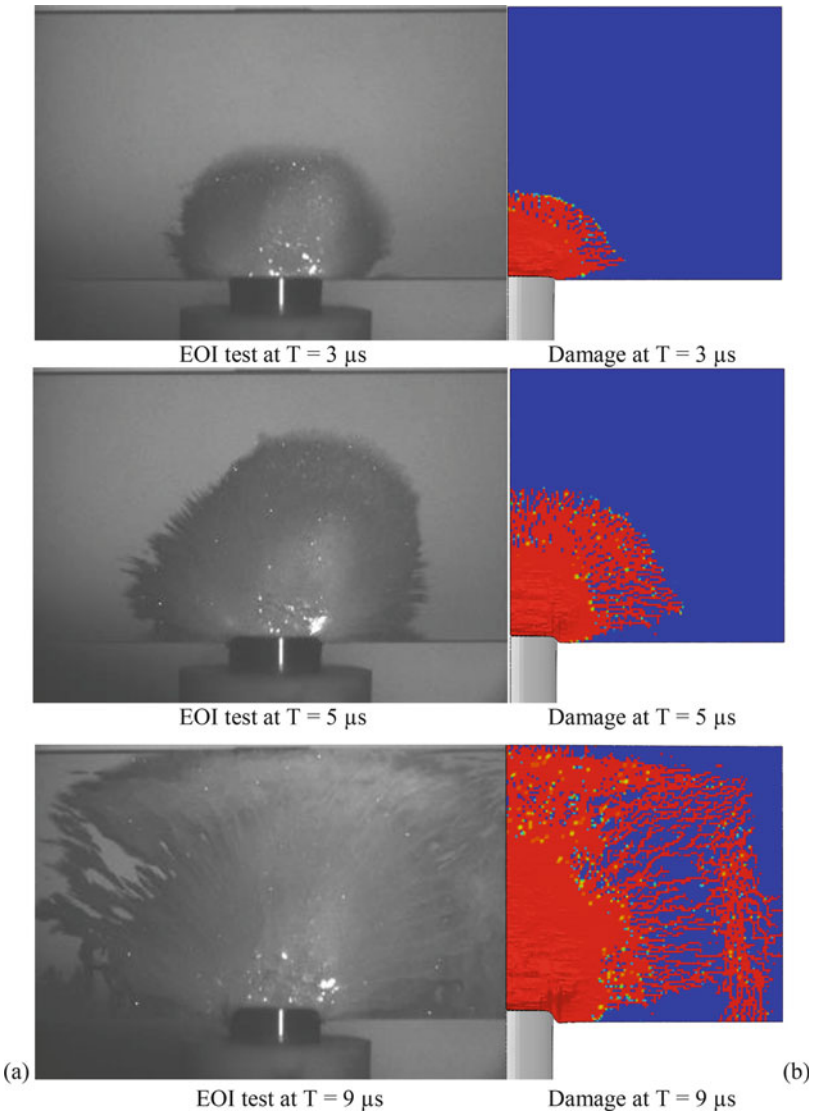

Fig. 2.5 Edge-on impact experiment performed at $V_{impact} = 175$ m/s. (**a**) Images of ultra-high speed camera. (**b**) Numerical simulation with DFH anisotropic damage model

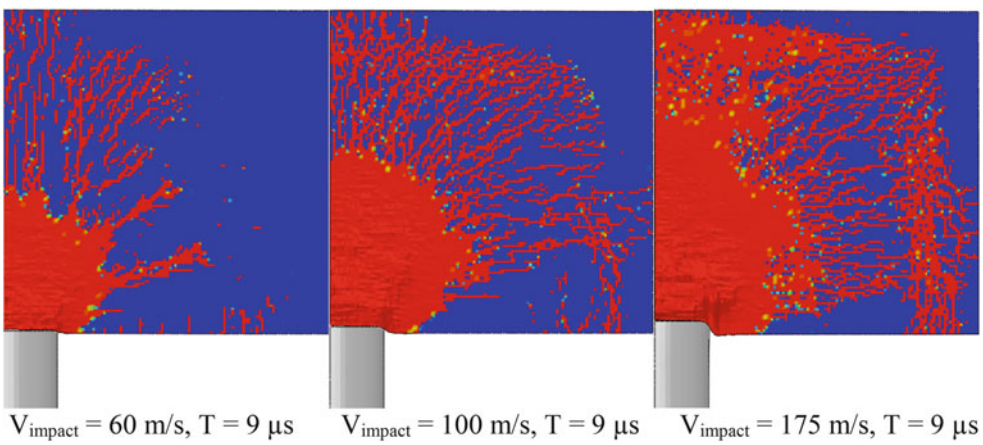

Fig. 2.6 Comparison of damage patterns predicted by DFH model considering three impact velocities

2.2 Conclusion

In the present work, edge-on impact tests have been performed with a transparent ZnS ceramic. A hemispherical end cap projectile hits the target at an impact velocity ranging from 60 to 175 m/s. The growth of damage in the target is visualized with an ultra-high speed camera. A fragmentation process made of a large number of oriented cracks develops in the target. The fragmentation pattern is composed of radial cracks induced by high-strain-rate tensile hoop stresses, cracks initiated on the rear face due to "release waves", cracks triggered at the impacted edge or at the lateral edges.

Numerical simulations have been performed with Abaqus-explicite finite-element code. The fragmentation of the target is model by means of the DFH (Denoual-Forquin-Hild) anisotropic damage model. Based on the concept of obscuration this model provides a micromechanical description of crack initiation, crack propagation and obscuration of critical defects due to crack previously triggered. The parameters used in the model (elastic parameter, Weibull parameters) have been identified from quasi-static experiments. The model enables predicting the damage in the target and the propagation of the damage front as function of time. As observed in experiments, the numerical calculation reproduces the increase of damage intensity and velocity of damage front with the impact velocity of the projectile.

References

1. Riou, P., Denoual, C., Cottenot, C.E.: Visualization of the damage evolution in impacted silicon carbide ceramics. Int. J. Impact Eng. **21**(4), 225–235 (1998)
2. Denoual, C., Hild, F.: A damage model for the dynamic fragmentation of brittle solids. Comp. Math. Appl. Mech. Eng. **183**, 247–258 (2000)
3. Forquin, P., Hild, F.: Dynamic fragmentation of an ultra-high strength concrete during edge-on impact tests. ASCE J. Eng. Mech. **134**(4), 302–315 (2008)
4. Zinszner, J.-L., Forquin, P., Rossiquet, G.: Experimental and numerical analysis of the dynamic fragmentation in a SiC ceramic under impact. Int. J. Impact Eng. **76**, 9–19 (2015)
5. Forquin, P., Erzar, B.: Dynamic fragmentation process in concrete under impact and spalling tests. Int. J. Fracture **163**, 193–215 (2010)
6. Grange, S., Forquin, P., Mencacci, S., Hild, F.: On the dynamic fragmentation of two limestones using edge-on impact tests. Int. J. Impact Eng. **35**, 977–991 (2008)
7. Erzar, B., Forquin, P.: Experiments and mesoscopic modelling of dynamic testing of concrete. Mech. Mater. **43**, 505–527 (2011)
8. Forquin, P., Hild, F.: A probabilistic damage model of the dynamic fragmentation process in brittle materials. Adv. Appl. Mech. **44**, 1–72 (2010)
9. Kanninen, M.F., Popelar, C.H.: Advanced Fracture Mechanics. Oxford University Press, Oxford (1985)
10. Denoual, C., Hild, F.: Dynamic fragmentation of brittle solids: a multi-scale model. Eur. J. Mech. A Solids **21**(1), 105–120 (2002)
11. Forquin, P., Tran, L., Louvigné, P.-F., Rota, L., Hild, F.: Effect of aluminum reinforcement on the dynamic fragmentation of SiC ceramics. Int. J. Impact Eng. **28**, 1061–1076 (2003)
12. Brajer, X., Forquin, P., Gy, R., Hild, F.: The role of the surface and volume for the fracture of glass under quasi-static and dynamic loadings. J. Non Cryst. Solids **316**, 42–53 (2003)

Chapter 3
Effects of Chain Extender on Dynamic Properties of PLLA/PBSL Blends

Masahiro Nishida, Yuma Takeuchi, Shun Furuya, Tetsuo Takayama, and Mitsugu Todo

Abstract The effects of the additive amount of a chain extender, with a weight ratio of 3–5 %, on stress-strain curves of poly(lactic acid) (PCL) and poly(butylene succinate-co-L-lactate) (PBSL) polymer blends were examined with a mixing ratio of PLA to PBSL of 70/30. The additive increased the elongation at break, and the strain rate decreased elongation at break.

Keywords Bioplastics • Strain rate • Tensile split Hopkinson pressure bar method • Polymer alloy • Crosslinking agent

3.1 Introduction

Biodegradable plastics and bioplastics are being investigated extensively, and new biodegradable plastics and bioplastics continue to be developed. Poly(lactic acid) (PLA) is a typical biodegradable bioplastic. Many studies have been conducted to develop various industrial products that can be manufactured using biodegradable plastics and bioplastics. However, such applications are currently limited to machine parts that are not subjected to high loading. Because PLA is brittle, its mechanical properties have been improved by polymer blends or natural-fiber reinforcement [1–3]. Because poly(butylene succinate-co-lactate) (PBSL) is a ductile and biodegradable polymer, PLA/PBSL polymer blends have great potential for high strength and toughness [4–7]. In order to increase their compatibility, a chain extender, Joncryl (ADR4370S, BASF), was added.

In this study, we examined the effects of different amounts of the chain extender (crosslinking agent) additive, 3–5 %, on dynamic and static tensile properties, with a mixing ratio of PLA to PBSL of 70/30, using a tensile split Hopkinson bar method and a universal testing machine. After dynamic and static tensile tests, the fracture surfaces of the specimens were observed.

3.2 Experimental Methods

3.2.1 Materials

Polymer blends of PLA and PBSL were prepared using PLA pellet from Nature Works Co. (Ingeo, 3100D) and PBSL pellet from Mitsubishi Chemical Co. (GS Pla® AZ91T). Because PBSL is ductile, there are many possibilities for high mechanical properties (for example, high impact strength) in polymer blends with PLA. Figure 3.1 illustrates the chemical structural formula of PLA and PBSL.

The mixing ratio (mass fraction) of PLA to PBSL was fixed at 70/30. During melt mixing, the chain extender (BASF, Joncryl ADR 4370-S) of the weight ratio of 3, 4, or 5 % was added. After melt mixing in a conventional melt mixer at 190 °C for 20 min, the blend mixtures were press processed using a conventional hot press at 190 °C and 30 MPa for 30 min.

M. Nishida (✉) • Y. Takeuchi • S. Furuya
Department of Mechanical Engineering, Nagoya Institute of Technology, Gokiso-cho, Showa-ku, Nagoya, Aichi 466-8555, Japan
e-mail: nishida.masahiro@nitech.ac.jp

T. Takayama
Graduate School of Science and Engineering, Yamagata University, 4-3-16 Jonan, Yonezawa, Yamagata 992-8510, Japan

M. Todo
Research Institute for Applied Mechanics, Kyushu University, 6-1 Kasuga-koen, Kasuga, Fukuoka 816-8580, Japan

B. Song et al. (eds.), *Dynamic Behavior of Materials, Volume 1*,
Conference Proceedings of the Society for Experimental Mechanics Series, DOI 10.1007/978-3-319-22452-7_3

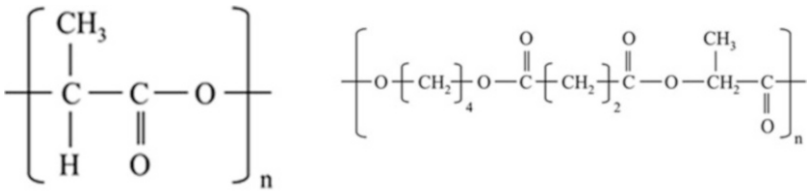

Fig. 3.1 Chemical structural formula. (**a**) PLA. (**b**) PBSL

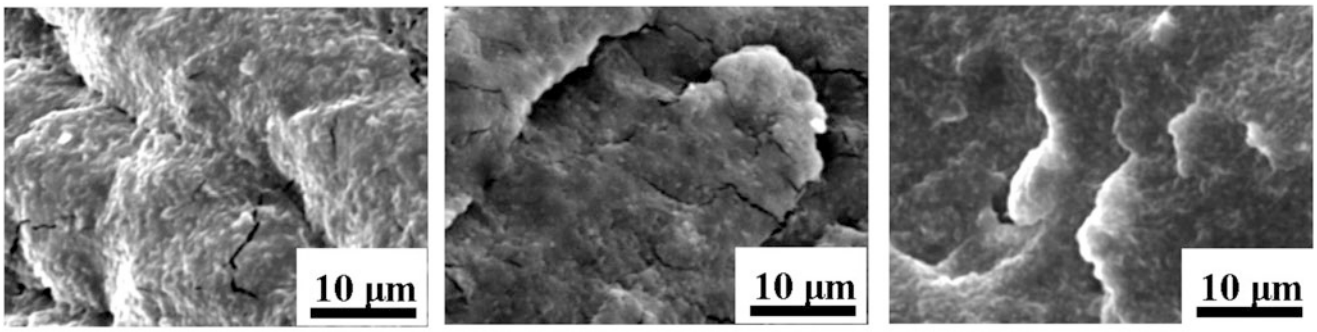

Fig. 3.2 SEM photographs before tensile tests. (**a**) Joncryl = 3 wt%. (**b**) Joncryl = 4 wt%. (**c**) Joncryl = 5 wt%

Fig. 3.3 Photograph of tensile test specimens. (**a**) Static tensile test (gauge area 2 mm by 5 mm, gauge length 10 mm). (**b**) Dynamic tensile test (gauge area 2 mm by 5 mm, gauge length 4 mm)

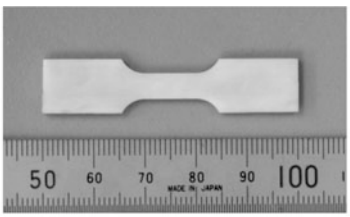

(a) Static tensile test (gauge area 2mm by 5mm, gauge length 10 mm)

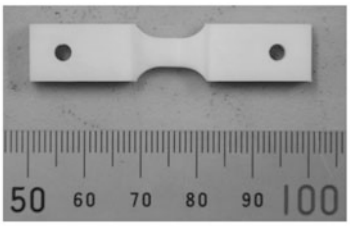

(b) Dynamic tensile test (gauge area 2mm by 5mm, gauge length 4 mm)

Photographs of the cryo-fractured surfaces, taken using a scanning electron microscope (SEM), are shown in Fig. 3.2. Clear two-phase structures were not observed by a scanning electron microscope when the chain extender was added. The chain extender improved the compatibility of PLA and PBSL.

3.2.2 Static Tensile Tests

Quasi-static tensile tests were conducted at a crosshead speed of 0.2 mm/min (strain rate of 0.9×10^{-4} to 2.2×10^{-4} s^{-1}) using a universal testing machine. The strain was calculated by images of the gauge area taken by digital camera. Dimensions of the specimens of static and dynamic tensile tests are shown in Fig. 3.3a.

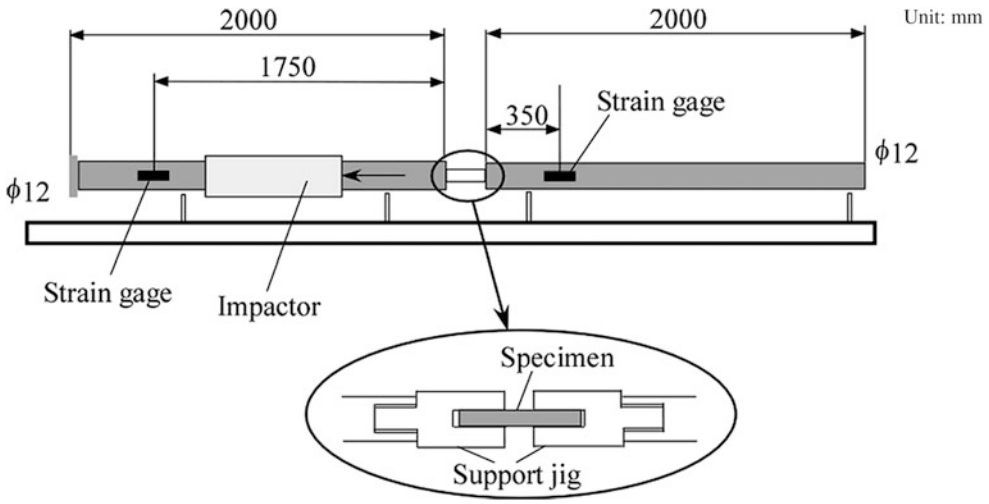

Fig. 3.4 Experimental setup for tensile Hopkinson bar (Kolsky bar) method

Table 3.1 Material constants of input and output bars used in calculations

	Density [kg/m^3]	Elastic wave velocity in bar, c_3 [m/s]	Young's modulus E [GPa]
Stainless steel, SUS304	8.0×10^3	4970	200

3.2.3 Dynamic Tensile Tests

At high strain rates, the dynamic properties of the specimens were examined by the tensile split Hopkinson bar test, as shown in Fig. 3.4. The diameters and lengths of input and output bars were 12 and 2000 mm respectively. Strain gages were applied to both sides of the input and output bars at distances of 1750 and 350 mm from the specimen, respectively. The stresses and strains of the specimens [8, 9] were calculated from the strains of the bars measured by strain gages, based on the following equations:

$$\sigma(t) = \frac{AE}{A_S}\varepsilon_T(t) \tag{3.1}$$

$$\varepsilon(t) = \frac{2c_3}{L}\int_0^t [\varepsilon_I(t) - \varepsilon_T(t)]\ dt \tag{3.2}$$

where ε_I and ε_T are the axial strains in the input bar induced by the incident wave and the axial strain in the output bar induced by the transmitted wave, respectively. E and c_3 are the Young's modulus and the elastic wave velocity of the input and output bars, respectively. L is the specimen's thickness. A and A_s are the cross-sectional areas of the input/output bars and the specimens. The input and output bars were made of stainless steel (SUS304), and their material constants used in the calculations are listed in Table 3.1. We preserved the specimens in a desiccator at a humidity of 30–40 % until just before use in order to avoid the effects of moisture absorption on the specimens. During the experiments, our laboratory was maintained at a temperature of 25 ± 2 °C and a humidity of 19–54 %. Dimensions of the specimens of dynamic tensile tests are shown in Fig. 3.3b.

3.3 Results and Discussion

The nominal stress-strain curves of the static tensile tests (Fig. 3.5) showed strain softening (work softening), which is defined as the reduction of stress with an increase in strain. When the additive was 5 %, the strain softening was not clear. The maximum stress with the 4 % additive was larger than those of 3 and 5 %. The elongation at break was almost the same among 3, 4 and 5 % additive ratios. At high strain rates, the stress-strain curves of the dynamic tensile tests (Fig. 3.6) did not show strain softening (work softening). The maximum stress and elongation at break were compared (Figs. 3.7 and 3.8);

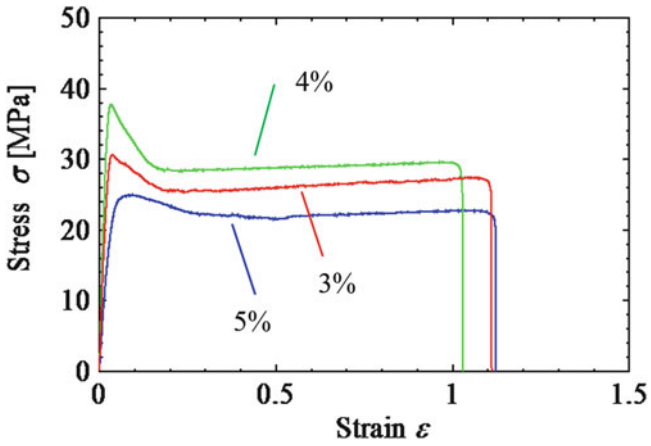

Fig. 3.5 Stress-strain curves of static tensile test

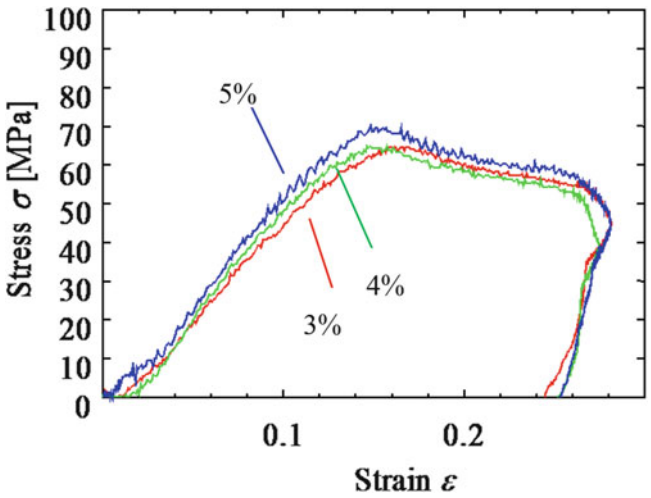

Fig. 3.6 Stress-strain curves of dynamic tensile test (850–1400 s^{-1})

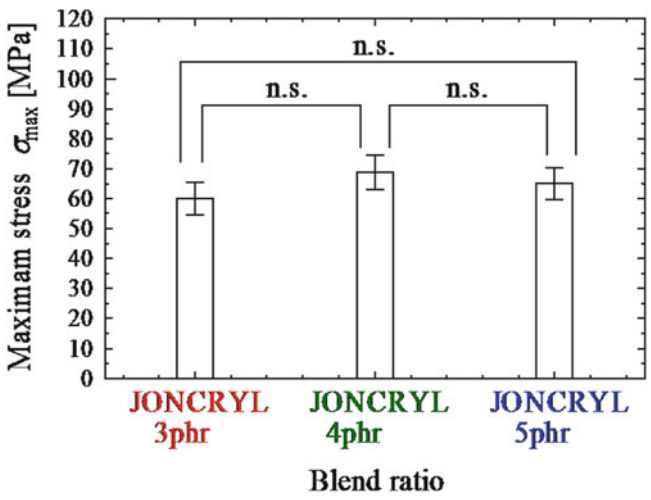

Fig. 3.7 Effects of mixing ratio on maximum stress

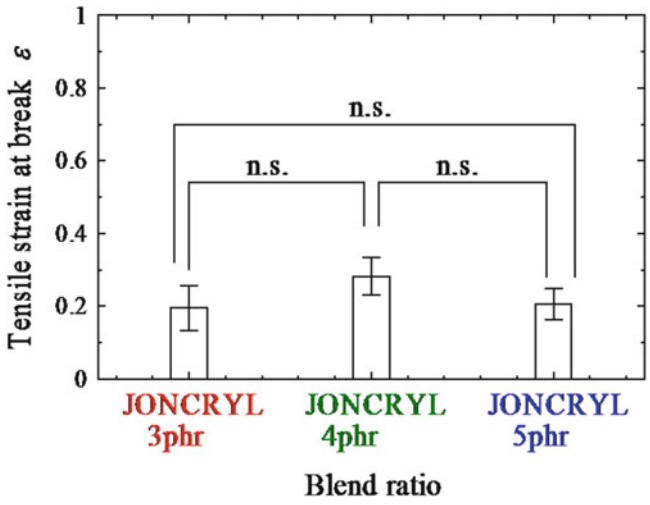

Fig. 3.8 Effects of mixing ratio on elongation at break

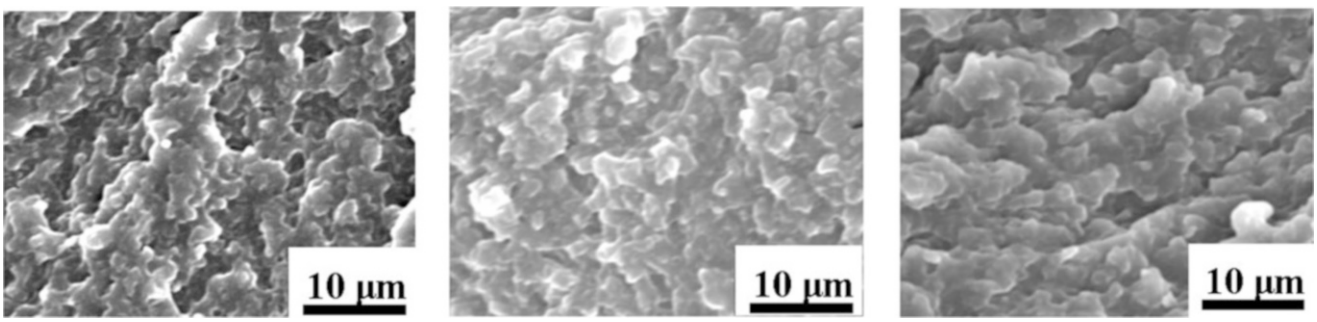

Fig. 3.9 Fracture surfaces of specimens at high strain rate

however, the comparisons showed no significant differences. Figure 3.9 shows SEM photographs of the fracture surface. The fracture surface was flat, and no clear elongation was observed. It seems that the elongation of materials decreased at high strain rate.

3.4 Conclusions

Dynamic tensile properties of a bioplastic PLA/PLBS blends were investigated experimentally using a tensile split Hopkinson bar and a universal testing machine. The additive clearly increased elongation at break at low strain rate. However, the additive increased slightly elongation at break. At low strain rate, stress-strain curves showed strain softening.

Acknowledgment Dynamic tensile properties of bioplastic PLA/PLBS blends were investigated experimentally using a tensile split Hopkinson bar and a universal testing machine. At low strain rate, the additive clearly but only slightly increased elongation at break. At low strain rate, stress-strain curves showed strain softening.

References

1. Ikeda, E.: Enhancement of Degradation Rate of Plastics for Suppression of Environmental Pollution by Plastics Waste. J. Soc. Mater. Sci. Jpn. **46**(12), 1347–1354 (1997)
2. Tsukamoto, N., Maruyama, H., Nishida, N.: Biodegradable Plastic Gears. Trans. Jpn. Soc. Mech. Eng. A **60**(58), 4318–4324 (1994)

3. Nishimura, Y., Kato, K., Kobayashi, H.: Development of the Biodegradable String-type Contact Material, Aichi Industrial Technology Institute Report, vol. 1, pp. 242–245 (2002–2012)
4. Vilay, V., Todo, M., Takayama, T., Jaafar, M., Ahmad, Z., Pasomsouk, K.: Effect of lysine triisocyanate on the mode I fracture behavior of polymer blend of poly(L-lactic acid) and poly(butylene succinate-co-L-lactide). J. Mater. Sci. **44**(11), 3006–3009 (2009)
5. Vilay, V., Mariatti, M., Ahmad, Z., Todo, M., Pasomsouk, K.: Effect of Copolymer on the Mechanical and Thermal Properties and Morphological Behavior of Biodegradable Poly (L-lactic acid) (PLLA) and Poly (Butylene Succinate-co-L-Lactate) (PBSL) Blends. Polymer. Adv. Tech. **22**, 1786–1793 (2011)
6. Kuno, S., Nishida, M., Kawashima, I., Takayama, T., Todo, M.: Dynamic Property Evaluation of PLLA/PBSL Polymer Blends using Compressive and Tensile Split Hopkinson Bar Methods. J. JSEM **12**(Special Issue), s198–s204 (2012)
7. Takeuchi, Y., Nishida, M., Takayama, T., Todo, M.: Effect of chain extender on impact properties of poly (lactic acid) and poly (butylene succinate-co-L-lactate) blends. Proceedings 4th Asian Conference on Mechanics of Functional Materials and Structures, pp. 283–284 (2014)
8. Gray III, G.T.: Classic split Hopkinson pressure bar testing. In: ASM Handbook, vol. 8, Mechanical Testing and Evaluation, pp. 462–476. ASM, Materials Park (2000)
9. Chen, W., Song, B.: Split Hopkinson (Kolsky) Bar: Design, Testing and Applications. Springer, New York (2010)

Chapter 4
Observation and Modeling of Cone Cracks in Ceramics

Brady Aydelotte and Brian Schuster

Abstract Ceramics undergo a complex failure process when subjected to impact by a projectile. Projectile impacts on thick ceramic targets produce varying levels of comminution, cone cracking, and radial cracking. Sphere impacts result in limited penetration and comminution relative to projectiles with a longer aspect ratio, yet significant radial and cone cracking is produced, and it is similar to Hertzian indentation. Sphere impact is a good way to study ceramics and a good validation problem to study the ability of hydrocodes to predict the formation and extent of radial and cone fractures in ceramic materials. Experimental results from normal and oblique sphere impacts on hot-pressed boron carbide cylinders are reported. Oblique sphere impacts created curved cone cracks, which did not appear oriented perpendicular to the impact surface. Cone angles appear to be the same for normal and oblique impacts for the impact conditions tested. Hydrocode predictions captured some but not all of the experimentally observed features.

Keywords Cone crack • Impact • Indentation • Ceramic • Damage

4.1 Introduction

Damage due to normal impact on ceramics has received considerable attention (see for example [1–6]). Evidently less effort has been directed towards the study of damage resulting from oblique impacts, particularly how it differs from damage resulting from normal impacts on armor grade ceramics. The terminology used in this paper to discuss different types of damage in a ceramic target from projectile impact is shown in Fig. 4.1. We could not find any published literature on oblique impact of ceramics, though there do exist some sliding indentation studies on polycrystalline ceramic materials [7–9]. Some work has also been done on oxide glasses [10–12].

In order to address this deficiency and further the study of the mechanical behavior of ceramics, we conducted impact experiments to explore the effects of oblique impacts on ceramics. We compared the cone cracking induced by normal and oblique impacts from tungsten carbide spheres on hot-pressed boron carbide (PAD B_4C) targets.

4.2 Experimental Setup

PAD B_4C cylinders 38.1 mm (1.5 in) diameter × 25.4 mm (1.0 in) length were procured from BAE Advanced Ceramics which is now owned by Coorstek. Some properties for PAD B_4C are listed in Table 4.1 for the reader's benefit.

The ceramic cylinders were impacted with 6.35 mm diameter (0.25 in) tungsten carbide-6 % cobalt (WC) spheres. Impact experiments were conducted at three different obliquities: 0°, 30°, and 60° from horizontal. Foam target holders were machined to orient the ceramic cylinders with an accuracy of plus or minus one degree. The spheres were fired out of a 0.30 caliber smooth-bore laboratory powder gun using plastic, two-piece, discarding sabots. WC projectile velocities were limited to between 200 and 500 m/s with emphasis on 300, 350, and 400 m/s impact velocities. The experimental setup is diagrammed in Fig. 4.2.

Two orthogonal pairs of 150 kV flash X-rays were used to determine projectile velocity. Additional 150 kV flash X-rays were used to capture late time (>100 μs post impact) images of fractures within the B_4C targets. The targets were recovered for future analysis. All angles were measured using FIJI [14] with repeated measurements to assess error.

B. Aydelotte (✉) • B. Schuster
US Army Research Laboratory, RDRL-WML-H321 Colleran Road, Aberdeen Proving Ground, MD 21005, USA
e-mail: brady.b.aydelotte.civ@mail.mil

B. Song et al. (eds.), *Dynamic Behavior of Materials, Volume 1*,
Conference Proceedings of the Society for Experimental Mechanics Series, DOI 10.1007/978-3-319-22452-7_4

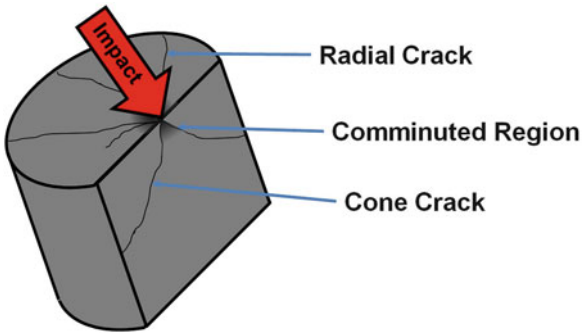

Fig. 4.1 Schematic of the damage produced by projectile impact on a thick cylindrical ceramic target showing our terminology for cone cracks, radial cracks, and a comminuted region. Comminution is the process of microcrack formation and intersection that converts a brittle solid into a granular material

Table 4.1 Selected mechanical properties of hot-pressed (PAD) B_4C from Vargas-Gonzalez et al. [13]

Density	Elastic modulus	Knoop hardness (HK2)	Fracture toughness
2.50 kg/m^3	445.5 GPa	2019 $\pm$ 60 kg/mm^2	2.90 $\pm$ 0.4 MPa$\sqrt{m}$

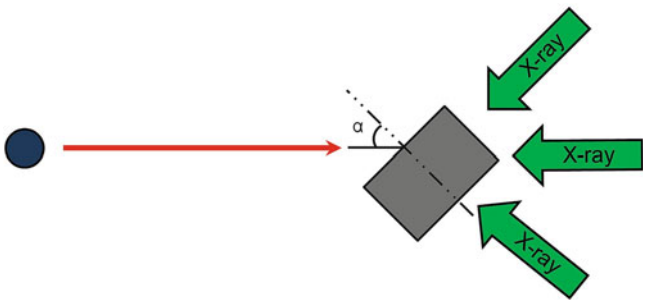

Fig. 4.2 Schematic of the impact experiments showing the obliquity measurement

4.3 Experimental Results and Analysis

Some selected results of the sphere impacts are shown in Fig. 4.3 for roughly three different velocities: 300, 350, and 400 m/s. There was considerable velocity scatter because it was difficult to hit low velocities with our current laboratory gun setup.

Cone cracks which form as a result of normal impacts are axisymmetric (unless the impact is off-center). Near the impact surface, the cone angle is constant. Away from the impact surface near the cylindrical sides of the target, the cone crack curves out to be normal to the sides of the cylinder. This is evident in Fig. 4.3a, d, g and is consistent with the PAD B_4C images published by LaSalvia et al. [4].

Cone cracks which form as a result of oblique impacts have concave down curvature on the leading edge and concave up curvature on the trailing edge. This behavior is evident in the oblique impacts in Fig. 4.3, and it is also shown schematically in Fig. 4.4. The curvature of cone cracks due to oblique impacts was also observed by Chaudhri and Liangyi [10] in soda-lime glass. We believe this is a result of cone crack surfaces locally reorienting themselves due to the spatially and temporally varying stress field from the projectile and/or debris sliding along the surface, changing the location of the maximum pressure. Chaudhri and Liangyi [10] also concluded that the movement of the point of contact was the cause of the curved cone cracks they observed in soda-lime glass. There may also be some effect from applying a shear load to the surface, though Chaudhri and Liangyi [10] didn't believe this effect was significant.

LaSalvia et al. [4] reported sphere impacts on PAD B_4C at 103, 209, and 312 m/s. The cone angles for the cone cracks in the targets impacted at 103 and 209 m/s measured 102°$\pm$ 2° and 82°$\pm$ 2° respectively. The outer cone of the PAD B_4C target impacted at 312 m/s measured 89°$\pm$ 2°, and the inner cone measured 31°$\pm$ 2°. The cone crack angles for the normal impacts reported in this work measured 78°$\pm$ 3°, 80°$\pm$ 3°, and 86°$\pm$ 3° for impacts at 284, 363, and 415 m/s respectively. This somewhat consistent with measurements of LaSalvia et al. [4] cone crack angles for impacts at 209 and 312 m/s.

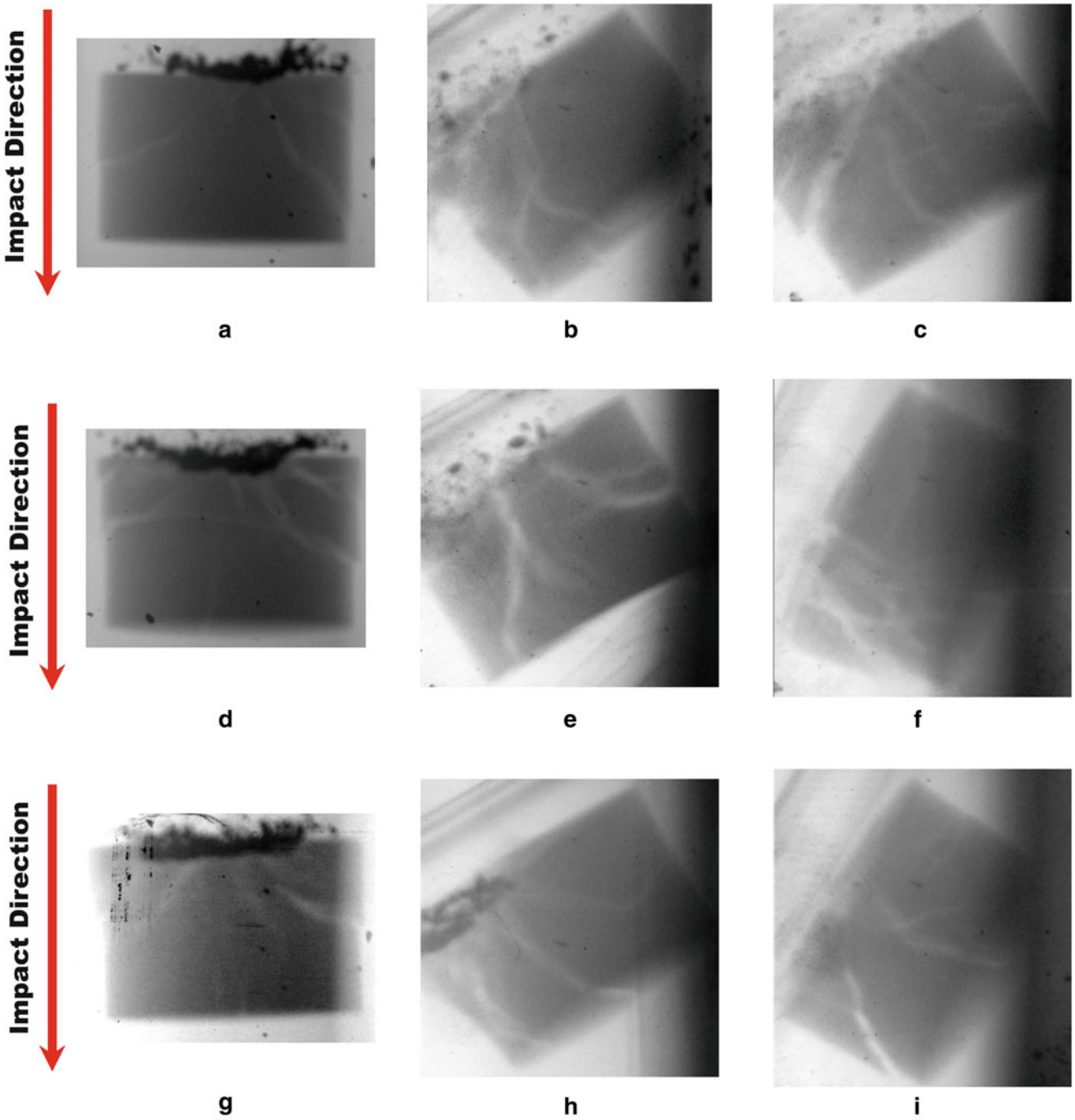

Fig. 4.3 Collected results of normal and oblique sphere impacts. Note that (**c**) is a 30° obliquity target. No 60° obliquity X-rays were captured around 300 m/s impact velocity. (**a**) V_{imp}: 284 m/s Obliquity: 0° Cone Angle: 78 ± 3°, (**b**) V_{imp}: 291 m/s Obliquity: 30° Cone Angle:? (**c**) V_{imp}: 310 m/s Obliquity: 30° Cone Angle: 78 ± 3°, (**d**) V_{imp}: 363 m/s Obliquity: 0° Cone Angle: 80 ± 3°, (**e**) V_{imp}: 392 m/s Obliquity: 30° Cone Angle: 82 ± 4°, (**f**) V_{imp}: 404 m/s Obliquity: 60° Cone Angle:?, (**g**) V_{imp}: 415 m/s Obliquity: 0° Cone Angle: 86 ± 3°, (**h**) V_{imp}: 431 m/s Obliquity: 30° Cone Angle: 75 ± 5°, (**i**) V_{imp}: 422 m/s Obliquity: 60° Cone Angle: 73 ± 5°

The oblique impacts which had measurable cone angles are shown in Fig. 4.3c,e,h,i. All had cone angles close to those measured for the normal impacts and roughly similar to those measured from the images in LaSalvia et al. [4]. Cone angle doesn't appear to be altered by target obliquity.

Nested cone cracks are commonly observed in impacts on ceramic targets with sufficient velocity. Most of the target X-rays in Fig. 4.3 show evidence of nested cone cracks; Nested cone cracks resulting from oblique impacts also tend to show

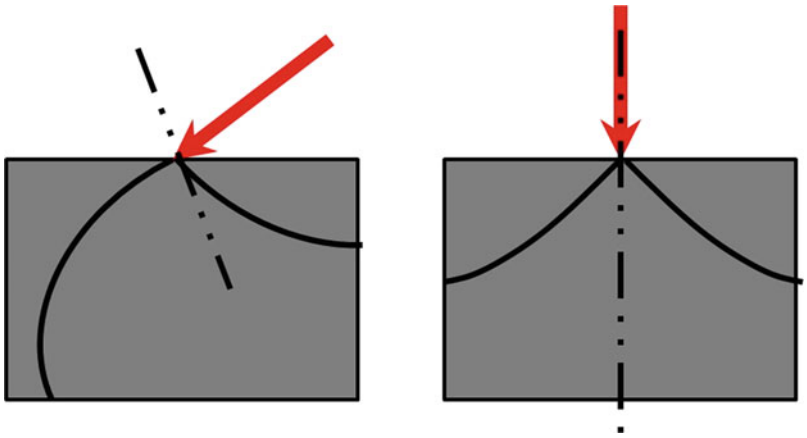

Fig. 4.4 Difference in cone orientation and shape for an oblique and normal impact respectively on a cylindrical ceramic target

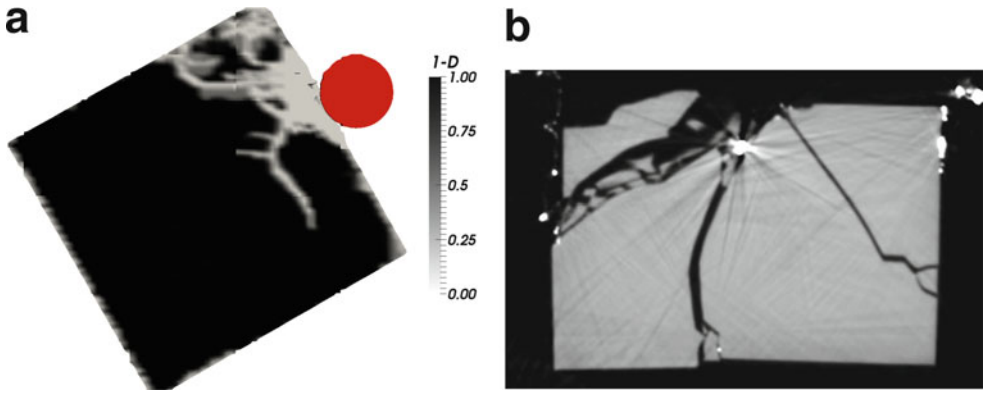

Fig. 4.5 (**a**) Simulated tungsten carbide sphere striking a B_4C cylinder target at an obliquity of 60°, 20 μs post-impact. Damaged ceramic appears white and undamaged ceramic appears black. The trailing portion of the cone crack is convex up and is similar to that seen in experiments. (**b**) Image produced by X-ray computerized tomography (CT) of a recovered target impacted at 310 m/s (also shown in Fig 4.3c). Note that the top of the cone crack is near the surface of the target, rather than a large region of comminuted material. The bright spots are tungsten carbide fragments which are embedded in the ceramic or in the foam target holder. The lines emanating from the tungsten carbide fragments are image artifacts from the tungsten carbide blocking X-rays inside the CT scanner as it revolved around the sample.

the curvature typical of oblique impacts. Figure 4.3e shows an interesting case where the outer cone crack is roughly symmetric, measuring 82°± 4° and the inner cone crack shows the concave down leading edge and the concave up trailing edge. The inner cone crack measures 46°± 3°.

4.4 Numerical Modeling

Preliminary efforts were made to model the sphere impact problems to gain greater insight into the evolution of damage and the development of cone cracks. A tungsten carbide sphere striking a boron carbide target at 300 m/s was modeling using the ALEGRA hydrocode [15]. The tungsten carbide sphere was modeled as elastic. Boron carbide was modeled with the KAYENTA geomaterial model [16].

The model accurately predicted the formation of the convex up region of the trailing end of the cone crack seen in Fig. 4.5a. The model didn't correctly predict the convex down region of the leading edge of the cone crack and it over-predicted the size of fully damaged regions underneath the sphere as seen in Fig. 4.5a,b. The differences between the model prediction and the impacted targets suggest that under the projectile, high hydrostatic compression results in very high strength in the boron carbide. This implies that our parameterization of the KAYENTA model could be reasonably adjusted to allow for higher strength at high pressure. This will be the subject of further investigation.

4.5 Conclusions

Sphere impacts on oblique ceramic targets have received no attention. Oblique impacts of this sort are similar to the classical Hertzian contact problem, but have the additional feature of some shear load applied on the surface as well as a changing center of maximum applied load. These additional features lead to substantial differences in the shape of the resulting cone cracks, but no apparent change in cone crack angle close to the impact surface. Hydrocode modeling of the impact was able to predict some of the features observed in experiments, the concave up trailing edge of the cone crack, but not the concave down leading edge of the cone crack.

Acknowledgements The authors acknowledge the helpful comments of Brian Leavy (ARL) and his assistance with the KAYENTA material model for boron carbide, Debjoy Mallick, and the ALEGRA development team at Sandia National Laboratory. We also acknowledge Cyle Teal (ARL) for his work on the 10 flash X-ray system, the laboratory technicians at ARL for assisting in these experiments, and the Department of Defense High Performance Computing Modernization Program for a grant of processing time.

References

1. Wilkins, M.L.: Mechanics of penetration and perforation. Spec. Issue: Penetration Mech. **16**(11), 793–807 (1978)
2. Shockey, D.A., Marchand, A., Skaggs, S., Cort, G., Burkett, M., Parker, R.: Failure phenomenology of confined ceramic targets and impacting rods. Int. J. Impact Eng. **9**(3), 263–275 (1990)
3. LaSalvia, J.C., Normandia, M.J., Miller, H.T., Mackenzie, D.E.: Sphere impact induced damage in ceramics: I. Armor-Grade SiC and TiB2. In: Advances in Ceramic Armor: A Collection of Papers Presented at the 29th International Conference on Advanced Ceramics and Composites, January 23–28, 2005, Cocoa Beach, Florida. Ceramic Engineering and Science Proceedings, pp. 170–181. Wiley, Hoboken, NJ, USA, (2005)
4. LaSalvia, J.C., Normandia, M.J., Miller, H.T., Mackenzie, D.E.: Sphere impact induced damage in ceramics: II. Armor-Grade B4c and WC. In: Advances in Ceramic Armor: A Collection of Papers Presented at the 29th International Conference on Advanced Ceramics and Composites, January 23–28, 2005, Cocoa Beach, Florida. Ceramic Engineering and Science Proceedings, pp. 183–192. Wiley (2005) Hoboken, NJ, USA
5. LaSalvia, J.C., Normandia, M.J., MacKenzie, D.E., Miller, H.T.: Sphere impact induced damage in ceramics: III. Analysis. In: Advances in Ceramic Armor: A Collection of Papers Presented at the 29th International Conference on Advanced Ceramics and Composites, January 23–28, 2005, Cocoa Beach, Florida. Ceramic Engineering and Science Proceedings, pp. 193–202. Wiley (2005) Hoboken, NJ, USA
6. LaSalvia, J., Leavy, R., Houskamp, J., Miller, H., MacKenzie, D., Campbell, J.: Ballistic impact damage observations in a hot-pressed boron carbide. In: Advances in Ceramic Armor V: Ceramic Engineering and Science Proceedings Volume 30, Issue 5, 2009, vol. 30, pp. 45–55. Wiley (2009)
7. Chiang, S.-S., Evans, A.G.: Influence of a tangential force on the fracture of two contacting elastic bodies. J. Am. Ceram. Soc. **66**(1), 4–10 (1983)
8. Laugier, M.: The surface fracture of alumina under a sliding spherical indenter. J. Mater. Sci. Lett. **5**(3), 253–254 (1986)
9. Ren, L., Zhang, Y.: Sliding contact fracture of dental ceramics: principles and validation. Acta Biomater. **10**, 3243–3253 (2014)
10. Chaudhri, M., Liangyi, C.: The orientation of the Hertzian cone crack in soda-lime glass formed by oblique dynamic and quasi-static loading with a hard sphere. J. Mater. Sci. **24**, 3441–3448 (1989)
11. Salman, A., Gorham, D., Verba, A.: A study of solid particle failure under normal and oblique impact. In: 8th International Conference on Erosion by Liquid and Solid Impact, vol. 186–187, Part 1, pp. 92–98 (1995)
12. Grant, P., Cantwell, W., McKenzie, H., Corkhill, P.: The damage threshold of laminated glass structures. Int. J. Impact Eng. **21**, 737–746 (1998)
13. Vargas-Gonzalez, L., Speyer, R.F., Campbell, J.: Flexural strength, fracture toughness, and hardness of silicon carbide and boron carbide armor ceramics. Int. J. Appl. Ceram. Technol. **7**(5), 643–651 (2010)
14. Schindelin, J., Arganda-Carreras, I., Frise, E., Kaynig, V., Longair, M., Pietzsch, T., Preibisch, S., Rueden, C., Saalfeld, S., Schmid, B., et al.: Fiji: an open-source platform for biological-image analysis. Nat. Methods **9**, 676–682 (2012)
15. Robinson, A.C., Carroll, S.K., Drake, R.R., Hansen, G.A., Hensinger, D.M., Kramer, R., Labreche, D.A., Love, E., Luchini, C.B., Mosso, S.J., et al.: ALEGRA User Manual. No. SAND2014-16031 (2014)
16. Brannon, R., Fossum, A., Strack, O.: Kayeta: Theory and User's Guide. No. SAND2009-2282 (2009)

Chapter 5
Dynamic Crack Propagation in Layered Transparent Materials Studied Using Digital Gradient Sensing Method: Part-II

Balamurugan M. Sundaram and Hareesh V. Tippur

Abstract Dynamic fracture behavior of bi-layered PMMA samples are studied using Digital Gradient Sensing (DGS) in conjunction with high-speed photography. DGS exploits elasto-optic effect exhibited by transparent solids subjected to a non-uniform state of stress causing deflection of light rays propagating through the material. The current work builds on authors' previous report concerning crack trapping, interfacial bifurcation, and mixed-mode penetration into the second layer when a dynamically growing mode-I crack in the first layer encounters a normally oriented interface of different strengths. The current work specifically focuses on the role of the interface location within the bi-layered specimen relative to the initial crack tip on fracture behavior with an intention of examining the effect of the incident crack speed and the associated stress intensity factors for select interfacial fracture toughness. The location of the interface is varied sequentially from 'near' to 'far' from the initial notch tip to accomplish this task. Preliminary results suggest that crack growth in both the interface and the second layer are greatly affected by the location of the interface. That is, the velocity and stress intensity factors of the incident crack affect the outcome of the overall fracture behavior of bi-layered samples including interfacial trapping and penetration into the second layer.

Keywords Digital gradient sensing • Transparent material • Layered material • Dynamic fracture • Crack path selection

5.1 Introduction

Optically transparent, impact resistant materials are used in various aerospace, automotive and military applications as windshields, protective canopy, face-shields, etc. In these applications, layered material architectures are routinely employed (e.g., safety or laminated glass). The ability of such materials to bear load and structurally survive impact loading is critical, especially when human lives and mission critical instruments are involved. Hence, it is essential that the mechanical failure characteristics of transparent materials and structures under impact loading conditions are well understood.

Many works reported in the literature focus on crack-interface interactions involving a growing crack and an inclined interface [1], resulting in a dominant penetrated crack in the subsequent layer following interfacial crack growth. Yet, relatively few reports exist on a more common and practical scenario of growing cracks interacting with normally oriented interfaces [2]. Accordingly, this work investigates the fracture response of an elastically homogeneous PMMA bi-layer with a discrete plane of weakness. The goal here is to study the fracture response when dynamically growing cracks of different velocity and stress intensity factor reach an interface oriented *perpendicularly* to the crack growth direction. The stress intensity factor evaluation is accomplished by using an optical technique called Digital Gradient Sensing in conjunction with high-speed photography. This study is a continuation of the previous work by the authors on the same material system/geometry with different interfacial fracture toughness. In this study the effect of the position of the layer within the geometry is studied. Of particular interest are dynamic crack deflection, bifurcation and penetration mechanisms across an interface located in the path of a dynamically propagating crack when the interface location is varied.

5.2 Digital Gradient Sensing

Full-field optical measurement techniques are preferable to point-wise methods in fracture and failure studies. In recent years, digital image correlation (DIC) has become increasingly popular as they require ordinary white light illumination, relatively simple optics, digital electronics and little/no surface preparation. With the introduction of ultrahigh-speed digital

B. M. Sundaram • H.V. Tippur (✉)
Department of Mechanical Engineering, Auburn University, Auburn, AL 36849, USA
e-mail: htippur@eng.auburn.edu

B. Song et al. (eds.), *Dynamic Behavior of Materials, Volume 1*,
Conference Proceedings of the Society for Experimental Mechanics Series, DOI 10.1007/978-3-319-22452-7_5

cameras, DIC has been extended to study transient problems [3] including dynamic fracture. In this context, a technique called Digital Gradient Sensing (DGS) [4] that employs 2D DIC for quantifying elasto-optic effects in transparent materials has been introduced. The optical measurements in this method represent two orthogonal in-plane stress gradients under plane stress conditions and offer several advantages for studying transparent materials.

In transmission-mode DGS [4] a speckle decoration on a planar surface, called the 'target', is photographed through a planar, optically transparent sheet under investigation. White light illumination is used for recording gray scales on the target. The speckle pattern is first photographed through the specimen in its undeformed state to record a reference image. Upon loading, the non-uniform stresses due to the applied loads change the local refractive index. Additionally, the Poisson effect produces a non-uniform thickness change. A combination of these, commonly known as the *elasto-optic effect*, cause the light rays to deviate from their initial path. The speckle pattern is once again photographed through the specimen in this deformed state. The local deviations of light rays can be quantified by correlating speckle images belonging to deformed and reference states to find displacement components. Under paraxial approximations, the angular deflections of light rays in two orthogonal planes (x-z and y-z planes with z-axis coinciding with the optical axis of the setup and x-y being the specimen plane coordinates) can be computed using these displacement components if the distance between the specimen plane and the target plane is known. A detailed analysis (see, [4]) suggests that the local angular deflections are related to the gradients of in-plane normal stresses as,

$$\phi_x = C_\sigma B[\partial(\sigma_x + \sigma_y)/\partial x], \phi_y = -C_\sigma B[\partial(\sigma_x + \sigma_y)/\partial y] \tag{5.1}$$

where C_σ is the elasto-optical constant of the material and B is its thickness.

5.3 Specimen Geometry and Preparation

The bi-layered specimens with interface normally oriented to the prospective crack growth direction were prepared by bonding two cast PMMA sheets using a commercially available acrylic adhesive to form a rectangular layered material system of approximate dimension $6'' \times 4''$ and thickness $\times$ $0.33''$. The interfacial fracture toughness of interface (100 μm thick) was [5] approximately 50 % of the virgin PMMA (~1.3 MPa$\sqrt{m}$). By varying the position of the interface with respect to the initial crack tip, various specimen configurations were obtained. Figure 5.1 shows the different specimen configurations used in this work.

The specimen preparation involved sanding the bond surfaces using 400 grit sand paper. The adhesive was applied to one of the two surfaces and both the surfaces were squeezed against each other using a bench-vise. A spacer of 100 μm thickness was placed between the two layers to control the interface thickness [5]. This was repeated for various interface positions. At least two specimens of each configuration were prepared to check experimental repeatability.

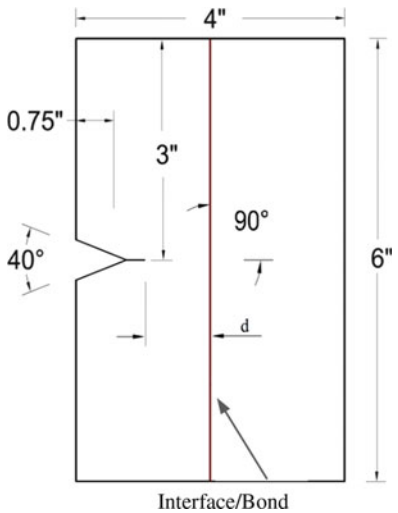

Fig. 5.1 Bi-layered material system with a normally oriented interface. The distance 'd' = 9 mm, 17 mm, 28 mm and 42 mm were used.

5.4 Experimental Details

The schematic of the experimental setup used for dynamic fracture tests is shown in Fig. 5.2. The setup included a 6 ft long, 1 in. diameter long-bar with a wedge shaped tip held against the unconstrained specimen with an identical wedge shaped notch and a 12 in. long, 1 in. diameter striker held inside the barrel of a gas-gun. Both the long-bar and the striker were of the same diameter and made of aluminum 7075 to eliminate the impedance mismatch between them. The striker was launched towards the long-bar using the gas-gun at a velocity of ~14 m/s. When the striker contacted the long-bar, a compressive stress wave propagated along the bar before transmission into the specimen in contact.

A target plate with random black and white speckles was placed behind the specimen at a fixed distance (~25 mm) to measure deformations using DGS. The speckle pattern was photographed through the specimen using a Cordin-550 ultrahigh-speed digital camera. It has 32 independent CCD image sensors positioned radially around a rotating mirror which sweeps image over these sensors. Prior to loading, a set of 32 reference images were recorded at a rate of ~200,000 frames per second at a resolution of 1000 × 1000 pixels per image. When the striker contacted the long-bar, a trigger signal initiated recording of a second set of 32 images at the same framing rate recording the fracture event.

Thus each reference image had a corresponding deformed image. The corresponding reference and deformed images from same sensor were paired. The paired sets of images were then correlated to obtain in-plane displacements before evaluating angular deflections of light rays at a 2-D array of spatial positions in the field of view.

5.5 Crack Path Selection

In Fig. 5.3a–d the 'V' notch is extended using a diamond impregnated blade to form the initial crack tip. The crack growth occurs from left to right in these photographs. There is a single crack initiated at the crack tip in layer-I which is predominantly mode-I in nature. In Fig. 5.3a it can be seen that when the interface at ~9 mm from the initial crack tip a

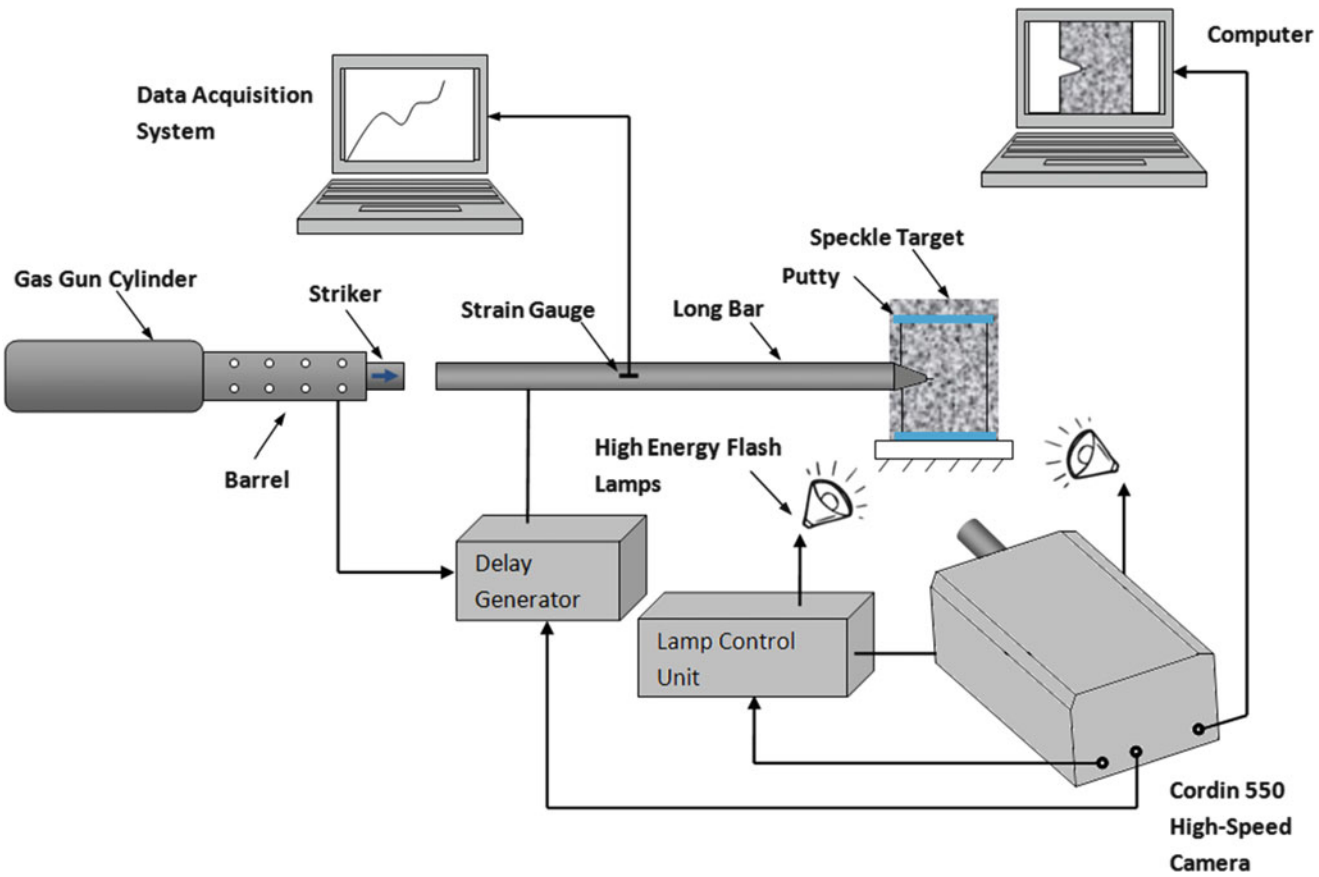

Fig. 5.2 Schematic of the experimental setup

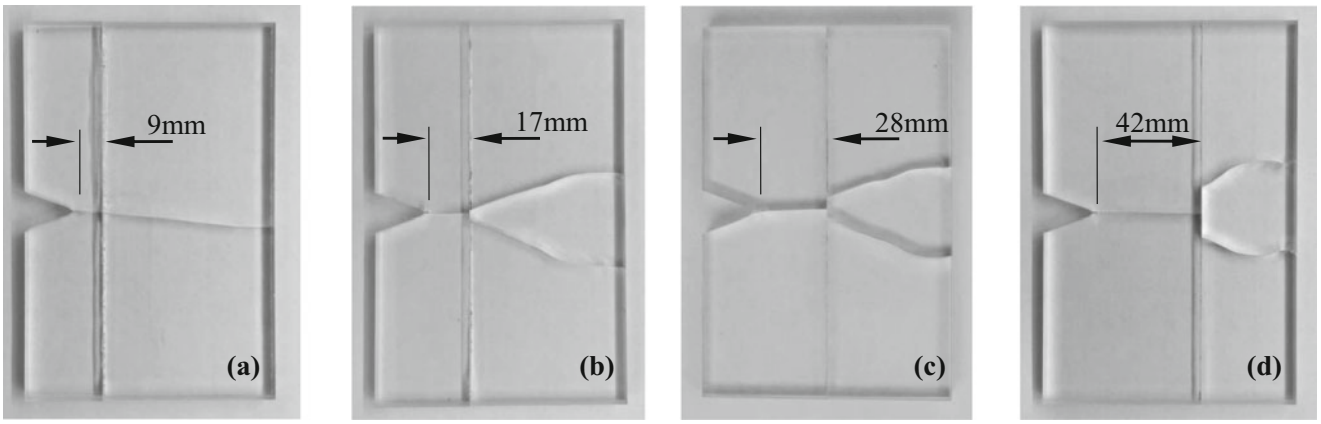

Fig. 5.3 Photographs of fractured specimens showing crack path (growth from *left* to *right*) selection upon interacting with a normal weak interface. The incident crack speed for different interface locations differ.

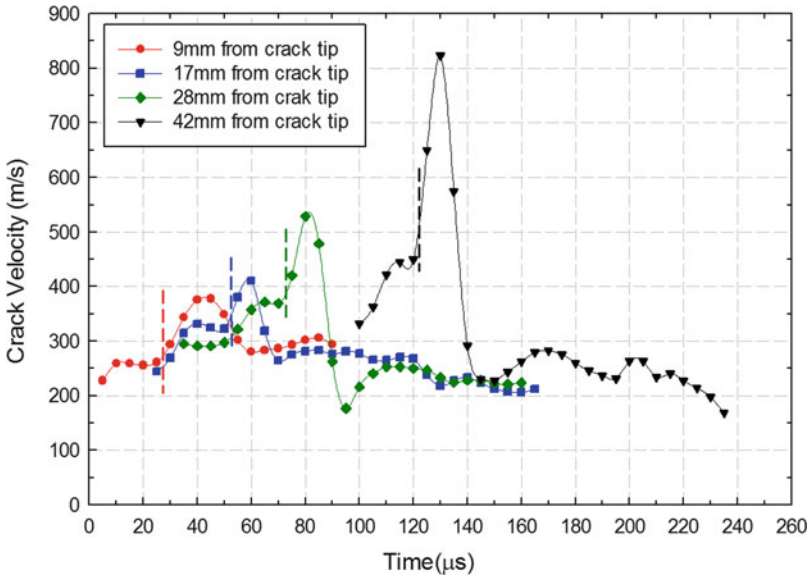

Fig. 5.4 Crack velocity histories for different interfacial locations in the samples. *Dotted vertical line* represent the approximate time at which the crack reaches the interface.

single crack emerges into the layer-II which is also predominantly mode-I type. On the other hand, in Fig. 5.3b–d two complex growth patterns involving crack bifurcation and interfacial crack growth followed by mixed-mode penetrated crack branches in layer-II can be seen. The two daughter cracks produced in layer-II travel symmetrically (relative to the specimen configuration) throughout their propagation. It can be seen that the distance travelled by the two daughter cracks in the interface were 2, 12, 22 mm for interface positions of 17, 28 and 42 mm, respectively. There is a clear evidence of increase in interfacial trapping/crack growth as the interface is located further away from the initial crack tip. There is also evidence of different crack angles at crack penetration into layer-II.

Figure 5.4 shows plots of crack velocity histories for all the four configurations. It can be seen that all the configurations show similar crack growth patterns in terms of velocity histories. In each configuration, the velocity when the crack impinges on the interface is different. There is a noticeable increase in the velocity when the crack approaches the interface. The increase in the distance of the interface from the initial notch also produces an increase incident velocity. From this, one could infer that the velocity of the crack when it impinges on the interface is a key factor in the subsequent interfacial bifurcation, and penetration/branching mechanisms observed. It should also be noted that the final crack velocity observed in layer-II in case of farthest interface (42 mm) from the initial crack tip is the lowest (~160 m/s) compared to the other configurations (~300 m/s for the 9 mm case). Furthermore, the crack speed reached by the bifurcated cracks within the

interface also attain higher values when the interface is situated farther away from the initial notch tip or the incident crack velocity is higher (>800 m/s vs. <400 m/s in the 42 mm vs. 9 mm cases, respectively). This is a rather counterintuitive observation that needs further investigation.

5.6 Optical Measurements

The recorded reference and deformed images were correlated using ARAMIS™ to obtain contours of constant angular deflections near a propagating crack tip. The details are avoided here for brevity. The resulting contours in Figs. 5.5 and 5.6 represent the angular deflections of light rays in various configurations(42mm and 9mm respectively) and represent the

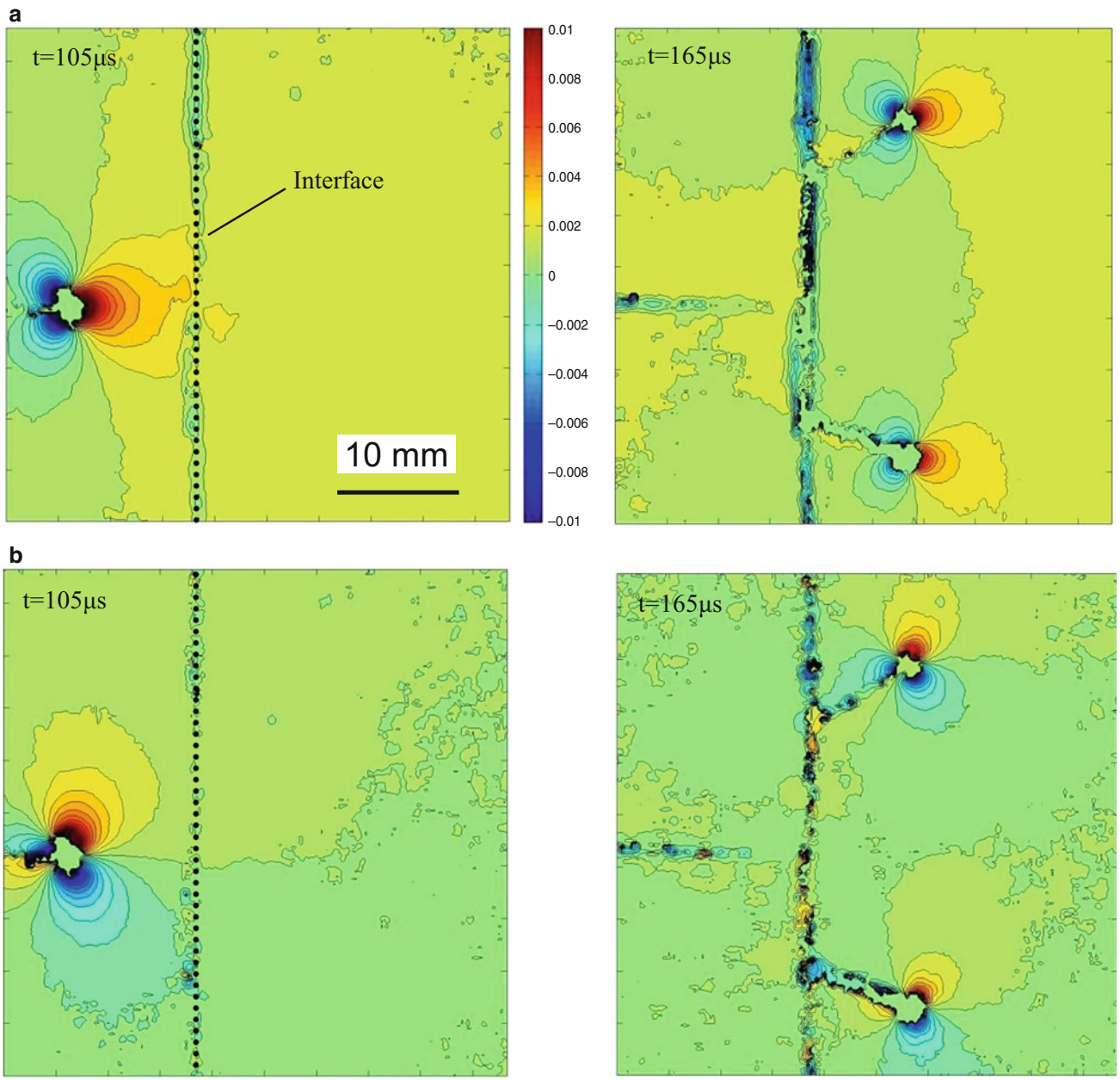

Fig. 5.5 Angular deflection contour plots proportional to stress-gradients in the *x*- and *y*-directions for an interface at 42 mm from initial crack tip. (**a**) ϕ_x contour. (**b**) ϕ_y contours

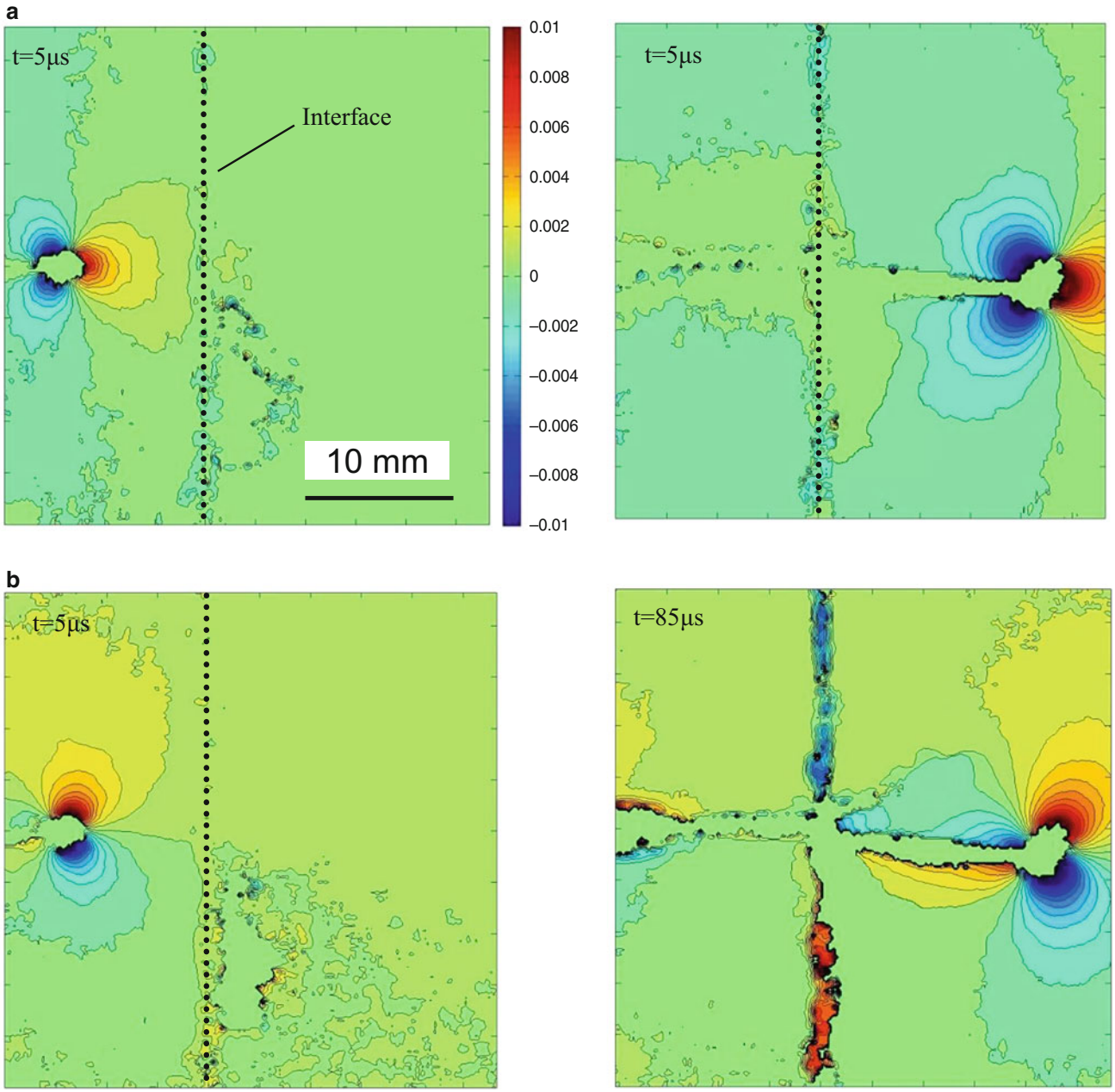

Fig. 5.6 Angular deflection contour plots proportional to stress-gradients in the *x*- and *y*-directions for an interface at 9 mm from the initial crack tip. (**a**) $\boldsymbol{\phi_x}$ contours (**b**) $\boldsymbol{\phi_y}$ contours

stress gradients [5] in two mutually perpendicular directions. Here only few representative plots for a few select cases are shown and $t = 0$ μs represents the time at which the crack initiates. The vertical dotted line represents the interface. In case of specimen with interface at 42 mm from crack tip (See, Fig. 5.5), two symmetrically propagating daughter cracks can be observed in second layer, whereas, for specimen with interface at 9 mm from crack tip (See, Fig. 5.6), a single crack is observed in the second layer.

5.7 Work-in-Progress

The equation for obtaining stress intensity factors form the measured data were formulated during the previous study on dynamic crack propagation reported in [3, 5]. The authors intend to evaluate the SIF histories for all the configurations to establish an empirical relationship between the observed crack growth mechanisms across the interface.

5.8 Conclusion

The results indicate that the position of the layer within a PMMA based bi-layer system can alter the crack growth morphology along the interface and in the second layer of an elastically homogeneous bi-layered brittle solid with a plane of weakness oriented normal to the initial crack growth direction. If the interface is positioned very close to the initial crack tip, a crack growth pattern involving single crack is observed in the second layer. Whereas, if the layer is positioned farther away from the initial crack tip, a pattern involving multiple daughter cracks occurs in layer-II. The factors affecting these dramatically different fracture patterns are incident crack velocity and stress intensity factor when impingement on the interface occurs. Further study on investigating these in detail is currently underway.

Acknowledgment The authors would like to thank the U.S. Army Research Office for supporting this research through grant W911NF-08-1-0285.

References

1. Xu, L.R., Huang, Y.Y., Rosakis, A.J.: Dynamic crack deflection and penetration at interfaces in homogeneous materials: experimental studies and model predictions. J. Mech. Phys. Solid. **51**(2003), 461–486 (2003)
2. Park, H., Chen, W.: Experimental investigation on dynamic crack propagating perpendicular through interface in glass. J. App. Mech. **78**(5) (2011)
3. Kirugulige, M.S., Tippur, H.V.: Measurement of surface deformations and fracture parameters for a mixed-mode crack driven by stress waves using image correlation technique and high-speed photography. Strain **45**(2), 108–122 (2009)
4. Periasamy, C., Tippur, H.V.: A full-field digital gradient sensing method for evaluating stress gradients in transparent solids. Appl. Optics **51**(12), 2088–2097 (2012)
5. Sundaram, B.M., Tippur, H.V.: Dynamic crack propagation in layered transparent materials studied using digital gradient sensing method. In: Proceedings of 2014 SEM Annual Conference, Greenville, SC (2014)
6. Periasamy, C., Tippur, H.V.: Measurement of crack-tip and punch-tip transient deformations and stress intensity factors using digital gradient sensing technique. Eng. Fract. Mech. **98**, 185–199 (2013)

Chapter 6
Measurement of the Dynamic Fracture Toughness of Alumina Ceramic

Pengwan Chen, Jingjing Chen, Baoqiao Guo, and Haibo Liu

Abstract In this study, the dynamic fracture toughness of the alumina ceramic at various loading rates was measured by using three test methods. A split Hopkinson pressure bar was used to apply dynamic loading. The three-point bending (TPB) test with a pre-crack and semi-circular bending (SCB) test with a pre-crack, and the flattened Brazilian disc (FBD) test without a pre-crack were used to measure the dynamic fracture toughness of alumina ceramic. The dynamic fracture toughness of alumina ceramic obtained by the three methods were compared and analyzed. The results by the three methods show a good consistency. The dynamic fracture toughness of alumina ceramic exhibits an obvious rate dependence upon the loading rate. Considering easy preparation of FBD specimens without fabricating a pre-crack, FBD test is recommended as an alternative method for measuring the dynamic fracture toughness of brittle materials.

Keywords Dynamic fracture toughness • Alumina ceramic • Three-point bending test • Semi-circular bending test • Flattened Brazilian disc test

6.1 Introduction

Due to its high strength and hardness, high temperature resistance and low cost, alumina ceramics are widely used in a large range of applications such as armor systems, aerospace industry. In these cases, the ceramic materials inevitably subjected to dynamic loading, its dynamic mechanical properties consequently become the criterion. The ceramics are typical brittle materials, of which the tensile strength is much lower than the compressive strength. As well-known, the direct tensile test is difficult to perform on the brittle materials due to the difficulty in sample preparation. It's also hard to measure the dynamic fracture toughness of ceramic materials.

Because of the simplicity of the sample preparation and the experiment process, the Brazilian test has become a standard method and widely used in measuring the dynamic tensile strength of brittle materials such as rock, concrete and ceramic [1–3]. As the most common dynamic impact loading device, the split Hopkinson pressure bar (SHPB) is widely used in mechanical study of brittle material [4–6]. Wang *et al*. [8] measured dynamic tensile strength of a brittle rock using FBD test, but the time to equilibrium and pattern of stress distribution for different FBD specimen was given by finite element analysis.

The dynamic fracture toughness plays an important role in mechanical properties of alumina ceramics. Samborski presented the experimental results of static and dynamic fracture toughness of alumina, and analyzed the influence of porosity fraction on fracture toughness [9]. However, the loading rate effect on the fracture toughness was not investigated. Xia *et al*. studied the loading rate dependence of fracture toughness on rock [10] and PMMA [11]. Based on the standard Brazilian test, Wang *et al*. [12, 13] proposed the FBD test, by which the indirect tensile strength and the fracture toughness of brittle materials could be determined. Zhou *et al*. [14] studied the static fracture toughness of a polymer-bonded explosive simulant using the TPB, SCB and FBD test, but did not given the dynamic consequence.

In this study, the dynamic fracture toughness of the alumina ceramic was experimentally investigated by using a SHPB apparatus. The dynamic fracture toughness at different loading rates was measured by three test methods: the TPB test, the SCB test and the FBD test. The results were analyzed and the test method for testing dynamic properties of brittle materials was discussed.

P. Chen (✉) • J. Chen • B. Guo • H. Liu
State Key Laboratory of Explosion Science and Technology, Beijing Institute of Technology, Beijing 100081, China
e-mail: pwchen@bit.edu.cn

B. Song et al. (eds.), *Dynamic Behavior of Materials, Volume 1*,
Conference Proceedings of the Society for Experimental Mechanics Series, DOI 10.1007/978-3-319-22452-7_6

6.2 Sample Preparation and Experimental Setup

The samples made of fine alumina ceramics powder, were prepared by cold compression molding and then sintered under very high temperature. The relative density is about 94.3 %. The diameter and thickness of disc-like samples are Φ40 × 16 mm. The FBD and SCB specimens were machined from the original disc specimens. The diameters of those two specimens are the same with the original disc specimen. The flat angel of the flat Brazilian disc is 30°.

In this work, a SHPB system was used as the dynamic loading device. The samples were placed between the incident bar and the transmitted bar. The incident, reflected and transmitted pulses from the strain gages attached on the bars, were recorded by the dynamic strain indicator. The SHPB apparatus with three different samples was shown in Fig. 6.1.

6.3 TPB Test

The three-point bending test is common method to determine the fracture toughness of metal materials. The fracture toughness K_{IC} of the long rectangular specimen with a pre-crack can be determined by:

$$K_{IC} = \frac{P_q \cdot S}{B \cdot W^{3/2}} f\left(\frac{a}{W}\right) \tag{6.1}$$

$$f\left(\frac{a}{W}\right) = \frac{3x^{1/2}[1.99 - 2.15x(1-x) - 3.93x + 2.7x^2]}{2(1+x)(1-x)^{3/2}}, \quad x = \frac{a}{W} \tag{6.2}$$

where $B \times W \times S$ are the thickness, height and the length between the two supports, a is the length of pre-crack, and Pq is the failure load. In the current study, the dimension of the three-point bending specimen is $B \times W \times S = 5$ mm $\times$ 10 mm $\times$ 30 mm, and the length of pre-crack is 2 mm (Fig. 6.2).

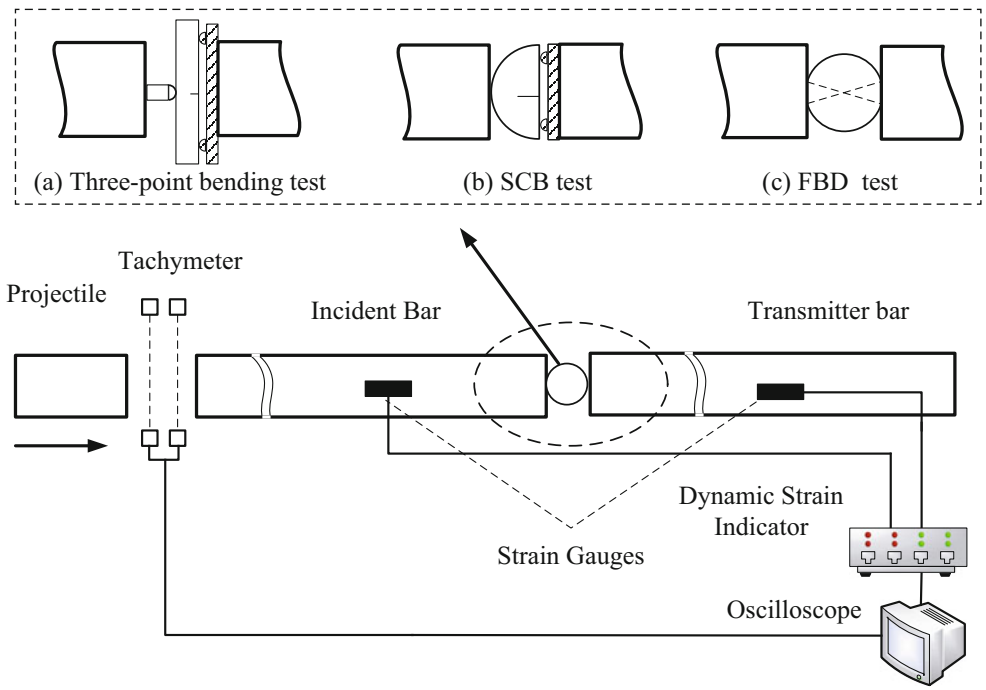

Fig. 6.1 Schematic of the experimental setup

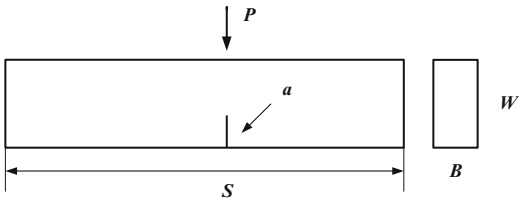

Fig. 6.2 Schematic of TPB test

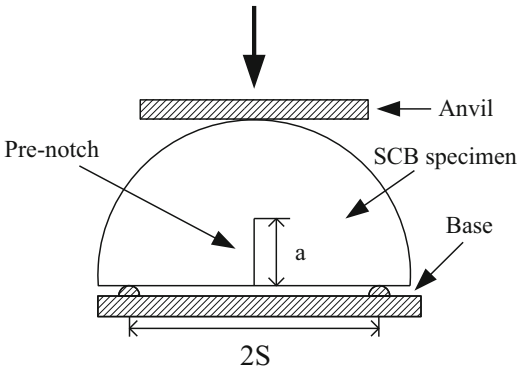

Fig. 6.3 Schematic of SCB test

6.4 SCB Test

Proposed by Chong and Kuruppu [15], the dynamic fracture toughness of brittle materials such as rock was studied by the semi-circular bending (SCB) test. Compare to the three point bending test, the SCB sample is compact. That's great advantage for sample preparation and also the dynamic test with SHPB device. As shown in Fig. 6.6, the SCB sample with a pre-fabricated crack is supported by two brackets, and the load is applied in the middle of sample. The fracture toughness of SCB can be determined by

$$K_{IC} = \frac{P_Q\sqrt{\pi a}}{DB} Y_K \tag{6.3}$$

$$Y_K = 4.47 + 7.4\frac{a}{D} - 106\left(\frac{a}{D}\right)^2 + 433.3\left(\frac{a}{D}\right)^3 \tag{6.4}$$

where P_Q is critical damage load; D is the diameter of specimen; B is the thickness of specimen; α is the pre-fabricated crack length, Y_K is a function of α/D and $2S$ is the bending span. Equations (6.3) and (6.4) are valid only when the conditions are satisfied: $0.25 \leq \alpha/D \leq 0.35$ and $2S/D = 0.8$. The pre-fabricated crack length of the SCB specimen is 12 mm.

6.5 FBD Test

In standard Brazilian test, the stress concentration on the loading points may cause the pre-crack. As an alternative, Wang *et al*. [17] proposed the FBD test. As shown in Fig. 6.3, two parallel planes are processed as the loading surface. The load is applied on the flat planes. Both the tensile strength and fracture toughness can be achieved by this proposed test. According to Griffith's strength theory, the crack initiates in the center of the FBD sample in condition that the loading angle $2\alpha \geq 20°$, which is the critical prerequisite for the validation of the tensile strength and the fracture toughness. The tensile strength of FBD sample is expressed as:

$$\sigma_t = k\frac{2P_t}{\pi DB} \tag{6.5}$$

The fracture toughness of FBD sample can be obtained by

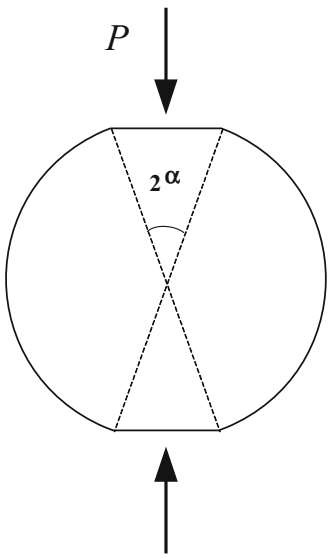

Fig. 6.4 Schematic of FBD test

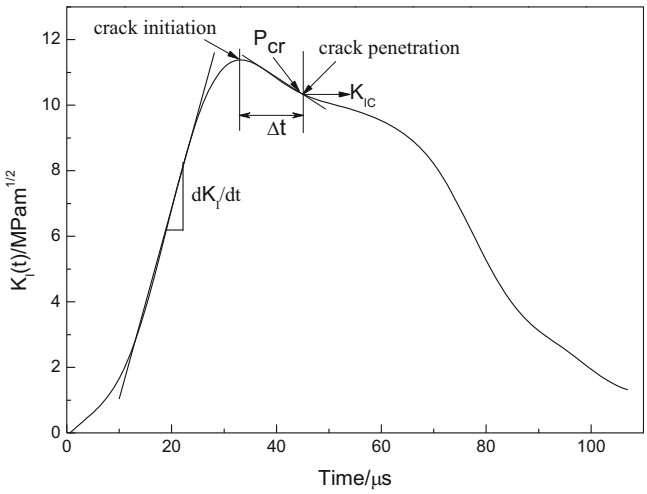

Fig. 6.5 Typical stress intensity factor curve of FBD test

$$K_{IC} = \frac{P_{cr}}{B\sqrt{D/2}}\Phi \tag{6.6}$$

where P_{cr} is on the local inflection point after the failure load P_t, k and Φ are two coefficients relevant to load angle. From the finite element analysis on the FBD sample by Wang *et al.* [12], the crack initiates in the sample center when the flat angel is under the condition $20° \leq 2\alpha \leq 30°$. Two coefficients k and Φ can also be achieved by from the numerical analysis. In this study, the loading angel is $2\alpha = 30°$, so $k = 0.9205$, $\Phi = 0.5895$ (Fig. 6.4).

6.6 Results and Analysis

As presented in the precedent section, the FBD test not only can achieve the strength, but also can provide the fracture toughness. Furthermore, the sample is compact and it's not necessary to fabricate the pre-crack. It's a big advantage in sample preparation for brittle material. The curve of stress intensity factor $K_I(t)$ can be obtained according to the Eq. (6.6), as shown in Fig. 6.5. After the collision and compaction process at initial contact, the stress intensity factor KI(t) curve changes over time with the load increases. There is a linear phase before the peak in the $K_I(t)$ curve, the slope of the linear phase is the

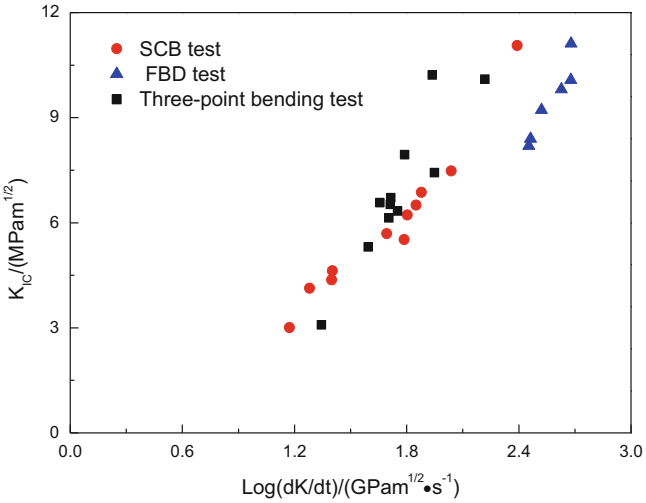

Fig. 6.6 Dynamic fracture toughness in function of strain rate by three test methods

dynamic loading rate dK_I/dt. Because the section of circular samples along the loading direction is not constant, the loading rate instead of the strain rate is presented in this study. The damage occurs when the load reaches the maximum; the cracks appeared in the center of the disc, and growth with the loading increase. And the crack went throughout the disc only when the load down decreased to local inflection load. Therefore, P_{cr} at inflection point represents the load of fracture toughness.

Based on the previous analysis, the crack initiate at the maximum load, and crack penetrate at the local minimum load P_{cr}. The time interval (Δt in Fig. 6.5) between the maximum load and P_{cr} can be determined. As the radius of the disc is known, the crack propagation velocity of alumina ceramic can be determined in the FBD test. The velocity is determined about 2317 $\pm$ 198 m/s.

For the SCB test with the pre-fabricated crack, the fracture toughness of alumina ceramics can be calculate with relevant parameters according to Eqs. (6.5) and (6.6). The dynamic loading rate calculation method of SCB test is the same with the FBD test. The relationship between fracture toughness of alumina ceramics with two densities measured by TPB test, FBD test and SCB test and loading rate is shown in Fig. 6.6. The fracture toughness measured by three methods are increased with the loading rate, and the three methods have good consistency. The loading rate dependence of alumina ceramics fracture toughness is presented by Kishi [16], it is consistent with the result of in this work. The effectiveness of FBD test to measure fracture toughness of the brittle material was verified by comparing those three methods. The FBD test has certain advantages in the aspect of toughness measurement for brittle material fracture because of sample preparation is simple and it does not need to prefabricate crack in the sample.

6.7 Conclusion

In this study, we made a comparative study of the dynamic fracture toughness of alumina ceramic by three test methods: the TPB test, the SCB test and the FBD test. The dynamic fracture toughness of alumina ceramic exhibits an obvious rate dependence upon the loading rate. The result shows the reliability of the three methods to determine the dynamic fracture toughness of brittle materials. However the FBD specimens are not necessary to fabricate a pre-crack. In addition, the FBD test can also measure the dynamic tensile strength. Considering these advantage, the FBD test is recommended as an alternative method for measuring the dynamic fracture toughness of brittle materials.

References

1. Johnstone, C., Ruiz, C.: Dynamic testing of ceramics under tensile stress. Int. J. Solid. Struct. **32**(17/18), 2647–2656 (1995)
2. Zhao, J., Li, H.B.: Experimental determination of dynamic tensile properties of a granite. Int. J. Rock Mech. Min. Sci. **37**(5), 861–866 (2000)
3. Rafael, J., Proveti, C., Michot, G.: The Brazilian test: a tool for measuring the toughness of a material and its brittle to ductile transition. Int. J. Fract. **139**, 455–460 (2006)
4. Zhu, J., Hu, S., Wang, L.: An analysis of stress uniformity for concrete-like specimens during SHPB tests. Int. J. Impact Eng. **36**, 61–72 (2009)
5. Wang, S., Liu, K.X.: Experimental research on dynamic mechanical properties of PZT ceramic under hydrostatic pressure. Mater. Sci. Eng. A **528**, 6463–6468 (2011)

6. Chang, H., Binner, J., Higginson, R., Myers, P., Webb, P., King, G.: High strain rate characteristics of 3-3 metal-ceramic interpenetrating composites. Mater. Sci. Eng. A **528**, 2239–2245 (2011)
7. Dong, S., Xia, K., Huang, S., Yin, T.: Rate dependence of the tensile and flexural strengths of glass-ceramic Macor. J. Mater. Sci. **46**, 394–399 (2011)
8. Wang, Q.Z., Li, W., Xie, H.P.: Dynamic split tensile test of flattened Brazilian disc of rock with SHPB setup. Mech. Mater. **41**, 252–260 (2009)
9. Samborski, S., Sadowskiw, T.: Dynamic fracture toughness of porous ceramics. J. Am. Ceram. Soc. **93**(11), 3607–3609 (2010)
10. Dai, F., Xia, K., Zheng, H., Wang, Y.X.: Determination of dynamic rock Mode-I fracture parameters using cracked chevron notched semi-circular bend specimen. Eng. Fract. Mech. **68**, 2633–2644 (2011)
11. Huang, S., Luo, S., Xia, K.: Dynamic fracture initiation toughness and propagation toughness of PMMA. In: Proceedings of the SEM Annual Conference, Albuquerque, 1–4 June 2009
12. Wang, Q.Z., Xing, L.: Determination of fracture toughness KIC by using the flattened Brazilian disk specimen for rocks. Eng. Fract. Mech. **64**, 193–201 (1999)
13. Wang, Q.Z., Jia, X.M., Kou, S.Q., et al.: The flattened Brazilian disc specimen used for testing elastic modulus, tensile strength and fracture toughness of brittle rocks: analytical and numerical results. Int. J. Rock Mech. Min. Sci. **41**, 245–253 (2004)
14. Zhou, Z., Chen, P., Duan, Z., Huang, F.: Comparative study of the fracture toughness determination of a polymer-bonded explosive simulant. Eng. Fract. Mech. **68**, 2991–2997 (2011)
15. Chong, K.P., Kuruppu, M.D.: New specimen for fracture toughness determination for rock and other materials. Int. J. Fract. **26**, 59–62 (1984)
16. Kishi, T.: Dynamic fracture toughness in ceramics and ceramics matrix composites. Eng. Fract. Mech. **40**(415), 785–790 (1991)

Chapter 7
Shock and High Strain Rate Characterization of HTPB with Varying Plasticizer

Jennifer Jordan, Didier Montaigne, Christopher Neel, George Sunny, and Christopher Molek

Abstract Hydroxyl-terminated polybutadiene (HTPB) has long been used as a binder in propellants and explosives. However, cured HTPB rubbery polyurethanes have not been characterized in a systematic fashion as function of plasticizer content. In this study, three isocyanate-cured HTPB variants with different amounts of plasticizer have been formulated. The materials were characterized using quasi-static and dynamic compression experiments. Additionally, the shock Hugoniot was measured on the two extremes of the material—no plasticizer and maximum plasticizer.

Keywords Hydroxyl-terminated polybutadiene • HTPB • Polyurethane • High strain rate • Shock

7.1 Introduction

Hydroxyl-terminated polybutadiene (HTPB) resin is used as the basis of a family of rubbery polyurethanes with varying amounts of plasticizer and curing agent, which results in materials with varying glass transition temperature. This results in materials that vary from rigid to highly flexible at room temperature. These materials are used in such applications as adhesives, elastomeric wheels and tires, and binders for rocket propellants and explosives.

HTPB is a crosslinked elastomer, containing the main, crosslinked network (gel) and the material not attached to the network (sol). The addition of plasticizer to the system results in a change in the way the network forms, not just density of crosslinks.

Several studies have investigated the quasi-static mechanical properties as a function of composition [1–7]. The mechanical properties of HTPB can be modified by the choice of isocyanate and chain extenders [2, 6], and the degree of crosslinking strongly correlates with strength [4, 5]. There have been a few studies in the literature investigating the high strain rate properties of HTPB [7, 9], which found that the strength of HTPB increases with increasing strain rate and decreasing temperature. For the most part, these studies have focused on a particular HTPB composition. Finally, there have been a few studies of the shock Hugoniot response of HTPB [10, 11], which found that the material shows a linear relationship between U_s and u_p.

In this study, three HTPB materials were prepared with varying amounts of plasticizer. The compressive mechanical properties of the three polymers were investigated across a range of strain rates. Additionally, the shock Hugoniots of the materials were determined.

7.2 Experimental Approach

Three HTPB-based polymers were prepared using varying amounts of plasticizer as described in Table 7.1. These materials had varying amounts of plasticizer to change the mechanical properties of the polymers. The polymers were prepared and cast into molds of appropriate sample sizes for testing.

Quasi-static compression experiments were conducted at room temperature using an Instron model 55R4201. Samples were nominally 12.7 mm long by 12.7 mm diameter. The strain in the sample was determined by tracking relative displacement of two dots nominally 3 mm above and below the centerline of the sample with Instron's Advanced Video

J. Jordan (✉)
Air Force Office of Scientific Research, Arlington, VA 22203, USA
e-mail: jennifer.jordan.6@us.af.mil

D. Montaigne • C. Neel • G. Sunny • C. Molek
Air Force Research Laboratory, Eglin AFB, FL 32542, USA

B. Song et al. (eds.), *Dynamic Behavior of Materials, Volume 1*,
Conference Proceedings of the Society for Experimental Mechanics Series, DOI 10.1007/978-3-319-22452-7_7

Table 7.1 Composition of HTPB materials

Sample	Density (g/cm^3)	% HTPB	% Plasticizer	% Isocyanate
HTPB0	0.910	90.928	0	9.072
HTPB1	0.914	47.871	47.394	4.736
HTPB2	0.916	32.303	64.458	3.239

Extensometer (model 2663-821), and the stress was determined from the load cell output. The strain rates tested were approximately 3×10^{-2}, 3×10^{-3}, and 3×10^{-4} s^{-1}. All data was acquired using Instron's Bluehill 2.15 software.

Dynamic compression experiments (approximately 2×10^{3} s^{-1}) were conducted using a split Hopkinson pressure bar (SHPB) system located at AFRL/RWME, Eglin AFB, FL [12]. The 6061-T6 aluminum incident and transmitted bars were 1524 mm long and 19.05 mm diameter. The striker is 610 mm long and made of the same material as the other bars. The samples, which were nominally 12.3 mm diameter and 7 mm long, are positioned between the incident and transmitted bars. The bar faces are lightly lubricated with grease to reduce friction. A thin copper pulse shaper was used to control the input pulse to the sample. The bar system uses semiconductor strain gages (Kulite AFP-500-90) in a voltage divider to acquire the incident and transmitted signals. The voltage pulses are converted to force using a measured calibration [12]. A dispersion correction algorithm was used to correct for bar wave dispersion [13, 14]. The data presented in this paper has been corrected for dispersion.

Planar shock experiments were conducted using a 60 mm diameter powder gun at Eglin AFB. A 4 mm thick aluminum impactor was used to impact a 2 mm thick aluminum driver plate at velocities ranging from 300 to 1400 m/s. The 4 mm thick HTPB sample was mounted on the rear surface of the aluminum driver plate. A 12.7 mm thick PMMA window, which was coated with a thin layer of aluminum on one side, was mounted on the rear surface of the HTPB. The thin aluminum coating served as a reflector for laser-based velocity interferometry diagnostics. Photonic Doppler Velocimetry (PDV) and Velocity Interferometry System for Any Reflector (VISAR) were used to measure the velocity at the mirrored surface of the PMMA, which was in contact with the HTPB sample. Additionally, PDV was used the measure the impact velocity of the projectile, and the free surface velocity of the aluminum driver plate.

7.3 Results and Discussion

The HTPB polymers were tested at three quasi-static strain rates using an Instron load frame (3×10^{-2}, 3×10^{-3}, and 3×10^{-4} s^{-1}) and one high strain rate using a split Hopkinson pressure bar (2.5×10^{3} s^{-1}). HTPB 1 was not tested at 3×10^{-3} s^{-1}. Figure 7.1a shows the response of the materials at the highest quasi-static rate, and Fig. 7.1b shows the response of the three polymers at the highest strain rate tested. Increasing the amount of plasticizer resulted in decreased strength in the material. There is considerable scatter in the data, as seen from Fig. 7.1b, which may be inherent in testing these soft materials.

It can be seen from Fig. 7.2 that increasing the strain rate resulted in an increased strength in the material, and, from Fig. 7.1, an increase in the slope of the stress–strain curve. At low strain rates, there is little strain rate dependence. However, at dynamic strain rates, the measured stress increases greatly over what would be expected from an extrapolation from the quasi-static data.

The shock response of the two HTPB materials tested, those with the most and no plasticizer, is shown in Fig. 7.3. Two HTPB materials tested by Millett et al. [11] are included for comparison, where HTPB 1 is a proprietary composition of Royal Ordnance, Glacoed, UK and HTPB 2 is 88 % HTPB and 12 % IPDI. The data from this study shows that increasing the amount of plasticizer results in a decrease in the shock velocity for a given particle velocity. Millett's HTPB 2 material corresponds with the HTPB0 materials from this study, which is expected since both samples have the same isocyanate and no plasticizer and, subsequently similar densities. The proprietary formulation has a different slope than the other materials tested, which demonstrates that the response of "HTPB" can vary greatly based on the underlying composition of the material.

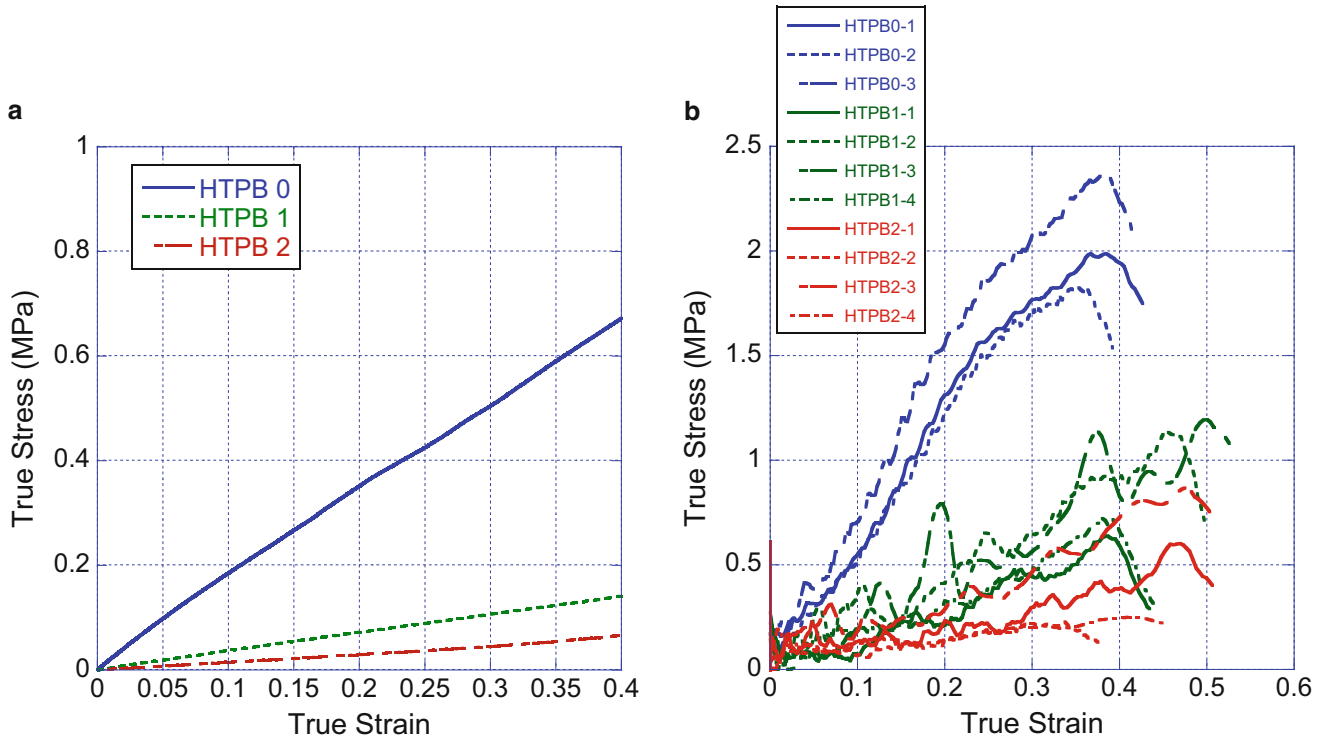

Fig. 7.1 (**a**) Quasi-static and (**b**) dynamic (~2.5 × 10^3 s^{-1}) compressive stress strain response of three HTPB materials with varying amounts of plasticizer

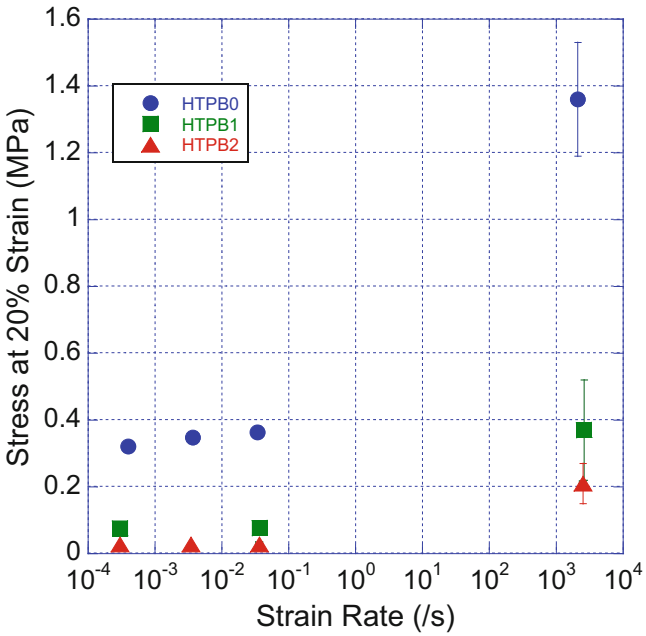

Fig. 7.2 Stress vs. strain rate for three HTPB polymers with varying amounts of plasticizer

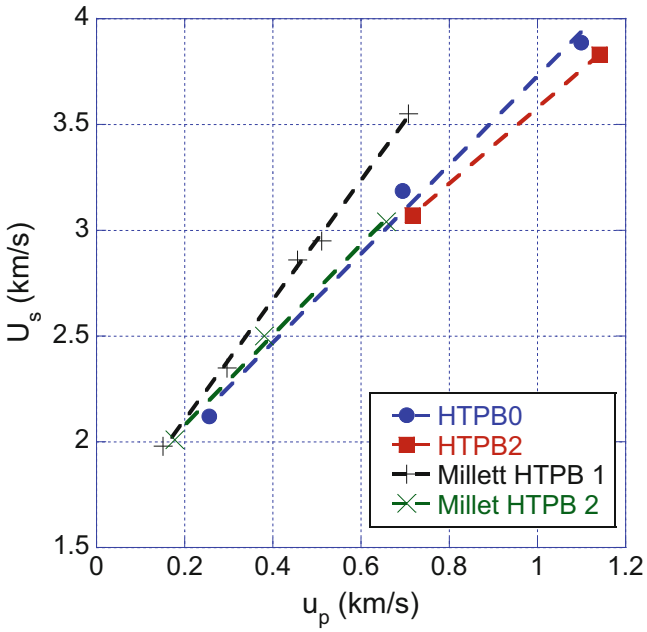

Fig. 7.3 Shock velocity versus particle velocity for HTPB0 and HTPB2 from this study in comparison with two HTPB materials from Millett et al. [11]. The linear fit to HTPB0 is $U_s = 1.63 + 2.1\ u_p$. The linear fit for HTPB2 is $U_s = 1.79 + 1.79\ u_p$

7.4 Summary

Hydroxyl-terminated polybutadiene (HTPB) has long been used as a binder in propellants and explosives. In this study, three isocyanate-cured HTPB variants with different amounts of plasticizer were formulated. The materials were characterized quasi-static and dynamic compression experiments, and the shock Hugoniot was measured on the two extremes of the material—no plasticizer and maximum plasticizer. Increasing the amount of plasticizer resulted in decrease stress in the material during compression experiments and decrease in shock velocity for a given particle velocity for shock experiments. All three materials showed significant strain rate dependence at high strain rates.

Acknowledgments This work was funded by the Munitions Directorate, Air Force Research Laboratory. The authors would like to thank Mr. Tomislav Kosta for his assistance with testing. Opinions, interpretations, conclusions, and recommendations are those of the authors and are not necessarily endorsed by the United States Air Force.

References

1. Chen, T.K., Hwung, C.J., Hou, C.C.: Effects of number-average molecular weight of network chain on physical properties of cis-polybutadiene-containing polyurethane. Polym. Eng. Sci. **32**(2), 115–121 (1992)
2. Vilar, W., Akcelrud, L.: Effect of HTPB structure on prepolymer characteristics and on mechanical properties of polybutadiene-based polyurethanes. Polym. Bull. **35**(5), 635–639 (1995)
3. Panicker, S.S., Ninan, K.: Effect of reactivity of different types of hydroxyl groups of HTPB on mechanical properties of the cured product. J. Appl. Polym. Sci. **63**(10), 1313–1320 (1997)
4. Haska, S.B., et al.: Mechanical properties of HTPB-IPDI-based elastomers. J. Appl. Polym. Sci. **64**(12), 2347–2354 (1997)
5. Sekkar, V., et al.: Polyurethanes based on hydroxyl terminated polybutadiene: modelling of network parameters and correlation with mechanical properties. Polymer **41**(18), 6773–6786 (2000)
6. Wingborg, N.: Increasing the tensile strength of HTPB with different isocyanates and chain extenders. Polym. Test. **21**(3), 283–287 (2002)
7. De La Fuente, J.L., Fernández-García, M., Cerrada, M.L.: Viscoelastic behavior in a hydroxyl-terminated polybutadiene gum and its highly filled composites: effect of the type of filler on the relaxation processes. J. Appl. Polym. Sci. **78**(7), 1705–1712 (2003)
8. Cady, C., et al.: Mechanical properties of plastic-bonded explosive binder materials as a function of strain-rate and temperature. Polym. Eng. Sci. **46**(6), 812–819 (2006)
9. Siviour, C.R., et al.: High strain rate properties of a polymer-bonded sugar: their dependence on applied and internal constraints. Proc. R. Soc. A Math. Phys. Eng. Sci. **464**(2093), 1229–1255 (2008)
10. Meziere, Y., et al.: The Shock Hugoniot of hydroxy-terminated polybutadiene. In: AIP Conference Proceedings (2004)
11. Millett, J., Bourne, N., Akhavan, J.: The response of hydroxy-terminated polybutadiene to one-dimensional shock loading. J. Appl. Phys. **95**(9), 4722–4727 (2004)
12. Jordan, J.L., Foley, J.R., Siviour, C.R.: Mechanical properties of Epon 826/DEA epoxy. Mech. Time-Depend. Mater. **12**(3), 249–272 (2008)
13. Gorham, D.: A numerical method for the correction of dispersion in pressure bar signals. J. Phys. E Sci. Instrum. **16**(6), 477 (1983)
14. Bacon, C.: An experimental method for considering dispersion and attenuation in a viscoelastic Hopkinson bar. Exp. Mech. **38**(4), 242–249 (1998)

Chapter 8
Modified Hopkinson Apparatus to Investigate Fluid Cavitation as a Potential Source of Injury

Michael Bustamante, Dilaver Singh, and Duane S. Cronin

Abstract Mild Traumatic Brain Injury (mTBI) has been recognized as an important issue for persons exposed to blast. Specifically, this injury has been associated with exposure to blast overpressure and more recently relatively large negative pressures have been identified as occurring at the posterior regions of the brain in experimental and in numerical studies of frontal blast exposure. These negative pressures are caused by the reflection of the incident bar stress wave from the free surface of the skull, and may be intensified due to focusing effects from the curvature of the skull. Under certain circumstances, this negative pressure is hypothesized to cause cavitation of cerebrospinal fluid (CSF) surrounding the brain, potentially resulting in injury to the brain. Unfortunately the cavitation pressure of CSF has not been directly measured, so the consequence of negative pressures in numerical head models exposed to blast cannot be accurately predicted. The cavitation pressure of fluids is highly variable, depending on the presence of impurities in the fluid and the presence of dissolved gasses. In this study, a modified Compressive Split Hopkinson Pressure Bar (CSHPB) apparatus incorporating a sealed confinement chamber was used to generate negative pressures in distilled water to investigate the cavitation properties of water as a surrogate for CSF. The negative pressures in the fluid were measured using a pressure transducer designed for compression and validated in comparison to the input signal on the modified Hopkinson bar apparatus, as well as verified by a numerical model of the experiment. The CSHPB apparatus was used to generate initial compressive waves ranging from 1.85 to 7.85 MPa to produce cavitation in distilled water. The experimental tests were simulated with good agreement and used to obtain water peak negative pressures ranging from −1.32 to −5.64 MPa. Future tests will be undertaken to investigate cavitation properties of CSF.

Keywords Cavitation • Split Hopkinson pressure bar • Mild traumatic brain injury • Negative pressure • Impedance mismatch

8.1 Introduction

Mild Traumatic Brain Injury (mTBI) has become an increasingly important and prevalent issue for persons exposed to blast. The United States Department of Defence defines mTBI as a head injury that results in alteration or loss of consciousness [1]. In the last decade, blast events in theatre account for up to 80 % of the TBI experienced by US service members, of which approximately 75 % are classified as mTBI [1]. Currently, mTBI is diagnosed through clinical assessment with functional deficits and neurological tests [2]. Service members that are exposed to non-physically-impairing injury from blasts are evaluated to determine their ability to return to duty [1]. These assessments and evaluations are based on approaches used to address sports concussions, which may not translate well to service members exposed to blast [1].

There are four commonly referenced mechanisms that can cause bodily harm to an individual from blast exposure (Fig. 8.1). The injuries caused by these mechanisms are described as the primary, secondary, tertiary, and quaternary blast injury. Primary blast injury is defined as any injury caused by the initial blast wave created by the rapid expansion of gases during an explosive detonation [3, 4]. This large overpressure generated by a blast, when interacting with the body can produce contusions, lacerations, and herniation of internal organs [4, 5]. Projectiles and debris propelled by the blast that pierce the skin, such as shrapnel, are categorized as secondary blast injury [3, 4]. Tertiary blast injuries occur when the body experiences large accelerations from a blast resulting from whole body translations such as being thrown against a wall, or acceleration of non-penetrating masses towards the body [3–6]. All other injuries, such as chemical, thermal, and nuclear effects of blasts are categorized under quaternary blast injuries [3–6].

M. Bustamante (✉) • D. Singh • D.S. Cronin
Department of Mechanical Engineering, University of Waterloo, 200 University Ave. W., Waterloo, ON, Canada N2L3G1
e-mail: mcbustam@uwaterloo.ca

B. Song et al. (eds.), *Dynamic Behavior of Materials, Volume 1*,
Conference Proceedings of the Society for Experimental Mechanics Series, DOI 10.1007/978-3-319-22452-7_8

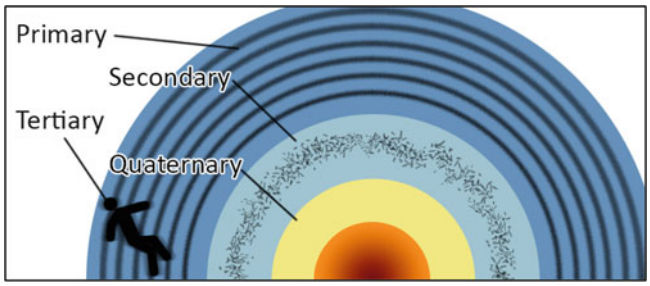

Fig. 8.1 Blast mechanisms which can cause bodily harm

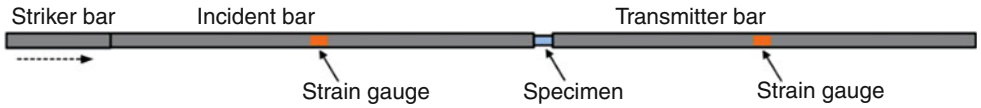

Fig. 8.2 Traditional CSHPB setup consisting of a striker, incident, and transmitter bar of the same material [13]

Due to the ethical concerns of using human *in vivo* measurements of brain response exposed to blast, studies often use animal models or numerical head models to determine the effects of the primary blast wave on the brain. It is hypothesized that cavitation of cerebrospinal fluid (CSF) due to transient negative intracranial pressure is a possible injury mechanism that can lead to mTBI. Cavitation is the generation of voids or cavities (i.e. bubbles) in a liquid due to localized pressure changes. When these bubbles collapse they can create jets of liquid that can produce large forces on surrounding materials [7]. The limits of CSF cavitation are currently unknown and many numerical studies that examine the effects of CSF cavitation in the brain use the cavitation limit of water which ranges from 0.1 to 120 MPa [8]. Published literature has shown that negative pressures can occur in the brain during the initial positive pressure phase of a blast. An experimental study by Bir (2011) measured negative pressures during frontal blast exposure in the parietal and occipital lobe using optical pressure sensors installed in fresh unembalmed post-mortem head surrogates. Negative pressures were noted for all specimens tested and reflected the change in orientation of the blast (i.e. negative pressures occurred at the contrecoup) [8]. A numerical study by Singh et al. (2013) modelled primary blast injury to the head using sagittal and transverse models of the head. These models showed the greatest negative intracranial pressures occurring at the posterior ranging from −211 to −760 kPa for the load cases considered in that study [10]. Panzer et al. (2012) modelled a 2D slice of the head in the transverse plane and assumed a CSF pressure cut-off of −100 kPa which was found to produce cavitation in the model before the negative pressure phase of the blast [11]. Zhang et al. (2013) tested the effects of an Advanced Combat Helmet on the numerical Wayne State University Head Injury Model (WSUHIM), and reported that a 0.35 MPa peak overpressure produced negative pressures ranging from −300 to −480 kPa occurring at the contrecoup [12].

It is hypothesized that the acoustic impedance mismatch between the skull and free surface of the head at the contrecoup may cause the large negative pressures observed in the brain during blast conditions. Due to a higher impedance of the skull compared to the free surface of the head, an incoming compressive wave is reflected as a tensile wave that may cause negative pressures leading to cavitation of CSF. An important property to determine whether cavitation of CSF is an injury mechanism in primary blast is to determine cavitation pressure limits for the CSF. This study will investigate cavitation in distilled water caused by a reflected compressive wave generated by a modified Compressive Split Hopkinson Pressure Bar (CSHPB). A CSHPB is an apparatus that can generate controlled high-rate loading in compression. A traditional CSHPB consists of a striker, incident, and transmitter bar of the same material (Fig. 8.2). When struck by the striker, a compressive wave is generated in the incident bar, travels down the incident bar, through the specimen, and into the transmitter bar.

The compressive wave that is generated in the incident bar is called the incident wave. When the incident wave reaches the incident bar and specimen interface, a portion of the wave is transmitted through the specimen and into the transmitter bar (i.e. the transmitted wave) and the balance of the wave is reflected at the interface and travels back through the incident bar (i.e. the reflected wave) (Fig. 8.3). Analysis of the incident, transmitted, and reflected waves can be used to determine the dynamic behaviour of the specimen. The fraction of the incident wave that is reflected is determined by the impedance mismatch between the bars and specimen (Eqs. 8.1 and 8.2), where σ is stress, ρ is density, C is acoustic waves speed. The product of density and acoustic wave speed is defined as the acoustic impedance of the material. The impedance mismatch between materials also describes the change in sense of the reflected wave when the incident wave travels from a higher to a lower impedance material (Fig. 8.4). This explains how an entire compressive wave is effectively reflected in

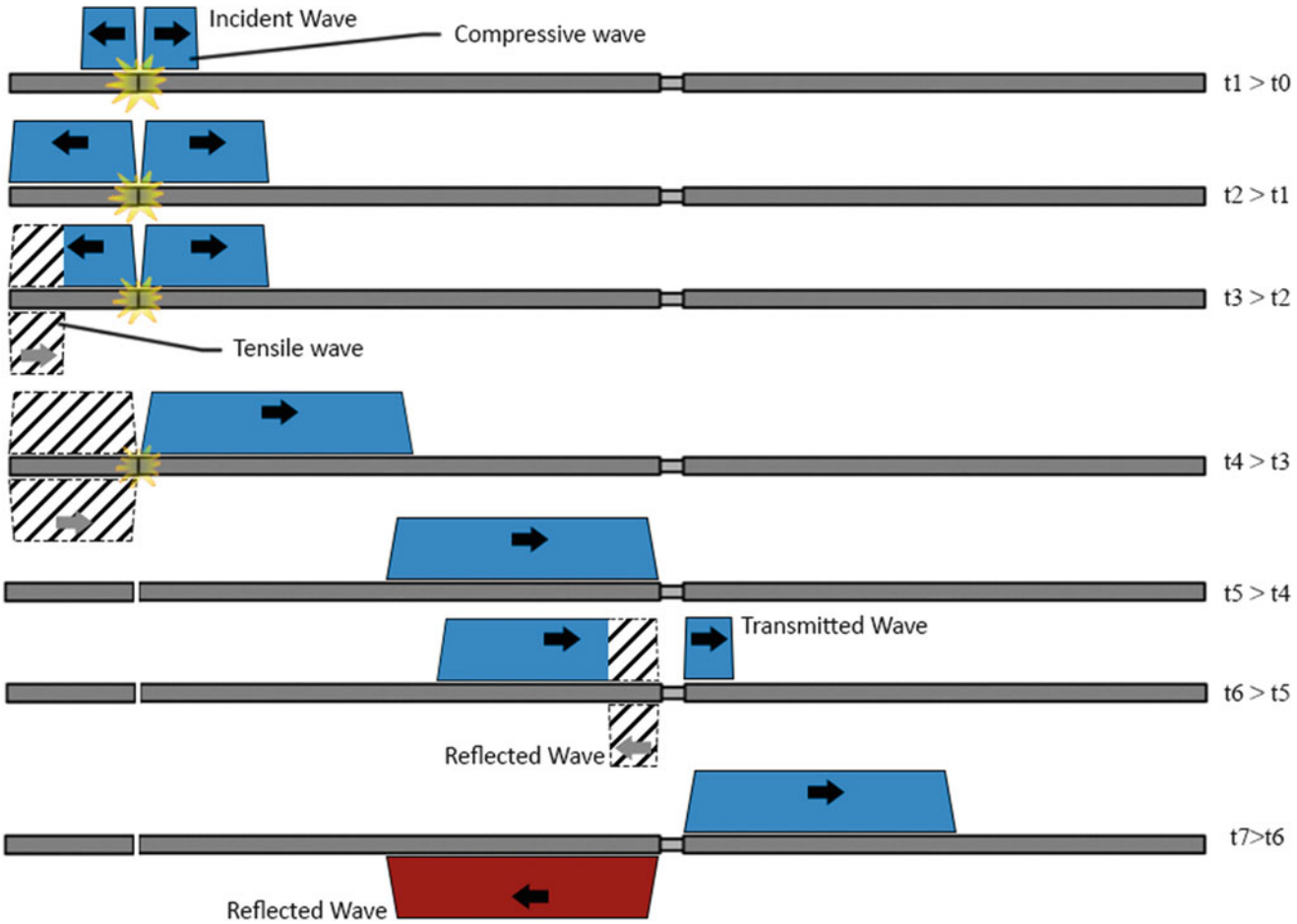

Fig. 8.3 Generation and propagation of incident wave, transmitted wave, and reflected wave in CSHPB after striker impact, where *dashed waves* indicate superposition

tension at the end of a bar, where the adjacent material is of lower impedance (e.g. an aluminum bar end exposed to air, since the impedance of air is far less than that of aluminum).

$$\frac{\sigma_{Reflected}}{\sigma_{Incident}} = \frac{(\rho C)_{material2} - (\rho C)_{material1}}{(\rho C)_{material1} + (\rho C)_{material2}} \tag{8.1}$$

$$\frac{\sigma_{Transmitted}}{\sigma_{Incident}} = \frac{2(\rho C)_{material2}}{(\rho C)_{material1} + (\rho C)_{material2}} \tag{8.2}$$

The traditional CSHPB can be altered to a Tensile Split Hopkinson Pressure Bar (TSHPB) that generates an initial tensile wave by replacing the striker bar with a striker tube and affixing an anvil onto the end of the incident bar. The striker tube impacts the anvil generating a tensile wave travelling down the incident bar, through the specimen, and into the transmitter bar. Preliminary tests by Singh et al. (2014) were conducted on a TSHPB apparatus along with a confinement chamber containing distilled water to show cavitation from tensile wave superposition at the interface between the specimen (i.e. distilled water) and transmitter bar (Fig. 8.5) [13]. The TSHPB apparatus was further modified by removing the transmitter bar and replacing the confinement chamber with a single-entry chamber to increase the stiffness of the boundary of interest (Fig. 8.5). A pressure transducer was also mounted flush to the inside wall of the chamber to determine static pressure of the contained water. The modified TSHPB produced cavitation in the distilled water at a negative pressure of approximately −80 kPa from an incident tensile wave with a magnitude of 3.1 MPa. Another similar study by Hong et al. (2014) achieved similar results by producing cavitation in water at a negative pressure of approximately −82 kPa using an initial tensile wave [14]. The pressure transducers used by both Singh and Hong were designed for compression and may not accurately

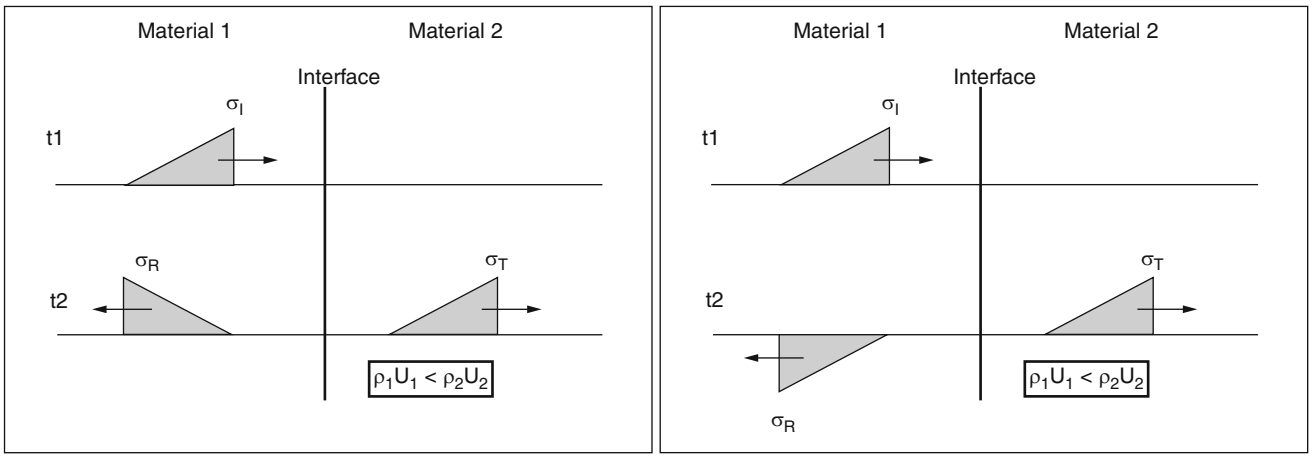

Fig. 8.4 Acoustic impedance difference between two materials, noting the effect on the sense of the reflected wave [16]

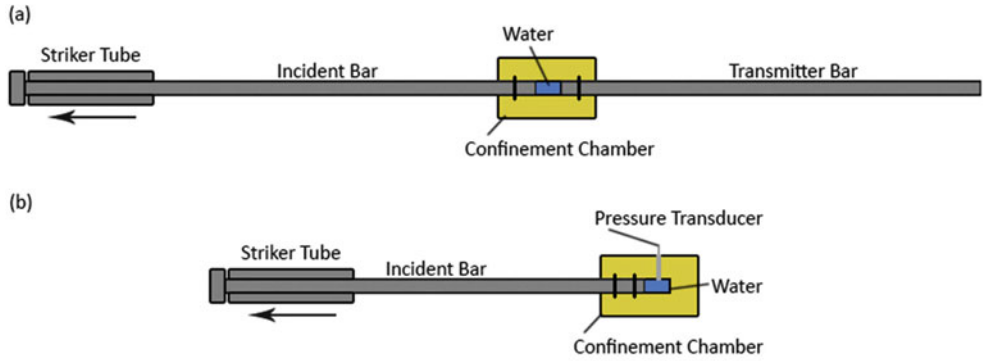

Fig. 8.5 (**a**) TSHPB setup consisting of a striker tube, incident bar, and transmitter bar of the same material. (**b**) Modified TSHPB with single-entry confinement chamber

describe the negative pressures in the water. Additionally, these studies used an initial tensile wave rather than an initial compressive wave experienced in blast exposure. In this study a modified CSHPB apparatus was developed to investigate cavitation of distilled water as a result of a reflected compressive wave as hypothesized in blast exposure. The applicability of a pressure transducer designed for compression on measuring negative pressure was also investigated.

8.2 Methods

The experimental setup in this study used a modified CSHPB and an acrylic confinement chamber filled with distilled water (Fig. 8.6). Water was used as a surrogate for CSF, since CSF is primarily water [15, 17]. The striker and incident bar were used to generate a compressive wave that traveled through the water and into the acrylic, and then reflect as a tensile wave at the acrylic and air interface. The CSHPB comprises 25.4 mm diameter aluminum bars with lengths of 2435 and 1068 mm for the incident and striker bars, respectively. The confinement chamber was made of acrylic with an inner diameter of 25.7 mm and an outer diameter of 89 mm. The pressure in the water was measured using a pressure transducer designed for compression (PCB Piezotronics Model 113B21) mounted flush to the inside wall of the chamber. Two o-rings were used to seal the chamber and bar interface to prevent water leakage during tests. A thin layer of dish soap was applied to the inside of the confinement chamber to create a hydrophobic surface to reduce the amount of bubbles developing at the inner wall of the chamber during filling. Distilled water was placed into the chamber through the transducer mount port using a syringe. A syringe was used to minimize the amount of bubbles that would occur if the water were simply poured into the

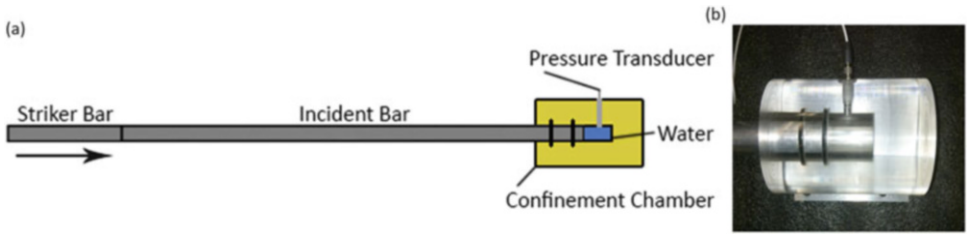

Fig. 8.6 (**a**) Modified CSHPB with aluminum bars and an acrylic confinement chamber. (**b**) Photograph of chamber end

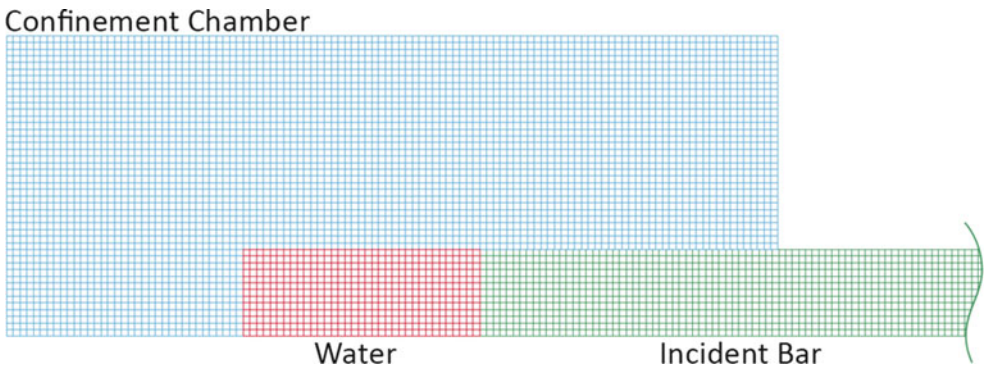

Fig. 8.7 Axisymmetric FE model of experimental CSHPB setup. Striker bar not shown

confinement chamber. Teflon tape was used on the threads of the transducer to seal the chamber. To generate a compressive wave, the striker bar was accelerated to initiate impact with the incident bar. The strain in the bar was measured by strain gages mounted on the incident bar. Measurements are obtained at 2 MHz using LABView 2014 Data Acquisition hardware and software. High-speed imaging of the water was captured at 100,000 fps with a 320 × 192 resolution.

An axisymmetric model of the experimental test was created using an explicit multi-physics finite element program (LS-DYNA, Version 971 Revision 6.1.1) (Fig. 8.7). The experimental setup was modelled with a total of 50,669 axisymmetric elements. The aluminum bars were modelled as an elastic material with a density of 2700 kg/m^3, Young's modulus of 68.9 GPa and Poisson's ratio of 0.35. The acrylic chamber was also modelled as an elastic material with a density of 1178 kg/m^3, Young's modulus of 3.47 GPa and Poisson's ratio of 0.35. The water was modelled as a viscous fluid material with a density of 1000 kg/m^3 and bulk modulus of 2.19 GPa. The interfaces between the incident bar, water, and confinement chamber have incorporated shared nodes since the surfaces were not expected to separate during the simulation time considered. Simulations were performed using striker velocities (V) calculated from Eq. (8.3) where σ is the incident bar stress measured, ρ is the bar density, and C is the bar acoustic wave speed.

$$\sigma = \frac{1}{2}\rho C V \tag{8.3}$$

8.3 Results

Eight experimental tests were performed with striker velocities ranging from 0.27 to 1.15 m/s resulting in incident bar stress amplitudes ranging from 1.85 to 7.85 MPa, and with peak compressive water pressures ranging from 1.16 to 4.69 MPa (Table 8.1). All tests performed showed cavitation occurring with bubbles developing throughout the volume of the water, with the majority of the bubbles at the interfaces of the water and acrylic and aluminum (Fig. 8.8). Bubbles showed growth and collapse duration of 0.62 ms during the 0.27 m/s impact velocity test. All eight experimental tests were simulated using the striker velocities in Table 8.1. Simulations resulted in incident bar stress amplitudes ranging from 1.86 to 7.88 MPa, positive peak water pressures ranging from 1.27 to 5.38 MPa, and negative peak water pressures ranging from −1.32 to −5.64 MPa (Table 8.2).

Table 8.1 Incident bar stress amplitude, peak water pressure, and calculated striker velocity values for all eight experimental tests

Striker velocity (m/s)	Incident bar stress (MPa)	Peak water pressure (MPa)
0.27	1.85	1.16
0.40	2.75	1.57
0.42	2.88	1.51
0.46	3.12	2.15
0.52	3.58	2.17
0.57	3.90	2.38
1.05	7.17	4.11
1.15	7.85	4.69

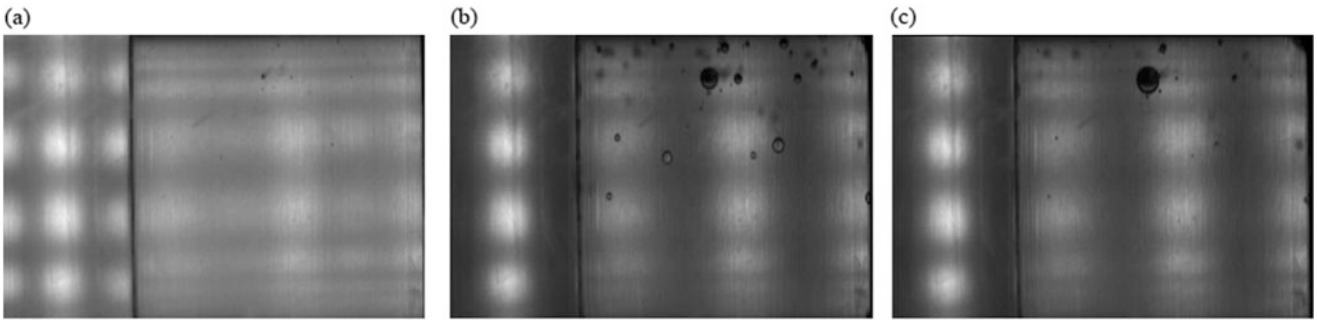

Fig. 8.8 High-speed imaging showing bubble locations and time duration of growth and collapse. (**a**) Before bubble development. (**b**) Growth: 0.31 ms. (**c**) Collapse: 0.62 ms

Table 8.2 Incident bar stress amplitude, positive and negative peak water pressure, and defined striker velocity values for all eight simulations

Striker velocity (m/s)	Incident bar stress (MPa)	Positive peak water pressure (MPa)	Negative peak water pressure (MPa)
0.27	1.86	1.27	−1.32
0.40	2.67	1.88	−1.97
0.42	2.89	1.88	−2.07
0.46	3.13	2.13	−2.24
0.52	3.59	2.44	−2.57
0.57	3.92	2.67	−2.8
1.05	7.19	4.92	−5.16
1.15	7.88	5.38	−5.64

Incident bar stress and water pressure versus time from experimental and numerical data for a striker velocity of 1.15 m/s are compared (Fig. 8.9). Trends of water pressure versus incident bar stress are compared for experimental and numerical data for all test cases performed (Fig. 8.10). Trends of initial water pressure wave (IWPW) versus incident bar stress are compared for experimental, numerical, and analytical data for all test cases performed (Fig. 8.11). The IWPW is the peak pressure measured by the pressure transducer before the first reflection at the water and acrylic interface travels back to the transducer. The analytical data for IWPW was obtained from Eq. (8.2) using experimental incident bar stress values in Table 8.1. The IWPW values of experimental tests are obtained at the same time as the easily visible IWPW values in the numerical simulations.

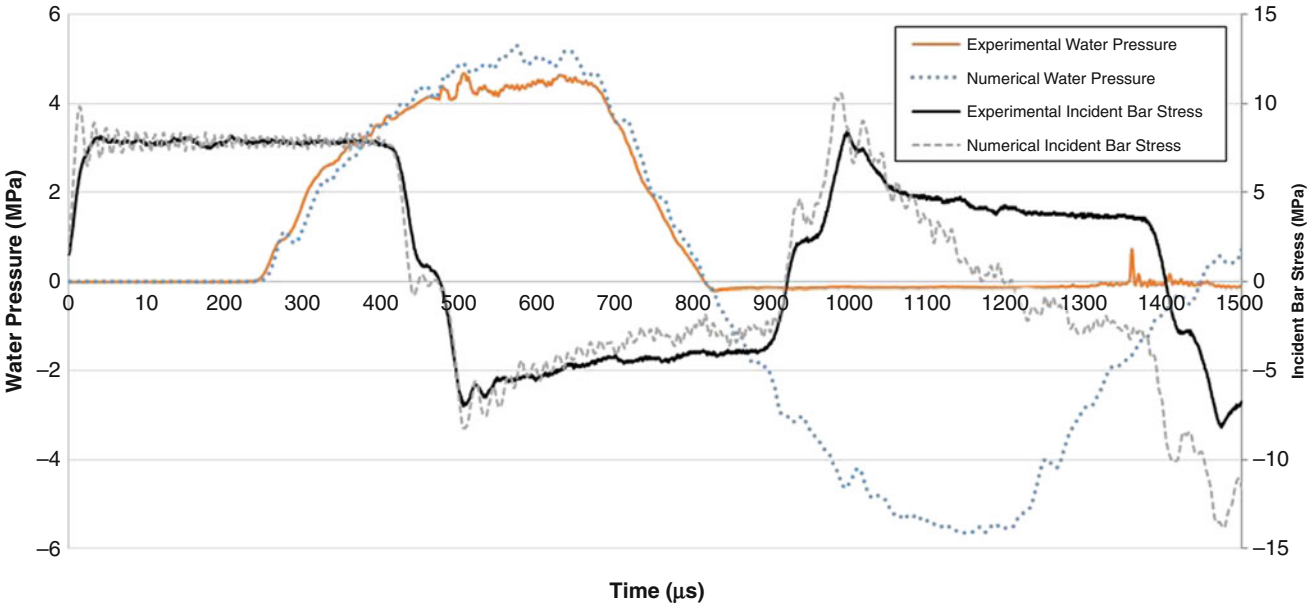

Fig. 8.9 Experimental and numerical water pressure and incident bar stress versus time plot for 1.15 m/s striker velocity

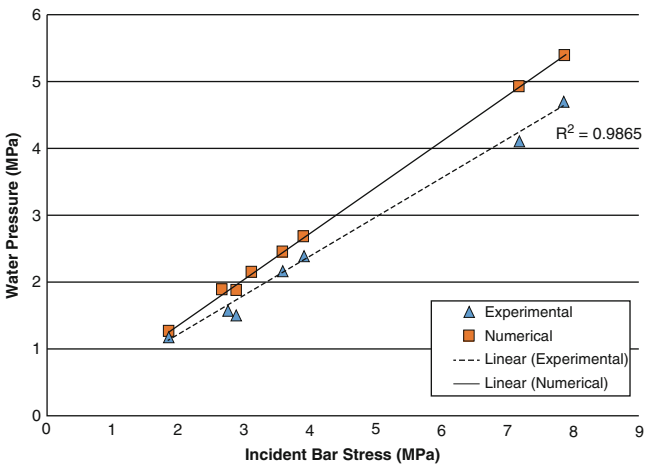

Fig. 8.10 Experimental and numerical data comparison of water pressure versus incident bar stress trends

8.4 Discussion and Conclusions

Figure 8.9 shows good agreement between the experimental data and numerical simulation for the 1.15 m/s striker velocity test. There was a small difference between the measured and predicted reflected waves in the bar, attributed to losses in the system due to friction from the o-rings. A small difference was also noted between the measured and simulated positive water pressures that can be attributed to the o-rings sealing the confinement chamber which may decrease the stiffness in the experiment compared to the model. As expected, the negative pressure in the water was not accurately measured for all test cases, due to the inability of the pressure transducer to measure negative pressures. Due to the good agreement of the positive pressures in the water, the maximum negative pressures that can be achieved in the experimental tests can be assumed to be approximately that of the negative pressures predicted by the numerical simulations. Cavitation of the water was not defined in the numerical model, therefore the predicted magnitude of the negative pressure in the model could be larger than that achieved in the experimental test, when it exceeds the cavitation pressure of the actual fluid.

The experimental and numerical trends of peak water pressure versus incident bar stress shown in Fig. 8.10 show good agreement. The lesser slope of the experimental trend can be attributed to the compliance of the experimental setup compared to the numerical model, particularly at higher water pressures. The experimental and numerical trends of

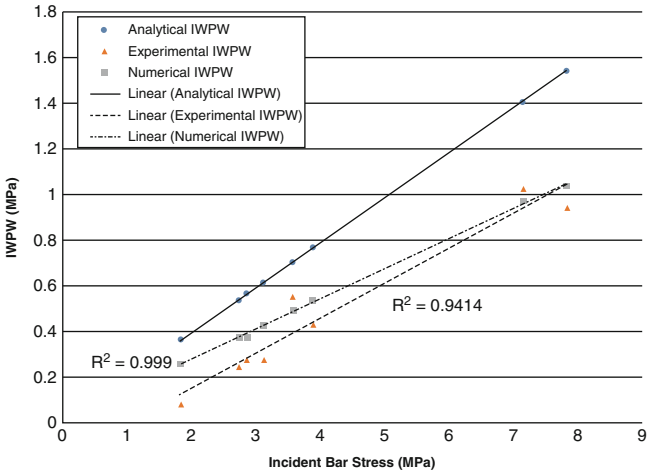

Fig. 8.11 Experimental, numerical, and analytical data comparison of IWPW versus incident bar stress trends

IWPW versus incident bar stress shown in Fig. 8.11 also show good agreement. As expected, the analytical values of IWPW are highest because this analysis assumes one-dimensional wave propagation, unlike the numerical and experimental approaches. Likewise, it is expected that the experimental values would have the lowest IWPW values because of the losses in the system that are not included in the numerical model.

Cavitation was observed for all eight tests performed even with a striker velocity as low as 0.27 m/s, suggesting that for future work a different material should be used for the incident and striker bars. Using a bar material with a lower impedance compared to aluminum will reduce the incident wave generated. Changing the bar material is preferred over reducing the striker velocity because vibrational and frictional effects become more significant at lower velocities.

A traditional CSHPB apparatus was modified into a TSHPB to perform preliminary tests investigating the cavitation properties of distilled water. The apparatus was further developed by removing the transmitter bar and using a single-entry confinement chamber to increase the stiffness of the reflection boundary, as well as mounting a pressure transducer to measure static pressure of the water. Both apparatuses were able to produce cavitation in the distilled water using an initial tensile incident wave. To better reproduce the conditions of blast exposure, the apparatus was again modified to generate an initial compressive incident wave. This current CSHPB apparatus has successfully produced cavitation in the distilled water using a reflected compression wave, and the experimental measurements were in good agreement with numerical simulations for all test cases. It was also suggested that the pressure transducer designed for compression inaccurately measures negative pressure and those obtained in the numerical model are the maximum achievable negative pressures that can occur in the experimental tests. Future work will consider alternate bar materials, and testing of CSF.

Acknowledgment The authors would like to acknowledge the financial and technical support of Defence Research and Development Canada—Suffield.

References

1. Scherer, M.R., Weightman, M.M., Radomski, M.V., Davidson, L.F., McCulloch, K.L.: Returning service members to duty following mild traumatic brain injury: exploring the use of dual-task and multitask assessment methods. Phys. Ther. **83**, 1254–1267 (2013)
2. Harrigan, T.P., Roberts, J.C., Ward, E.E., Merkle, A.C.: Correlating tissue response with anatomical location of mTBI using a human head finite element model under simulated blast conditions. In: IFMBE Proceedings, College Park, pp. 18–21 (2010)
3. Rosenfeld, J.V., McFarlane, A.C., Bragge, P., Armonda, R.A., Grimes, J.B., Ling, G.S.: Blast-related traumatic brain injury. Lancet Neurol. **12** (9), 882–893 (2013)
4. Schmitt, K.-U., Niederer, P.F., Cronin, D.S., Muser, M.H., Walz, F.: Trauma Biomechanics, 4th edn. Springer, Berlin (2014)
5. El Sayed, T., Mota, A., Fraternali, F., Ortiz, M.: Biomechanics of traumatic brain injury. Comput. Methods Appl. Mech. Eng. **197**(51–52), 4692–4701 (2008)
6. Bass, C.R., Panzer, M.B., Rafaels, K.A., Wood, G., Shridharani, J., Capehart, B.: Brain injuries from blast. Ann. Biomed. Eng. **40**(1), 185–202 (2012)
7. Thiruvengadam, A.: Handbook of Cavitation Erosion, Rev. edn. Hydronautics, Laurel (1974)
8. Herbert, E., Balibar, S., Caupin, F.: Cavitation pressure in water. Phys. Rev. E **74**(4), 041603 (2006)
9. Bir, C.: Measuring Blast-Related Intracranial Pressure within the Human Head. Final Report, U.S. Army Medical Research and Material Command, Award No. W81XWH-09-1-0498. (2011)

10. Singh, D., Cronin, D.S., Haladuick, T.N.: Head and brain response to blast using sagittal and transverse finite element models. Int. J. Numer. Meth. Bio. Eng. **30**(4), 470–489 (2013)
11. Panzer, M.B., Myers, B.S., Capehart, B.P., Bass, C.R.: Development of a finite element model for blast brain injury and the effects of CSF cavitation. Ann. Biomed. Eng. **40**(7), 1530–1544 (2012)
12. Zhang, L., Makwana, R., Sharma, S.: Brain response to primary blast wave using validated finite element models of human head and advanced combat helmet. Front. Neurol. **4**, 88 (2013)
13. Singh, D., Cronin, D.S.: Investigation of cavitation using a modified Hopkinson apparatus. In: Proceedings of SEM, Greenville (2014)
14. Hong, Y., Canchi, S., King, M., Lee, S.J., Sarntinoranont, M., Subhash, G.: Development of a test system to study brain tissue damage due to cavitation, pp. 2–3 (2014)
15. Conn, P.M.: Neuroscience in Medicine, 2nd edn. Humana, Totowa (2003)
16. Cronin, D.S.: Explicit finite element method applied to impact biomechanics problems. In: IRCOBI, Krakow (2011)
17. Kandel, E., Schwartz, J., Thomas, J.: Principles of Neural Science, 4th edn. McGraw-Hill Medical, New York (2013)

Chapter 9
Dynamic Energy Absorption of Eco-Core and Other Commercial Core Materials

Rafid M. Kully

Abstract Eco-Core is a fire resistant syntactic foam that was developed to be used as a core material for sandwich structures. Core materials are subjected to multiaxial stress state in general and potentially to high strain rates. To evaluate the suitability of Eco-Core for applications involve dynamic effects as for blast mitigation and shock absorption military applications, its energy absorption needed to be evaluated. Also, it needed to be compared with energy absorption of other commercial core materials to determine its reliability. Specimens of 11 mm diameter and 3.2 mm length were prepared using Eco-Core (500 kg/m^3), PVC foam (100 kg/m^3), Balsa wood (202 kg/m^3) and Rohacell-A (75 kg/m^3). All specimens were confined with aluminum sleeve of 11 mm inner diameter and 0.9 mm thickness. Confined specimens were tested on Split Hopkinson Pressure Bar (SHPB) apparatus at strain rate ranged from 3120/s to 3490/s. Test results showed that energy absorption per unit volume of Eco-Core (11 MPa) is far superior to other tested commercial core materials (more than twice of Balsa wood the nearest material). The energy absorption per unit mass of Eco-Core (22 kN m/kg) is marginally better than other tested commercial core materials (as good as Balsa wood).

Keywords Energy absorption • Eco-Core • PVC foam • Balsa wood • Rohacell-A

9.1 Introduction

Composite sandwich structures have been receiving considerable amount of interest because of their superior stiffness-to-weight ratio, strength-to-weight ratio, resistance to corrosion and other properties such as thermal and acoustic insulations. Core material type has major impact on the overall properties of sandwich structure. It controls important mechanical properties of the structure like fatigue and shear characterization; bending stiffness; and energy absorption, the most important property. It determines the reliability of the structure for energy absorption applications like shock absorption, blast mitigation and others. Therefore, to extend the scope of any core material usage in different applications, its energy absorption capability needs to be studied. In real applications core is subjected to multiaxial stress state as shown in Fig. 9.1. When an axial force is applied on a sandwich structure, the core under that force tends to deform axially. Also, it tends to deform laterally due to Poisson effect. The rest of the core material constrains the lateral expansion that develops a lateral stress (q). Thereby, the core is under multiaxial stress state even when the applied stress is uniaxial. To simulate the multiaxial conditions on specimen, it has to be confined to develop the lateral stress in addition to the axial stress. The confinement approach by the mean of encasing the specimen inside sleeve was used in several dynamic and static studies before as in [1–4].

The objective of this study is to determine the dynamic energy absorption capability of Eco-Core and other core materials like PVC foam, Balsa wood and Rohacell-A and compare them to each other's. The approach of this work is to develop a test fixture to apply axial and lateral stresses on the specimen during dynamic tests, use the test fixture with Split Hopkinson Pressure Bar (SHPB) apparatus to conduct dynamic tests at high strain rates (3000/s–3500/s), determine the stress strain response for each material and calculate the energy absorptions form the areas under the stress strain curves.

R.M. Kully (✉)
97th Air Mobility Wing, Air Education and Training Command, United States Air Force, 97th CES, Bldg 358, Room 1082, 401 L Ave., Altus AFB, Altus, OK 73523, USA
e-mail: rafid.kully@us.af.mil

B. Song et al. (eds.), *Dynamic Behavior of Materials, Volume 1*,
Conference Proceedings of the Society for Experimental Mechanics Series, DOI 10.1007/978-3-319-22452-7_9

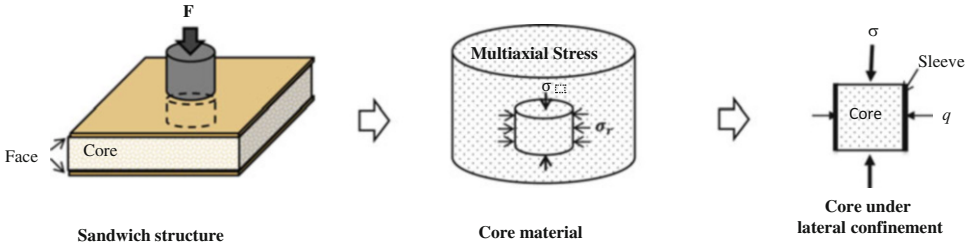

Fig. 9.1 Schematic of multiaxial stress state of sandwich structure core material

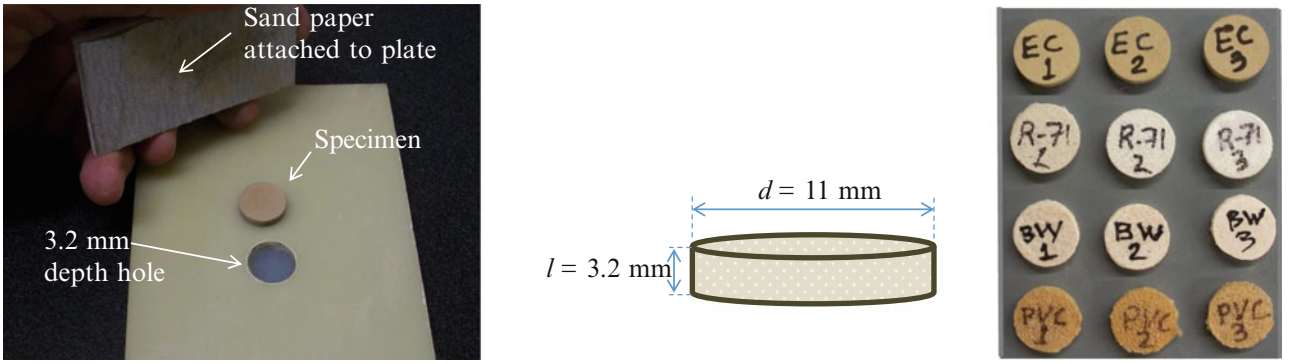

a) Specimen fabrication fixture b) Specimen's schematic c) Specimens' photograph

Fig. 9.2 Fabrication process, schematic and photograph of specimens

9.2 Materials and Specimens

Four core materials were used in this test, Eco-Core (500 kg/m^3), PVC foam (100 kg/m^3), Balsa wood (202 kg/m^3) and Rohacell-A (75 kg/m^3) . Eco-Core panels were fabricated from fly ash known as Cenosphere and small percentage of high char yield resin known as (Phenol-formaldehyde resole resin). More details about the fabrication process are available in reference [5]. The rest of the core material were provided in the form of panels by McMaster-Carr [6]. Rectangular panels of 100×100 mm^2 dimensions were prepared to fit in the vise of the drill machine. Cylindrical specimens of 11 mm diameter were cut from the panels using an 11 mm inner diameter core cutter. Specimens were at different lengths according to the different thicknesses of the used panels. 5 mm length specimens were cut from the different length specimens. At this stage the specimens' length was 30–40 % longer than final desired length. Each specimen was sanded down by 400-grit sand paper to 3.2 mm length within 25 μm variation using the fixture appears in Fig. 9.2a. This process insured that the two faces of the specimen were perfectly parallel to minimize the misalignment with the test fixture. The final dimensions of all specimens were $d = 11$ mm and $l = 3.2$ mm as appear in Fig. 9.2b. These dimensions were selected after many trails and according to many specimen design considerations. The aspect ratio of the specimen (l/d) was 2.9, which was within the recommended range for testing soft material [7]. Photographs of all specimens appear in Fig. 9.2c.

9.3 High Strain Rate Confined Compression Testing

High strain rate confined compression tests for core materials were conducted using SHPB test apparatus and using a specially designed test fixture. Before modifying SHPB to conduct confined tests, it was independently validated by data in the literature. Solid specimens of polycarbonate and nylon 6/6 were tested at 1200/s and 1250/s strain rates, respectively. Measured responses were compared to and validated by results of Salisbury [8] and Chou et al [9]. More details about the used SHPB for this test and the validation process are available in reference [5]. The validated SHPB apparatus along with the specially designed test fixture were used to test core materials.

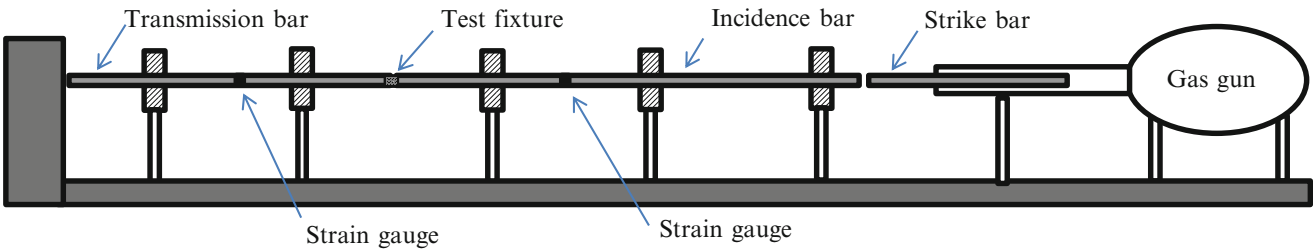

Fig. 9.3 Schematic of SHPB apparatus

9.3.1 SHPB Apparatus and Analysis

SHPB apparatus appears in Fig. 9.3 consists of two bars known as incidence bar and transmission bar and a third projectile bar driven by the pressure of a gas gun, known as strike bar. When testing with SHPB a test specimen is sandwiched between incidence bar and transmission bar. A stress/strain compression wave is generated by the impact of the strike bar on the impact end of the incidence bar. The stress/strain pulse propagates through the incidence bar toward the specimen, called incident pulse, $\varepsilon_i(t)$. When the pulse reaches the specimen-incidence bar interference, part of the pulse passes through the specimen to the transmission bar, called transmitted pulse, $\varepsilon_t(t)$. The other part of the incident pulse reflects back to the incidence bar as a tensile pulse, called reflected pulse, $\varepsilon_r(t)$. Pulse reflection occurs because of the difference in the material impedance of specimen and bar. The incident and reflected pulses are measured by a strain gauge installed on the incidence bar and the transmitted pulse is measured by a strain gauge installed on the transmission bar. The two gauges are at the same distance from the specimen (0.9 m). During the test, the specimen undergoes deformation until it reaches its dynamic limit.

The concept of the one dimensional stress wave propagation theory is used to calculate the strain rate in the specimen from the reflected wave signal, $\varepsilon_r(t)$ as:

$$\dot{\varepsilon}(t) = \frac{2c_b\varepsilon_r(t)}{l} \tag{9.1}$$

Where C_b is the speed of sound in the bars, l is the specimen length. The strain is calculated by integrating the strain rate (9.1) with respect to time as:

$$\varepsilon(t) = \frac{2c_b}{l}\int_0^t \varepsilon_r(t)dt \tag{9.2}$$

The axial stress in the specimen as a function of time is calculated from transmitted wave signal, $\varepsilon_t(t)$ as:

$$\sigma(t) = \frac{A_bE_b}{A_s}\varepsilon_t(t) \tag{9.3}$$

Where A_b is the cross-section area of incidence/transmission bar, A_s is the cross-section area of the specimen and E_b is the elastic modulus of bars' material. The stress strain response of the specimen is obtained by (9.2) and (9.3). This method of computation is given in number of text books and references on impact, for example [9–12].

9.3.2 Test Fixture

Test fixture consists of two plugs and sleeve. Sleeve was made of aluminum 6061/T6 with 11 mm diameter, 0.9 mm thickness and 6 mm length. Length of sleeve was selected to sufficiently encase the specimen and the ends of the two plugs. Plugs were made of aluminum 7075/T6 to match the impedance of the SHPB bars and avoid pulse dispersion. Figure 9.4a, b show schematic with dimensions and photograph of the test fixture, respectively. The left plug butts against the specimen

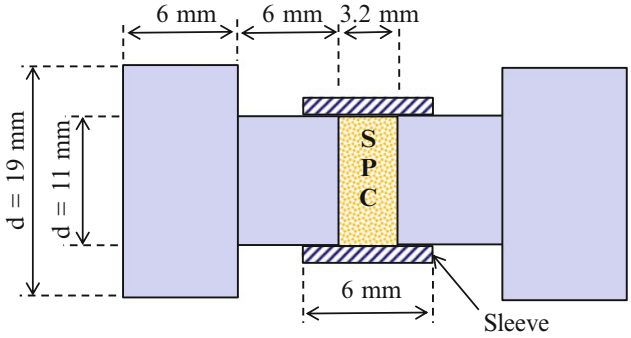

a) Schematic of test fixture

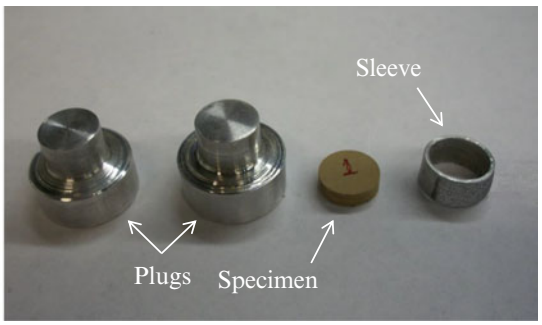

b) Photograph of test fixture

Fig. 9.4 Schematic and photograph of text fixture

and the transmission bar and the right plug butts against the specimen and the incidence bar. The specimen snug fits the sleeve within 25 μm clearance; the two plugs slide into the sleeve within 50 μm clearance.

9.3.3 Test

After SHPB apparatus was validated, confined compression tests for core materials were conducted. Starting with Eco-Core, specimen of $d = 11$ mm and $l = 3.2$ mm was inserted gently inside the aluminum sleeve. Specimen location was adjusted carefully such that it is in the mid-length of the sleeve as shown in Fig. 9.4a. The whole fixture was placed in between the incidence and transmission bars. The center of the incidence plug was aligned to the center line of the incidence bar and they were taped together without leaving any gap in between. The same process was repeated on the transmission side of the specimen. The gas gun of the apparatus was charged to 124 kPa pressure (This value was determined according to calibration process between the gas gun pressure and resulted strain rate). The trigger of the oscilloscope was turned on standby position. Then the system was fired, the strike bar impacted the incidence bar. The stress wave was generated at the impact site, traveled along the incidence bar, specimen and then to the transmission bar. The data acquisition system acquired the strain gauge signals from the incidence and transmission bars at rate of 0.5 MHz. The original waveform signals were filtered to reduce the noise by using the Xviewer software. Three specimens of Eco-Core were tested at the same gas gun pressure to insure the repeatability of the test. Also, three specimens of each of the other core materials were tested in the same manner at the same gas gun pressure. All the signals were saved to be reduced to strain rate, strain and stress.

9.4 Test Results

9.4.1 Basic Results

A typical time history of strain pulse signals for dynamic confined compression test of Eco-Core is shown in Fig. 9.5a. The figure shows the three strain/stress pulses of the bars (incident, transmitted and reflected pulses). The duration of the incident pulse ($T/2$) was about 415 μs (1135−720 μs) and the frequency ($f = 1/T$) was 1.2 kHz. Calculation of pulse frequency helped to select the suitable sampling rate of the data acquisition system (Oscilloscope), which was 0.5 MHz in this present case. Note that selecting higher sampling rate results in oscillatory data due to high frequency noise. On the other hand, lower sampling rate results in missing important phenomenons like peak strains/stress. The dynamic equilibrium of the specimen during the entire test period was verified by comparing the incident pulse to the sum of transmitted and reflected pulses. The pulses time history in Fig. 9.5b shows that the two values were close to each other's. It indicates that the strains of the bars on both sides of the specimen were almost equal. Since the bars have the same area and modulus of elasticity, then the stresses on both sides of the specimen were equal as well. That verified the dynamic equilibrium of the confined specimen over the entire test period and confirmed the right selection of specimen's dimensions.

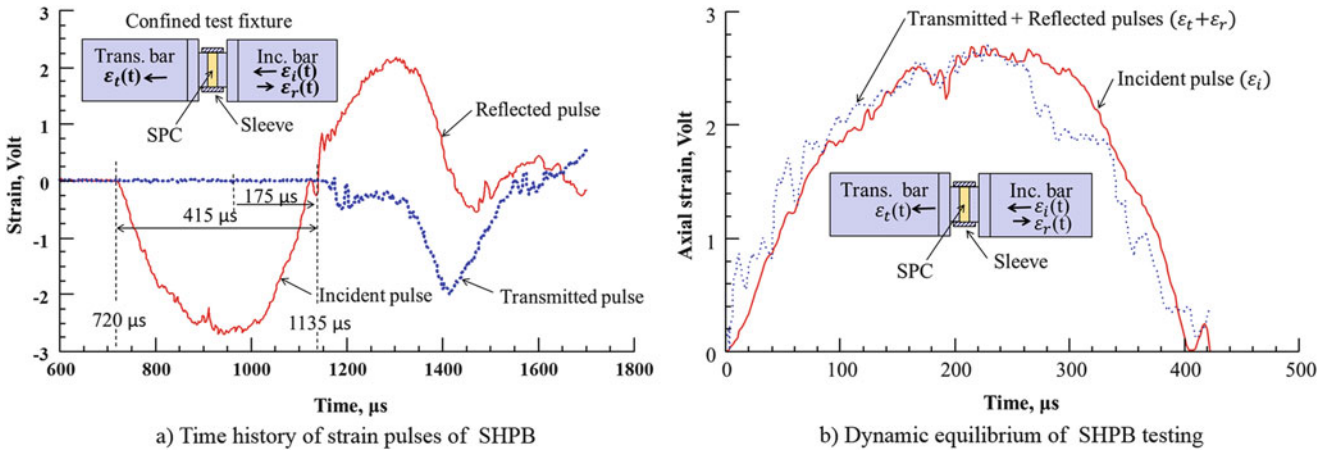

Fig. 9.5 Time history of strain pulses and dynamic equilibrium of confined compression test of Eco-Core at 3120/s

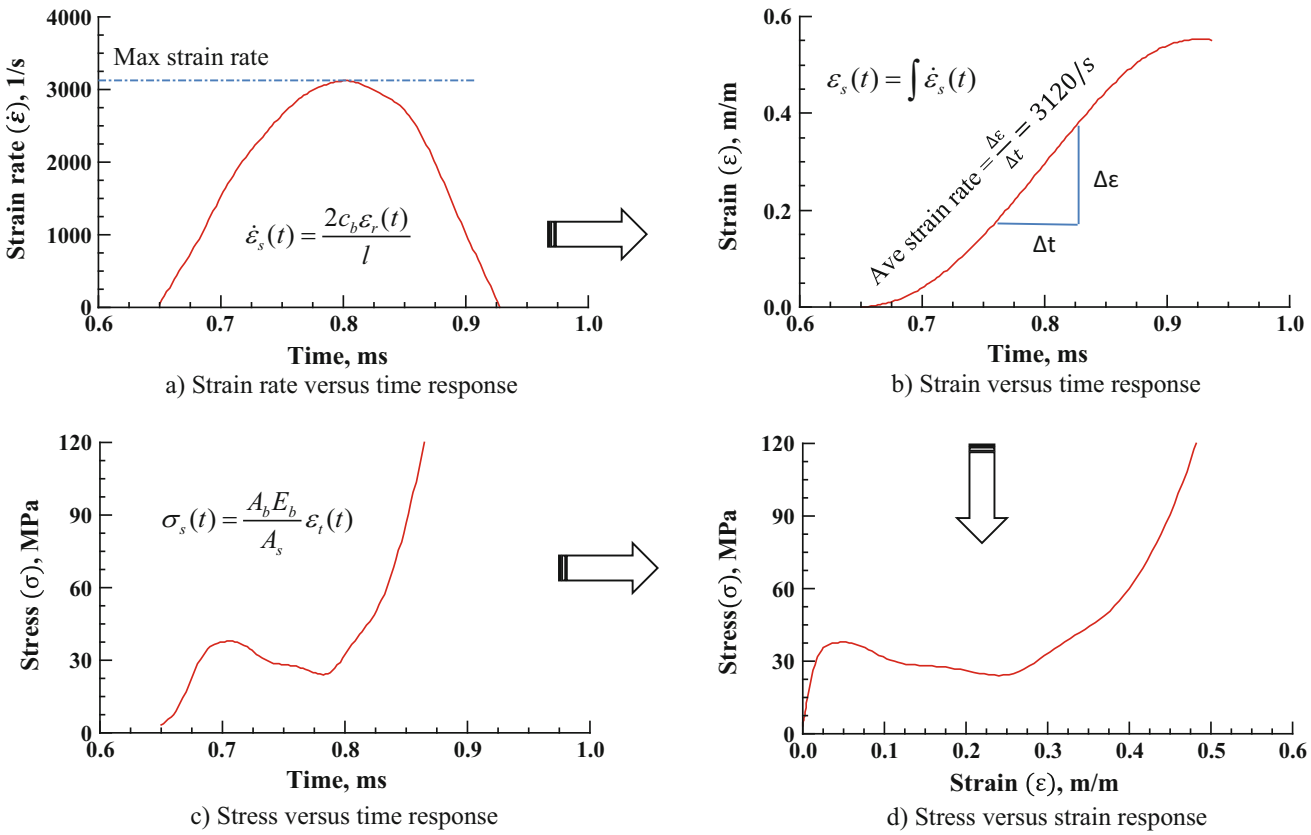

Fig. 9.6 Strain rate, strain and stress versus time responses and stress strain response of Eco-Core at 3120/s strain rate

Basic strain rate, strain and stress results were derived from the reflected and transmitted pulses time history. They were calculated by applying (9.1), (9.2) and (9.3), respectively. The parameters used with the equations were: A_b = 285 mm^2, A_s = 95 mm^2, E_b = 71.7 GPa, C_b = 5051 m/s and l = 3.2 mm. Results were reduced to stress versus strain response. Figure 9.6a–d show respectively the basic strain rate, strain, stress versus time responses and the derived stress versus strain response of Eco-Core at 3120/s. Stress strain responses for three specimens of each core materials were determined. In all cases the three responses agreed very well with each other's to indicate good repeatability of the test. The middle response out of the three responses of each material was used with its associated strain rate for further comparison and analysis.

9.4.2 *Energy Absorption Results*

Energy absorption per unit volume of each core material was calculated from the area under its stress strain response curve until the densification limit (ε_d). Approximated densification limit for each material was determined from the intersection between the tangent to the crushing phase curve and the tangent to the densification phase curve (see Fig. 9.7a). The stress strain response for each of Eco-Core, PVC foam, Balsa wood and Rohacell-A and their densification limits were determined and plotted in Figs. 9.7a–d, respectively. Area under each material response curve was determined by integrating the products of stress of small interval by the stain deference of the interval from 0 to the densification limit as:

$$A = \int_0^{\varepsilon_d} \sigma \, d\varepsilon \tag{9.4}$$

Where σ is the stress of small interval (2 μs) and $d\varepsilon$ is the strain difference during the small interval. The energy absorption per unit volume for all materials were calculated and compared to each other's in Fig. 9.8a. Since the weight of the core material curies significant importance toward its overall properties, then energy absorption per unit mass was calculated as well. It was called specific energy absorption in this study and calculated by dividing the energy absorption per unit volume by the density of the material. Specific energy absorptions for all materials were plotted in Fig. 9.8b.

Also, the energy absorption results for all materials at 3120/s–3490/s strain rates in addition to the densities and static yielding strengths were all summarized in Table 9.1. Results as appear in the last figure and table show that the energy absorption per unit volume of Eco-Core (11 MPa) is more than twice that of Balsa wood (4.4 MPa), more than five time that of PVC foam (1.9 MPa) and more than nine times that of Rohacell A (1.1 MPa). That means energy absorption per unit volume of Eco-Core is superior to other core materials. On the other hand, energy absorption per unit mass of Eco-Core

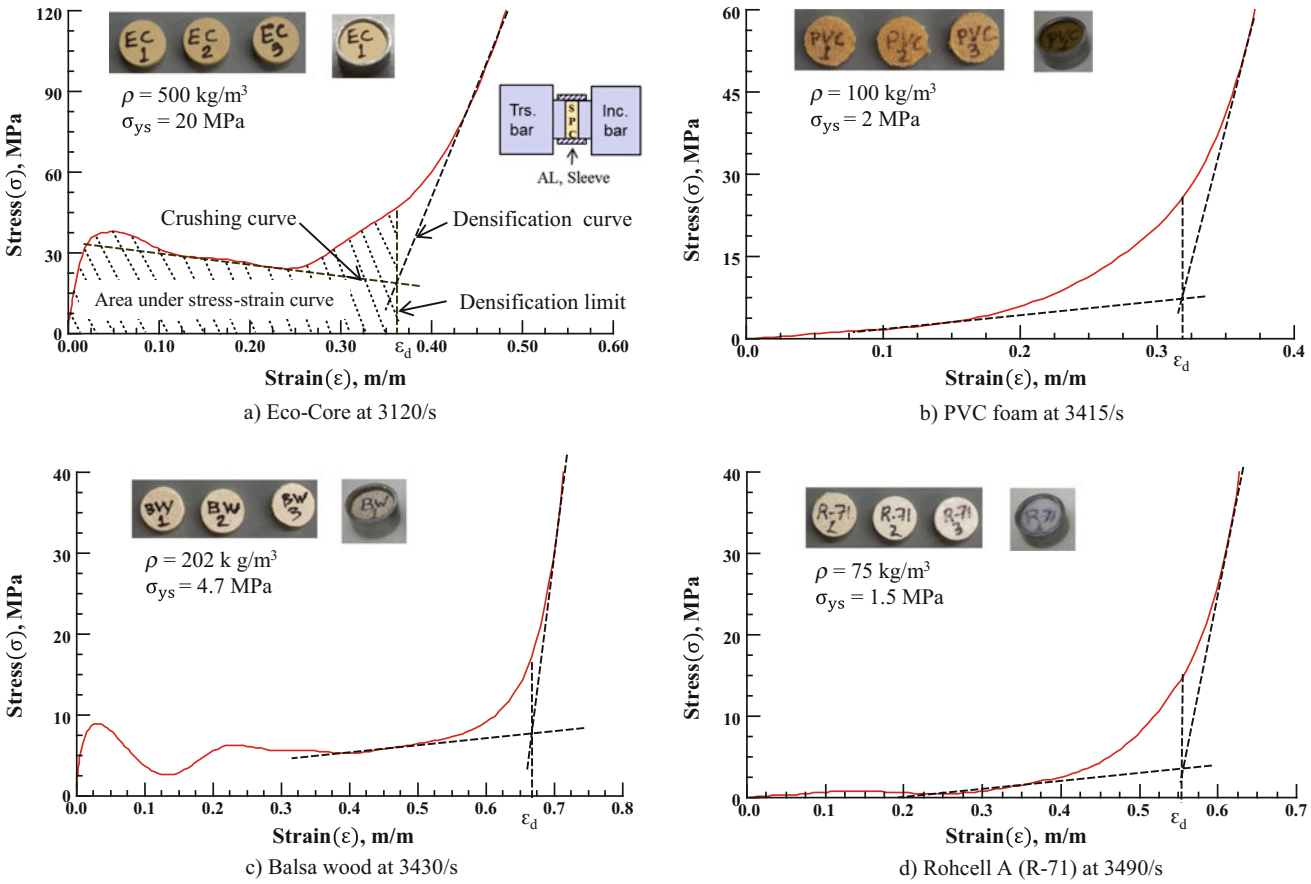

Fig. 9.7 Stress strain responses of core materials and determination of area under responses curves

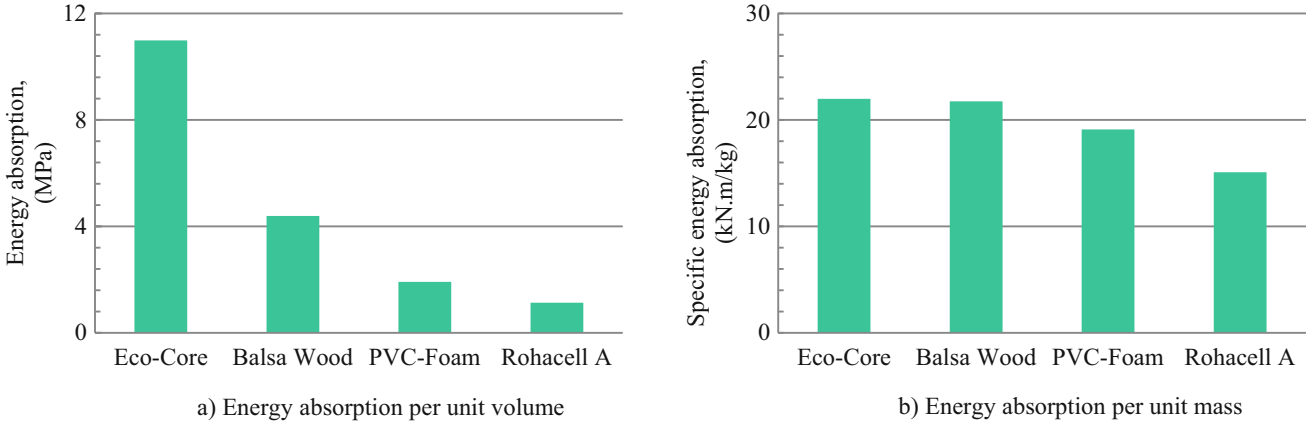

Fig. 9.8 Energy absorption per unit volume and per unit mass for core materials at 3120/s–3490/s strain rates

Table 9.1 Energy absorption per unit volume and per unit mass of core materials at 3120/s–3490/s strain rates

Material	Density, kg/m^3	Static yielding strength, MPa	Energy absorption per unit volume, MPa	Energy absorption per unit mass, kN m/kg
Eco-Core	500	20	11.0	22.0
Balsa wood	202	4.7	4.4	21.7
PVC Foam	100	2	1.9	19.1
Rohacell A (R-71)	75	1.5	1.1	15.1

(22 kN m/kg) is still better than that of other core materials (21.7, 19.1 and 15.1 kN m/kg for Balsa wood, PVC foam and Rohacell A, respectively), but, the difference is marginal. According to these results Eco-Core is highly recommended for applications with fire safety and energy absorptions requirements where weight of the structure is not an important factor like stationary applications as in bunkers. Also, it is still recommended for mobile applications like transportations, air-crafts, aerospace and naval wherever possible.

9.5 Conclusion

High strain rate (3120/s–3490/s) confined compression tests were performed on Eco-Core and other core materials (Balsa wood, PVC foam and Rohacell A). SHPB apparatus along with special test fixture to apply axial and lateral stresses on specimen were used to perform the tests. Specimens of all materials were of 11 mm diameter and 3.2 mm length. Test results showed that the energy absorption per unit volume of Eco-Core (11 MPa) is far superior to other tested commercial core materials (more than twice of Balsa wood the nearest material). The energy absorption per unit mass of Eco-Core (22 kN m/kg) is marginally better than other tested commercial core materials (As good as Balsa wood). Accordingly, Eco-core is highly recommended for stationary applications where the weight is not a significant factor as in stationary applications as in bankers and still recommended for mobile applications like transportations, air-crafts, aerospace and naval wherever possible.

References

1. Song, B., et al.: Confinement effects on the dynamic compressive properties of an epoxy syntactic foam. Compos. Struct **67**(3), 279–287 (2005)
2. Panduranga, R., Russell, L., Jr, Shivakumar, K.: Energy absorption of eco-core a syntactic foam. In 48th AIAA/ASME/ASCE/AHS/ASC Structural, Structural Dynamic and Material Conference, Waikiki, 2007
3. Subhash, G., Liu, Q.: Quasistatic and dynamic crushability of polymeric foams in rigid confinement. Int. J. Impact Eng. **36**(10), 1303–1311 (2009)

4. Kully, R., Shivakumar, K.: Constitutive equation of syntactic foam under lateral constraint. In 29th ASC Technical Conference, San Diego (2014)
5. Rafid Kully, K.S.: Dynamic constitutive equation for a syntactic foam under multi-axial stress state. Dissertation, Mechanical Engineering, North Carolina A&T State University, Greensboro (2014)
6. McMaster-Carr, http://www.mcmaster.com/
7. Chen, W., Zhang, B., Forrestal, M.: A split Hopkinson bar technique for low-impedance materials. Exp. Mech. **39**(2), 81–85 (1999)
8. Salisbury, C.: Spectral analysis of wave propagation through a polymeric Hopkinson bar. Dissertation, Mechanical Engineering, University of Waterloo, Waterloo (2001)
9. Chou, S., Robertson, K., Rainey, J.: The effect of strain rate and heat developed during deformation on the stress-strain curve of plastics. Exp. Mech. **13**(10), 422–432 (1973)
10. Meyers, M.A.: Dynamic Behavior of Materials. Wiley, Hoboken, NJ (1994)
11. Panduranga, R., Shivakumar, K.: The high strain rate compression response of a fire resistant syntactic foam. In 27th ASC Technical Conference, Arlington (2012)
12. Panduranga, R.: High strain rate response of eco-core and its modification. Dissertation, Mechanical Engineering. NC A&T State University, Greensboro (2010)

Chapter 10
Harmonic Vibration Test for the Analysis of the Dynamic Behaviour of Polyurethane Foams

O. Duboeuf, R. Dupuis, E. Aubry, and M. Lauth

Abstract The main goal of this paper is to describe experimental techniques and identification of dynamic properties of flexible polyurethane foam. Indeed, automotive seat comfort level is established with considering quasi-static—density core, hysteresis loss and compression stress— and dynamic— transmissibility and damping— properties of flexible polyurethane foams. Our dynamic system, modeled as a single degree-of-freedom system, is composed of an experimental device with a free mass on the top and a shaker on the basement. The first one, a rigid block, is mounted on a 100 × 100 × 50 mm cube sample of foam material and the second one excites the device with harmonic vibration. The steady-state response of a polyurethane foam sample—after the same number of cycles—to harmonic vibration is analyzed for different excitation amplitude level and for different initial compression level, corresponding respectively to various road surface conditions and to various apparent-mass. The transmitted vibration between the shaker and the free mass is measured to determine the damping effect and the filter band of polyurethane foam, and enables to trace the Bode magnitude and phase plots of the dynamic stiffness function of the system. The results presented here compare three types of foams.

Keywords Polyurethane foams • Dynamic behavior • Dynamic stiffness function • Harmonic vibration • Bode plots

10.1 Introduction

Comfort in automotive applications is not just driving pleasure; it is the best player for the safety and health of passengers of the vehicle. For example, an uncomfortable seat transmits vibrations from the road, the engine, and the frame to the occupant and therefore can leads to back and neck pain due to poor filtration. The effect of these vibrations on health is a known phenomenon and has been already studied by many Scientists [1]. But the remaining key point is still "how can we make them more comfortable?"

A full seat consists of a frame, foam paddings and a headrest. Flexible polyurethane foam (PU foam) is very often used in automotive seat padding comfort application. Indeed, PU foam is characterized by a large spectrum of mechanical properties [2] such as: low density, the ability to absorb the strain energy and low stiffness. Moreover, by modifying the chemical formulation of foam, it is also possible to impact upon the static and dynamic mechanical properties, and consequently upon the comfort of seat users.

Using the mechanical field, we can study foam by four different ways: static behavior [2–4], quasi-static behavior [5–8], dynamic behavior [8–12] and ageing behavior [13, 14]. All this ways are a part of the comprehension of behavior of automotive seating, together with other test such as approach comfort, ride comfort and overall durability of seat. To control the vibration transmitted to the seat and then to increase the comfort, we need to model a complex mechanical behavior of polyurethane foams and therefore to identify its dynamic and quasi-static properties. In our study, using our harmonic vibration test method, three kinds of foams with similar properties are tested. This paper explains the test method and operation results we have obtained.

O. Duboeuf (✉)
Laboratoire MIPS, Université de Haute Alsace, 12 rue des frères Lumière, Mulhouse 68093, France

Laboratoire R&D Foam Chemistry, Faurecia Automotive Seating, 17 rue de la Forge, Lure 70202, France
e-mail: olivier.duboeuf@uha.fr

R. Dupuis • E. Aubry
Laboratoire MIPS, Université de Haute Alsace, 12 rue des frères Lumière, Mulhouse 68093, France

M. Lauth
Laboratoire R&D Foam Chemistry, Faurecia Automotive Seating, 17 rue de la Forge, Lure 70202, France

B. Song et al. (eds.), *Dynamic Behavior of Materials, Volume 1*,
Conference Proceedings of the Society for Experimental Mechanics Series, DOI 10.1007/978-3-319-22452-7_10

10.2 Experimental Study: Tested Materials

In this work, we study polyurethane foams, designed by Foam A, B and C, large used in automotive seating application and whose chemical, morphological and mechanical properties are shown in Table 10.1. As you can notice those characteristics are similar in term of chemistry, only the quantity of reinforcing particulate copolymer polyol (CPP) is different. Copolymer polyol plays a great role in polyurethane foam formulation. It is a "grafted" polyol, used to improved hardness, strength, foam processing, and cell opening. It also increases the cross-linking degree [15].

Density, compression stress and resilience are determined by the methods recommended in standards ASTM D3574 [16]. The average cell size is determined through the Microvision-Ellix device and an adaptation of "Visiocell" method detailed in the study of Ju [17].

10.3 Experimental Methodology

All the tests presented in this paper have been carried out on a vibration-testing device, shown in Fig. 10.1. It is composed by a shaker on the basement (INSTRON 8800), a bottom plate fixed on the basement and a sliding top plate guided in a single direction of translation by four guides. To limit the internal friction of the stems on the guides (e.g. ball bearings), our experimental setup uses air bearing. The friction coefficient is then practically zero. Between the two plates, a cubic sample of foam is fixed.

The actuator is used to create the excitation signal whose characteristics will be given later. During the tests, the displacement of the bottom plate x_{bottom} (t) (displacement under the foam sample) and the displacement of the sliding top

Table 10.1 Chemical, morphological and mechanical foams characteristics

Designation	Foam A	Foam B	Foam C
Foam types	Flexible	Flexible	Flexible
Isocyanate	TDI-LVOC	TDI-LVOC	TDI-LVOC
Polyol—CPP rate	Polyol PA—**15 parts**	Polyol PA—**30 parts**	Polyol PA—**55 parts**
Water rate	3.5 parts	3.5 parts	3.5 parts
Fabrication process	Molded	Molded	Molded
Type of cells	Open	Open	Open
Dimensions ($L_0 \times l_0 \times h_0$) m^3	0.1 × 0.1 × 0.05	0.1 × 0.1 × 0.05	0.1 × 0.1 × 0.05
Density ($kg.m^{-3}$)	45	46	46
Compression stress (kPa)	5.8	8.1	10.4
Resilience (%)	81	78	74
Average cell size (μm)	424	428	430

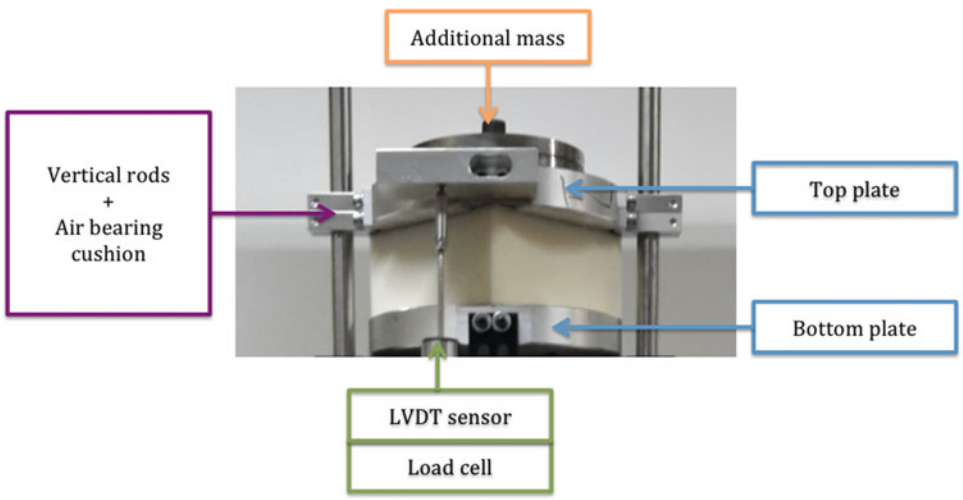

Fig. 10.1 Testing device

Table 10.2 Initial compression levels for three tests

Test	Designation (%)	Foam A	Foam B	Foam C
Test 1	Initial compression level for preload M1	3.0	2.5	1.5
Test 2	Initial compression level for preload M2	15.0	7.5	5.0
Test 3	Initial compression level for preload M3	33.5	16.5	8.0

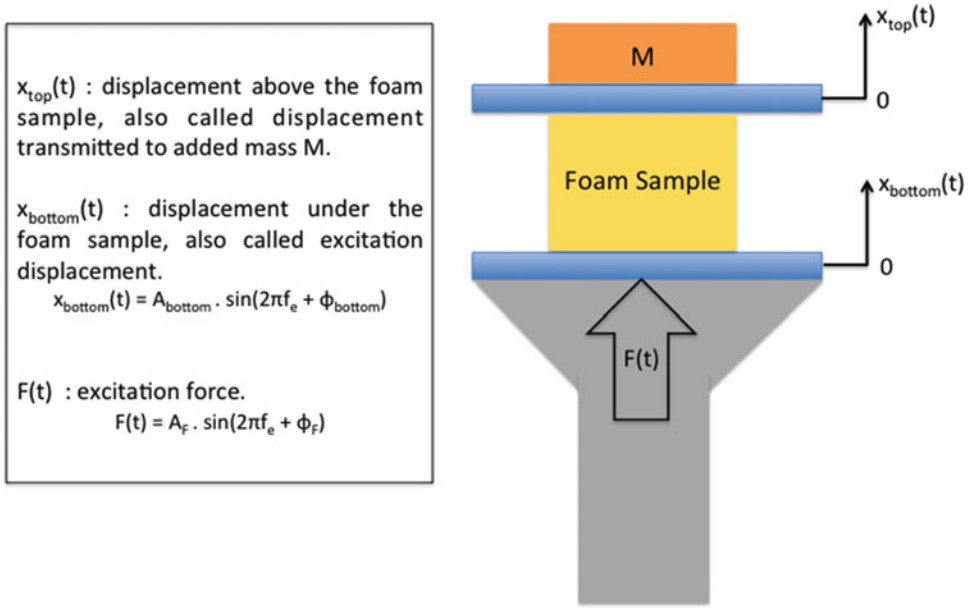

Fig. 10.2 Schematization of the testing procedure

plate x_{top} (t) (displacement above the foam sample) are measured with LVDT linear sensors. We also measured the excitation force under foam sample $F(t)$ with a load cell placed between the actuator and the base plate.

Actually, the initial compression level of the foam car seat is a function of the occupant weight. In this study, we compare the three foams for three "persons" (about 5th, 50th andt 90th percentile), so for three preload above the sample. As a result, put the same additional mass M on the three samples induce different initial compression levels (Table 10.2) due to different compression stress.

The harmonic vibration test consists in shaking the bottom plate with a sinusoidal signal. The excitation frequency f_e is varying from initial value $f_{min} = 1$ Hz to final value $f_{max} = 20$ Hz by raising step of 0,5 Hz. The foam is excited for a significant amount of cycles at each frequency to achieve a steady state (about 100 cycles). Then, the three measurements (displacement of the sliding top plate, displacement of the bottom plate and excitation force under foam sample) are recorded during 100 cycles. A Fourier Transforms are finally realized on each signal recorded. To make sure the repeatability of our tests, each trial is carried out at least three times, always with a new sample of foam from the same population.

The Fig. 10.2 displays a schematization of the experimental test device, signals and procedure.

In this work, all samples used in harmonic vibration test have the same mechanical and environmental histories: they are virgin, extracted from the core of a new foam molded block (0.4 × 0.4 × 0.07 m) produced in laboratory, cut to the following dimensions 0.1 × 0.1 × 0.05 m and being conditioned during at least 24 h in a climate room (temperature at 23 (±2) °C and relative humidity at 50(±5) %).

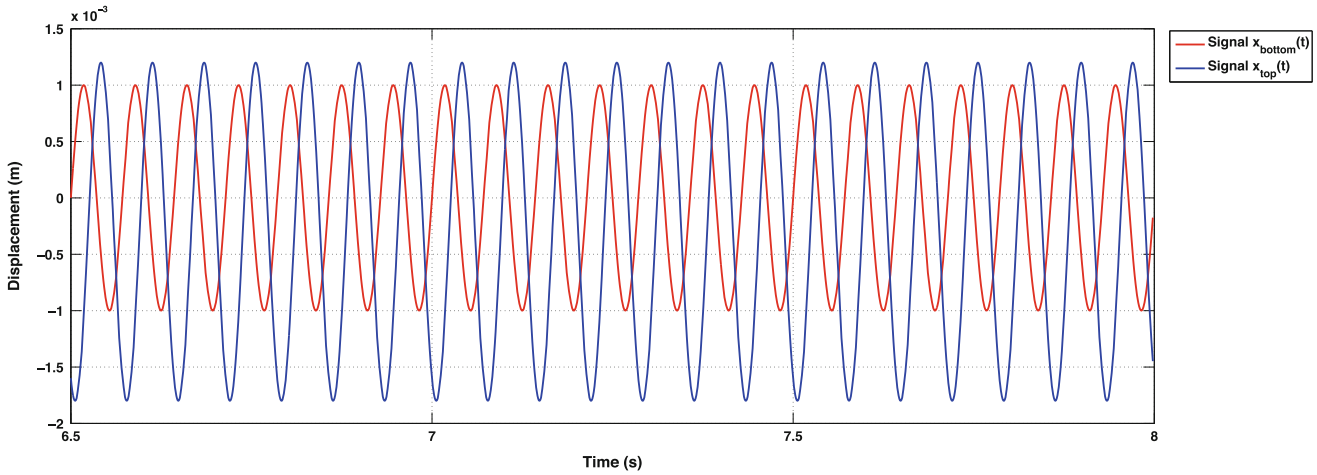

Fig. 10.3 Difference between $x_{top}(t)$ and $x_{bottom}(t)$ at 14 Hz

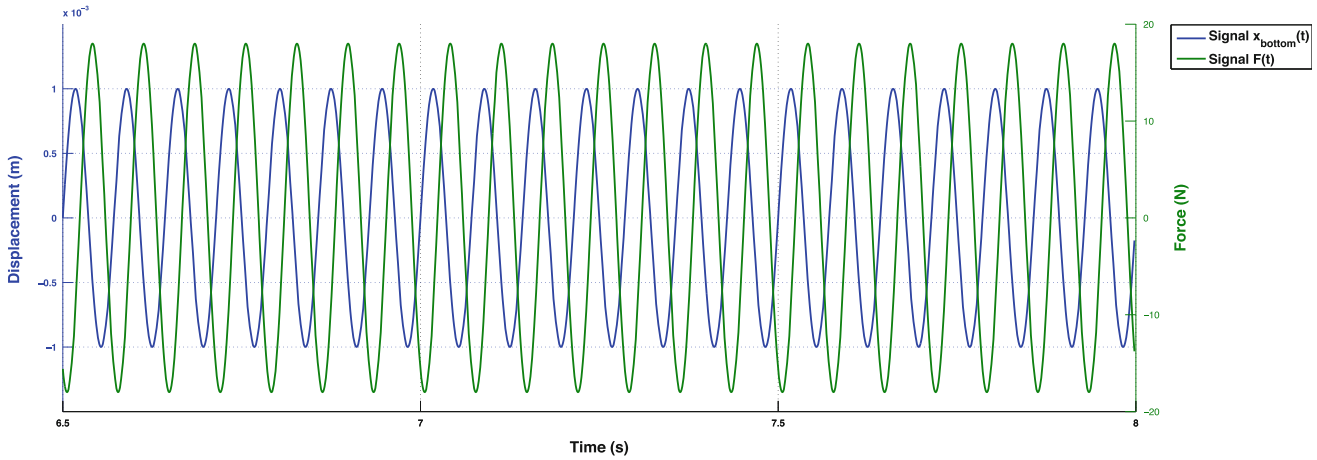

Fig. 10.4 Difference between $x_{top}(t)$ and F(t) at 14 Hz

10.4 Results and Discussions

10.4.1 Time Domain Analysis

At first, to prove that the dynamic behavior of the polyurethane foam is complex, we observed the two temporal signals recorded. On the one hand, we have the excitation displacement (displacement under the foam, $x_{bottom}(t)$) and on the other hand, we have the displacement transmitted to the free mass (displacement above the foam, $x_{top}(t)$). They have both the same main frequency in the steady state, but the second one present a permanent and constant offset to the initial position. This offset depends on the frequency value. This offset is due to several facts. Indeed, after each loading and unloading cycle, we can observe an accumulation of residual strain. This phenomenon is also observable in the quasi-static behavior (Fig. 10.3).

The evaluation two temporal signals recorded could also be with the excitation force under the foam $F(t)$ and the displacement transmitted to the free mass $x_{top}(t)$. In the same way, there is an offset between 0 and $\frac{\pi}{2}$ at various excitation frequencies, due to the viscoelastic behavior of the polyurethane foam (Fig. 10.4).

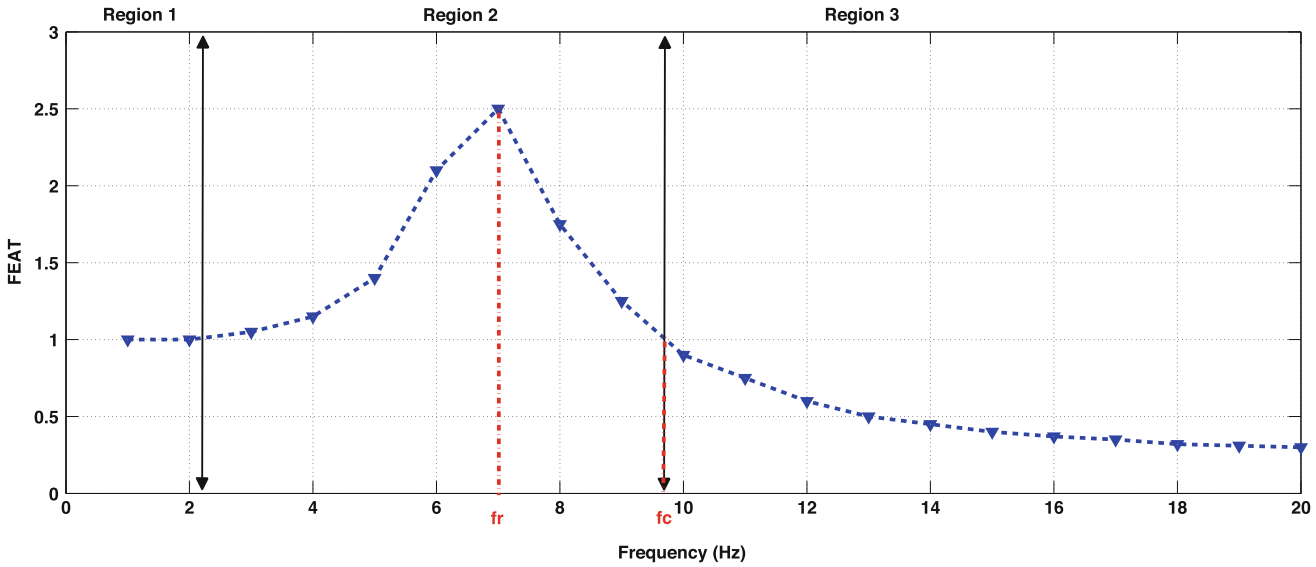

Fig. 10.5 Example for a FEAT ratio

10.4.2 Frequency Response Analysis

There are several methods to evaluate the comfort of a car seat. For example, automotive OEM's calculate the ratio between the vibration level above the car seat (on the passenger) and the excitation at the basement of the seat (due to engine, structure and road vibrations) [18]. This one is known as "SEAT factor" (Seat Effective Amplitude Transmissibility). All information about this method to evaluate seat comfort is detailed in ISO 2631-1 standard [19].

In the same way, our laboratory uses a ratio to determine the ability of the foam to reduce vibrations. This ratio is known as "FEAT factor" for "Foam Effective Amplitude Transmissibility" which is calculated following a sinusoidal excitation at constant amplitude and constant frequency for each initial compression level [8]. FEAT ratio is:

$$FEAT\ (A_{bottom}, f_e) = \frac{RMS_{top}}{RMS_{bottom}} = \sqrt{2}\,\frac{RMS_{top}}{A_{bottom}} \tag{10.1}$$

where:

- RMS_{top} is the root mean square values of free mass displacement above the foam sample.
- A_{bottom} is the amplitude of the excitation sinusoidal signal.

As shown on the Fig. 10.5, we can divide the FEAT representation into three regions. In the first one, FEAT ratio is equal to one. The foam has a rigid body behavior. The vibration is transmitted through the foam without amplification or attenuation. Then, FEAT ratio is greater than 1. The level of vibration transmitted by the foam is amplificated. This region could be divided into two sub-regions: FEAT ratio is growing up from one to a maximal value, the natural frequency f_r, in the resonance region and then, it is decrease until the value one, the filtration frequency f_c. All the frequency between 1 Hz and the filtration frequency is the bandwidth. In the bandwidth, the foam is always transmitting or amplifying the excitation signal. It is the worst frequency region for a passenger on a seat. The third region is the most interesting and attractive for passengers. Indeed, the FEAT ratio is under one, so the level of vibration transmitted by foam is lower than the excitation level. This is the foam vibration damping power.

All the test presented here has been proceed on the three foams A, B and C. Table 10.3 presents the dynamic characteristics resulting of the harmonic vibration tests and Fig. 10.6 shows this results.

As it was explained before, reinforcing particulate copolymer polyol (CPP) is used to increase the cross-linking degree. We can observe an impact on the compression stress and the resilience after four cycles. A higher content of copolymer polyol into the formulation will lead to harder foam characterized by a higher compression stress and a lower resilience.

Moreover, compression stress and resilience are immediately in relation with dynamic results. Indeed, the FEAT ratio is greater when the resilience is lower, and the natural frequency is lower when the compression set is lower too.

Table 10.3 Dynamic characteristics of our foams for different preload

Dynamic results	Foam A			Foam B			Foam C		
Preload (kg)	M1	M2	M3	M1	M2	M3	M1	M2	M3
Natural Frequency f_r (Hz)	7.5	5.3	3.7	10.0	7.2	5.4	13.0	10.0	8.0
Maximal FEAT value	2.5	2.4	2.6	2.7	2.6	2.4	3.1	2.8	2.6
Filtration frequency f_c (Hz)	9.0	6.7	5.2	12.4	9.2	6.8	15.5	12.3	9.7
Stiffness (N/m)	6662	4353	2659	11891	8277	5820	20,077	15,634	12,602
Damping (N.s/m)	37.2	39.2	46.2	31.9	44.4	50.6	33.1	42.2	48.1

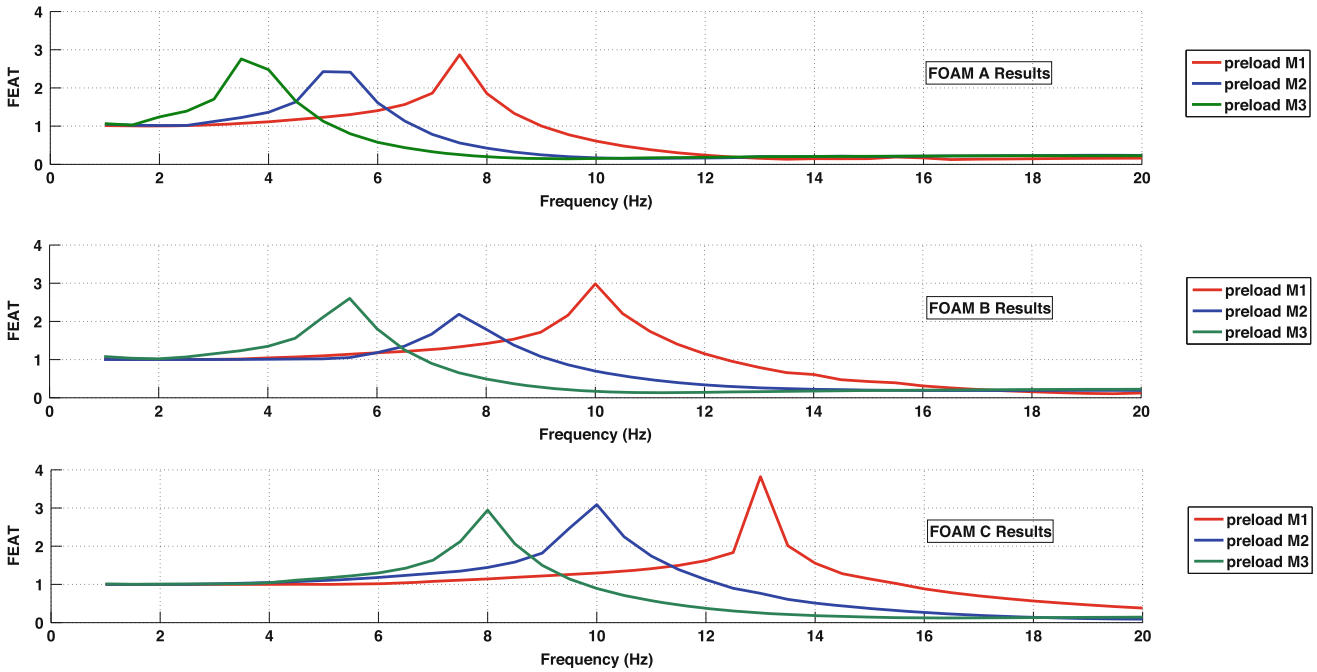

Fig. 10.6 FEAT ratio for each foams at different preload

As shown in Table 10.3, dynamic characteristics of foam are in relation with stiffness and damping effect. A foam, whose CPP rate level is low, will have a shorter bandwidth and therefore better vibration filtration power. In the opposite side, the amplification at natural frequency will be smaller. A foam with a high CPP rate level will have a greater bandwidth so a lower vibration filtration power.

In addition, the loading upon a seat (i.e. the initial compression level, representing normal human weight on cushion) changes its physical characteristics. As we know, stiffness is directly function of both the mass and the natural frequency. In addition, damping is also related to the mass, the natural frequency and the quality factor (in relation with the maximum value FEAT). Therefore, loader the seat will be charged, lower will be its natural frequency and filtration frequency.

10.5 Conclusions

This experimental study shows that the dynamic behavior of our polyurethane foams has a complex behavior. The study of the influence of the copolymer polyol in the initial formulation shows that the natural frequency and filtration frequency have been improved while the copolymer polyol rate is lower, for a specified compression stress.

In addition, the amplitude level of the excitation as well the initial quasi-static compression level given by the customer passenger are also following the same trade. Thus, the choice of the polyurethane foam for a given application must be carried out through a statistical study of the real solicitation conditions (range of dominant frequency of excitation, the highly probable excitation levels, etc.).

References

1. Rakheja, S., Dong, R.G., Patra, S., Boileau, P.E., Marcotte, P., Warren, C.: Biodynamics of the human body under whole-body vibration: synthesis of the reported data. Int. J. Ind. Ergon. **40**(6), 710–732 (2010)
2. Gibson, L.J., Ashby, M.F.: Cellular Solids: Structure and Properties, 2nd edn. Cambridge University Press, Cambridge (1997)
3. Goangseup, Z., Byeong, M.K., Yoon, K.H., Young, H.L.: An experimental study on static behaviour of a GFRP bridge deck filled with a polyurethane foam. Compos. Struct. **82**(2), 257–268 (2008)
4. Tu, Z.H., Shim, V.P.W., Lim, C.T.: Plastic deformation modes in rigid polyurethane foam under static loading. Int. J. Solids Struct. **38**(50–51), 9267–9279 (2001)
5. Dupuis, R., Aubry, E.: Development and comparison of foam comprehensive law in great deformation. In SEM XI International Congress, Orlando (2008)
6. Ouellet, S., Cronin, D., Worswick, M.: Compressive response of polymeric foams under quasi-static, medium and high strain rate conditions. Polym. Test. **25**(6), 731–743 (2006)
7. Deng, R., Davies, P., Bajaj, A.K.: A nonlinear fractional derivative model for large uni-axial deformation behaviour of polyurethane foam. Signal Process. **86**(10), 2728–2743 (2006)
8. Jmal, H.: Identification du comportement quasi-statique et dynamique de la mousse de polyurethane au travers de modèles à mémoire. Ph.D. thesis, Univesité de Haute-Alsace, Mulhouse (2012)
9. Deng, R.: Modeling and characterization of flexible polyurethane foam. PhD thesis, School of Mechanical Engineering, Purdue University, West Lafayette (2004)
10. Singh, R., Davies, P., Bajaj, A.K.: Initial condition response of a viscoelastic dynamical system in the presence of dry friction and identification of system parameters. J. Sound Vib. **239**(5), 1086–1095 (2001)
11. Singh, R., Davies, P., Bajaj, A.K.: Estimation of dynamical properties of polyurethane foam through use of Prony series. J. Sound Vib. **264**(5), 1005–1043 (2003)
12. White, S.W.: Dynamic modelling and measurement of occupied car seats and seating foam. Master's Thesis, School of Mechanical Engineering, Purdue University, West Lafayette (1998)
13. Bezazi, A., Scarpa, F.: Tensile fatigue of conventional and negative Poisson's ratio open cell PU foams. Int. J. Fatigue **31**(3), 488–494 (2009)
14. Rizov, V., Mladensky, A.: Model fatigue fracture behavior of Divinucell H-30 structural foam—a non-linear approach. Comput. Mater. Sci. **46** (1), 255–260 (2009)
15. Kaushiva, B.D., Dounis, D.V., Wilkes, G.L.: Influences of copolymer polyol on structural and viscoelastic properties in molded flexible polyurethane foams. J. Appl. Polym. Sci. **78**, 766–786 (2000)
16. ASTM D 3574-86, Test B1, Standard Methods of Testing Flexible Cellular Materials—Slab, Bonded, and Molded Urethane Foams
17. Ju, M.: Contribution à la modélisation du comportement visco-hyper-élastique de mousses de polyurethane—Validation expérimentale en quasi-statique. PhD thesis, Université de Haute-Alsace, Mulhouse (2014)
18. Gunaselvam, J., Van Niekerk, J.L.: Seat selection guidelines to reduce whole-body vibration exposure levels in the SA mining industry. J. South. Afr. Inst. Min. Metall. **105**(10), 675–686 (2005)
19. ISO 2631-1:1997, Mechanical vibration and shock—evaluation of human exposure to whole-body vibration—Part 1: general requirements

Chapter 11
Statistical Characterizations for Tensile Properties of Co-polymer Aramid Fibers: Loading Rate Effects

J.H. Kim, N.A. Heckert, Kai-Li Kang, W.G. McDonough, K.D. Rice, and G.A. Holmes

Abstract High strength polymer fibers such as poly(*p*-phenylene terephthalamide) (PPTA), and poly(*p*-phenylene benzobisoxazole), (PBO) have been used for ballistic body armors. In addition to these para-oriented fibers, copolymer aramid fibers are being considered. Although mechanical properties of these fibers measured under quasi-static loading conditions are reported to be excellent, fiber tensile properties measured at comparable loading conditions for ballistic impact are rarely reported. In this study, we measure single fiber tensile properties at high rate loading conditions by clamping a fiber to the grips of a mini Kolsky bar, and investigate their statistical distributions as well as fiber morphologies.

Keywords Single fiber • Tensile test • Co-polymer aramid fiber • Statistical analysis • High strain rate

11.1 Introduction

Soft body armors (SBAs) to protect the human body from ballistic impact typically consist of high strength polymer fibers. Polymer fibers used in armor application include poly(*p*-phenylene benzobisoxazole) (PBO), ultra high molecular weight polyethylene (UHMWPE) fibers, and poly(*p*-phenylene terephthalamide) (PPTA). A co-polymer aramid fiber containing 5-amino-2-(p-aminophenyl)-benzimidazole is also being considered in armor applications. Numerous studies on PPTA and UHMWPE fiber have been carried out, but mechanical properties of co-polymer aramid fiber are rare.

When a projectile strikes fibers of body armor, longitudinal and transverse waves propagate from the impact zone, which create fiber deformations in several different directions (i.e. tension along the longitudinal, transverse and deflection of fibers) over a short period of time. Among the many parameters influencing performance of SBA, the material properties are critical such as dimensionless fiber property defined by the product of the specific fiber toughness and tensile wave velocity [1]. Until recently, tensile tests to measure fiber properties at strain rates comparable to those of ballistic impact were carried out using yarns assumed to be sharing an equal load. In order to measure fiber tensile properties at high strain rates, a miniaturized tension Kolsky bar has been developed [2], and a single fiber gripping method specifically adopted to increase test throughput [3].

Fiber strengths obtained by the single fiber tensile test typically exhibit large variation, so statistical analyses are often carried out to model dispersions of strength data. Weibull analyses for single fiber strengths are carried out here to investigate the effects of loading rate on tensile strengths of co-polymer aramid fibers.

J.H. Kim • W.G. McDonough • G.A. Holmes (✉)
Materials Science and Engineering Division (M/S 8541), National Institute of Standards and Technology, Gaithersburg, MD 20899, USA
e-mail: gale.holmes@nist.gov

N.A. Heckert
Statistical Engineering Division (M/S 8980), National Institute of Standards and Technology, Gaithersburg, MD 20899, USA

K.-L. Kang • K.D. Rice
Materials Measurement Science Division (M/S 8102), National Institute of Standards and Technology, Gaithersburg, MD 20899, USA

B. Song et al. (eds.), *Dynamic Behavior of Materials, Volume 1*,
Conference Proceedings of the Society for Experimental Mechanics Series, DOI 10.1007/978-3-319-22452-7_11

11.2 Ballistic Models

Numerous models have been developed to analyze the ballistic performance of SBAs, including semi-empirical [4], analytical [5, 6] and numerical models [7, 8]. Figure 11.1 illustrates an orthogonal woven fabric with 2-dimensional rhombus shaped deformation from an impact on a three-dimensional tetrahedron shape [6]. In this model, planer woven fabric is modeled as perpendicular crossed nonwoven yarns (i.e. weft and warp). The strain energy of fabrics can be divided into two parts: one the result of the fracture work of yarns (i.e. principal yarns) contacted by the projectile, the other the elastic strain energy and plastic strain energy of yarns affecting the rhombus region excluding principal yarns.

That the total energy (W) of single layer fabric is equal to the sum of strain energy (W_s) and kinetic energy (W_k) can be verified experimentally:

$$W = W_s + W_K = \frac{1}{2}m\left(V_i^2 - V_r^2\right) \tag{11.1}$$

where V_i and V_r are initial and residual velocities (after the impact) of the projectile. The strain energy and kinetic energy of the multiple layers of the fabric are equal to the product of absorbed energy for single layers and the number of layers. The time interval Δt from the beginning of impact to the yarn breakage (or projectile arrest) is used to calculate the kinetic energy of the projectile. Δt is estimated from strain rate ($\dot{\varepsilon}$) by:

$$\Delta t = \frac{\Delta\varepsilon}{\dot{\varepsilon}} \tag{11.1}$$

where $\Delta\varepsilon$ is defined as $\varepsilon_{max} - \varepsilon_{ins}$, and ε_{ins} is the instantaneous strain in fiber induced by a longitudinal wave. The strain rate used in the reference [6] was in the range of 500–1500 s^{-1} depending on the projectile velocity.

11.3 Experimental Procedure

11.3.1 Fiber Samples and Single Fiber Tensile Tests

Single co-polymer aramid fibers were collected from yarns in plain woven fabric. Fibers in yarns were held tightly so separation of single fibers from yarn required very careful handling. PMMA (poly(methyl methacrylate)) was used as clamping material for the single fiber tensile tests based on a previous study [3]. For the quasi-static loading, a single fiber was clamped in the grips of a screw-driven machine with approximately 1 mN of pretension using a weight. Fiber lengths of 2, 5, and 8 mm were used as gauge lengths. For the high rate loading, the miniaturized Kolsky bar was used in conjunction with a quartz-piezoelectric load cell due to a very small transmitted force signal through a single fiber. A laser optical system [9] was used to measure the displacement of the Kolsky bar. Fiber lengths of 2, 5, and 8 mm were used as the gauge lengths of the high rate tests and fiber diameters were measured over five equally spaced locations for each fiber under optical microscope using × 60 objective lens and CCD camera.

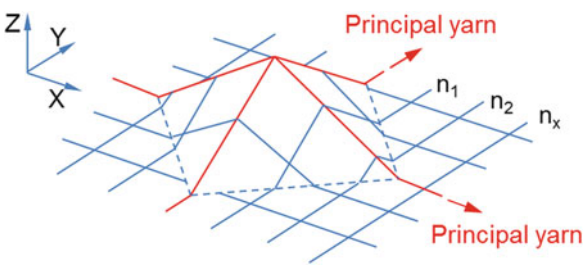

Fig. 11.1 Schematic of the impact model for orthogonal woven fabric and 2-dimensional rhombus region deformed from the impact

11.4 Results and Discussion

11.4.1 Fabric and Fiber Surface Conditions

Figure 11.2 shows an image of fabric surfaces obtained by an optical microscope and fiber surface images taken by scanning electron microscope. A single yarn with approximately 0.8 mm width was carefully divided in several subgroups. Some of the separated fibers displayed an uneven surface that appears to consist of additional layers. Since the fibers were collected from a woven fabric, one might expect that this resulted from additional weaving processes for the virgin fibers.

11.4.2 Graphical Statistical Analyses of the Tensile Strengths

The fiber tensile strengths obtained by the quasi-static test were investigated graphically using nonparametric analyses. Figure 11.3 shows a relative histogram of the tensile strength at 5 mm. A relative histogram is normalized so that the area under the histogram, rather than the sum of the relative counts, is equal to 1. Thus, the histogram represents an estimate of the underlying probability density. The main peak location in Fig. 11.2 is between 3.5 and 4 GPa, although smaller values are also exhibited below 3 GPa.

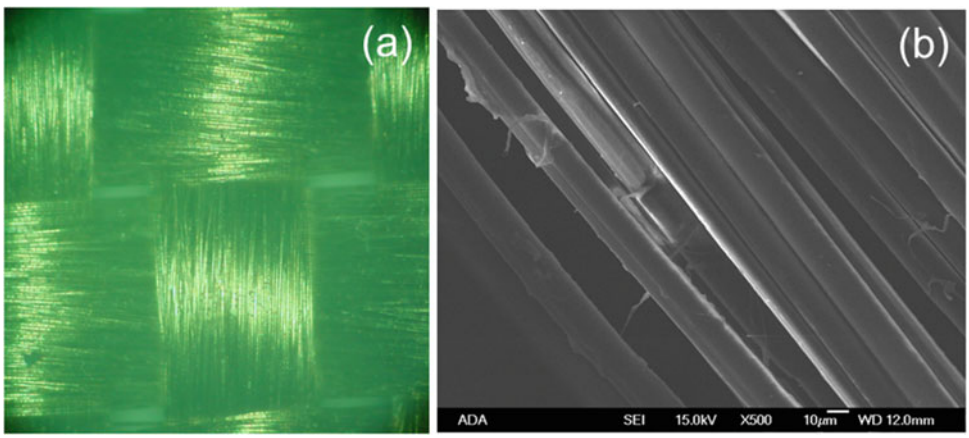

Fig. 11.2 The optical image of the fabric (**a**) and (**b**) electron microscopic image of co-polymer fibers

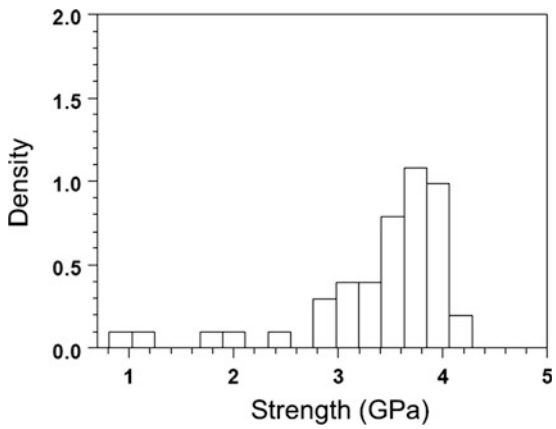

Fig. 11.3 The relative histogram for the tensile strengths of the 5 mm fibers

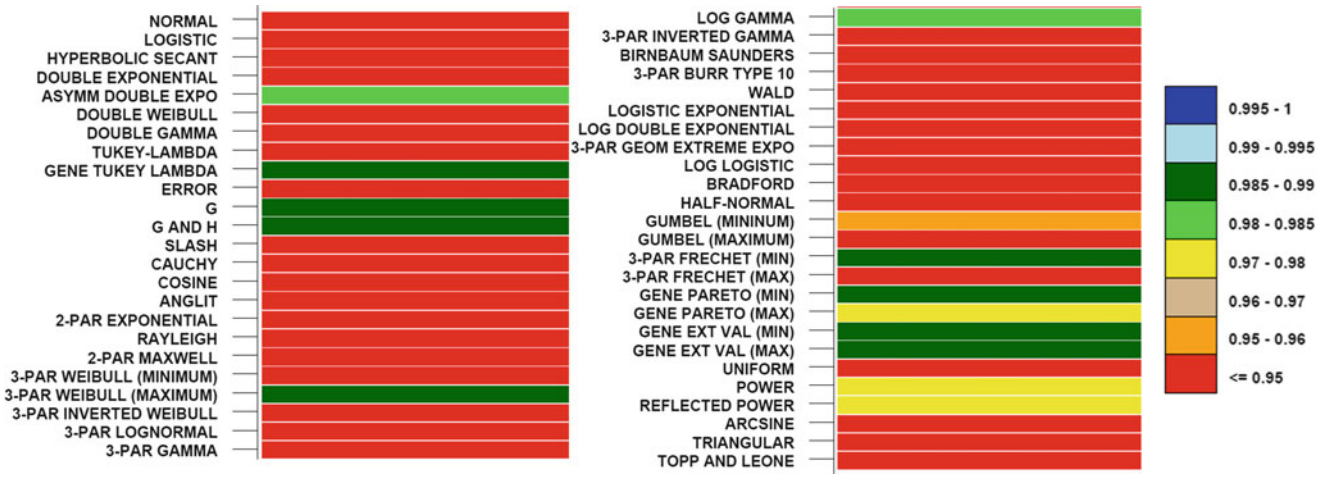

Fig. 11.4 Color-coded screening plots comparing goodness-of-fit by PPCC criterion for tensile strengths for the 5 mm fibers

11.4.3 Screening Goodness of Fit

Screening plots to find potentially best fitting distributions were carried out using a PPCC (probability plot correlation coefficient)-based algorithm. The PPCC goodness of fit criterion is based on the correlation coefficient of the line fitted to the points on a probability plot for the given distribution. Therefore, higher PPCC values mean better fit with the given distribution. In Fig. 11.4, a screening plot of the fiber strengths obtained using 5 mm fibers is shown with PPCC values. Dark blue (PPCC $>$ 0.99) and cyan (PPCC $>$ 0.995) indicate good to excellent fit, green (PPCC $>$ 0.98) and dark green (PPCC $>$ 0.985) indicate acceptable fit, and brown, orange, and red indicate poor fit (PPCC $<$ 0.95). Yellow indicates (0.97 $<$ PPCC $<$ 0.98) marginal fit. Most distributions exhibit poor fits with the strengths of the 5 mm fiber, with PPCC values lower than 0.95. Considering the surface conditions of the separated fibers and dispersion of the relative histogram, apparent poor fits for the distributions are probably attributed to dispersion in the lower tail.

11.5 Concluding Remarks

Single co-polymer aramid fibers were collected from a plain woven fabric and their strengths were measured under quasi-static condition. The fiber surface after separation from the yarn showed unevenness. A normalized histogram for the tensile strengths of 5 mm fibers showed relatively wide dispersion in the lower tail. The presence of strengths in the lower tail could explain the generally poor fits of the screening plot.

References

1. Cheeseman, B.A., Bogetti, T.A.: Ballistic impact into fabric and compliant composite laminates. Compos. Struct. **61**(1–2), 161–173 (2003)
2. Cheng, M., Chen, W., Weerasooriya, T.: Experimental investigation of the transverse mechanical properties of a single Kevlar KM2 fiber. Int. J. Solids Struct. **41**(22–23), 6215–6232 (2004)
3. Jae Hyun, K., Heckert, N.A., Mates, S.P., Seppala, J.E., McDonough, W.G., Davis, C.S., Rice, K.D., Holmes, G.A.: Effect of fiber gripping method on the single fiber tensile test: II. Comparison of fiber gripping materials and loading rates. J. Mater. Sci. **50**(5), 2049–2060 (2015)
4. Cunniff, P.M.: A semiempirical model for the ballistic impact performance of textile-based personnel armor. Text. Res. J. **66**(1), 45–59 (1996)
5. Phoenix, S.L., Porwal, P.K.: A new membrane model for the ballistic impact response and V-50 performance of multi-ply fibrous systems. Int. J. Solids Struct. **40**(24), 6723–6765 (2003)
6. Gu, B.H.: Analytical modeling for the ballistic perforation of planar plain-woven fabric target by projectile. Compos. Part B **34**(4), 361–371 (2003)

7. Grujicic, M., Glomski, P.S., He, T., Arakere, G., Bell, W.C., Cheeseman, B.A.: Material modeling and ballistic-resistance analysis of armor-grade composites reinforced with high-performance fibers. J. Mater. Eng. Perform. **18**(9), 1169–1182 (2009)
8. Grujicic, M., Glomski, P.S., Pandurangan, B., Bell, W.C., Yen, C.F., Cheeseman, B.A.: Multi-length scale computational derivation of Kevlar ((R)) yarn-level material model. J. Mater. Sci. **46**(14), 4787–4802 (2011)
9. Lim, J., Chen, W.N.W., Zheng, J.Q.: Dynamic small strain measurements of Kevlar 129 single fibers with a miniaturized tension Kolsky bar. Polym. Test. **29**(6), 701–705 (2010)

Chapter 12
Longitudinal Wave Propagation Including High Frequency Component in Viscoelastic Bars

T. Tamaogi and Y. Sogabe

Abstract The purpose of this study to evaluate the attenuation and the dispersion properties for viscoelastic materials over a wide range of frequencies. The viscoelastic properties within the frequency of around 200 kHz were examined by using the solid and hollow bars of polymethyl methacrylate (PMMA). The PMMA properties were testes by the longitudinal impact experiments in the lower frequency area of up to around 15 kHz and the ultrasonic propagation experiments using the ultrasonic transducers in the high frequency area from 20 to 200 kHz. Consequently, it was found that the second-mode vibration as well as the first-mode should be considered in the high frequency area. It was also confirmed that the second-mode vibration influenced deeply as the radial thickness became thin.

Keywords Dynamic properties • Propagation • Viscoelastic • Ultrasonic • Transducer

12.1 Introduction

Polymer materials are widely used in various fields because of their impact resistance or the vibration control. It is well known that the deformation of the materials remarkably depends on the time or the strain rate. The shape of a stress wave in a viscoelastic bar changes as it propagates because of the attenuation and the dispersion that mainly depend on the material damping characteristics. The dynamic properties of viscoelastic materials have been evaluated by some techniques such as the wave propagation method [1, 2] and the viscoelastic SHB method [3, 4] based on the elementary theory. Taking the geometric dispersion or the three-dimensional effect into account, more precise theories have been demonstrated [5, 6].

The dynamic properties of viscoelastic materials in the high frequency area are complex, but it is difficult to evaluate the properties only by the impact experiment. In this work, the ultrasonic propagation experiments as well as the longitudinal impact experiments were performed using PMMA materials in order to evaluate the attenuative and dispersive features over a wide range of frequencies based on the three-dimensional exact theory.

12.2 Viscoelastic Theory

12.2.1 Viscoelastic Model

In the case of a thin and uniform viscoelastic bar, the constitutive equation about for a one-dimensional longitudinal wave is written in the following form:

$$P(D)\sigma(x,t) = Q(D)\varepsilon(x,t), \tag{12.1}$$

where x is the coordinate along the rod axis, t is the time, ρ is the material density, σ and ε are stress and strain along the x-axis, respectively. D denotes the differentiation with respect to time $D=\partial/\partial t$, $p(D)$ and $Q(D)$ are linear differentiation operators.

T. Tamaogi (✉)
Department of Mechanical Engineering, National Institute of Technology, Niihama College, 7-1 Yakumo-cho, Niihama, Ehime 792-8580, Japan
e-mail: takatamajp@yahoo.co.jp

Y. Sogabe
Department of Mechanical Engineering, Ehime University, 3 Bunkyo-cho, Matsuyama, Ehime 790-8577, Japan

B. Song et al. (eds.), *Dynamic Behavior of Materials, Volume 1*,
Conference Proceedings of the Society for Experimental Mechanics Series, DOI 10.1007/978-3-319-22452-7_12

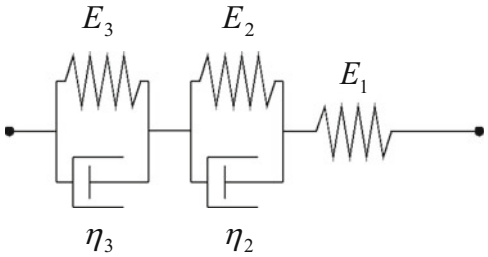

Fig. 12.1 Viscoelastic models for determining mechanical properties

The complex compliance, which represents one of the viscoelastic properties of the material, is defined by the ratio of strain to stress in the frequency domain as

$$J^*(\omega) = {J_1}^*(\omega) - i\ {J_2}^*(\omega). \tag{12.2}$$

The viscoelastic characteristics of materials are identified as 5-element model in this paper as shown in Fig. 12.1. The relation between viscoelastic parameters of 5-element model and the real and the imaginary part of the complex compliance are given by

$$\left.\begin{aligned} {J_1}^*(\omega) &= \frac{1}{E_1} + \frac{E_2}{{E_2}^2 + (\omega\eta_2)^2} \\ {J_2}^*(\omega) &= \frac{\omega\eta_2}{{E_2}^2 + (\omega\eta_2)^2} \end{aligned}\right\}. \tag{12.3}$$

The Poisson's ratio of a viscoelastic medium ν can be assumed to be a real constant as well as the elastic medium. The complex Lame's functions $\lambda^*(\omega)$ and $\mu^*(\omega)$ are shown as follows by using ν and $J^*(\omega)$:

$$\left.\begin{aligned} \lambda^*(\omega) &= \frac{\nu}{(1+\nu)(1-2\nu)J^*(\omega)} \\ \mu^*(\omega) &= \frac{1}{2(1+\nu)J^*(\omega)} \end{aligned}\right\}. \tag{12.4}$$

12.2.2 Three-Dimensional Exact Theory

Consider a stress wave propagating in an infinite cylindrical elastic bar. The equation of motion is written in the following

$$\rho\frac{\partial^2 \mathbf{u}}{\partial t^2} = (\lambda + 2\mu)\mathrm{grad}\Delta - 2\mu\mathrm{rot}\ \boldsymbol{\Omega}, \tag{12.5}$$

where $\mathbf{u}$ denotes the displacement vector, λ and μ are the Lame coefficients, Δ=div$\boldsymbol{u}$, $2\boldsymbol{\Omega}$=rot$\boldsymbol{u}$. Assuming axial symmetry, and applying the Fourier transformation with respect to the time and the correspondence principle [7] to (12.5), the following equations for a viscoelastic medium on the cylindrical coordinate plane are deduced:

$$\left.\begin{aligned} -\rho\omega^2 U_r &= \left(\lambda^* + 2\mu^*\right)\frac{\partial D}{\partial r} - 2i\xi\mu^* W \\ -\rho\omega^2 U_z &= \left(\lambda^* + 2\mu^*\right)(-i\xi)D - 2\mu^*\left(\frac{\partial W}{\partial r} + \frac{W}{r}\right) \end{aligned}\right\}, \tag{12.6}$$

where the displacement $\overline{u}_r(r,z,\omega)$=$U_r(r,\omega)\cdot\exp(-i\xi z)$ and $\overline{u}_z(r,z,\omega)$=$U_z(r,\omega)\cdot\exp(-i\xi z)$, the volumetric strain $\overline{\Delta}(r,z,\omega)$=$D(r,\omega)\cdot\exp(-i\xi z)$, the rotation vector $\overline{\Omega}_\theta(r,z,\omega)$=$W(r,\omega)\cdot\exp(-i\xi z)$, $\xi(\omega)$=$k(\omega) - i\alpha(\omega)$ respectively. Solving (12.7) in D and W of solid and hollow bars, the Bessel's differential equations are obtained. The solutions can be expressed as follows: The subscript s and h means solid and hollow bars, respectively.

$$\left.\begin{aligned} D_s(r,\omega) &= A_0 J_0(pr) \\ W_s(r,\omega) &= A_1 J_1(qr) \end{aligned}\right\}, \tag{12.7}$$

$$\left.\begin{aligned} D_h(r,\omega) &= A_0 J_0(pr) + B_0 Y_0(pr) \\ W_h(r,\omega) &= A_1 J_1(qr) + B_1 Y_1(qr) \end{aligned}\right\}, \tag{12.8}$$

where J_0, and J_1 are the Bessel functions of first kind, Y_0, and Y_1 are those of second kind. A_0, A_1, B_0 and B_1 are the arbitrary functions of ω, $p^2=\rho\omega^2/\left(\lambda^*+2\mu^*\right)-\xi^2$, $q^2=\rho\omega^2/\mu^*-\xi^2$, respectively. The displacement and Stress are calculated from above equations. Considering stress free boundary conditions at the external surface of the bar, the following frequency equation results of solid and hollow bars:

$$\begin{vmatrix} c_{11} & c_{12} \\ c_{21} & c_{22} \end{vmatrix} = 0, \tag{12.9}$$

$$\begin{vmatrix} c_{11} & c_{12} & c_{13} & c_{14} \\ c_{21} & c_{22} & c_{23} & c_{24} \\ c_{31} & c_{32} & c_{33} & c_{34} \\ c_{41} & c_{42} & c_{43} & c_{44} \end{vmatrix} = 0, \tag{12.10}$$

where $c_{11}=\left(q^2-\xi^2\right)J_0(pa)-2pJ_1(pa)/a$, $c_{12}=(2i\xi)[qJ_0(qa)-J_1(qa)/a]$, $c_{13}=\left(q^2-\xi^2\right)Y_0(pa)-2pY_1(pa)/a$, $c_{14}=(2i\xi)[qY_0(qa)-Y_1(qa)/a]$, $c_{21}=2i\xi pJ_1(pa)$, $c_{22}=\left(q^2-\xi^2\right)J_1(qa)$, $c_{23}=2i\xi pY_1(pa)$, $c_{24}=\left(q^2-\xi^2\right)Y_1(qa)$, $c_{31}=\left(q^2-\xi^2\right)J_0(pb)-2pJ_1(pb)/b$, $c_{32}=(2i\xi)[qJ_0(qb)-J_1(qb)/b]$, $c_{33}=\left(q^2-\xi^2\right)Y_0(pb)-2pY_1(pb)/b$, $c_{34}=(2i\xi)[qY_0(qb)-Y_1(qb)/b]$, $c_{41}=2i\xi pJ_1(pb)$, $c_{42}=\left(q^2-\xi^2\right)J_1(qb)$, $c_{43}=2i\xi pY_1(pb)$, $c_{44}=\left(q^2-\xi^2\right)Y_1(qb)$,

a and b are the outer and inner radii, respectively.

Solving (12.9) and (12.10) for complex wave number $\xi(\omega)$ numerically, the attenuation coefficient $\alpha(\omega)$, the wave number $k(\omega)$ and the phase velocity $C(\omega)$ are given by

$$\alpha(\omega) = -\mathrm{Im}[\xi(\omega)], \tag{12.11}$$

$$k(\omega) = \mathrm{Re}[\xi(\omega)], \tag{12.12}$$

$$C(\omega) = \frac{\omega}{k(\omega)}. \tag{12.13}$$

12.3 Experimental Methods

The longitudinal wave propagation experiments and the ultrasonic propagation experiments using the ultrasonic transducers were carried out. The experimental methods and dimensions using the PMMA solid bars were indicated in reference [8].

Figure 12.2 shows a schematic diagram of an ultrasonic wave propagation experiment using wave packets generated by the ultrasonic transducers when the PMMA hollow bars are used. The length and outer and inner diameter are 1000 mm, 15 mm and 9 mm, respectively. Six kinds of ultrasonic transducers having several characteristic frequencies from 20 to 200 kHz are prepared as shown in Table 12.1. The ultrasonic transducer is attached to the one side of the specimen. Four semiconductor strain gages are situated on the outer surface separated by equal intervals. The transducer is vibrated at the natural frequency by giving the voltage amplified with an AC amplifier.

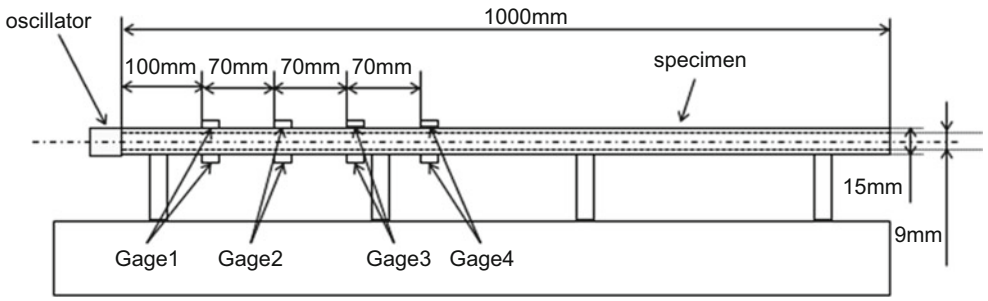

Fig. 12.2 Schematic diagram of propagation experiment using wave packets generated by ultrasonic transducer

Table 12.1 Properties of ultrasonic transducers (Fuji Ceramics Corporation)

Type		Frequency kHz	Diameter mm	Length mm	Capacitance pF
①	0.05Z15D	49.75	15	26.20	136
②	0.075Z15D	74.95	15	16.40	220
③	0.1Z15D	99.60	15	10.50	339
④	0.13Z10D	131.40	10	8.40	192
⑤	0.15Z20D	148.50	20	8.40	788
⑥	0.2Z15D	198.70	15	6.20	564

12.4 Experimental Results and Analyses

12.4.1 Measurement Results and Attenuative and Dispersive Features

The measured strain waves using the ultrasonic transducer type ① (49.75 kHz) on a PMMA hollow bar is denoted in Fig. 12.3a as a typical example. It is found that the attenuation and dispersion generate as the waves propagate. The frequency spectrum of each wave are represented in Fig. 12.3b. The frequency spectrums have a lot of frequency elements of in the frequency around 50 kHz. The values of 46.9–50.3 kHz, which are 70 % of the maximum values of the frequency spectrums, are used for evaluation of the attenuative and dispersive features.

The strain wave propagating on the surface of the bar is obtained by the following equation [8]:

$$\overline{\varepsilon}_z = \overline{\varepsilon}_0 \exp\{-(\alpha + ik)\}z, \tag{12.14}$$

where z is the coordinate along the rod axis, $\overline{\varepsilon}$ indicates the strain in the frequency domain. Using the least square method, the attenuation coefficient and phase velocity can be determined from the experimental data [8].

The attenuation coefficient and phase velocity on the hollow and solid bar (the diameter is 8 mm) are shown in Figs. 12.4 and 12.5. The plots in the figures show average experimental values, and the vertical bars indicate the standard deviation. The solid line is the analytical values obtained by the solution for the first mode of the complex wave number using 5-element model shown in Fig. 12.1. The viscoelastic values E_1, E_2, η_2, E_3 and η_3 are 5.89 GPa, 58.4 GPa, 2.80 MPa·s, 122 GPa, 0.39 MPa·s.

It is found that the experimental and model's predicted values for both $\alpha(\omega)$ and $C(\omega)$ on solid bar are almost identical in Fig. 12.5a, b. It is enough to evaluate the properties for the PMMA solid bar of a wide range of frequencies using the first mode of the complex wave number. In contrast, the experimental and model's predicted values for both $\alpha(\omega)$ and $C(\omega)$ on hollow coincide with each other within the low frequency area in Fig. 12.4a, b. However, experimental and analytical values are disagreement in the high frequency area. It is considered that the high-order mode vibrations are generated.

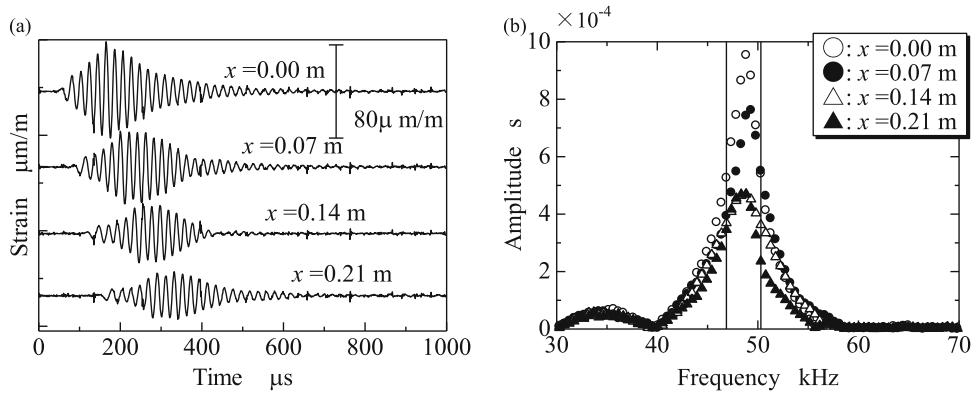

Fig. 12.3 Experimental results on propagation test using wave packets generated by ultrasonic transducer type ① (49.75 kHz) on PMMA hollow bar. (**a**) Measured strain waves; (**b**) frequency spectrums

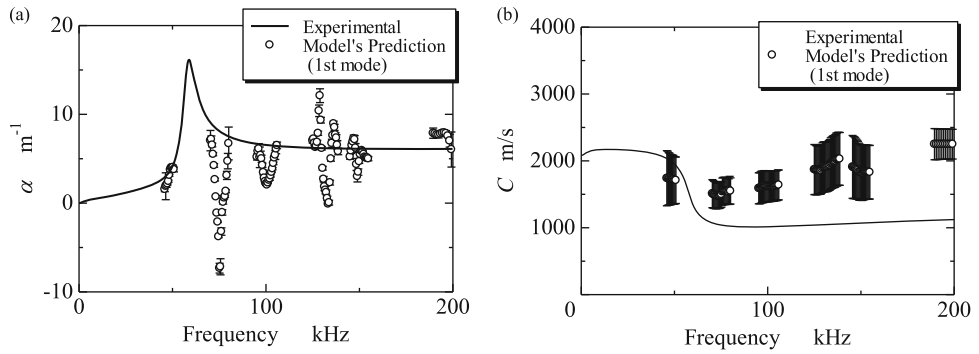

Fig. 12.4 Experimental and analytical values for $\alpha(\omega)$ and $C(\omega)$ on PMMA hollow bar. (**a**) Attenuation coefficient; (**b**) phase velocity

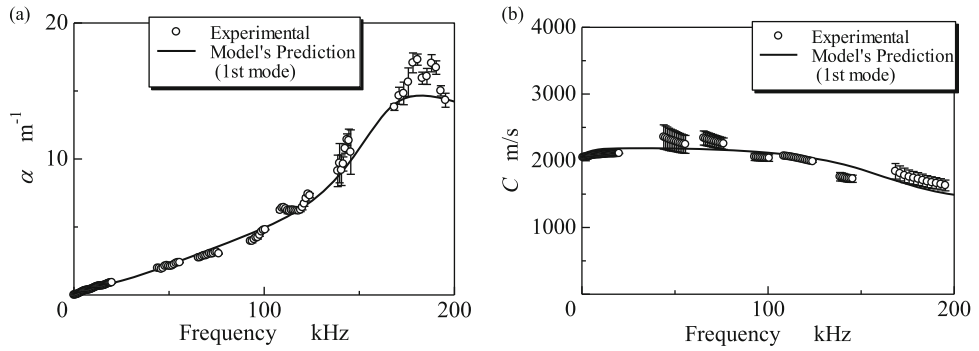

Fig. 12.5 Experimental and analytical values of $\alpha(\omega)$ and $C(\omega)$ on PMMA solid bar with diameter of 8 mm. (**a**) Attenuation coefficient; (**b**) phase velocity

12.4.2 Effect of High-Order Mode for Hollow Bar

Figure 12.6 shows the model's predicted values of first and second mode solutions for $\alpha(\omega)$ and $C(\omega)$ on the hollow bar with the outer and inner diameter of 15 and 9 mm. It is seen that the value of the second mode become small remarkably in the frequency around 65 kHz, and is almost the same value of the first mode. It is verified that the disagreement between the experimental and the analytical values in the high frequency area in Figs. 12.4a, b is due to the higher-order mode vibration. Therefore, it can be said that the higher-order mode vibration as well as the first mode vibration propagate on the hollow bar in the high frequency area.

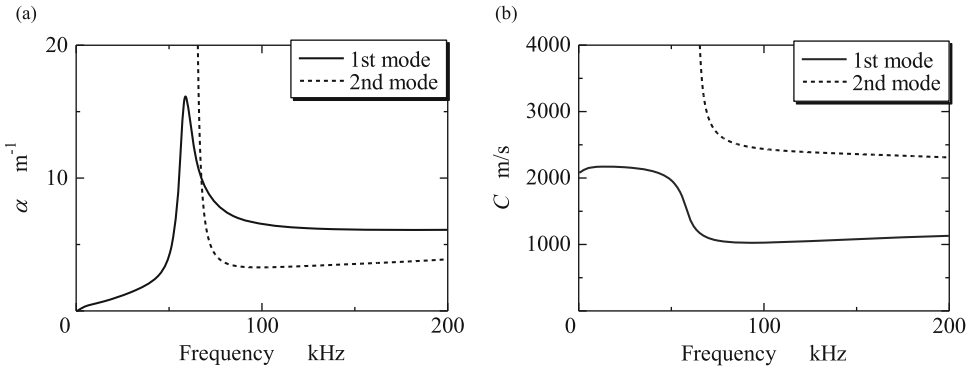

Fig. 12.6 Analytical values of first and second mode for $\alpha(\omega)$ and $C(\omega)$ on PMMA hollow bar. (**a**) Attenuation coefficient; (**b**) phase velocity

12.5 Conclusions

The conclusions obtained from the present study are summarized as follows:

- The attenuation and dispersion properties for viscoelastic material over the wide range of frequencies were examined by the ultrasonic propagation experiments using the ultrasonic transducers having several characteristic frequencies.
- It was found that the viscoelastic properties on PMMA solid and hollow bars in the low frequency area could be evaluated by the first mode vibration using the 5-element model based on the three-dimensional exact theory.
- The higher-order mode vibration as well as the first mode vibration propagated on the hollow bar in the high frequency area.

References

1. Sackman, J.L., Kaya, I.: On the determination of very early-time viscoelastic properties. J. Mech. Phys. Solids **16**(2), 121–132 (1968)
2. Sogabe, Y., Tsuzuki, M.: Identification of the dynamic properties of linear viscoelastic materials by the wave propagation testing. Bull. JSME **29**(254), 2410–2417 (1986)
3. Sogabe, Y., Yokoyama, T., Yokoyama, T., Nakano, M., Kishida, K.: A split Hopkinson bar method for testing materials with low characteristic impedance. Dyn. Fract. **300**, 137–143 (1995)
4. Juea, Z., Shishengb, H., Lili, W.: An analysis of stress uniformity for viscoelastic materials during SHPB tests. Lat. Am. J Solids Struct **3**(2), 125–148 (2006)
5. Zhao, H., Gary, G.: A three dimensional analytical solution of the longitudinal wave propagation in an infinite linear viscoelastic cylindrical Bar. Application to experimental techniques. J. Mech. Phys. Solids **43**(8), 1335–1348 (1995)
6. Benatar, A., Rittel, D., Yarin, A.L.: Theoretical and experimental analysis of longitudinal wave propagation in cylindrical viscoelastic rods. J. Mech. Phys. Solids **51**(8), 1413–1431 (2003)
7. Flügge, W.: Viscoelasticity, p. 159. Springer, New York (1975)
8. Tamaogi, T., Sogabe, Y.: Attenuation and dispersion properties of longitudinal waves in PMMA Bar over a wide range of frequencies (in Japanese). J. JSEM **12**(3), 264–269 (2013)

Chapter 13
Quasistatic to Dynamic Behavior of Particulate Composites for Different Temperatures

Nadia Bahlouli, Kui Wang, Rodrigue Matadi Boumbimba, Christiane Wagner-Kocher, and Saïd Ahzi

Abstract In automotive industry, polypropylene based composites are generally used in the manufacturing of car bumpers. In such a case, a detailed study of high strain rate and temperature sensitivities of polypropylene based composites is essential since the bumpers undergo compressive impact loading in a wide range of temperatures. The considered fillers consisted of ethylene octane copolymer and talc. The investigated filler content was 0, 10. and 20 wt. The dynamic behavior was investigated by using split Hopkinson pressure bars, at different strain rates and temperatures. We found that neat polypropylene and polypropylene talc composites were brittle at low temperatures. The addition of ethylene octane copolymer inclusions improved the impact resistance of materials. The dynamic properties are correlated with the morphological investigations of the studied composites by means of the optical microscopy. Finally, we also identify the effect of soft and rigid fillers in the quasi static to dynamic transition.

Keywords Polypropylene • Talc • Nodules • Dynamic • Temperature

13.1 Introduction

Polypropylene (PP) is one of the most widely used plastics in the automotive industry. In a continuously increasing part of this market, the material needs to be recycled. Actually, the growing plastics waste forces governments to legislate for the limitation of such waste by introducing the concept of isofunctional recycling [1]. The recycling effects on polypropylene based materials were studied [2–8]. Degradations induced by the ageing and the recycling of composite based polypropylene were quantified under quasi-static loading by Bahlouli et al., Pessey et al., and Luda et al [2–4]. After multiple extrusion/crushing processes, the main result is that polymer chain scission induces the degradation of the mechanical properties. The recyclability of other PP composites has also been investigated by Bahlouli et al. [2] and Wang et al. [5, 6, 8]. The purpose of this study has been to examine the effect of recycling on the properties of PP-based composites (rubber nodules)/PP and talc/PP) using extrusion process. Rheological, mechanical and structural properties of the composites have been determined and compared after each extrusion cycle. The results showed that the melt viscosity of the composites decreases with processing number in the same way of pure PP [9], as well as the mechanical properties of the composites decreased with processing number. All noted changes in the composites properties have been caused by the changes in the structural properties of the composites during the processing cycle. The obtained results from this work made possible the optimization of the recycling process and a better use of the recycled materials in components design. In view of these results, recycled materials suppliers must regenerated recycled materials so they can be upgraded in parts of structures. Different ways can be used to regenerate

N. Bahlouli (✉)
ICUBE Laboratory—CNRS, University of Strasbourg, 2 Rue Boussingault, Strasbourg 67000, France
e-mail: nadia.bahlouli@unistra.fr

K. Wang
Qatar Environment and Energy Research Institute, Qatar Foundation, PO Box 5825, Doha, Qatar

R.M. Boumbimba
Laboratory of Mechanics, Biomechanics, Polymers and Structures, National Engineering School of Metz, 1 route d'Ars Laquenexy, Metz 57078, France

C. Wagner-Kocher
ENSISA-LPMT, Université de Haute Alsace, 11 rue Alfred Werner, Mulhouse Cedex 68093, France

S. Ahzi
ICUBE Laboratory—CNRS, University of Strasbourg, 2 Rue Boussingault, Strasbourg 67000, France

Qatar Environment and Energy Research Institute, Qatar Foundation, PO Box 5825, Doha, Qatar

B. Song et al. (eds.), *Dynamic Behavior of Materials, Volume 1*,
Conference Proceedings of the Society for Experimental Mechanics Series, DOI 10.1007/978-3-319-22452-7_13

polypropylene [9–11]. Changing the grade of the polymer is one of these methods. Depending on the desired mechanical properties, the compounder will provide a polypropylene grade. By doing that, suppliers will be able to change the grade of recycled polypropylene by adding particles. For a low-grade polypropylene, elastomeric particles have been added. To get a higher grade of polypropylene, talc has been added. But the addition of particles not only impacts the grade of polypropylene. Indeed, the mechanical properties of a polymer strongly depend on the grade of polymers. It is important to notice that the addition of particles not only impacts the grade of polypropylene. Actually, the mechanical properties of a polymer strongly depend upon the grade of polymers. Previous rheological and morphological analyses were performed to highlight the effect of the adjunction of talc and rubber nodules on the thermal and rheological properties of polypropylene [5, 6]. This work explores the strong effects of the addition of soft particles and rigid particles in polypropylene on the thermo mechanical behavior over a wide range of strain rates. Experimental work has been conducted for a wide range of temperatures and strain rates for different filler content in PP in both quasi-static and split-Hopkinson tension bar test rigs. DMA tests were also carried out to position the temperatures tested against the different phase's transitions.

13.2 Materials and Methods

A highly isotactic polypropylene (PP) was supplied by LyondellBasell for this study (reference Moplen HP500N, Frankfurt am Main, Germany). This PP had a melt flow index (MFI) of 12 g/10 min and a density of 0.9 g/cm^3 [12]. To study the effects of soft fillers on mechanical properties of the PP, an impact modifier of PP was used. This impact modifier of PP is a metallocene ethylene octene copolymer (EOC) supplied by ExxonMobil (reference Exact TM 8230, Brussels, Belgium). This EOC had a MFI of 30 g/10 min and a density of 0.882 g/cm^3, and it contained 72 wt. % of ethylene and 28 wt. % of octene. The effect of rigid particles in PP was identified by the adjunction of talc powder which was kindly offered by Luzenac (referenced Steamic T1 CF, Toulouse, France), and had a density of 2.78 g/cm^3 and a median diameter (D50) of 1.9 μm.

PP blends containing 0 wt. %, 10 wt. % and 20 wt. % of EOC or talc (PP/EOC, 100/0, 90/10, 80/20, or PP/talc, 100/0, 90/10, 80/20, respectively) were prepared by extrusion. PP with 20 wt. % of EOC and 10 wt. % of talc (PP/EOC/Talc 70/20/10) was also processed. These compositions are similar to available commercial PP composites for car bumpers [2]. The talc powder was dried for 12 h at 80 °C before mixing. The mixing of the materials was conducted with a single screw BUSS Kneader extruder model PR46 (Pratteln, Switzerland), with a screw diameter (D) of 46.5 mm and a length/diameter ratio L/D of 11, at 200 °C and 50 rpm and under air conditions. The obtained molten filaments of PP-based composites were quenched by a cold water bath and were subsequently pelletized using a rapid granulator. The pellets were dried in an air-circulating oven for 60 min to minimize the moisture for the subsequent step [13].

The viscoelastic properties of the materials were characterized by dynamic mechanical analysis (DMA) using a NETZSCH DMA 242C instrument (Selb, Germany). Specimens of dimensions of 16 × 10 × 3 mm were carefully cut from the tensile specimens, tested with the single—cantilever bending mode at the frequency of 1 Hz and with a constant static force of 0.5 N. During this procedure, the materials were tested from −100 to 140 °C with a heating rate of 2 °C/min. For DMA, we report averaged values and representative curves resulting from three experiments per tested material.

Mechanical properties for both virgin and recycled materials were evaluated using uniaxial tension with a servohydraulic Instron testing machine model 8031 (Norfolk, Massachusetts, USA) at the room temperature (25 ± 1 °C). Based on the standard ASTM D638, the Young's modulus and yield stress were determined at a crosshead speed of 1 mm/min and the strain at break was determined at the crosshead speed of 50 mm/min. The Young's modulus and the yield stress were calculated from the initial slop of stress–strain curves and the maximum stress of stress–strain curves during the transition between viscoelastic and viscoplastic stages, respectively. Since the tensile specimens have a gauge length of 50 mm, the corresponding strain rates are 0.0033/s for 1 mm/min and 0.017/s for 50 mm/min. The engineering stress (σ_{eng}) and strain (ε_{eng}) were determined from the measured load (F) and displacement (Δl) using the original specimen cross-sectional area (S_0) and length (l_0). (σ_{eng}) and (ε_{eng}) can be used to determine the true stress (σ_{true}) -true strain (ε_{true}) curves. At least five tests were performed per strain rate, which allows determining the averaged values of each mechanical parameter.

A homemade split Hopkinson pressure bars (SHPB) was used to perform the uniaxial compressive high strain rate testing. This apparatus consisted of three parts, a striker, an input bar and an output bar made of 316L steel, with lengths of 500 mm, 2903 mm and 2890 mm, respectively, and the same diameter of 22 mm. The cylindrical samples with a diameter of 8 mm and a thickness of 3 mm were cut from the injected tensile samples and placed between the input bar and the output bar. Petroleum jelly was used as lubricant to limit the friction between the bars and the sample. A furnace with two symmetrical resistance heaters was installed for high temperature testing. For the low temperature testing, liquid nitrogen was mixed with different contents of absolute ethyl alcohol depending on the required testing temperature. Based on the classical elastic wave propagation theory, when the stress and strain fields were uniform in the specimen, the nominal stress ($\sigma_n(t)$), the

nominal strain ($\varepsilon_n(t)$) and the nominal strain rate ($\dot{\varepsilon}_n(t)$) of the tested materials were computed by the classical expressions given in [13, 15]. The recorded strain signals are post-processed with the software package DAVID to reconstruct the time histories of strain at the end of the incident and transmitter bars, following the procedures described in [16, 17]. In this study, dynamic tests were carried out at various temperatures ranging from −30 to 85 °C (−30, 0, 25, 50 and 85 °C), and various strain rates ranging from 592 s^{-1} to 3346 s^{-1} ($\dot{\varepsilon}_1 = 592p\backslash pm6.5\%\ s^{-1}$, $\dot{\varepsilon}_2 = 1276p\backslash pm7.9\%\ s^{-1}$, $\dot{\varepsilon}_3 = 2221p\backslash pm5.6\%\ s^{-1}$ and $\dot{\varepsilon}_4 = 3346p\backslash pm4.3\ s^{-1}$). Each test was repeated five times and hence, averaged strain rates and averaged curves were reported here. In the manuscript, these four strain rates were denoted as Strain-rate-1, Strain-rate-2, Strain-rate-3 and Strain-rate-4, respectively.

13.3 Results and Discussion

Attention is first focused on the impact of the EOC and the talc on the viscoelastic properties of the PP characterized by DMA, and in particular on the storage modulus (Fig. 13.1). For PP/EOC composites (Fig. 13.1 left), the storage modulus decreases with the content of EOC due to the increased amount of soft rubber phase. For the evolution of the damping factor *tan δ* with temperature (Fig. 13.1), we observed three relaxation peaks: (1) the glass transition of EOC (β_{EOC}), (2) the glass transition of PP (β_{PP}), and (3) the crystalline phase relaxation of PP (α_{PP}). It is to be noted that the crystalline phase relaxation of EOC (α_{EOC}) was not detected due to the overlapping of the α_{EOC} relaxation with the much more intense β_{EOC} relaxation [18–20]. The peak position of each relaxation process provided the corresponding relaxation temperature. For PP/talc composites (Fig. 13.1 left), the storage modulus increased with the addition of talc due to the presence of rigid talc fillers. The increase in rigidity was also explained by the formation of an interphase between the PP matrix and the rigid talc fillers, having an intermediate rigidity between that of talc and that of PP [21]. Comparing with the glass transition temperature of PP phase for neat PP and PP/talc composites, we found that the addition of talc filler slightly decreased the glass transition temperature of PP. The talc particles acted as nucleation agents of PP, and hence, the presence of talc within PP matrix resulted in a faster crystallization rate that caused an amorphous phase with a higher motion in comparison with neat PP [21]. On the contrary, the α_{PP} relaxation temperature of PP increased with the presence of talc. This is attributed to the fact that talc fillers increased the lamella thickness of PP.

Elastic properties from tensile stress–strain curves non presented here were obtained (Fig. 13.1). For PP/EOC composites (Fig. 13.2), the addition of EOC inclusions decreases the yield stress and Young's modulus of neat PP, which is consistent with the storage modulus of PP and PP/EOC blends assessed by DMA. We also measured the elongation at break of the materials (Fig. 13.2). Firstly, the elongation at break of the material increases in the following order: PP < PP/EOC 80/20 < PP/EOC 90/10. It was expected that neat PP had a lower elongation at break than the PP/EOC blends due to the toughening effect of the rubber particles, but surprisingly elongation behavior seems not to increase with the increasing

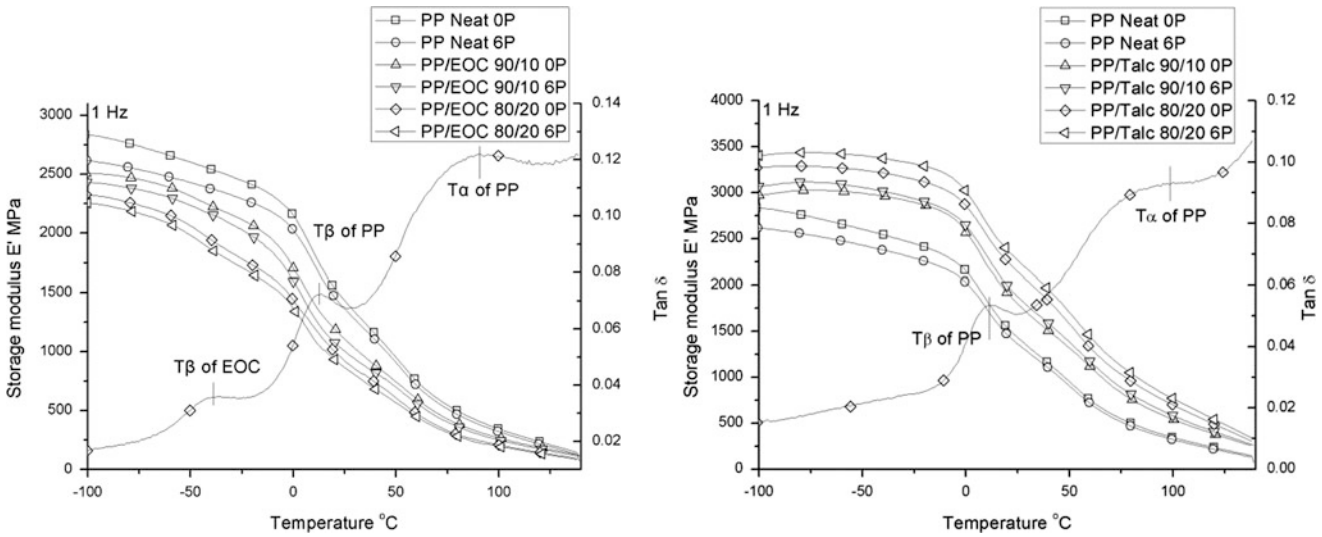

Fig. 13.1 EOC (*left*) and talc (*right*) content effect on PP storage modulus at 1 Hz

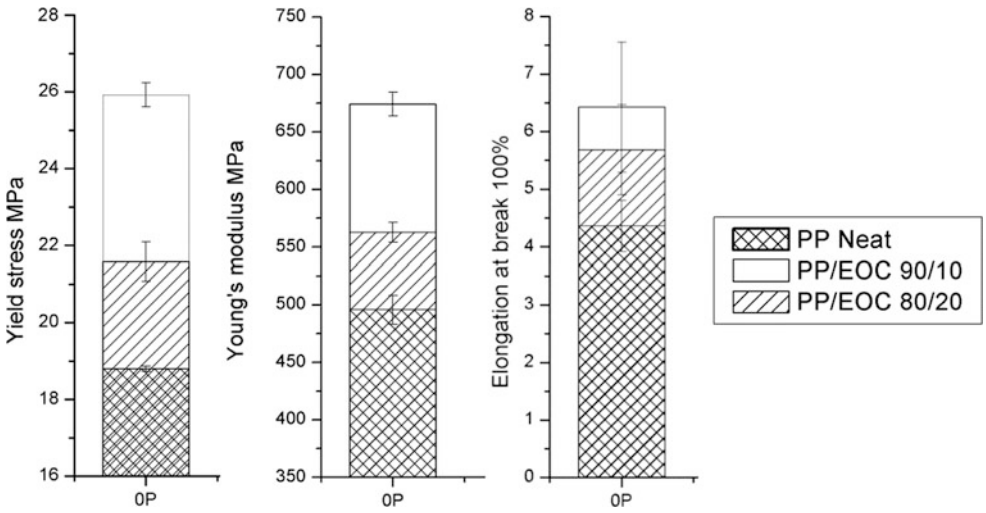

Fig. 13.2 Elastic properties for the different filler contents for quasistatic tensile tests

content of EOC. According to the currently accepted toughening theories during loading, the rubbery particles act as sites of stress concentration. Therefore, as soon as the stress around the particles overcomes the yield stress of the matrix, the deformation mechanism such as crazing and/or shear yielding become active [22, 23]. Consequently, the ductility behavior of neat PP is improved by the addition of EOC dispersed phase. It should be noted that the ductility behavior of PP/rubber blends is not persistent increasing with the increasing of the rubber concentration. This behavior is influenced by both the nature of matrix and the rubber volume fraction. At low volume fraction of rubber, the generation of crazing around the rubber particles eliminates the tendency of the matrix to strain hardening. The whitening of the specimen and the inconspicuous cross-sectional areas change between the yield stress and the failure point indicate that crazing, rather than shear yielding, is the main energy dissipation mechanism [22]. For high volume fraction of rubber, the shear bands around rubber particles interact, and microcracks develop at the areas of high mechanical constraints, leading to reduce the elongation at break [24]. On the other hand, the elongation at break appears related to the amount of β phase (Fig. 13.2): the higher the amount of β phase, the higher the ductility of PP blends. These two mechanisms can be used to explain why the elongation at break of PP/EOC 90/10 is higher than that of PP/EOC 80/20 in our case.

For PP/talc composites (Fig. 13.2), the introduction of the talc filler significantly increased the Young's modulus of neat PP For the two crosshead speeds. However, the presence of talc increased the tensile yield stress of neat PP at the lower rate (1 mm/min), but decreased the tensile yield stress at the higher rate (50 mm/min). When the talc was mixed with PP, it may accommodate one part of macroscopic stress, with limited or delayed cavitation mechanisms by debonding. In the case of a low strain rate, the accommodation of stress by the talc particles is important, resulting in an increase of yield stress and limited cavitation. For the case of high strain rates, the accommodation of stress by the talc particles is low, which results in marked cavitation mechanisms and a low yield stress [25–28]. Besides this, Zhou et al. [29] attributed the decrease of PP/talc composite yield stress compared to neat PP to the presence of thermal residual stresses in the case of the composite. In particular, the coefficients of thermal expansion of PP matrix and talc are quite different, which may induce important thermal residual stresses within the composites and hence may decrease the yield stress during the tensile test in comparison with neat PP.

Yield stress/temperature is plotted versus strain rates for the different tested materials (Fig. 13.3). A strong sensitivity to the strain rate is obtained. The neat PP and the PP/talc composites presented a brittle behavior at −30 and 0 °C. This is due to the glass transition temperature of non-recycled PP which is around 12 °C. With increasing the testing temperature, the ductility of PP and PP/talc increased gradually. This phenomenon is probably due to the increased mobility of polymer chains with increasing temperature that delays the material rupture. Concerning the yield point of these materials, it tends to increase with the content of talc particles at −30 and 0 °C. However, for higher temperatures, the yield stress of PP/talc 90/10 was higher than that of PP/talc 80/20. This result may be attributed to the damage mechanisms by matrix/filler debonding during dynamic testing. In particular, it is hypothesized that PP/talc 80/20 may exhibit more damage than PP/talc 90/10. From 0 °C, the yield point of PP and PP/talc decreased with increasing temperature.

The PP/EOC had a ductile dynamic response for all the investigated temperatures. This is due to the addition of EOC inclusions as toughening agents of PP matrix that obviously increase the impact resistance of the material. Whatever the

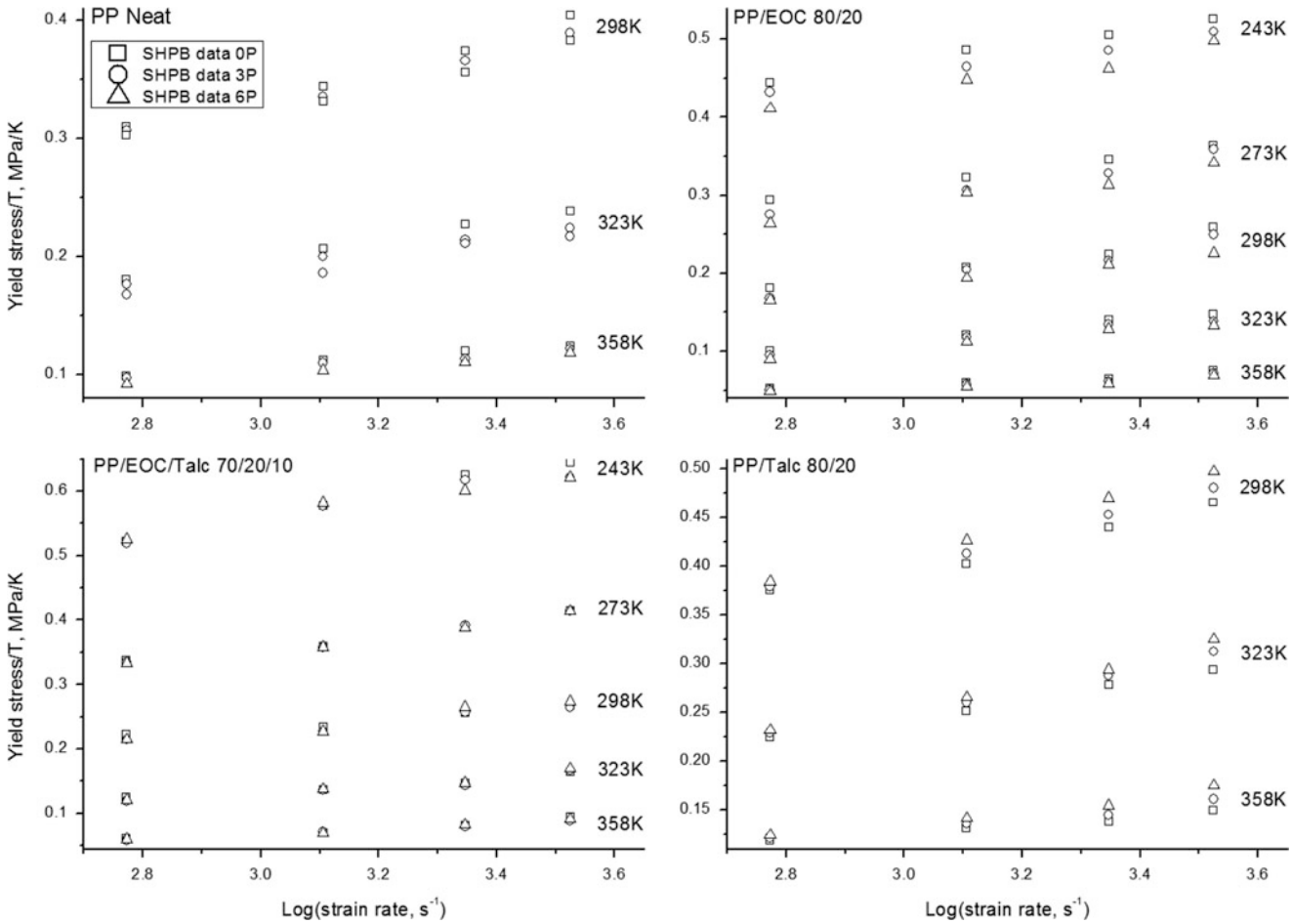

Fig. 13.3 The dependences of yield stress in dynamic compression on strain rate and recycling number at five temperatures

testing temperature, in the case of PP/EOC composites, the yield stress decreased with the amount of EOC. This can be explained by the increased amount of this soft rubber phase. With increasing temperature, the yield point of PP/EOC and PP/EOC/talc gradually decreased. In addition, we noted that the yield stress of PP/EOC/talc 70/20/10 was lower than that of PP/EOC 90/10 for the investigated testing conditions.

13.4 Conclusions

The results showed that the considered materials were strain-rate and temperature sensitive. The addition of EOC decreased the Young's modulus and yield stress of PP while the presence of talc fillers increased the Young's modulus of PP. However, the yield stress for PP/talc 80/20 was slightly lower than that of PP/talc 90/10 probably due to more important damage mechanisms by matrix/filler debonding in PP/talc 80/20 compared to PP/talc 90/10 during the dynamic testing.

Acknowledgements The authors would like to acknowledge the financial support provided by the Ministry of the Innovation and Research, the ADEME, France and the Region Alsace.

References

1. Directive 2003/53/CE, du Parlement Européen et du Conseil. Journal Officiel de l'Union Européenne. (2003)
2. Bahlouli, N., Pessey, D., Raveyre, C., Guillet, J., Ahzi, S., Hiver, J.M., Dahoun, A.: Recycling effects on the rheological and thermomechanical properties of polypropylene-based composites. Mater. Des. **33**(1), 451–458 (2012)
3. Pessey, D., Bahlouli, N., Raveyre, C., Guillet, J., Hiver, J.M., Dahoun, A., Ahzi, S.: Characterization of the contamination on two composites based polypropylene. Polym. Sci. Eng. (in press)
4. Luda, M.P., Ragosta, G., Musto, P., Pollicino, A., Caminom, G., Recca, A., Nepote, V.: Natural ageing of automotive polymer components: characterisation of new and used poly(propylene) based car bumpers. Macromol. Mater. Eng. **287**, 404–411 (2002)
5. Wang, K., Bahlouli, N., Addiego, F., Ahzi, S., Rémond, Y., Ruch, D., Muller, R.: Effect of talc content on the degradation of re-extruded polypropylene/talc composites. Polym. Degrad. Stab. **98**(7), 1275–1286 (2013)
6. Wang, K., Addiego, F., Bahlouli, N., Ahzi, S., Rémond, Y., Toniazzo, V., Muller, R.: Analysis of thermomechanical reprocessing effects on polypropylene/ethylene octene copolymer blends. Polym. Degrad. Stab. **97**(8), 1475–1484 (2012)
7. Aurrekoetxea, J., Sarrionanda, M.A., Urrutibeascoa, I., Maspoch, M.L.I.: Effects of recycling on the microstructure and the mechanical properties of isotactic polypropylene. J. Mater. Sci. **36**, 2607–2613 (2001)
8. Wang, K., Addiego, F., Bahlouli, N., Ahzi, S., Remond, Y., Toniazzo, V.: Impact response of recycled polypropylene-based composites under a wide range of temperature: effect of filler content and recycling. Combust. Sci. Technol. **95**, 89–99 (2014)
9. Gaoa, Z., Kanekoa, T., Amasakib, I., Nakadaa, M.: A kinetic study of thermal degradation of polypropylene. Polym. Degrad. Stab. **80**(2), 269–274 (2003)
10. Luda, M.P., Ragosta, G., Musto, P., Acierno, D., Di Maio, L., Camino, G., Nepote, V.: Regenerative recycling of automotive polymer components: poly(propylene) based car bumpers. Macromol. Mater. Eng. **288**, 613–620 (2003)
11. Zhong-Wei, W., Guang-Fu, L., Shou-Xu, S., Shao-Bo, P.: Regeneration and recycling of waste thermosetting plastics based on mechanical thermal coupling fields. Int. J. Precis. Eng. Manuf. **15**(12), 2639–2647 (2014)
12. Wang, K., Boumbimba, R.M., Bahlouli, N., Ahzi, S., Muller, R., Bouquey, M.: Dynamic behaviour of a melt mixing polypropylene organoclay nanocomposites. J Eng Mater Technol **134**(1), 010905 (2012)
13. Matadi, R., Hablot, E., Wang, K., Bahlouli, N., Ahzi, S., Avérous, L.: High strain rate behaviour of renewable biocomposites based on dimer fatty acid polyamides and cellulose fibres. Compos Sci Technol **71**(5), 674–682 (2011)
14. Gray, G.T.: Classic split-Hopkinson pressure bar testing. ASM International, Materials Park (2000)
15. Gray, G.T., Blumenthal, W.R.: Split-Hopkinson Pressure Bar Testing of Soft Materials. In: Kuhn, H., Medlin, D. (eds.) ASM Handbook, vol. 8, pp. 462–476. ASM International, Materials Park (2000)
16. Gary, G.: Instruction manual of David, SHPB tests analysis software, https://www.sites.google.com/site/hopkinsonbars/home/david (2005)
17. Zhao, H., Gary, G.: The testing and behaviour modelling of sheet metals at strain rates from 10^{-4} to 10^{4} s^{-1}. Mat. Sci. Eng. A **207**, 46 (1996)
18. Jaziri, M., Mnif, N., Massardier-Nageotte, V., Perier-Camby, H.: Rheological, thermal, and morphological properties of blends based on poly (propylene), ethylene propylene rubber, and ethylene-1-octene copolymer that could result from end of life vehicles: effect of maleic anhydride grafted poly(propylene). Polym. Eng. Sci. **47**, 1009–1015 (2007)
19. Al-Malaika, S., Peng, X., Watson, H.: Metallocene ethylene-1-octene copolymers: influence of comonomer content on thermo-mechanical, rheological, and thermo-oxidative behaviours before and after melt processing in an internal mixer. Polym. Degrad. Stab. **91**, 3131–3148 (2006)
20. Benavente, R., Pérez, E., Yazdani-Pedram, M., Quijada, R.: Viscoelastic relaxations in poly(ethylene-co-1-octadecene) synthesized by a metallocene catalyst. Polymer **43**, 6821–6828 (2002)
21. Díez-Gutiérrez, S., Rodríguez-Pérez, M.A., De Saja, J.A., Velasco, J.I.: Dynamic mechanical analysis of injection-moulded discs of polypropylene and untreated and silane-treated talc-filled polypropylene composites. Polymer **40**, 5345–5353 (1999)
22. Guerrica-Echevarria, G., Eguiazabal, J.I., Nazabal, J.: Effects of reprocessing conditions on the properties of unfilled and talc-filled polypropylene. Polym. Degrad. Stab. **53**, 1–8 (1996)
23. Greco, R., Mancarella, C., Martuscelli, E., Ragosta, G., Yin, J.: Polyolefin blends: 2. Effect of EPR composition on structure, morphology and mechanical properties of iPP/EPR alloys. Polymer **28**, 1929–1936 (1987)
24. Jancar, J., DiAnselmo, A., DiBenedetto, A.T., Kucera, J.: Failure mechanics in elastomer toughened polypropylene. Polymer **34**, 1684–1694 (1993)
25. Addiego, F., Di Martino, J., Ruch, D., Dahoun, A., Godard, O., Lipnik, P., Biebuyck, J.-J.: Cavitation in unfilled and nano-CACO3 filled HDPE subjected to tensile test: revelation, localization, and quantification. Polym. Eng. Sci. **50**, 278–289 (2010)
26. Hadal, R.S., Misra, R.D.K.: The influence of loading rate and concurrent microstructural evolution in micrometric talc- and wollastonite-reinforced high isotactic polypropylene composites. Mater. Sci. Eng. A **374**, 374–389 (2004)
27. Azizi, H., Faghihi, J.: An investigation on the mechanical and dynamic rheological properties of single and hybrid filler/polypropylene composites based on talc and calcium carbonate. Polym. Compos. **30**, 1743–1748 (2009)
28. Addiego, F., Dahoun, A., G'Sell, C., Hiver, J.M., Godard, O.: Effect of microstructure on crazing onset in polyethylene under tension. Polym. Eng. Sci. **49**, 1198–1205 (2009)
29. Zhou, Y., Rangari, V., Mahfuz, H., Jeelani, S., Mallick, P.K.: Experimental study on thermal and mechanical behavior of polypropylene, talc/polypropylene and polypropylene/clay nanocomposites. Mater. Sci. Eng. A **402**, 109–117 (2005)

Chapter 14
A Kolsky Bar for High-Rate Micro-compression: Preliminary Results

Daniel Casem, Emily Huskins, Jonathan Ligda, and Brian Schuster

Abstract Initial results from a Kolsky bar with a 127 μm diameter are presented. The small diameter is used achieve high strain-rates and for compatibility with small (tens of microns) specimens. The bar is instrumented optically; a transverse displacement interferometer is used to measure the input and reflected pulses within the input bar and a normal displacement interferometer is used to measure the transmitted pulse in the output bar. It is shown using a simple elastic impact experiment that the pulses within the bars propagate as uniaxial stress waves according the elementary theory used in the standard analysis. An example application is also given where a niobium sample is loaded at a strain rate greater than 1 M/s.

Keywords Split Hopkinson Pressure Bar • Kolsky Bar • High-rate testing • Interferometers • Compression testing

14.1 Introduction

The Kolsky bar, or Split Hopkinson Pressure Bar, is widely used for mechanical testing at elevated strain-rates. In compression and tensile configurations, the maximum strain-rates achievable are in part related to the diameter of the bar; all other things being equal, a bar with a smaller diameter will have an increased temporal resolution of specimen stress and strain measurements and therefore permit higher rate testing. See for example [1–4]. Miniature bars are also compatible with small scale specimens, providing the potential to conduct high-rate micromechanical testing.

One practical limitation of miniaturization is instrumentation. Typical strain gages (Fig. 14.1a) cannot be used reliably with bar diameters less than approximately 3 mm. For this reason, Casem et al. [5] have adapted the interferometer instrumentation used in the Pressure Shear Plate Impact [6] experiment to the Kolsky bar, and have applied it to bars with diameters as small as 794 μm. This instrumentation is depicted in Fig. 14.1b, and involves the use of a Transverse Displacement Interferometer (TDI) in place of the input/incident bar strain gages and a Normal Displacement Interferometer (NDI) in place of the output/transmitter bar strain gages.

In this paper, we describe a system with a 127 μm diameter. The motivation for this is to develop a capability to test ductile metals with dimensions on the order of ~10 to 70 μm, which approach the realm of true micro-mechanical testing capable of obtaining material properties at the mesoscale. We refer to is as a "micro Kolsky bar" (μKB) to emphasize the ability to deal with specimens sizes on the order of tens of microns. Data from preliminary experiments of an elastic impact and on a specimen of pure niobium are given below.

14.2 Experimental Set-Up

The μKB described here is 127 μm in diameter. It is centerless ground from fine grained HSS steel with a hardness of Rc 63. The input bar is 35 mm long and the output bar is 25 mm long. A solid model is shown in Fig. 14.2, which shows the barrel, striker, and input bar. The bars and barrel are aligned in brass bushings that rest in an aluminum v-notch.

D. Casem (✉)
U.S. Army Research Laboratory, RDRL-WMP-C, Aberdeen Proving Ground, Aberdeen, MD 21005-5069, USA
e-mail: daniel.t.casem.civ@mail.mil

E. Huskins
United States Naval Academy, 323 Rickover Hall, Annapolis, MD, USA

J. Ligda • B. Schuster
U.S. Army Research Laboratory, RDRL-WML-H, Aberdeen Proving Ground, Aberdeen, MD 21005-5069, USA

B. Song et al. (eds.), *Dynamic Behavior of Materials, Volume 1*,
Conference Proceedings of the Society for Experimental Mechanics Series, DOI 10.1007/978-3-319-22452-7_14

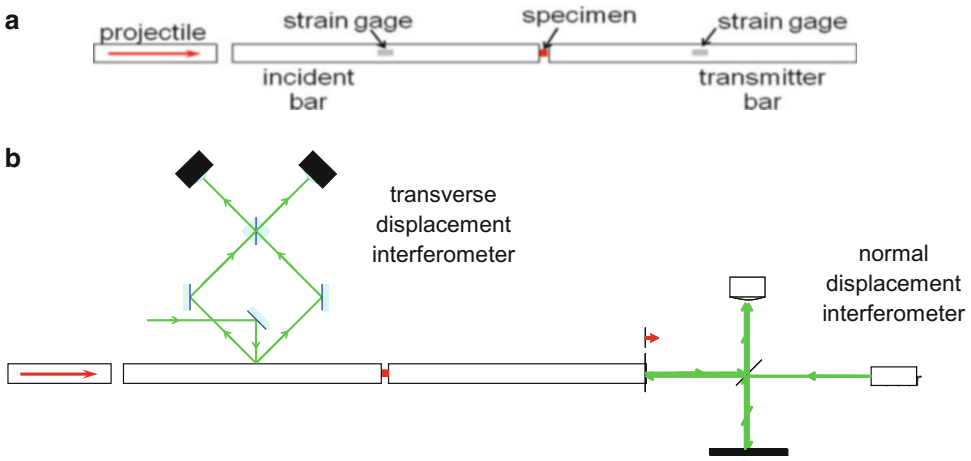

Fig. 14.1 (**a**) A standard Kolsky bar instrumented with strain gages. (**b**) An optically instrumented Kolsky bar after [5]

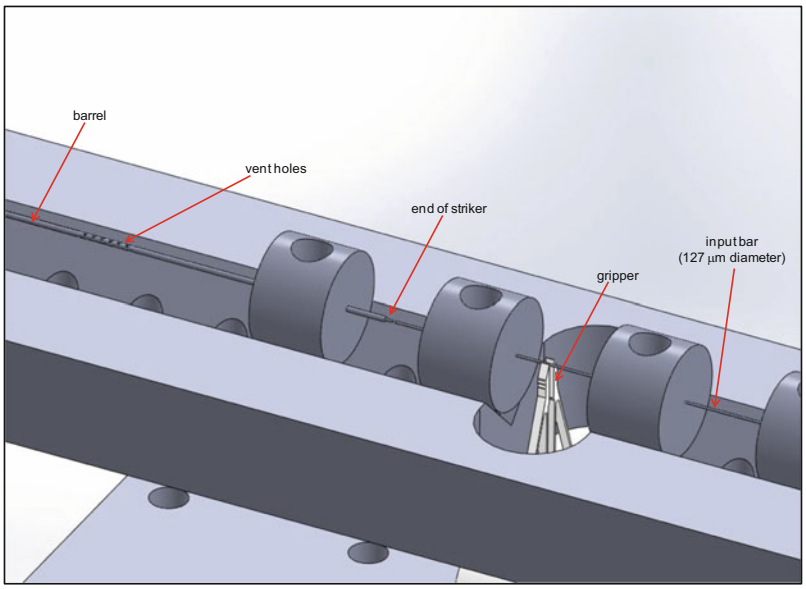

Fig. 14.2 A model of the uKB showing the barrel, striker, and input bar. A piezoelectric microgripper is used for positioning

The bushings fasten from beneath the v-notch. A piezoelectric microgripper is shown and is used to position the input bar. It is mounted on mechanical translation stages and a goniometer that allow precise positioning and rotation (about the axis) of the bar.

The TDI requires a diffraction grating at the midpoint of the bar. This is machined with a Focused Ion Beam (FIB) and is shown in Fig. 14.3. The grating needs to be on a flat surface, achieved by first polishing a flat along the entire length of the input bar. This flat is visible in the figure and only reduces the area/impedance of the input bar by a few percent, and is ignored in these preliminary experiments. Note a better arrangement would use two TDIs diametrically opposed to one another to account for bending waves [7, 8]. However only one TDI is used in the experiments described below.

14.3 Results: Elastic Impact

Figure 14.4 shows results from a simple elastic impact of a 101 μm diameter striker, 13 mm in length. There is no specimen and the input and output bars are in contact (no gap between the bars). Thus we expect the simple propagation of a rectangular pulse through the bars that is first measured by the TDI on the input bar (the input or incident pulse) and next by

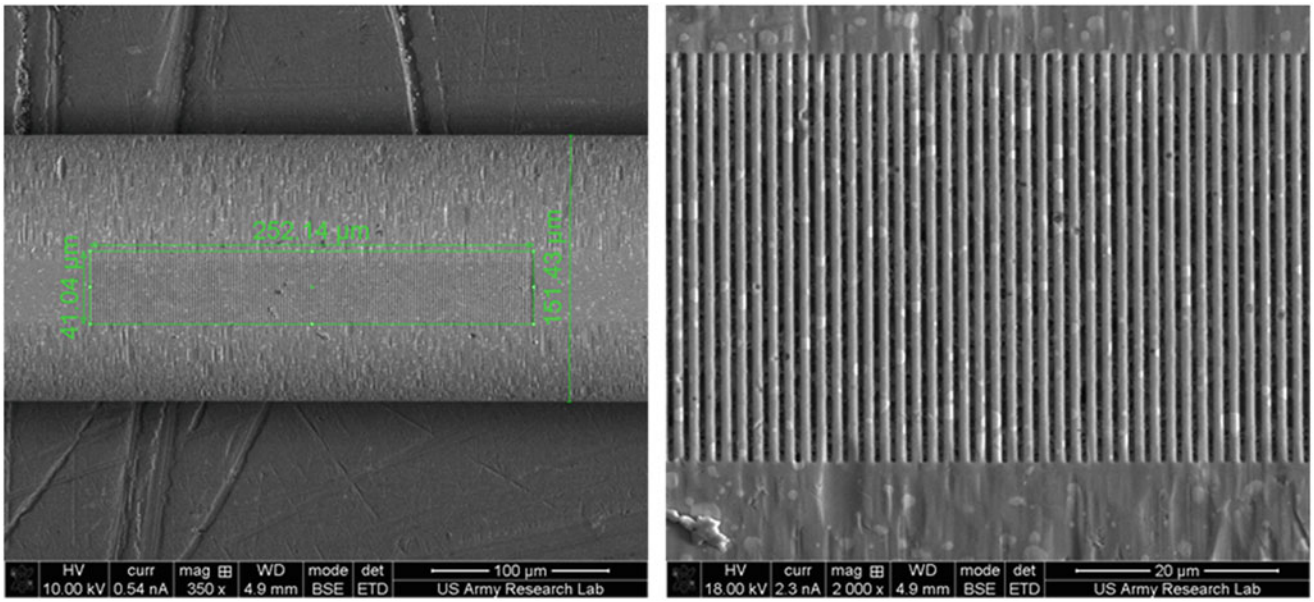

Fig. 14.3 A diffraction grating is needed at the mid-point of the incident bar for the TDI. It is machined onto a polished flat with a FIB

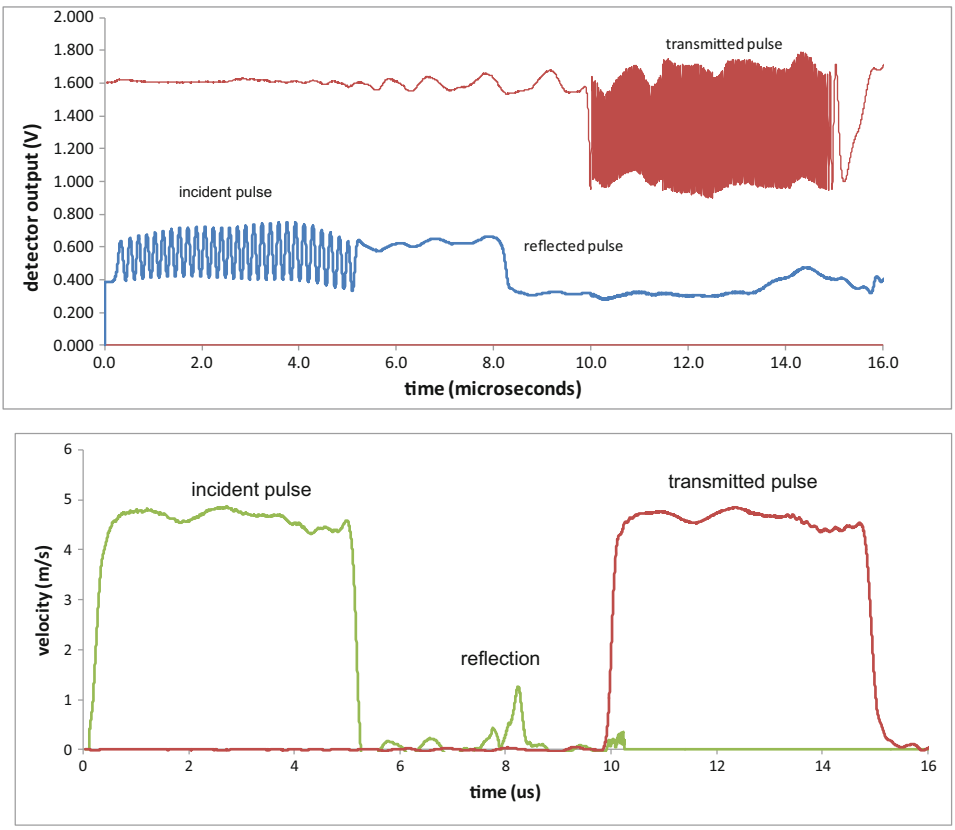

Fig. 14.4 An elastic pulse propagates through the input and output bars (no gap between the bars). The pulse is not square; this deviation is attributed to buckling of the projectile

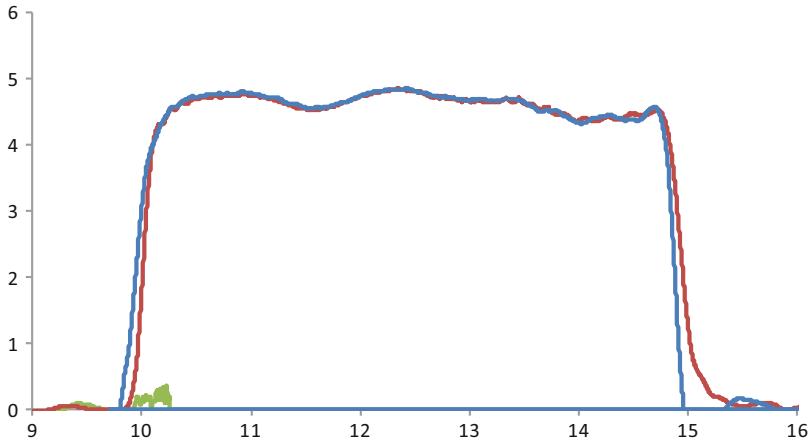

Fig. 14.5 The input and output pulse are overlaid and show essentially the same shape, demonstrating that the wave is a one-dimensional elastic wave (not affected by flexure)

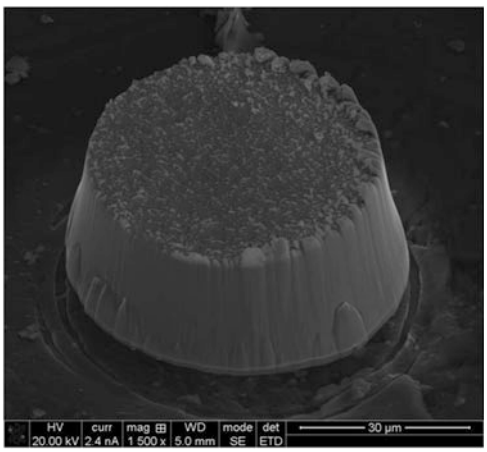

Fig. 14.6 Nb specimen laser-milled and final machined via FIB

the NDI at the end of the output bar (the output or transmitted pulse). The detector outputs from the TDI and NDI are shown at the top and the particle velocity (proportional to the more commonly measured strain according to $\varepsilon = \pm v/c$) calculated from this data is shown below. Two things are notable from this data. First, there is a small reflection, most likely due to an imperfect interface between the input and output bars. The second is that the pulse is not a perfect square wave. It is suspected that this is due to buckling/bending of the striker at impact. Because of the small sizes, it was initially feared that any slight debris on the striker or in the barrel would cause the projectile to jam in the barrel. For this reason, an oversized barrel inner diameter of 152 µm was used. This is a large clearance, and considering the large L/D ratio of this projectile (130) it is reasonable to suspect considerable bending on impact due to buckling and/or a non-centric impact. This can explain the oscillations on the measured pulse.

Note these oscillations are not indicative of bending in the input and output bars. Bending waves in these bars typically travel at speeds less than 3000 m/s, as opposed to a bar wave speed of $c = 4900$ m/s, and do not have time to reach the measurement locations during the times considered here. Furthermore, it can be shown that the pulse travels without change in form at the bar wave speed, a strong indication that the pulse propagates as a uniaxial stress wave unaffected by bending by translating the pulses in time so that they overlay on the same time scale. This is shown in Fig. 14.5 (no dispersion correction has been applied).

14.4 Results: High-Rate Compression of Niobium

This section presents data from an experiment on a niobium sample. The sample was rough machined from a 25 µm thick foil (99.9 % pure, annealed) with a fs laser mill. Final machining was performed with a FIB, and the finished sample is shown Fig. 14.6. The diameter, nominally at 50 µm, tapers considerably due to the FIB process.

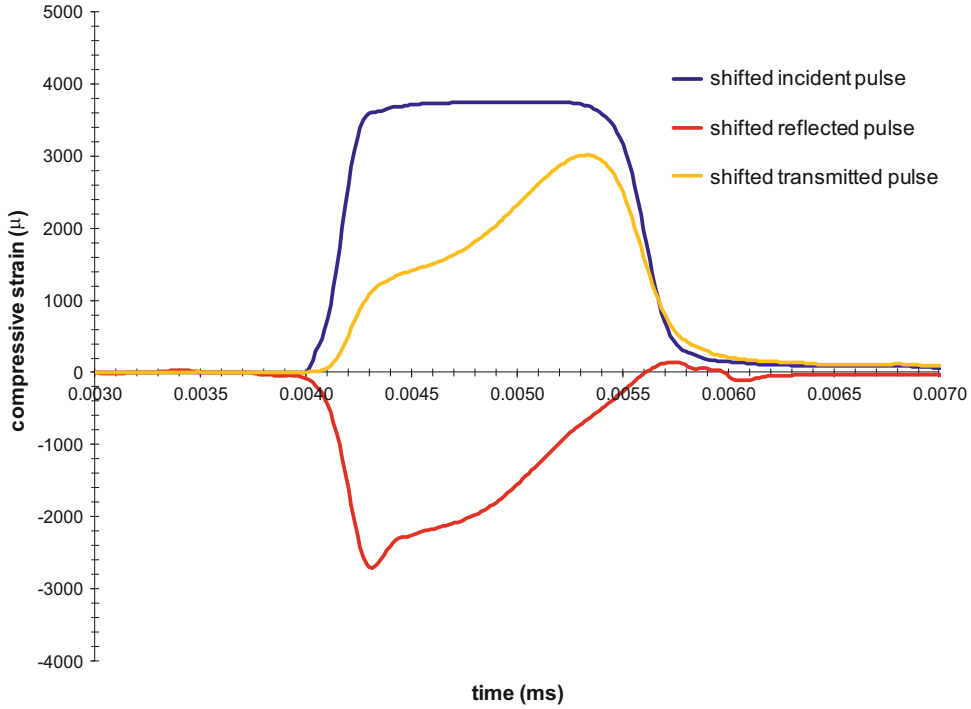

Fig. 14.7 Incident, reflected, and transmitted pulses for an experiment on Nb

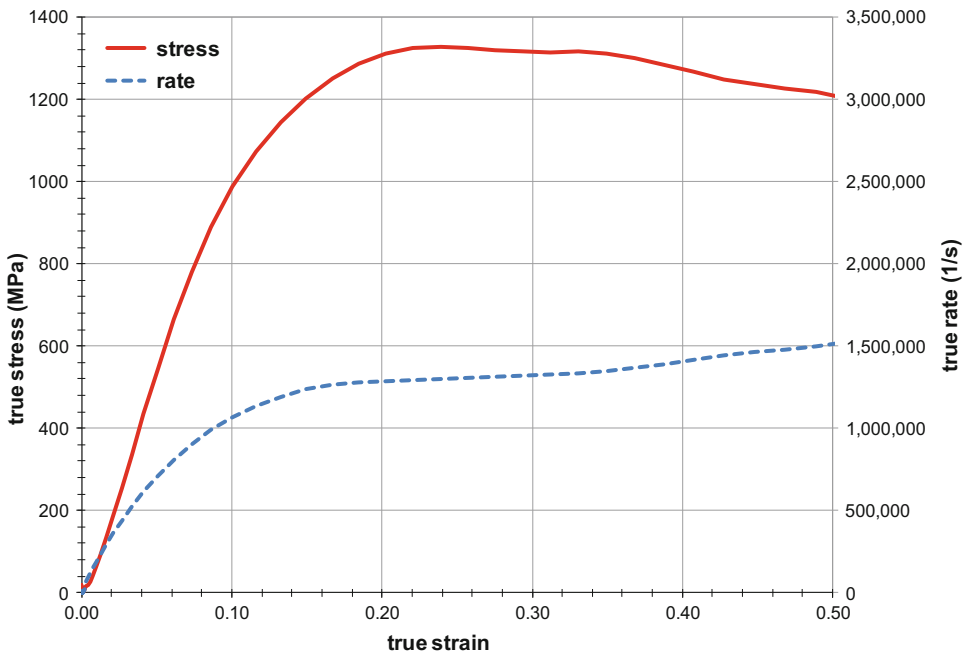

Fig. 14.8 Stress–strain data for Nb (note considerable error due to tapered geometry). Note the strain-rate in excess of 1 M/s

Figure 14.7 shows the pulses, in terms of strain, measured with the NDI and TDI, translated in time to the time they act at the specimen. Following a standard analysis, specimen stress and strain are calculated and plotted in Fig. 14.8. Note the large strain-rate, initially at 1 M/s and increasing to almost 1.5 M/s.

14.5 Discussion and Conclusion

A Kolsky bar facility with 127 μm diameter bars has been constructed and preliminary results are promising. Experiments with elastic impacts demonstrate one-dimensional stress-wave propagation within the bars, free from significant effects of flexure or bar heterogeneity. Oscillations in the incident pulse were observed and attributed to flexure of long thin strikers. We are currently developing an improved barrel and striker bar configuration. Experiments with Nb demonstrate the ability to achieve strain-rates in excess of 1 M/s, and that the NDI and TDI instrumentation are adequate for experiments at these time and length scales. Current work for improvement in this regard includes a better method for machining specimens to reduce the surface finish and eliminate the taper.

Acknowledgement The authors would like to thank Stephanie Slaughter (Army College Qualified Leaders program) for her help in preparing the niobium specimens.

References

1. Lindholm, U.S.: Deformation maps in the region of high dislocation velocity. In: Kawata, K., Shioiri, J. (eds.) High Velocity Deformation of Solids, pp. 26–35. Springer, New York (1977)
2. Jia, D., Ramesh, K.T.: A rigorous assessment of the benefits of miniaturization in the Kolsky bar system. Exp. Mech. **44**, 445–454 (2004)
3. Casem, D.T.: A Small Diameter Kolsky bar for High-rate Compression. In: Proceedings of the 2009 SEM Annual Conference and Exposition on Experimental and Applied Mechanics, Albuquerque, 1–4 June 2009
4. Ames, R.G.: Limitations of the Hopkinson Pressure Bar for High-Frequency Measurements. In: Furnish, M.D., Elert, M., Russell, T.P., White, C.T. (eds.) Shock compression of condenser matter, pp. 1233–1237 (2005)
5. Casem, D.T., Grunschel, S.E., Schuster, B.: Normal and transverse displacement interferometers applied to small diameter Kolsky bars. Exp. Mech. **52**, 173–184 (2012)
6. Kim, K., Suk, X., Clifton, R.J., Kumar, P.: A combined normal- and transverse-displacement interferometer with an application to impact of y-cut quartz. J. Appl. Phys. **48**(10), 4132–4139 (1977)
7. Huskins, E.L., Casem, D.T.: Compensation of bending waves in an optically instrumented miniature Kolsky bar. J. Dynamic Behavior Mater. **1**, 65–69 (2015)
8. Casem, D.T., Zellner, M.: Kolsky bar wave separation using a photon doppler velocimeter. Exp. Mech. **53**, 1467–1473 (2013)

Chapter 15
Multi-Scale Mechanical Performance of High Strength-High Ductility Concrete

Ravi Ranade, William F. Heard, and Brett A. Williams

Abstract A new fiber-reinforced cement-based composite, called High Strength-High Ductility Concrete (HSHDC) with unparalleled combination of compressive strength (>150 MPa) and tensile ductility (>3 %), has been recently developed. Due to such unique combination of properties, the specific energies of HSHDC under tension and compression at both pseudo-static and high strain rates are extremely high. The design of this engineered material is based on the fundamental principles of micromechanics which focus on the synchronous functioning of the fiber, the cementitious matrix, and their interface to achieve the desired material properties for a given structural application. For such micromechanics-based design to succeed, the material has been researched at several length scales ranging from micro-scale fiber/matrix interactions to structural-scale impact resistance of HSHDC slabs. This paper summarizes the mechanical properties of HSHDC at various length scales to facilitate further development of this material and explore its potential for use in enhancing structural impact and blast resistance.

Keywords High strength-high ductility concrete • Impact resistance • High performance concrete • Micromechanics • Rate effects

15.1 Introduction

Impact and blast resistance of a material, particularly concrete for protective structures, requires high rate energy absorption, which cannot be met only by increasing the material's compressive strength. Despite this known fact, there had been a race to achieve the strongest concrete, at least until 1980s, as it offered a clear economic incentive of making lightweight structures due to the high strength-to-weight ratio of the high/ultra-high strength concretes. In the last two decades, the focus has shifted away from high strength to high performance and tensile ductility in cement-based materials. This led to the creation of ultra-ductile concretes such as Engineered Cementitious Composites (ECC) [1]. ECC can absorb large amount of energy per unit volume; however, it does not possess similar strength-to-weight ratio as ultra-high strength concretes (UHSC). The ultra-high performance concretes (UHPC) [2], extension of UHSC with the addition of fibers and microstructure improvements, do offer a good strength-to-weight ratio but their energy absorption is limited due to tension-softening behavior. This motivated the development of High Strength-High Ductility Concrete (HSHDC), which offer the performance advantages of both ECC (tensile ductility) and UHPC (compressive strength).

HSHDC, as the name suggests, combines ultra-high compressive strength (>150 MPa) and tensile ductility (>3 %) in one material [3]. The microstructure of HSHDC is tailored specifically to meet these target composite properties. The mix design of HSHDC is given in Table 15.1, and the properties of the ultra-high molecular weight polyethylene (PE) fiber used in HSHDC are given in Table 15.2. In this paper, the multi-scale mechanical characterization and investigation of HSHDC from micro-scale to composite scale to structural element scale is reviewed. At the structural scale, thin slabs of HSHDC are evaluated under drop-weight impact and are compared with similar-sized fiber-reinforced UHPC (FR-UHPC) slabs.

R. Ranade (✉)
State University of New York at Buffalo, 135 Ketter Hall, Buffalo, NY 14260, USA
e-mail: ranade@buffalo.edu

W.F. Heard • B.A. Williams
Engineer Research and Development Center (ERDC) of the US Army Corps of Engineers,
3909 Halls Ferry Rd, Vicksburg, MS 39180, USA

B. Song et al. (eds.), *Dynamic Behavior of Materials, Volume 1*,
Conference Proceedings of the Society for Experimental Mechanics Series, DOI 10.1007/978-3-319-22452-7_15

Table 15.1 Mix proportions of HSHDC

Constituent	Particle size range, μm (1 μm = 3.9 × 10^{-5} in.)	Mix proportions (by weight)	Weight per unit volume	
			(kg/m^3)	(lb/yd^3)
Cement (Class H)	30–80	1	907	1528
Microsilica (Silica Fume)	0.1–1	0.389	353	595
Ground Silica (Silica Flour)	5–100	0.277	251	423
Silica Sand	100–600	0.700	635	1070
Tap Water	–	0.208 w/cm = 0.15	189	318
HRWRA	–	0.018	16	27
PE Fiber[a]	–	0.0214	19	33

[a]Properties of the PE fiber are given in Table 15.2

Table 15.2 Geometry and mechanical/physical properties of the PE Fiber

Diameter	Length	Volume fraction	Tensile strength	Young modulus	Elongation at break	Specific gravity	Melting temp.
28 mm	12.7	2 %	3000 MPa	100 GPa	3.1 %	0.97	150 °C

15.2 Micromechanics-Based Design of HSHDC

Unlike the design of most other cementitious materials which is typically based on empirical results, the design of HSHDC is grounded in the principles of fracture mechanics at the micro-scale (micromechanics). The micromechanics-based design (originally developed for designing ECC) relies primarily on investigating and favorably tailoring the interactions between these phases (particularly fiber/matrix interactions) for achieving desirable composite tensile properties. The excellent compressive properties of HSHDC are achieved by adopting the long-standing design principles of UHPC which include reducing matrix porosity, dense particle packing, promoting mix homogeneity, using sound quality aggregates, and microstructure enhancements through heat curing. Such systematic design of HSHDC facilitates the achievement of the unique combination of compressive strength and tensile ductility.

The major steps involved in the micromechanics-based design procedure for tailoring the tensile properties of HSHDC are shown in Fig. 15.1 below. This procedure typically starts with a matrix optimized for compressed strength, along with certain types of high performance fibers (shortlisted based on strength, modulus, water/cement ratio of the matrix, etc.). The goal of this design procedure is to select the fiber type and geometry which can optimally work with matrix; although, slight matrix modifications are expected to accommodate the fiber.

Starting with the single fiber pullout tests, the fiber/matrix interaction parameters are determined. These parameters are fed into a statistical scale-linking model [4], along with an assumed fiber geometry (diameter and length), to determine the collective bridging stress (σ) of the fibers as a function of the crack opening (δ), known as the σ-δ relation. This σ-δ relation acts as a constitutive law of crack bridging for this particular fiber/matrix system, and is used to infer the maximum complementary energy of fiber bridging (J_b') and the fiber bridging stress capacity (σ_{ult}). The fiber geometry is optimized to maximize J_b' and σ_{ult}. J_b' and σ_{ult} are maximized because the micromechanics principles require (1) σ_{ult} to be greater than the matrix cracking strength (σ_{fc}), and (2) J_b' to be greater than the crack tip toughness J_{tip} to ensure multiple cracking and tensile ductility of HSHDC. Greater ratios σ_{ult}/σ_{fc} and J_b'/J_{tip} lead to greater tensile ductility and robustness of multiple cracking [5].

In case, any of the two necessary micromechanics-based conditions [(1) or (2) above] is violated, the matrix modifications such as lowering the matrix fracture toughness or introducing artificial flaws are investigated, and/or the fiber/matrix bond is altered through fiber coatings or treatments. Even when both the conditions for multiple cracking are satisfied, the design of HSHDC may be limited by the commercial availability of the optimized fiber geometry or the processability of the fibers (e.g. the high aspect ratio of the fibers may make them harder to mix homogenously, particularly in low water/cement ratio matrices such as the HSHDC matrix). The processability and fiber dispersion is improved by controlling the matrix viscosity. If none of the above corrections are successful, the same process is repeated with the next fiber until the most suitable fiber is found for that particular matrix. Composite-scale experiments are performed to verify the tensile and compressive properties of HSHDC.

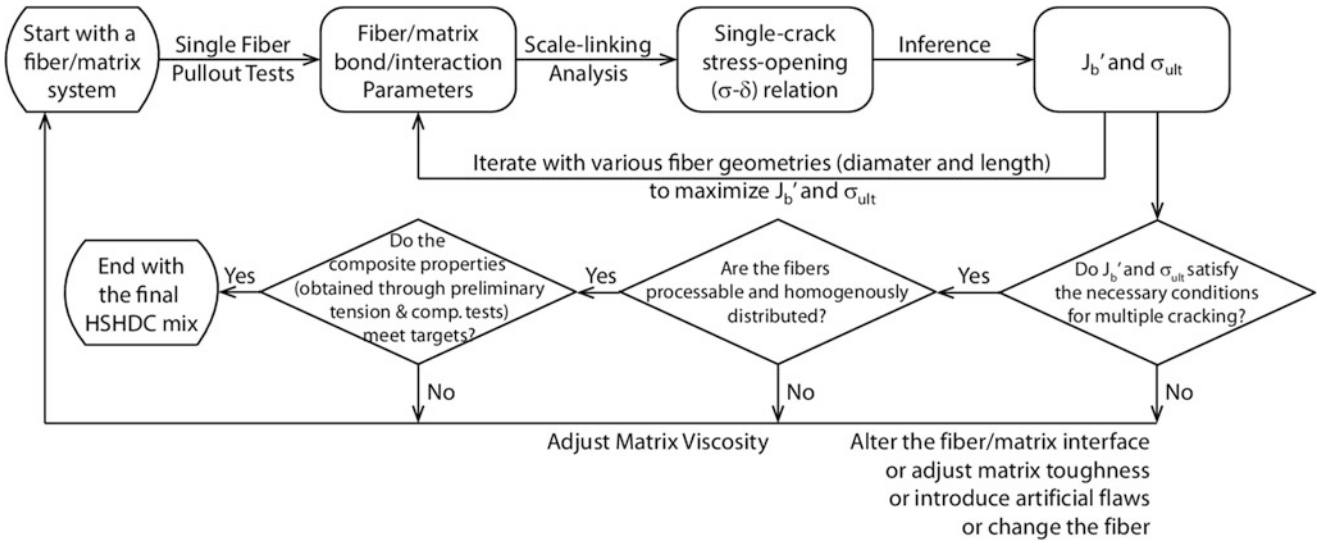

Fig. 15.1 Micromechanics-based procedure for designing HSHDC

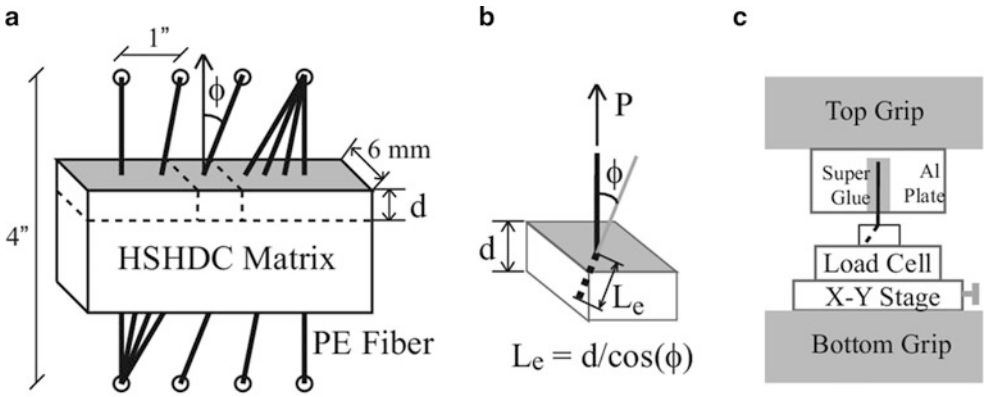

Fig. 15.2 Single-fiber pullout (SFP) test (**a**) specimen preparation for polymer fibers (**b**) individual polymer fiber SFP specimen (**c**) experimental setup

The micromechanical investigation of HSHDC is reported in Ranade et al. [6]. The average fiber/matrix interaction parameters of HSHDC obtained from several single fiber pullout tests (Fig. 15.2). The PE fiber forms high interfacial frictional bond (τ_0) of about 1.52 MPa facilitated by dense particle packing of the very high strength matrix. This high τ_0 accompanied by a negligible chemical bond (G_d), results in a high complementary energy (J_b') favorable for macroscopic strain-hardening response of HSHDC under direct tension. For comparison, the measured τ_0 for the same fiber in a moderate strength matrix has been reported to be 0.54–0.76 MPa [7]. Other fiber/matrix interaction properties of HSHDC determined in this research are snubbing coefficient ($f = 0.59$) and slip hardening parameter ($\beta = 0.003$). All micromechanical properties show wide scatter due to material inhomogeneity (similar to SHCC) at micro-length scale.

A new inclination-dependent hardening mechanism of fiber pullout in HSHDC is also discovered in Ranade el al [6], as the existing fiber/matrix interaction mechanisms [8] developed for similar strain-hardening concretes (such as ECC) are insufficient in completely describing the experimentally observed inclined fiber pullout behavior of PE fibers embedded in a very high strength HSHDC matrix. The SHCC micromechanical model in the pullout phase is modified to incorporate this mechanism. The SEM micrographs (Fig. 15.3) provide evidence for this mechanism and its mathematical formulation. The newly defined inclination hardening parameter, μ (constant property of the composite), is 386 N/(m-rad) for HSHDC.

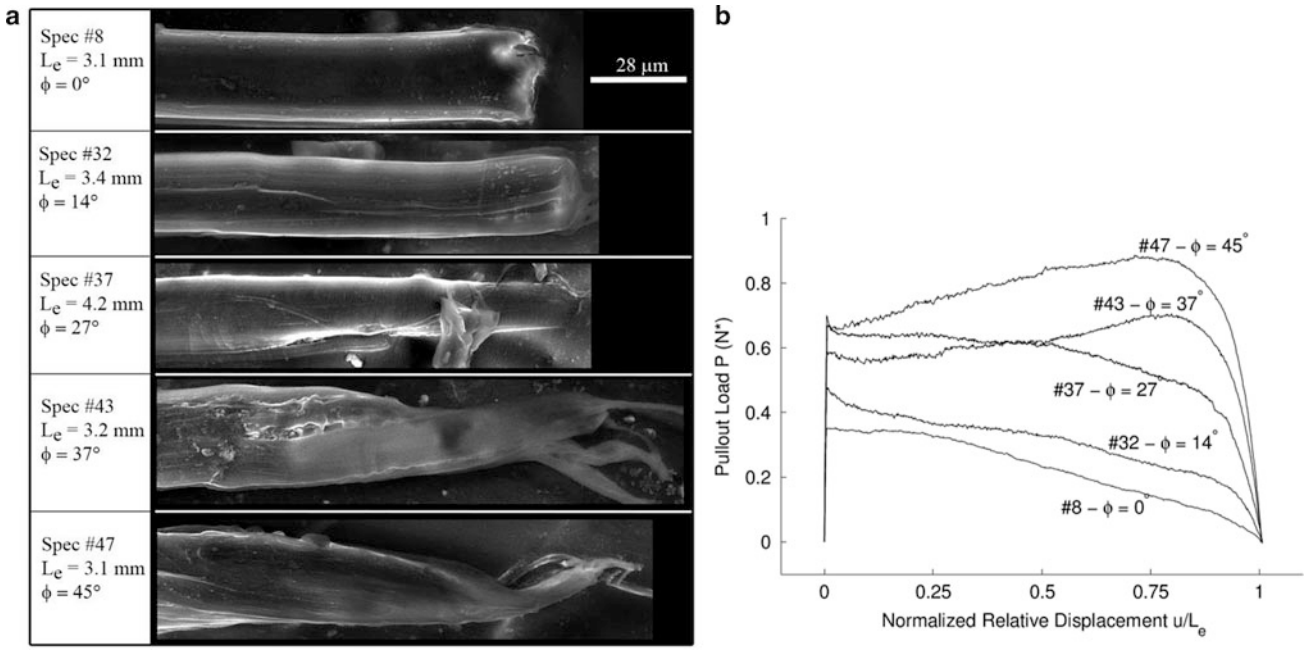

Fig. 15.3 (**a**) SEM micrographs showing increasing fibrillation of highly inclined fibers supporting the presence of inclination hardening in HSHDC observed in (**b**) Single fiber pullout curves of PE fibers embedded in HSHDC matrix

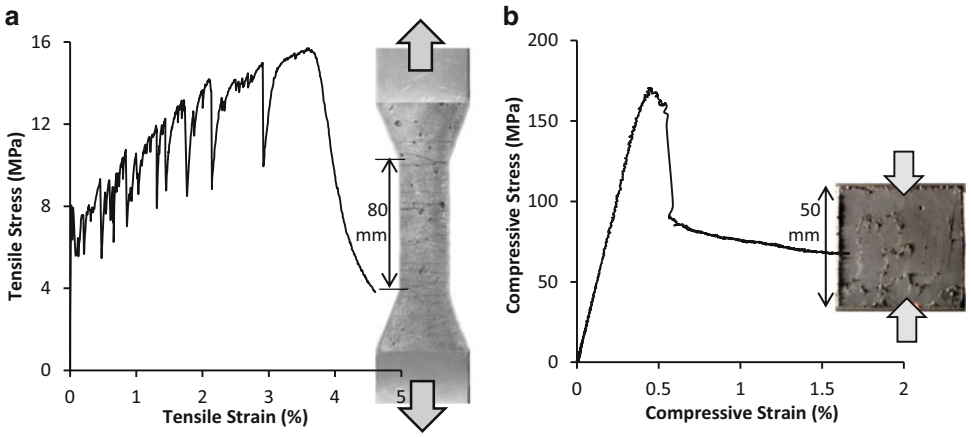

Fig. 15.4 Composite behavior of HSHDC under (**a**) direct uniaxial tension (**b**) direct uniaxial compression

15.3 Composite Properties of HSHDC

The composite-scale characterization of HSHDC is reported in Ranade et al. [3]. The behavior of HSHDC under direct uniaxial tension is shown in Fig. 15.4a. The average tensile stress capacity of HSHDC is about 14.5 MPa and average tensile strain capacity is 3.5 %. As the load increases from zero, the tensile stress inside the composite increases linear-elastically. The matrix cracks for the first time when the stress intensity factor exceeds the fracture toughness of the matrix, typically at the largest internal flaw. The crack propagates almost instantaneously throughout the section under steady-state (a direct result of micro-mechanical tailoring [9]) causing sudden drop in tensile stress as the load transfer capacity of the matrix at the section is lost. However, the fiber bridging capacity is not exceeded at the matrix cracking stress (another result of micromechanics-based design), and the tensile stress is gradually regained exceeding the first crack stress. The tensile stress increases until another crack is triggered at the next largest flaw and the process repeats until the fiber bridging capacity is exceeded by the applied tensile stress at one of these cracked sections. After this point, the tensile stress reduces

monotonically following the bridging stress-crack opening relation. Thus, the micromechanics-based design of HSHDC facilitates multiple micro-cracking of the matrix under tension which is the fundamental reason behind the extraordinary tensile ductility and specific energy of the composite.

The behavior of HSHDC under uniaxial compression is shown in Fig. 15.4b. The pre-peak branch of these curves is extremely linear and elastic, which is typical of VHSC/UHPCs. Near the peak (within about 20 % of the peak load), the stress-strain curve of HSHDC becomes non-linear and inelastic due to the nucleation of microcracks at grain boundaries, micro-defects, and other micro-scale heterogeneities. These cracks are stabilized through fiber-bridging in HSHDC resulting in a more ductile response and a flattened peak (in HSHDC) instead of a sharp peak typically observed in VHSC/UHPCs [2, 10]. Furthermore, it can be seen in Fig. 15.4b that the post-peak stress after the axial splitting of an HSHDC cube does not suddenly drop to near zero but to a residual stress value of 60–80 MPa. Thereafter, the stress gradually decreases to zero with increasing compressive displacement. Overall, HSHDC shows linear elastic behavior under uniaxial compression until 80 % of its peak strength, followed by a relatively ductile near-peak and post-peak response.

The flexural behavior of HSHDC under four-point bending (using 100 × 100 × 300 mm beams) is investigated in Ranade et al. [3]. The average modulus of rupture (MOR) of HSHDC beams is about 32 MPa and the average mid-point net deflection of the beam at MOR is about 2.5 % of the span length. The high flexural strength and ductility of HSHDC are direct results of its high compressive strength and tensile ductility. For instance, the MOR of HSHDC beams can be predicted from its properties under uniaxial tension and compression using the analytical model developed by Maalej and Li [11]. The average MOR/σ_{tc} ratio of HSHDC is 3.8, which agrees well with the analytical prediction.

15.4 Tensile Rate Effects in HSHDC

The properties of HSHDC, similar to other cement-based materials [12], are influenced by the strain/load rate [13]. As the strain rate is increased from 0.0001/s to 10/s, average first crack strength (σ_{fc}) and average ultimate tensile strength (σ_{ult}) of HSHDC dogbone specimens increase by about 53 % and 42 %, respectively, as observed in Fig. 15.5a. In spite of a relatively constant ratio of σ_{ult}/σ_{fc} with strain rate, the tensile strain capacity decreases to 2.9 % at 0.1/s and plateaus after that. Such variation in tensile strain capacity is attributable to a similar trend in average crack width which reduces from 160 μm at 0.0001/s to 120 μm at 0.1/s and plateaus for higher strain rates.

These tensile rate effects at the composite scale are caused due to the rate effects at the micro-scale, reported in Ranade et al. [13]. Almost all the fiber/matrix interaction properties, fiber properties, and matrix fracture toughness exhibit changes with displacement rate (equivalent to the strain rate in composite testing) to varying degrees. The interfacial frictional bond (τ_0) increases only slightly (by 14 %) over the six orders of displacement rates investigated in this study (0.009–900 mm/s). The absence of chemical bond between the PE fiber and HSHDC matrix makes the overall fiber/matrix bond relatively

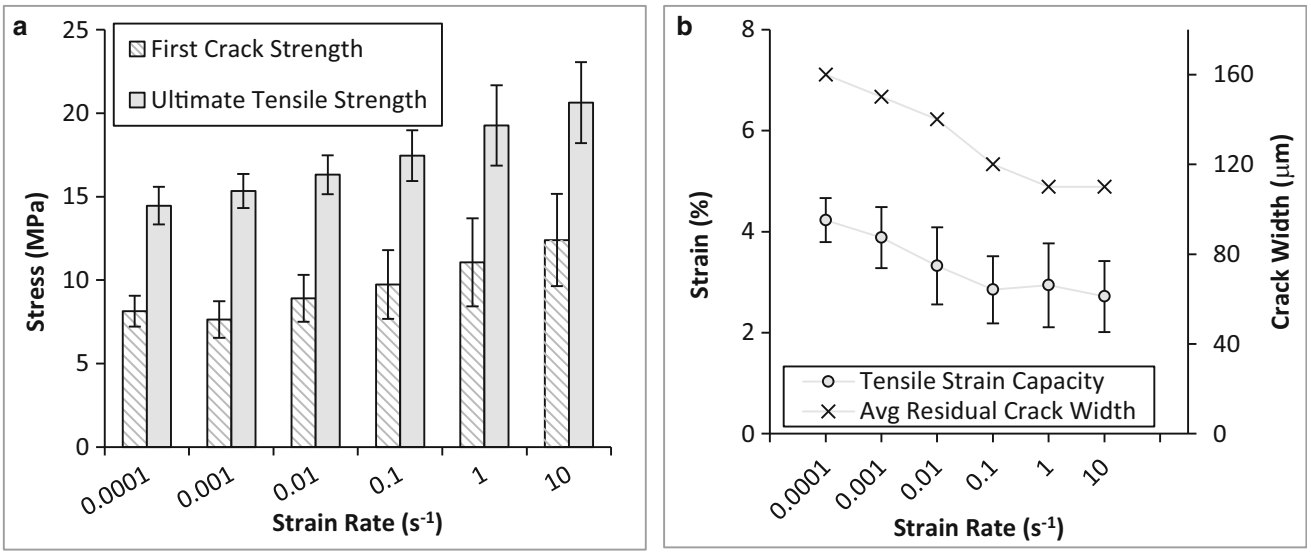

Fig. 15.5 Composite scale rate effects in HSHDC. (**a**) First crack strength and Ultimate tensile strength (**b**) Tensile strain capacity and average residual crack width

insensitive to rate effects. The changes that are the most consequential for fiber-bridging in HSHDC are the increases in PE fiber strength and modulus with displacement rate. At the fastest rate, the PE fiber strength and modulus increase by about 21 and 85 % of their respective quasi-static values. However, these increase in fiber strength and modulus, along with the increase in fiber/matrix interaction properties, result in the reduction of complementary energy (J_b') of fiber-bridging. Nevertheless, J_b' remains significantly greater (about six times) than the crack tip toughness even at the highest strain rate investigated in this study, which coupled with constant σ_{ult}/σ_{fc} ratio (due to comparable increases in matrix fracture toughness and fiber-bridging capacity) facilitates multiple cracking and energy absorbing capacity of HSHDC at all strain rates investigated in this study.

15.5 Impact Resistance of HSHDC

The behavior of thin slabs of HSHDC under multiple, moderate-velocity impacts is investigated utilizing preliminary drop-weight impact experiments (Fig. 15.6) [14]. The behavior of HSHDC slabs (300 × 300 × 25 mm) is compared with the behavior of same-sized slabs made of a fiber-reinforced Ultra-high Performance Concrete (FR-UHPC) with compressive strength greater than 200 MPa. A constant weight of 16.04 kg was dropped repeatedly on both HSHDC and FR-UHPC slabs using a cylindrical steel impact head of diameter 75 mm from a height of 1.40 m. The impacts are repeated for either 20 times or until slab failure, whichever occurs first. Almost zero rebound of the impact head either due to flexural failure of the slab or due to head penetration in the slab is deemed as 'slab failure'.

The performance of HSHDC slabs (solid curves) under repeated impacts is compared with that of the FR-UHPC slabs (dashed curves) in Fig. 15.7. Each impact produces significant inelastic tensile strains, which accumulate with increasing number of impacts. As soon as the deflection-hardening capacity of the FR-UHPC slab is exceeded, it starts to lose its impact load bearing capacity as observed by the drops in the peak contact force (PCF) in Fig. 15.7a. The drop in PCF of FR-UHPC slabs occurs rapidly after seventh to eighth impacts. In contrast, PCF in HSHDC slabs remains almost constant for all the impacts. While the FR-UHPC slabs fail under flexure before 20 impacts, HSHDC slabs maintain their integrity and continue to rebound the drop-weight assembly during all the 20 impacts. The damage tolerance of HSHDC, which is significantly higher than FR-UHPC under tension, allows the HSHDC slabs to absorb more impact energy, while maintaining their structural integrity, compared to the FR-UHPC slabs.

15.6 Modelling HSHDC in LS-Dyna

In order to investigate the structural applications of HSHDC for impact and blast resistance, the MAT_072R3 material model in the LS-Dyna library is employed. Although the MAT_072R3 model (also known as K&C model) was originally developed by Malvar et al. [15] for concrete and tension-softening FRCs, it can be adopted for HSHDC (and similar strain-hardening concretes) because it has (1) three separate fixed 'loading surfaces' (yield, ultimate, and residual), and (2) independent parameters for controlling the damage evolutions in tension and in compression. While the mathematical details of the MAT_072R3 model are presented in Malvar et al. [15] and other texts on concrete plasticity, the main features and

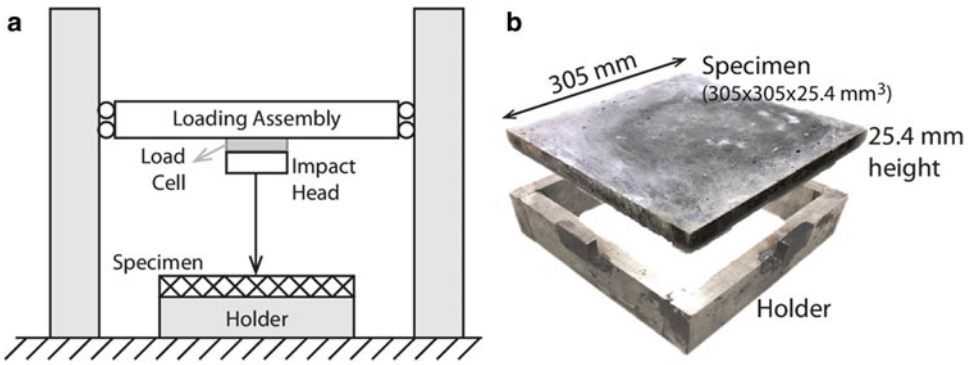

Fig. 15.6 Drop-weight impact experiment (**a**) Test setup (**b**) Specimen dimensions

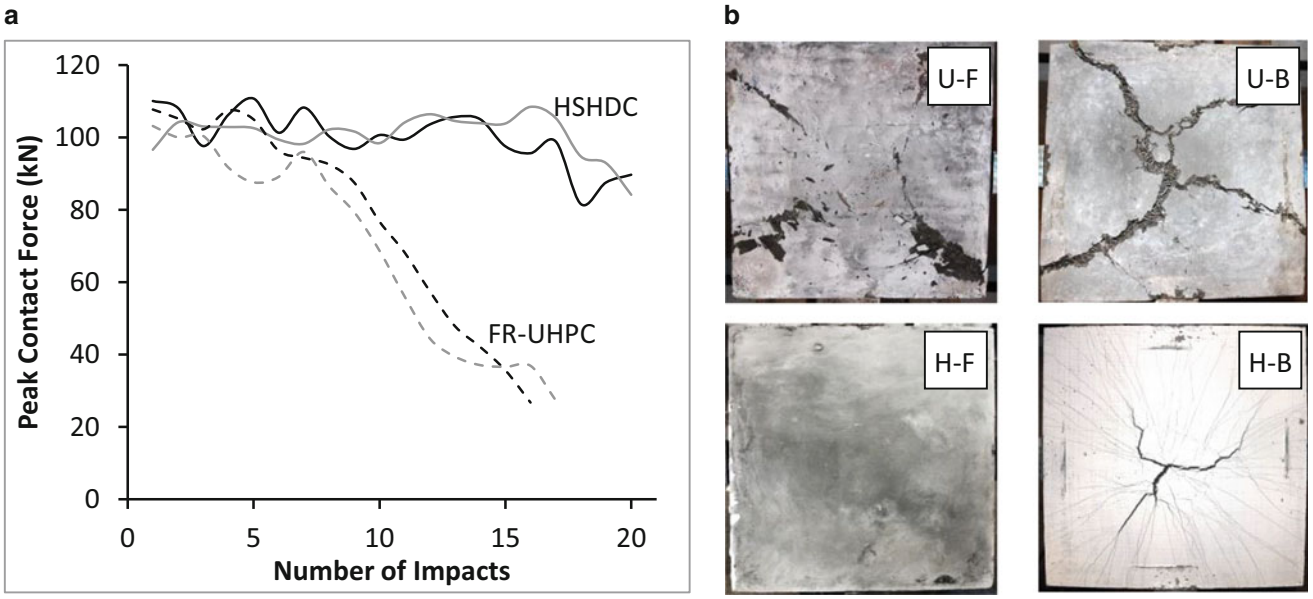

Fig. 15.7 Comparison of HSHDC and FR-UHPC slabs under multiple impacts (**a**) Peak contact force (**b**) Visual damage in the slabs of both materials*. *U is FR-UHPC and H is HSHDC; F denotes front (compression) face and B denotes back (tensile) face

Table 15.3 MAT_072R3 loading surface parameters for modelling HSHDC

a_{0y} (MPa)	a_{1y}	a_{2y} (MPa^{-1})	a_0	a_1	a_2	a_{1f}	a_{2f}
22.6×10^6	0.397	1.2×10^{-9}	24×10^6	0.366	4.91×10^{-10}	0.356	4.80×10^{-10}

setup of this model with all the inputs required for simulating HSHDC using the MAT_072R3 model are given in Ranade et al. [15].

The input parameters for the MAT_072R3 material model in LS-Dyna can be broadly classified into three categories: (1) loading surfaces, (2) damage accumulation, and (3) other inputs [15]. The eight parameters of MAT_072R3 grouped as: (a_{0y}, a_{1y}, a_{2y}), (a_0, a_1, a_2), and (a_{1f}, a_{2f}) describe the $p - \Delta\sigma$ loading curves on the compressive meridian of yield, maximum, and residual loading surfaces, respectively. As noted in Malvar et al. [15], the 3D failure surface in the post-elastic stage moves between three fixed 'loading surfaces', namely yield, maximum, and residual. Mathematically, at a particular damage state represented by damage parameter η in MAT_072R3, the failure surface is a linear combination of either the yield and the maximum or the maximum and the residual loading surfaces with coefficients η and $(1 - \eta)$. A combination of uniaxial test results conducted by the authors and previous multi-axial tests on concretes with similar compressive strength are used as known data points (p, Δσ) to determine the eight parameters for modelling HSHDC, noted in Table 15.3.

The damage parameter η is defined as a function of cumulative effective plastic strain parameter, λ in MAT_072R3. The parameter λ above is computed from the tensorial plastic strains, ε_{ij}^{p}, in the MAT_072R3 [15]. The η-λ damage function is input by the user (Table 15.4) based on the shape of the material's experimental uniaxial compressive behaviour. The values of the damage scaling parameters b_1 and b_2 used for the SHCC in this study are determined by matching the computed stress-strain responses of a single element with the experimental curves, and are set equal to −0.55 and −20, respectively.

Other parameters required as inputs in the MAT_072R3 model are density (2400 kg/m^3), Poisson ratio (0.20), and localization width of the crack (LOCWIDTH = 2 mm). LOCWIDTH is assumed equal to the element size, which is 2 mm, to prevent localization instabilities and spurious mesh sensitivity. Decreasing LOCWIDTH increases the observed ductility in both tension and compression.

All the model parameters discussed thus far for defining the failure surface capture only the *deviatoric* behavior of the material, and therefore, an 'equation of state' (EOS), which defines the *hydrostatic* behavior of a material by relating the hydrostatic pressure to the volumetric strain, is needed to completely describe the material behavior [15]. For this purpose, the EOS of type 8 (EOS 8) in LS-Dyna, which inputs tabulated pressure-volumetric strain data points (linear variation is assumed between the specified points) along with instantaneous bulk modulus at these points (for unloading), is used. The

Table 15.4 MAT_072R3 damage function $\eta-\lambda$ for modelling HSHDC

λ	0	1.2×10^{-5}	2.4×10^{-5}	4×10^{-5}	5.6×10^{-5}	7.2×10^{-5}	8.8×10^{-5}	1.0×10^{-4}	2.5×10^{-4}	7.0×10^{-4}	2.5×10^{-3}	10	1.0×10^{10}
η	0	0.85	0.97	0.99	1	0.99	0.88	0.3	0.2	0.1	0	0	0

rate effect on the material strength is incorporated in the model by specifying a 'load curve' in LS-Dyna, by relating dynamic increase factors (DIF) to strain rate. Failure of the material is defined using tensile and compressive erosion criteria in this study. The erosion criterion (using MAT_ADD_EROSION keyword in LS-Dyna) for tensile strain is set at 2.9 %, and that for hydrostatic pressure is set at 400 MPa. Using all the above parameters, the observed uniaxial stress-strain curves of HSHDC are satisfactorily modeled at various strain rates. Furthermore, the impact performance of HSHDC slabs (discussed above) is also satisfactorily modeled using this material model; for details, the reader is referred to Ranade [14].

15.7 Conclusions and Future Research and Applications

The development of HSHDC has opened a new avenue for material research and development, which, instead of trading-off strength for ductility/durability (and vice-versa), achieves both the objectives simultaneously. The tensile rate effects investigation reveals that the material remains ductile at high rates, which, is promising for high energy applications such as impacts and blasts; however, the strain rates are a lot higher in such events and the material is yet to be tested at these rates. Furthermore, the behavior of HSHDC with conventional steel reinforcement must be quantified in the future, as most potential structural applications of HSHDC will contain such reinforcement. In addition to structural resilience, HSHDC is also expected to be an extremely durable material owing to its tight crack width and tensile ductility. Integrated life cycle assessments investigating both the resilience and sustainability of a structure together are expected to further reveal the potential uses of HSHDC in civil and military infrastructure.

Acknowledgments The authors would like to thank Lafarge, Holcim, WR Grace, US Silica, and Honeywell for providing the materials for this research. Permission to publish was granted by the Director, Geotechnical and Structures Laboratory at ERDC.

References

1. Li, V.C.: On engineered cementitious composites (ECC)—a review of the material and its applications. J. Adv. Concr. Technol. **1**(3), 215–230 (2003)
2. Russell, H.G., Graybeal, B.A.: Ultra-high performance concrete: a state-of-the-art report for the Bridge Community, Publication No. FHWA-HRT-13-060, pp. 1–25. US DoT, Federeal Highway Administration, McLean, VA (2013)
3. Ranade, R., Li, V.C., Stults, M.D., Heard, W.F., Rushing, T.S.: Composite mechanical properties of high strength-high ductility concrete. ACI Mater. J. **110**(4), 413–422 (2013)
4. Li, V.C., Wang, Y., Backer, S.: A micromechanical model of tension-softening and bridging toughening of short random fiber reinforced brittle matrix composites. J. Mech. Phys. Solids **39**(5), 607–625 (1991)
5. Kanda, T., Li, V.C.: Multiple cracking sequence and saturation in fiber reinforced cementitious composites. Concr. Res. Technol. **9**(2), 19–33 (1998)
6. Ranade, R., Li, V.C., Stults, M.D., Rushing, T.S., Roth, J., Heard, W.F.: Micromechanics of high strength-high ductility concrete. ACI Mater. J. **110**(4), 375–384 (2013)
7. Li, V.C., Maalej, M.: Effect of plasma treatment of polyethylene fibers on interface and cementitious composite properties. J. Am. Ceram. Soc. **79**(1), 74–78 (1996)
8. Lin, Z., Kanda, T., Li, V.C.: On interface property characterization and performance of fiber reinforced cementitious composites. J. Concr. Sci. Eng. **1**, 173–184 (1999)
9. Li, V.C., Wang, S., Wu, C.: Tensile strain-hardening behavior of PVA-ECC. ACI Mater. J. **98**(6), 483–492 (2001)
10. Wight, J.K., MacGregor, J.G.: Stress-strain Curves for Concrete. In: Wight, J.K., MacGregor, J.G. (eds.) Reinforced Concrete: Mechanics and Design, 5th ed, pp. 64–70. Upper Saddle River, NJ: Prentice Hall (2009)
11. Maalej, M., Li, V.C.: Flexural/tensile-strength ratio in engineered cementitious composites. J. Mater. Civ. Eng. **6**(4), 513–528 (1994)
12. Bischoff, P.H., Perry, S.H.: Compressive behavior of concrete at high strain rates. J. Mater. Struct. **24**, 425–450 (1991)
13. Ranade, R., Li, V.C., Heard, W.F.: Tensile rate effects in high strength-high ductility concrete. Cem. Concr. Res. **68**, 94–104 (2014)
14. Ranade, R.: Advanced cementitious composites development for resilient and sustainable infrastructure, pp. 216–297. Ph.D. Dissertation, University of Michigan (2014)
15. Malvar, L.J., Crawford, J.E., Wesevich, J.W., Simons, D.: A plasticity concrete material model for DYNA3D. Int. J. Impact Eng. **19**(9–10), 847–873 (1997)
16. Ranade, R., Li, V.C.: Material model for SIMULATING SHCC in LS-Dyna. In: Proceedings of RILEM SHCC-3, pp. 235–242, Dordrecht, Netherlands, 3–5 Nov 2014

Chapter 16
PZT Experimental Detection of Natural Frequencies for Compressed Thin-Walled Beams

E. Lofrano, A. Carpinteri, R. Malvano, A. Manuello, G. Piana, and G. Ruta

Abstract By means of PZT pickups, we experimentally measured the natural frequencies of an aluminum thin-walled open profile under centered compression, and investigated the effects of end warping constraints on free vibration and buckling loads. The specimen was mounted on a MTS testing machine, controlling the axial displacement imposed to a beam end by the hydraulic jack. The free vibration frequencies were detected for different values of the compressive force. The experimental results are compared to those provided by an in-house numerical code, which investigates the elastic stability of thin-walled beams in a dynamic setting. Indeed, the code is able to follow the paths of natural frequencies versus the applied load, accounting for the effect of cross-sectional warping on both natural frequencies and buckling loads. The experimental results show that piezoelectric pickups, like the disk adopted, can be efficiently used for the experimental modal analysis of engineering structures.

Keywords Natural frequencies • PZT sensors • Thin-walled beams • Warping constraints • Buckling • Numerical simulations

16.1 Introduction and Outline of the Investigation

It is well known that the mechanical characteristics of thin-walled beams with open profile are their appreciable bending stiffness about at least one principal axis of inertia, and, by contrast, their negligible torsion stiffness. Moreover, since in general the placement of their centroid is different from that of their center of shear, bending and torsion are coupled both in the linear and nonlinear range. As a consequence, their elastic buckling modes are coupled, and the post-buckling behavior is unstable [1]. In addition, also due to their geometry, it is known that Saint-Venant's principle does not hold, and boundary effects propagate throughout the beam length [2]: this makes the effect of warping, and of warping constraints, appreciable, if not dominant, also because of the additional contribution of torsion couple [2, 3]. Due to the widespread applications of such profiles, the investigation of the critical load for such beams has always been an interesting subject in many fields of engineering; some of the authors have published on the matter [4–6].

In the current literature on the critical loads for thin-walled beams, it is usually assumed that the pre-buckling equilibrium path is trivial, i.e., it is taken as reasonable that the applied load does not sensibly deform the considered element [1–3]. This may be a physically reasonable assumption for beams with solid cross-sections, the axial stiffness of which is remarkable; the coupling between bending and torsion is not so important, and warping effects are negligible too. However, when dealing with thin-walled beams, the pre-buckling path can have much effect on the critical load, and investigations on non-trivial

E. Lofrano • G. Piana • G. Ruta (✉)
Department of Structural and Geotechnical Engineering, Sapienza University, Via Eudossiana 18, Rome 00184, Italy
e-mail: giuseppe.ruta@uniroma1.it

A. Carpinteri • A. Manuello
Department of Structural, Geotechnical and Building Engineering, Politecnico di Torino,
Corso Duca degli Abruzzi 24, Torino 10129, Italy

R. Malvano
Department of Mechanical and Aerospace Engineering, National Institute of Metrological Research—INRIM,
C/o Politecnico di Torino, Corso Duca degli Abruzzi 24, Torino 10129, Italy

B. Song et al. (eds.), *Dynamic Behavior of Materials, Volume 1*,
Conference Proceedings of the Society for Experimental Mechanics Series, DOI 10.1007/978-3-319-22452-7_16

equilibrium paths leading to buckling can be of interest. Some of the authors have performed numerical investigations on the subject [7–9], by elaborating an *in-house* finite differences code based on the model dealt with in [4–6]. Further refinements of the model have been proposed in [10], and additional refinements of the numerical code are in progress, to take into account fully non-conservative loads.

In the meanwhile, some others among the authors have investigated, numerically and experimentally, the variation of the natural frequencies of compressed beams [11], taking advantage of a vast experience on experimental settings. Indeed, it is important, from the point of view of applications, to detect how natural frequencies change as a function of the state of stress of the considered structural element: such knowledge may result to be useful for design, monitoring, and damage detection.

Now, it is well known that the buckling critical load is attained when the relevant natural frequency vanishes following a load path in which the same natural frequency diminishes as the load increases, i.e., as the apparent stiffness of the beam goes down. It has been straightforward, then, to design an experimental campaign of validation of the results obtained numerically for thin-walled beams with open profile, with the aim of: (a) generalizing the experimental investigations already performed, to keep into account warping and warping constraints, so typical of thin-walled profiles, by designing and realizing suitable end constraint devices to match the analytical conditions introduced in the numerical investigation; (b) finding experimental validation of the numerical results obtained so far; and (c) highlighting, by experimental evidence, the role of the pre-buckling equilibrium path, usually neglected in the literature.

Since this is a long-term project, the research group has begun investigating the effect of compressive loads operated by a universal MTS testing machine on simple specimens, suitably constrained at the ends by devices designed and made on purpose, to take into account the warping properties of thin-walled profiles. In [11] some of the authors have adopted laser techniques to detect the natural frequencies of the tested beams, suitably curved to simulate a known imperfection, or a pre-buckling path. Here, however, we report how the use of PZT pickups, characteristic of musical technologies, is effective, precise, robust, and reliable in the experimental campaign.

The first set of specimens was with cruciform cross-sections; in this contribution, we fully describe the obtained results, and the comparisons with the corresponding numerical ones. Another set of specimens, with doubly symmetric cross-section to simplify the experimental apparatus in these first campaigns, but with non-negligible warping stiffness, is under consideration, and the obtained results will be reported in due course.

16.2 Experimental Setup, Equipment, and Testing Procedure

In order to design, calibrate, and validate an experimental setup useful for the experimental investigation of the stability and dynamics of thin-walled profiles, a first set of specimens endowed with cruciform cross-section was chosen. The physical and mechanical properties of the specimen are reported in Table 16.1. In particular, while the geometrical quantities and the mass density were measured, the elastic constants (the Young's modulus and the Poisson's ratio) were assumed based on the characteristics declared by the manufacturer. Since this was a preliminary phase of a more general study, the specimen's profile was not rectified, therefore some small variations in the geometrical dimensions of the cross section were present along the beam axis.

Figure 16.1 shows the experimental setup adopted for the tests. A servo-hydraulic MTS testing machine, with a closed-loop electronic control and a maximum loading capacity of 100 kN, was used to provide the loading. The specimen was positioned vertically, and constrained to the testing machine by means of connections that were able to prevent displacements, rotations and twist of the end sections (Fig. 16.1a). In particular, two brass elements were manufactured in order to allow the insertion of the beam ends, with the possibility of preventing or permitting the warping deformation of the terminal sections respectively by means of the removal (Fig. 16.1b, left) or the introduction (Fig. 16.1b, right) of suitable screws. Moreover, the position of the lower joint could be adjusted in the horizontal plane in order to ensure the required vertical alignment with the upper joint (Fig. 16.1c). During the tests, the loading was operated by controlling the vertical displacement transmitted to the lower beam end by the hydraulic jack.

As regards to the measuring devices, a laser displacement transducer (laser sensor) and a piezoelectric disk buzzer (PZT sensor or pickup) were adopted. In principle, both possess characteristics such that dynamic identification tests can be

Table 16.1 Physical and mechanical properties of the specimen

Unconstrained length, mm	Total web width, mm	Web thickness, mm	Young's modulus, N m^{-2}	Poisson's coefficient	Mass density, kg m^{-3}
670	32	1.0	70×10^9	0.3	2600

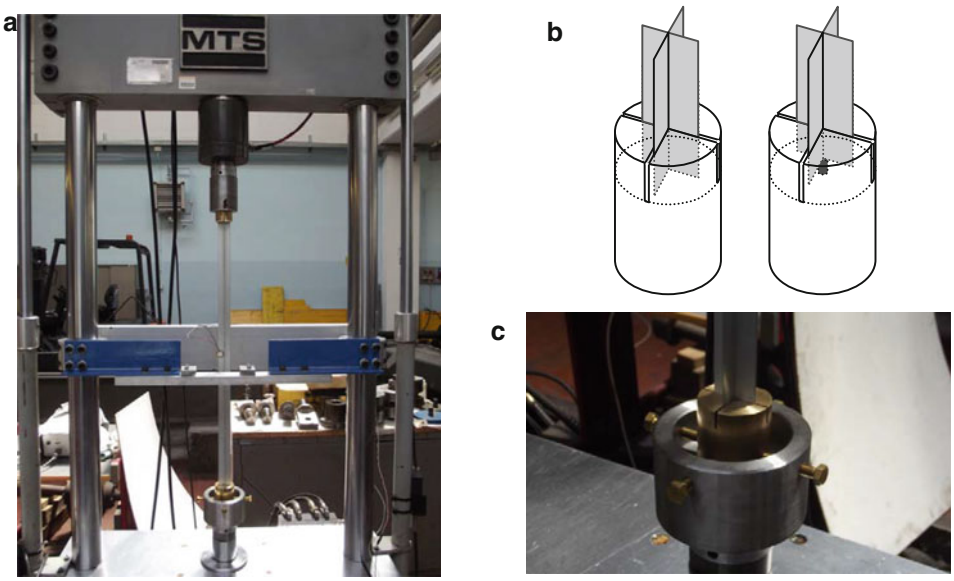

Fig. 16.1 Experimental setup: (**a**) testing machine, (**b**) detail and (**c**) picture of an end joint

Table 16.2 Main characteristics of the laser and PZT sensors

Laser sensor		PZT sensor	
Measuring range, mm	20	External diameter, mm	20
Start of measuring range, mm	30	Frequency range, kHz	~0 to 20
End of measuring range, mm	50	Resonant frequency, kHz	6.0 ± 0.5
Frequency range, Hz	0–750	Operating temperature, °C	−20 to +50
Resolution, μm	10	Weight, g	0.91

conducted without perturbing the mass of the specimen. Nevertheless, for the present application, the PZT pickup presents several advantages with respect to the adopted laser sensor, which instead presents strong limitations instead.

The adopted laser sensor is the optoNCDT 1302-20, a triangulating displacement sensor produced by Micro-Epsilon. It has a resolution of 10 μm for dynamic acquisitions at the maximum frequency of 750 Hz, and a default measuring range equal to 20 mm (it can be narrowed by the user to utilize the maximum resolution on a reduced range of distance); the midrange is positioned at 40 mm far from the surface of the transducer. The adopted PZT sensor is a transducer that produces an electric voltage signal when subjected to dynamic deformation (direct piezoelectric effect), thus it does not need any supply. The generated signal can be amplified if necessary, acquired by audio acquisition devices as well as classical data acquisition devices, and therefore recorded and post-processed. This sensor can be connected to the surface of the specimen simply by using a glue or a thin film of gel, and their usage do not require any calibration. An assessment of the capabilities of PZT disks for the experimental modal analysis was conducted by some of the authors [12]. The main features of the adopted laser and PZT sensors are reported in Table 16.2. As can be easily seen, the operating frequency range of the laser sensor is much smaller than that of the PZT sensor; this represents a crucial point in our experimental campaign.

During the tests, both the laser and PZT sensors were located at mid-height with respect to the specimen: the setup is shown in Fig. 16.2. The laser sensor was mounted on an adjustable slider (in order to regulate the distance from the surface of the specimen), which in turn was sustained by a transverse connected to the testing machine frame (Fig. 16.2a). The PZT sensor was attached to the surface of the beam by a thin film of gel.

The natural frequencies were therefore extracted for different values of the compressive axial force. For the frequency identification, only one measuring point was adopted. Signals coming from both the laser sensor and the PZT disk were acquired by using a NI 9215 data acquisition device produced by National Instruments. This is a four channels-device, with a resolution of 16 bits, a maximum sampling frequency of 100 kHz, and an operating voltage range from −10 to 10 V. The adopted sampling frequencies were equal to 750 Hz and 3 kHz for the laser sensor and the PZT sensor, respectively. In the case of the PZT sensor, signals were pre-amplified by means of an operational amplifier. Acquisition, processing and post-processing of measured signals were made using the software LabVIEW.

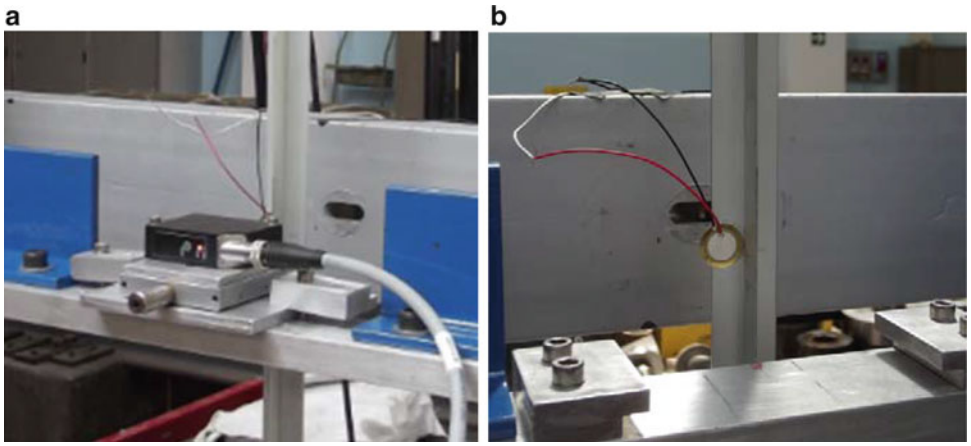

Fig. 16.2 (**a**) Laser and (**b**) PZT measuring system

Table 16.3 Frequencies detected during the experimental tests (unloaded specimens)

Mode	Laser *f*, Hz	PZT *f*, Hz	Diff., %
1	160.92	161.87	0.59
2	–	275.47	–
3	–	284.18	–
4	–	325.43	–
5	–	486.13	–
6	–	667.84	–
7	–	741.30	–
8	–	767.53	–
9	–	813.39	–

16.3 Experimental Results

The results obtained in terms of natural frequencies of the unleaded beam for the experimental setup described in the previous section are listed in Table 16.3. The specimen was excited with several impulses, and the dynamic responses were post-processed by performing a Fast Fourier Transform to obtain the first nine natural frequencies. Only the responses were measured (i.e., an operational modal analysis was performed), and the frequencies were detected using the Peak Picking technique. As one can see, by using the laser sensor it has been possible to detect only the fundamental frequency, while the PZT sensor has been able to catch also the higher ones. Nevertheless, the percentage difference found for the first frequency indicates that PZT sensors are able to identify resonant frequencies with a precision comparable to that of a non-contact transducer such as the adopted laser sensor.

To follow the frequency paths for increasing values of the axial compressive load, the same procedure was repeated step by step for a series of progressive displacement increments imposed by the MTS. The results obtained for the fundamental frequency are collected in Table 16.4. The small values of the standard deviations, σ, for both laser and PZT measurements indicate that all processed data were reliable, while the small percentage difference between the two sets of data points out that also the frequency-load path can be efficiently detected by the pickup. The comparison among the curves provided by the laser and the PZT sensor for the first frequency is shown in Fig. 16.3a, while Fig. 16.3b shows the first nine frequency-load paths obtained with the PZT pickup when the warping of the end sections was constrained or allowed. As expected, the results in Fig. 16.3b show that the curves obtained constraining and releasing the warping motion are practically indistinguishable (a small shift appears for the ninth frequency, but reasonably this difference is due to some problem connected to the measurement, rather than to warping). As regards to the warping effect, which is obviously negligible for this kind of section, it was therefore verified that the realized end joints system is actually able not to affect the frequency-load curves of interest.

Table 16.4 Comparison among frequencies detected by laser and PZT sensors for different values of the imposed displacement

Load, kN	Displacement, mm	Laser		PZT		Diff., %
		Frequency f, Hz	Standard deviation σ, Hz	Frequency f, Hz	Standard deviation σ, Hz	
0.00	0.00	161.73	1.06	161.87	0.69	0.09
0.24	0.12	156.88	0.40	159.12	0.03	1.43
0.49	0.19	154.08	0.70	156.42	0.45	1.52
1.00	0.34	150.04	0.45	151.69	0.56	1.10
1.41	0.45	146.6	0.56	149.22	0.31	1.79
2.02	0.61	142.44	0.85	145.42	0.46	2.09
2.46	0.73	139.6	0.46	142.33	0.63	1.96
2.98	0.85	135.94	0.64	138.24	0.28	1.69
3.43	0.97	132.33	0.37	134.61	0.92	1.72
3.95	1.14	130.96	0.34	131.33	1.26	0.28

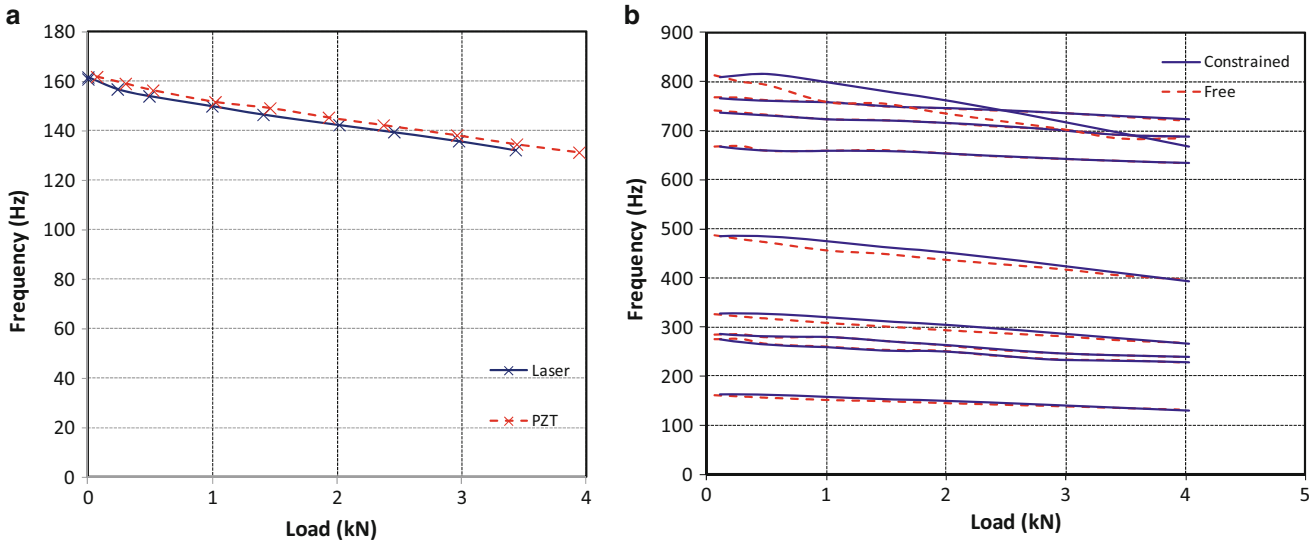

Fig. 16.3 Frequencies vs. load plots: (**a**) comparison among the curves provided by the laser and the PZT sensor (first frequency) and (**b**) effect of warping constraints (first nine frequencies, PZT sensor)

16.4 Numerical Simulations and Comparisons

In this section, starting from the properties listed in Table 16.1, and recalling that the end joints of the beam were capable to prevent the displacements as well as the rotations and the twist of the end sections (like a double clamped beam with an imposed displacement at the bottom), two numerical models were built. The first was achieved by using a finite element commercial code (Lusas) and it was used to validate the physical and mechanical characteristics listed in Table 16.1, as well as the frequency values obtained with the PZT sensor (see Table 16.3). The second model was implemented in a *in-house* finite differences code, developed by some of the authors of this work [8], here used to follow the frequency-load responses and to evaluate the critical load.

16.4.1 Finite Element Analyses

Three finite element models were implemented: a thin shell, a thick shell, and a brick (i.e., 3-d solid) model. For the first model, the QSL8 finite element was selected: it includes both membrane and bending behaviors, while shear deformability is neglected. QTS8 thick shell elements were adopted for the second model: these elements have five

degrees of freedom per node (three displacements and two rotations) and include shear deformability, in addition to membrane and bending deformability. In this case, the meshing was made by adopting 180 subdivisions along the beam axis, and 4 subdivisions per side (16 in total) in the cross-sectional plane. Lastly, HX20 3D solid elements were used for the brick model: this element has three displacement degrees of freedom per node and its formulation is based on the classical isoparametric approach; in the specific case, a quadratic interpolation of nodal displacements was adopted. This element presents a regular geometry, therefore no aspect-ratio problems are attended. The mesh was realized by adopting 180 subdivisions along the beam axis, 4 subdivisions per side (16 in total) along the web directions, and 1 subdivision along the web thickness.

For sake of explanation, Fig. 16.4 shows the first mode shape and relevant frequency obtained for each model. A comparison among the first nine frequencies (of the unloaded beams) obtained with the FEM code (linear eigenvalue analysis) and the ones revealed by experimental tests (see Table 16.3) is shown in Table 16.5: the percentage differences state that the numerical models are in good agreement with the experimental evidence, although the mean values of the discrepancies return a stiffer numerical response. Of course, this stiffening effect is consistent with the kinematic FEM modeling, and tends to vanish passing from the thin shell case (1.40 %), to the thick shell case (1.04 %), and thence to the brick case (0.87 %). It is worth noting that, for the sake of completeness, the table also points out the type of motion, "L" if lateral or "T" if torsional (of course, coupled motions cannot appear because of the double-symmetry of the cross-section). We also point out that, for the present geometry, the fundamental frequency is associated to a torsional mode of vibration, as well as the critical load is associated to a purely torsional buckling.

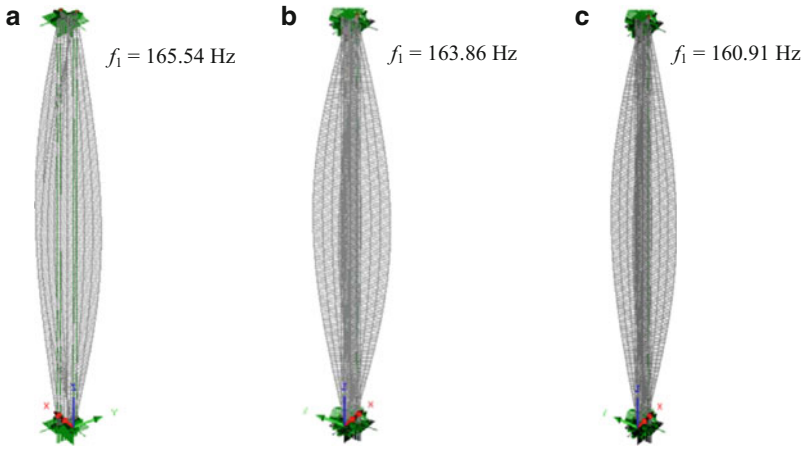

Fig. 16.4 Extruded views of the finite element models: first mode shape and relevant frequency for the (**a**) thin shell, (**b**) thick shell and (**c**) brick model

Table 16.5 Comparison among experimental (PZT) and numerical (FEM) frequencies (unloaded beams)

		Test (PZT)	FEM (thin shell)		FEM (thick shell)		FEM (brick)	
Mode	Motion	f, Hz	f, Hz	Diff., %	f, Hz	Diff., %	Diff., %	Diff., %
1	T	161.87	165.54	2.2	163.86	1.2	160.91	−0.6
2	L	275.47	278.43	1.1	278.43	1.1	270.75	−1.7
3	L	284.18	284.99	0.3	284.99	0.3	281.59	−0.9
4	T	325.43	331.75	1.9	328.40	0.9	329.69	1.3
5	L	486.13	499.22	2.6	494.22	1.6	484.58	−0.3
6	L	667.84	668.52	0.1	661.87	−0.9	676.69	1.3
7	T	741.30	749.31	1.1	749.32	1.1	749.29	1.1
8	L	767.53	766.70	−0.1	766.71	−0.1	765.76	−0.2
9	L	813.39	840.35	3.2	832.09	2.2	816.26	0.4
			Mean abs. val. diff., %		Mean abs. val. diff., %		Mean abs. val. diff., %	
			1.40		1.04		0.87	

16.4.2 *Results from* In-House *Code*

The beam model used in [4–10] is direct and one-dimensional, and is based on the standard theory of beams with shearing deformation (a.k.a. Timoshenko beam model), enriched with a coarse descriptor of warping and the possibility to describe kinematics with respect to the two parallel axes of the centroids and of the shear centers. In this way, it is possible to describe kinematics exactly, and to obtain linearized measures of strain pulled back to the reference configuration, which is fundamental in the investigations of elastic buckling. The addition of a coarse scalar descriptor of warping has the same meaning as the introduction of a new state parameter, that is, the warping descriptor is not, in principle, a displacement at a point, but rather a measure of how the cross-section has come out of its original plane. This makes it possible to introduce standard constraints of literature [1–3] between the warping descriptor and the torsion curvature, and to find the usual balance equations of force and couple, plus the auxiliary equation for the bi-shear and the bi-moment, in a straightforward way from a standard procedure based on the balance of power (or, otherwise, virtual work), plus localization and regularity arguments.

In order to take into account a general behaviour, non-linear hyper-elastic constitutive relations complete kinematics and balance, and reflect known results of the literature on thin-walled models. This makes it possible to investigate perturbations of non-trivial equilibrium paths, and examine their stability by means of standard Ljapounov criteria; for the details on the model and on the derivation of the governing equations, we refer to [4–10].

Since closed-form solutions are not possible in these cases, we search them numerically by an *in-house* code based on a proposal of literature [13]. Intrinsic balance, compatibility and constitutive equations are written in terms of finite differences and their numerical solution is searched for; then, stability is analyzed. Starting from a central finite differences scheme, the numerical analysis is developed as follows: all derivatives (e.g., f') are rewritten as

$$\frac{f_{n+1} - f_n}{\Delta L_n}, \qquad n = 1, 2, \ldots N$$

and all other unknowns and quantities (e.g., g) are expressed as

$$\frac{g_{n+1} + g_n}{2}, \qquad n = 1, 2, \ldots N$$

where f_n and g_n are the nodal values of two generic functions f and g, ΔL_n is the distance between two nodes (the length of an interval or finite element) and N the total number of elements. This technique is similar to a finite element approach and yields a powerful discretization of the governing equations. The scheme is completed by boundary conditions; the solution of this set of equations provides the equilibrium paths for the considered structure. These are in general non trivial and may be found by a numerical analysis that can be performed by means of one of the non-linear solvers available in many computing environment (i.e., without *ad hoc* modeling approximation). In order to study the stability of these paths, the governing equations and the boundary conditions are linearized about the known equilibrium configurations, thus reducing the stability analysis to the non standard eigenvalue problem

$$[C]\{dX/dt^*\} = [B]\{X^*\}$$

where $\{X^*\}$ is a small perturbation of the unknowns $\{X\}$ characterizing equilibrium. Then we look for solutions in the form

$$\{X^*\} = \{X_0^*\}\mathrm{e}^{\lambda t}$$

leading to an eigenvalue problem, in which the imaginary parts of the eigenvalues λ represent the free-vibration frequencies of the considered beam around the equilibrium configuration. The stability of the system relies on the real part of λ: when all eigenvalues have negative real part, equilibrium is stable; when an eigenvalue is real and positive, or has a real positive part, buckling or flutter occurs.

For the implementation of the described procedure, in addition to the values of length L, Young's modulus E, Poisson's coefficient ν (from which the tangential elastic modulus $G = E/[2(1+\nu)] = 26.92 \times 10^9 \quad N\,m^{-2}$) and density ρ, also the sectional properties are needed. Starting from the dimensions of edge and thickness of Table 16.1, and defined $\{O, x_1, x_2, x_3\}$ as centroidal principal cartesian system, Table. 16.6 lists the numerical values of the sectional quantities, where: A, A_j are the area and the shear shape modified areas; A_{ij} are the mixed shear shape modified areas; J is the Saint-Venant torsion inertia

Table 16.6 Sectional properties of the specimen

A, mm^2	$A_2 = A_3$, mm^2	$A_{23} = A_{32}$, mm^2	J, mm^4	I_c, mm^4	$I_2 = I_3$, mm^4	$x_{c2} = x_{c3}$, mm	$I_{f2} = I_{f3}$, mm^5	Γ, mm^6
64	32	0	21	5462	2731	0	0	0

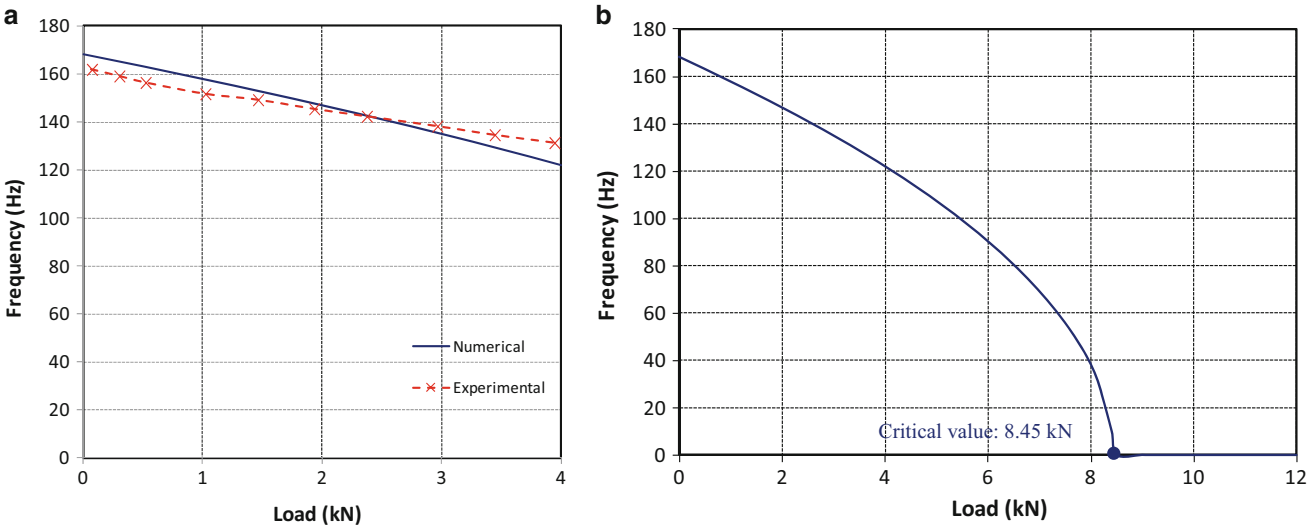

Fig. 16.5 First frequency vs. load plots: (**a**) comparison among the numerical and the experimental (PZT sensor) curves and (**b**) numerical response with increasing load

factor; I_c is the polar moment of inertia with respect to the shear centre; I_j are the centroidal principal moments of inertia; x_{cj} are the coordinates of the shear centre in the centroidal principal cartesian system; I_{fj} are the flexural-torsion constants and Γ is the warping inertia of the cross-section (with i,j=2, 3).

Since the cross-section is symmetric, the mixed shear shape modified areas, the coordinates of the shear centre and the flexural-torsion constants vanish, that is, $A_{ij} = x_{cj} = I_{fj} = 0$. Moreover, for the particular shape of the cross-section, also the warping inertia of the cross-section is negligible, i.e., $\Gamma = 0$.

The results obtained through the *in-house* code (with a dense discretization of 20 elements) are shown in Fig. 16.5. In detail, Fig. 16.5a compares the numerical first frequency-load curve with the relevant experimental one (PZT sensor, see Fig. 16.3a): the results show that the two curves are in good agreement each other.

In order to numerically check the stability condition (which will be studied soon also experimentally), the loading is increased until the critical configuration. The results of Fig. 16.5b clearly highlight the critical compressive axial load: since it is a torsion motion, when this value is attained the cross-sections rotate around the beam-axis, that remains straight, exhibiting therefore a torsion buckling.

16.5 Influence of Warping Rigidity and Constraints

The set of specimens considered in experiments so far has zero warping stiffness [1–3], so the effects of warping and warping constraints on the critical load of more general thin-walled open profiles cannot be put into evidence by the experimental campaign. With the aim of moving a step forward, we purchased a new set of specimens at a company specialized in precision machining. The cross-section of these new beams is as shown in Fig. 16.6: it is characterized by a cross with end flanges, that is, a shape with remarkable warping stiffness. This implies that suitable end constraints, preventing warping or leaving it free, will have a sensible effect on the critical load.

The experimental campaign on these beams is underway, and the relevant results and the comparisons with the numerical results will be reported in due course.

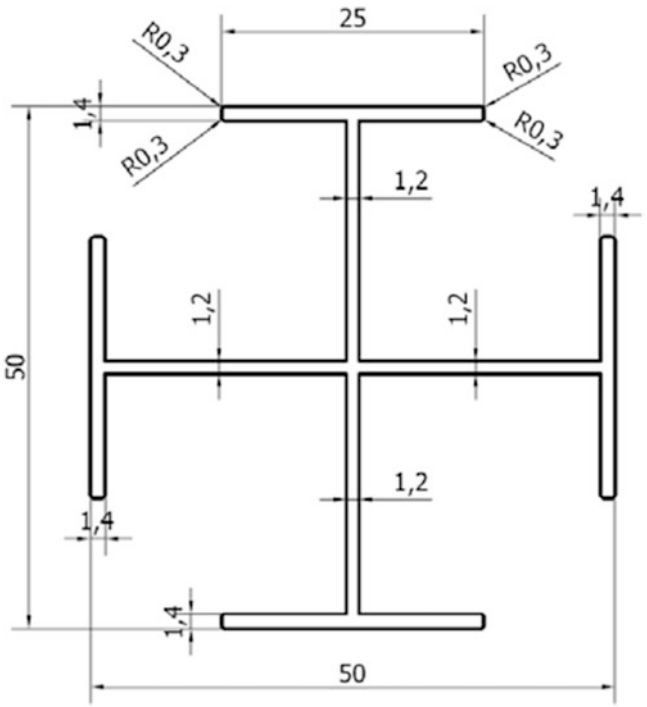

Fig. 16.6 Cross-section of the new set of specimens (dimensions in mm)

16.6 Concluding Remarks

This contribution introduces a new way of detecting physical quantities for the experimental measurements of natural frequencies in thin-walled beams with open profile. Indeed, by the help of PZT disk buzzers attached to the specimen, mounted on a universal testing machine and subjected to a progressive load, it has been possible to follow with a great precision the curves load vs. characteristic displacement and load vs. natural frequencies. These PZT sensors are disks of small diameter, low weight, require a small amount of cables, and calibration is not needed. Typical data acquisition devices can be adopted, or, more conveniently, a simple audio acquisition board of musical applications can be used. They have shown the same reliability of laser instruments, with the advantage of not requiring a continuous precise positioning of the laser setting towards the specimen, and, most importantly, offering a much wider operating frequency range, achievable at a very low cost (conversely, high frequency precision laser sensors are generally rather expensive). By following the variation of the first natural frequency with the load and the deformation, one has reliable information on the possibility of attaining a zero value of the natural frequency, i.e., a critical buckling load in the neighbourhood of a non-trivial equilibrium configuration. Such results are of a great importance from the point of view of both the design against buckling and the setting of a precise, yet simple and affordable, experimental set. This first set of experiments was performed on beams with cruciform cross-sections and vanishing warping stiffness. These results have been satisfactorily compared with those obtained numerically by an *in-house* finite difference code. The latter is able to follow the equilibrium paths for the considered beams, investigating their stability. The second set of experiments, on beams with a cross-section exhibiting remarkable warping stiffness, is in progress and its results will be reported in a future contribution.

References

1. Pignataro, M., Rizzi, N., Luongo, A.: Stability, Bifurcation, and Postcritical Behaviour of Elastic Structures. Elsevier, Amsterdam (1991)
2. Timoshenko, S., Gere, J.M.: Theory of Elastic Stability. McGraw-Hill, New York (1961)
3. Vlasov, V.Z.: Thin-Walled Elastic Beams. Monson, Jerusalem (1961)
4. Ruta, G., Pignataro, M., Rizzi, N.: A direct one-dimensional beam model for the flexural-torsional buckling of thin-walled beams. J. Mech. Mater. Struct. **1**, 1479–1496 (2006)
5. Ruta, G., Pignataro, M., Rizzi, N.: A beam model for the flexural-torsional buckling of thin-walled members. Thin-Walled Struct. **46**, 816–822 (2008)

6. Pignataro, M., Rizzi, N., Ruta, G., Varano, V.: The effects of warping constraints on the buckling of thin-walled structures. J. Mech. Mater. Struct. **4**, 1711–1727 (2010)
7. Lofrano, E., Paolone, A., Ruta, G.: Stability of non-trivial equilibrium paths of beams on partial visco-elastic foundation. Acta Mech. **223**, 2183–2195 (2012)
8. Lofrano, E., Paolone, A., Ruta, G.: A numerical approach for the stability analysis of open thin-walled beams. Mech. Res. Commun. **48**, 76–86 (2013)
9. Brunetti, M., Lofrano, E., Paolone, A., Ruta, G.: Warping and Ljapounov stability of non-trivial equilibria of non-symmetric open thin-walled beams. Thin-Walled Struct. **86**, 76–86 (2015)
10. Brunetti, M., Paolone, A., Ruta, G.: On inner shearing constraints for a direct beam model coarsely describing warping. Meccanica **48**, 2439–2451 (2013)
11. Carpinteri, A., Malvano, R., Manuello, A., Piana, G.: Fundamental frequency evolution in slender beams subjected to imposed axial displacements. J. Sound Vib. **333**, 2390–2403 (2014)
12. Piana, G., Brunetti, M., Carpinteri, A., Malvano, R., Manuello, A., Paolone, A.: On the use of piezoelectric sensors for experimental modal analysis. In: SEM 2015 Annual Conference and Exposition on Experimental and Applied Mechanics, Costa Mesa, 8–11 June 2015
13. Hodges, D.H.: Geometrically exact, intrinsic theory for dynamics of curved and twisted anisotropic beams. AIAA J. **41**, 1131–1137 (2003)

Chapter 17
On the Use of Piezoelectric Sensors for Experimental Modal Analysis

G. Piana, M. Brunetti, A. Carpinteri, R. Malvano, A. Manuello, and A. Paolone

Abstract Piezoelectric disk buzzers are commonly used on stringed musical instruments to acquire the sound in the form of a voltage signal. Aim of the present investigation is to assess the possibility of using these transducers for experimental modal analysis. Piezoelectric disks were therefore used in the laboratory to extract the natural vibration frequencies and mode shapes of an aluminum cantilever beam and of a steel arch. The results are compared with theoretical predictions and with other experimental values obtained using a laser displacement transducer and accelerometers. Due to their high accuracy, small dimensions, low weight, easy usage, and low cost, piezoelectric disks seem to be an attractive tool for experimental modal analysis of engineering structures.

Keywords Experimental modal analysis • Piezoelectric sensor • Accelerometer • One-dimensional structures

17.1 Introduction and Overview of the Present Study

Conventional experimental modal analysis is essentially based on measurement of displacement, velocity or acceleration, as well as of the excitation force [1–3]. This approach, sometimes referred to as Displacement Modal Testing (DMT), is a very broad and well developed branch of applied mechanics and engineering. A wide literature on this subject exists, with papers being continuously published in international journals and conference proceedings devoted to modal analysis, structural dynamics, and vibration. At the same time, a less developed alternative approach which is based on strain measurements exists; in this case we speak of Strain Modal Testing (SMT) [4–13]. By using this technique, a direct measure of the dynamic strain can be obtained, and therefore even stresses can be evaluated. Main cons of SMT are related to the practical use of strain gauges and strain sensors, with drawbacks that strongly limit its applicability (e.g., need of proper calibration, inadequate sensitivity at high frequency, phase delay, amplitude loss, etc.). Recently, a novel miniaturized piezoelectric strain sensor, which avoids the main drawbacks of strain gauge measurements, has been tested for application in experimental modal analysis [14]. In this case, the main disadvantage regards the cost of this piezoelectric strain sensor, that (at present time) is rather high if compared to that of standard mono-axial accelerometers.

In music technology, piezoelectric pickups are used to make high quality recordings of the sound produced by stringed musical instruments, like electric or acoustic guitars, violins, etc. They capture mechanical vibrations and convert them to an electrical signal. Since piezoelectric disk beepers (or buzzers) have little dimensions, low weight, and wide frequency range, they can be suitable for experimental modal analysis. In the present work, we assess their capabilities in this field on two simple one-dimensional structures: a cantilever beam and a parabolic arch. Another important advantage of these transducers is the reduced cost (a few Euros).

In the first part of this study, we tested the accuracy in extracting the natural frequencies of both the analyzed structural elements. For the cantilever, we used two piezoelectric pickups having different diameters, as well as a laser displacement transducer, in order to make some comparisons. The influence of the self-weight on the fundamental frequency was also evaluated through both the piezoelectric pickup and the laser sensor. For all cases, analytical predictions were

G. Piana (✉) • M. Brunetti • A. Paolone
Department of Structural and Geotechnical Engineering, Sapienza University, Via Eudossiana 18, Rome 00184, Italy
e-mail: gianfranco.piana@polito.it

A. Carpinteri • A. Manuello
Department of Structural, Geotechnical and Building Engineering, Politecnico di Torino, Corso Duca degli Abruzzi 24, Torino 10129, Italy

R. Malvano
Department of Mechanical and Aerospace Engineering, National Institute of Metrological Research—INRIM, C/o Politecnico di Torino, Corso Duca degli Abruzzi 24, Torino 10129, Italy

B. Song et al. (eds.), *Dynamic Behavior of Materials, Volume 1*,
Conference Proceedings of the Society for Experimental Mechanics Series, DOI 10.1007/978-3-319-22452-7_17

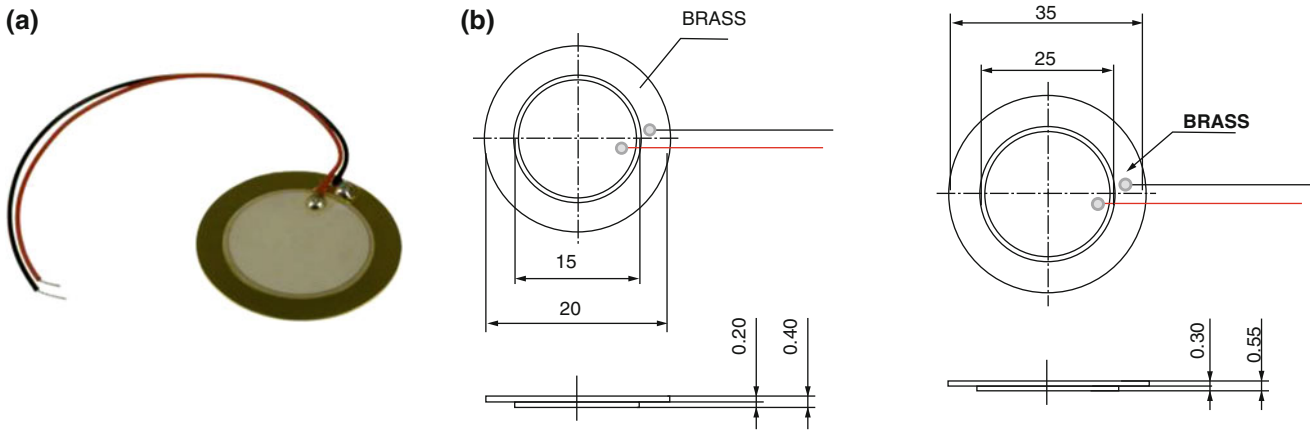

Fig. 17.1 (**a**) Photo and (**b**) schematic (dimensions in mm) of the adopted piezoelectric disk buzzers

Table 17.1 Main characteristics of the adopted piezoelectric sensors

Sensor	External diameter (mm)	Frequency range (kHz)	Resonant frequency (kHz)	Operating temperature (°C)	Weight (g)
JPR-PLUSTONE 400-403	20	~0 to 20	6.0 ± 0.5	−20 to +50	0.91
JPR-PLUSTONE 400-411	35		3.0 ± 0.5		2.79

adopted as reference values. In the case of the arch, only the smaller piezoelectric pickup was used; it was placed in different locations in order to investigate on the influence of the positioning on the extraction of the natural frequencies. In this case, the experimental results were compared to those coming from finite element analyses and other experimental results obtained in a previous study conducted by one of the authors [15], where mono-axial accelerometers were used. Then, in a second phase, we moved to the extraction of mode shapes, by placing several piezoelectric pickups at the same time. In the case of the cantilever beam, experimental results were compared to the analytical solution, whereas for the arch, results obtained from finite element modeling and other experiments were used for the comparison with our experimental results.

17.2 Features and Usage of the Adopted Piezoelectric Sensors

The adopted piezoelectric disk buzzers are transducers that produce an electric voltage signal when subjected to dynamic deformation (direct piezoelectric effect), thus they do not need any supply. The generated signal can be amplified if necessary, acquired by audio acquisition devices as well as classical data acquisition devices, and therefore recorded and analyzed or manipulated. These sensors can be connected to the surface of the object of interest simply by using a glue or a thin film of gel, and their usage do not require any calibration. Figure 17.1 shows a picture and a schematic of the type of sensors adopted in the present study, while their main features are reported in Table 17.1. Two different diameters were selected for testing, i.e. 20 and 35 mm (sensors JPR-PLUSTONE 400-403 and 400-411, respectively).

17.3 Modal Testing of an Aluminium Cantilever Beam

17.3.1 Experimental Setup

The tested cantilever was an aluminum bar of rectangular cross section ($b \times t = 25 \times 1.97$ mm). The element was clamped for a length equal to 10 cm, while the free length of the cantilever was $L = 470$ mm. The value of the Young's modulus, $E = 62$ GPa, was obtained from static deflection measurements, while the material mass density is $\rho = 2600\,\mathrm{kg/m^3}$ (mass

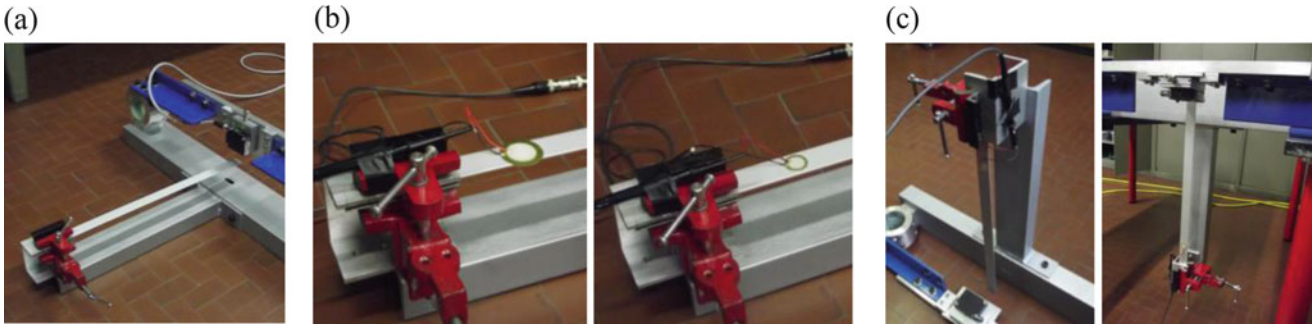

Fig. 17.2 Experimental setup for extraction of natural frequencies: (**a**) laser sensor (**b**) piezoelectric pickups ($\phi = 35$ mm, *left*; $\phi = 20$ mm, *right*), (**c**) cantilever subjected to axial force due to the self weight (stretched, *left*; compressed, *right*)

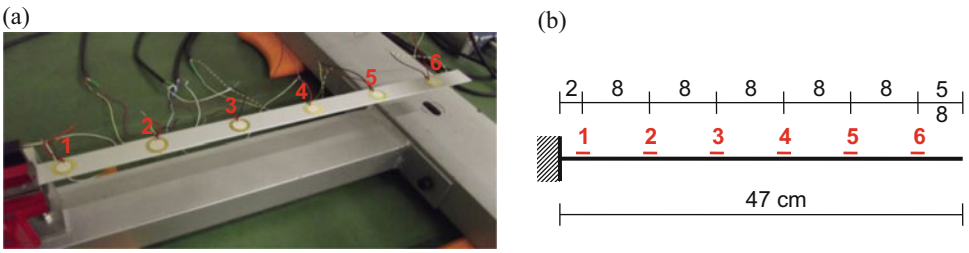

Fig. 17.3 Experimental setup for extraction of modal curvatures and mode shapes: (**a**) picture and (**b**) locations of sensors

per unit length $\mu = 0.128$ kg/m). Figure 17.2 shows the setup adopted for the evaluation of the natural frequencies. In Fig. 17.2a, a laser displacement transducer is positioned in correspondence of the cantilever tip, while in Fig. 17.2b, a piezoelectric pickup is located near the fixed end ($\phi = 35$ mm, left; $\phi = 20$ mm, right). The laser sensor is the optoNCDT 1302-20, a triangulating displacement sensor produced by Micro-Epsilon. It has a resolution of 10 μm for dynamic acquisitions at the maximum frequency of 750 Hz, and a default measuring range equal to 20 mm (it can be narrowed by the user to utilize the maximum resolution on a reduced range of distance); the midrange is positioned at 40 mm far from the surface of the transducer. The piezoelectric pickups were connected to the element surface by means of a thin film of gel. With respect to their location, they were positioned close to the clamped end, i.e. close to the region with the maximum deformation. This is a fundamental difference with respect to DMT: like in SMT, piezoelectric disks must preferably be located in regions where deformations are higher. Conversely, in the case of modal testing based on acceleration measurements, for example, accelerometers must preferably be located in regions where the displacement is higher. Therefore, while bad locations for accelerometers are the regions close to the nodes, bed positions for piezoelectric buzzers are the regions were strains are zero (like the tip of a cantilever, for example). Figure 17.2c shows the setup adopted to evaluate the variation of the fundamental frequency induced by the self weight, when the cantilever was stretched (left) or compressed (right). In this first phase of the investigation, signals coming from both laser sensor and piezoelectric buzzers were acquired, without any pre-amplification, by using a NI 9215 data acquisition device produced by National Instruments. This is a four channels-device, with a resolution of 16 bits, a maximum sampling frequency of 100 kHz, and a operating voltage range from −10 to 10 V. Acquisition, processing and post-processing of measured signals were made using the software LabVIEW.

Figure 17.3 shows the experimental setup adopted for the extraction of the mode shapes. A total of six pickups were placed in the positions indicated in Fig. 17.3b. In this case, only piezoelectric sensors with a diameter of 20 mm were adopted (Fig. 17.3a). In this second part of the investigation, an audio acquisition device was used to catch the signals generated by the pickups; therefore, this time, WAV (Waveform Audio File Format) files were obtained. The adopted device was the Audiobox 1818VSl produced by PreSonus. This is a eight channels device which allows to record with a resolution of 24 bits at different frequencies: 44.1, 48.0, 88.2, and 96.0 kHz. The sample frequency of 44.1 kHz was chosen for our measurements. Processing and recording of acquired signals were done by using Studio One 2 (a sound recording software by PreSonus), while Matlab and Maple were used for post-processing.

17.3.2 Results and Comparisons

The natural frequencies were obtained by the Fourier analysis of the measured free response signals (only the output was registered). For each adopted sensor, six impulsive excitations plus six imposed displacement initial conditions were given to the beam in order to study the consequent free response. Table 17.2 proposes a comparison among the natural frequencies obtained by the adopted sensors and the corresponding theoretical values predicted by the analytical solution [1]. In these tests, the sample frequency was set equal to the maximum value for the laser sensor, i.e. 750 Hz. As can easily be seen, the laser was not able to capture the fourth frequency (241.90 Hz), which conversely was seen by the two pickups. In all cases, the percentage differences between experimental and theoretical values are extremely small (Table 17.2). Moreover, we must notice that piezoelectric pickups did not perturbed the mass of the specimen, so their results are absolutely comparable to those of a non-contact transducer, like the used laser sensor. Table 17.3 collects the first ten natural frequencies extracted with the 20 mm piezoelectric pickup when it was operating with a sample frequency equal to 20 kHz. The small values of the standard deviation, σ, reported in the same table, indicate the low dispersion of the obtained values.

The capabilities of the piezoelectric disks were also tested by checking if they were able to appreciate the variation of the fundamental frequency induced by the axial load generated by the self weight of the cantilever beam, when disposed in vertical position. An increase (decrease) in the fundamental frequency is produced when the cantilever beam is disposed vertically with its tip directed downward (upward). Due to the low magnitude of the axial load induced by the self weight, this variation was indeed very small. Table 17.4 collects the experimental results, compared to the theoretical values. The self weight produced a uniformly distributed axial load $p = \pm 1.26$ N/m (positive for tensile, negative for compressive load). With good approximation, a linear relationship between the square of the fundamental frequency and the distributed axial load can be assumed [16]: $\left(f_1/f_{1,0}\right)^2 = 1 + p/|p_{cr}|$, where $f_{1,0}$ is the fundamental frequency of the unloaded cantilever beam (i.e., for $p = 0$), and p_{cr} is the critical load for buckling [16] ($p_{cr} \cong -7.837EI/L^3 \cong -74.54$ N/m, being EI the flexural rigidity of the cantilever beam). Results show that both piezoelectric disks were able to appreciate the small variation in the fundamental frequency produced by the axial load due to the self weight, with numerical values comparable to those of a non-contact transducer such as the adopted laser sensor.

The extraction of the mode shapes was therefore performed by adopting the setup shown in Fig. 17.3. In this case, only the pickup with a diameter of 20 mm was used. The Peak Picking Method was adopted [1–3]. Three impulses were

Table 17.2 Comparison among natural frequencies from laser and PZT sensors at a sample frequency of 750 Hz

	Theoretical	Laser		PZT ($\phi = 35$ mm)		PZT ($\phi = 20$ mm)	
Mode	f (Hz)	f (Hz)	Diff. (%)	f (Hz)	Diff. (%)	f (Hz)	Diff. (%)
1	7.03	7.00	−0.4	7.00	−0.4	7.00	−0.4
2	44.09	44.20	0.2	43.90	−0.4	44.02	−0.2
3	123.45	123.40	0.0	120.75	−2.2	122.17	−1.0
4	241.90	–	–	233.30	−3.7	239.48	−1.0

Table 17.3 Natural frequencies from PZT ($\phi = 20$ mm) at a sample frequency of 20 kHz (σ denotes the standard deviation)

Mode	f (Hz)	σ (Hz)	Mode	f (Hz)	σ (Hz)
1	7.11	0.38	6	596.43	0.63
2	43.76	0.51	7	829.03	0.91
3	123.29	0.25	8	1102.22	1.07
4	242.37	1.21	9	1418.85	2.06
5	396.94	0.49	10	1779.99	1.06

Table 17.4 Variation of the fundamental frequency induced by the axial load due to the self weight (positive p means tension)

	Theoretical		Laser		PZT ($\phi = 35$ mm)		PZT ($\phi = 20$ mm)	
Axial load due to self weight	f_1 (Hz)	Variat. (%)	f_1 (Hz)	Variat. (%)	f_1 (Hz)	Variat. (%)	f_1 (Hz)	Variat. (%)
$p = 0$	7.03	–	7.02	–	7.03	–	7.01	–
$p = 1.26$ N/m	7.09	0.85	7.08	0.85	7.08	0.71	7.08	0.99
$p = -1.26$ N/m	6.98	−0.72	6.97	−0.72	6.97	−0.86	6.96	−0.72

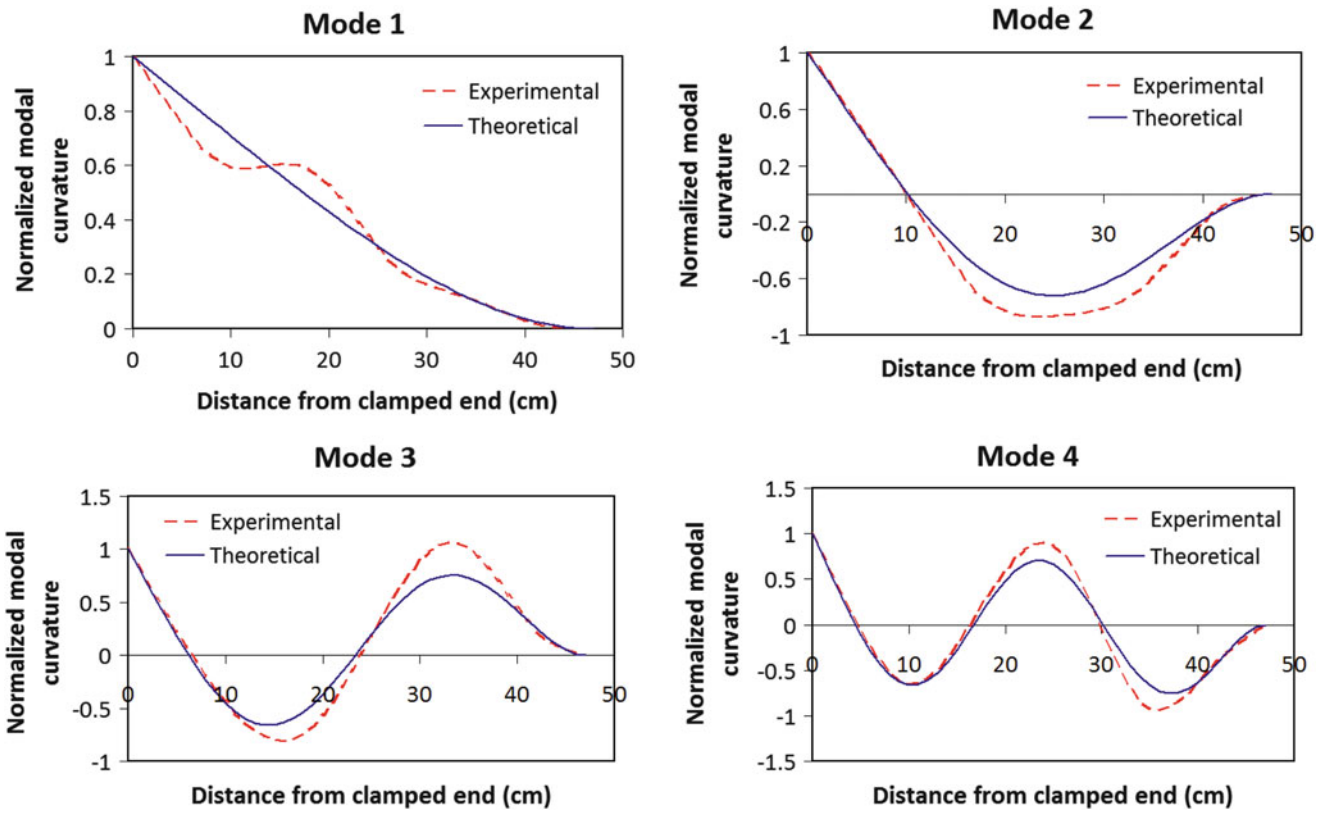

Fig. 17.4 First four normalized modal curvatures for the cantilever in Fig. 17.3

transmitted in correspondence of each one of the following points: midpoint between sensors 1–2, 2–3, 3–4, 4–5, 5–6, and between sensor 6 and the tip. The amplitude of the acquired voltage signal have proved to be proportional to the cantilever surface deformation. Thus, the modal curvatures were directly detected as follows. For each acquired response signal, all measured voltage values were normalized with respect to the value assumed in correspondence of the clamped end and a zero value was added in correspondence the cantilever tip (zero deformation); those values were therefore interpolated via cubic splines, in order to evaluate the modal curvature on the whole domain. Once the modal curvatures were determined, a double integration with respect to the space variable, with the opportune boundary conditions, lead to the functions describing the mode shapes (the linearized expression of the curvature was adopted in this phase). Figures 17.4 and 17.5 show a comparison between experimental and theoretical results in terms of modal curvatures and mode shapes, respectively. As can be seen in Fig. 17.4, the adopted piezoelectric disk was able to extract the modal curvatures with high precision. Figure 17.5 shows that the results are rather good also in terms of mode shapes, with the only exception of the fourth mode for which the result is unsatisfactory; in the case of the first mode, in particular, the experimental and theoretical curves are practically superposed.

The correlation between experimental and theoretical results, for both modal curvatures and mode shapes, were quantitatively evaluated by the Modal Assurance Criterion (*MAC*) [17] and the Normalized Modal Difference (*NMD*) [17]. The results are reported in Table 17.5 and indicate a very high correlation between experimental and analytical modal curvatures. A good correlation was also obtained for mode shapes 1 and 3, and a less good correlation was found for mode 2. Conversely, the fourth experimental and analytical mode shapes were completely uncorrelated, even if the correlation between the corresponding modal curvatures was excellent (see Table 17.4): this fact suggests that the deduction of the mode shapes from modal curvatures needs to be reconsidered with more attention. The results shown in Figs. 17.4 and 17.5, as well as the corresponding *MAC* and *NMD* values reported in Table 17.5, come from some of the acquired data: a complete and systematic statistical analysis of all the experimental data is still a work in progress at present.

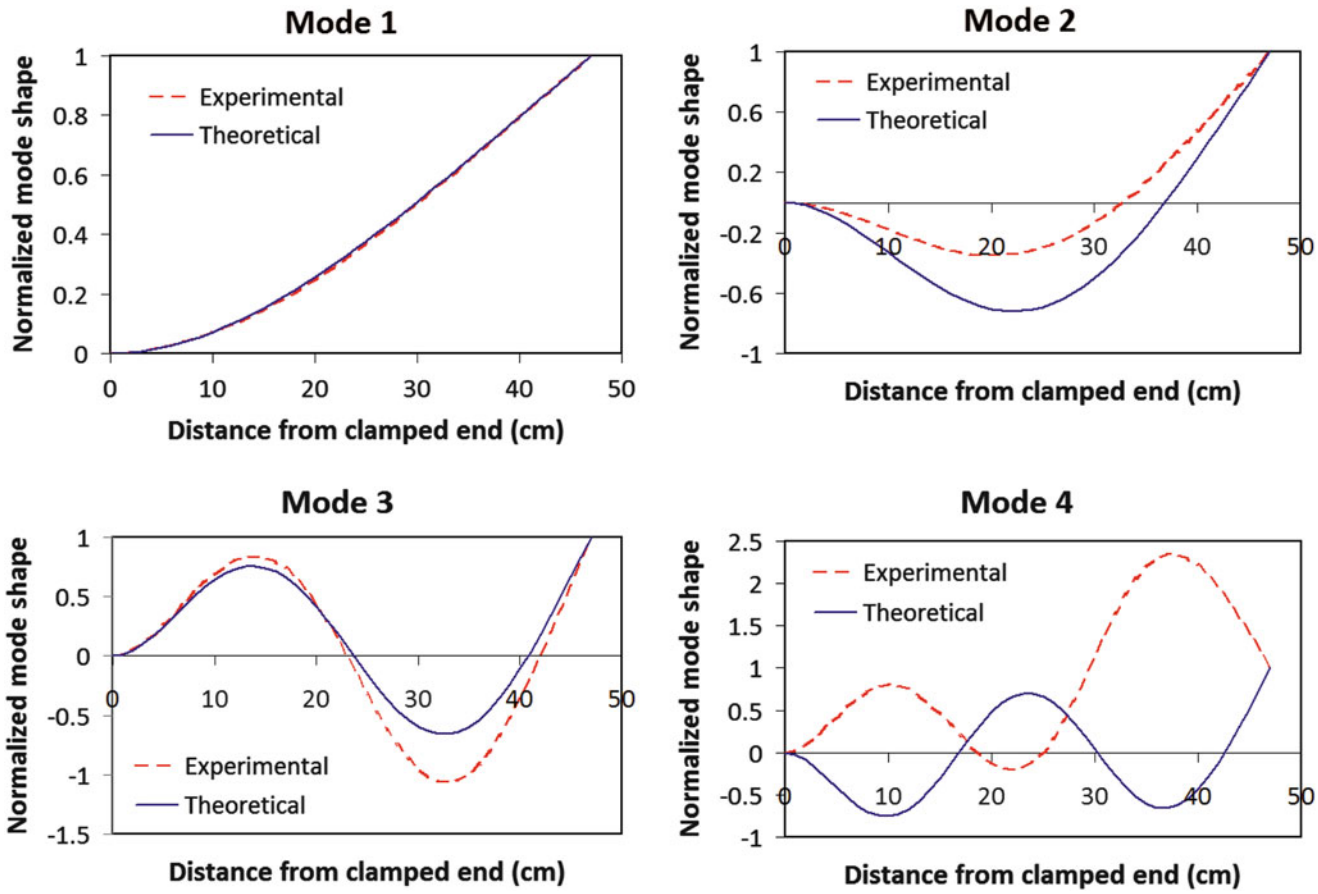

Fig. 17.5 First four normalized mode shapes for the cantilever in Fig. 17.3

Table 17.5 *MAC* and *NMD* values for modal curvatures and mode shapes shown in Figs. 17.4 and 17.5

	Modal curvatures		Mode shapes	
Mode	*MAC*	*NMD*	*MAC*	*NMD*
1	0.9858	0.1199	0.9999	0.0088
2	0.9840	0.1270	0.7200	0.6200
3	0.9750	0.1610	0.9320	0.2680
4	0.9710	0.1740	0.2940	1.5400

17.4 Modal Testing of a Double-Hinged Steel Parabolic Arch

17.4.1 Experimental Setup

Figure 17.6 shows the setup adopted during the tests. The specimen was constituted by a double-hinged parabolic steel arch. The centerline of the arch has a span of 1010 mm and a rise of 205 mm (rise-to-span ratio of 0.203); the cross section is rectangular, with a width $b = 40$ mm and a depth $h_u = 8$ mm (Fig. 17.6a). The material properties are the Young's modulus, $E = 2.050 \times 10^5$ MPa, the Poisson's ratio, $\nu = 0.3$, and the mass density, $\rho = 7.849 \times 10^{-6}$ kg/mm^3. Red circles in Fig. 17.6a indicate the instrumented sections.

Figure 17.6b shows the setup adopted for the tests performed using the piezoelectric pickup (the disk with a diameter of 20 mm was used). For the extraction of the natural frequencies, only one pickup was adopted. It was positioned in correspondence of sections 4, 5, 6, and 7 indicated in Fig. 17.6a. In this case, the signals were pre-amplified by means of a differential amplifier and therefore acquired using the NI 9215 data acquisition device by National Instruments. LabVIEW programs were used for acquisition, processing and post-processing operations. For the extraction of the modal curvatures

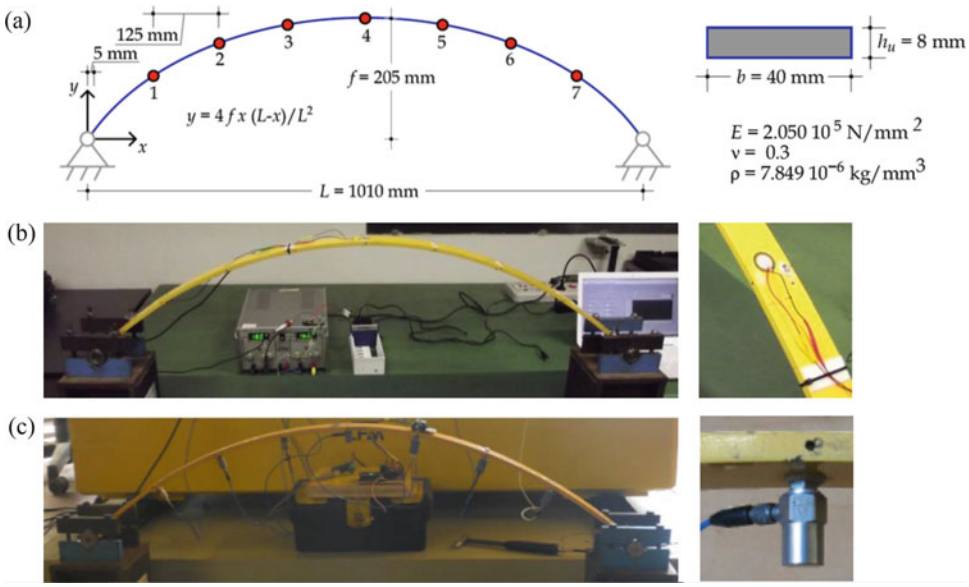

Fig. 17.6 Experimental setup for the steel parabolic arch: (**a**) geometry and mechanical properties (*red circles* indicate the instrumented sections), (**b**) setup for testing with piezoelectric pickup, (**c**) setup for testing with accelerometers [15]

and mode shapes, seven pickups were placed at the same time in correspondence of sections 1–7 in Fig. 17.6a. As for the case of the cantilever, the Audiobox 1818VSl and the software Studio One 2 by PreSonus were used to acquire and processing the signals, while the post-processing was done using Matlab and Maple. Lastly, Fig. 17.6c shows the setup realized in a previous study [15], where seven uni-axial piezoelectric accelerometers were placed in correspondence of sections 1–7 in Fig. 17.6a.

17.4.2 Results and Comparisons

The first six natural frequencies of in-plane vibration were extracted using the same procedure adopted for the cantilever, i.e., by means of Fourier analysis of the free response signals. The adopted sampling frequency was equal to 3 kHz. The arch was excited by external impulses (five for each point) transmitted in correspondence the following positions (see Fig. 17.6a): 1, 2, midpoint between 2 and 3, and 4. Also in the case of the arch, only the output was registered (in other words, an operational modal analysis was performed). Table 17.6 summarizes the statistics for the identified frequencies: mean values, μ, standard deviations, σ, and coefficients of variation, $CV = \mu/\sigma$, are reported. The values of standard deviation and coefficient of variation indicate the low dispersion and reliability of all data.

Finite element models were implemented in order to evaluate the frequencies of interest through a linear dynamic eigenvalue analysis. The models were built by modeling the centerline of the arch by curved Timoshenko-like beam elements; in the case of the accelerometers, also the additional masses were taken into account. A comparison between experimental and numerical frequencies is shown in Table 17.7 for both the present campaign (piezoelectric disk) and a previous one (accelerometers) [15]. As can be seen, a good agreement between numerical and experimental results was found for all the identified frequencies. However, we must notice that the frequencies obtained using the accelerometers are lower than the frequencies identified by means of the piezoelectric disk, because of the additional masses of the accelerometers (and cables), whose values were not negligible with respect to the mass of the arch. As a general comment, we observe that the adopted piezoelectric pickup has allowed a precise determination of the resonant frequencies also in the case of a curved structural element such as the parabolic arch analyzed in this study. Moreover, its mass is so small that the mass of the specimen was not perturbed.

The results related to the extraction of modal curvatures and mode shapes will be presented at the Conference: comparisons among the results obtained using piezoelectric disks and those coming from finite element analyses and modal tests based on accelerometers will be discussed.

Table 17.6 Identified natural frequencies: mean values, μ, standard deviations, σ, and coefficients of variation, CV

Frequency	μ (Hz)	σ (Hz)	CV (%)
f_1	54.6	0.49	0.89
f_2	127.0	1.06	0.84
f_3	231.1	0.76	0.33
f_4	360.0	0.70	0.19
f_5	521.4	0.90	0.17
f_6	721.7	0.84	0.12

Table 17.7 Comparison between experimental and numerical frequencies

	Present study (piezoelectric disks)			Previous study (accelerometers) [15]		
Frequency	Experim. (Hz)	FEM (Hz)	Diff. (%)	Experim. (Hz)	FEM[a] (Hz)	Diff. (%)
f_1	54.6	52.8	−3.30	50.3	51.9	3.10
f_2	127.0	127.5	0.39	123.8	124.9	0.81
f_3	231.1	233.3	0.96	224.7	228.6	1.69
f_4	360.0	364.3	1.21	359.3	357.6	−0.47
f_5	521.4	530.8	1.80	509.9	520.7	2.11
f_6	721.7	721.4	−0.04	716.3	708.1	−1.15

[a]The masses of the accelerometers were considered in the model

17.5 Concluding Remarks

Piezoelectric disk buzzers were used in the lab (as long as we know, for the first time) to extract modal parameters of structural elements such as a cantilever beam and a double-hinged parabolic arch. Comparisons with theoretical predictions and other experimental data were made in terms of natural frequencies, modal curvatures, and mode shapes. Results indicate that the adopted sensor proved to be an efficient tool for detecting natural frequencies and modal curvatures/shapes of metallic specimens, at least at the laboratory scale; this for both straight (cantilever) and curved (arch) elements. The voltage signal generated by the adopted piezoelectric disk during vibration, is proportional to the specimen surface deformation (elastic curvature, in our case). This fact implies that it is better to position this kind of sensor in regions where deformations (not displacements) are higher. In this sense, our application is pretty close to Strain Modal Testing, even though, probably, a measure of the effective strain cannot be obtained through piezoelectric disk buzzers, at least without any calibration; this problem has not been addressed by the present study. In any case, these sensors could be suitable for damage identification based on modal testing, where the modal curvature is one of the prime parameters [19]. Given the advantages stated in the abstract and the results obtained in the present study, the authors believe that further investigations on the effectiveness of adopting piezoelectric disk buzzers for experimental modal analysis would be of interest. For example, their response on non-metallic specimens, like concrete or masonry, as well as the application on full-scale real structures, should be assessed by new investigations. Moreover, the capability of extracting modal damping from measured signals should be analyzed as well.

References

1. De Silva, C.W.: Vibration: Fundamentals and Practice. CRC Press, Boca Raton (2000)
2. Ewins, D.J.: Modal Testing: Theory, Practice and Application, 2nd edn. Research Studies Press, Baldock (2000)
3. Fu, Z.-F., He, J.: Modal Analysis. Butterworth-Heinemann, Oxford (2001)
4. Hillary, B., Ewinns, D.J.: The use of strain gauges in force determination and frequency response function measurement. In: Proceedings of the 2nd IMAC, pp. 627–634 (1984)
5. YI, S., Kong, F.R., Chang, Y.S.: Vibration modal analysis by means of impulse excitation and measurement using strain gauges. In: Proceedings of the IMechE C308/84, pp. 391–396 (1984)
6. Stacker, C.: Modal analysis efficiency improved via strain frequency response functions. In: Proceedings of the 3rd IMAC, pp. 612–617 (1985)
7. Song, T, Zhang, P.Q., Feng, W.Q., Huang, T.C.: The application of the time domain method in strain modal analysis. In: Proceedings of the 4th IMAC, pp. 31–37 (1986)
8. Debao, L., Hongcheng, Z., Bo, W.: The principle and techniques of experimental strain modal analysis. In: Proceedings of the 7th IMAC, pp. 1285–1289 (1989)
9. Bernasconi, O., Ewins, D.J.: Application of strain modal testing to real structures. In: Proceedings of the 7th IMAC, pp. 1453–1464 (1989)
10. Bernasconi, O., Ewins, D.J.: Modal strain/stress fields. Int. J. Anal. Exp. Modal Anal. **4**(2), 68–79 (1989)

11. Yam, L.H., Leung, T.P., Li, D.B., Xue, K.Z.: Theoretical and experimental study of modal strain analysis. J. Sound Vib. **191**(2), 251–260 (1996)
12. Rovšček, D., Slavič, J., Boltežar, M.: The use of strain sensors in an experimental modal analysis of small and light structures with free-free boundary conditions. J. Vib. Control. **19**(7), 1072–1079 (2013)
13. Kranjc, T., Slavič, J., Boltežar, M.: The mass normalization of the displacement and strain mode shapes in a strain experimental modal analysis using the mass-change strategy. J. Sound Vib. **332**, 6968–6981 (2013)
14. Mucchi, E., Dalpiaz, G.: On the use of piezoelectric strain sensors for experimental modal analysis. In Menghetti U., Maggiore A., Parenti Castelli V., Settima giornata di studio Ettore Funaioli, 19 luglio 2013: Quaderni del DIEM—GMA—Atti di giornate di studio 7, pp. 293–301. Società Editrice Esculapio, Bologna. http://amsacta.unibo.it/4064/ (2014)
15. Lofrano, E., Paolone, A., Romeo, F.: Damage identification in a parabolic arch through the combined use of modal properties and empirical mode decomposition. In: Proceedings of the 9th International Conference on Structural Dynamics, EURODYN 2014, Porto, 30 June–2 July 2014
16. Virgin, N.L.: Vibration of Axially Loaded Structures. Cambridge University Press, New York (2007)
17. Allemang, R.J., Brown, D.L.: A correlation coefficient for modal vector analysis. In: Proceedings of the 1st IMAC, Orlando (1982)
18. Maya, N.M.M., Silva, J.M.M. (eds.): Theoretical and Experimental Modal Analysis. Research Studies Press, Taunton (1997)
19. Dessi, D., Camerlengo, G.: Damage identification techniques via modal curvature analysis: overview and comparison. Mech. Syst. Signal Process. **52–53**, 181–205 (2015)

Chapter 18
Characterization of Vibrational Mechanical Properties of Polyurethane Foam

Raphaël Dupuis, Olivier Duboeuf, Bertrand Kirtz, and Evelyne Aubry

Abstract Polyurethane foam (PU) is widely used in numerous comfort applications such as automotive seat cushioning and mattresses. The present paper is devoted to describe experimental techniques and identification of dynamic properties of thin flexible polyurethane foam used in automotive seats. In the experimental device, a free mass is mounted on a 0.1 m^2 of different foams used in car upholstery. The foam is the only flexible component. The device is excited with an electrodynamic shaker with frequencies varying between 10 and 200 Hz. The response of foam samples to sweep sine excitation is analyzed for different excitation acceleration amplitude (1–2.5 mm s^{-2}) and for different free masses.

In order to answer the issue of replacement, different multilayer products and single foam samples have been characterized and comparisons have been carried out. The results of this study show interesting properties in terms of dynamic behavior of multilayer products when compared to the PU foams.

Keywords Polyurethane foam • Upholstery • Dynamic behavior • Natural frequency • Filtration frequency

18.1 Introduction

In order to propose some alternative soft cellular solids usable in the automotive interior, it is necessary to have an accurate knowledge of the dynamic characteristics of the existing materials. The new European Directives such as 2000/53/CE [1] imposes strict rules concerning the recycling with an aim of 85 % of recyclable products and 95 % re useable products. These new constraints imposes car manufacturers and their partners to review the automotive specifications for the materials used in the automotive interior as the headliner facings, the loudspeaker housing, the insulation material, car upholsteries, etc... The materials currently used as seat upholsteries are complex materials generally composed of three layers (Fig. 18.1). The first layer is a knitted or woven fabric, for the appearance, generally made of polyester (PET). The second layer is polyurethane foam between 2 and 8 mm thickness. The third layer is usually a knitted polyamide (PA) or polyester fabric. The use of polyurethane will bring comfort in the case of flexible foams and excellent thermal insulation in the case of rigid foam [2].

The realization of automotive complex fabrics, usually done by flame lamination, produces the emission of dangerous volatile components [2], and inhibit the recyclability of this complex. Indeed, the delaminating process of these complex materials is quite impossible because traces of foam remain in the polyester or polyamide after separation of the different layers and pollute the extracted components. Some alternative products to polyurethane foam are existing, often made by a single component material (100 % polyester p.e.), leading to an easier recyclability. To be accepted by automotive original equipment manufacturer, these alternative materials must have the same mechanical characteristics, particularly in terms of humid aging and dynamic characteristics, than the replaced foam. Moreover, it must meet the requirements of the automotive industry in terms of weight, implementation and cost [3].

R. Dupuis (✉) • E. Aubry
Laboratoire MIPS, Université de Haute Alsace, 12, rue des frères Lumière, Mulhouse Cedex 68093, France
e-mail: raphael.dupuis@uha.fr

O. Duboeuf
Laboratoire MIPS, Université de Haute Alsace, 12, rue des frères Lumière, Mulhouse Cedex 68093, France

Laboratoire R&D Foam Chemistry, Faurecia Automotive Seating, 17 rue de la Forge, Lure 70202, France

B. Kirtz
Acouvib, 2 Rue du Rhône, Mulhouse 68100, France

B. Song et al. (eds.), *Dynamic Behavior of Materials, Volume 1*,
Conference Proceedings of the Society for Experimental Mechanics Series, DOI 10.1007/978-3-319-22452-7_18

In this paper, different polyurethane foams have been studied. The methods of physical and mechanical characterization of foams will be presented. First, the characterization methods and free mass vibration tests will be detailed, then the results will be analyzed and a critical analysis of the dynamic behavior of these materials will be carried out.

Many authors have published as well paper than books about foam mechanical properties. The reference is obviously the work of Gibson and Ashby [4]. Thus, they have shown that the characteristics of foams depend on various parameters such as cell morphology, size, arrangement, connections between them... Static mechanical behavior of foams has been well described by Gibson and Ashby [4], particularly in the effect of a compressive force. On the stress-strain curves of polyurethane foam, three main parts can be highlighted. First a linear elasticity at low stress followed by a long collapse plateau, and finished by a densification of the material in which the stress rises steeply.

Concerning dynamic studies on polyurethane foam, Pritz [5] has proposed in 1980 to study the complex modulus of soft materials using a free mass device. Since then, the team of Bajaj and Davies has conducted numerous studies on the polyurethane foam, both experimental [6–9] with a free mass device guided with ball bearing, and in modeling using memory integer models [8], or memory fractional models [9, 10]. Jmal has also developed an interesting approach with memory integer models [11]. All of these studies have focused on samples of thick foam (75 mm), but never to the cover of the seat.

18.2 Tested Materials

The study focused on polyurethane foams commonly used in automotive trim. The foam is soft cellular structure [8]. The cells can be modeled geometrically by a pentagon. A method of characterization [12] adapted from the VISIOCELL® method (Fig. 18.2) has been used to evaluate the average diameter of foam cells. The tested foams A and B were respectively open and closed cells.

All the parameters issued of these characterization methods are shown in Table 18.1.

Table 18.1 presents the main physical characteristics of foams studied.

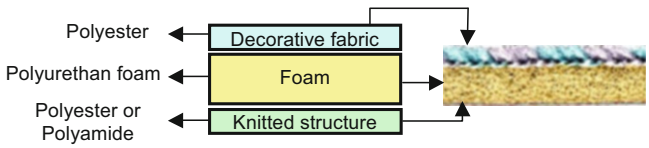

Fig. 18.1 Automotive complex composition

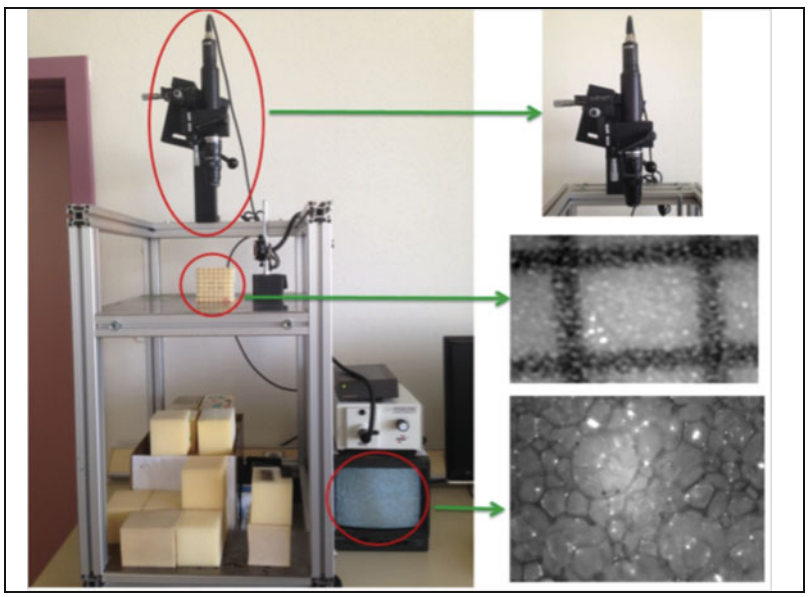

Fig. 18.2 Polyurethane foam structure [12]

For each foam, we applied the experimental methodology to determine the compression behaviour presented in 2009 [13] and we calculated the energy of the hysteresis and the maximum stress at 50 % of initial thickness deformation at the fourth cycle (Table 18.2).

18.3 Experimental Methodology

All the tests have been carried out on an electrodynamic shaker (LDS V455, Bruel and Kjaër) driven by a vibration control system (COMET, Bruel and Kjaër) (Fig. 18.3). The foam plates are glued by a perfectly hardening adhesive (3M™ Double Coated Tape 9832) to thin metal plates, which are bolted on the base of the shaker and on the free mass to prevent the free mass from losing contact with the foam during vibration. In order to vary the compression level, additional weights can be placed on the top mass (Fig. 18.3).

The frequency of excitation was varied from 10 to 200 Hz with a 1 oct/min sweep rate, with constant input acceleration, and the amplitude and phase of the response was recorded. Two piezoelectric CCLD accelerometers (type 4507B, Bruel and Kjaër) were used to measure the input acceleration of the shaker and the output response of the free mass. The amplitude and phase responses were recorded for four additional free mass (1.0, 1.6, 2.2 and 2.8 kg) in order to modify the foam compression levels and four excitation acceleration amplitudes (1.0, 1.5, 2.0 and 2.5 m/s^2 peak amplitude).

The test procedure is the following: according to the recommendations given by White et al. [6], the sample is first loaded during 30 min to reach his static steady state. Then, the system is excited at constant acceleration amplitude at a 10 Hz

Table 18.1 Physical characteristics of tested foams

Designation	Foam A	Foam B
Foam types	Flexible	Flexible
Isocyanate	TDI polyester	TMDI
Fabrication process	Slabstock	Slabstock
Type of cells	Closed	Open
Dimensions ($L_0 \times l_0 \times h_0$) m^3	0.1 × 0.1 × 0.004	0.1 × 0.1 × 0.004
Density (kg m^{-3})	45.2	46.1
Average longitudinal cell size (μm)	190	348
Average transversal cell size (μm)	117	241

Table 18.2 Compression behaviour properties of tested foams

Designation	Foam A	Foam B
Energy dissipated during the 4th cycle of compression (J)	1.9	1.45
Maximum stress at 50 % of initial thickness deformation at the fourth cycle (kPa)	11	6.7

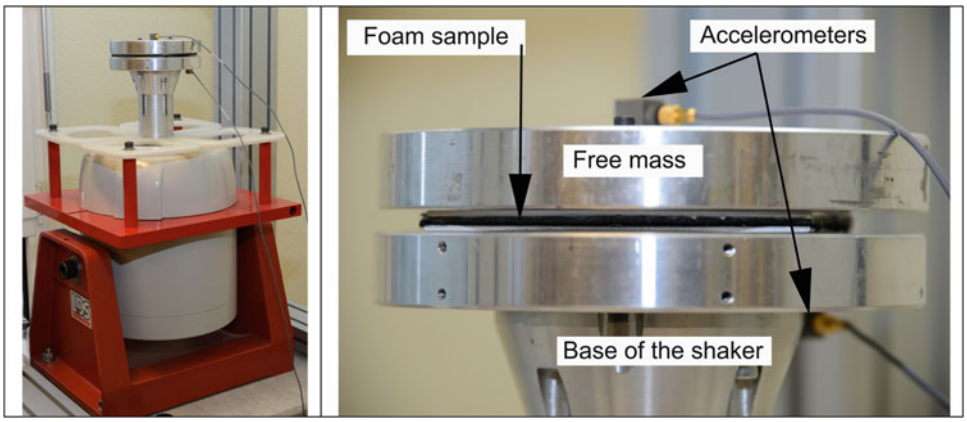

Fig. 18.3 LDS shaker and free mass system

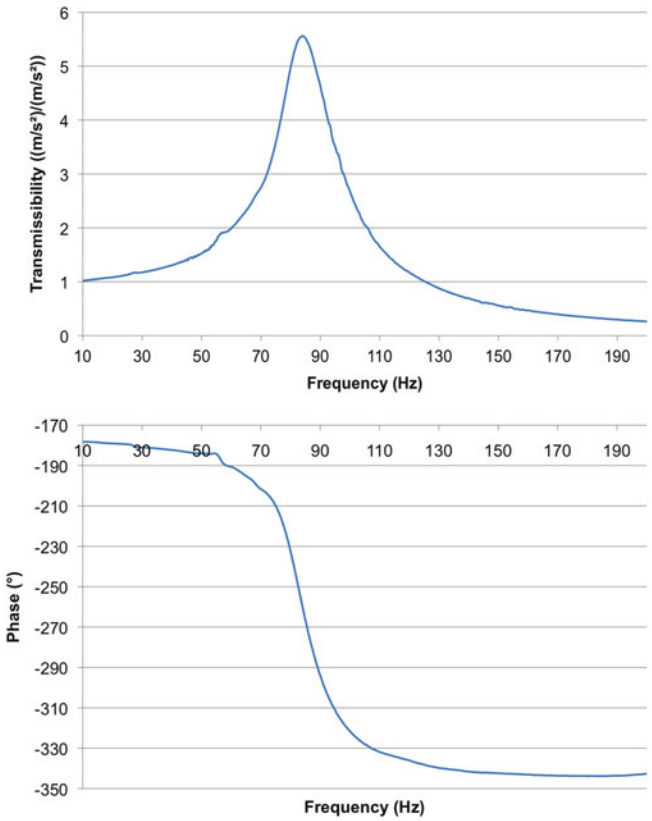

Fig. 18.4 Classical transmissibility–frequency and phase–frequency curves of polyurethane foam

frequency during 10 min. At least, the sweep sine is applied from low to high frequency and then from high back to low frequency.

At the end of the test, the transmissibility is calculated and plotted (Fig. 18.4), and we can calculate the natural frequency, the Q factor, the gain at the resonance and the filtration frequency.

18.4 Results and Discussions

For each mass and each excitation acceleration level, we measured the natural frequency, the filtration frequency, the magnitude at resonance, and we calculated the stiffness of each foam. The results were plotted curves (Figs. 18.5, 18.6, 18.7 and 18.8).

The first parameter we analyzed is the stiffness (Fig. 18.5). We can notice that for foam B, whatever the mass we applied and whatever our excitation acceleration level, the stiffness is quite constant, excepted for the heaviest mass and highest acceleration. This can be explained by the structure of open cellular foam B. For the foam A, according to our testing conditions, the stiffness is not constant. When we load the foam with our lowest mass, we can observe that the stiffness is more important. Our excitation acceleration level of excitation doesn't seem to have a great influence on the stiffness of foam A. For each level of mass, the stiffness doesn't vary when the excitation acceleration level changes. This can be explained by the highly nonlinear comportment of closed cell polyurethane foams described by Gibson and Ashby [4].

Concerning the natural frequency (Fig. 18.6), when we use our two heaviest masses (2.2 or 2.8 kg), the natural frequency is comprised inside the 0–50 Hz band which is the frequencies classically excited in automotive seat. In addition, the filtration frequency of foam B is lower than 50 Hz. That means that foams never filter, and sometimes amplifies the vibrations of the seat.

The results of filtration frequency are presented in Fig. 18.7. We observe that the filtration frequency is quite constant for foam B, into the band of masses and excitation acceleration level we choosed. The foam A presents a constant filtration

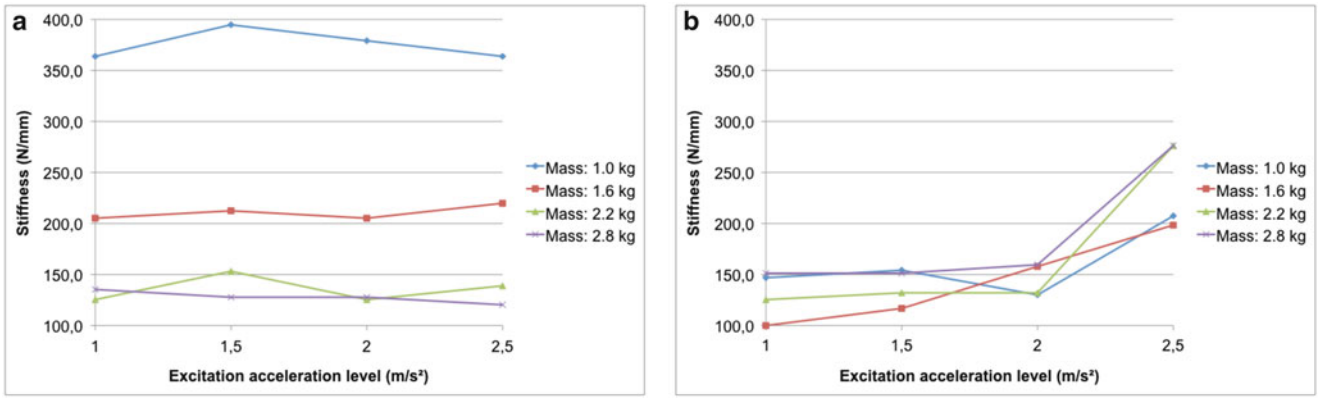

Fig. 18.5 Stiffness of foam A (**a**) and B (**b**)

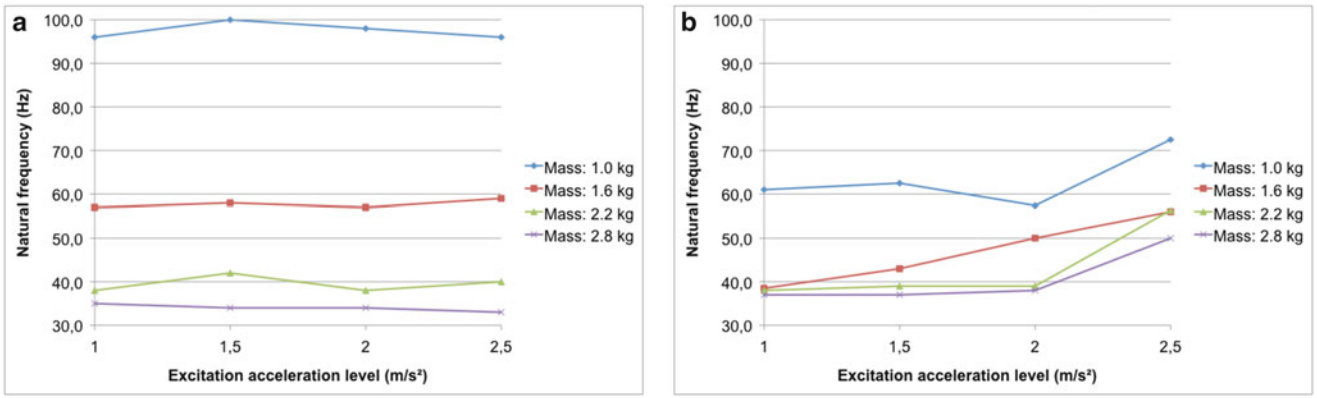

Fig. 18.6 Natural frequency for foam A (**a**) and B (**b**)

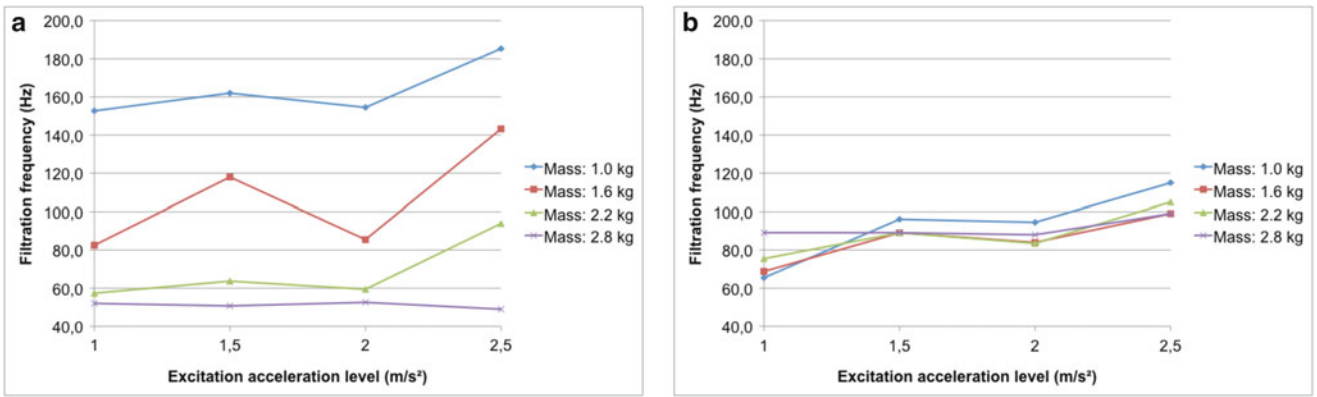

Fig. 18.7 Filtration frequency for foam A (**a**) and B (**b**)

frequency when our excitation acceleration level is varying between 1 and 2.5 m/s^{-2}, but at the opposite, the filtration frequency is highly dependant of the mass. For the masses of 1.0 or 1.6 kg, the filtration frequency are lower than for masses of 2.2 or 2.8 kg.

In term of maximal transmissibility (Fig. 18.8), the two foam types show an important level of amplification. The mass and the acceleration level of excitation don't seem to have influence on the maximal transmissibility for each type of foam. We can suppose that the maximal transmissibility is correlated to a material parameter, like the size cell for example.

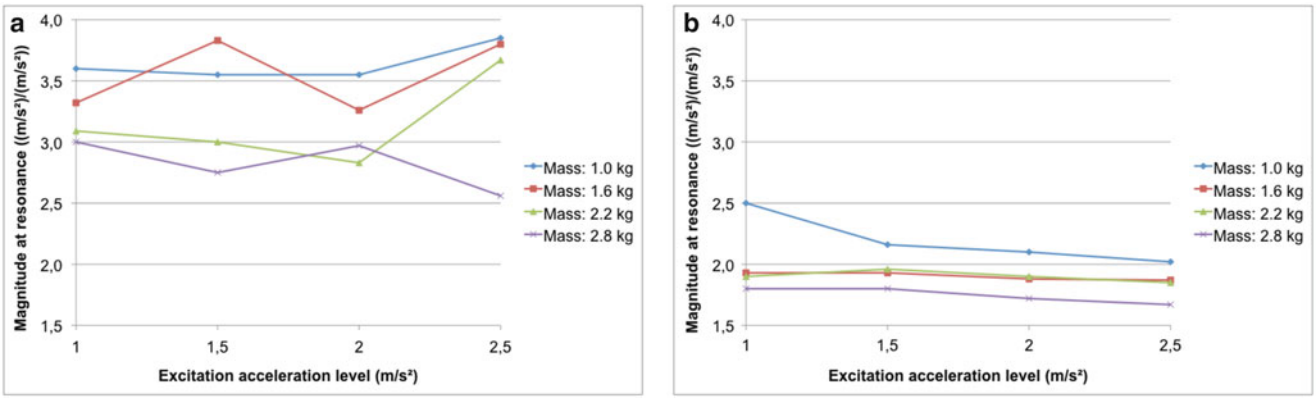

Fig. 18.8 Magnitude at resonance for foam A (**a**) and B (**b**)

18.5 Conclusions

In this study, a method for testing the vibrational mechanical properties of thin soft cellular materials used in automotive upholsteries has been developed and detailed. This method has been used to test two types of polyurethane foams. The results showed that the tested polyurethane foams have different behavior probably due to the type of cells (open or closed). The results demonstrate the inability of thin foams to filter the vibration transmitted to the seat. Indeed, the natural frequencies and the filtration frequencies are in the band of 0–50 Hz classically excited at the base of the seat. The results also highlight that the transmissibility is absolutely not negligible for all the accelerations and preload charges on the foams.

These results have to be confirmed by testing other foams, and will allow us to fully characterize new eco friendly materials dedicated to replace the current polyurethane foams.

References

1. Directive 200/53/CE du parlement Européen et du conseil du 18 septembre 2000 relative aux véhicules hors usage, Journal official des Communautés européennes (2000)
2. Caudron, J.-C.: Etude du marché du polyuréthane et Etat de l'art de ses techniques de recyclage. Agence de l'Environnement et de la Maîtrise de l'Energie (2003)
3. Demangeat, O.: Etude économique et veille technologique. société N. Schlumberger (2000)
4. Gibson, L.J., Ashby, M.F.: Cellular Solids. Pergamon, Oxford (1992)
5. Pritz, T.: Transfer function method for investigating the complex modulus of acoustic materials: spring-like specimen. J. Sound Vib. **72**(3), 317–341 (1980)
6. White, S.W., Kim, S.K., Bajaj, A.K., Davies, P., Showers, D.K., Liedtke, P.E.: Experimental techniques and identification of nonlinear and viscoelastic properties of flexible polyurethane foam. Nonlinear Dyn. **22**(3), 281–313 (2000)
7. Singh, R., Davies, P., Bajaj, A.K.: Initial condition response of a viscoelastic dynamical system in the presence of dry friction and identification of system parameters. J. Sound Vib. **239**(5), 1086–1095 (2001)
8. Singh, R., Davies, P., Bajaj, A.K.: Estimation of dynamical properties of polyurethane foam through use of Prony series. J. Sound Vib. **264**(5), 1005–1043 (2003)
9. Deng, R.: Modeling and characterization of flexible polyurethane foam. Ph.D. thesis, School of Mechanical Engineering, Purdue University, West Lafayette, IN 46907 (2004)
10. Deng, R., Davies, P., Bajaj, A.K.: A nonlinear fractional derivative model for large uni-axial deformation behaviour of polyurethane foam. Signal Process. **86**(10), 2728–2743 (2006)
11. Jmal, H.: Identification du comportement quasi-statique et dynamique de la mousse de polyurethane au travers de modèles à mémoire. Ph.D. thesis, Université de Haute-Alsace, Mulhouse (2012)
12. Ju, M.L.: Contribution à la modélisation du comportement visco-hyper-élastique de mousses de polyuréthane—Validation expérimentale en quasi-statique. Ph.D. thesis, Université de Haute-Alsace, Mulhouse (2014)
13. Njeugna, N., Schacher, L., Adolphe, D.C., Dupuis, R.L., Aubry, E., Schaffhauser, J.-B., Strehle, P.: Comparison of compression behaviour of PU foam and 3D nonwoven. In: The Fiber Society Fall Meeting and Technical Conference, Boucherville (2008)

Chapter 19
High Strain-Rate Ductile to Brittle Transition in Nanoporous Zeolite

Phillip Miller and Junlan Wang

Abstract Synthetic nanoporous zeolite was investigated by nanoindentation at low strain-rates and laser-generated stress waves at high strain-rates. Under quasi-static conditions zeolite has enhanced ductility and resilience. Under high strain-rate conditions zeolite undergoes a ductile to brittle transition. Compressive, uniaxial strain loading was achieved with an acoustically matched windowing material to prevent tension in the zeolite. Stresses as low as 400 MPa resulted in multiple fractures not originating from a single flaw. Under tension the spallation strength of zeolite was measured as 215 MPa with transgranular fracture observed as the dominant spallation feature, further indicating the brittle failure at high strain-rates.

Keywords Nanoporous • Zeolite • High strain rate • Ductile • Brittle

19.1 Introduction

Zeolites form a class of nanoporous and crystalline aluminosilicates. They are naturally occurring minerals, but synthetic zeolites are also highly desired. This is due to their nanoscale porosity allowing unique applications as molecular sieves and ion-exchangers. The crystalline pore structure allows simultaneous high porosity and mechanical stability. Synthesizing zeolites allows fine control of the aluminum to silicon ratio, which dictates the materials ion-exchange capability, influencing the materials performance and allowing tuning for a desired application. Low silica zeolites, whose aluminum to silicon ratio is ~1 find widespread application as ion-exchangers. It is also possible to synthesize zeolites without aluminum, known as pure silica zeolites. These have found recent interest as a next generation low dielectric constant material for the semiconductor industry due to the high porosity [1]. Zeolites have also been investigated for applications as environmentally friendly wear and corrosion resistant coatings [2]. Wear resistance is provided by their high mechanical strength and resilience, which is comparable to that of chromium. Corrosion resistance is provided by high and pure silica zeolites, which are only aggressively attacked by hydrofluoric acid [3].

In general, porous materials provide several responses which make them good candidate materials for impact and shock. Due to the presence of voids and pores in the material they undergo compaction and densification during compression. While the strength of the porous material may be lower than that of its bulk counterpart, energy must be consumed for the initial collapsing of the pores. This process of reducing the material from its large specific volume to its standard volume involves not only overcoming elastic and plastic response, but also friction and other dissipative mechanisms. Additionally, the porous nature of the material allows wave interactions, such as transverse relief, to operate at a small scale and dissipate additional energy. Thus compaction of porous materials is highly dissipative and even modest porosity can achieve significant stress attenuation. Dynamic compaction may also be localized to the area of applied loading, with little effect on the surrounding material. Counterintuitively, the compression of a porous material to a given volume requires more energy than compressing the bulk material to the same volume. This is due to the compression of the porous material being accompanied by larger thermal energy, and hence thermal stress, than experienced by the bulk material [4]. The spallation behavior of porous materials can be sensitive to the compressive plastic strain experienced during the initial loading as well as ductile or brittle response. The quasi-static response of zeolite is ductile, as reported previously by Chow and Wang [2]. However, under the high strain rate loading performed in the current study, it is observed that the zeolite undergoes a ductile to brittle transition and demonstrates brittle fracture.

P. Miller • J. Wang (✉)
Department of Mechanical Engineering, University of Washington, Seattle, WA 98195, USA
e-mail: junlan@uw.edu

B. Song et al. (eds.), *Dynamic Behavior of Materials, Volume 1*,
Conference Proceedings of the Society for Experimental Mechanics Series, DOI 10.1007/978-3-319-22452-7_19

19.2 Sample Preparation, Zeolite Growth, and Structure Confirmation

Substrates were chosen for this study based on their response to laser generated stress wave loading and their applicability as materials whose performance would be improved by being coated with zeolite. 4130 chromoly steel and 6061 aluminum alloy find wide use as structural materials, but require surface coating in many applications to overcome a specific deficiency. 4130 steel has poor corrosion resistance, while 6061 aluminum alloy has poor hardness and wear resistance. The substrates were cut into thin disks from bulk bar stock. Grinding, lapping, and polishing were performed on both surfaces to provide an ideal surface for both the zeolite film growth, as well as to accommodate our optical interferometer, which relies on an optically flat, specular reflective surface.

The zeolite studied is ZSM-5, an MFI framework zeolite first reported by Kokotailo et al. [5]. The ZSM-5 framework consists of two interpenetrating porous networks. A straight, nearly circular channel running parallel to [010] with dimensions of 5.4×5.6 Å, and an elliptical zigzag channel along [100] with dimensions of 5.1×5.4 Å. ZSM-5 are orthorhombic crystals and belong to space group No. 62, Pnma, with cell parameters of $a = 20.07, b = 19.92,$ and $c = 13.42$ Å [6]. Zeolite film growth is achieved by hydrothermal deposition and follows the procedure of Lew et al. [1]. A solution was prepared with aluminum powder, tetrapropylammonium hydroxide (TPAOH), tetraethylorthosilicate (TEOS), and sodium hydroxide (NaOH) in de-ionized water with a molar composition of 0.16TPAOH:0.64NAOH: TEOS:92H_2O:0.0018Al. The initial step in the solution synthesis procedure is mixing 0.0104 g Al power, 100 g de-ionized water, and 5.36 g NaOH pellets for 30 min at 400 RPM. 17.03 g TPAOH is then added and stirred for an additional 15 min. Subsequently 236 g of de-ionized water is added and stirred for 15 min. Final solution synthesis step is the dropwise addition of 43.6 g TEOS while stirring. Solution is aged for 24 h while stirred at 800 RPM. After aging the solution is placed in a Teflon lined autoclave, in which the 4130 steel of 6061 aluminum alloy thin disk substrates have been suspended by copper wires. After ensuring the substrates are fully immersed with adequate separation from one another, the autoclave is sealed and placed in an oven at 175 °C for 24 h, after which film growth rates drops. In order to achieve the thickness of films needed for this study, the hydrothermal synthesis process is repeated as needed, using a fresh solution for each 24 h growth stage.

SEM imaging of the surface of the as synthesized zeolite film was performed to examine the surface and crystal morphology. Figure 19.1a is a low magnification micrograph showing island-like surface features which are dominant above 10 μm length scale. Surface profiling of the as synthesized surface is shown in Fig. 19.1b, with a measured RMS surface roughness of 4.5 μm. Figure 19.1c shows the high degree of intergrowth and twinning with no preferred orientation, a trademark morphology for this specific zeolite and synthesis procedure, which was optimized to be a thin film membrane coating. Figure 19.1d shows individual crystals ranging in size from 5 to 20 μm, which were used to measure the length-to-width ratio of 3.5. This ratio is consistent with the growth temperature of 175 °C. For ZSM-5 the individual crystal size is limited by the Al atom concentration, since the nucleation rate is proportional to the Al^{3+} concentration [7].

X-ray diffraction (XRD) was used to confirm the crystal structure by comparing measured XRD data with that of the known zeolite ZSM-5 structure [8]. Quantitative XRD was obtained by Rietveld refinement [9, 10] using the MAUD [11, 12] software. Reference data comes from the Database of Zeolite Structures [13], with the ZSM-5 XRD data originating from van Koningsveld et al. [8]. Overall good agreement between the measured XRD data and the Rietveld refinement is observed, with corresponding refined cell parameters of $a = 20.03, b = 19.92,$ and $c = 13.40$ Å (Fig. 19.2).

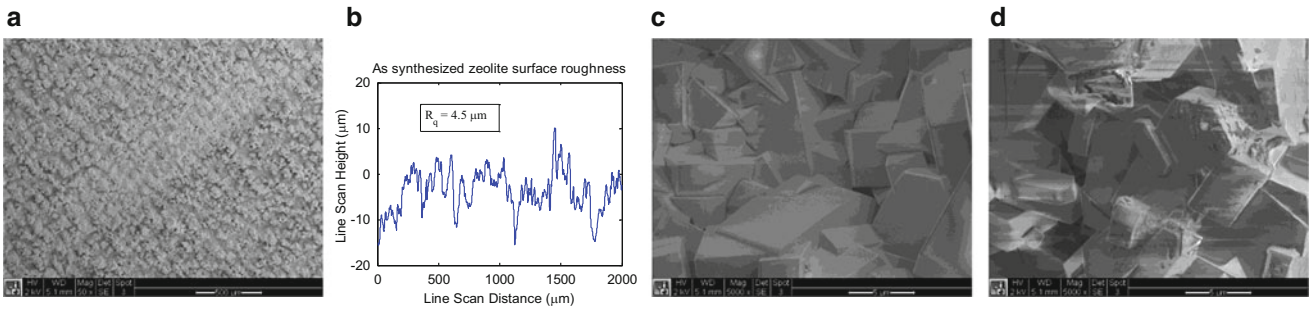

Fig. 19.1 SEM images of the as synthesized zeolite surface morphology (**a**, **c**, **d**), and profile of surface roughness (**b**)

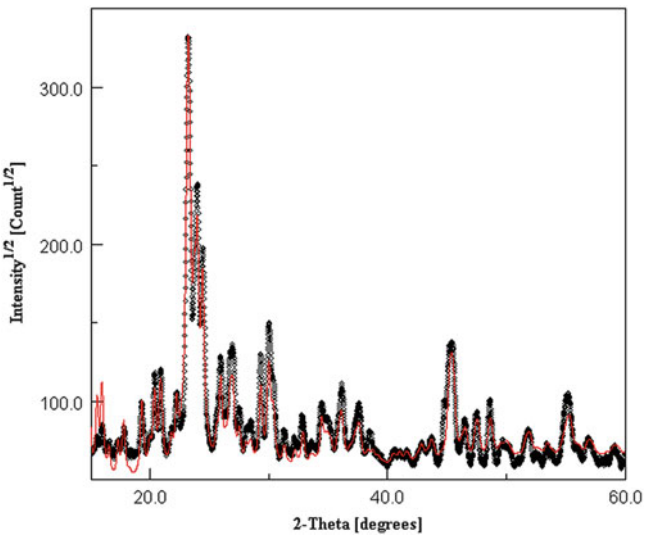

Fig. 19.2 XRD measurements (*black*) and Rietveld refinement results (*red*), with corresponding cell parameters of $a = 20.03$, $b = 19.92$, and $c = 13.40$ Å

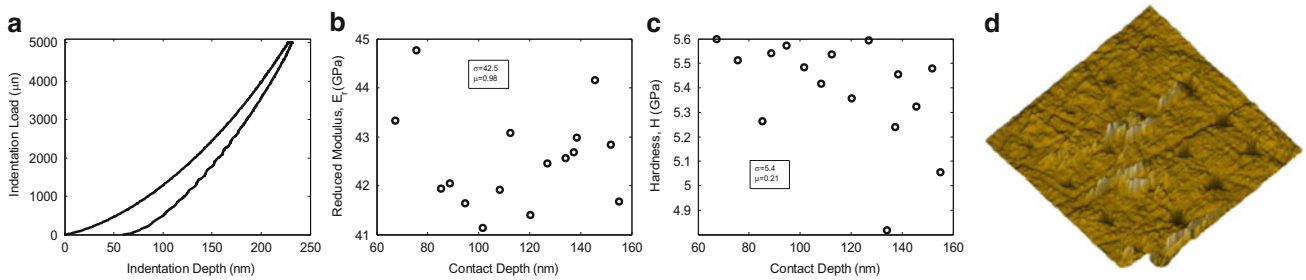

Fig. 19.3 (**a**) Indentation load–displacement curve for a 5000 μN load, showing the large amount of recovery. (**b**) & (**c**) Reduced modulus and hardness, 42.5 and 5.4 GPa respectively. (**d**) SPM image of the sample surface after indentation

19.3 Experimental Methods

19.3.1 Quasi-Static Testing by Nanoindentation

Instrumented nanoindentation with simultaneous load and displacement measurement was performed on the pristine polished sample surfaces. Measurement of the reduced modulus and hardness is accomplished using the well-known method of Oliver and Pharr [14, 15]. The indentation load was ramped up over 5 s to the maximum load, held for 5 s, then ramp unloaded over 5 s. A 4 × 4 indentation array was conducted with maximum load ranging from 1500 to 5000 μN using a Berkovich tip, a representative load is shown in Fig. 19.3a. The reduced modulus was measured to be 42.5 GPa with a standard deviation of 0.98 GPa, while the hardness was 5.4 GPa with a standard deviation of 0.21 GPa, both shown in Fig. 19.3b, c. Scanning probe microscopy (SPM) was achieved using the nanoindentation tip scanning the surface with a closed-loop load control of 2 μN, providing the surface topography in Fig. 19.3d. These results are consistent with those reported previously for this zeolite using nanoindentation [2]. At the quasi-static loading, the zeolite behaves ductile, with significant deformation recovery after unloading, and the indents showed no cracking or fracture even at all load level applied.

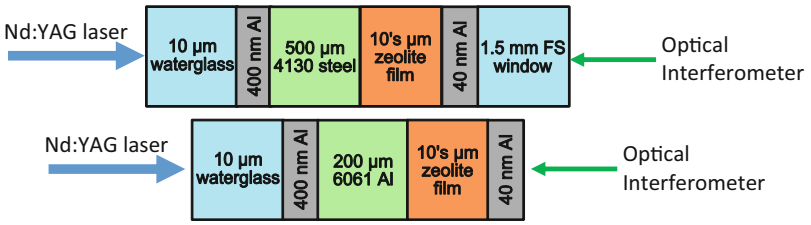

Fig. 19.4 Zeolite sample geometry for compression (*top*) and spallation (*bottom*) experiments. Compression: 4130 steel substrate was coated with MFI zeolite films of 10's μm thickness. Standard Al energy absorbing layer and spin coated waterglass confining layer was used to augment and control stress generation. 1.5 mm fused silica was used as a windowing material, with the inner surface coated with a thin aluminum reflective film. Tension: thick zeolite films was grown on thin 6061 aluminum alloy substrate. The zeolite will be coated with a thin aluminum reflective film

19.3.2 High Strain-Rate Testing by Laser Generated Stress Waves

For the high strain rate study, the experimental setup is that of the standard laser spallation experiment [16, 17]. Thin (several hundred microns) 4130 steel or 6061 aluminum alloy substrates were coated with 10's μm thick MFI zeolite using the synthesis process described in Section 19. 2. For compression experiments the substrate is 4130 steel. The motivation for using a steel substrate is that the stress profile has a smooth Gaussian profile, with a width comparable to that of the 5 ns loading laser. In order to elicit only the compressive behavior of the ZSM-5, a fused silica window was used to minimize tensile stress which would normally develop from reflection at the free surface. The sample geometry is shown in Fig. 19.4 (top). Fused silica is closely acoustically matched to ZSM-5, allowing the compressive stress (applied from the left by a 5 nm Nd:YAG pulse laser) to be efficiently transmitted into the substrate. The inner surface of the 1.5 mm fused silica window was coated with a thin 40 nm sputter deposited aluminum film, thus forming a back surface mirror needed for the interferometer. The back surface of the substrate, which faces the loading laser, has an energy absorbing layer (400 nm Al) as well as a spin coated waterglass confining layer. When the 5 ns Nd:YAG laser pulse is absorbed by the confined Al energy absorbing layer, a compressive stress wave is generated which is propagated toward the right to compress the zeolite sandwiched between steel substrate and fused silica window.

In addition to compression, spallation experiments were also conducted, with 6061 aluminum alloy as the substrate material. The sample geometry is shown in Fig. 19.4 (bottom). Without the fused silica window, the compressive stress is reflected into tensile wave at sample free surface which eventually load the zeolite in tension. 6061 aluminum alloy for the substrate was chosen due to its close acoustic match to the zeolite substrate, allowing both high stress generation and efficient coupling to the zeolite. A downside of the 6061 aluminum alloy substrate is the large distortion of the stress profile due to plasticity. This does not hinder the measurement of the spallation strength, though, since spallation creates unique signal features, allowing property extraction even in the presence of wave distortion from plasticity. Since the aim of these experiments is spallation, the laser-induced stress wave is allowed to reflect at the zeolite free surface into a tensile wave. Actual tension in the substrate is only achieved once the reflected tensile wave meets the unloading portion of the incoming compressive stress. If the tensile stress generated from the superposition of the free surface reflected wave and the compressive unloading wave exceeds the dynamic tensile strength of the zeolite, the spallation strength will be measured. The side of the sample facing the 5 ns Nd:YAG loading laser is coated with the typical 400 nm energy absorbing layer and 10 μm spin coated waterglass. For the spallation experiment it is important that the confining layer is thin enough to ensure that the unloading wave intersects with the free surface reflected tensile wave within the zeolite thickness and away from the 6061 aluminum alloy-zeolite interface, thus ensuring the measured spallation strength is that of the bulk zeolite, and not influenced by the interface.

19.3.2.1 Compression Experiment with Thick Zeolite Films

Compression experiments were carried out for several 4130 steel substrate samples, with and without zeolite coatings. The principal goal was to measure the wave profile for coated and uncoated samples to determine if there was any distortion to the stress wave. Figure 19.5 shows typical interferometer signal (top) and stress history (bottom) for a 560 μm thick 4130 steel bare substrate (left) and a substrate with the same thickness and a 20 μm thick zeolite coating (right). Both profiles are

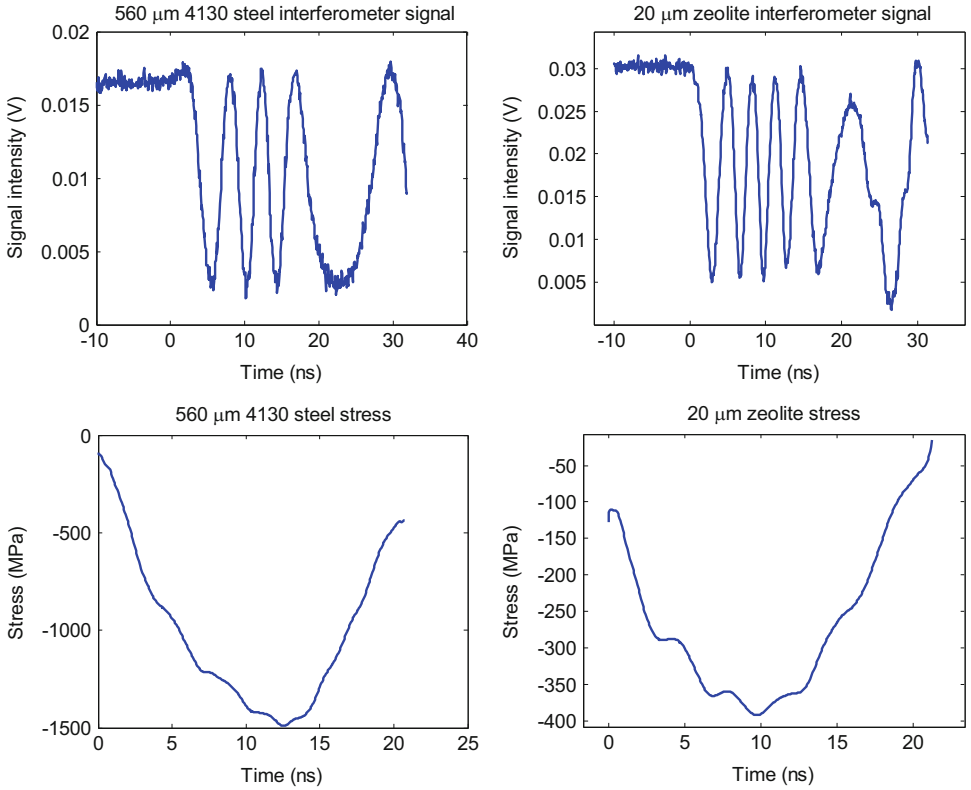

Fig. 19.5 Interferometer signal (*top*) and stress history (*bottom*) for 560 μm thick 4130 bare substrate (*left*) and the same substrate coated with 20 μm thick ZSM-5 (*right*). Peak stress in the bare steel substrate was 1.5 GPa, while for the sample coated with the zeolite coating the peak stress is 400 MPa

Gaussian with time constants of 6.1 ns for the 4130 and 6.3 ns for zeolite. Peak stress achieved in the uncoated substrate is 1.5 GPa, while that of the coating is 400 MPa.

To increase the amount of interaction of the stress wave with the zeolite coating, a much thicker coating was grown via sequential hydrothermal synthesis. The resulting film was 63 μm thick, grown on a 290 μm thick 4130 substrate. Compression experiment with a 1.5 mm fused silica window were conducted, which simulates measurement of the in situ particle velocity. For fused silica windowing with moderate stress amplitude, no corrections are needed other than the stress calculations no longer having a one-half prefactor, which was previously required for free surface reflection since the incoming compressive wave and reflected tensile wave both displace the surface in the same direction. Figure 19.6 (top-left) shows the recorded interferometer signal and (top-right) the stress history for the 63 μm thick zeolite on 330 μm thick 4130 substrate. For the thicker coating the stress profile is not asymmetric. Peak stress ranges from 300–400 MPa, with an average near 330 MPa. SEM imaging, shown in Fig. 19.6 (bottom), of the front surface revealed two distinct features: (1) some areas show spallation-like deformation; (2) surface cracking. The asymmetry of the stress profile can be attributed to the thinner substrate, which shows more elastic–plastic behavior than longer propagation distances in the thicker substrate.

19.3.2.2 Spallation Experiment with Bulk Zeolite

Due to the onset of brittle fracture observed during the compression experiments, and the observation of spallation for areas in which there was poor contact with the fused silica window, it was determined that more information on the dynamic response of zeolite could be extracted from spallation experiments. For this testing the substrate chosen was 6061 aluminum alloy, which has a higher stress transmission coefficient $\beta_t = 0.72$. While 6061 aluminum alloy will plastically deform even at moderate stress levels and alter the stress profile, this will not inhibit spallation measurement as long as the zeolite experiences sufficient stress. Initial testing of an uncoated 6061 aluminum alloy substrate measured peak stresses of 3.5^{+} GPa. For the stress transmission coefficient from aluminum to zeolite we can expect stress levels of ~2.5 GPa.

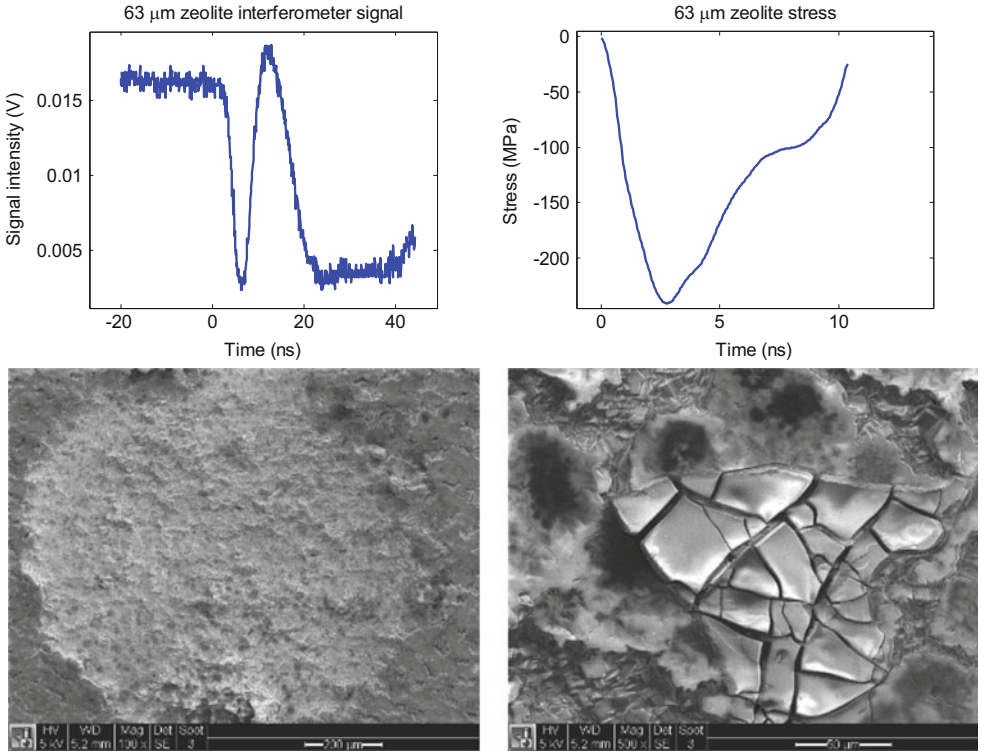

Fig. 19.6 *Top*: Interferometer signal (*left*) and substrate stress history (*right*) for 63 μm zeolite. The thicker zeolite coating displays an asymmetric stress profile, with a peak stress of 300 MPa. *Bottom*: SEM images of resulting spallation and surface cracking

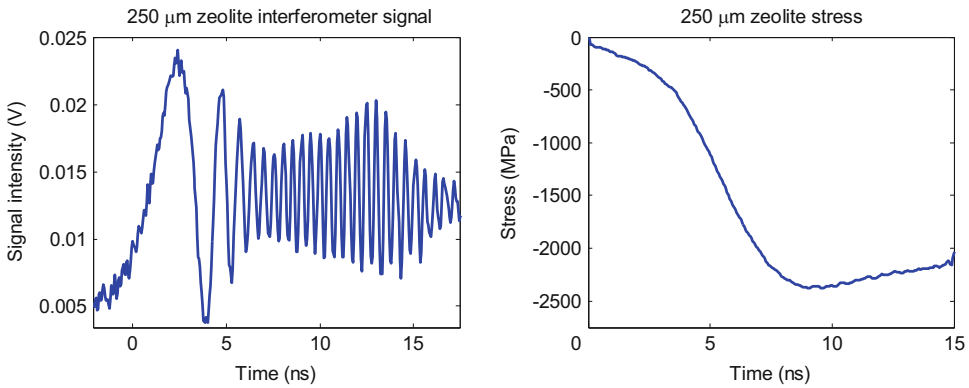

Fig. 19.7 Interferometer signal (*left*) and substrate stress history (*right*) for 250 μm thick zeolite on 150 μm thick 6061 Al substrate. Usable fringe data only lasts for ~20 ns, before complete unloading. Peak stress measured is ~2.5 GPa

Figure 19.7 shows the measured interferometer signal and derived stress history for the zeolite loaded at fluence of ~33 J/cm^2. Peak stress of 2.5 GPa was measured, consistent with peak stress measurement for the uncoated aluminum combined with the stress transmission efficiency. The elastic precursor and elastic–plastic transition from the 6061 substrate is clearly visible in the loading signal. Due to degraded interferometry signal for some of the data collected, a new analysis technique was required which does not depend on data reduction at the individual half-fringe level. Instead, a spectral technique was used, following the technique of Strand et al. [18], in which the frequency response as a function of time was interpreted by a shifting Fourier analysis. Fourier analysis was performed on 10 ns intervals, using a Blackman windowing function on each interval to ensure periodicity. A continuous spectrum is generated by advancing a single data point, 50 ps, for each spectrum analysis. The fringe frequency can be converted to surface velocity by multiplying by the fringe constant,

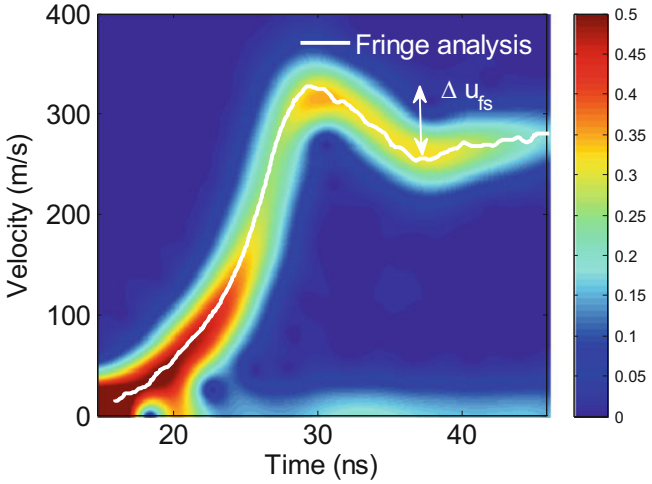

Fig. 19.8 Velocity spectrograph compared with the fringe based data reduction. Δu_{fs}, the velocity pullback, is also indicated

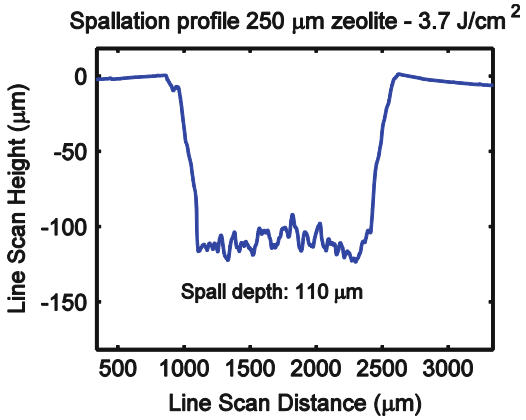

Fig. 19.9 Profilometer measurement of spallation depth. Mean spallation depth was measured as 110 μm, while the spallation width is ~1.5 mm

$\lambda/2$. Figure 19.8 shows the spectrograph of the surface velocity in comparison with the velocity derived from fringe analysis, resulting from loading of 3.7 J/cm^2. Very good agreement is observed for the two profiles. While the fringe interpreted surface velocity shows sharper features, noise is more detrimental. The velocity spectrum is naturally smoothed by both the frequency resolution, as well as analyzing 10 ns at a time.

Also shown in Fig. 19.8 is the signature of spallation, the pullback signal. The velocity pullback, Δu_{fs}, is labeled for convenience. The pullback signal is the result of the free surface reflected wave interacting with the unloading wave, creating a spall pulse. Within the "acoustic approach" the spallation strength can be extracted from the pullback signal by [19]:

$$\sigma_{\text{spall}} = \frac{1}{2}\rho c_L \Delta u_{\text{fs}} \tag{19.1}$$

where ρ is the density, c_L is the longitudinal wave speed, and Δu_{fs} is the aforementioned velocity pullback. Another spallation analysis technique depends on the spallation depth. If the stress history is known, then the stress at any depth, h, can be computed by:

$$\sigma(t;h) = \sigma(t - h/c_L) - \sigma(t + h/c_L) \tag{19.2}$$

Figure 19.9 shows measurement of the spallation depth by scanning contact profilometry. The spallation depth was measured to be 110 μm, with a width of ~1.5 mm. This corresponds to a stress transit time of 20 ns. Spallation strength

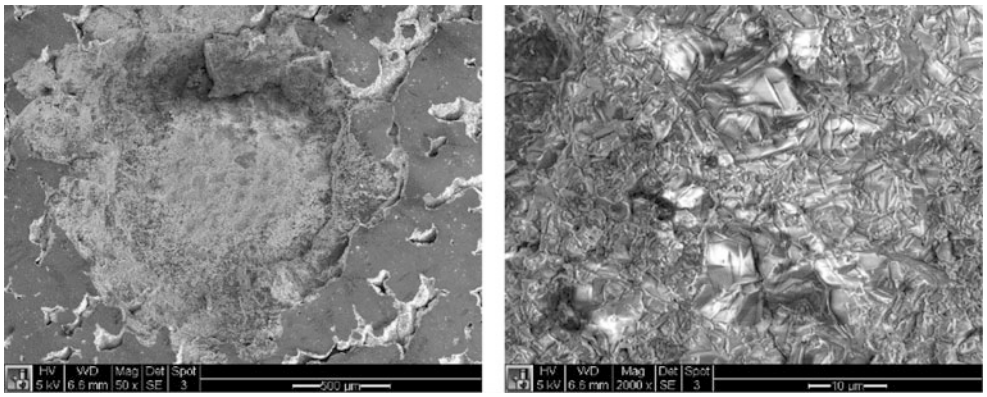

Fig. 19.10 SEM images of spallation surface. *Left* image at ×50 shows the large scale fracture structure, with noticeable steps away from the center of the spallation plane. *Right* image, zoomed to ×2000, shows the dominance of transgranular fracture, with some fracture facets of individual grain typical of intergranular fracture

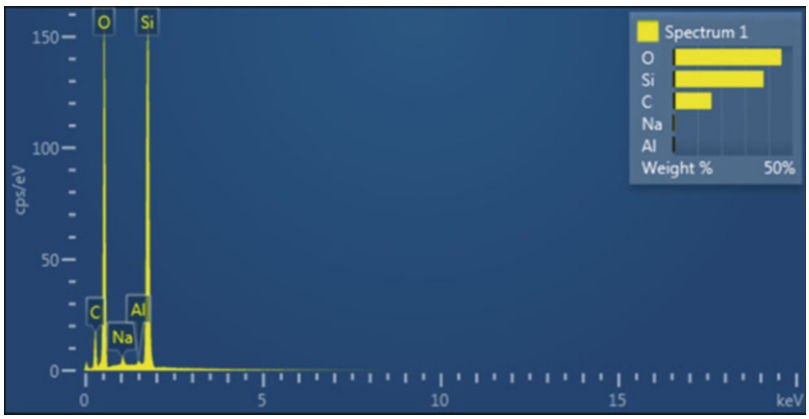

Fig. 19.11 EDS analysis of the spallation area shown in Fig. 19.10. Highest elemental percentages correspond to silicon and oxygen, as expected. Si-Al-O weight ratio agrees with that of the zeolite stoichiometry

analysis using the spallation depth requires interferometry data for a time of at least $2h/c_L$, or 40 ns for this data. Interferometry data is not reliable for this duration, so spallation strength based on the velocity pullback must be used.

Figure 19.10 shows SEM images of the spallation surface at magnifications of ×50 and ×2000, respectively. While image resolution is limited due to the charge buildup of the insulating zeolite, it is clear that dominant fracture feature is intergranular failure. Some large planar faces are also visible, which may be from transgranular failure.

Due to the depth of the measured spallation, it was important to determine if the spallation was due to the bulk material failure, or being influenced by the substrate/zeolite interface. Energy-dispersive x-ray spectroscopy (EDS) generates characteristic x-rays which can originate from 5 to 10 μm deep within the sample. EDS was performed on the spall plane to determine if the composition matches that expected for the ZSM-5 zeolite, and the results are shown in Fig. 19.11. The stoichiometry of uncalcinated ZSM-5 is $|((C_3H_7)_4NOH_4)|[Si_{95.7}Al_{0.3}O_{192}]$, with an expected Si-Al-O weight percentage of ~46.5-0.5-53 %. The actual EDS measurements are ~45.1-0.4-54.5 %. This indicates the spallation happened far enough away from the substrate such that no additional Al signal is measured.

Correlation analysis was performed with the measurement values for laser energy, peak stress, spallation strength, and spallation depth, shown in Fig. 19.12. Correlation coefficient for each variable pair is on the graph of the intersection of the row and column variable. Significant correlations are highlighted in red. Strongly correlated variable pairs are laser energy, peak stress, and spall depth. The spallation strength was measured with a mean of 215 MPa and standard deviation of 70 MPa. The intersection of a variable with itself shows the histogram of the measurements. Laser pulse energy, thus peak stress, was varied to determine if the zeolite spallation strength exhibits any trend. There is a small, positive correlation between peak stress and spallation strength, but the trend is far smaller than the data scatter.

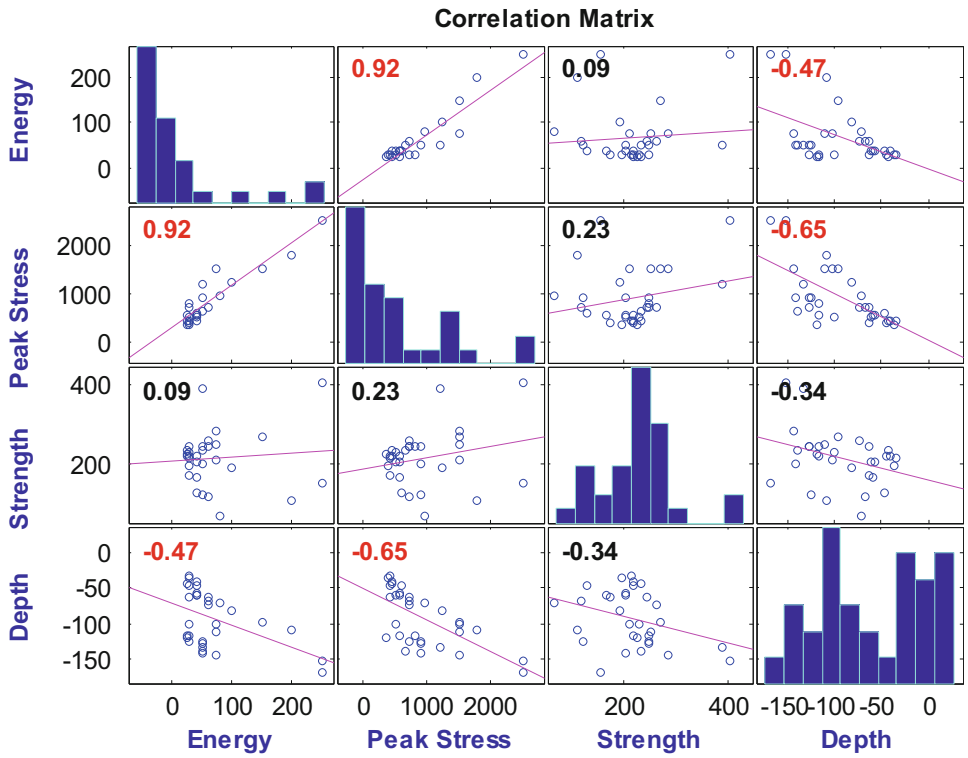

Fig. 19.12 Correlation matrix for laser pulse energy, peak stress, spallation strength, and spallation depth. The *numbers* in each plot shows the correlation coefficient between the intersection of the row and column variable, with those in *red* showing significant correlation. Correlated variables are energy, peak stress, spall strength, and depth

19.4 Discussion

Quasi-static testing of zeolite by instrumented nanoindentation demonstrates that the behavior of crystalline, nanoporous zeolite is considerably different from that of fully dense, bulk silicates. Whereas quartz and fused silica have high hardness and modulus, and tend to form radial fractures along the indenter edges, the zeolite studied here instead has a very ductile response. It also has lower hardness and modulus, which contributes to its enhanced resilience. Zeolite is also superior in its elastic recovery from the maximum load. All of these features arise from the nanoporous crystalline nature of zeolites, which can accommodate a much larger degree of recoverable deformation without fracturing, and yields in a ductile manner.

High strain-rate compression experiments using the 5 ns Tempest laser at fluences ~33 J/cm^2 on the zeolite coated and uncoated 4130 steel substrates showed several interesting behaviors. For both thin and thick coatings the stress history is an accurate temporal copy of the uncoated stress history. The 560 μm thick 4130 steel showed a Gaussian stress profile, with time constants for the uncoated and coated close to that of the loading laser. This is the expected elastic and long term propagation behavior for the stress wave away from the stress generation region. While at first inspection it would appear that the zeolite coating is quite remarkable in its attenuation capability, reducing the incident stress amplitude of 1.5 GPa from the 4130 substrate to only 400 MPa, this response can be explained with purely elastic behavior. Upon arrival of the stress wave at the interface of the 4130 substrate and zeolite coating, stress and acceleration continuity are required. The result is that there is transmission and reflection at the interface. The transmission coefficient from steel to zeolite is given by:

$$\beta_t = \frac{2(\rho c_L)^{\mathrm{ZSM-5}}}{(\rho c_L)^{\mathrm{ZSM-5}} + (\rho c_L)^{4130}} = 0.32 \tag{19.3}$$

where ρ is the density, c_L is the longitudinal wave speed, and the superscript indicates the density and wave speed specified for either the zeolite (ZSM-5) or the steel (4130). A transmission coefficient of 0.32 is very close to the observed ratio of 0.27 and well within the error level associated with data reduction.

The observation of spallation of the zeolite coating is unexpected. Zeolite is very closely acoustically matched to the fused silica window material, allowing nearly all of the incident compressive stress to be efficiently transmitted from the zeolite to the window. Fused silica has a slightly higher acoustic impedance than zeolite, which results in the reflected wave at the zeolite-fused-silica interface to have the same sign as the incoming wave, i.e. a compressive wave is reflected at the surface, not a tensile wave. It may be possible that the tensile stress needed for spallation was generated from the free surface reflection at the fused silica window. While this wave will eventually interact with the film, fused silica is a highly nonlinear elastic solid. For stresses under 3.5 GPa it is dominated by negative nonlinear stress–strain behavior. The result of the negative nonlinear behavior is that low amplitude stress propagates faster than high amplitude stress [19, 21]. While the wave propagates through the window it will attenuate and stretch, leading to much lower stress. Additionally, the interface between the window and zeolite is unlikely capable of supporting significant tensile stress. Investigation of the fringe record reveals that the areas with spallation had abnormally high stresses, twice as high as any other data. Stress and displacement twice that of the norm corresponds exactly to the expected behavior from a free surface reflection. A set of data were taken without the windowing material, which matched that of the anomalously high stress data where spallation was observed. In these areas the contact between the zeolite and the window was poor, resulting in a free surface for the zeolite coating.

The final SEM observation, shown at bottom right in Fig. 19.6, is surface cracking of the zeolite. Surface cracking was observed with good interferometry data that indicated uniform contact with the fused silica window. Surface fracturing at moderate stress levels of 300–400 MPa is in sharp contrast with the mechanical response of zeolite under nanoindentation [2, 22], where no fracture features are observed even under maximum loading conditions, which represent contract stresses in excess of 3 GPa. There are two contributions to the observation of surface cracking at much lower stresses than observed for nanoindentation. The first contribution is the zeolite coatings used for this study are of a thickness where they behave as bulk materials. Nanoindentation is a local probe of the material property, unless done specifically near existing defect, e.g. grain boundaries [23]. For thin films defect concentration and flaw size generally grow with film thickness, as principal sites of defect concentration like grain boundaries become significant. As the typical zeolite crystal size ranges from 5 to 20 μm, any film thicker than this will begin to behave more as a bulk material. The second contribution to the observed zeolite behavior may be attributed to the very high strain-rate associated with laser loading. At very high strain-rates materials may undergo a ductile to brittle transition. Such a transition is possible when the stress rate, related to the elastic strain-rate, far exceeds the plastic strain-rate, which is responsible for crack tip blunting [24]. Nanoindentation results show that zeolite has simultaneous high hardness (6.3 GPa) and low elastic modulus (51 GPa), resulting in high resilience [2]. For such materials under high strain-rate loading energy can be supplied to the crack tip faster than can be dissipated from blunting and crack advance. The appearance of multiple intersecting fractures also corroborates the possibility of a strain-rate driven ductile to brittle transition, as lower rate crack growth tends to initiate at a single area that has reached a critical stress level leading to catastrophic growth and branching before other flaws are activated [24].

Spallation experiments on 6061 aluminum alloy substrates with peak compressive stresses ranging from 250 to 3000 GPa were conducted to determine the dynamic tensile failure behavior of bulk zeolite. The brittle nature of zeolite under high strain-rate conditions was confirmed by the spallation study. SEM images of the spallation morphology show that the spallation is dominated by brittle transgranular fracture, but accompanied by some degree of intergranular fracture. Profile measurement and SEM images indicate the spallation area is larger than the loading area, indicating long term failure development after the initial onset of spallation, a typical response for brittle materials. Due to reduced signal quality at time scales relevant to the first wave interaction with the surface, a spectral analysis technique was adopted to extract the relevant spallation feature from the interferometer data, the velocity pullback signal. EDS analysis performed within the spallation area indicates a close stoichiometric match to the bulk zeolite material, indicating the spallation happened far enough away from the interface that the true bulk spallation strength was measured. The bulk spallation strength of 215 MPa is substantially lower than that of the interfacial strength, measured to be 326 MPa [25]. Brittle material spallation strength can be sensitive to the initial compressive loading, as the compressive wave can act on preexisting flaws, microcracks, and grain boundaries to initiate the fracture process before arrival of the release wave. Correlation analysis shows there is no significant dependence of the spallation strength on the loading parameters, e.g. laser pulse energy or peak stress, as is observed with some brittle materials such as alumina [26]. Strong correlation is observed between laser energy and peak stress, as expected, and also between energy/peak stress and spallation depth. This is further indication that the final spallation depth is determined by long term (post initial stress wave) fracture and fragmentation.

19.5 Conclusions

Under high strain-rate dynamic loading by short pulse laser-generated stress waves the behavior of bulk zeolite is that of a brittle solid. The only significant stress attenuation can be attributed to the acoustic mismatch between the substrate material and the bulk zeolite coating. Under moderate compressive loading of only several hundred MPa peak stress, surface fracturing is observed. The surface fracture morphology indicates simultaneous nucleation and propagation of cracks, a predominately high strain-rate brittle behavior. Spallation experiments with peak stress ranging from 250 to 3000 MPa were conducted. Spectral analysis of the interferometry data was used to extract the velocity pullback signal. The spallation strength was measured from the velocity pullback, with mean value of 215 MPa. This value is lower than that of the interfacial strength of zeolite. EDS analysis on the spallation area indicated no excess aluminum, indicating spallation occurred away from the interface and the true bulk spallation strength was measured. SEM imaging showed the predominance of brittle transgranular fracture. No correlation was observed between the peak compressive stress and spallation strength.

References

1. Lew, C.M., Cai, R., Yan, Y.: Zeolite thin films: from computer chips to space stations. Acc. Chem. Res. **43**(2), 210–219 (2010). doi:10.1021/ar900146w
2. Chow, G., Bedi, R.S., Yan, Y., Wang, J.: Zeolite as a wear-resistant coating. Microporous Mesoporous Mater. **151**, 346–351 (2012). doi:10.1016/j.micromeso.2011.10.013
3. Flanigen, E.M., Bennett, J.M., Grose, R.W., et al.: Silicalite, a new hydrophobic crystalline silica molecular sieve. Nature **271**, 512–516 (1978). doi:10.1038/271512a0
4. Zel'dovich, Y., Raizer, Y.P.: Physics of Shock Waves and High-Temperature Hydrodynamic Phenomena, vol. 2, 2nd edn. Academic, New York (1967)
5. Kokotailo, G., Lawton, S., Olson, D.: Structure of synthetic zeolite ZSM-5. Nature **272**, 437–438 (1978)
6. Olson, D.H., Kokotailo, G.T., Lawton, S.L., Meier, W.M.: Crystal structure and structure-related properties of ZSM-5. J. Phys. Chem. **85**, 2238–2243 (1981). doi:10.1021/j150615a020
7. Yokomori, Y., Idaka, S.: The structure of TPA-ZSM-5 with Si/Al = 23. Microporous Mesoporous Mater. **28**, 405–413 (1999). doi:10.1016/S1387-1811(98)00311-4
8. Van Koningsveld, H., van Bekkum, H., Jansen, J.C.: On the location and disorder of the tetrapropylammonium (TPA) ion in zeolite ZSM-5 with improved framework accuracy. Acta Crystallogr. Sect. B: Struct. Sci. **43**, 127–132 (1987). doi:10.1107/S0108768187098173
9. Rietveld, H.: Line profiles of neutron powder-diffraction peaks for structure refinement. Acta Crystallogr. **22**, 151–152 (1967)
10. Rietveld, H.: A profile refinement method for nuclear and magnetic structures. J. Appl. Crystallogr. **2**, 65–71 (1969)
11. Lutterotti, L.: MAUD (material analysis using diffraction): a user friendly Java program for Rietveld texture analysis and more. In: Proceeding of the Twelfth International Conference on Textures of Materials, vol. 1, McGill University, Montreal, 9–13 Aug 1999
12. Lutterotti, L., Matthies, S., Wenk, H.: MAUD: a friendly Java program for material analysis using diffraction. IUCr Newslett. CPD **21**, 14–15 (1999)
13. Baerlocher, C., McCusker, L.B.: Database of zeolite structure. http://www.iza-structure.org/databases/
14. Pharr, G.M.: Measurement of mechanical properties by ultra-low load indentation. Mater. Sci. Eng. A **253**, 151–159 (1998). doi:10.1016/S0921-5093(98)00724-2
15. Oliver, W.C., Pharr, G.M.: An improved technique for determining hardness and elastic modulus using load and displacement sensing indentation experiments. J. Mater. Res. **7**, 1564–1583 (2011). doi:10.1557/JMR.1992.1564
16. Gupta, V., Argon, A.S., Cornie, J.A., Parks, D.M.: Measurement of interface strength by laser-pulse-induced spallation. Mater. Sci. Eng. A **126**, 105 (1990)
17. Wang, J., Sottos, N., Weaver, R.: Tensile and mixed-mode strength of a film-substrate interface under laser induced pulse loading. J. Mech. Phys. Solids **52**, 999–1022 (2004)
18. Strand, O.T., Goosman, D.R., Martinez, C., et al.: Compact system for high-speed velocimetry using heterodyne techniques. Rev. Sci. Instrum. **77**, 083108 (2006). doi:10.1063/1.2336749
19. Novikov, S., Divnov, I., Ivanov, A.: The study of fracture of steel, aluminium and copper under explosive loading. Fiz. Met. Metalloved. **21**, 608–615 (1966)
20. Barker, L.M.: Shock-wave studies of PMMA, fused silica, and sapphire. J. Appl. Phys. **41**, 4208 (1970). doi:10.1063/1.1658439
21. Wang, J., Weaver, R., Sottos, N.: Laser-induced decompression shock development in fused silica. J. Appl. Phys. **93**, 9529–9535 (2003)
22. Johnson, M., Li, Z., Wang, J., Yan, Y.: Mechanical characterization of zeolite low dielectric constant thin films by nanoindentation. Thin Solid Films **515**, 3164–3170 (2007). doi:10.1016/j.tsf.2006.01.048
23. Lian, J., Garay, J.E., Wang, J.: Grain size and grain boundary effects on the mechanical behavior of fully stabilized zirconia investigated by nanoindentation. Scr. Mater. **56**, 1095–1098 (2007). doi:10.1016/j.scriptamat.2007.02.027
24. Freund, L.B.: Dynamic Fracture Mechanics, pp. 469–470, 509. Cambridge University Press, Cambridge (1998)
25. Hu, L., Wang, J., Li, Z., et al.: Interfacial adhesion of nanoporous zeolite thin films. J. Mater. Res. **21**, 505–511 (2006)
26. Rozenberg, Z.: The response of ceramic materials to shock loading. In: Schmidt, R.D., Forbes, J.W., Tasker, D.G. (eds.) Shock Compression of Condensed Matter—1991, pp. 439–444. Elsevier, Amsterdam (1991)

Chapter 20
Dynamic High-Temperature Tensile Characterization of an Iridium Alloy

Bo Song, Kevin Nelson, Ronald Lipinski, John Bignell, G.B. Ulrich, and E.P. George

Abstract Iridium alloys have been utilized as structural materials for certain high-temperature applications due to their superior strength and ductility at elevated temperatures. In some applications where the iridium alloys are subjected to high-temperature and high-speed impact simultaneously, the high-temperature high-strain-rate mechanical properties of the iridium alloys must be fully characterized to understand the mechanical response of the components in these severe applications. In this study, the room-temperature Kolsky tension bar was modified to characterize a DOP-26 iridium alloy in tension at elevated strain rates and temperatures. The modifications include (1) a unique cooling system to cool down the bars while the specimen was heated to high temperatures with an induction heater; (2) a small-force pre-tension system to compensate for the effect of thermal expansion in the high-temperature tensile specimen; (3) a laser system to directly measure the displacements at both ends of the tensile specimen independently; and (4) a pair of high-sensitivity semiconductor strain gages to measure the weak transmitted force. The dynamic high-temperature tensile stress–strain curves of the iridium alloy were experimentally obtained with the modified high-temperature Kolsky tension bar techniques at two different strain rates (~1000 and 3000 s^{-1}) and temperatures (~750 and 1030 °C).

Keywords Kolsky bar • High temperature • Dynamic tension • Iridium alloy • Stress–strain response

20.1 Introduction

Iridium alloys possess unique property combinations of high melting temperature, high-temperature strength and ductility, and excellent oxidation and corrosion resistance [1–5], making them ideal for specialized applications. In these applications, the high-temperature impact response of the material must be fully understood in order to verify that the component safety envelope is sufficient. High-strain-rate and high-temperature stress–strain tensile data are thus needed to develop strain-rate and temperature dependent material models for safety analysis. The dynamic high-temperature compressive response has been experimentally investigated [6] earlier.

It has been very challenging to conduct high-temperature Kolsky tension bar experiments. The concept of cold contact time (CCT), which is commonly used in high-temperature Kolsky compression bar experiments, is no longer applicable to high-temperature Kolsky tension bars. In a Kolsky tension bar test, the specimen has to be firmly attached to the bar ends before heating and dynamic loading. In order to minimize the heat transfer from the high-temperature tensile specimen to the room-temperature pressure bars, Scapin et al. [7] applied a Cortex-tube-based air cooling system to cool down the bars while the specimen was heated up to 400 °C. However, this air cooling system may not be sufficient for the experiments at higher temperatures, i.e., 750 and 1030 °C, in this study. In addition, when characterizing thin sheet iridium specimens, special fixtures are needed. However, the complex specimen fixtures may modify the stress wave propagation. For instance, a stress wave reflection may be generated at each interface within the joints/fixtures between the specimen and the bars. In this case, the reflected wave, which is usually used to calculate the strain rate and strain in the specimen, is no longer reliable. Direct displacement measurements, i.e. non-contact optical measurements, on both ends of the specimen are required. The thermal expansion in the small and thin iridium tensile specimen may generate additional measurement issues that need to be properly addressed.

B. Song (✉) • R. Lipinski • J. Bignell
Sandia National Laboratories, Albuquerque, NM 87185, USA
e-mail: bsong@sandia.gov

K. Nelson
Sandia National Laboratories, Livermore, CA 94550, USA

G.B. Ulrich • E.P. George
Oak Ridge National Laboratory, Oak Ridge, TN 37831, USA

B. Song et al. (eds.), *Dynamic Behavior of Materials, Volume 1*,
Conference Proceedings of the Society for Experimental Mechanics Series, DOI 10.1007/978-3-319-22452-7_20

In this study, the conventional Kolsky tension bar was modified to characterize dynamic tensile stress–strain response of thin-sheet DOP-26 iridium alloy specimens at elevated temperatures. Specimens were characterized at two different strain rates (~1000 and 3000 s^{-1}) and temperatures (~750 and 1030 °C) in order to determine the effects of strain rate and temperature on the tensile stress–strain response.

20.2 Modified High-Temperature Kolsky Tension Bar System

Figure 20.1a shows a schematic of the modified high-temperature Kolsky tension bar system and Fig. 20.1b–e show the detailed modifications for high-temperature experiments. A flat dog-bone shaped tensile specimen and corresponding fixture are shown in Fig. 20.1b. The fixture was machined with a slot with the same dimensions as the non-gage section of

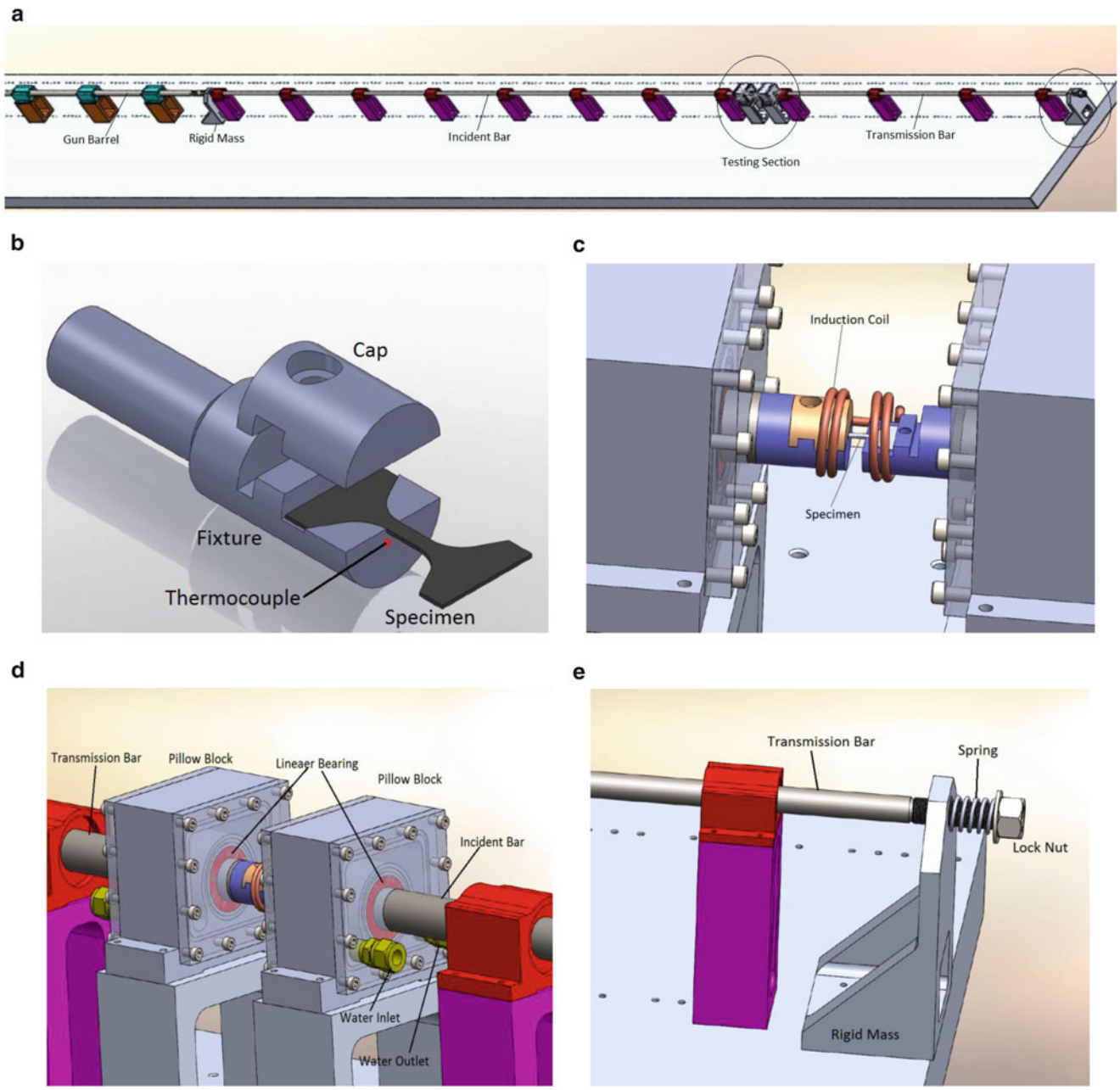

Fig. 20.1 Schematic of Kolsky tension bar with pulse shaping (**a**) Schematic of the modified high-temperature Kolsky bar system (**b**) Specimen fixture (**c**) Heating and testing section (**d**) Water cooling system (**e**) Spring-loaded pre-tension system

the specimen such that the whole non-gage section of the specimen was placed into the slot of the fixture. This design allows the load to be applied through the specimen shoulders to the gage section. The specimen was then covered with a semicircular cap. Both the fixtures and the semicircular caps were made of Inconel 718 steel, which has a relatively high strength at elevated temperatures. An induction coil heater was installed on the testing section, as shown in Fig. 20.2c. When the fixtures were heated with the induction coil, the heat was transferred to both the specimen and the bars simultaneously. In order to prevent heating of the bars, a pair of hollow water-cooled pillow blocks was installed on the bar ends, as shown in Fig. 20.2d. A splitting-beam laser extensometer presented in Ref. [8] was employed in this study to independently measure the displacements at both ends of the specimen. In this study, the laser detectors had been calibrated to exhibit a perfect linearity but with different factors: 0.732 mm/v at the incident bar side and 0.258 mm/v at the transmission bar side. The specimen strain can be calculated as

$$\varepsilon = \frac{L_1 - L_2}{L_s} \tag{20.1}$$

where L_1 and L_2 are displacements of the specimen ends attached to the incident and transmission bars, respectively; L_s is the gage length of the specimen. As shown in Fig. 20.1a, the non-gage sections of the specimen were enclosed in the fixtures. Equation (20.1) maximizes the representation of the actual deformation of the gage section without the need for correction with respect to the deformation in the non-gage sections.

A spring-loaded pre-tension system, as shown in Fig. 20.1e, was developed to prevent the specimen from buckling due to thermal expansion during heating. The spring was placed between a rigid mass and a flange (Fig. 20.1e). The flange was screwed toward the rigid mass to compress the spring, which in turn generated a tension load in the tension bar system including the tensile specimen. Another rigid mass was placed against the gun barrel (Fig. 20.1) to prevent the bar system from moving backwards when the whole bar system was pre-loaded in tension [9]. In this study, the spring was set to generate a pre-tension load of approximately 18 N which is sufficient to straighten the iridium specimen during heating but insufficient to produce further stretch on the iridium specimen.

Another high temperature testing issue is thermal softening of the specimen. A pair of semiconductor strain gages was used to replace the regular resistor strain gages on the transmission bar. The semiconductor strain gages had a gage factor of 139, which is approximately 70 times more sensitive than the regular resistor strain gages. The specimen stress is calculated as

$$\sigma = \frac{E_0 A_0 \varepsilon_t}{A_s} \tag{20.2}$$

where E_0 is Young's modulus of the bar material; A_0 is the cross-sectional area of the transmission bar; ε_t is the transmitted strain; and A_s is the cross-sectional area of the specimen. Combining the measurements of the semiconductor strain gages (20.2) and the laser system (20.1) for specimen stress and strain histories, respectively, yields the stress–strain curve of the specimen under investigation.

20.3 Dynamic High-Temperature Tensile Characterization of Iridium Alloy

The iridium tensile specimens were removed from prime DOP-26 alloy blanks using electrical discharge machining (EDM) with zinc-coated brass wire. The specimens were ground to remove the residual EDM layer, and then deburred and polished. All specimens were acid cleaned and then heat treated at 1375 ± 25 °C for 1 h ± 10 min in vacuum (1×10^{-4} Torr). The tensile specimens had a thickness of 0.66 mm, a width of 2.54 mm, and a gage length of 6.35 mm. The detailed dimensions of the iridium specimens used in this study are shown in Fig. 20.2.

Figure 20.3 shows typical strain gage signals on the incident and transmission bars for the incident, reflected, and transmitted waves at the test temperature of 1030 °C. It is noted again that, the reflected pulse was not reliable and could not be used for specimen strain measurement. Instead, we used the laser system to directly track the movements of the specimen ends that were attached to the incident and transmission bars. The laser outputs shown in Fig. 20.4 clearly show significant change in the laser output for the front end (on the incident bar side) but no significant change for the back end (on the transmission bar side). This is because the transmitted force was too small to generate significant displacement on the transmission bar side.

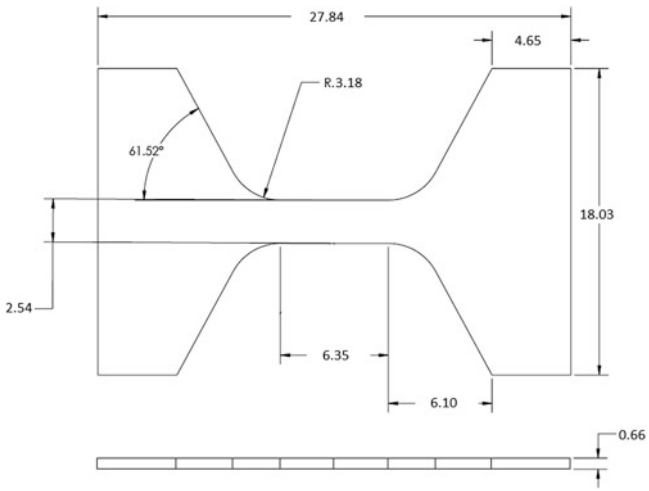

Fig. 20.2 Iridium tensile specimen design (mm)

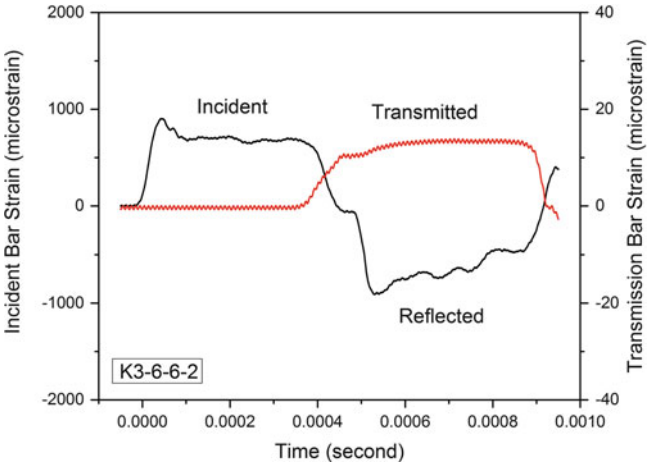

Fig. 20.3 Typical strain-gage signals

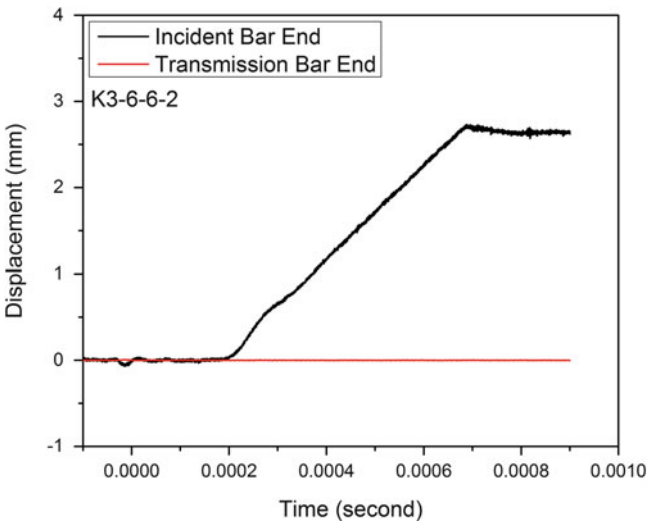

Fig. 20.4 Laser outputs

The engineering stress and strain histories in the specimen, which were calculated with (20.2) and (20.1), respectively, are shown in Fig. 20.5. The strain rate was then calculated with the slope of the strain history as a nearly constant 860 s^{-1}. The stress history exhibits oscillations because of the effect of the electromagnetic field generated by the induction coil on the highly-sensitive semiconductor strain gage signals. In this study, the raw data of stress history was filtered to remove

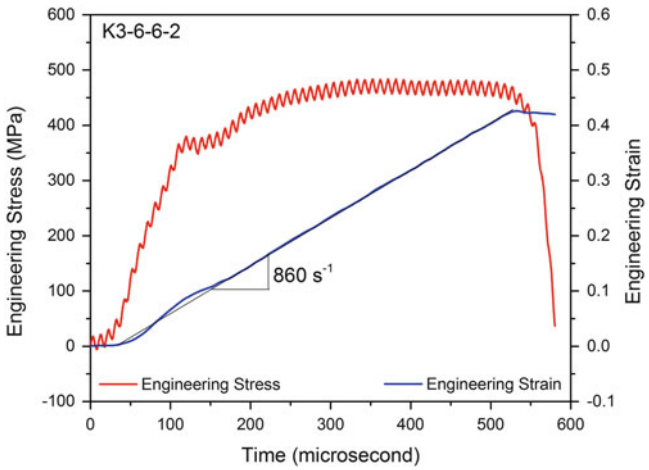

Fig. 20.5 Stress and strain histories

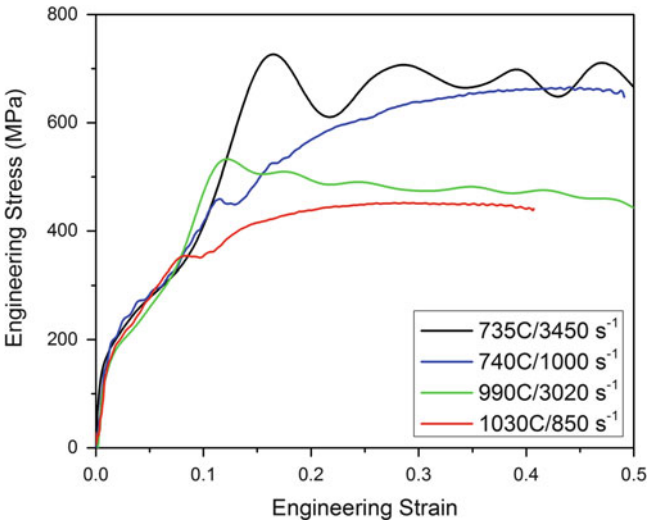

Fig. 20.6 Tensile stress–strain curves of iridium alloy at different strain rates and temperatures

the oscillations. Based on the stress and strain histories shown in Fig. 20.5, the tensile stress–strain curve at 860 s^{-1} and 1030 °C was obtained.

Following the same procedure, the iridium alloy was characterized in tension at two different strain rates (~1000 and 3000 s^{-1}) and temperatures (~750 and 1030 °C). Three specimens were tested at each condition. The results were consistent (within 10 %) for each testing condition. Figure 20.6 shows the mean tensile stress–strain curves of the iridium alloy at different strain rates and temperatures. Due to the superior ductility of the iridium alloy at elevated temperatures, the specimens did not fail during the first dynamic tensile load except for the testing condition of 735 °C/3450 s^{-1}. At the 735 °C/3450 s^{-1} condition, the engineering failure strains varied between 0.5 and 0.7. It is noted that the engineering failure strains were not representative of the actual failure strain since significant strain localization and necking occurred in the specimens before failure. Therefore, the stress–strain curves are plotted up to a strain of 0.5 in Fig. 20.6. The dynamic high-temperature stress–strain curves of the iridium alloy show different profiles than quasi-static curves [3]. All stress–strain curves show an initial elasticity followed by significant work hardening behavior when the strain is below 10 %. This phenomenon may be related to a change in microstructure or deformation mechanism at high strain rates and elevated temperatures. More oscillatory behavior was recorded in the stress–strain curve at 735 °C/3450 s^{-1}., The reason for this is still unknown and under investigation. When the strain is below 10 %, the stress–strain curves show neither strain-rate nor temperature effects. When the strain increases, the stress–strain curves show plastic flow with significant strain-rate and temperature effects. At strains greater than 10 % and similar strain rates the flow stresses decrease when the temperature increases from 750 to 1030 °C, showing significant thermal-softening behavior. At the same temperature, the flow stresses increase when the strain rate increases from ~1000 to 3500 s^{-1}, showing a positive strain-rate sensitivity.

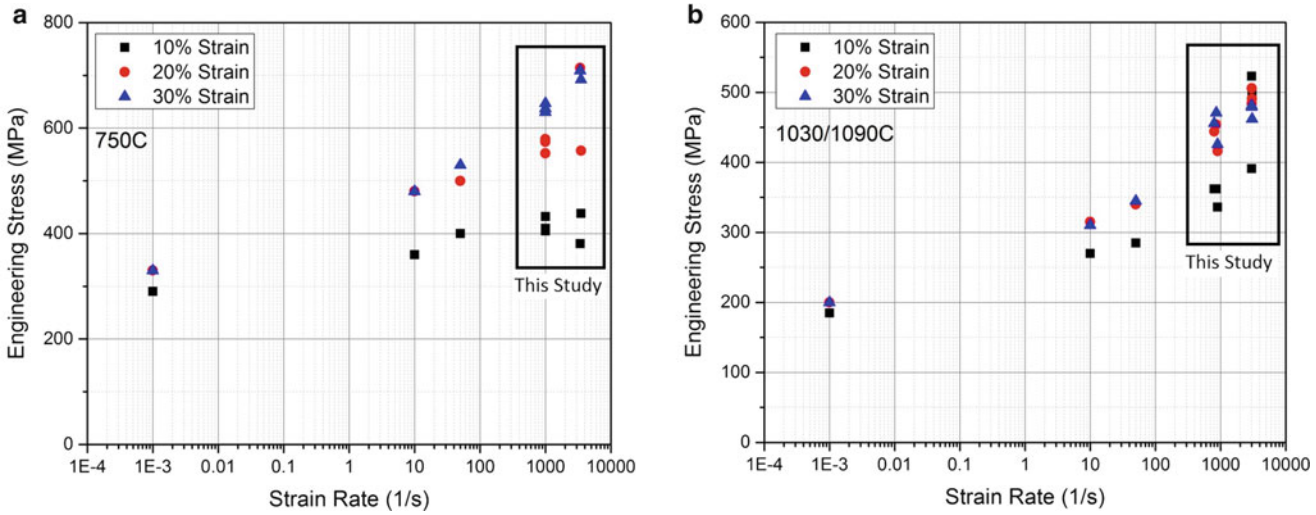

Fig. 20.7 Effect of strain rate on the tensile stress–strain response of iridium alloy at different temperatures (**a**) Strain rate effect at 750 °C (**b**) Strain rate effect at 1030/1090 °C

Figure 20.7 shows the detailed strain-rate effects including the quasi-static data at different strain rates and temperatures presented in [3]. The data obtained from this study are marked while the rest are from the reference [3] in both figures. Figure 20.7 clearly shows a significant strain-rate effect on the tensile flow stress of the iridium alloy at both temperatures. The strain-rate sensitivities are slightly different at the two temperatures and are also dependent on the level of strain.

20.4 Conclusions

The conventional direct-tension Kolsky bar was modified for high-temperature tensile characterization of the DOP-26 iridium alloy. An induction coil was applied to heat the iridium specimen to elevated temperatures up to 1030 °C while the specimen ends of the incident and transmission bars were cooled to reduce the thermal gradient in the bars. A pair of semiconductor strain gages on the transmission bar were used to directly measure the force/stress in the specimen during dynamic loading. A laser system was developed to independently measure the displacements at the specimen ends on the incident- and transmission-bar sides so that the specimen strain could be calculated. A spring-loaded pretension system was installed on the free end of the transmission bar to prevent the high-temperature specimen from buckling during heating. Dynamic tensile stress–strain curves of the iridium alloy were obtained at two temperatures (750 and 1030 °C) and strain rates (~1000 and 3000 s^{-1}). The iridium alloy shows high ductility at elevated temperatures and strain rates. The effects of strain rate and temperature on the tensile stress–strain response of the iridium alloy were also determined. The iridium alloy exhibits little sensitivity to strain rate or temperature when the strain is below 10 %, but strong sensitivities to both strain rate and temperature when the strain is greater than 10 %.

Acknowledgements The authors would like to acknowledge the support of Dr. Helena Jin for the preliminary DIC work and Kevin Connelly for his initial specimen and fixture design support.

This work was sponsored by the United States Department of Energy (DOE) Office of Space and Defense Power Systems (NE-75). The authors gratefully acknowledge the support and guidance of Ryan D. Bechtel of the US Department of Energy.

Sandia National Laboratories is a multi-program laboratory managed and operated by Sandia Corporation, a wholly owned subsidiary of Lockheed Martin Corporation, for the U.S. Department of Energy's National Nuclear Security Administration under contract DE-AC04-94AL85000.

Oak Ridge National Laboratory is a multi-program research laboratory managed by UT-Battelle, LLC, for the US DOE under contract DE-AC05-00OR22725.

References

1. Ohriner, E.K.: Processing of iridium and iridium alloys, methods from purification to fabrication. Platin. Met. Rev. **52**, 186–197 (2008)
2. George, T.G.: High-strain-rate, high-temperature biaxial testing of DOP-26 iridium. Los Alamos National Laboratory Report, LA-11065 (1998)
3. Schneibel, J.H., Carmichael, C.A., George, E.P.: High strain rate tensile testing of DOP-26 iridium. Oak Ridge National Laboratory Report, ORNL/TM-2007/81 (2007). Oak Ridge National Laboratory
4. McKamey, C.G., George, E.P., Lee, E.H., Ohriner, E.K., Cohron, J.W.: Impurity effects on high-temperature tensile ductility of iridium alloys at high strain rate. Scr. Mater. **42**, 9–15 (2000)
5. George, E.P., Bei, H., Lee, E.H., Braden, J.D.: Tensile impact ductility and fracture behavior of DOP-26 iridium at 500–900 °C, Oak Ridge National Laboratory Report, ORNL/TM-2004/239 (2004)
6. Song, B., Nelson, K., Lipinski, R., Bignell, J., Ulrich, G., George, E.P.: Dynamic high-temperature testing of an iridium alloy in compression at high-strain rates. Strain **50**, 539–546 (2014)
7. Scapin, M., Peroni, L., Fichera, C.: Investigation of dynamic behaviour of copper at high temperature. Mater. High Temp. **31**, 131–140 (2014)
8. Nie, X., Song, B., Loeffler, C.M.: A novel splitting-beam laser extensometer technique for Kolsky tension bar experiment. J. Dyn. Behav. Mater. **1**(1), 70–74 (2015)
9. Song, B., Lu, W.-Y.: Preload high-rate tension techniques. In Proceedings of SEM XII International Congress and Exposition on Experimental and Applied Mechanics, Costa Mesa, (2012)

Chapter 21
Dynamic Friction Properties of Stainless Steels

P.H. Hsu, Sheng-Yu Huang, C.C. Chiang, L. Tsai, S.H. Wang, and N.S. Liou

Abstract Stainless steels have been used extensively in the industry areas. In this research, the dynamic shear and friction properties of stainless steel 304 and stainless steel 316 were examined using Modified Torsional Kolsky Bar (MTKB). The dynamic shear modulus and the dynamic coefficient of friction of stainless steel 304 and 316 were observed respectively. The dynamic shear properties of stainless steels were also examined using commercial software Deform-3D. The fracture surfaces and shear bands were observed using SEM.

Keywords: Stainless steel • Deform-3D • MTKB • Dynamic mechanical properties

21.1 Introduction

The Fe-Cr-Ni alloys, or simply stainless steels, have been widely applied in various engineering fields since 1912. Among them, 300 series stainless steels were most widely adopted which amounts up to 85 % of stainless steel usage in the world. Stainless steels were currently used in power machinery, petroleum products, chemicals, load pressure vessels, boilers, steam pipes, gas pipes and today's most advanced semiconductor devices. Stainless steels have become inseparable in our daily life.

300 series stainless steels, which have Face-centered cubic (FCC) crystalline structure, have good corrosion resistance, weldability, ductility, mechanical strength and moldability. There are two main stainless steel forming technologies [1]:

1. Hot-rolling
2. Cold-rolling

But, either hot rolling or cold rolling, there were a lot of technical difficulties during the production process. Hence, in this research, the dynamic shearing response of stainless steel 304 and 316 will be explored using modified torsional Kolsky bar.

Khosravifard et al. have examined the dynamic torsional properties of high manganese steel in 2013 [2]. But there were relatively few study focus on the high strain rate torsion properties of stainless steels which utilizing Kolsky Bar. In this research, the dynamic torsion and friction properties of stainless steels were examined at strain rates between 500 and 1000 s^{-1}.

21.2 Method and Material

21.2.1 MTKB

To study the dynamic shear and friction properties of stainless steels, two different experimental setups were carried out. In Fig. 21.1, the specimen was sandwiched between an incident and a transmitted bar, it's called the split bar method. In this

P.H. Hsu • S.-Y. Huang • C.C. Chiang • L. Tsai (✉)
National Kaohsiung University of Applied Sciences, Kaohsiung, Taiwan
e-mail: liren@cc.kuas.edu.tw

S.H. Wang
I-Shou University, Kaohsiung, Taiwan

N.S. Liou
Southern Taiwan University of Science and Technology, Tainan, Taiwan

B. Song et al. (eds.), *Dynamic Behavior of Materials, Volume 1*,
Conference Proceedings of the Society for Experimental Mechanics Series, DOI 10.1007/978-3-319-22452-7_21

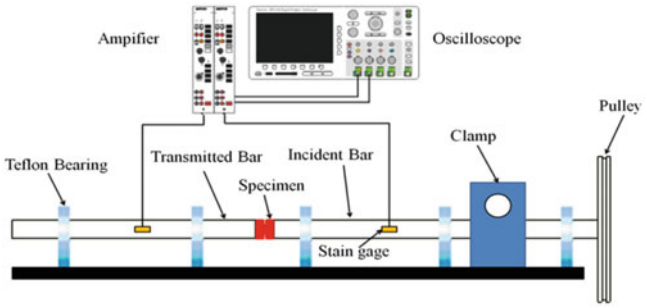

Fig. 21.1 Torsional Kolsky bar chematic diagram

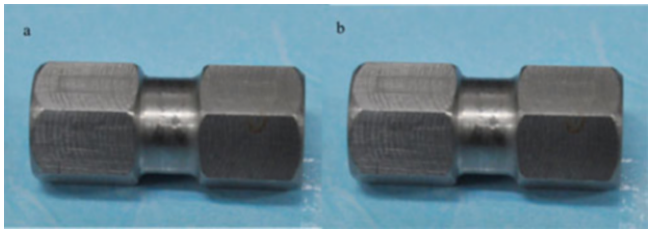

Fig. 21.2 Schematic diagram of the split-bar specimen

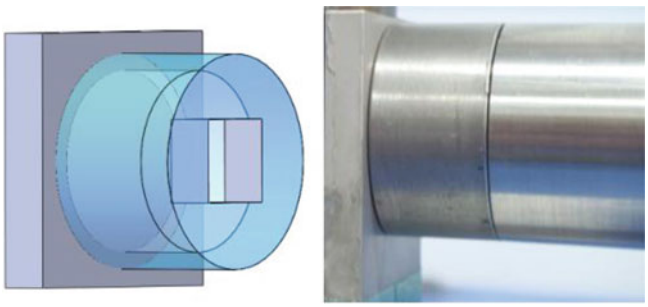

Fig. 21.3 Contact condition between the specimen and rigid support in single bar setup

Table 21.1 Composition of stainless steel 304

Type	Composition %							
Austenitic types								
	C	Mn	Si	Cr	Ni	P	S	Other
304	0.08	2.00	1.00	18.0–20.0	8.0–10.5	0.045	0.03	

setup, the specimen was machined to be thin walled dog-bone shape, as shown in Fig. 21.2. When the applied torsion arrive the specimen, the specimen will fracture due to excessive shear deformation. Another experimental setup utilizes only the incident bar, as shown in Fig. 21.3, it's called the single bar method. In this setup, the specimen was machined to a cylinder-shape and compressed against a rigid support. The dynamic torsion would force the specimen to slide on the rigid support, which is also a stainless steel surface.

21.2.2 SS304

Stainless steel 304 is a kind of austenitic stainless steels. It has been widely used in our daily life, because of their better corrosion resistance in aggressive environments. The main components of stainless steel 304 is shown in Table 21.1 [3, 4]. Stainless steel 304 also has good strength, toughness and low maintenance demand, which was often used in a more hostile environment, such as the buildings close to the beach, water treatment facilities, nuclear energy and chemical industry. Stainless steel 304 is current the most widely used in the industry.

Table 21.2 Composition of stainless steel 316

Type	Composition %							
Austenitic types								
	C	Mn	Si	Cr	Ni	P	S	Other
316	0.08	2.00	1.00	16.0–18.0	10.0–14.0	0.045	0.03	2.0–3.0 Mo

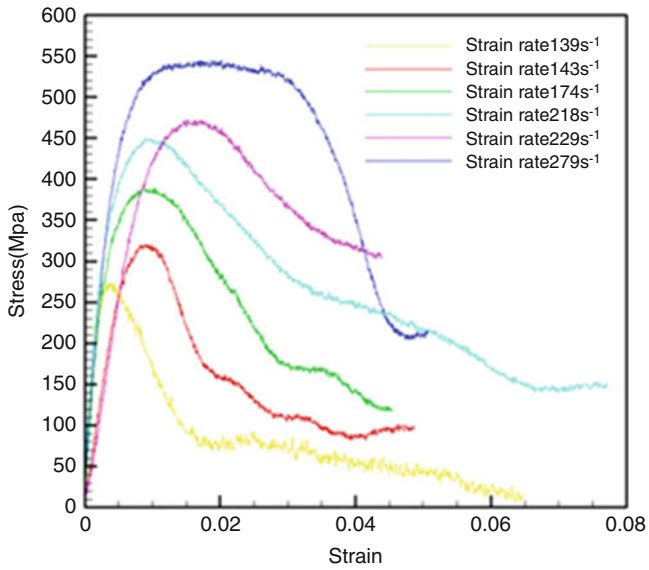

Fig. 21.4 Stress-strain curves of stainless steel 304

21.2.3 SS316

Stainless steel 316 also is a kind of austenitic stainless steels and is currently second only to stainless steel 304 as one of the most frequently used stainless steel. Compare to stainless 314, in stainless steel 316 the composition of molybdenum (Mo), and nickel (Ni) increased. The main components of stainless steel 316 are shown in Table 21.2 [4].

21.3 Result and Discussion

In the present study, MTKB experiments were performed at room temperature. Stress-strain curves of stainless steel 304 and 316 were shown in Figs. 21.4 and 21.5, respectively. The trends of the stress-strain curves were found to be quite similar within the tested strain rate rage. Figure 21.4 shows the stress-strain curves of stainless steel 304 with six different strain rates: 139, 143, 174, 218, 229 and 279 s^{-1}. The maximum shear stresses were 270, 320, 390, 450, 470 and 550 MPa, respectively. The effect of strain rates to the dynamic torsional response of stainless steel 304 is quite obvious.

Figure 21.5 shows the stress-stain curves of stainless steel 316 in ten different strain rates: 214, 227, 270, 276, 279, 299, 304, 384, 403 and 406 s^{-1}, respectively. The observed maximum shear stresses were 265, 278, 309, 310, 344, 381, 406, 424, 471 and 512 MPa, respectively. Both stainless steels have higher elastic moduli with increasing strain rate. The strain hardening phenomena was also quite obvious for both materials.

When comparing the high strain rate performance between stainless steel 304 and 316, as shown in Fig. 21.6, it is quite obvious that stainless steel 304 is more sensitive to the strain rates and possess higher dynamic elastic moduli and maximum shearing stress, which could be because the composition of Ni is higher in stainless steel 316. Therefore, stainless steel 316 possess better mechanical properties to withstand dynamic shear loading, which could be very useful for seismic resistant buildings.

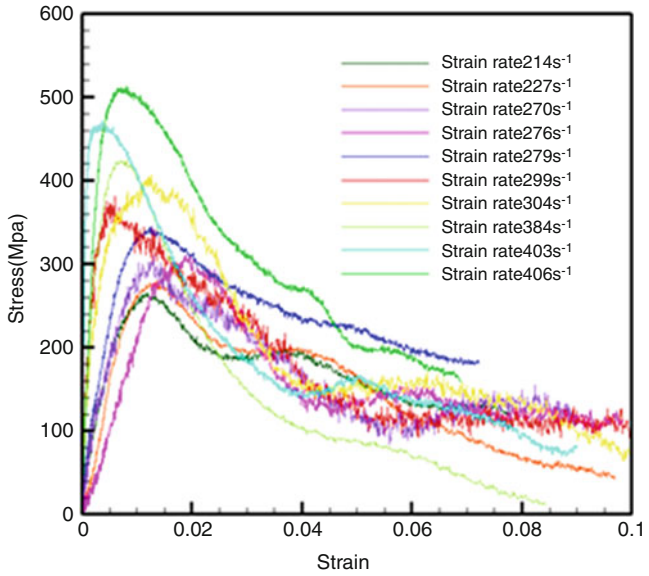

Fig. 21.5 Stress-strain curves of stainless steel 316

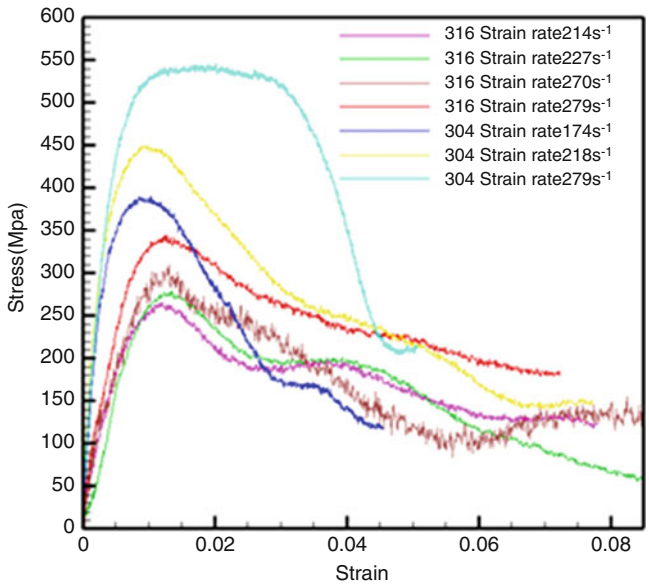

Fig. 21.6 Stress-strain curves of stainless steel 304 and 316

21.3.1 SEM

To understand the fracture mechanism of the two stainless steel materials, the surface morphology of the fracture surfaces was observed using SEM. It can be found that both materials have significant dimple, obviously belong to cut ductile failure. Figure 21.7 shows the SEM picture of stainless steel 304 under shear loading at strain rate 279 s^{-1}.

21.3.2 FEM

In order to monitor the fracture mechanism and to determine the proper specimen size the wall thickness for split bar experiments, a set of DEFORM-3D simulation was performed, as shown in Fig. 21.8. The formation of shear bending in Fig. 21.8e is quite obvious, but in this simulation, it is only good for determine the proper fracture strain but not well enough for determine the exact material response during dynamic shear loading.

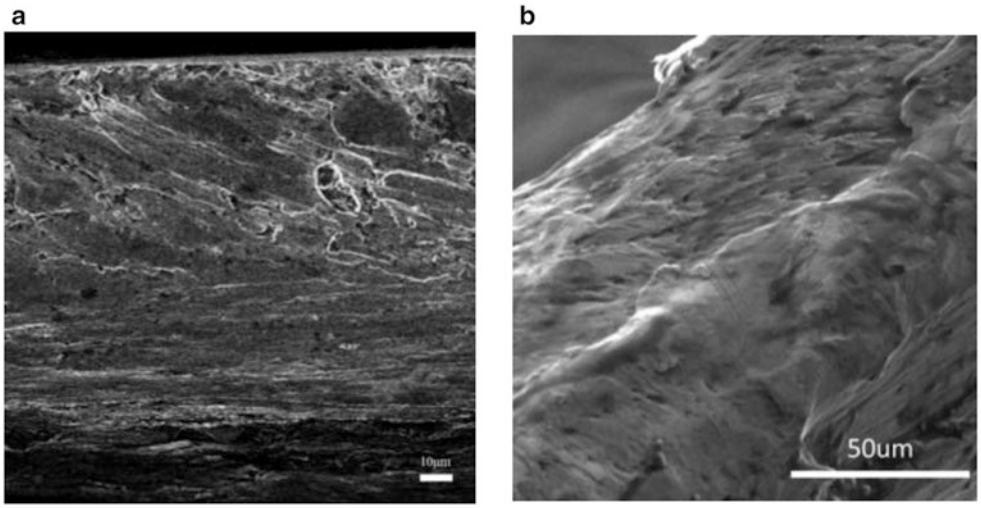

Fig. 21.7 SEM figure of stainless steel 304 under (**a**) ×200 times and (**b**) ×1000 times magnifications under strain rate 279 s^{-1} shear loading

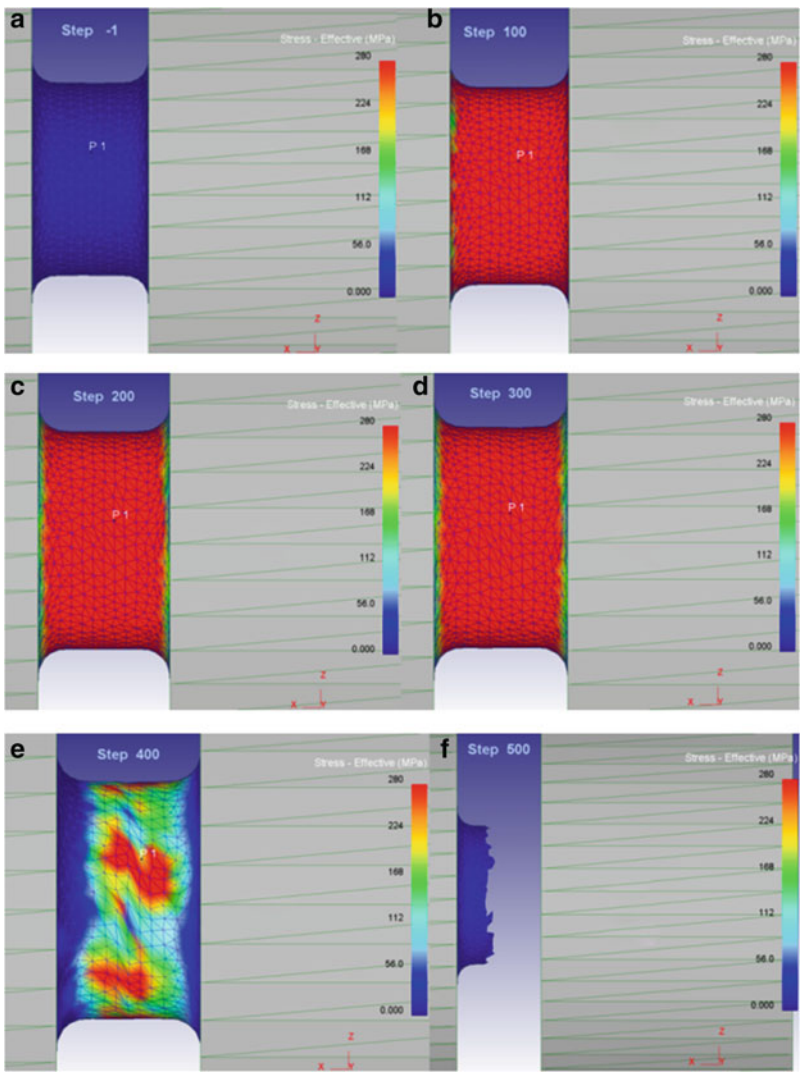

Fig. 21.8 The simulation process diagram in 304 stainless steel from (**a**) step 1 to (**f**) step 500 at strain rates of 139 s^{-1}

21.4 Conclusion

MTKB was utilized to test the dynamic shear response of two stainless steel materials. For two kinds of steel material, cut part using different strain rates to tested, combined with the results of macroscopic and microscopic make the following conclusions:

stainless steel 304 shear stress, obviously influenced by the strain rate, with the increase in strain rate, shear stress of the specimen has a clear upward trend, stainless steel 304 is the material can be proved by the strain rate effect, in contrast, stainless steel 316 with strain rate rise, shear of specimen has gone up, but upward trend is not quite clear, comparison of two steel material, stainless steel 304 showing the strain rate 218, 229, 279 s^{-1} and stainless steel 316 in strain rate 214, 227, 279 s^{-1}, can be found to increase with increasing strain rate and shear gap between the two steel materials also increased.

By SEM observation of two steel material fracture surface, it can be found at low strain rate the broken section has twisted or torn happens, at high strain rates is relatively flat. It can be found smooth dimple on the fracture surface, with deep dimples organization and cut absolutely tropical. These are the evidence of ductile shear fracture. It can be seen under high strain rate case, both steel materials reduced smooth dimple area, the number of deeper dimples increased.

The experiment results for single bar apparatus is currently under examinations. The dynamic friction properties of both stainless steel 304 and 316 will be presented in the near future.

Acknowledgments This research was supported by the Taiwan National Science Council under grant no. 101-2221-E-151-014, and National Kaohsiung University of Applied Sciences, Taiwan.

References

1. Lee, J.M., Park, W.S., Yoo, S.W., Kim, M.H.: Strain-rate effects on the mechanical behavior of the AISI 300 series of austenitic stainless steel under cryogenic environments. Mater. Des. **31**, 3630–3640 (2010)
2. Khosravifard, A., Moshksar, M.M., Ebrahimi, R.: High strain rate torsional testing of a high manganese steel: design and simulation. Mater. Des. **52**, 495–503 (2013)
3. Sudesh, T.L., Wijesinghe, L., Blackwood, D.J.: Characterisation of passive films on 300 series stainless steels. Appl. Surf. Sci. **253**, 1006–1009 (2006)
4. Shimada, M., Kokawa, H., Wang, Z.J., Sato, Y.S., Karibe, I.: Optimization of grain boundary character distribution for intergranular corrosion resistant 304 stainless steel by twin-induced grain boundary engineering. Acta Mater. **50**, 2331–2341 (2002)

Chapter 22
Dynamic Tensile Behavior of a Quenched and Partitioned High Strength Steel Using a Kolsky Bar

Steven Mates and Fadi Abu-Farha

Abstract Dynamic tension tests were performed on a quenched and partitioned high strength steel grade, QP980, using a direct tension Kolsky Bar method. In this method, the steel incident bar consists of a tube section and a solid section of equal impedance mated through a threaded connection. The striker is pneumatically launched within the tube section into an impact cap to create the tensile loading pulse. The transmission bar, which is constructed of aluminum to improve the force measurement sensitivity, is not impedance matched to the incident bar, and as a result the wave analysis technique was modified accordingly. The sample geometry follows ISO 26203-1:2010. Strain-time histories of the specimens obtained by the wave analysis were compared to high speed DIC strain field measurements, and the latter were used to correct the compliance of the test setup. Material tests were performed parallel to, perpendicular to, and at 45° with respect to the rolling direction. Specimens were taken to failure and to several intermediate strain levels by using momentum traps on the incident and transmission bars. Specimen gauge length, gas pressure and striker bar length were changed to achieve different strain rates, covering the range needed for crash simulations. The dynamic behavior of the material is compared to its quasi-static behavior.

Keywords: Kolsky bar • High strain rate • Advanced high strength steels • Automotive light-weighting • High speed digital image correlation

22.1 Introduction

Efforts to improve fleet fuel economy through vehicle weight reduction are currently focused on replacing existing high strengths steels with even higher strength grades, known as Advanced High Strength Steels (AHSSs). While some already introduced AHSSs meet the target strength levels (tensile strength higher than 1 GPa), they typically lack the target ductility levels. This not only implies limitations to the sheet formability needed for cold stamping, but also the toughness (energy absorption) needed to meet the desired crashworthiness characteristics. Multi-phase steels containing a retained austenite phase have the potential to provide additional ductility at high strength levels due to the transformation of the retained austenite into martensite in response to plastic deformation. The recently developed class of quenched and partitioned (QP) steels is an example of such multi-phase steels, with a carbon-rich retained austenite phase produced by a partitioning heat treatment, leading to uniform tensile ductility in excess of 10 % at 1 GPa tensile strength [1]. Although not in use in mass-produced automotive components yet, QP steels have great potentials for a wide range of applications in next-generation lightweight vehicles, and they are thus gaining more attention. QP steels have been in commercial production for several years. While their quasi-static deformation behavior has been investigated, efforts characterizing their high rate behavior are very limited. To assess the crashworthiness of these steels, and to supply the data needed for full scale crash simulations using finite element analysis, high strain rate deformation data must be acquired.

In this paper we describe high strain rate tensile measurements of a selected grade of QP steels, the QP980. We use a direct tension Kolsky Bar method in order to facilitate high-speed Digital Image Correlation (DIC) measurements by virtue of unobstructed optical access to the specimen. Tests are performed at different strain rates and different sheet orientations. Moreover, tests are performed to fracture and to intermediate strains (interrupted testing) using momentum trapping to eliminate multiple loadings on the specimen that would otherwise occur due to the reverberation of elastic energy in the Kolsky bar. Data from fracture tests is used to compare the behavior of the material at high rates to that obtained at quasi-

S. Mates (✉)
National Institute of Standards and Technology, 100 Bureau Drive, Gaithersburg, MD, USA
e-mail: steven.mates@nist.gov

F. Abu-Farha
Clemson University—International Center for Automotive Research, Greenville, SC 29607, USA

B. Song et al. (eds.), *Dynamic Behavior of Materials, Volume 1*,
Conference Proceedings of the Society for Experimental Mechanics Series, DOI 10.1007/978-3-319-22452-7_22

static conditions. Intermediate strain tests are useful to investigate the microstructural evolution due to the applied dynamic strain, including the change in the retained austenite volume fraction, which will be performed in the future.

22.1.1 Experimental Method

A schematic of the NIST tension Kolsky bar is shown in Fig. 22.1. It utilizes a tubular incident bar concept conceived by Frew and colleagues [2]. This method simplifies the use of pulse-shaping, which is used here to eliminate oscillations in the incident pulse. The incident barrel is constructed of 4340 steel, while the solid portion of the incident bar and the specimen grips are made of hardened maraging steel. The solid portion of the incident bar is 26 mm in diameter and is impedance matched to the barrel. The transmission bar is 20 mm in diameter and made of 7075-T6 aluminum, which provides better force measurement sensitivity compared to steel due to its lower Young's modulus value. Fracture tests are performed using a 1 m long, 20 mm diameter striker bar launched at impact speeds between 6.25 ± 0.05 m/s and 11.4 ± 0.05 m/s. Interrupted strain tests are performed with a 375 mm long, 20 mm diameter striker impacting at 11.6 ± 0.05 m/s. The incident bar momentum trap consists of a 375 mm tube that is impedance matched to the incident barrel. It is placed at a specific distance from the barrel such that it contacts the barrel in time to trap the first pulse that is reflected from the specimen. The transmission bar momentum trap consists of a 375 mm long aluminum tube that is impedance matched to the transmission bar. It is placed concentric with the transmission bar and in contact with a flange fixed to the end of the bar, as shown in Fig. 22.1.

Strain gage data are obtained from 1000-Ω metal foil gages bonded to the incident and transmission bars. Both axial and Poisson strain gages are used on the transmission bar to boost the force sensitivity compared to two axial gages alone. The four gages are arranged in a Wheatstone bridge circuit with a 24 V battery as the excitation source. The sensitivity of the measurement is approximately 81 με/mV ± 1 μm/m/mV. The bridge output voltage is recorded at 2 MHz with 14 bit resolution on a 200 mV scale.

Figure 22.2 describes the two sample geometries used for this study. Both specimens follow the recommendations of ISO 26203-1:2010 with regard to the ratio of gage width to gage length (greater than or equal to 2), and to the fillet radius (1.5 mm). Specimens following these geometries were prepared from 1.4 mm thick QP980 sheets using waterjet cutting, followed by precision machining to introduce the grip holes. Two precision alloy steel pins, arranged symmetrically about the load axis, are used on each tab. The pin holes are slightly undersized compared to the pin diameter (5.556 ± 0.008 mm)

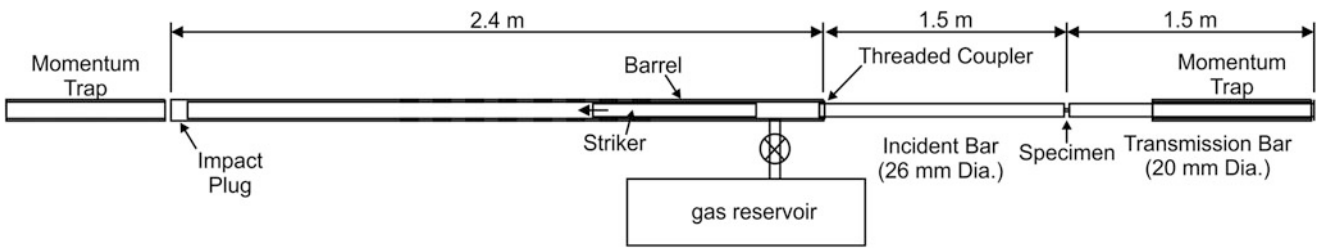

Fig. 22.1 Schematic of NIST direct tension Kolsky bar. Not to scale

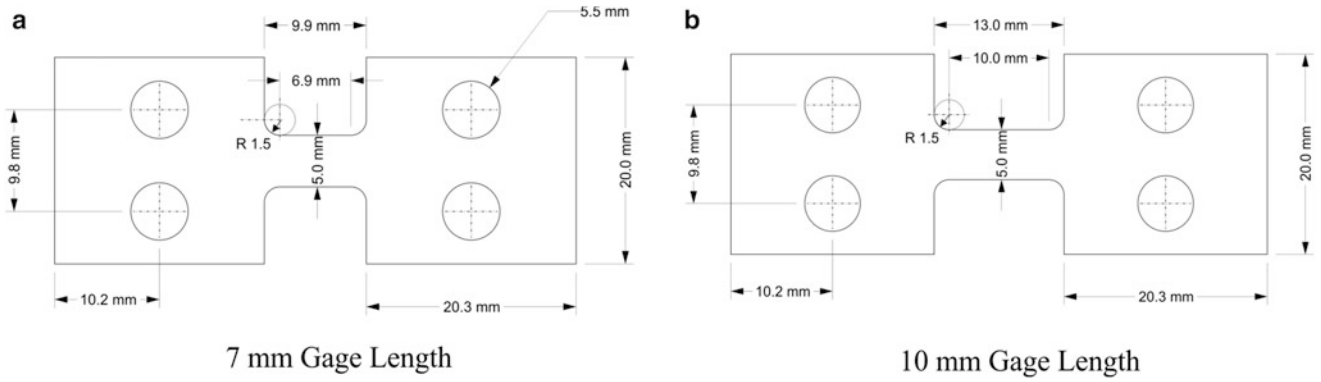

Fig. 22.2 Sample geometries with dimensions in mm, drawn to scale. The specimens are 1.4 mm thick

to promote a small amount of plastic deformation during insertion, which helps prevent slippage during dynamic testing. No adhesive is used. The grips are attached to the bars with ½-20 threads that are treated with Teflon tape to prevent loosening.

Three dimensional digital image correlation (DIC) measurements of the deforming specimen are obtained at 62,500 frames per second with a resolution of 192 by 336 pixels, giving a field of view of approximately 10.3 mm by 18.1 mm, or about 0.05 mm per pixel. Correlation calculations are performed on 21 pixel subsets with a 7 pixel offset. The optical resolving power of the setup, as measured by the 1951 Air Force Target, is 7.13 line pairs per mm. Illumination is provided by a high intensity flash unit operating at 125 W·s with a pulse duration of approximately 1.5 ms. The flash is triggered off the striker bar velocity sensor with a delay programmed to begin the flash at between 5 and 10 frames (80 and 160 μs) prior to the arrival of the tension pulse. The electronic shutter on the cameras is set to 1 μs to eliminate motion blur.

22.1.2 Kolsky Bar Data Analysis

To synchronize the DIC strain-time data with the stress-time data provided by the strain gage output, the DIC strain history, computed by averaging strains over the entire gage area, is first aligned with the strain-time data from the strain gages, which is in turn synchronized with the stress-time data using known wave propagation times between the gages and the sample. The sample strain rate and stress histories are determined using the usual one-dimensional elastic wave analysis with force equilibrium assumed. Using the "3-wave" method for calculating the strain rate, the expression for our Kolsky bar is:

$$\dot{\varepsilon} = \frac{\left[c_i \cdot (\varepsilon_i - \varepsilon_r) - c_t \cdot \left(\frac{E_i A_i}{E_t A_t}\right) \cdot (\varepsilon_i + \varepsilon_r)\right]}{L} \tag{22.1}$$

In (22.1), ε is strain, c is elastic wave speed, E is Young's modulus, A is area and L is length, which can be either instantaneous length for true strain rate, or original length for engineering strain rate. The subscripts i, r and t denote incident, reflected and transmitted, respectively. The expression for stress is:

$$\sigma = \frac{E_t A_t}{A_s} \varepsilon_t. \tag{22.2}$$

This expression gives the engineering stress if the original cross-sectional area of the specimen (A_s) is used, or the true stress if the instantaneous area is used.

22.2 Results

Figure 22.3 shows a typical result for a fracture test for a specimen with a 0° orientation with respect to the rolling direction. In this test we use 1 m striker impacting at 9 m/s (+/−0.05 m/s). The top left graph shows the raw strain gage data. In this test there is no momentum trapping, so there are large amplitude reverberations in the strain gage data, as shown in the plot top left. The top right plot shows the strain-time data from the wave analysis method computed using (22.1) and compares the result to the DIC true strain averaged over the entire gage section. As this plot shows, the wave analysis indicates much higher strains in the gage section compared to the DIC average strain. The DIC strain results are considered more accurate since they are derived from localized surface deformation measurements and make no assumption regarding the extent of the deformation zone in the specimen, as the wave analysis method does. The exaggerated strain value provided by the wave analysis is due to deformation occurring outside the nominal gage section (compliance). As such, the wave analysis result is corrected to match the more accurate DIC result using a correction factor, P, that is less than one. In the experiment shown in Fig. 22.3, $P = 0.75$, which is a typical result for these experiments. In general, P may depend on the specimen geometry, the grip technique, and material behavior. The bottom left plot of Fig. 22.3 shows the engineering stress–strain behavior along with the strain-rate versus strain for the experiment. The strain rate increases significantly in the middle of the test, due to localized necking. From this plot, the tensile strength of the steel is about 1120 MPa, and the fracture strain is just over 20 %. However, these results are based on the assumption that the strain distribution within the gage section is uniform until necking begins. The bottom right plot of Fig. 22.3 shows that, while the axial strain distribution is quite symmetric over the gage section, it is never uniform. In this plot the true strain is averaged over cross sections of the specimen along the gage

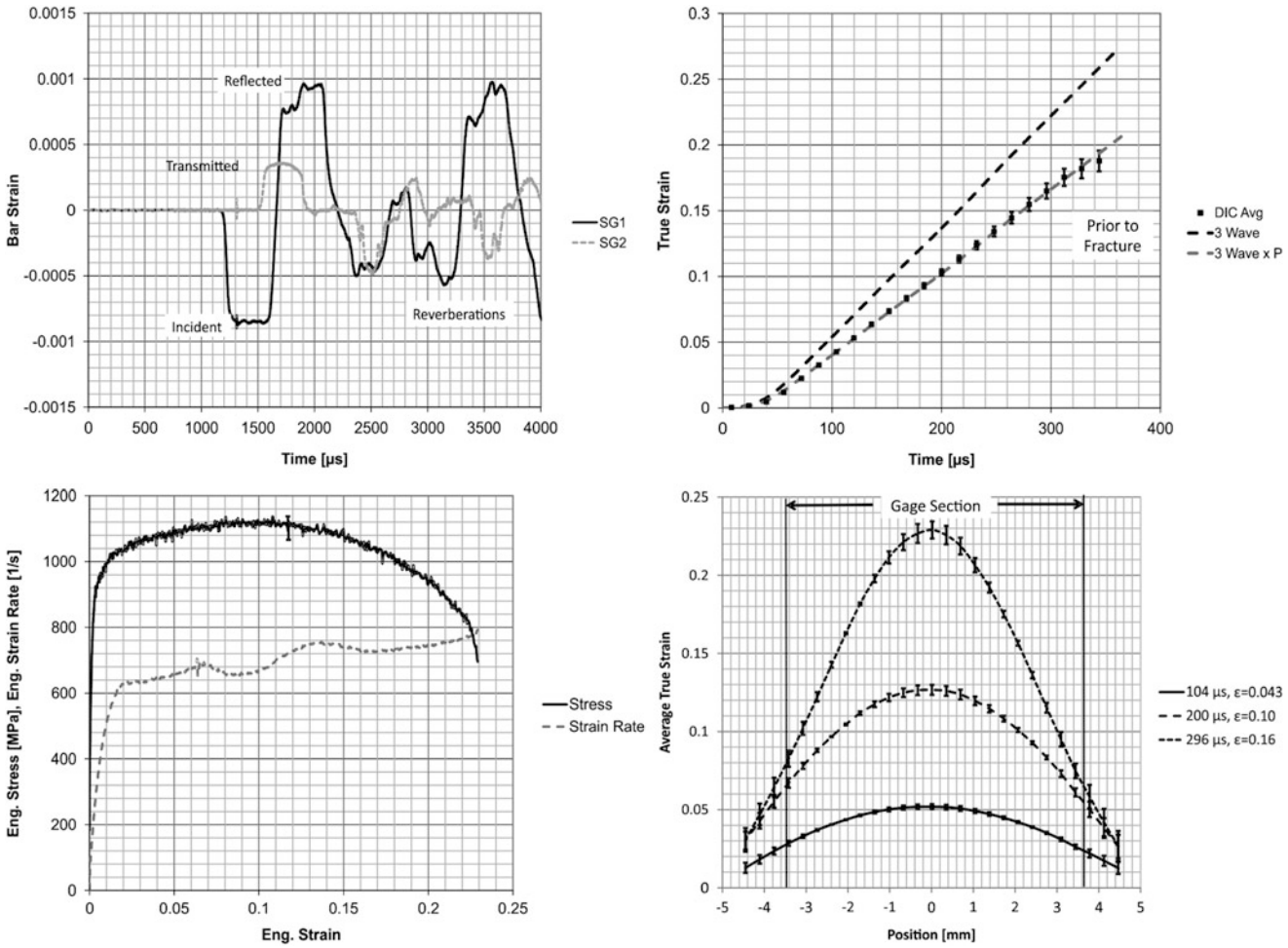

Fig. 22.3 *Top left*: raw strain gage signals from fracture experiment (7 mm gage length, not synchronized with plot *top right*). *Top right*: strain-time from strain gage analysis and average DIC strain over the gage area (DIC error bars are 2 standard deviations of the mean). *Bottom left*: dynamic stress–strain curve and strain rate versus strain. Error bar on stress represents the expanded uncertainty with k = 2. *Bottom right*: axial strain distribution along gage length, averaged at each cross section (error bars are one standard deviation)

length. The symmetric profiles indicate good force equilibrium during the test. However, as the plot shows, the distribution is highly peaked. The maximum strain that occurs in the center of the specimen is 20–40 % higher than the average strain, with the proportion increasing with average strain. We believe this is the underlying cause of the observation that fracture always occurred in the center of the specimen in our tests. The highly peaked strain distributions seen here agree generally with recently published numerical simulations of dynamic tension tests with similar gage-length to gage-width ratios [3]. Because the strains are so non-uniform over the gage length, the engineering stress–strain curve shown in Fig. 22.3 is not a very meaningful representation of the real material behavior. The data remain useful, though, for examining the relative effects of strain rate and rolling direction. Going forward, DIC measurements must be better leveraged to determine the dynamic tensile behavior of this material up to and beyond necking, using either a Bridgman-like correction technique [4] or finite element modeling and inverse methods.

Figure 22.4 describes an interrupted strain experiment for a 0° orientation specimen using a 375 mm striker impacting at 11.6 m/s (+/−0.05 m/s). In this experiment the momentum traps are engaged, so the amplitude of the reverberations is much smaller compared to the results shown in Fig 22.3. The top right plot shows the DIC average strain versus time for this test along with the compensated strain result from the wave analysis (here $P = 0.77$). The specimen experiences just over 10 % engineering strain and has yet to begin localized necking. As with the fracture test presented in Fig. 22.3, the present test has a non-uniform, yet highly symmetric, axial strain distribution. The DIC measurements capture the elastic recovery that occurs as the load is removed, amounting to 0.65 %. This value corresponds well to the expected amount of elastic strain in the specimen at the peak load level, considering a nominal Young's modulus of 200 GPa for this material. The elastic

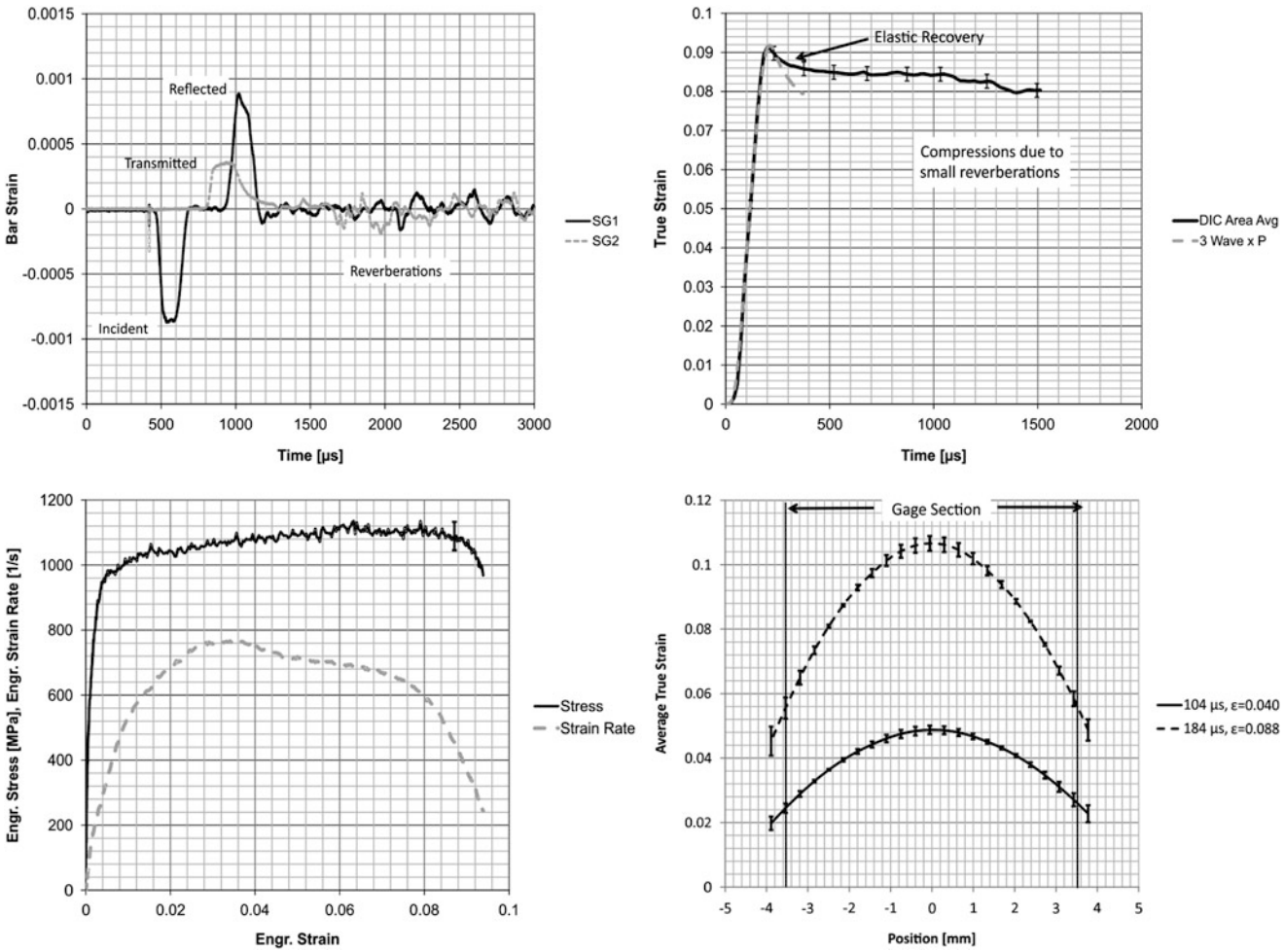

Fig. 22.4 *Top left*: raw strain gage signals from a recovery experiment (7 mm gage length, not synchronized with plot *Top right*). *Top right*: strain-time from strain gage analysis and average DIC strain over the gage area (DIC data error bars are twice the standard deviation of the mean). *Bottom left*: dynamic stress–strain curve and strain rate versus strain. Error bar on stress represents the expanded uncertainty with k = 2. *Bottom right*: axial strain distribution along gage length, averaged at each cross section (error bars are one standard deviation)

recovery occurs within 300 μs of the peak load, after which the average strain settles to a constant level. Then, at 1100 μs and again at 1400 μs, the specimen experiences a small compressive strain (about 0.25 % in aggregate) due to reverberations in the bar that remain despite the momentum trapping.

Figure 22.5 shows three experiments for the 7 mm gage length and the 0° orientation where the striker velocity is increased to examine the effect of strain rate on the plastic behavior. As the plot shows, there is little difference in the curves until the peak stress. At the lowest dynamic strain rate the specimen did not fracture, so the drop off in stress occurs because the load pulse comes to an end. As a result, no ductility information is available at this strain rate. The highest strain rate shows slightly less ductility at fracture compared to the intermediate strain rate, although the difference is small. Compared to the quasi-static strength (measured following ASTM E8), QP980 shows measureable strain rate hardening, which generally agrees with the trends observed in other multi-phase steels with retained austenite in the microstructure, such as TRIP steels [5]. It is note mentioning here that the stress–strain curves for both the quasi-static and high rate cases show similar hardening behaviors with comparable uniform strains (~12 %); the high rate curves stretch further in the non-uniform deformation portion simply due to the smaller specimens with lower gage width-to-length ratio. Figure 22.6 examines the effect of orientation with respect to the rolling direction for this sheet steel. As the figure shows, there is very little influence of rolling direction on the dynamic fracture behavior. Thus, whatever preferred texture is introduced into the grain structure via the rolling process has little influence over the dynamic strength and ductility of this particular high strength steel.

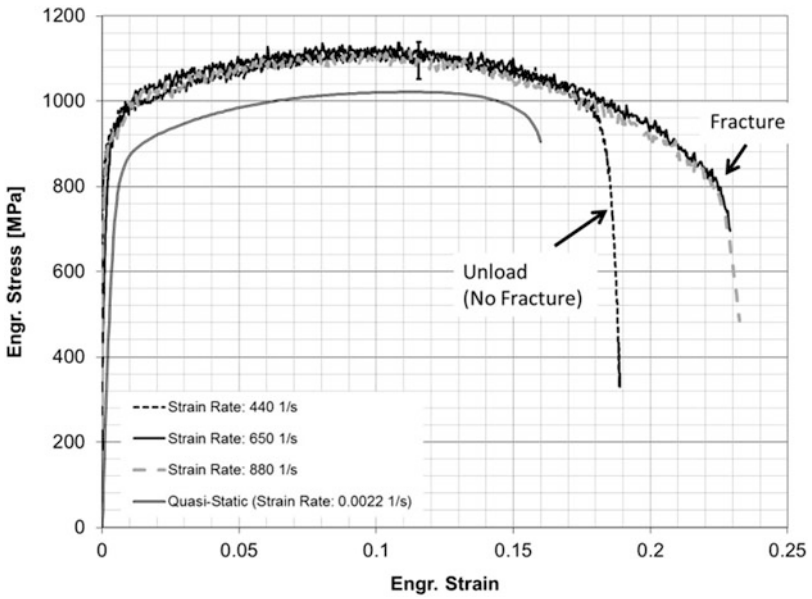

Fig. 22.5 The effect of strain rate on QP980, using 7 mm gauge length specimens. Error bar represents 2k expanded uncertainty and is typical for all tests

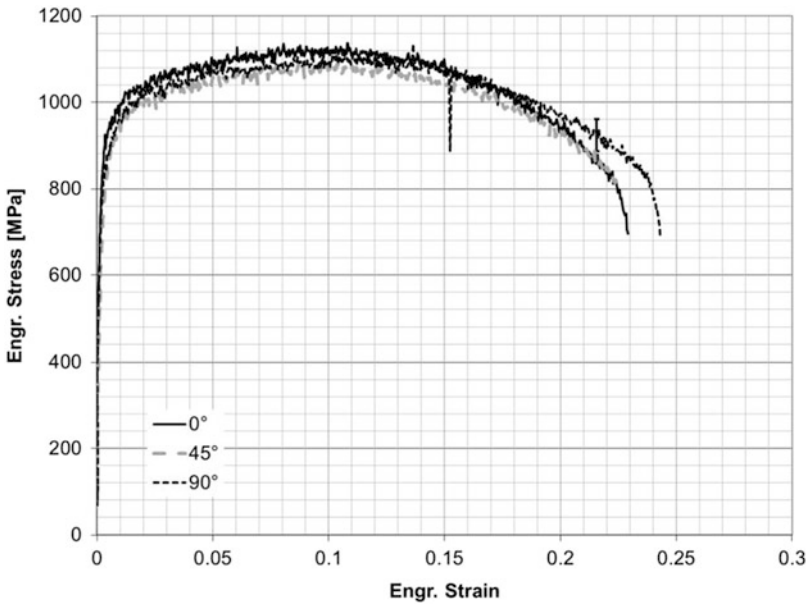

Fig. 22.6 The effect of orientation with respect to the rolling direction on QP980 fracture behavior. Tests are conducted with 7 mm gauge length specimens at a strain rate of 650 s^{-1}. Error bar represents the expanded uncertainty with k = 2

22.3 Conclusions

High strain rate tension tests are conducted on a quenched and partitioned high strength steel grade (QP980) to compare with the material behavior at quasi-static rates, for crashworthiness assessment. High speed 3D DIC is used to measure the strain distribution of the specimens during deformation. Interrupted strain tests are performed to several intermediate strains to investigate the microstructural evolution resulting from large strain dynamic tensile deformation. The DIC measurements showed that significantly less strain occurs in the gage section compared to the strain indicated by the strain gage analysis method, which assumes all displacement that occurs between the grips converts to strain within the gage section. This turned out to be an invalid assumption in these experiments. The DIC measurements were also able to capture the magnitude of elastic recovery that occurs in the specimens during interrupted-strain testing. Finally, the DIC measurements showed that while axial strain distributions are highly symmetric they are also very non-uniform. Finally, the orientation of the specimen with respect to the rolling direction nor a factor of two increase in strain rate (from 440 1/s to 880 1/s) had much influence on

the mechanical behavior of this material. The results obtained here for the QP980 will be used for comparison with other grades of conventional AHSSs. Moreover, they will serve as the baseline for comparisons with future generations of AHSSs that are currently under development.

Acknowledgment/Disclaimer This material is based upon work supported by the Department of Energy under Cooperative Agreement Number DE-EE0005976, with United States Automotive Materials Partnership LLC (USAMP). This support is greatly appreciated.

References

1. Speer, J., Assuncao, F., Matlock, D., Edmonds, D.: The “quenching and partitioning” process: background and recent progress. Mater. Res. **8**, 417–423 (2005)
2. Guzman, O., Frew, D.J., Chen, W.: A Kolsky tension bar technique using a hollow incident tube. Meas. Sci. Technol. **22**, 9 (2011)
3. Rotbaum, Y., Rittel, D.: Is there an optimal gauge length for dynamic tensile specimens? Exp. Mech. **54**(7), 1205–1214 (2008)
4. Bridgman, P.W.: The stress distribution at the neck of a tension specimen. Trans. ASM **32**, 553 (1944)
5. Huh, H., Kim, S., Song, J., Lim, J.: Dynamic tensile characteristics of TRIP-type and DP-type steel sheets for an auto-body. Int. J. Mech. Sci. **50**, 918–931 (2008)

Chapter 23
Dynamic Flow Response of Rigid Polymer Foam Subjected to Direct Impact

Behrad Koohbor, Addis Kidane, and Wei-Yang Lu

Abstract In this work, the dynamic response of closed-cell PMDI foam specimens with different initial densities subjected to direct impact loading was investigated using a shock-tube apparatus and digital image correlation. Cylindrical foam specimens with different densities were affixed on a rigid frame on one side while the impact load was applied to the other side. The full-field deformation of the polymeric foam specimen during the loading process was captured using stereovision high speed camera system. The load was measured using quartz impact force sensors located between the rigid frame and the specimen, while the full-field displacement and strain distributions were obtained using 3D DIC. A simple one-dimensional model was also proposed to calculate the change of specimen density at any given time during the deformation. The inertia stresses developed during high strain rate deformation were determined using the instantaneous density and the full-field acceleration distribution obtained from the displacement field measured by DIC. By using the load cell data, the calculated inertia stresses and the strain components obtained from DIC, the full field stress–strain distribution over the entire region of interest was extracted. The average stress–strain response of the specimens was also presented as a function of foam density.

Keywords: Polymeric foam • Dynamic loading • Digital image correlation • Shock tube • Direct impact

23.1 Introduction

Polymeric foams are widely used in engineering applications where light weight structural design and/or energy mitigation characteristics are important. These applications include but are not limited to sandwich structures, cushioning structures (e.g. helmet liners), automotive components and packaging. Since many of the aforementioned applications entail high loading rates, investigation of the deformation response of these materials at elevated strain rates has been a subject of interest. However, due to the rather complicated characteristics of these materials, particularly in high strain rate conditions, a precise evaluation of the material response in dynamic loading conditions has always been a challenging task. The complexity of the analysis of the foam materials subjected to dynamic loading is mainly due to their substantial strain rate sensitivity, cell structure, compressibility and low wave propagation speed [1, 2]. For instance, the compressive wave speed is low in polymeric foams, which results in the delayed time to reach equilibrium and makes the conventional measurement of load and deformation at specimen end inadequate [3, 4].

In this work, the dynamic flow response of polymeric foams subjected to impact loading is investigated through the use of high speed photography in conjunction with 3D digital image correlation (DIC). The full-field displacement distribution during loading is obtained through DIC and is later used to calculate the acceleration field as well as the local density. The acceleration field and the density are then used to determine the inertia stresses developed in the material during exposure to dynamic loading. Finally the inertia stress distribution is calculated and superimposed to the data collected at the specimen end to determine the actual stress distribution within the specimen. In this way, the level of inaccuracy due to the delayed state of dynamic equilibrium has been significantly lowered.

B. Koohbor (✉) • A. Kidane
Department of Mechanical Engineering, University of South Carolina, 300 Main Street, Columbia, SC 29208, USA
e-mail: koohbor@email.sc.edu

W.-Y. Lu
Sandia National Laboratories, Livermore, CA, USA

B. Song et al. (eds.), *Dynamic Behavior of Materials, Volume 1*,
Conference Proceedings of the Society for Experimental Mechanics Series, DOI 10.1007/978-3-319-22452-7_23

23.2 Materials and Methods

Rigid closed-cell PMDI foams with initial nominal densities of 320 and 640 kg/m^3 were examined. The differences in the cell structure of the materials have been illustrated in Fig. 23.1a, b. Cylindrical specimens of 25.4 mm in diameter and 25.4 mm in length were extracted from the as-received billets using a waterjet machine. To facilitate the use of DIC, a high contrast random speckle pattern was manually applied on the specimen surface, as typically shown in Fig. 23.1c.

A shock tube apparatus was used to apply dynamic loading on the specimens in this work. The details and the design aspects of the shock tube can be found elsewhere [2, 5, 6]. In the present work, an aluminum projectile was used to apply direct impact loading on the foam specimens. The projectile was machined from high strength 7068 aluminum alloy and was also speckled in order to enable measuring its velocity prior and during incidence with the specimen. The specimen was affixed on a custom made fixture with the use of lithium-based grease which also serves as the lubricant. Three load cells were placed inside the mentioned fixture and behind the specimen. An oscilloscope was used for triggering of the camera system and to collect the load data from the load-cells. A high speed stereo camera system composed of a pair of Photron SAX-2 cameras each equipped with a 100 mm lens was used to record the deformation process at a rate of 1.8×10^5 fps and a 256×168 pix^2 resolution. A high intensity LED light system was also used for the illumination.

The images acquired during the loading process were exported to the 3D digital image correlation software Vic-3D® for further analysis. The DIC analysis was performed using subset and step sizes of 25 and 3 pixels, respectively, resulting in a spatial resolution of 54 μm/pix. The experimental setup showing the shock tube and the stereo camera arrangement is demonstrated in Fig. 23.2.

23.3 Data Analysis

The stress–strain response of a material in uniaxial loading conditions is conventionally calculated from the load and displacement measured at specimen ends. However, in the case of low impedance materials subjected to dynamic loading conditions, the conventional method might introduce substantial error due to two main reasons. First, owing to the delayed state of equilibrium, the stress and strains distribution will be non-homogeneous, particularly in earlier stages of the deformation [3]. Second, the inertia effect at high loading rate cannot be neglected. To overcome these limitations,

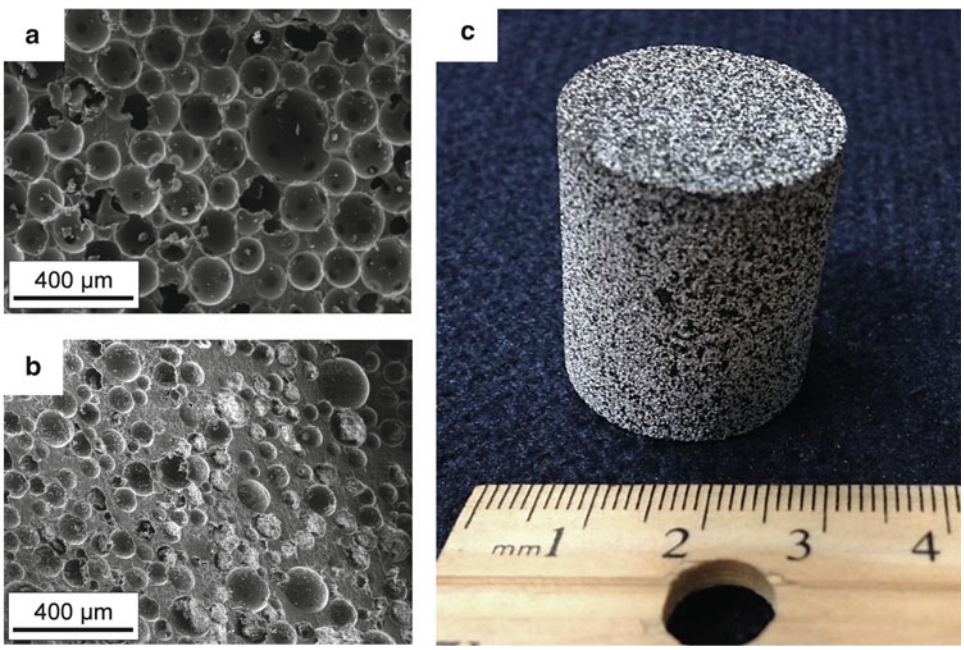

Fig. 23.1 The SEM images of the specimens with (**a**) 320 kg/m^3 and (**b**) 640 kg/m^3 nominal densities. A typical cylindrical specimen has also been demonstrated in (**c**)

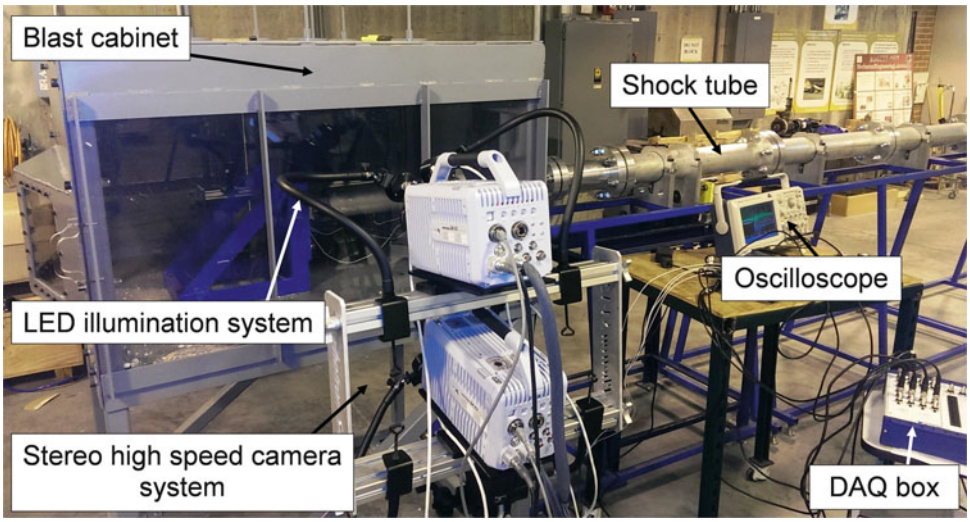

Fig. 23.2 The experimental setup used in this work to apply dynamic loading on the foam specimens

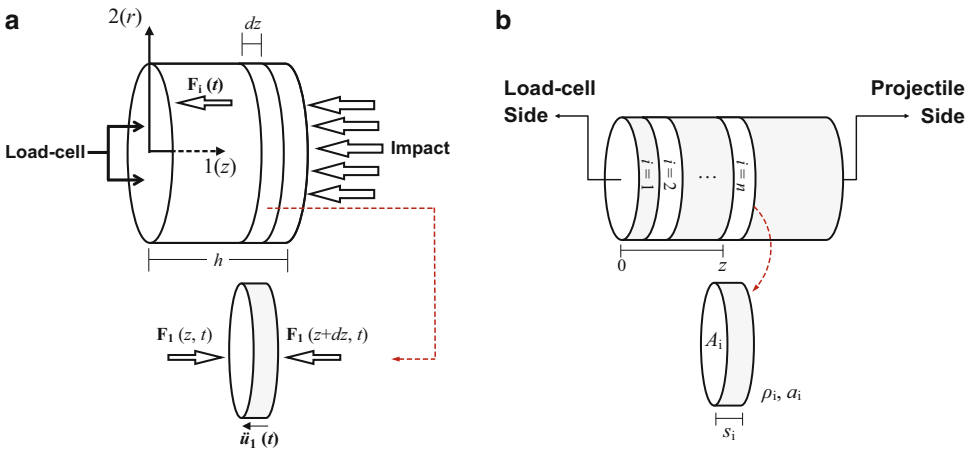

Fig. 23.3 Schematic view of (**a**) the cylindrical specimen subjected to direct impact, and (**b**) the specimen sliced into finite number of thinner segments, used to determine the inertia forces and stresses

Pierron [4, 7, 8], has suggested that the deformation measured from DIC can be used to calculate the inertia term and hence to establish a dynamic-equilibrium state at any time during deformation. He further shows that, through an inverse analysis, the force and hence the stress at any given time and at any given position within the field of view can be calculated [4, 7, 8]. Following a similar procedure, in this work an inverse analysis was performed, in which the full-field deformation obtained from DIC is used to include the inertia stresses into the analysis.

Consider a schematic cylindrical specimen, as shown in Fig. 23.3a, subjected to direct impact on its projectile side. Considering Newton's law of motion and the free body diagram of the sliced section, the following equation can be written:

$$F_1(z+dz,t) - F_1(z,t) = \rho(z,t)A(z,t)dz\frac{\partial^2 u_1}{\partial t^2}(z,t) \tag{23.1}$$

Where, $\rho(z, t)$, $A(z, t)$ and $u_1(z, t)$ represent the specimen local density, cross sectional area and displacement along the axial direction, at position z and time t, respectively. Upon rewriting in differential form and integration, (23.1) can be expressed as:

$$F_1(z,t) = F_1(0,t) + \int_{\xi=0}^{\xi=z} \rho(\xi,t)A(\xi,t)\frac{\partial^2 u_1}{\partial t^2}(\xi,t)d\xi \tag{23.2}$$

Using (23.2), the force applied on any given position z and at any time t can be reconstructed by knowing the force acting on the location $z = 0$, i.e. the load cell side along with the acceleration, density and cross sectional area at position z. Note that the local acceleration data can readily be calculated using a simple central difference scheme applied on the local displacement components obtained directly from DIC.

Similar to the force, the axial stress component can also be reconstructed at any given point over the entire region of interest as:

$$\sigma_1(z,t) = \frac{F_1(0,t)}{A(0,t)} + \int_{\xi=0}^{\xi=z} \rho(\xi,t)\frac{\partial^2 u_1}{\partial t^2}(\xi,t)d\xi \tag{23.3}$$

With $\sigma_1(z, t)$ denoting the axial stress magnitude at position z and time t. In practice, the integral on the right hand side of (23.2) and (23.3) can be approximated as:

$$\int_{\xi=0}^{\xi=z} \rho(\xi,t)\frac{\partial^2 u_1}{\partial t^2}(\xi,t)d\xi \approx \sum_{i=1}^{n} \rho^{(i)}a^{(i)}s^{(i)} \tag{23.4}$$

Where $\rho^{(i)}$ and $a^{(i)}$ are the local density and axial acceleration values at section i, respectively. $s^{(i)}$ represents the thickness of section i and n denotes the total number of slices up to the location z, as shown in Fig. 23.3b. It should be noted here that the density and acceleration values on each slice were calculated by averaging these parameters over the entire volume of the thin sliced section.

The material compressibility was considered in the analysis by proposing a simple mathematical equation based on the principle of mass conservation, capable of predicting the local density of the material, $\rho(z, t)$, as a function of its initial density, ρ_0, axial strain component, $\varepsilon_1(z, t)$, and the local plastic Poisson's ratio, $\upsilon(z, t)$, as:

$$\rho(z,t) = \rho_0(\exp[\varepsilon_1(z,t)])^{2\upsilon(z,t)-1} \tag{23.5}$$

The local plastic Poisson's ratio of the material was measured as the ratio of local radial and axial strain components at any given position along the axis of the deforming specimen, as:

$$\upsilon(z,t) = -\frac{\varepsilon_2(z,t)}{\varepsilon_1(z,t)} \tag{23.6}$$

Where the subscripts '1' and '2' denote the axial and radial directions, respectively. The radial component of strain was obtained by first assigning a cylindrical coordinate system to the undeformed specimen. Then, by tracking the local radial expansion measured by DIC, the local radial strain component was determined. Having obtained both components of strain, i.e. radial and axial, the local plastic Poisson's ratio can be calculated using (23.6).

23.4 Results and Discussion

To calculate the average strain rate applied on the specimens during direct impact loading, the magnitude of the axial strain component was averaged over the entire region of interest and plotted with respect to the deformation time. The slope of the best linear fit was calculated as the average strain rate applied on the specimens, as shown in Fig. 23.4. An average strain rate of 2540 s^{-1} was applied on the specimens of both initial densities in this work.

It should be noted that the axial strain is not distributed uniformly along the specimen axis. The non-uniform distribution of axial strain has been illustrated in Fig. 23.5 as a time shift between the curves plotted at different locations along the specimen axis. The time shift between the curves of Fig. 23.5b shows the transient state of the deformation and is consistent

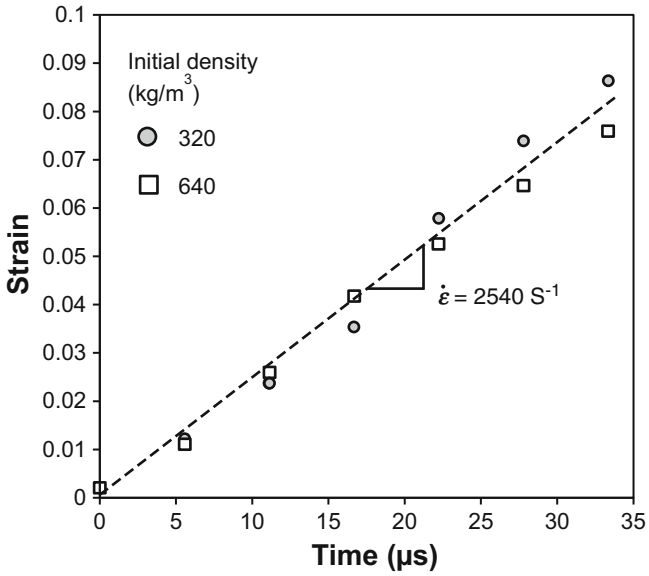

Fig. 23.4 The evolution of axial strain component with time. The slope of the best linear fit indicates the average strain rate applied on the specimens

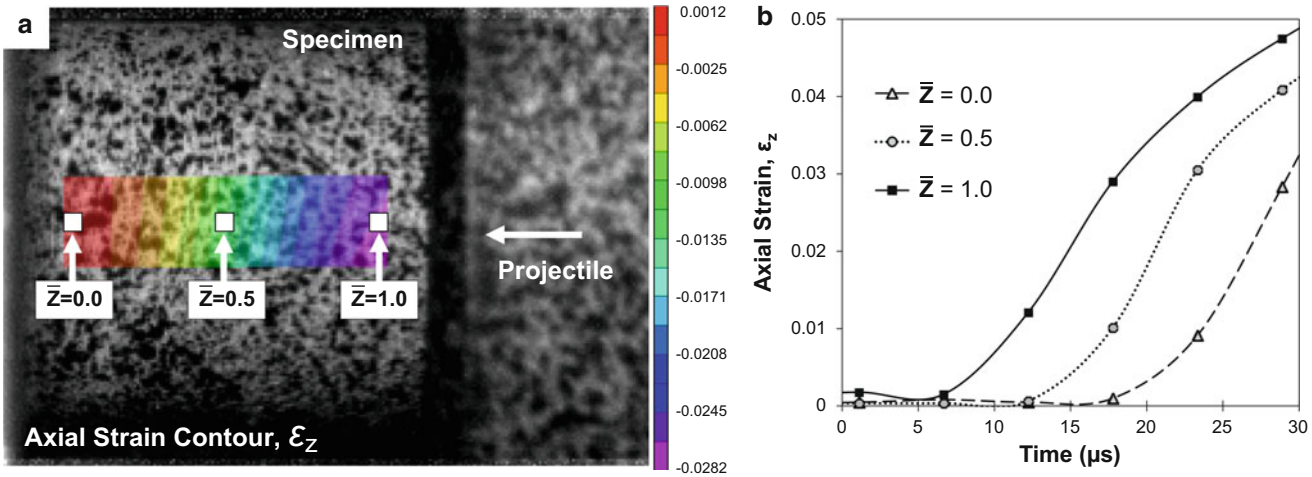

Fig. 23.5 (**a**) The non-uniform strain distribution map at $t = 15$ μs. (**b**) The strain–time curves extracted from the points marked in (**a**). $\overline{Z}$ represents the normalized distance from the load-cell side

with the wave propagation speed in these materials. Note that depending on the specimen density, a 15 ~ 30 μs time is required for the compressive wave to propagate through the specimen. The rather long time shifts shown above necessitates the inclusion of the inertia stresses into the analysis, particularly for the analysis of the specimen deformation at earlier stages of the deformation [9].

The local Poisson's ratio and local density were calculated next. Typical evolution of local Poisson's ratio and accordingly, the local density are shown in Fig. 23.6 for the specimen with 640 kg/m^3 initial density. It is observed that both Poisson's ratio and local change of density vary along specimen axis. The calculated local Poisson's ratios show lower values at locations closer to the load-cell side of the specimen, i.e. $\overline{Z} = 0$, on which the local change in the density is higher.

The full-field acceleration was obtained from the full-field axial displacement obtained directly from DIC, and using central difference method. The full field axial strain and acceleration for the specimen with 640 kg/m^3 initial density are shown in Fig. 23.7. The axial displacement contours show a rather circumferentially-homogeneous distribution, while acceleration field is demonstrated to be distributed in a more inhomogeneous pattern, particularly at earlier stages of deformation. To give a better insight, the axial acceleration magnitude is averaged over the entire region of interest and plotted against time as shown in Fig. 23.8. For both cases, i.e. 320 and 640 kg/m^3 foams, the acceleration distribution shows

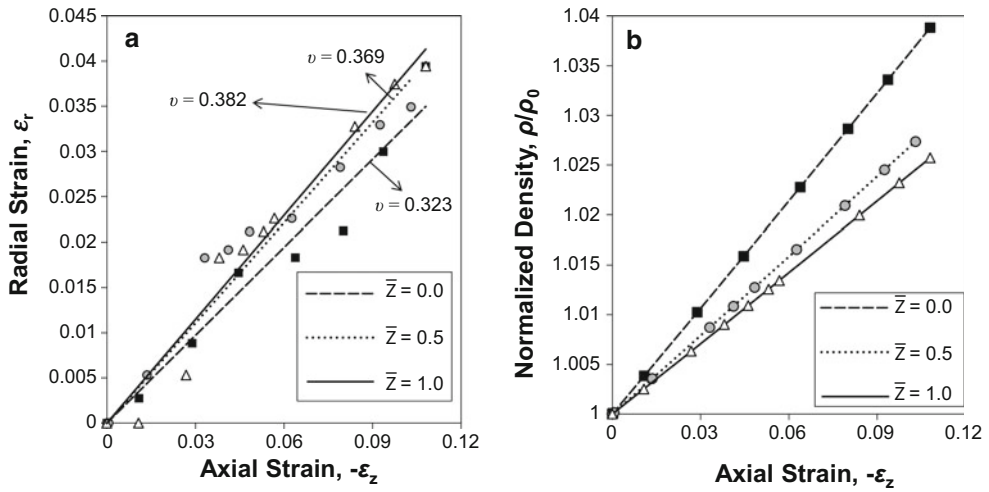

Fig. 23.6 Variation of local (**a**) Poisson's ratio and (**b**) normalized density for the specimen with 640 kg/m^3 initial density subjected to impact loading

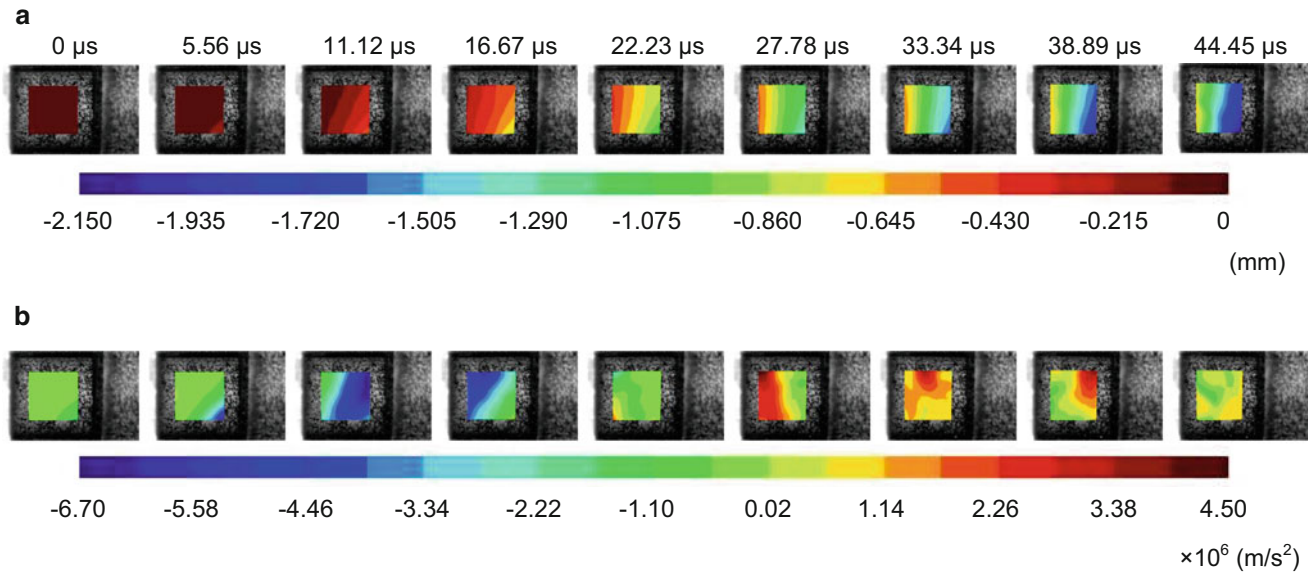

Fig. 23.7 Full-field contours of (**a**) axial displacement and (**b**) axial acceleration for the specimen with 640 kg/m^3 initial density

higher magnitudes at earlier stages, i.e. $t < 25$ μs. The high values of acceleration obtained at $t < 25$ μs will significantly increase the inertia stresses, as also previously documented in [3].

Based on the full-field acceleration and density distributions, and following the procedure detailed earlier, the full-field stress–strain response of the foam specimens subjected to impact loading was obtained. The local stress–strain curves obtained for the three representative locations, i.e. $\overline{Z} = 0.0, 0.5, 1.0$, are plotted in Fig. 23.9, along with the average flow curves calculated for each specimen. The nonhomogeneous distribution of local stress is obvious in this figure, while the so-called non-uniform deformation response is attributed to the influence of inertia forces developed in each specimen. It is also observed that due to the more prominent effect of inertia stresses, the difference between the local stress–strain curves and the average curve for each specimen is larger at earlier stages of the deformation.

Comparing the average stress–strain curves for the two specimens, a remarkable change in the constitutive response of the specimens is observed. The difference can be explained through the different cell structures in the specimens.

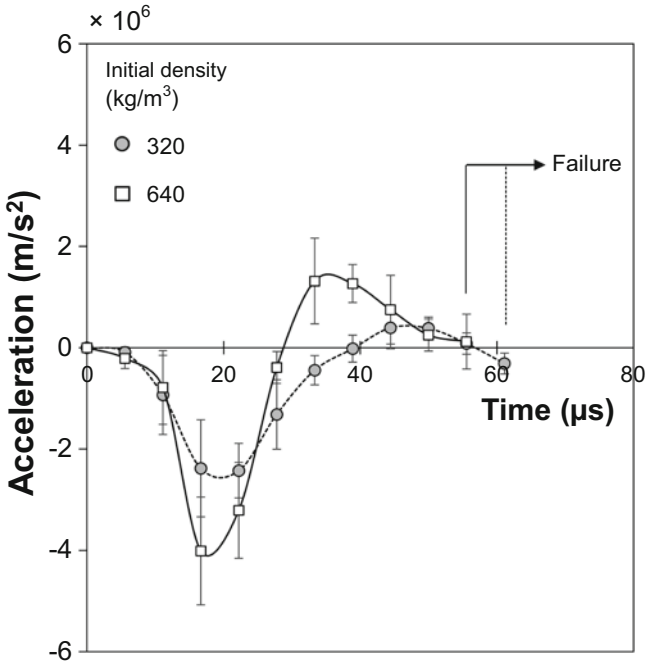

Fig. 23.8 Variation of the axial acceleration averaged within the domain of interest against deformation time

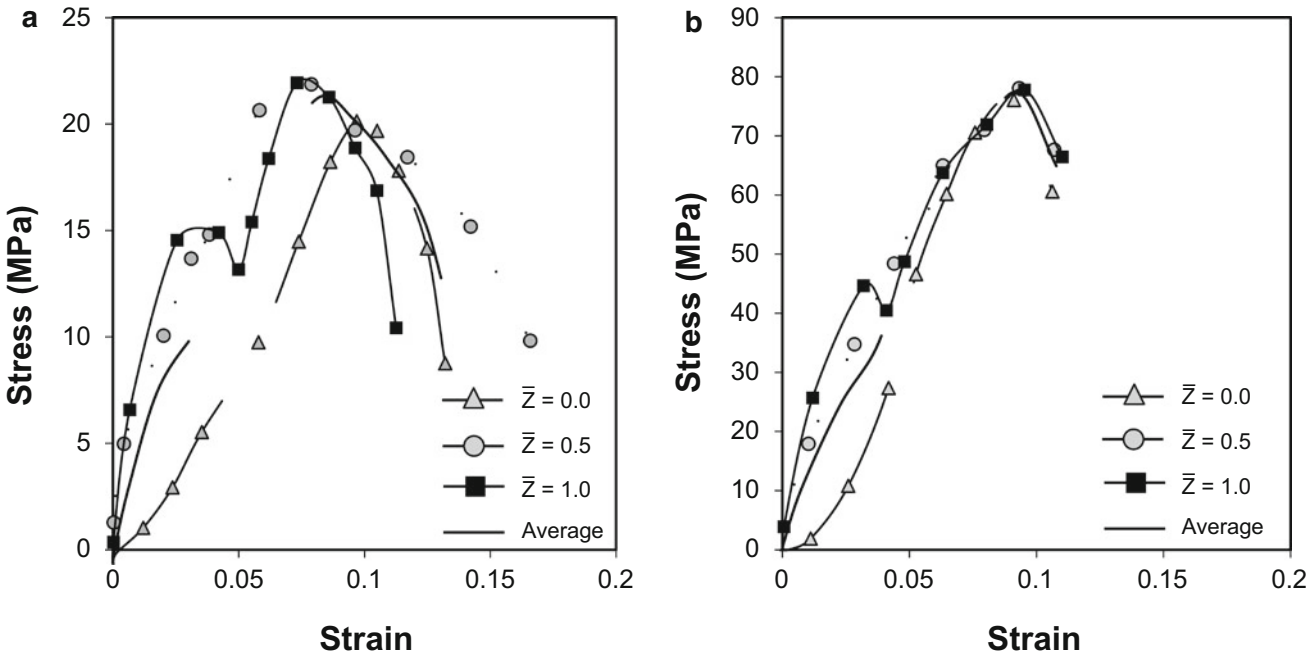

Fig. 23.9 Local stress–strain curves obtained at different locations along the specimen axis, for the specimens with (**a**) 320 kg/m^3 and (**b**) 640 kg/m^3 initial density

As previously demonstrated in Fig. 23.1, the thickness of the cell walls changes remarkably with density. The thinner cell walls present in the material with lower initial density make them more susceptible to micro-buckling under a smaller far-field load. On the other hand, the specimen with higher initial density is made of cells with thicker wall sections and will exhibit higher strength as well as a larger magnitude of energy absorption before failure [9].

23.5 Summary

The dynamic compressive response of closed-cell PMDI foams was investigated. PMDI foams with different nominal densities were subjected to direct impact, while their deformation response was observed and analyzed using high speed photography in conjunction with 3D DIC. The full-field acceleration distribution was obtained from the displacement distribution. Then, considering the one-dimensional equation of motion, the full-field inertia stresses were determined and superimposed to the stress magnitude measured from the load-cells. Having obtained the full-field stress–strain distribution over the entire region of interest, local and average flow response of the specimens were presented.

Acknowledgements Sandia National Laboratories is a multi-program laboratory managed and operated by Sandia Corporation, a wholly owned subsidiary of Lockheed Martin Corporation, for the U.S. Department of Energy's National Nuclear Security Administration under contract DE-AC04-94AL85000.

References

1. Gibson, L.J., Ashby, M.F.: Cellular Solids: Structure and Properties, 2nd edn. Cambridge University Press, Cambridge (1997)
2. Mallon, S., Kidane, A., Lu, W.Y.: Full-field deformation observation of polymer foam subjected to shock loading. In: Song, B., Casem, D., Kimberley, J. (eds.) Dynamic Behavior of Materials. Proceedings of the 2014 Annual Conference on Experimental & Applied Mechanics, vol. 1, pp. 83–89. Springer, Cham (2015). DOI:10.1007/978-3-319-06995-1_14
3. Othman, R., Aloui, S., Poitou, A.: Identifications of non-homogeneous stress fields in dynamic experiments with a non-parametric method. Polym. Test. **29**, 616 (2010)
4. Pierron, F., Zhu, H., Siviour, C.: Beyond Hopkinson's bar. Phil. Trans. R. Soc. A **372**, 2013195 (2014)
5. Mallon, S., Koohbor, B., Kidane, A., Sutton, M.A.: Fracture behavior of prestressed composites subjected to shock loading: a DIC-based study. Exp. Mech. **55**, 211–225 (2014). doi:10.1007/s11340-014-9936-5.0
6. Mallon, S., Koohbor, B., Kidane, A.: Fracture of pre-stressed woven glass fiber composite exposed to shock loading. In: Song, B., Casem, D., Kimberley, J. (eds.) Dynamic Behavior of Materials. Proceedings of the 2014 Annual Conference on Experimental & Applied Mechanics, vol. 1, pp. 213–219. Springer, Cham (2015). DOI:10.1007/978-3-319-06995-1_32
7. Pierron, F., Forquin, P.: Ultra-high-speed full-field deformation measurements on concrete spalling specimens and stiffness identification with the virtual fields method. Strain **48**, 388 (2012)
8. Zhu, H., Pierron, F., Siviour, C.: Latest results in novel inertial high strain rate tests. In: Song, B., Casem, D., Kimberley, J. (eds.) Dynamic Behavior of Materials. Proceedings of the 2014 Annual Conference on Experimental & Applied Mechanics, vol. 1, pp. 21–26. Springer, Cham (2015). DOI:10.1007/978-3-319-06995-1_5
9. Koohbor, B., Mallon, S., Kidane, A., Lu, W.Y.: The deformation and failure response of closed-cell PMDI foams subjected to dynamic impact loading. Polym. Test. 44. 112 (2015)

Chapter 24
Differences in the Hydrostatic Implosion of Metallic and Composite Tubes Studied Using Digital Image Correlation

Michael Pinto, Sachin Gupta, and Arun Shukla

Abstract A comparative experimental study is conducted to investigate the mechanisms and energies associated with the hydrostatic implosion of hollow cylinders of different materials. Experiments are performed in a 2.1 m diameter spherical pressure vessel designed to provide constant hydrostatic pressure through the collapse event. Aluminum, glass/polyester, and carbon-fiber/epoxy tubes are studied to explore the effect of material type on the modes of failure. 3-D Digital Image Correlation technique, which is first calibrated for the underwater environment, is used to capture the full-field real-time deformation during the implosion event. Dynamic pressure transducers measure the pressure pulses generated by the implosion event and evaluate its damage potential. Using these measurement techniques, the differences in mechanisms of failure as well as their effects on the local pressure history are characterized.

Keywords: Composite tubes • Filament-winding • Hydrostatic implosion • Digital image correlation • High-speed photography

24.1 Introduction

The implosion of a submerged structure is a type of buckling, occurring when external pressure reaches a critical value and resulting in a rapid and often catastrophic collapse. During this collapse, walls of the structure and nearby fluid are accelerated to high velocities and stop suddenly once the collapse is completed. This sudden change in momentum releases a pressure wave into the surrounding fluid, which can damage nearby structures [1, 2]. Because of this, the implosion problem has gained much attention in recent decades. The implosion of glass spheres has been studied by several authors who characterized the pressure pulse emitted during collapse as well as its potential for damage to nearby structures [3–5]. The implosion of aluminum cylinders has also been studied recently. Turner identified key stages of the implosion event in relation to the local pressure about the collapsing structure [6]. Farhat et al. studied the implosion of aluminum cylinders with varying length to diameter ratios to produce both mode 2 and mode 4 failures [7]. In this work, the authors were able to observe the differences in the emitted pressure pulse as well as the collapse progression due to the change in buckling mode.

The use of composites has attracted attention in underwater marine applications due to the array of advantages offered by these materials. Composite materials offer alternatives with reduced weight, improved corrosion resistance, and for submerged structures, greater potential operating depths. In addition, these materials provide improved stealth qualities by having very low thermal, acoustic, and magnetic signatures, increasing their appeal for military applications. For these reasons, the presence of composite materials in marine industries is increasing, and they are currently used in several naval applications, such as sonar domes, masts, and hull sheathings [8]. One of the biggest obstacles to widespread adaptation of composite materials is a lack of complete understanding and simple design rules for these materials, especially under extreme loading conditions [8]. For this reason, this work looks to expand the current knowledge of composite behavior by examining the problem of implosion.

The implosion of composite cylinders under hydrostatic loading has also been experimentally studied in a few previous publications. Moon et al. examined implosion of filament-wound carbon/epoxy composite tubes with different winding angles both experimentally and computationally to determine collapse pressures and modes [9]. Both Ross and Smith performed experiments on carbon/E-glass tubes to determine critical buckling pressure, buckling modes, and create design tables for these structures [10, 11]. Hernandez-Moreno et al. tested filament-wound glass/epoxy composite tubes with a

M. Pinto • S. Gupta • A. Shukla (✉)
Dynamics Photomechanics Laboratory, Department of Mechanical,
Industrial and Systems Engineering, University of Rhode Island, Kingston, RI 02881, USA
e-mail: shuklaa@egr.uri.edu

B. Song et al. (eds.), *Dynamic Behavior of Materials, Volume 1*,
Conference Proceedings of the Society for Experimental Mechanics Series, DOI 10.1007/978-3-319-22452-7_24

winding angle of 55° to examine effects of winding pattern on the collapse pressure [12]. Hur et al. examined the buckling modes, loads, and failure of carbon/epoxy tape layup tubes both experimentally and computationally [13].

Recent work by the authors studied the implosion of both carbon and glass fiber reinforced composite tubes along with aluminum tubes using high-speed photography and Digital Image Correlation [14–16]. This study expands on that work by comparing the implosion of composite tubes of different types to that of aluminum tubes, and identifying key differences caused by changes in material.

24.2 Materials

The impodable volumes in this study are carbon/epoxy and glass/polyester(PE) filament wound composite tubes and aluminum 6061-T6 tubes. The carbon/epoxy tubes consist of seven layers of unidirectional carbon fabric reinforcement arranged in a [±15/0/±45/±15] layup with a 60.3 mm inner diameter and a 381 mm unsupported length. These cylinders are manufactured by Rock West Composites (West Jordan, UT) with a nominal wall thickness of 1.63 mm and are thoroughly sanded on the exterior surface for excellent finish and tolerances. The glass/PE tubes consist of five layers of unidirectional E-glass fabric reinforcement arranged in a [±55/±55/0] layup with a 57.2 mm inner diameter and 381 mm unsupported length. These cylinders are manufactured by Nor'Easter Yachts (Milford, CT) with a nominal wall thickness of 2 mm. Aluminum 6061-T6 tubes were extruded with an inner diameter of 54.6 mm, a wall thickness of 1.27 mm, and a length of 406 mm. The dimensions are selected as to provide specimens with a relatively low expected collapse pressure, and a high R/t ratio so that thin-wall assumptions may be utilized.

24.3 Experimental Methods

All implosion experiments are conducted in a 2.1 m diameter spherical pressure vessel with a maximum pressure rating of 6.89 MPa and designed to provide constant hydrostatic pressure throughout the collapse event (see Fig. 24.1). Several Plexiglass windows mounted about the midspan of the pressure vessel allow the specimens to be viewed by cameras and adequately lit by two high powered light sources.

The specimens are sealed using two aluminum end caps, and are then suspended horizontally in the center of the pressure vessel. A random high-contrast speckle pattern is applied to a region spanning the entire length of the specimen and approximately half of the circumference using flat black and white paint. To measure the changes in local pressure during the collapse event, several high pressure blast transducers (PCB 138A05, PCB Piezotronics, Inc., Depew, NY) are mounted at different locations about the specimen both axially and circumferentially. The amplified outputs of this sensor are monitored by an Astro-med Dash® 8HF-HS portable data recorder (Astro-Med Inc., West Warwick, RI) at a sampling rate of 2 MHz.

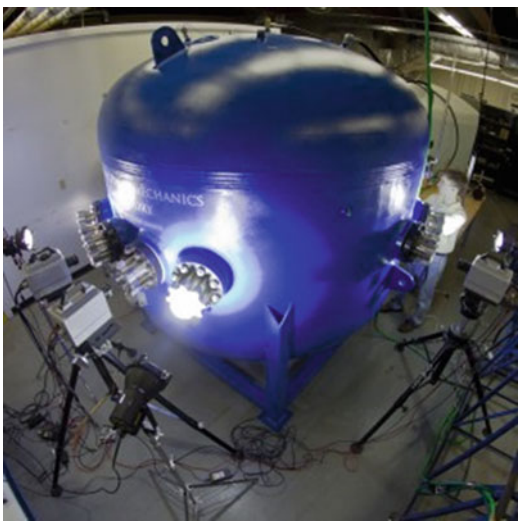

Fig. 24.1 Pressure vessel used for implosion experiments

The vessel is then flooded with water, leaving a small air pocket at the top. Once the vessel is filled, nitrogen gas is introduced into the air pocket to pressurize the enclosed water. The pressure inside the vessel is increased slowly (0.083 MPa/min) until the specimen collapsed. At this point, the cameras and pressure sensors are end triggered to record the data occurring 1 s prior to triggering. In this way, data is collected for the entire collapse event by all recording devices.

Two high-speed cameras (Photron SA1, Photron USA, Inc.), offset by 17° are used to capture stereo high-speed images of the patterned region of the specimen at 20,000 frames/s for glass/PE tubes, and 50,000 frames/s for both carbon/epoxy tubes and aluminum tubes. The stereo images are analyzed using commercially available digital image correlation (DIC) software, VIC3D 2012 (Correlated Solutions, Inc., Columbia, SC) to determine real-time, full-field displacements across the viewable surface of the specimen throughout the implosion event.

24.4 Results

Aluminum tubes were observed to fail at 2.04 MPa in a mode 2, or flattening buckling shape. The local pressure history measured about the midspan of these specimens is seen in Fig. 24.2 (left) and DIC contours of displacement and velocity across the length of the tube are plotted in Fig. 24.2 (right).

The pressure history measured for these specimens is quite consistent with reports of previous studies [6.7]. At the start of the collapse, the local pressure decays smoothly to a minimum just prior to $t = 0$ ms. This corresponds with an acceleration of the center of the tube, as shown by DIC contours.

At $t = 0$ ms, contact is made between opposing walls of the tube. This is evidenced by the velocity contour which shows a sudden drop in velocity at the center of the tube to zero at this time. This is accompanied by a very sharp spike in the local pressure at this time, indicating the acoustic pulse released due to this contact. Shortly thereafter a very large spike in pressure is observed with considerable impulse. This pulse is caused by the change in momentum to the surrounding fluid, which had accelerated inward along with the walls of the structure. Following this pulse is a lower magnitude pressure tail that corresponds with the axial propagation of the buckle through the length of the tube, as seen in the displacement and velocity contours. An interesting feature seen in the velocity contour is the acceleration of the collapse as the buckle propagates. Starting at approximately $t = 0.2$ ms, the velocity of the region just behind the zero velocity zone increases to significantly higher magnitude than the maximum velocity at the center of the tube. This corroborates with previous buckling experiments performed on long pipes which showed the propagation velocity of the buckle accelerates as it travels along the length of the pipe [17].

Filament-wound glass fiber specimens fail at 2.05 MPa in a mode 2 buckling shape, becoming completely flat. The local pressure history measured about the midspan of these specimens is seen in Fig. 24.3 (left) and DIC contours of displacement and velocity across the length of the tube are plotted in Fig. 24.3 (right). Qualitatively, this pressure trace at first appears very much like those measured for aluminum tubes with a gradual decay in pressure followed by a pressure spike and a broad overpressure region. However, the underpressure region shows some unique characteristics.

From the start of the dynamic event to $t = -0.80$ ms, a slow and gradual decay in pressure is observed, as reflected in the slow ovalling seen in the displacement contour. The unstable collapse appears to initiate after $t = -0.80$ ms, where a sharp

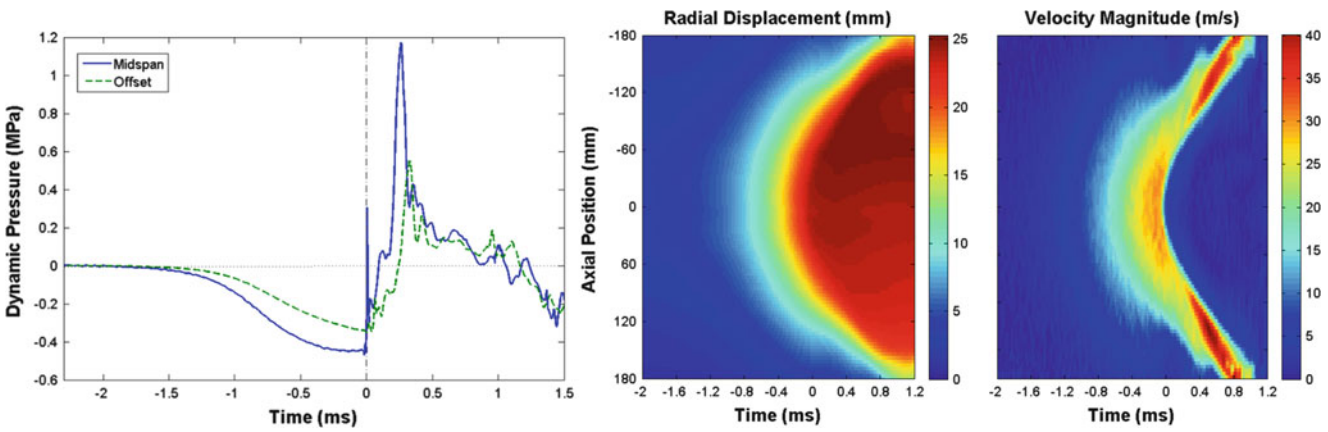

Fig. 24.2 Pressure history (*left*) and deflection and velocity contours (*right*) measured in the collapse of aluminum tubes

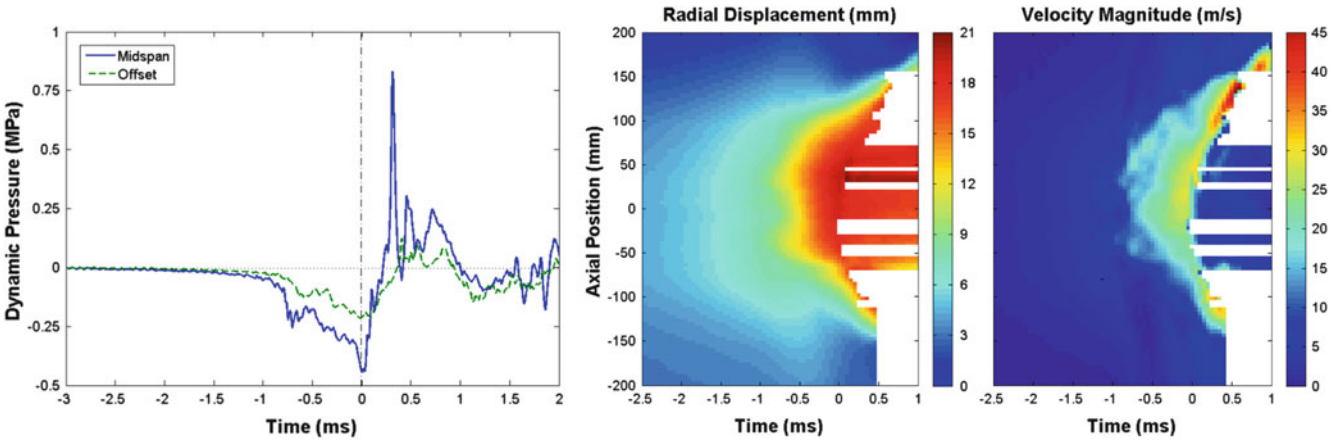

Fig. 24.3 Pressure history (*left*) and deflection and velocity contours (*right*) measured in the collapse of glass/PE tubes

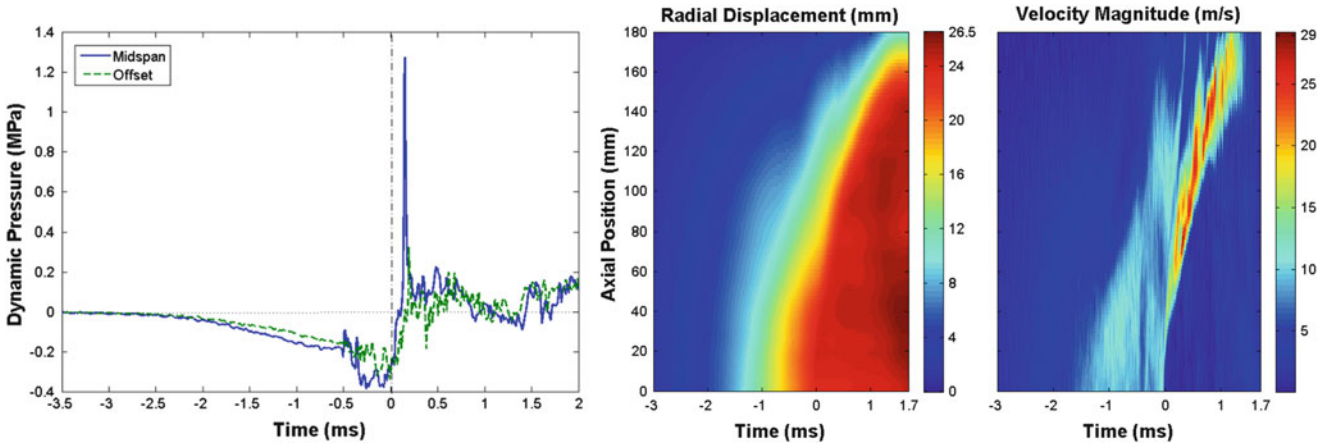

Fig. 24.4 Pressure history (*left*) and deflection and velocity contours (*right*) measured in the collapse of carbon/epoxy tubes

drop in pressure is seen, coupled with a sudden increase in velocity at two axial locations, representing the formation of local buckles. These local buckles converge into a single global buckle at $t = -0.45$ ms, as evidenced by the displacement and velocity contours, and pressure continues to drop at a near-constant rate. At $t = 0.00$ ms, wall contact is made and is followed by a relatively small acoustic pulse emitted by the contact itself. As the contact spreads, the surrounding fluid is suddenly arrested, and that rapid change in momentum results in the high magnitude pressure pulse seen at $t = 0.30$ ms. There is then a lower magnitude pressure tail as the wall contact spreads axially through the until the entire specimen has flattened. As was the case for aluminum tubes, the buckle front accelerates to very high velocities as it propagates.

The carbon fiber reinforced specimens fail at 0.97 MPa in a mode 2 buckle shape. The local pressure history measured about the midspan of these specimens is seen in Fig. 24.4 (left) and contours of displacement and velocity are included in Fig. 24.4 (right).

Initially, the unstable collapse is characterized by a smooth and gradual decay in pressure up to $t = -0.48$ ms. At this time, a distinct spike in pressure is recorded followed by a sharp drop to a minimum of -0.43 ± 0.05 MPa. This spike is a result of longitudinal cracks that initiate at the apexes of the two buckling lobes, releasing an acoustic pulse. This cracking causes a sudden loss of structural stability, allowing the tube walls to accelerate, and, consequently, causing a more rapid drop in pressure. The remainder of the underpressure region shows an approximate maintenance of a minimum pressure, similar to observations made in the implosion of glass tubes by Turner [5]. The drop in pressure seen in this region is sufficient to support the initiation of cavitation near the apexes of the buckle lobes. It is also noted that between $t = -0.48$ ms and $t = 0.00$ ms, the pressure trace shows minor spikes superimposed on the minimum pressure. This phenomenon is a result of cavitation bubbles forming due to low pressure. After growing to a critical size they collapse upon themselves, releasing acoustic pulses upon collapse which are recorded by the nearby pressure transducers.

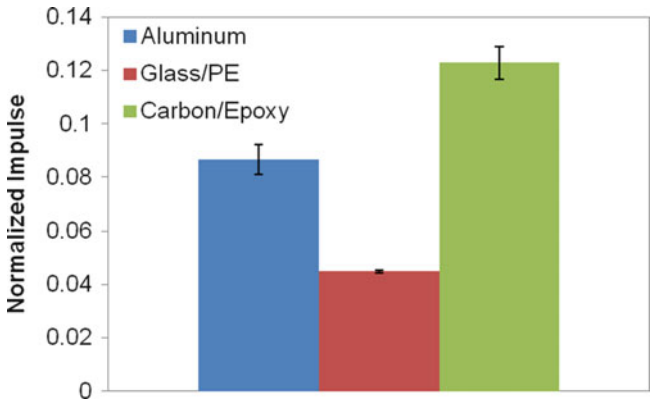

Fig. 24.5 Normalized impulse, defined by Eq. 24.1

The occurrence of wall contact is confirmed by the DIC generated velocity contour at that time which shows the appearance of a small region of zero velocity at the center of the specimen. Immediately after wall contact, a small, sharp spike is recorded as the local pressure begins to rise. This represents the minor acoustic pulse released as a result of the wall contact, as has been observed in both glass/PE and aluminum tubes. Following wall contact, pressure rises rapidly to a maximum as a result of the momentum change imparted to surrounding fluid. DIC displacement and velocity contours show that the midspan of the specimen has flattened completely, and this buckle has begun to propagate axially, as evidenced by the expanded area of zero velocity combined with the greater region of radial displacement close to the inner radius of the tube. Following this pulse, the buckle shape continues to propagate through the length of the structure and pressure measurements are dominated by reflections. As in the previous cases, the buckle is seen to accelerate as it propagates.

The damage potential of the pressure pulses released in these implosions may best be compared through the impulse generated. Here impulse is defined as the time integral of the pressure profile. To normalize for the difference in collapse pressure, and to remove the effect of reflections from the tank boundary, the following normalized impulse is defined:

$$\bar{I} = \frac{\int_0^{t^-} \Delta p dt}{\int_0^{t^-} P_0 dt} \tag{24.1}$$

Where P_0 is the hydrostatic pressure during the collapse event, Δp is the dynamic pressure at time t, and t^- is the time at wall contact. This normalized impulse is plotted for each specimen in Fig. 24.5.

This plot shows that of the specimens studied, carbon/epoxy tubes released the strongest pressure pulse, and glass/PE tubes released the weakest. The reason for this difference is in the particular damage mechanics present in each material. During collapse, the main mode of damage in glass/PE tubes, matrix cracking and fiber pull-out, is significantly more energy intensive than the plasticity that dominates the collapse of aluminum tubes. This causes more of the potential hydrostatic energy available prior to collapse to be dissipated in damage, thereby reducing the impulse released into the environment. Carbon/epoxy tubes were seen to possess the greatest generated impulse, primarily due to the catastrophic nature of their collapse. The main mode of damage in carbon/epoxy tubes is through-thickness cracking, which enhanced collapse velocity to the point of causing surface cavitation. This increase in velocity also enhanced the magnitude of impulse generated, and consequently increased the damage potential of the shockwave released.

24.5 Conclusions

As a result of this study, the failure, damage progression, and pressure pulse released during the hydrostatic collapse of filament wound composite tubes and aluminum tubes is characterized and compared. It is found that composite materials possess unique failure mechanisms that have a profound effect on the local pressure history during an implosion. Because of the energy intensive damage mechanisms at play, glass/PE tubes release pressure pulses with the smallest damage potential upon their collapse. This makes structures of this material an ideal choice to mitigate the risk to adjacent structures in the event of an implosion.

Acknowledgment The authors kindly acknowledge the financial support provided by Dr. Yapa D. S. Rajapakse, under the Office of Naval Research (ONR) Grant No. N00014-10-1-0662.

References

1. Accident grounds neutrino lab—physicsworld.com [WWW Document]: http://physicsworld.com/cws/article/news/2001/nov/15/accident-grounds-neutrino-lab (n.d.). Accessed 2 Oct 2014
2. Ling, J., Bishai, M., Diwan, M., Dolph, J., Kettell, S., Sexton, K., Sharma, R., Simos, N., Stewart, J., Tanaka, H., Viren, B., Arnold, D., Tabor, P., Turner, S., Benson, T., Wahl, D., Wendt, C., Hahn, A., Kaducak, M., Mantsch, P., Sundaram, S.K.: Implosion chain reaction mitigation in underwater assemblies of photomultiplier tubes. Nucl. Instrum. Methods Phys. Res., Sect. A **729**, 491–499 (2013)
3. Orr, M., Schoenberg, M.: Acoustic signatures from deep water implosions of spherical cavities. J. Acoust. Soc. Am. **59**, 1155–1159 (1976)
4. Harben, P.E., Boro, C.: Implosion source development and Diego Garcia reflections. Presented at the 23rd Department of Defense/Department of Energy Seismic Research Review, Jackson Hole, Wyoming (2001)
5. Turner, S.E.: Underwater implosion of glass spheres. J. Acoust. Soc. Am. **121**, 844–852 (2007)
6. Turner, S.E.: Underwater implosion of cylindrical metal tubes. J. Appl. Mech. **80**(1), 011013 (2012)
7. Farhat, C., Wang, C.G., Main, A., Kyriakides, S., Lee, L.H., Ravi-Chandar, K., Belytschko, T.: Dynamic implosion of underwater cylindrical shells: experiments and computations. Int. J. Solids Struct. **50**(19), 2943–2961 (2013)
8. Mouritz, A.P., Gellert, E., Burchill, P., Challis, K.: Review of advanced composite structures for naval ships and submarines. Compos. Struct. **53**(1), 21–42 (2001)
9. Moon, C.J., In-Hoon, K., Bae-Hyeon, C., Jin-Hwe, K., Choi, J.H.: Buckling of filament-wound composite cylinders subjected to hydrostatic pressure for underwater vehicle applications. Compos. Struct. **92**(9), 2241–2251 (2010)
10. Ross, C.T.F., Little, A.P.F., Haidar, Y., Waheeb, A.A.: Buckling of carbon/glass composite tubes under uniform external hydrostatic pressure. Strain (2009). doi:10.1111/j.1475 1305.2008.00475.x
11. Smith, P.T., Ross, C.T.F., Little, A.P.F.: Collapse of composite tubes under uniform external hydrostatic pressure. J. Phys. Conf. Ser. **181**, 156–157 (2009)
12. Hernández-Moreno, H., Douchin, B., Collombet, F., Choqueuse, D., Davies, P.: Influence of winding pattern on the mechanical behavior of filament wound composite cylinders under external pressure. Compos. Sci. Technol. **68**(3–4), 1015–1024 (2008)
13. Hur, S.H., Son, H.J., Kweon, J.H., Choi, J.H.: Postbuckling of composite cylinders under external hydrostatic pressure. Compos. Struct. **86** (1–3), 114–24 (2008)
14. Pinto, M., Gupta, S., Shukla, A.: Study of implosion of carbon/epoxy composite hollow cylinders using 3-D digital image correlation. Compos. Struct. **119**, 272–286 (2014)
15. Pinto, M., Gupta, S., Shukla, A.: Hydrostatic implosion of GFRP composite tubes studied by digital image correlation. J. Press. Vessel. Technol. **137**, 051302 (2015)
16. Gupta, S., Parameswaran, V., Sutton, M.A., Shukla, A.: Study of dynamic underwater implosion mechanics using digital image correlation. Proc. R. Soc. A Math. Phys. Eng. Sci. **470**(2172), 20140576 (2014)
17. Kyriakides, S., Corona, E.: Mechanics of Offshore Pipelines. Elsevier, Amsterdam (2007)

Chapter 25
Novel Protection Mechanism of Blast and Impact Waves by Using Nanoporous Materials

Weiyi Lu

Abstract Recently, a novel nanoporous materials functionalized liquid (NMFL) system was developed to reduce the incident stress wave and keep it lower than the safety threshold efficiently. The inner surface of the nanopores is nonwettable to the liquid phase by applying special surface treatment. When the nanoporous particles are immersed into the liquid, due to the capillary effect, the nanopores remain empty. The blast wave front, typically with the rising time around 100 μs, can generate high local pressure which compresses the liquid into the nanopores in a few microseconds. A significant amount of the incident energy is converted into heat due to the interfacial tension. Moreover, a considerable fraction of the incident energy can be "captured" through a non-dissipative process due to the small ligament length and the effective multilayer structure with large impedance mismatch of the nanoporous structure.

Keywords: Energy capture • Stress wave • Nanoporous materials functionalized liquid • High strain rate • Mechanical impedance

25.1 Introduction

Bombs, mines, and other improvised explosive devices (IEDs) were a major threat to the U.S. troops, vehicles, and infrastructures. The intensive stress waves associated with these devices lead to traumatic brain injury (TBI)—a signature injury and invisible wound in the battle field [1, 2]. The long-term life quality of the injured soldiers is negatively impacted and the health care cost is tremendous. To prevent the damage caused by the stress waves, energy absorption materials and systems have been developed to mitigate the energy.

Various "soft materials", such as foams [3, 4], CNT forests [5], micro-trusses [6], have been synthesized and utilized as the key component of stress wave mitigation systems by converting incident energy into heat. To maximize the energy mitigation efficiency, the total deformability of these materials can reach 98 % under compression [6, 7]. However, to match the failure strength of the protection target, for instance, biological tissue and brain, the working pressure of these protection systems is pre-determined. By given this, there is no degree of freedom (DoF) for the design. Even worse, the working pressure has to be kept low to ensure the materials are effective for protection and comfortable to wear, and thus, the energy absorption efficiency is low and negligible compared to the amount of input energy. This intrinsic confliction between high efficiency and effectiveness cannot be solved by conventional energy dissipation mechanisms. At least, one more DoF needs to be introduced into the system.

The recently invented nanoporous materials functionalized liquid (NMFL) [8, 9] possesses the extra DoF. It is a liquid suspension of nanoporous particles (NPs). At ambient condition, the nanopores remain empty because of the special treated nanopores surface which is non-wettable to the liquid phase. When the working pressure of the system is reached, the liquid overcomes the energy barrier at the solid-liquid interface and intruded into the nanopores. Due to the extremely large specific surface area of NPs, considerable amount of energy is dissipated into heat. At high strain rate, once the liquid molecules—the energy carrying media, infiltrates into the nanopores, because of the mechanical impedance mismatch between the confined liquid molecules and the rigid nanopore walls and the small ligament length of the nanoporous framework, the energy would be locked inside and the energy transmission path is severely interrupted by the complex microstructure of the nanoporous materials. This non-dissipative protection mechanism is named as Energy Capture [10, 11]. The extra DoF associated with this novel mechanism is that the amount of "captured" energy is independent from the working pressure of the protection system. Be specific, the wave pressure carried by the liquid molecules is always higher than the working

W. Lu (✉)
Department of Civil and Environmental Engineering, Michigan State University, 428 S. Shaw Ln, East Lansing, MI 48824, USA
e-mail: wylu@egr.msu.edu

B. Song et al. (eds.), *Dynamic Behavior of Materials, Volume 1*,
Conference Proceedings of the Society for Experimental Mechanics Series, DOI 10.1007/978-3-319-22452-7_25

pressure of the system, otherwise the system would not be activated. With the higher pressure, the energy locked inside is much larger than the amount of energy dissipated in conventional methods.

In this paper, the working pressure of NMFL is characterized by quasi-static compression test and the dynamic behavior of the NMFL at high strain rate is evaluated by Split Hopkinson Pressure Bar (SHPB) tests. The protection efficiency of the system is analyzed by an energy approach.

25.2 Experiments

25.2.1 Quasi-Static Compression Test

The as received hydrophobic mesoporous silica gel (Sigma-Aldrich, 60755) was surface treated by chloro-dimethyl-octyl-silane. The particle size of the NPs was in the range of 15–35 μm. Gas adsorption analysis was conducted by Tristar 3000 (Micromeritics Corp.) to characterize the porous structure of the NPs. The measured average pore size and specific pore volume were 7.8 nm and 0.55 cm^3/g, respectively. The selected non-wettable liquid phase was saturated lithium chlorid (LiCl) solution (46 wt%).

About 0.4 g of the nanoporous silica gel was added into a stainless steel cell, as depicted in Fig. 25.1a. Then, 1.5 g of saturated LiCl solution was dropped into the cell slowly and the trapped air bubbles were carefully removed. The NMFL was sealed by a stainless steel piston with polyurethane o-ring. The strength and sealing effect of the o-ring were evaluated by compressing the cell filled with neat liquid. Neither leaking nor failure occurred in the testing pressure range. The diameter of the piston and the inner diameter of the cell were 19 mm and the cross-sectional area of the piston, A, was 286 mm^2.

The NMFL was compressed by an Instron 5582 model at a constant loading rate of 0.5 mm/min. When the peak load was reached, the load cell traveled back to its original position at the same rate. The displacement of the piston, d, as shown in Fig. 25.1, and the force applied on it were recorded. Due to the surface property of the nanopores, when the particles were immersed into the liquid phase, the nanopores were empty (Fig. 25.1a). With the aid of external force, the liquid molecules overcome the energy barrier at the solid-liquid interface and intruded into the nanopores. Eventually, the nanopores were fully filled by the liquid molecules (Fig. 25.1b).

25.2.2 Split Hopkinson Pressure Bat (SHPB) Tests

To evaluate the high strain rate behavior of NMFL, SHPB apparatus was employed. Figure 25.2 is the schematic of the experimental setup. The striker, incident bar, and transmission bar were made of stainless steel 17-4 h900 with the diameter

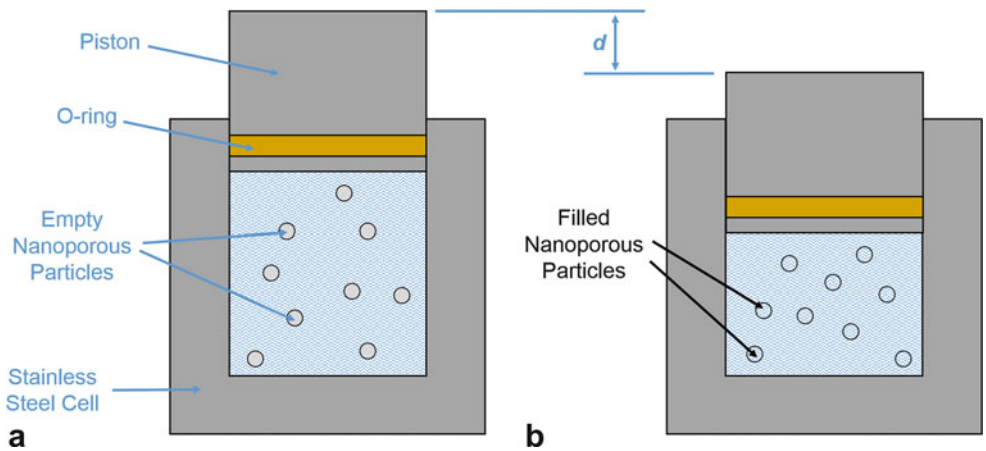

Fig. 25.1 Stainless steel testing cell and sealed NMFL: (**a**) before compression, non-wettable liquid and unoccupied nanopores; (**b**) after compression, the nanopores were fully filled by the infiltrated liquid molecules

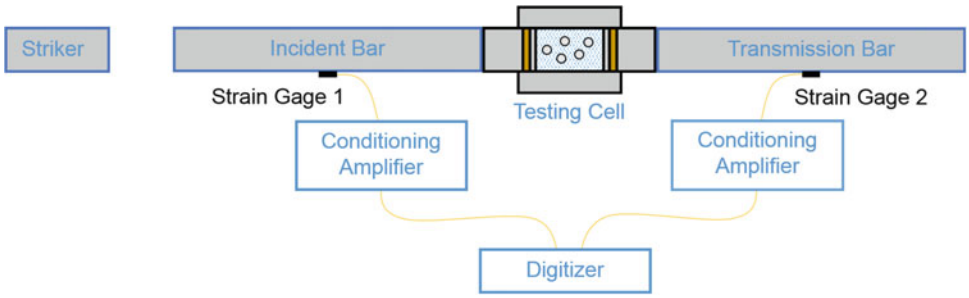

Fig. 25.2 Split Hopkinson Pressure Bar (SHPB) apparatus and dynamic testing setup

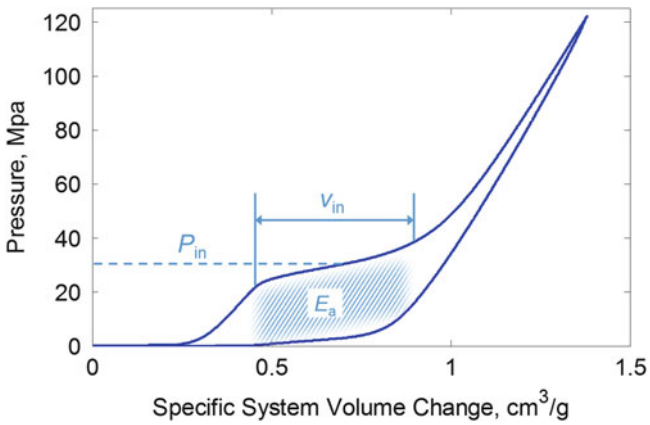

Fig. 25.3 Typical quasi-static loading-unloading curve of NMF liquid

of 12.7 mm and lengths of 304.8, 1219.2, and 1219.2 mm, respectively. The NMFL was sealed in a stainless steel tube with 12.7 mm inner diameter by two movable pistons made of the same stainless steel 17-4 h900 as the bars. The cross-section area, A_s, was 127 mm^2. The testing cell was sandwiched by the incident and transmission bars and thin layers of grease were applied at bar-piston interfaces to eliminate voids between contact surfaces. Since the pistons and bars were made of same material, the signal reflection at these two interfaces could be ignored. The striker was released from a gas chamber and impacted at the front end of the incident bar with a speed of v, which was controlled by the gas pressure in the chamber. The incident speed, the striker length, and the bar material determined the peak wave pressure and the duration of the incident pulse. Because of the aspect ratio and material of the bar, the wave propagation is one dimensional and wave dispersion is negligible. The incident pulse was partially reflected at the piston-NMFL interface and the rest propagated into the transmission bar.

The incident and reflected pulses were measured by a strain gage attached at the center of the incident bar while the transmitted pluse was measured by the strain gage attached at the center of the transmission bar. Two conditioning amplifiers (Vishay Micro-measurement, 2300) were used for each strain gage to amplify the electric signals acquired by the strain gages (Vishay Micro-measurement, WK-13-250BF-10C) and improve the signal-to-noise ratio. The gain was 500 and the cut-off frequency of the filter was 10 kHz. The amplified signals were recorded by a digitizer (National Instruments, PCI-5105) with sampling rate of 10^7 samples/s.

NMFLs with 0.13, 0.25, and 0.50 g NPs were impacted at speed of 5 m/s. In addition, NMFL with 0.25 g NPs was impacted at 10 m/s, and 15 m/s to evaluate the rate effect. The total length of the NMFLs was maintained at 20 mm as a constant. After tests, no leaking or breakage of the cell was observed.

25.3 Results and Discussion

25.3.1 Quasi-Static Compression Test

Figure 25.3 is a typical loading-unloading curve of NMFL under quasi-static compression test which is highly hysteretic and similar to those of conventional systems. The P_{in} and V_{in} in the figure are defined as the liquid infiltration pressure and the

infiltration volume, respectively. Specifically, the stress plateau associated with V_{in} is the process of liquid infiltration and the pressure at mid-point of the plateau is P_{in}. The starting point of the infiltration plateau is where the slope of loading curve is reduced by 50 %, while the ending point is where the slope increased by 50 %. The V_{in} is calculated as $\Delta d \cdot A/m$, where Δd is the total displacement of the piston for liquid infiltration and m is the mass of NPs. From the curve, V_{in} is around 0.5 cm^3/g which is consistent with the gas adsorption analysis result. The minor deficit must be attributed to the van der Waals distance between the liquid molecules and the modified nanopore surface. The infiltration plateau is not perfectly flat because of the narrow pore size distribution in the NPs. The liquid infiltration pressure is proportional to the reciprocal of the nanopore size and starts with the large pores. When the external loading is removed, the defiltration stress plateau with lower pressure was observed indicating the outflow of the liquid molecules from the nanopores.

The area between the infiltration and defiltration plateaus is defined as energy absorption efficiency of NMFL, E_a. As the first order approximation, it can be expressed as

$$E_a = P_{in} V_{in} = \Delta\gamma A_{NP} \tag{25.1}$$

Where $\Delta\gamma$ is the excessive solid-liquid interfacial tension and A_{NP} is the specific surface area of the NPs. At this extremely low strain rate, the main working mechanism of NMFL is energy dissipation. The input mechanical energy is dissipated as heat due to the excessive solid-liquid interfacial tension. The energy absorption efficiency of the NMFL is around 15 J/g which is already an order of magnitude higher than those of conventional foams, thanks to the extremely large specific surface area of the NPs. However, the working pressure of this NMFL is relatively high, around 30 MPa. Hence, it cannot be adopted as protection layer for targets with failure strength lower than P_{in}. With lower P_{in}, E_a would be decreased accordingly.

The elastic limit of the NPs was evaluated by crushing dry particles [12]. No buckling of the nanopore walls was observed until the external pressure reached 400 MPa which is an order of magnitude higher than the liquid infiltration pressure. Therefore, the hysteretic behavior of the NMFL liquid shown in Fig. 25.3 must be attributed to the liquid infiltration without permanent deformation on the NPs.

25.3.2 SHPB Tests

At low strain rate, the energy absorption efficiency of NMFL depends on the liquid infiltration pressure according to Eq. (25.1). Nonetheless, the liquid phase brings in an additional DoF as it is the energy carrying medium in wave propagation. Under dynamic loading conditions, when stress waves are generated, the effect of the liquid phase can be further evaluated. High strain rate tests are conducted on a customized SHPB apparatus. The peak wave pressure of incident pulses as shown in Fig. 25.4a is proportional to the impact speed of the striker which validates the precision of the system [13]. In addition, the momentum, M, of all the tests are conservative as listed in Table 25.1. The momentum of the wave pulses is calculated by Eq. (25.2) and the subscript, i, r, and t represent incident, reflected, and transmitted wave pulses, respectively.

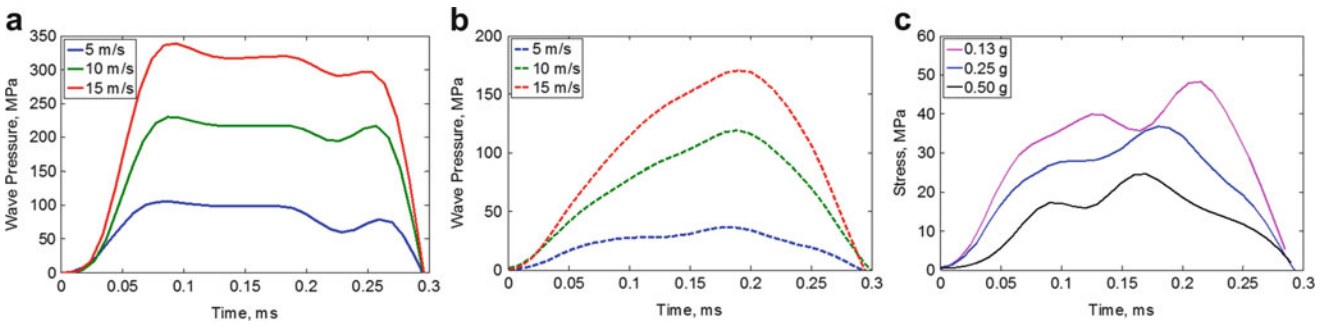

Fig. 25.4 SHPB tests on NMFL: (**a**) Incident pulses at various impact speeds; (**b**) transmitted pulses of NMFL containing 0.25 g NPs at various impact speeds; (**c**) transmitted pulses of NMFL containing different amount of NPs impacted at 5 m/s

Table 25.1 Incident, reflected, and transmitted momentums

NPs (g)	Impact speed (m/s)	M_i (N.s)	M_r (N.s)	M_t (N.s)	r %	t %
0.13	5.42	2.9	1.6	1.1	55.2	37.9
0.25	5.30	2.8	1.8	0.8	64.3	28.6
0.25	10.39	6.4	4.1	2.6	64.1	40.66
0.25	15.38	9.3	5.7	3.8	61.3	40.9
0.50	5.30	2.9	2.2	0.5	75.9	17.2

Table 25.2 Incident, reflected, and transmitted energies

Nps (g)	Impact speed (m/s)	E_i (J)	E_r (J)	E_t (J)	E_c (J)	R %	T %	C %	E_{ce} (J/g)
0.13	5.42	7.1	3.0	1.0	3.1	42.7	14.5	74.8	23.8
0.25	5.30	6.3	3.4	0.6	2.3	54.0	9.5	79.3	9.2
0.25	10.39	33.2	16.5	5.9	10.8	49.7	17.8	64.7	43.2
0.25	15.38	70.4	33.0	12.7	24.7	46.9	18.0	66.0	98.8
0.50	5.30	7.1	4.8	0.2	2.1	67.6	2.8	91.3	4.2

$$M = \int_0^T F dt = \int_0^T \sigma A_s dt = \int_0^T E\varepsilon A_s dt \tag{25.2}$$

Where F is the force applied on the bar, σ is the stress on the bar, E is the Young's modulus of the bar material, ε is the strain measured by the strain gages, and T is the time duration of the pulses.

The voids in NPs significantly reduce the mechanical impedance of NPs. When the mass ratio of NPs in the NMFL increases, the mechanical impedance of the mixture decreases leading to higher ratio of reflected momentum, r%. The NMFL can be regards as a soft material and the stress equilibrium for the SHPB tests may not be fully established, and, thus, the regular stress–strain analysis is not applicable to current study. Alternatively, data analysis approach from the aspect of energy is used. The wave energy (E_x, $x = i, r, t$) has two components—the strain energy (E_s) and the kinetic energy (E_k) of the bar and can be expressed by Eq. (25.3) [14].

$$E_x = E_s + E_k = \left[cA_s/(2E) + \rho A_s c^3/\left(2E^2\right)\right]\int_0^T \sigma^2 dt \tag{25.3}$$

Where c is the longitudinal 1-D wave speed in the bar material and ρ is the density of the bar. The energies of all wave pulses are listed in Table 25.2.

Two sets of SHPB tests were conducted on the NMFLs: (1) the incident speed was fixed at 5 m/s and the load of NPs in the NMFLs were 0.13, 0.25, and 0.50 g; (2) the NPs load was fixed at 0.25 g and the impact speed was adjusted from 5 to 15 m/s. The transmitted wave pulses are displayed in Fig. 25.4b, c.

For the first set of tests, when the load of NPs was increased, less energy transmitted through the NMFL. As mentioned above, this is not only attributed to the increased V_{in} but also related to the larger impedance mismatch between the bar material and the soft NMFL. From Table 25.2, the "energy absorption efficiency" of the NMFLs were 24.4, 9.2, and 4.2 J/g, respectively. Despite the smaller transmitted wave energy, the efficiency of the NMFLs were reduced. For systems with 0.25 and 0.50 g NPs, the efficiency was even lower than the energy absorption efficiency under quasi-static loading condition, E_a. This is because the pore volume of the NPs were not fully utilized, i.e., only a fraction of the NPs were involved in energy absorption while the rest remain empty since the incident energy level was relatively low. However, the "energy absorption efficiency" of the system with only 0.13 g NPs was higher than E_a indicating there must be additional protection mechanism of the NMFL at high strain rate.

In the second series of tests, the impact speed was enhanced as well as the incident energy. At higher impact speeds, the "energy absorption efficiency" of the NMFL was several times higher than E_a and the new energy absorption mechanism associated with the NMFL is energy capture. The energy capture efficiency, E_{ce}, were 43.2 and 98.8 J/g with 10 and 15 m/s impact speeds, respectively. More importantly, the transmitted energy was always 18 % of the incident one (T%). The reflected, transmitted, and capture energy ratios are defined as follows

$$R\% = E_r/E_i$$
$$T\% = E_t/E_i \tag{25.4}$$
$$C\% = E_c/(E_i - E_r) = (E_i - E_r - E_t)/(E_i - E_r)$$

The amount of captured energy by the NMFLs is the missing part from the energies carried by the incident, reflected, and transmitted wave pulses. The effective input energy of the NMFL is the energy difference between the incident pulse and the reflected one. For NMFL with 0.25 g NPs, about 50 % of the incident energy was applied onto it. Then, about 65 % of the effective incident energy was captured by the system. Under high strain rate loading conditions, certain fraction of the incident energy can be captured by the NMFL liquid instead of certain amount of energy can be dissipated as heat. Therefore, the energy capture efficiency of NMFL under dynamic loading is independent from and much higher than its energy absorption efficiency under quasi-static compression. The enhanced performance must be attributed to the interruption of wave propagation path.

The liquid molecules filled nanopores can be treated as a special sandwich structure—the trapped liquid molecules are the soft cores while the rigid nanopore walls are the hard shells. In addition, the wall thickness is at nanometer scale and the nanopore walls are incompressible by the stress waves. The large mechanical impedance mismatch in each sandwich layer suppresses the wave transmission. In a single NP, there may be millions or even billions layers of sandwich structure. This complex microstructure of NPs can efficiently disrupt the wave propagation in NMFL, and, thus, significantly mitigate the incident wave pressure and energy.

The captured energy is not necessary to be completely dissipated or converted into other forms of energy. The liquid infiltration takes place with the aid of external pressure, and thus, the flow rate is much faster than that of liquid defiltration. Given this, the captured energy can be released from the nanopores at a much slower rate. Hence, the intensity of the energy can be reduced to safety level.

25.4 Conclusions

Under dynamic loading conditions, the non-dissipative energy absorption mechanism—energy capture is the main working mechanism of stress wave mitigation. Since the working pressure of NMFLs and the amount of captured incident energy are independent, the energy capture efficiency can be much higher than the energy absorption efficiency. On the other hand, thanks to the liquid component, the protection layer is flexible and comfortable to wear. By using nanoporous materials with lower infiltration pressure, bio-tissues and human bodies can be effectively protected by a thin layer of NMFL. The solid-liquid ratio in NMFL can be further adjusted to optimize the energy capture efficiency.

Acknowledgments The concept generation, the theoretical analysis, and the system design were supported by the National Science Foundation under Grant No. ECCS-1028010. The experimental investigation was supported by the Army Research Office under Grant No. W91CRB-11-C-0112, and the materials preparation was supported by DARPA under Grant No. W91CRB-11-C-0112.

References

1. Lew, H.L., Otis, J.D., Tun, C., Kerns, R.D., Clark, M.E., Cifu, D.X.: Prevalence of chronic pain, posttraumatic stress disorder, and persistent postconcussive symptoms in OIF/OEF veterans: polytrauma clinical triad. J. Rehabil. Res. Dev. **46**(6), 697–702 (2009)
2. Ruff, R.L., Ruff, S.S., Wang, X.F.: Headaches among Operation Iraqi Freedom/Operation Enduring Freedom veterans with mild traumatic brain injury associated with exposures to explosions. J. Rehabil. Res. Dev. **45**(7), 941–952 (2008)
3. Jang, W.Y., Kyriakides, S.: On the crushing of aluminum open-cell foams: part II analysis. Int. J. Solids Struct. **46**(3–4), 635–650 (2009)
4. Jang, W.Y., Kyriakides, S.: On the crushing of aluminum open-cell foams: part I. Experiments. Int. J. Solids Struct. **46**(3–4), 617–634 (2009)
5. Daraio, C., Nesterenko, V.F., Jin, S.H.: Highly nonlinear contact interaction and dynamic energy dissipation by forest of carbon nanotubes. Appl. Phys. Lett. **85**(23), 5724–5726 (2004)
6. Schaedler, T.A., Jacobsen, A.J., Torrents, A., Sorensen, A.E., Lian, J., Greer, J.R., Valdevit, L., Carter, W.B.: Ultralight metallic microlattices. Science **334**(6058), 962–965 (2011)
7. Sun, H.Y., Xu, Z., Gao, C.: Multifunctional, ultra-flyweight, synergistically assembled carbon aerogels. Adv. Mater. **25**(18), 2554–2560 (2013)
8. Han, A.J., Lu, W.Y., Kim, T., Punyamurtula, V.K., Qiao, Y.: The dependence of infiltration pressure and volume in zeolite Y on potassium chloride concentration. Smart Mater. Struct. **18**(2), 1 (2009)

9. Liu, L., Chen, X., Lu, W.Y., Han, A.J., Qiao, Y.: Infiltration of electrolytes in molecular-sized nanopores. Phys. Rev. Lett. **102**(18), 184501 (2009)
10. Xu, B.X., Chen, X., Lu, W.Y., Zhao, C., Qiao, Y.: Non-dissipative energy capture of confined liquid in nanopores. Appl. Phys. Lett. **104**(20), 203107 (2014)
11. Xu, B.X., Qiao, Y., Chen, X.: Mitigating impact/blast energy via a novel nanofluidic energy capture mechanism. J. Mech. Phys. Solids **62**, 194–208 (2014)
12. Han, A., Punyamurtula, V.K., Lu, W.Y., Qiao, Y.: Deformation of a nanoporous silica under compressive loading. J. Appl. Phys. **103**(8), 084318 (2008)
13. Wang, Z.G., Meyer, L.W.: On the plastic wave propagation along the specimen length in SHPB test. Exp. Mech. **50**(7), 1061–1074 (2010)
14. Surani, F.B., Kong, X.G., Panchal, D.B., Qiao, Y.: Energy absorption of a nanoporous system subjected to dynamic loadings. Appl. Phys. Lett. **87**(16), 163111 (2005)

Chapter 26
Response of Material Under Blast Loading

Dan Schleh, Guojing Li, and Dahsin Liu

Abstract A shock tube based laboratory testing facility was used for simulating blast loading to characterize the response of circular metallic specimens. Measuring techniques including electrical resistance strain gages, fringe projection and others were used for recording and comparing the critical strains and deformation histories during and after blast loading.

Keywords Blast • Shock tube • Deformation • Strain • Fringe projection

26.1 Experimental Techniques

26.1.1 Shock Tube Based Blast Testing

In this study, a shock tube was used for generating blast waves. The shock tube was comprised of three pressure tubes-shaped chambers, namely the high-pressure chamber, the intermediate-pressure chamber and the low-pressure chamber. A blast containment chamber, as illustrated in Fig. 26.1, was joined to the end of the shock tube to enclose the specimen during blast testing. The high-pressure chamber and the low-pressure chamber store pressurized gases and are responsible for the ultimate output pressure from the shock tube for blast testing. The intermediate-pressure chamber is a small chamber situated between the high-pressure and the low-pressure chambers with one notched diaphragm on each of its ends. The notches are carefully designed and prepared to control the rupture of the diaphragms, hence providing a means to regulate the function of the blast tube. A piston may be added to the low-pressure chamber when significantly high output pressure is desired.

To operate the shock tube, the high-pressure and the low-pressure chambers along with the partitioned intermediate-pressure chamber, which is located between the high-pressure and the low-pressure chambers, are simultaneously pressurized with individual levels of gas to achieve a desired output pressure wave based on gas-dynamic analysis. When the gas in the intermediate-pressure chamber is vented out, a significant difference in pressure between the high-pressure chamber and the intermediate-pressure chamber can take place, resulting in the rupture of the diaphragm between the chambers. Almost instantaneously, the diaphragm separating the intermediate-pressure chamber and the low-pressure chambers also ruptures. The flow and expansion of the gas into the low-pressure chamber drives the piston positioned near the boundary between the intermediate-pressure chamber and the low-pressure chamber towards the nozzle located at the end of the shock tube, i.e. the end of the low-pressure chamber.

At the end of the low-pressure chamber, there exists a small-diameter tube, such as a nozzle, to further pressurize the gas in the low-pressure chamber. Hence, a third diaphragm should be installed between the low-pressure chamber and the nozzle. Consequently, as the piston moves down the low-pressure chamber and toward the nozzle, the gas that exists between the piston and the nozzle diaphragm compresses, causing the pressure to build up. When the pressure becomes sufficient high to rupture the nozzle diaphragm, it sends the pressure wave that has developed through the nozzle towards the specimen surface. Associated with the rapid change in pressure is the significant rise in temperature that last for a short duration. The high temperature that is produced as a result of the pressure change is high enough to cause combustion, resulting in bright flashes. The gas in the low-pressure chamber also serves to slow down the piston to prevent it from severely colliding onto the nozzle. The specimen to be tested is located at the end of the nozzle and inside the blast

D. Schleh • G. Li • D. Liu (✉)
Department of Mechanical Engineering, Composite Vehicle Research Center, Michigan State University,
2727 Alliance Drive, Lansing, MI 48910, USA
e-mail: liu@msu.edu

B. Song et al. (eds.), *Dynamic Behavior of Materials, Volume 1*,
Conference Proceedings of the Society for Experimental Mechanics Series, DOI 10.1007/978-3-319-22452-7_26

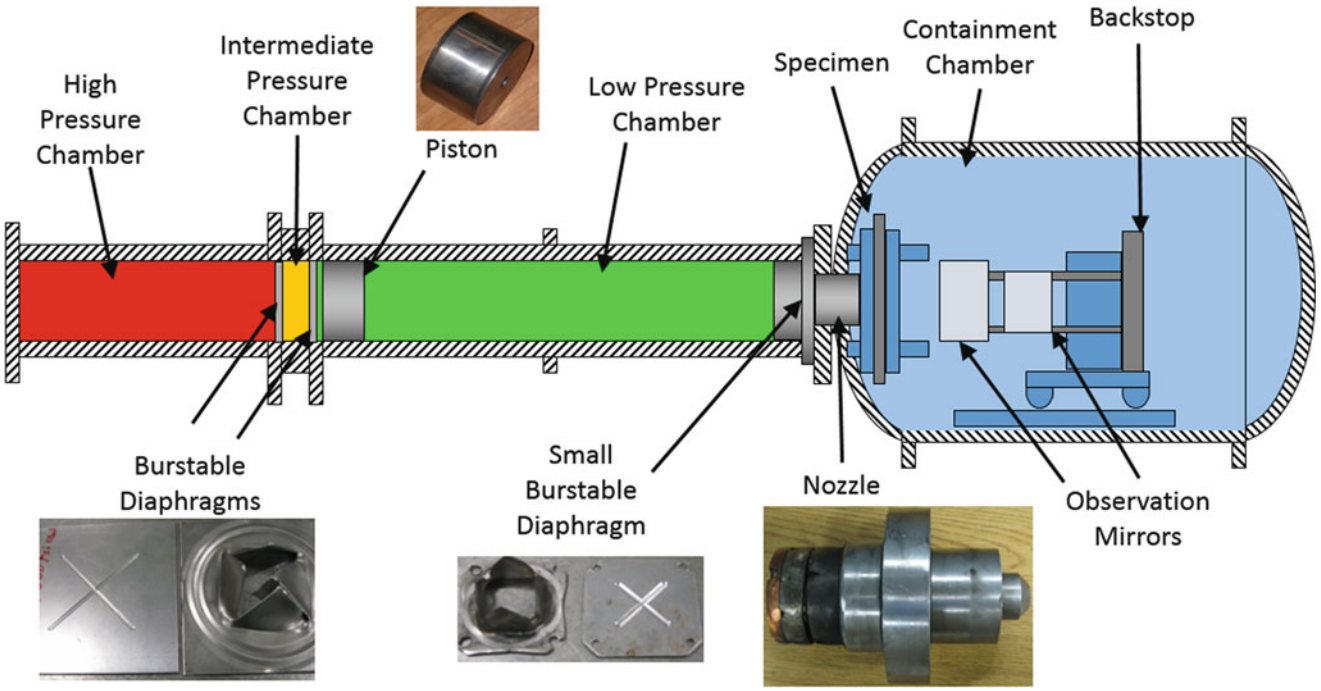

Fig. 26.1 Schematic of the shock tube with images of shock tube components

containment chamber during testing. Due to the high pressure environment, testing specimens are placed in a fixture which is fastened to the end of the low-pressure chamber as seen in Fig. 26.1.

26.1.2 Specimen Dimensions and Boundary Conditions

A metallic material was investigated in this study. Circular specimens with diameters of 76 and 178 mm were used. For each testing diameter, plates with both thicknesses of 1.59 and 3.18 mm were subject to shockwave loading. In performing the blast testing, each specimen must be firmly secured in a rigid fixture before being attached to a testing frame due to the violent testing environment.

For all the specimens tested, the thickness of the region clamped in contact with the fixture was 6.38 mm. For the specimens of 76 mm in diameter and 1.59 mm in thickness, initial test results demonstrated a shearing out of the test region right at the fixture opening. In an attempt to relieve the stress concentration developing at the boundary, a transition fillet was added to the subsequent 76 mm diameter and 1.59 mm thick specimens. The consequence of adding the fillet was that the test region on the specimen increased slightly in diameter. Despite the slight increase in diameter of the specimen, the diameter of the fixture providing support for the specimen remained unchanged at 76 mm.

26.1.3 Pressure Profiles

Pressure profiles served as the quantification of the shockwave loading applied to the specimens. The general controllable characteristics of the pressure waves were the magnitude and the duration of loading. To control these characteristics, several variables were adjusted. They included the magnitudes of the high-pressure and low-pressure chambers, the piston mass, and the nozzle diameter.

A number of different pressure profiles were explored while only six were specifically used for testing. For each of these six profiles, one of each specimen with a diameter of 76 or 175 mm and a thickness of 1.59 or 3.18 mm was tested. Graphical representations of the six pressure profiles can be seen in Fig. 26.2 while some specific values are given in Table 26.1. In Table 26.2, the 'Output (kPa*s)' is the integration of the pressure profiles of Fig. 26.2 with respect to time. The 'Total

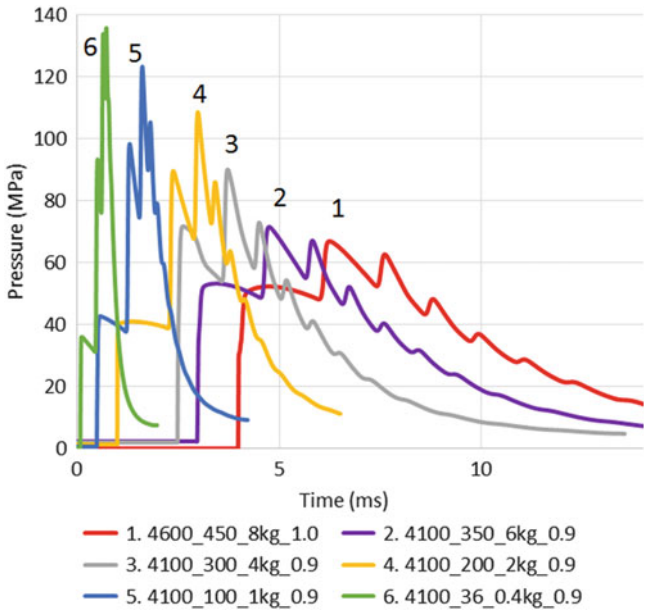

Fig. 26.2 Various pressure curves based on various pressure profiles

Table 26.1 Characteristics of pressure profiles

Pressure profile number	High pressure chamber, MPa (psi)	Low pressure chamber, MPa (psi)	Piston mass, kg	Nozzle diameter, mm (in)	Peak pressure, MPa	Total duration, ms	Output, kPa*s (psi*s)
1.	32.2 (4600)	3.15 (450)	8	25.4 (1)	62.7	12.38	416.4 (60.39)
2.	28.7 (4100)	2.45 (350)	6	22.86 (0.9)	71.5	10.16	350.2 (50.79)
3.	28.7 (4100)	2.1 (300)	4	22.86 (0.9)	90	7.68	277.6 (40.26)
4.	28.7 (4100)	1.4 (200)	2	22.86 (0.9)	108.5	6.51	246.5 (35.75)
5.	28.7 (4100)	0.7 (100)	1	22.9 (0.9)	123.2	3.98	146.5 (21.25)
6.	28.7 (4100)	0.252 (36)	0.4	22.86 (0.9)	133.7	2.17	69.8 (10.12)

Table 26.2 Apex displacements from digital indicator after tests

Pressure profile	Output, kPa*s (psi*s)	Al-3´´-1/16´´	Al-3´´-1/8´´, mm	Al-7´´-1/16´´	Al-7´´-1/8´´, mm
1. 4600psi-450psi-8kg-D1.0inch	416.4 (60.39)	Rupture	Rupture debris strike	Rupture	7.74
					10.6
2. 4100psi-350psi-6kg-D0.9inch	350.2 (50.79)	Rupture	6.30	Rupture	8.95
3. 4100psi-300psi-4kg-D0.9inch	277.6 (40.26)	Rupture	4.59	Rupture	9.09
4. 4100psi-200psi-2kg-D0.9inch	246.5 (35.75)	Rupture	7.57	Rupture	10.1
5. 4100psi-100psi-1kg-D0.9inch	146.5 (21.25)	Rupture	12	Rupture	14.5
6. 4100psi-36psi-0.4kg-D0.9inch	69.8 (10.12)	Rupture	9.18	Rupture	11.1

Duration (ms)' is the time between the initial sharp increase in pressure and the time required for the magnitude of the pressure to decrease to roughly 10 MPa.

The pressure curves given in Fig. 26.1 were obtained from theoretical calculations. These calculations were validated using pressure sensors positioned in the shock tube. Validation of the calculated profiles was neither conducted for every test nor for every testing scenario. It was assumed that for a given loading condition (high pressure, low pressure, piston mass and nozzle diameter) the pressure profile would be consistent. Simulation data, instead of measured data based on pressure sensor, was then used due to the cost of pressure sensors. For validating the simulation data, a Kulite HKS-11-375 high pressure dynamic transducer was used, which can withstand 206 MPa and 300 °F. After one to two tests, the sensor no longer produced an accurate signal despite their maximum pressure rating remaining within the high pressures in the shock tube. Validation tests where pressure transducers were inserted in the shock tube at multiple points were performed. Figure 26.3 compares the data from the calculation with that measured by the pressure transducer.

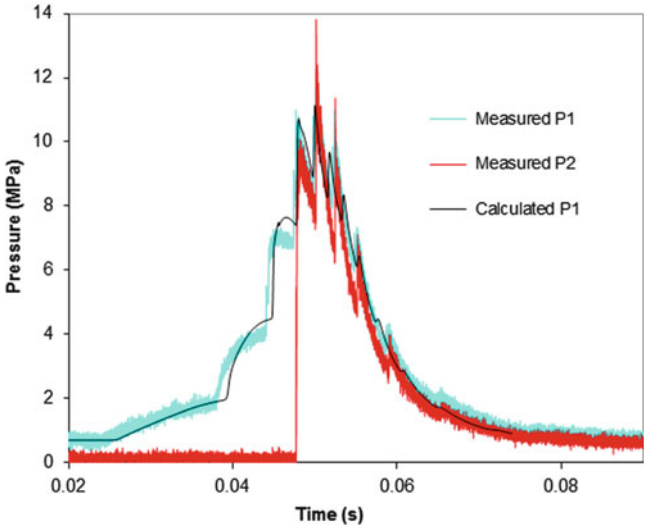

Fig. 26.3 Comparisons of pressure histories obtained from calculation and measurements

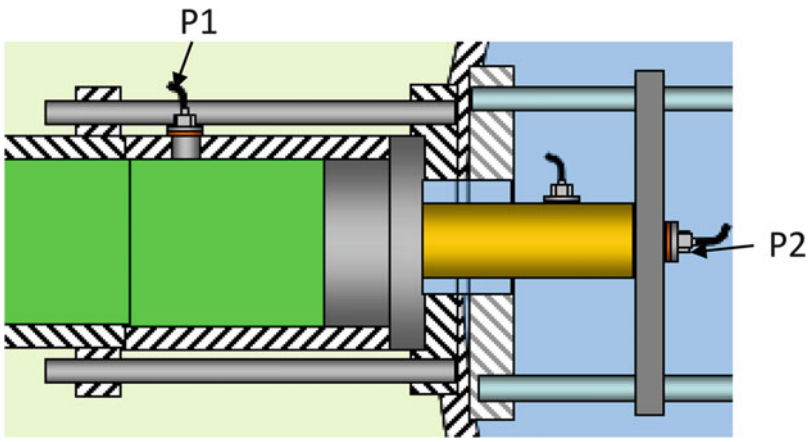

Fig. 26.4 Pressure transducer locations within shock tube

As shown in Fig. 26.3, the pressure curve obtained from transducer P1 (located close to the end of the low-pressure chamber as shown in Fig. 26.4) and that obtained from the calculated P1 demonstrates a good agreement. This confirms the feasibility of using the computational scheme in the design and application of pressure profiles for the concerned tests. The measured P2 (based on a transducer located at the end of the blast nozzle as shown in Fig. 26.4), however, shows a discrepancy from the pressure measured at P1 and the calculated P1 data set. The measured P2 has a very sharp increase in pressure while calculated P1 and measured P1 show a more gradual increase in pressure at the beginning of the curve. The difference is believed to come from the rupture of a small diaphragm imposed between the low pressure chamber and the nozzle as shown in Fig. 26.4. Both measured P1 and calculated P1, however, are obtained from within the low-pressure chamber. The bumps in the ascending portions of them are due to the movement of the piston toward the end of the low-pressure chamber while compressing the air in front of it. The measured P2, however, is neither in the low-pressure chamber nor any pressurized environment. It is subject to atmospheric pressure. The drastic pressure increase is sudden as it occurs due to the rupture of a small diaphragm that is positioned close to the sensor.

In the development of the pressure curves of Fig. 26.2, the differences among the measured P2, calculated P1 and measured P1 were taken into consideration. For the calculated curves to represent the loading at P2 in Fig. 26.3, the discrepancy at the beginning of loading between calculated P1 and measured P2 was removed from the calculated P1 to arrive at a pressure profile for application. In addition, it should be noted that the pressure sensor located at P2 for pressure verification testing was mounted in a steel block where no significant plastic deformation occurred. However, it is noted that specimen may deform as loading occurs, creating a gap between the end of the nozzle and the specimen surface. This could be influential as it allows pressure to dissipate. Due to the lack of a durable (for multiple uses) and accurate (without disturbing the pressure profile) sensor for monitoring high-pressure waves in tests, only limited tests were performed with pressure sensors. Some pressure profiles based on removing the initial portion of calculated P1 were used in this study.

26.2 Experimental Results

Several techniques were employed before and after testing for measurements of specimen response. During testing, fringe projection and strain gages were used in attempts to garner time-dependent data. Fringe projection produces whole-field out-of-plane displacements through images captured during testing by considering the changes that occur in projected shadows. Strain gages were adhered to the center of plates to measure strain data at the plate center during loading. After testing, the apex of test specimens was measured using a digital indicator. In some cases fringe projection was applied to gather an out-of-plane displacement profile through the apex of deformation as a function of position on the plate.

26.2.1 Fringe Projection During Testing

Fringe projection uses differences in shadows that take the form of lines to deduce out-of-plane differences between images. In the application of fringe projection to the dynamic testing environment of the shock tube, a high-speed camera and a strong light source were required. The light source was placed behind a grating and shadows from the grating were projected onto the test specimens through a lens. Images of the test specimen surface were recorded during the test. Because of the potential for damage to the high-speed camera and the light source projecting the shadows, both pieces of equipment were placed outside of the blast containment chamber. Two portals in the side of the blast containment chamber were used to allow visual access to the test specimen. Since the line of sight through the portals is perpendicular to the transverse axis of the test specimen, mirrors were required inside of the blast containment chamber to aid in viewing. The mirrors inside the blast containment chamber were mounted to a removable 200 kg cart that also serves as a back stop to blasts. Figure 26.5 shows the setup of the fringe projection system.

Fringe projection was applied to some tests. The test results generated from fringe projection were not always great due to the harsh operating environment existing during testing. Shock wave testing caused large changes in temperature which in turn may cause combustion of gases, grease and debris. When the combustion occurred, light was generated. The flashes of light interfered with image acquisition of the shadows as they not only drown out the shadows, but often the entire viewing window. Fringe projection was also challenging in shock tube testing due to vibrations and debris. When a test was run, there

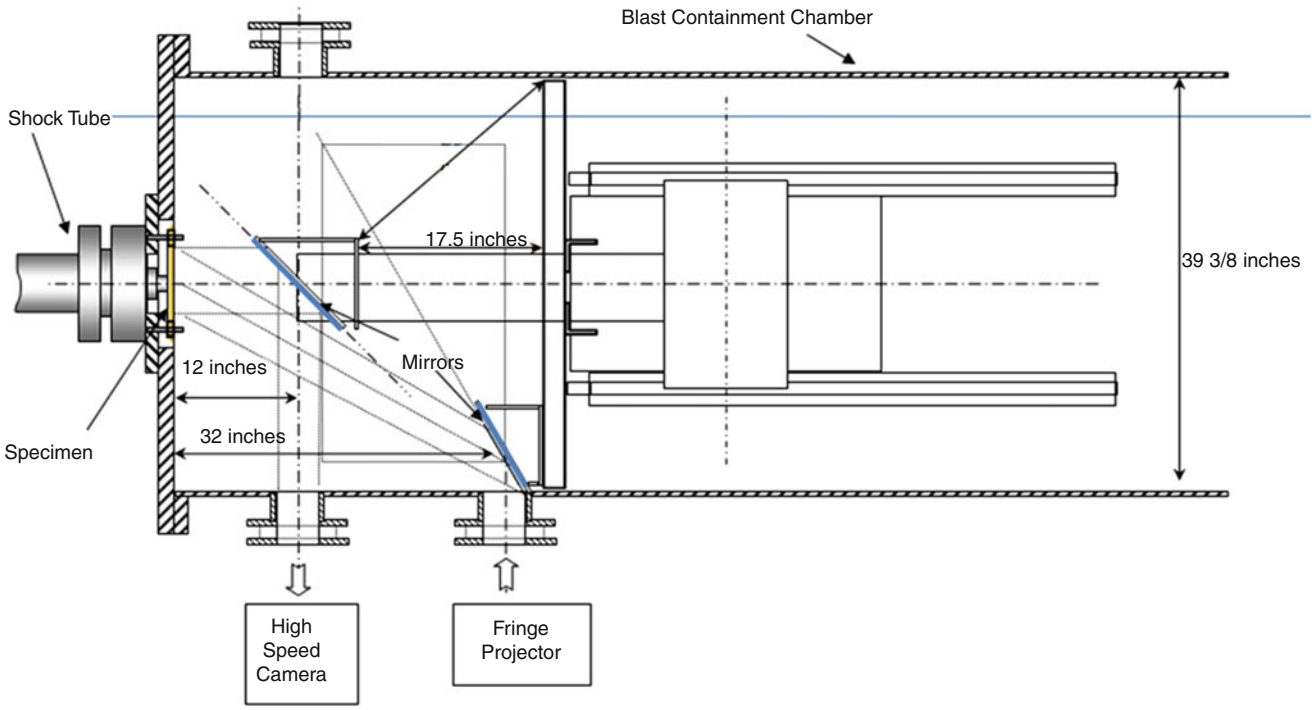

Fig. 26.5 Fringe projection system for shock tube testing

Table 26.3 Fringe projection and digital indicator apex measurements performed after testing

Metal 7″ Dia., 1/8″ thick plates		
Out-of-plane displacements (mm)		
Test designator	Digital indicator	Fringe projection
T4A	10.11	9.76
T14A	11.05	10.69
T20A	8.946	8.95
T33A	9.09	8.87
T46A	14.48	14.23
T56A	7.74	7.67
T60A	10.62	10.45

was significant vibration in many components of the shock tube and the cart supporting the mirrors was not immune to this. Consequently, when the mirrors shook, so did the view of the specimen, causing blurring of the projected shadows. Additionally, shock wave loading had a tendency to stir up any dust or debris that was in the blast containment chamber. Having extra dust in the air eventually caused the image to darken to the point where the specimen became unrecognizable. Dust could also obscure the projected shadows. To record images during testing, images must be collected at a high rate of capture, often 10,000 fps or above. High frame rates often resulted in a reduction in time that the sensor in camera had to collect light. This meant that images captured at high frame rates tended to be darker than those collected at low frame rates. Table 26.3 shows the comparison between those from fringe projection and a digital indicator at the apex of tested specimens. They seem to have good agreement.

26.2.2 Strain Gages During Testing

Strain gages were mounted on the surface of plates prior to testing to allow for the measurement of strain at the center of the plate during testing. The use of strain gages was attempted for a few tests. Strain gage results only captured a small segment of the loading sequence. The lead wires to the strain gages would often disconnect within 0.05 ms from the start of loading while loading durations of the shock wave can range from 0.5 to 10 ms.

26.3 Summary

The shock tube based blasting facility was proved to be effective for simulating thin metallic materials under blast loading. The measuring techniques, including strain gage and fringe projection, were also demonstrated to be capable of recording critical information up to some extent during and after the blast testing.

Acknowledgment The financial support from the U.S. Army RDECOM Tank-Automotive Research, Development & Engineering Center (TARDEC) is greatly appreciated.

Chapter 27
Using Richtmyer–Meshkov Instabilities to Estimate Metal Strength at Very High Rates

Michael B. Prime, William T. Buttler, Sky K. Sjue, Brian J. Jensen, Fesseha G. Mariam, David M. Oró, Cora L. Pack, Joseph B. Stone, Dale Tupa, and Wendy Vogan-McNeil

Abstract Recently, Richtmyer–Meshkov instabilities (RMI) have been proposed for studying strength at strain rates up to 10^7/s. RMI experiments involve shocking a metal interface that has geometrical perturbations that invert and grow subsequent to the shock. As these perturbations grow, their growth may arrest, or they may grow unstably and eventually fail. The experiments observe the growth and arrest to study the specimen's yield (deviatoric) strength. Along these lines we first review some RMI experimental results on Cu. Next, the paper presents explicit Lagrangian simulations used to help interpret the Cu RMI results and infer the strength, i.e. flow stress, of the target metal. A Preston-Tonks-Wallace (PTW) constitutive model is modified to be more accurate at the strain rates accessed in the experiment. The advantages and disadvantages of RMI, as compared to the Rayleigh–Taylor (shockless) instabilities that are used more commonly to infer strength, are discussed. The advantages of using simple velocimetry measurements in place of radiography are also discussed.

Keywords Richtmyer–Meshkov instabilities • Shock • High strain rate • Strength • Rayleigh–Taylor

27.1 Introduction

Rayleigh Taylor (RT) instabilities have long been used to infer material strength [1–3] and recently have been instrumental in developing sophisticated constitutive models for the high-pressure, high-rate regimes accessed in such experiments [4, 5]. Figure 27.1 illustrates a typical RT experiment. In the RT geometry, gaseous detonation products from a high explosive (HE) expand across a vacuum gap and shocklessly accelerate a sample that has initial geometric perturbations. Strength (meaning resistance to deviatoric, i.e., shear, deformation) moderates the growth rates of the instabilities. The perturbation growth rates, measured experimentally with radiography, are then used to indirectly estimate the strength of the sample at very high strain rates.

Only more recently, Richtmyer–Meshkov Instabilities (RMI) have also been shown to be sensitive to strength at strain rates up to 10^7/s [6–13]. Figure 27.2 illustrates an RMI experiment in the configuration fielded in recent experiments [8, 9]. In contrast to the RT experiments, the sample in the RMI experiment is loaded by a shock rather than by a shockless acceleration. Also, strength is determined by testing different sized perturbations and finding those where strength *arrests* the instability growth, as compared to measuring growth rates as is done in RT experiments.

Figure 27.2 shows an RMI experiment for the case of the perturbations on the free surface opposite of the shock loading (Atwood number $A_t = -1$). This free surface configuration is the only published experimental implementation of RMI for strength measurements [8, 9, 14] maybe partly because it is easier to diagnose a free surface but also because it studies the question of ejecta from a shocked surface [9, 14–19]. The original idea for RMI strength measurements [6, 7] described a configuration where the perturbations were an inner surface in the experiment (e.g., $A_t = +1$), which follows the more traditional fluid mechanics view of RMI, but are more difficult to experimentally field and diagnose. Note that in the configuration of Fig. 27.2, the shock releases quickly from the free surface, so most of the spike growth and arrest occurs at low pressure. In the traditional $A_t = +1$ configuration, the shock pressure is supported during spike growth and arrest.

M.B. Prime (✉) • W.T. Buttler • S.K. Sjue • B.J. Jensen • F.G. Mariam • D.M. Oró • C.L. Pack • J.B. Stone • D. Tupa • W. Vogan-McNeil
Los Alamos National Laboratory, P.O. Box 1663, Los Alamos, NM 87545, USA
e-mail: prime@lanl.gov

B. Song et al. (eds.), *Dynamic Behavior of Materials, Volume 1*,
Conference Proceedings of the Society for Experimental Mechanics Series, DOI 10.1007/978-3-319-22452-7_27

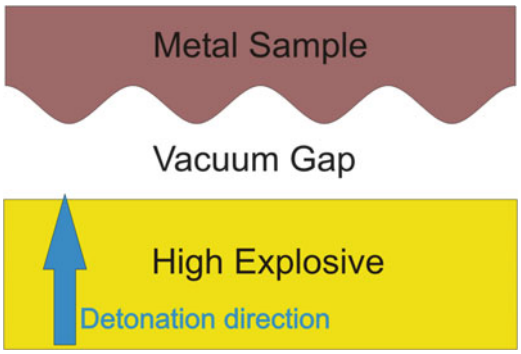

Fig. 27.1 Schematic of Rayleigh–Taylor instability experiment. The HE detonation products *shocklessly* accelerate the perturbed surface of the sample

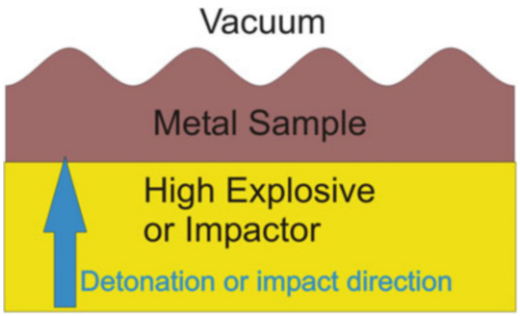

Fig. 27.2 Schematic of a Richtmyer–Meshkov instability experiment (for Atwood $= -1$). The perturbed surface of the sample is accelerated by a *shock* from an impact or from HE detonation

27.2 Experiment

A set of experiments performed in the Fig. 27.2 configuration, to study strength in Cu, are analyzed using hydrodynamic modeling to continue work from a previous study [13]. The new experiments reported here are virtually identical to a set of experiments reported in detail elsewhere [9, 14]. The experiment uses a plane wave lens and a momentum trapping target to approximate the ideal conditions illustrated in Fig. 27.2. The experiments were diagnosed using proton radiography [20] and Photon Doppler Velocimetry (PDV) [21]. The target uses OFHC Cu in the half-hard state with a total thickness of 8 mm. The sine wave perturbations have a wavelength, λ, of 550 μm. In the new study, five initial perturbation amplitudes were studied, $\eta_0 =$ 28–55 μm, to give non-dimensional $\eta_0 k$ (where $k = 2\pi/\lambda$) of 0.32, 0.38, 0.45, 0.53 and 063. These $\eta_0 k$'s were chosen to better constrain the previous results [9, 14], where a $\eta_0 k = 0.35$ case had significant spike growth and arrest, but where the next bigger $\eta_0 k$, 0.75 had unstable spike growth. By further mapping the $\eta_0 k$ regime where there is spike growth that arrests, the regime with the most sensitivity to strength, it is hoped to refine the strength information that can be extracted.

27.3 Modeling

Continuum simulations were performed using Flag, a Lagrangian hydrodynamics code [22, 23]. The simulations were similar to those used in a previous study [13], but with some updates. Each simulation used a two-dimensional plane strain mesh that modeled two full wavelengths of the perturbation, see Fig. 27.3, and had constraints on the top and bottom to prevent vertical displacements, effectively assuming periodic behavior.

The PBX 9501 HE was modeled using a JWL equation of state with constants from Dobratz [24] and programmed burn. The Cu sample was modeled using SESAME tabular equation of state 3336 [25], a Preston-Wonks-Wallace (PTW) deviatoric strength model [26], and the Tonks ductile damage and failure model [27–30]. The Tonks damage model was previously calibrated for Cu using flyer plate spall data and, notably, incipient spall data with experimentally measured distributions of porosity [31].

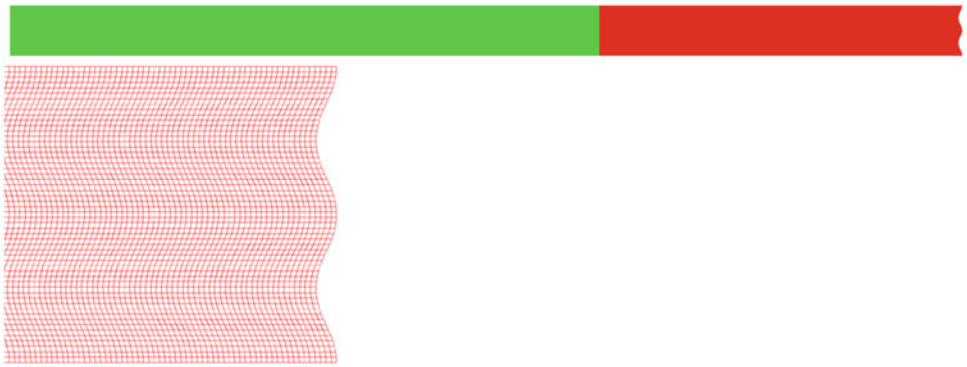

Fig. 27.3 (*Top*) The overall mesh for the simulation uses Cartesian 2D plane strain elements. The *top* and *bottom* surfaces have vertical displacement constraints to enforce periodicity. The *green* portion is 13 mm of PBX 9501 HE with a planar detonation at the left end at $t = 0$. The *red* potion is the Cu target. (*Left*) Zoomed in on the free surface showing that two full periods of the sine wave are modeled using 20 μm zoning

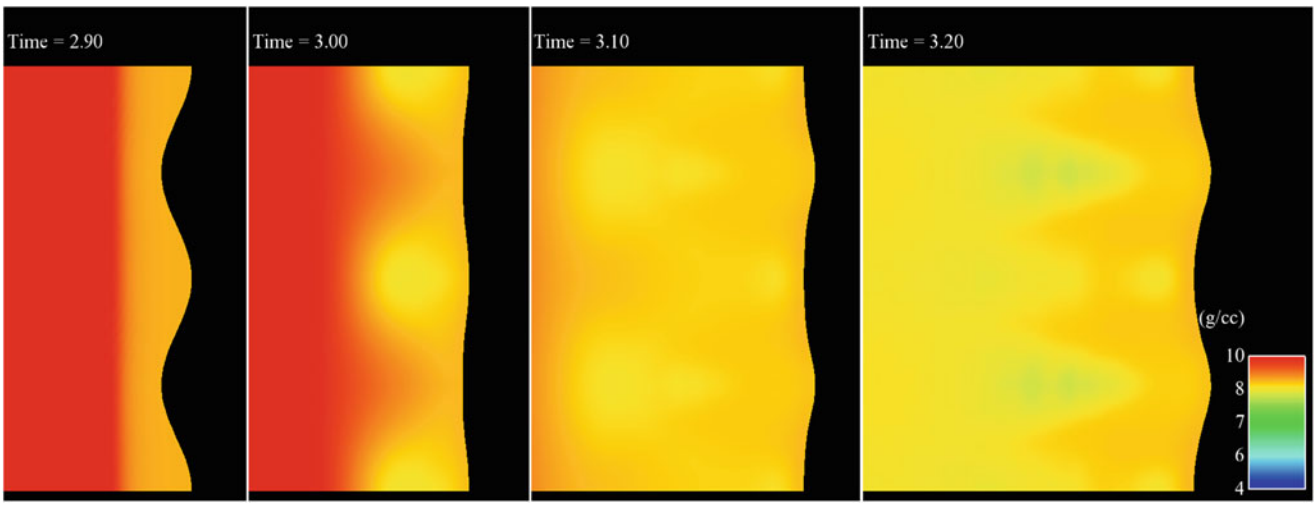

Fig. 27.4 Model snapshots of the inversion, growth and arrest of Richtmyer–Meshkov instabilities in Cu. The density coloration shows the incoming shock, free surface release, and the beginnings of porosity development from tension

27.4 Results

We present results from the $\eta_0 k = 0.45$ case, which arrested, because the cases with $\eta_0 k \geq 0.53$ grew unstably. Figure 27.4 shows several snapshots from the simulation, with times taken relative to detonation of the HE. At 2.9 μs, the rightward moving shock is about to reach the free surface with the initial perturbations. At 3.0- and 3.1-μs the perturbations invert and grow as the shock releases at the vacuum-surface interface. By 3.2 μs the perturbation growth has essentially arrested and the damage model has predicted some porosity growth caused by tension. The porosity growth can be seen by the regions with densities below the nominal.

Figure 27.5 shows the PDV-measured velocities for $\eta_0 k = 0.45$. The PDV spot size is sufficient to see a full perturbation wavelength, so the plotted velocity spectra includes the high and low spots of the final perturbations, also known as the spikes and bubbles. The peak velocity is that of the spike, which decays back to the 1.5 mm/μs level of the overall free surface, thus indicating arrest of the spike growth. Figure 27.6 shows the spike velocity, extracted from the data of Fig. 27.5, compared with the results of the hydrodynamic simulation. The simulation has predicted too low of a spike velocity. The total predicted spike growth, which equals the area between the spike velocity curve and the velocity of the overall free surface, is therefore significantly under predicted. Those discrepancies occur because the PTW strength model is too strong is this regime.

The PTW model was calibrated using quasi-static and Hopkinson bar stress-strain data taken at rates from 10^{-3}/s to 2800/s and temperatures from 77 to 473 K. The hydrodynamic simulation of this RMI experiment indicated that the spike

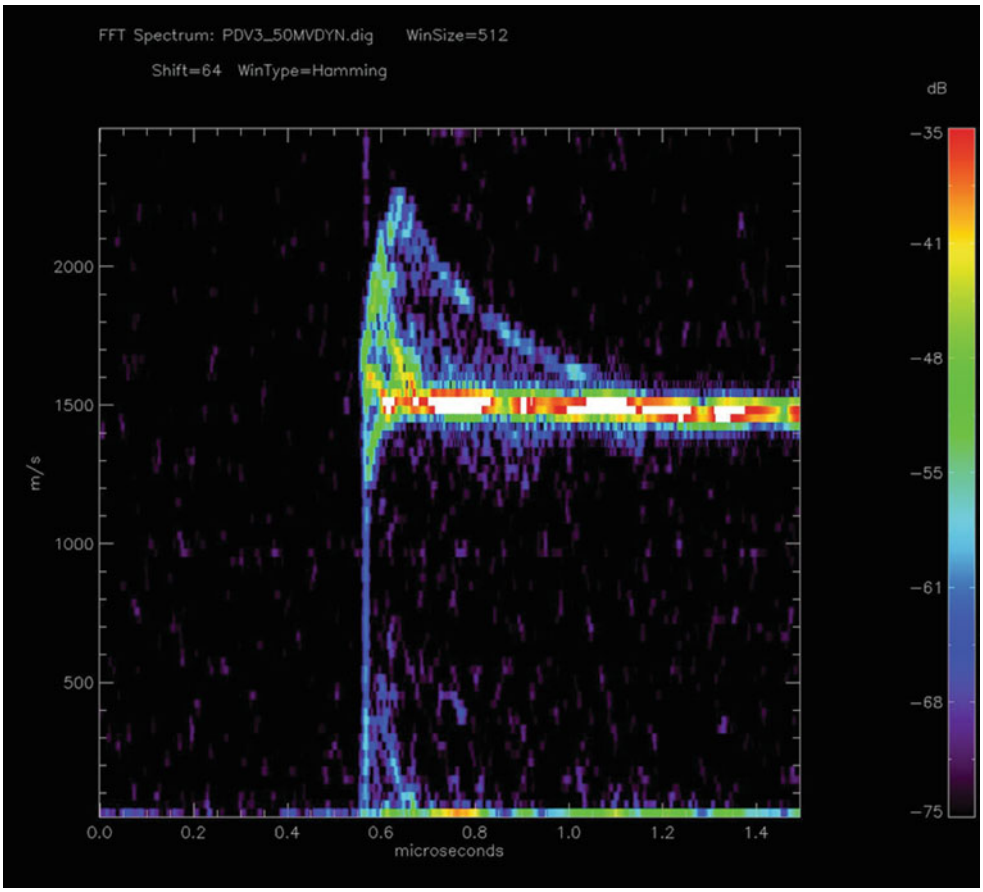

Fig. 27.5 Experimentally measured velocity spectra for the $\eta_0 k = 0.45$ case. The PDV probes simultaneously measures all the surface in its field of view, with the maximum value in this plot corresponding to the spike

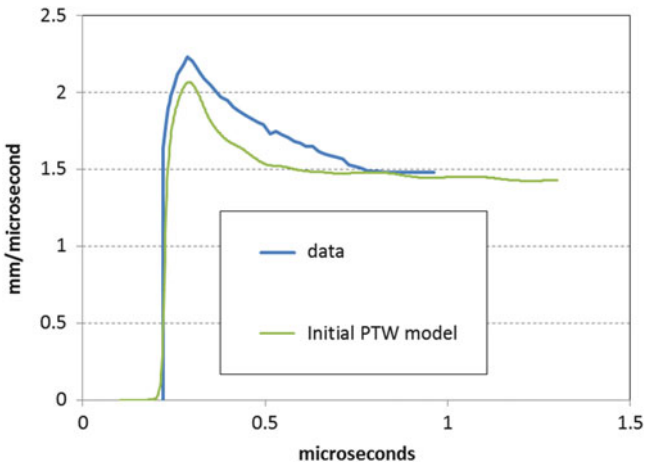

Fig. 27.6 The initial model prediction underestimates the velocity and therefore the total spike growth, which indicates that the model has the Cu too strong

growth and arrest occurs mostly at strain rates between 1.5×10^6 and 6.0×10^6/s. The analysis of the previous RMI experiments in this series [9], which includes a modification to the Piriz equation [7], estimated an average flow strength of 520 MPa. In this 10^6/s strain rate regime, the PTW model is transitioning from a thermally-activated dislocation glide regime for modest strain rates (say up to the calibration data of about 10^4/s) to the strong shock (phonon drag) regime of 10^9/s and up. There is no experimental basis for the PTW model parameters used for this transition region. For the half-hard copper in this experiment, the default parameters from annealed copper together with the thermally activated regime parameters fit

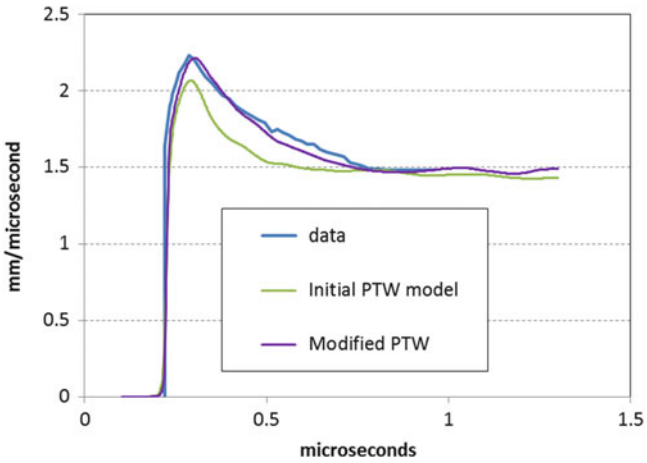

Fig. 27.7 The modified PTW strength model fits the data very well

Table 27.1 Comparing different types on dynamic instability-based experiments that can be used to infer strength at very high rates

	Rayleigh–Taylor	Richtmyer–Meshkov Atwood = +1	Richtmyer–Meshkov Atwood = −1
Acceleration	Shockless	Shock	Shock
Strain rate	High	High	High
Pressure	High (confined)	High (confined)	Low (free surface releases)
Diagnostics	Radiography	Radiography	Surface velocimetry (radiography can be added)
Measured behavior	Growth rate	Arrest—final spike height	Arrest—final spike height

to half-hard copper had the strength already transitioning to the much stronger phonon drag regime when the strain rates exceeded 10^6/s giving an initial yield strength of approximately 1600 MPa at a strain rate of 5.0×10^6/s.

A simple approach was used to modify PTW. The 520 MPa estimated strength, in spite of representing only a time and spatial average of strength, was used to modify two PTW parameters, y_1 and y_2, such that the yield strength passed approximately through 520 MPa at the strain rates between 1.5×10^6 and 6.0×10^6/s that were estimated for the experiment. The PTW model was not affected at lower rates. Effectively, this modification extended the thermally-activated regime strengths until the rates exceed about 10^7/s. Figure 27.7 shows the simulation results with the new PTW model, and the agreement with data is excellent. The simulations indicate that the total plastic strain reaches about 90 % in the spike for $\eta_0 k = 0.45$. Nonetheless, calculations indicate that the velocity predictions are more sensitive to yield stress than to saturation stress, as has been observed before [13]. Therefore, the saturation stress in the model was not modified. Note that Rayleigh Taylor instability experiments have also been used to constrain PTW models in a similar strain rate regime [32].

27.5 Conclusions

RMI experiments on Cu were used modify a PTW constitutive model in the regime between 10^4 and 10^7/s, where experimental data to constrain the model were lacking. The improved PTW model reproduces the experimental data quite well. This result is one indication that RMI experiments can be quite sensitive to material strength in a high strain rate regime that is difficult to otherwise access.

Table 27.1 summarizes the discussion in the Introduction about instability experiments used to infer material strength. Although they all access similar strain rates, up to about 10^7/s, there are significant differences between RT experiments and the two types of RMI experiments. RT experiments are shockless and RMI experiments involve a shock. Compared to the other two, the RMI experiment in the free surface configuration ($A_t = -1$) tests strength at lower pressure following a shock and release, and is the easiest to field experimentally because it can be diagnosed without radiography. In the other two configurations, instabilities evolve at higher pressures. To our knowledge, no RMI experiment in the Atwood = +1

configuration has ever been reported, presumably because of the difficulty of fabricating pieces with mating perturbations, and the difficulty with diagnosing the growth- and strain-rates. The RMI experiment in the free surface configuration can be successfully diagnosed without radiography, which makes experiments much simpler and less expensive.

Acknowledgments We acknowledge the support of the pRad team in acquiring these data. In addition, we appreciate contributions to these experiments by members of the LANL MST-7 group where our Cu targets were machined and characterized by F. Garcia, B. Day and D. Schmidt.

This work was performed at Los Alamos National Laboratory, operated by the Los Alamos National Security, LLC for the National Nuclear Security Administration of the U.S. Department of Energy under contract DE-AC52-06NA25396. By acceptance of this article, the publisher recognizes that the U.S. Government retains a nonexclusive, royalty-free license to publish or reproduce the published form of this contribution, or to allow others to do so, for U.S. Government purposes.

References

1. Barnes, J.F., Blewett, P.J., McQueen, R.G., Meyer, K.A., Venable, D.: Taylor instability in solids. J. Appl. Phys. **45**(2), 727–732 (1974). http://dx.doi.org/10.1063/1.1663310
2. Colvin, J.D., Legrand, M., Remington, B.A., Schurtz, G., Weber, S.V.: A model for instability growth in accelerated solid metals. J. Appl. Phys. **93**(9), 5287–5301 (2003). http://dx.doi.org/10.1063/1.1565188
3. Lebedev, A.I., Nizovtsev, P.N., Rayevsky, V.A., Solovyov, V.P.: Rayleigh–Taylor instability in strong media, experimental study. In: Young, R., Glimm, J., Boston, B. (eds.) Proceedings of the Fifth International Workshop on Compressible Turbulent Mixing (1996)
4. Barton, N.R., Bernier, J.V., Becker, R., Arsenlis, A., Cavallo, R., Marian, J., Rhee, M., Park, H.-S., Remington, B.A., Olson, R.T.: A multiscale strength model for extreme loading conditions. J. Appl. Phys. **109**(7), 073501 (2011). http://dx.doi.org/10.1063/1.3553718
5. Smith, R.F., Eggert, J.H., Rudd, R.E., Swift, D.C., Bolme, C.A., Collins, G.W.: High strain-rate plastic flow in Al and Fe. J. Appl. Phys. **110** (12), 123515 (2011). http://dx.doi.org/10.1063/1.3670001
6. Piriz, A.R., Cela, J.J.L., Tahir, N.A., Hoffmann, D.H.H.: Richtmyer-Meshkov instability in elastic-plastic media. Phys. Rev. E **78**(5), 056401 (2008)
7. Piriz, A.R., Cela, J.J.L., Tahir, N.A.: Richtmyer–Meshkov instability as a tool for evaluating material strength under extreme conditions. Nucl. Instrum. Methods Phys. Res., Sect. A **606**(1), 139–141 (2009)
8. Dimonte, G., Terrones, G., Cherne, F.J., Germann, T.C., Dupont, V., Kadau, K., Buttler, W.T., Oro, D.M., Morris, C., Preston, D.L.: Use of the Richtmyer-Meshkov instability to infer yield stress at high-energy densities. Phys. Rev. Lett. **107**(26), 264502 (2011)
9. Buttler, W.T., Oró, D.M., Preston, D.L., Mikaelian, K.O., Cherne, F.J., Hixson, R.S., Mariam, F.G., Morris, C., Stone, J.B., Terrones, G., Tupa, D.: Unstable Richtmyer-Meshkov growth of solid and liquid metals in vacuum. J. Fluid Mech. **703**, 60–84 (2012)
10. López Ortega, A., Lombardini, M., Pullin, D.I., Meiron, D.I.: Numerical simulations of the Richtmyer-Meshkov instability in solid-vacuum interfaces using calibrated plasticity laws. Phys. Rev. E **89**(3), 033018 (2014)
11. Mikaelian, K.O.: Shock-induced interface instability in viscous fluids and metals. Phys. Rev. E **87**(3), 031003 (2013)
12. Plohr, J.N., Plohr, B.J.: Linearized analysis of Richtmyer-Meshkov flow for elastic materials. J. Fluid Mech. **537**, 55–89 (2005)
13. Prime, M.B., Vaughan, D.E., Preston, D.L., Buttler, W.T., Chen, S.R., Oró, D.M., Pack, C.: Using growth and arrest of Richtmyer-Meshkov instabilities and Lagrangian simulations to study high-rate material strength. J. Phys. Conf. Ser. **500**(11), 112051 (2014)
14. Buttler, W.T., Oro, D.M., Preston, D., Mikaelian, K.O., Cherne, F.J., Hixson, R.S., Mariam, F.G., Morris, C.L., Stone, J.B., Terrones, G., Tupa, D.: The study of high-speed surface dynamics using a pulsed proton beam. AIP Conf. Proc. **1426**(1), 999–1002 (2012). http://dx.doi.org/10.1063/1.3686446
15. Asay, J.R., Mix, L.P., Perry, F.C.: Ejection of material from shocked surfaces. Appl. Phys. Lett. **29**(5), 284–287 (1976). http://dx.doi.org/10.1063/1.89066
16. Germann, T.C., Hammerberg, J.E., Holian, B.L.: Large-scale molecular dynamics simulations of ejecta formation in copper. AIP Conf. Proc. **706**(1), 285–288 (2004). http://dx.doi.org/10.1063/1.1780236
17. Zellner, M.B., Buttler, W.T.: Exploring Richtmyer–Meshkov instability phenomena and ejecta cloud physics. Appl. Phys. Lett. **93**(11), 114102 (2008). http://dx.doi.org/10.1063/1.2982421
18. Zellner, M.B., Dimonte, G., Germann, T.C., Hammerberg, J.E., Rigg, P.A., Stevens, G.D., Turley, W.D., Buttler, W.T.: Influence of shockwave profile on ejecta. AIP Conf. Proc. **1195**(1), 1047–1050 (2009). http://dx.doi.org/10.1063/1.3294980
19. Dimonte, G., Terrones, G., Cherne, F.J., Ramaprabhu, P.: Ejecta source model based on the nonlinear Richtmyer-Meshkov instability. J. Appl. Phys. **113**(2), 024905 (2013). http://dx.doi.org/10.1063/1.4773575
20. King, N.S.P., Ables, E., Adams, K., Alrick, K.R., Amann, J.F., Balzar, S., Barnes Jr., P.D., Crow, M.L., Cushing, S.B., Eddleman, J.C.: An 800-MeV proton radiography facility for dynamic experiments. Nucl. Instrum. Methods Phys. Res., Sect. A **424**(1), 84–91 (1999)
21. Holtkamp, D.B.: Survey of optical velocimetry experiments-applications of PDV, a heterodyne velocimeter. In: Kiuttu, G.F., Turchi, P.J., Reinovsky, R.E. (eds.) Proceedings of 2006 International Conference on Megagauss Magnetic Field Generation and Related Topics, pp. 119–128. IEEE, Santa Fe (2006). doi:10.1109/MEGAGUSS.2006.4530668
22. Caramana, E.J., Burton, D.E., Shashkov, M.J., Whalen, P.P.: The construction of compatible hydrodynamics algorithms utilizing conservation of total energy. J. Comput. Phys. **146**(1), 227–262 (1998). http://dx.doi.org/10.1006/jcph.1998.6029
23. Burton, D.E., Carney, T.C., Morgan, N.R., Runnels, S.R., Sambasivan, S.K., Shashkov, M.J.: A cell-centered Lagrangian hydrodynamics method for multi-dimensional unstructured grids in curvilinear coordinates with solid constitutive models. Los Alamos National Laboratory Report LA-UR-11-04995 (2011)
24. Dobratz, B.M., Crawford, P.C.: LLNL explosives handbook. Properties of chemical explosives and explosive simulants. Lawrence Livermore National Laboratory Report UCRL-52997 Change 2 (1985)

25. Lyon, S.P., Johnson, J.D.: Sesame: the Los Alamos National Laboratory equation of state database. Los Alamos National Laboratory Report LA-UR-92-3407 (1992)
26. Preston, D.L., Tonks, D.L., Wallace, D.C.: Model of plastic deformation for extreme loading conditions. J. Appl. Phys. **93**(1), 211–220 (2003)
27. Tonks, D., Zurek, A., Thissell, W., Vorthman, J., Hixson, R.: The Tonks ductile damage model. Los Alamos National Laboratory Report LA-UR-03-0809 (2002)
28. Zurek, A.K., Thissell, W.R., Johnson, J.N., Tonks, D.L., Hixson, R.: Micromechanics of spall and damage in tantalum. J. Mater. Process. Technol. **60**(1–4), 261–267 (1996). http://dx.doi.org/10.1016/0924-0136(96)02340-0
29. Tonks, D.L.: Percolation wave propagation, and void link-up effects in ductile fracture. J. Phys. IV **4**(C8), C8-665–C8-670 (1994)
30. Tonks, D.L., Zurek, A.K., Thissell, W.R.: Void coalescence model for ductile damage. AIP Conf. Proc. **620**(1), 611–614 (2002). http://dx.doi.org/10.1063/1.1483613
31. Tonks, D.L., Bronkhorst, C.A., Bingert, J.F.: Inertial effects in dynamical ductile damage in copper. Los Alamos National Laboratory Report LA-UR-11-05803 (2011)
32. Park, H.-S., Lorenz, K.T., Cavallo, R.M., Pollaine, S.M., Prisbrey, S.T., Rudd, R.E., Becker, R.C., Bernier, J.V., Remington, B.A.: Viscous Rayleigh-Taylor instability experiments at high pressure and strain rate. Phys. Rev. Lett. **104**(13), 135504 (2010)

Chapter 28
Study of Energy Contributions in Granular Materials During Impact

Nikhil Karanjgaokar and Guruswami Ravichandran

Abstract A drop-tower experimental setup was developed for the impact testing of 2D assembly of cylinders and 3D assembly of spheres with impactor velocity of around 6 m/s. This drop tower setup was used to load 2D granular assembly of polyurethane cylinders of 1″–1.25″ length with three different diameters of 1/4″, 3/8″ and 1/2″. A high speed camera was used for recording the images at speeds between 10,000 and 50,000 fps to monitor the deformation of the cylinders. The inter-particle forces in these experiments were calculated using a GEM based force inference technique. The resultant force networks in the granular assemblies were then qualitatively compared to the acceleration fields and strain fields observed during the experiments at different time instants. The conservation of energy was used to plot the evolution of energy components like kinetic energy, strain energy, friction and dissipative components during impact experiments.

Keywords Digital image correlation • Granular materials • Granular element method • Force chains

28.1 Introduction

Granular materials are conglomerations of discrete solid grains which in its dry state, lack cohesion and transmit forces via inter-granular contacts through rigid elastic interactions. There can be a wide variation of configurations in a granular systems owing to the differences in shape and size of individual grains and the packing of the grains in the granular media. This heterogeneous fabric of granular materials results in preferred paths for the force transfer in these materials. These preferred pathways results in formation of force chains in dry granular materials as evidenced by numerous experimental and numerical simulations.

The phenomenological description of macroscopic response of granular materials has long been viewed as a viable alternative to continuum modeling [1, 2]. In particular, inter-particle forces have been linked to the macroscopic behavior of granular media like constitutive behavior [3, 4], wave propagation [5] and friction [6]. Numerical modeling techniques linking inter-particle forces and macroscopic properties need to be validated through experiments at the particle scale. Photoelasticity based techniques have been used for inter-particle force visualization in granular media [7, 8]. However, these studies have been limited to birefringent grains and require the knowledge of the boundary conditions. Most recent techniques for force-inference in granular media require some inherent assumptions about grain shape or law governing the contact mechanics [9, 10].

The recently proposed Granular Element Method (GEM) [11–13] overcomes all of these challenges and is only restricted by the availability of experimental techniques to extract full-field grain displacement fields and particle edges. The extension of GEM method presented in [13] provides a new tool for quantitatively measuring dynamic inter-particle force transmission in granular media. In the current work, a drop-tower impact experiment was employed to load a 2D assembly of polyurethane cylinders and the deformation of individual grains was monitored using high speed imaging. Digital image correlation is used to obtain the particle kinematics and strain fields in the granular assembly. The experimental measurements like granular kinematics, contact points and strain fields are then used to infer the inter-particle forces using the GEM based approach described in [13]. The Sect. 28.2 of this paper discusses the experimental approach designed for the drop-tower testing of the granular assemblies while results obtained for impact of a random arranged polyurethane assembly are presented along with some discussion regarding energy contributions in Sect. 28.3. The final section explores future applications of this method and presents some of its limitations.

N. Karanjgaokar (✉) • G. Ravichandran
Graduate Aerospace Laboratories of the California Institute of Technology, 1200 E California Blvd. MC 105-50, Pasadena, CA 91106, USA
e-mail: nikhiljk@caltech.edu

B. Song et al. (eds.), *Dynamic Behavior of Materials, Volume 1*,
Conference Proceedings of the Society for Experimental Mechanics Series, DOI 10.1007/978-3-319-22452-7_28

28.2 Experimental Setup and Procedure

The drop-tower experimental setup used for testing granular assemblies in the current work is shown in Fig. 28.1a. As seen in the figure, hollow aluminum tube (9′ long) is mounted on a rigid load frame and a rigid impactor can free-fall under gravity through the hollow tube. The impactor velocity when it reaches fixture holding the granular assembly is around 6 m/s. The fixture holding the cylindrical grains has rigid walls on the sides and the bottom face while the slotted top face allows a flat slider to move vertically on impact.

The drop tower setup was used to conduct impact experiments on polyurethane (Durometer 80A). Cylindrical grains with a length of 1.25″ and three different diameters (1/4″, 3/8″ and 1/2″) were randomly arranged as granular assemblies. The elastic modulus for Polyurethane rods was measured to be 9.35 MPa with a Poisson's ratio $\upsilon = 0.49$. The coefficient of friction for polyurethane was experimentally measured to be 0.43. In order to facilitate the use of digital image correlation (DIC), the flat faces of the cylindrical grains were patterned with spray paint with appropriate speckle density for different diameters (see Fig. 28.1b). The images during the impact experiments were recorded with Phantom v710 high speed camera at an approx. resolution of 800 × 800 pixels between 10,000 and 55,000 fps.

The DIC software VIC-2D™ from Correlated Solutions was used to calculate the displacement and velocity fields for each grain separately. The displacement fields were then used to obtain the ε_{xx}, ε_{xy} and ε_{yy} strain fields in each grain and calculate the average strain in each grain. The velocity fields from DIC in each grain were then used to calculate the acceleration fields and average accelerations in the grains by numerical differentiation.

The recorded images were also used to obtain the position of the centroid and the locations of the particles contacts at each time instant. This was achieved by converting the recorded grayscale image to a binary image and the particle centroids and radius were then detected using a circular Hough transform with Matlab's image processing toolbox. The resulting centroids and radii were used to find contacting particles: if the distance between two centroids was less than two times the radii of the corresponding particles, the particles were taken to be contacting with appropriate normal and tangent vectors. Similarly, contact points between particles and the boundaries of the fixture were also detected.

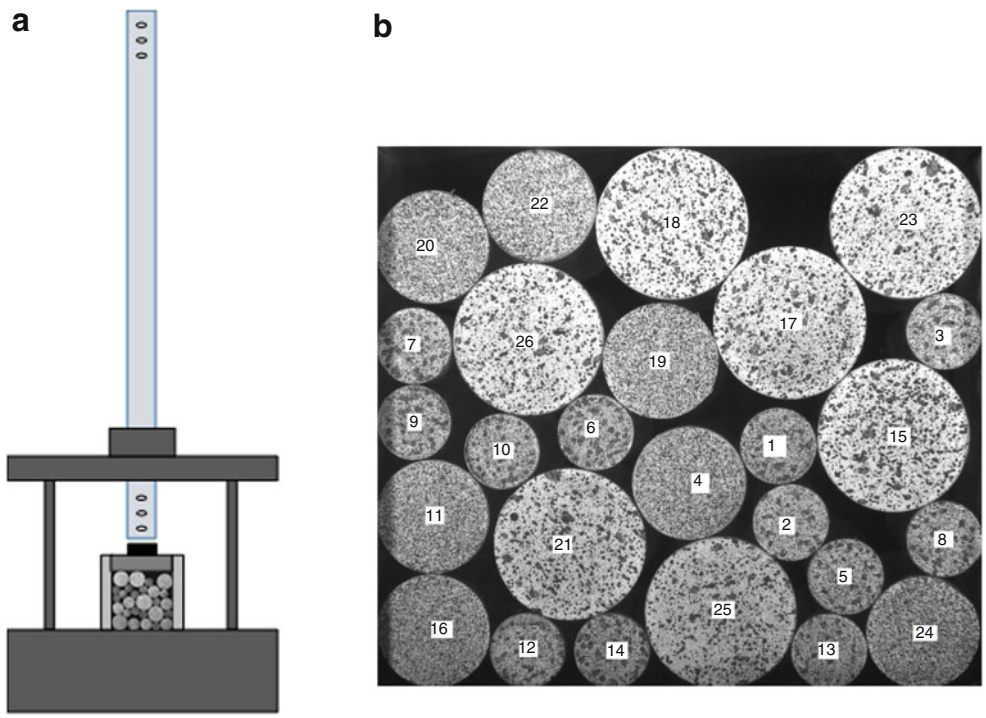

Fig. 28.1 (**a**) A schematic representation of the drop tower setup for loading the granular assembly of cylindrical grains, (**b**) a representative image recorded by the high speed camera for a granular assembly of polyurethane cylindrical grains of three different diameters with speckle-patterns

28.3 Results and Discussion

The Fig. 28.2 shows the representative ε_{xx}, ε_{xy} and ε_{yy} strain fields for polyurethane grains at some time instant during the impact experiment. A rate independent linear elastic model was used to compute the average stress values from average strain values for each grain. While the assumption is definitely valid for grains with small strains, it may no longer be valid for polyurethane grains with large strains. But hyperelasticity, plasticity and rate dependency based models for polyurethane are not considered for scope of this paper. The analysis of the velocity fields obtained from the DIC results reveals that

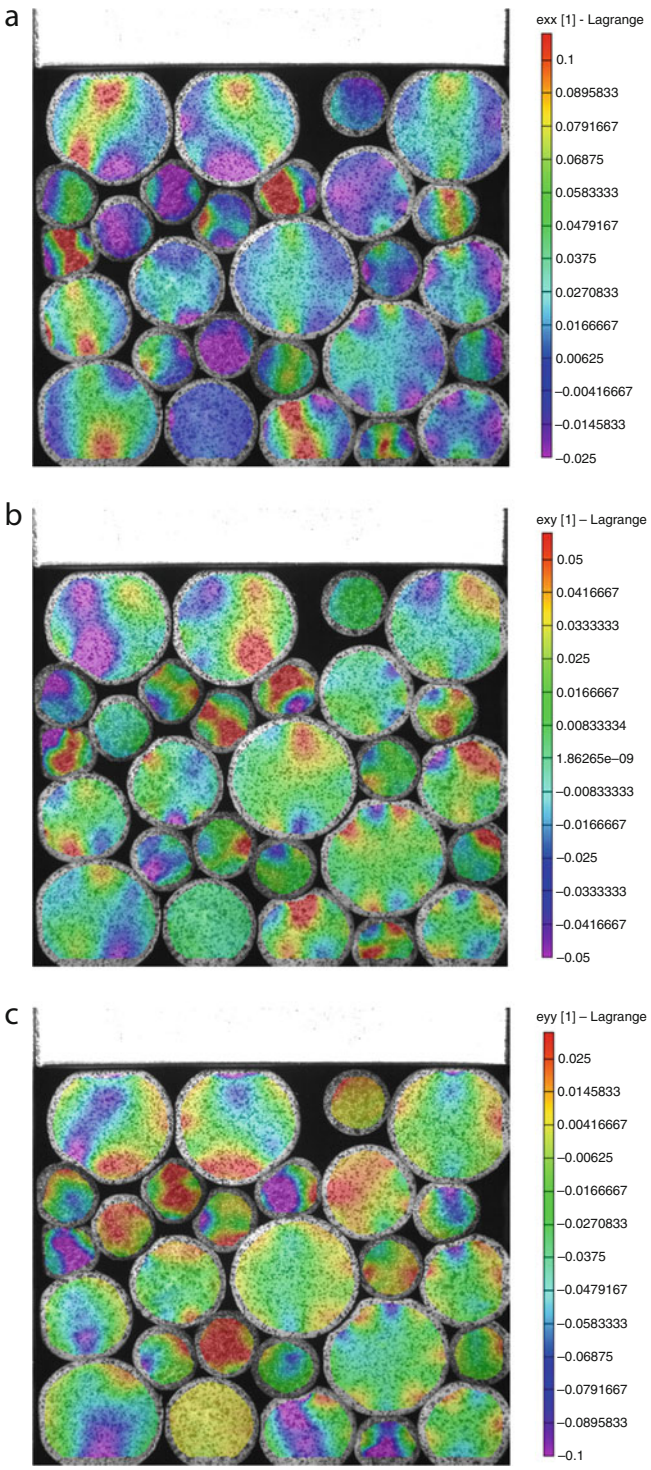

Fig. 28.2 The full-field strain for impact experiment for polyurethane grains for (**a**) εxx, (**b**) εxy and (**c**) εyy at some instant

although the wave velocity for the polyurethane is around 93 m/s, the wavefront moves at approximately 5 m/s through the granular media.

The numerical optimization presented in [13] links particle positions, accelerations, contact points, and stresses to inter-particle forces. Three particle-scale equations accomplish this connection: momentum balance, stress-force relations, and constraint equations. These equations are combined in a multi-objective optimization problem that can be solved to obtain inter-particle forces. In the current work, we have studied the effect of local acceleration gradients within the particles and have included integral terms with moments of local accelerations about the particle centroid. Ignoring influence of local acceleration fields does not result in large errors (<5 N) in the inter-particle force values in the current granular assembly. A similar analysis was also conducted for polycarbonate grains but due to the comparably higher wave speeds in polycarbonate, the impact event lasted for a shorter time and hence fewer images could recorded for the experiments. Since the polycarbonate grains undergo smaller deformations, the images were recorded at a higher magnification and inter-particle forces were calculated for plane strain and plane stress assumptions.

The monitoring of contribution of different components of energy enhances the understanding of the interaction of particles at the microscale and provides means to understand response mechanisms at the macroscale. The experimental approach developed here facilitates the monitoring the evolution of energy contributions from elastic energy, frictional losses and kinetic energy in a granular arrangement. The energy entering the system due to impact of the granular assembly with the top wall at any instant 't' is given by,

$$E_{in} = \sum_{t=0}^{t} \sum_{i=1}^{N_p} f_i^t \delta u_i \tag{28.1}$$

Where f_i^t is the instantaneous force between particle i and the top wall and δu_i is the corresponding incremental displacement of the top wall. The kinetic energy and the strain energy at any instant is given by,

$$E_{kinetic} = \frac{1}{2} \sum_{p=1}^{N_p} m_p \dot{u}_p^2 \tag{28.2}$$

$$E_{strain} = \frac{1}{2} \sum_{p=1}^{N_p} V_p \left(\sigma_{ij} \varepsilon_{ij}\right)_p \tag{28.3}$$

Similarly, the GEM approach also allows us to measure the frictional losses at each contact and the energy dissipated through frictional sliding can be obtained using,

$$E_{friction} = \sum_{t=0}^{t} \sum_{i=1}^{N_c} f_{slip}^t \delta u_{slip} = \sum_{t=0}^{t} \sum_{i=1}^{N_c} (f_i \cdot t_i) \left[(\delta u_i \cdot t_i)_{Grain\ 1} - (\delta u_i \cdot t_i)_{Grain\ 2} \right] \tag{28.4}$$

where δu_{slip} is the incremental slip displacement vector at the sliding contact for the 'N_c' total contacts at any instant. The contributions of these different energy contributions for the randomly arranged polyurethane assembly is shown in Fig. 28.3.

As seen in Fig. 28.3, the input energy representing the transfer of the kinetic energy of the impactor to the granular assembly follows a linear profile and lasted for around 0.5 ms for the random polyurethane assembly. The impactor bounces upwards after initial impact and results in another collision with the sliding top wall granular assembly and results in another smaller increase in the input energy as seen in the Fig. 28.3. This input energy enters the granular assembly as kinetic energy as evidenced by the high relative contribution of kinetic energy during the initial stages of impact. As the stress wave moves through the granular assembly at a particle velocity around 5 m/s, the contribution of kinetic energy decreases and the elastic strain energy of the system increases correspondingly. The second impact of the impactor with the top wall results in a small burst of kinetic energy and consequently the strain energy reaches its maximum as the granular assembly is compressed. The granular assembly subsequently slowly decompresses as the strain energy of the system is slowly released once again at much slower particle velocity and hence time for strain energy release (~3 ms) is much larger than time for transfer of initial impact. This energy leaves the system as the kinetic energy of the impactor as the impactor bounces off. Since the impactor is not necessarily in the field of view, it is difficult to account for the kinetic energy of the impactor. The high relative contribution of frictional losses is quite surprising since the magnitude of frictional forces are significantly low (f_t ~ 5–20 N)

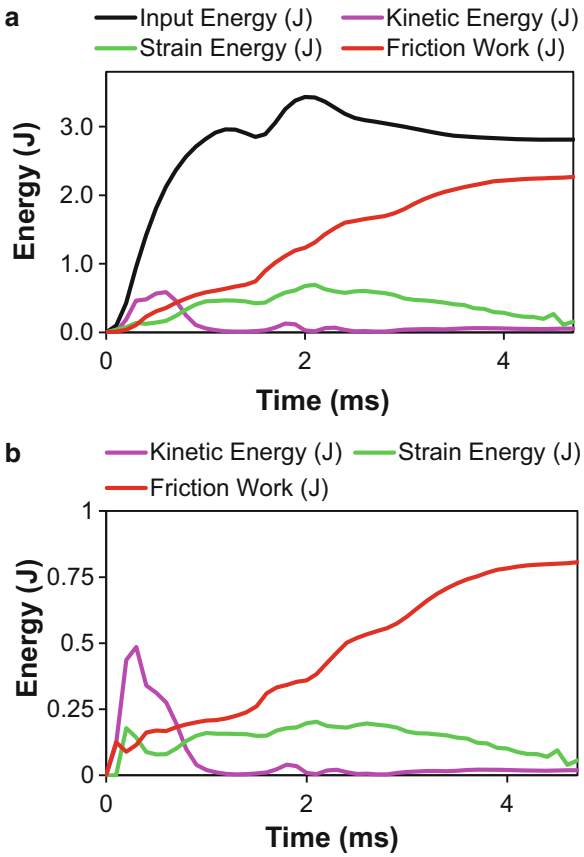

Fig. 28.3 (**a**) The evolution of different contributions of energy during the impact of a random assembly of polyurethane cylinders as a function of time, (**b**) the relative contribution of kinetic energy, strain energy and frictional losses normalized with respect to total input energy during impact of the random assembly of the polyurethane cylinders

as compared to normal contact forces which are at least order of magnitude higher at any instant. A closer look at the frictional losses for each contact reveals that the small amount of frictional losses are continually dissipated at each contact over time.

28.4 Conclusions

A method for quantitatively measuring dynamic inter-particle force transmission in granular materials is presented in the current work. The proposed method has been demonstrated to have the ability to test different materials with elastic modulus orders of magnitude apart. These results illustrate a new opportunity to experimentally validate theories linking microscopic inter-particle forces with macroscopic behavior in a variety of applications. The extension of the current approach to testing of stiffer materials is currently restricted by high-speed cameras that can provide high resolution images. The capacity to monitor energy modes during deformation of granular materials can facilitate the design of new hierarchical granular systems for preferential energy dissipation modes.

References

1. Andrade, J.E., Borja, R.I.: Capturing strain localization in dense sands with random density. Int. J. Numer. Methods Eng. **67**, 1531–1564 (2006)
2. Dafalias, Y.F., Popov, E.P.: A model of nonlinearly hardening materials for complex loadings. Acta Mech. **21**, 173–192 (1975)
3. Christoffersen, J., Mehrabadi, M.M., Nemat-Nasser, S.: A micromechanical description of granular material behavior. J. Appl. Mech. **48**(2), 339–344 (1981)
4. Bathurst, R.J., Rothenburg, L.: Observations on stress-force-fabric relationships in idealized granular materials. Mech. Mater. **9**(1), 65–80 (1990)

5. Somfai, E., Roux, J.-N., Snoeijer, J.H., Van Hecke, M., Van Saarloos, W.: Elastic wave propagation in confined granular systems. Phys. Rev. E **72**, 021301 (2005)
6. Clark, A.H., Kondic, L., Behringer, R.P.: Particle scale dynamics in granular impact. Phys. Rev. Lett. **109**, 238302 (2012)
7. Dantu, P.: Contribution a l'etiude mecanique et geometrique des milieux pulverulents. In: Proceedings of the 17th International Conference on Soil Mechanics and Foundation Engineering, vol. 1, pp. 144–148, Butterworths Scientific Publications, London (1957)
8. Wakabayashi T.: Photoelastic method for determination of stress in powdered mass. In: Proceedings of the 7th National Congress Applied Mechanics, Japan National Committee for Theoretical and Applied Mechanics, pp. 153–158, Science Council of Japan, Tokyo (1957)
9. Saadatfar, M., Sheppard, A.P., Senden, T.J., Kabla, A.J.: Mapping forces in a 3D elastic assembly of grains. J. Mech. Phys. Solids **60**(1), 55–66 (2012)
10. Zhou, J., Long, S., Wang, Q., Dinsmore, A.D.: Measurement of forces inside a three-dimensional pile of frictionless droplets. Science **312** (5780), 1631–1633 (2006)
11. Andrade, J., Avila, C.F.: Granular element method (GEM): linking inter-particle forces with macroscopic loading. Granul. Matter **14**, 51–61 (2012)
12. Hurley, R., Marteau, E., Ravichandran, G., Andrade, J.E.: Extracting inter-particle forces in opaque granular materials: beyond photoelasticity. J. Mech. Phys. Solids **63**, 154–166 (2014)
13. Hurley, R.C., Lim, K.W., Ravichandran, G., Andrade, J.E.: Dynamic inter-particle force inference in granular materials: Method and application. Exp. Mech., In press, EXME-D-14-00346R1, (2015)

Chapter 29
Ballistic Perforation of Double Reinforced Concrete as a Function of Energy

Christopher S. Meyer

Abstract In an effort to better understand the energy required to breach double-reinforced concrete (DRC) walls it was attempted to estimate by numerical simulations the minimum kinetic energy required to perforate a DRC target. To this end, a parametric numerical study was conducted at the U. S. Army Research Laboratory. Large scale, high-fidelity, three-dimensional numerical simulations were conducted using an Eulerian shock physics code considering both eroding penetration and rigid body penetration. The parametric study investigated right cylindrical steel rods with masses of 500–2000 g and length-to-diameter ratios (L/D) of 1–10 impacting with velocities ranging from 500 to 1500 m/s, and perforating rebar reinforced concrete targets with a range of presented areas. This paper explores the numerical simulation results to consider the kinetic energy of perforation of DRC for the described range of conditions. Experimental results from the literature are compared with the numerical results. An empirical fit to the data is reported.

Keywords Numerical simulation • Reinforced concrete • Kinetic energy • Perforation • Residual velocity

29.1 Introduction

The literature encompasses a significant amount of research in concrete penetration and perforation including experimental investigations involving depth of penetration into concrete, e.g., Luk et al. [1] and Gomez and Shukla [2], and perforation of concrete, e.g., Hanchak et al. [3], Cargile et al. [4], Jinzhu et al. [5]. In addition to experiments, models have been proposed for predicting depth of penetration into concrete by ogive and truncated ogive-nosed projectiles, e.g., Forrestal et al. [6], Lixin et al. [7], and Teland and Sjøl [8], and for predicting residual velocity for ogive and truncated ogive-nosed projectiles after perforation of concrete, e.g., Wu et al. [9]. Numerical simulations of rigid penetration, e.g., Liu et al. [10], and perforation, e.g., Huang et al. [11] of concrete have been conducted exploring penetration at normal and oblique angles and using Lagrangian and Arbitrary Lagrangian-Eulerian frames. Numerical simulations of eroding penetration of concrete have also been conducted, e.g., Nia et al. [12]. Analytical studies of normal and oblique concrete perforation by rigid projectiles have also been conducted, e.g., Chen et al. [13, 14].

Developing tools to remove both concrete and reinforcement and create a hole large enough for a person to go through is a challenging problem. Perhaps improved understanding of the energy necessary to perforate concrete and reinforcement will enlighten development of such tools. Latif et al. have examined the minimum kinetic energy for penetration of concrete by a rigid penetrator [15–17], and their work builds upon that by Li et al. [18] who developed an empirical formula that apparently predicts the minimum kinetic energy required for a projectile of a given diameter to perforate concrete of a given thickness and unconfined compressive strength. Latif et al. and Li et al. use data by Bainbridge [19] to validate their semi-empirical formula for the kinetic energy required for concrete perforation, but this data is apparently for thin targets with projectiles that are relatively large compared with the thicknesses of the concrete targets, that is, apparently the target thickness is five times the diameter of the projectile or less, with the majority of the data reported for target thicknesses of two times the projectile diameter or less. Additionally, the semi-empirical formula for the kinetic energy required for concrete perforation provided by Li et al. [18] considers ogive-nosed projectiles, and, while Latif et al. [16, 17] attempt to expand the Li et al. formula to account for different nose shapes including flat, the focus is on depth of penetration into concrete rather than perforation of concrete. The present work considers a flat-nosed projectile perforating a thick target, that is, a target whose thickness is ten times the diameter of the projectile perforating the target. Li et al. [18] (and likewise Latif et al. [15], who report the formulae by Li et al.) provide an equation, given in the present work as (29.1), for calculating the "critical impact energy for the occurrence of perforation" for a thick target, that is, with the ratio of target thickness to

C.S. Meyer (✉)
U.S. Army Research Laboratory, ATTN: RDRL-WML-H, Aberdeen Proving Ground, MD 21005-5066, USA
e-mail: christopher.s.meyer12.civ@mail.mil

B. Song et al. (eds.), *Dynamic Behavior of Materials, Volume 1*,
Conference Proceedings of the Society for Experimental Mechanics Series, DOI 10.1007/978-3-319-22452-7_29

Table 29.1 Input parameters, (a) relevant to the present work and (b) from Cargile et al. [4] and (c) from Hanchak [3], and results, based on these parameters, determined by calculating the "critical impact energy for the occurrence of perforation" using (29.1) reported by Li et al. [18]

	Projectile diameter, d (m)	Projectile mass, m (kg)	Target unconfined compressive strength, f'_c (MPa)	Target thickness, h (m)	Ratio of target thickness to projectile diameter, h/d	Critical impact energy for perforation, E_{cp} (kJ)	Minimum (critical) velocity for perforation, v_{cp} (m/s)	Experimental impact and residual velocity, $v_i - v_r$ (m/s)
(a)	0.02	1	33.6	0.2	10	15.7	177	?
(b)	0.05	2.32	39.9	0.284	5.7	112.5	311	309 − 0
	0.05	2.32	36.5	0.254	5.1	86.7	273	309 − 32
	0.05	2.33	39.9	0.254	5.1	90.7	279	470 − 257
(c)	0.0254	0.50	48.0	0.178	7.0	23.0	303	301 − 0
	0.0254	0.50	140.0	0.178	7.0	39.2	396	376 − 0
								382 − 0

projectile diameter of between 3.80 and 18.0 [18]. Applying this formula to the present work, for which equation parameters are given in Table 29.1, one finds that the energy required for target perforation is 15.7 kJ. Applying the median mass considered in the present work, 1000 g, to this energy, one finds a minimum impact velocity, using the well-known formula for kinetic energy, $½mv^2$, of 177 m/s. This is of course for an ogive-nose projectile, which the present work does not consider, and unfortunately, due to time constraints, the geometry and impact conditions (not to mention materials) of these data could not be numerically simulated using the approach taken in the subject work, so it is unclear whether the numerical results of the subject work are in agreement with this semi-analytical model. However, it is certain by comparison with the results presented later in the subject work, that this impact velocity is insufficient for a flat-nosed projectile to perforate a thick concrete target.

$$E_{cp} = 45.576\, d^3 \left(f_c^{'}\right)^{1/2} \left(\frac{h}{d} - 2.560\right) \quad \text{for } 3.80 < \frac{h}{d} < 18.0 \tag{29.1}$$

The data by Cargile et al. [4] and Hanchaks et al. [3], which were for ogive-nosed projectiles, were also compared with the equation by Li et al. [18], included here as (29.1), and found to be in agreement. Table 29.1 includes the results of this comparison.

The present work considers a flat-nosed projectile perforating a thick reinforced concrete target. To better understand the kinetic energy required for a blunt-nosed projectile to perforate a reinforced concrete target a parametric numerical study was conducted. Parameters considered in the study include the projectile initial velocity, mass, length-to-diameter ratio, and impact orientation. The area each projectile presented to the target scaled the initial kinetic energy of each projectile configuration and these data were compared with the projectile residual velocity. The data were then fit to determine an empirical expression that may be used to estimate whether a given projectile design will perforate reinforced concrete at a given impact velocity.

29.2 Numerical Simulations

An approach described by the author in prior related works [20–23] was used in the present work to model and simulate reinforced concrete penetration and perforation. Large scale, three-dimensional numerical simulations were conducted on Department of Defense Supercomputing Resource Center High Performance Computing systems using CTH, an Eulerian shock physics code [24]. Further detail of the modeling approach has been previously reported and to save space is not reported here, but the reader may find this detail in reference [23] with additional detail in references [20–22]. For reference, Table 29.2 contains some elastic properties for the materials used in the subject simulations.

The dynamic compressive material behavior of concrete was simulated using the Holmquist-Johnson-Cook (HJC) concrete constitutive model [25]. See also prior related work by the author for additional discussion on the HJC model [20, 21]. Concrete material parameters were derived from mechanical characterization data for SAM-35 concrete [26] and for RTC concrete [27] provided by the U.S. Army Corps of Engineers, Engineer Research and Development Center, Geotechnical and Structures Laboratory. These materials were selected for the subject study, as they are typical of concretes used in U.S. Army Research Laboratory testing.

Table 29.2 Sample elastic material parameters used in the numerical calculations

Material	Tensile yield strength (MPa)	Unconfined compressive strength (MPa)	Poisson's ratio	Density (kg/m^3)	Sound speed (m/s)
Projectile steel (4340)	1551		0.283	7842	4529
Rebar steel (A615)	924		0.28	785	4600
Concrete (SAM-35)		33.6	0.24	2092	3512
Concrete (RTC)		36.9	0.245	2242	3730

Concrete data provided by the U.S. Army Corps of Engineers, Engineer Research and Development Center, Geotechnical and Structures Laboratory [26, 27]

Table 29.3 Permutations of parameters examined

Mass (g)	Impact position	L/D	Length (cm)	Diameter (cm)	Presented area (cm^2)	Impact velocity (m/s)				
1000	End	0.88	5	5.696	25.48	500	800	1000	1200	1500
1000	End	2.48	10	4.027	12.74	500	800	1000	1200	1500
1000†	End	5.03	16	3.184	7.96	500	800	1000†	1200	1500†
1000	End	9.81	25	2.547	5.10	500	800	1000	1200	1500
1000†	Side	5.03	16	3.184	7.96	500†	800	1000†	1200	1500†
1000	Side	9.81	25	2.547	5.10	500	800	1000	1200	1500
500	End	0.89	4	4.503	15.92	500	800	1000	–	1500
500	End	5.20	13	2.498	4.90	500	800	1000	–	1500
500	End	9.93	20	2.014	3.18	500	800	1000	–	1500
2000	Side	4.97	20	4.027	80.55	500	800	1000	1200	1500
2000	Side	10.05	32	3.184	101.88	500	800	1000	1200	1500
2000	Side	9.81	25	2.547	5.10	500	–	1000	–	1500
2000*	Side	4.97	20	4.027	80.55	–	–	1000	1200	–

All are steel projectiles impacting SAM-35 concrete target except the last line (with *asterisk*), which is steel projectile impacting RTC concrete. Permutations with a *dagger*, in addition to standard CTH, were also run as rigid penetration using the boundary layer interface algorithm

Rebar reinforcement was placed in accordance with specification [28]. Rebar material was A615 steel and pressure response was modeled using the Mie-Grüneisen equation of state [29, 29] with CTH library parameters for alpha iron. The rebar steel strength behavior was modeled with the Johnson-Cook constitutive and damage model for metals [31] with user defined material parameters found by fitting stress-strain data [32]. Likewise, the penetrator material, 4340 steel [33, 34], was modeled with user-defined material parameters for the Mie-Grüneisen equation of state and the Johnson-Cook constitutive and damage model.

As mentioned, the Eulerian non-linear wave propagation computer code CTH [24] was used for the subject numerical simulations. It is well known that Eulerian codes such as CTH are well suited for eroding, long-rod penetration, e.g. [35]. However, due to mixed-cell averaging, these same codes are not well suited to rigid body motion, e.g. [36]. For this reason, the so-called boundary layer interface (BLINT) method [37] was incorporated into CTH for modeling rigid body penetration, e.g. [38]. Kmetyk and Yarrington [38] used CTH to simulate steel long-rod projectile penetration of concrete and they reported, "CTH with the boundary-layer algorithm is well-suited to predict the global or "rigid-body" response of the penetrator." The BLINT algorithm [37] in CTH was used for some simulations as highlighted by a dagger in Table 29.3.

The subject parametric study investigated right circular cylindrical steel rods impacting rebar reinforced concrete at two crossed (tied) rebar, as shown in Fig. 29.1. Cylindrical rods impacted DRC walls with orientations to target of either end-on (that is, in typical long-rod fashion) or side-on (that is, rotated 90° from typical long-rod fashion). Rods with masses of 500−2000 g and length-to-diameter ratios (L/D) of 1−10 were simulated impacting DRC targets with velocities ranging 500−1500 m/s. The presented area of the penetrators varied 3−120 cm^2 according to the penetrator L/D and impact orientation. The permutations of these parameters examined in the subject work are provided in Table 29.3. From the data given in Table 29.3, the initial energy of a given projectile may be computed from the well-known equation for kinetic energy, $\frac{1}{2}mv^2$. The presented area of the projectiles provided in Table 29.3 is calculated from the projectile's length, diameter, and impact orientation given in Table 29.3. Comparing the initial energy divided by the presented area of a projectile with the residual velocity of the projectile provides a means of evaluating a projectile's effectiveness at perforating a reinforced concrete target.

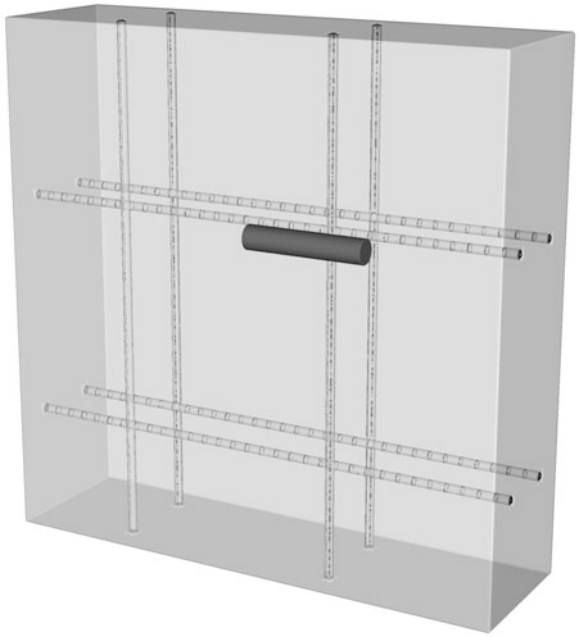

Fig. 29.1 3D CTH model. The target is modeled with semi-infinite boundary conditions on all four sides and is 20.3-cm (8-in.) thick. The *right* circular cylindrical projectile shown is 16-cm long by 3.184-cm in diameter, 1000-g with L/D = 5. Rebar placement is standard as described in ITOP 5-2-503 [28]

As mentioned earlier, the modeling approach has been validated in prior work [20, 21]. Most similar numerical work uses the Hanchak et al. [3] residual velocity data for validation (cf. [10–13]). This approach is approximately acceptable for initial validation, but is not necessarily predictive as there is wide variation in the unconfined compressive strengths of concretes, as demonstrated by Hanchak et al. [3] by testing 48 MPa (7 ksi) and 140 MPa (20 ksi) strength concrete, and the validation is therefore only truly appropriate for the particular concretes tested by Hanchak et al. [3]. The Hanchak et al. [3], similar experimental data (cf. Cargile et al. [4], Jinzhu et al. [5]), and, to this author's knowledge, all open literature concrete perforation data is for ogive-nosed and truncated ogive-nosed projectiles. Prior related work by this author [20–22] has suggested that it is necessary to characterize the material of interest, parameterize an appropriate constitutive model with this characterization data, and validate the constitutive model parameters with penetration and perforation experimental data all prior to considering a model predictive for the set of conditions for which the model was validated. Therefore, using these data, e.g. Hanchak et al. [3], Cargile et al. [4], and Jinzhu et al. [5], for model validation is not appropriate for the subject simulations for these reasons, i.e. not simulating the same concrete and not simulating an ogive-nosed projectile, however these data will still be included in the presentation of the results as a point of comparison.

29.3 Results and Discussion

The traditional way of looking at target perforation residual velocity data is an initial velocity versus residual velocity curve, often called a Vi-Vr curve. Figure 29.2 shows the initial velocity and residual velocity data for the permutations described in Table 29.3. No trends are apparent when these data are displayed this way. As described earlier, comparing the initial energy divided by the presented area of a projectile to the residual velocity of the projectile provides a means of evaluating a projectile's effectiveness. These results from the parametric numerical simulations are presented in Fig. 29.3. Examination of this chart suggests a trend in the data. The data are closely grouped for smaller residual velocities, perhaps related to the ballistic limit velocity of the target-penetrator system, but the scatter of the data increases among larger residual velocities.

If we make the assumption that penetration is a function of the target-penetrator material system, and plot all of the data on a single chart, as we have done in Fig. 29.3, and if we normalize the penetrator energy per unit area by the target resistance to penetration, which here is defined as the target density, ρ_T, times the target sound speed, C_T, squared times the target thickness, h, then we can fit a curve to the data and extract two empirical parameters. We will assume here that these two parameters apply to all target-penetrator material systems, which may not be a bad assumption considering that the data from the RTC concrete target simulations fit with the majority of the data but with residual velocity shifted slightly depending on the penetration resistance of the material, defined earlier. Note that we are using the same rebar material in all cases since it is

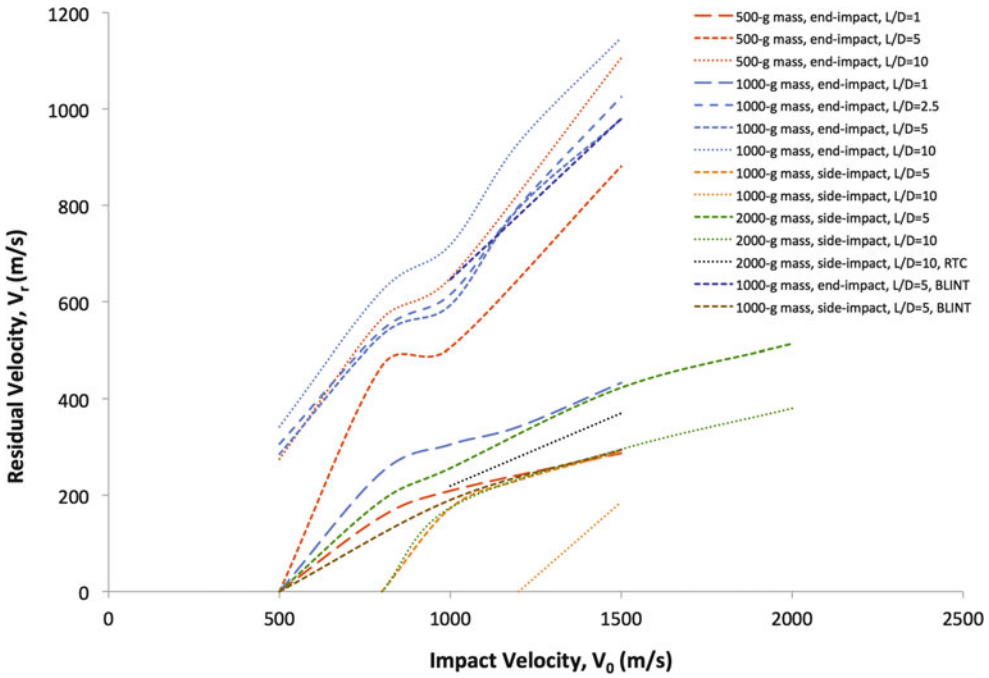

Fig. 29.2 Residual velocity results from parametric numerical simulations

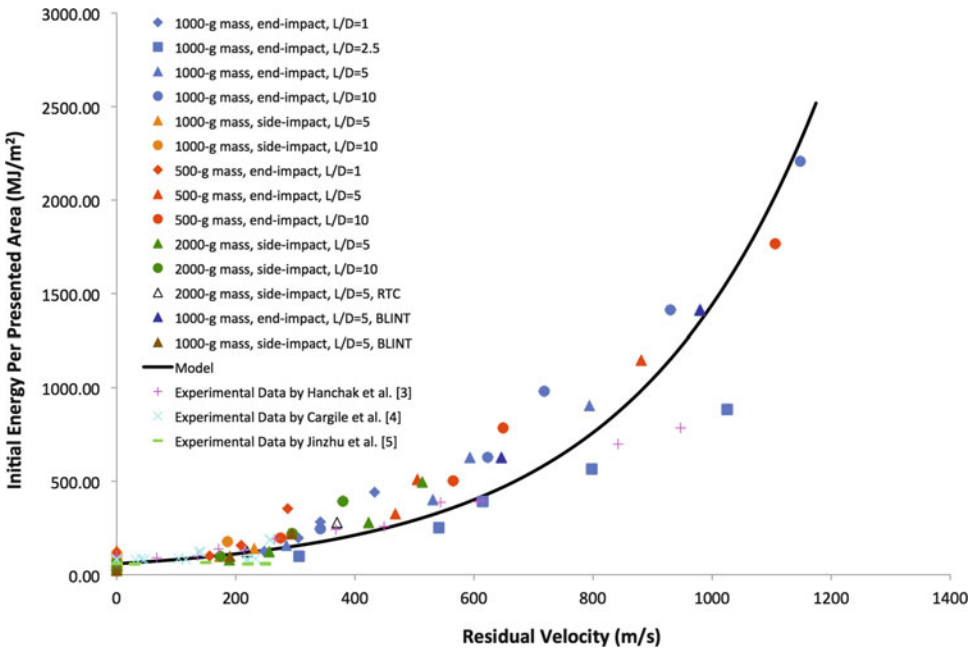

Fig. 29.3 Results from numerical simulations of variously dimensioned and oriented cylindrical projectiles with various impact velocities perforating a double reinforced concrete target. Initial energy is found from the data in Table 29.3 using the well-known formula for kinetic energy (i.e. $\frac{1}{2}mv^2$) and presented area is provided in Table 29.3. Model fit is for SAM-35 concrete with parameters for (29.2) given in Table 29.4. Fit $R^2 = 0.866$

assumed here that, in the Eulerian case, the rebar provides little resistance to penetration relative to the concrete since, in similar Eulerian simulations of the same target material and penetrator material but without rebar, the resulting residual velocity is only slightly different than simulations with rebar.

Equation 29.2 provides a fit ($R^2 = 0.866$) to the data presented in Fig. 29.3. Equation 29.2 includes two empirical parameters, A and B, which were determined for the fit to the data in Fig. 29.3, and are provided in Table 29.4.

Table 29.4 Empirical parameters, material parameters, and geometry for (29.2), determined for the empirical fit in Fig. 29.3

A (m/s)	B	ρ_P (kg/m^3)	ρ_T (kg/m^3)	C_T (m/s)	d (m)	h (m)
312.5	106.2	8050	2242	3730	0.02	0.20

A and B, are empirical parameters derived from the fitting of (29.2) to data for SAM-35 concrete perforated by a 4340 steel projectile. ρ_P is projectile density, ρ_T is target density, C_T is sound wave velocity in the target material (note that these target parameters are also provided in Table 29.1), d is projectile diameter, and h is target thickness

$$v_r = Aln\left(\frac{B\,\pi\,\rho_P\,d\,v_0^2}{\rho_T\,C_T^2\,h}\right) \tag{29.2}$$

Equation 29.2 normalizes the projectile energy per presented area (numerator of (29.2)) by target resistance to penetration (denominator of (29.2)) defined earlier. The parameter B incorporates a projectile shape factor, 1/4 for cylindrical projectiles or 1/6 for spherical projectiles.

Note that this work examines blunt projectile impacts to reinforced concrete targets, but the preponderance of experimental data available examines ogive or similarly sharp projectile impacts to concrete and is typically concerned with depth of penetration into concrete. Despite the lack of directly applicable experimental data, the experimental results of Hanchak et al. [3], Cargile et al. [4], and Jinzhu et al. [5] for ogive-nose penetration of concrete is compared with the numerical results as shown in Fig. 29.3. However, experimental validation is obviously an important subject for future exploration. This work was intended as an initial exploration into the kinetic energy required to perforate reinforced concrete and thus to provide a means of estimating whether a given projectile design will perforate reinforced concrete at a given impact velocity.

29.4 Conclusions

Using numerical simulations, a parametric study was conducted to determine the energy per unit area required to perforate a double reinforced concrete target with a right circular cylindrical projectile. An empirical equation was fit to the data from the numerical simulations. This equation may potentially be used to design projectiles for perforating reinforced concrete.

Much work is still needed in this effort. Evaluation of the empirical fit to the data should be conducted to determine any dependence of empirical parameters on the target-penetrator material system. Experimental exploration of the relationship between kinetic energy, projectile presented area, and target perforation residual velocity is needed.

References

1. Luk, V.K., Forrestal, M.J.: Penetration into semi-infinite reinforced-concrete targets with spherical and ogive-nose projectiles. Int. J. Impact Eng. **6**, 291–301 (1987)
2. Gomez, J.T., Shukla, A.: Multiple impact penetration of semi-infinite concrete. Int. J. Impact Eng. **25**, 965–979 (2001)
3. Hanchak, S.J., Forrestal, M.J., Young, E.R., Ehrgott, J.Q.: Perforation of concrete slabs with 48 MPa (7ksi) and 140 MPa (20ksi) unconfined compressive strengths. Int. J. Impact Eng. **12**, 1–7 (1992)
4. Cargile, J.D., Giltrud, M.E., Luk, V.K.: Perforation of thin unreinforced concrete slabs. In: International Symposium on Interaction of Nonnuclear Munitions with Structures, Panama City (1993)
5. Jinzhu, L., Zhongjie, L., Hongsong, Z., Fenglei, H.: Perforation experiments of concrete targets with residual velocity measurements. Int. J. Impact Eng. **57**, 1–6 (2013)
6. Forrestal, M.J., Altman, B.S., Cargile, J.D., Hanchak, S.J.: An empirical equation for penetration depth of give-nose projectiles into concrete targets. Int. J. Impact Eng. **15**, 395–405 (1994)
7. Lixin, Q., Yunbin, Y., Tong, L.: A semi-analytical model for truncated-ogive-nose projectiles penetration into semi-infinite concrete targets. Int. J. Impact Eng. **24**, 947–955 (2000)
8. Teland, J.A., Sjøl, H.: Penetration into concrete by truncated projectiles. Int. J. Impact Eng. **29**, 447–464 (2004)
9. Wu, H., Fang, Q., Zhang, Y., Gong, Z.: Semi-theoretical analyses of the concrete plate perforated by a rigid projectile. Acta Mechanica Sinica **28**, 1630–1643 (2012)
10. Liu, Y., Ma, A., Huang, F.: Numerical simulations of oblique-angle penetration by deformable projectiles into concrete targets. Int. J. Impact Eng. **36**, 438–446 (2009)
11. Huang, F., Wu, H., Jin, Q., Zhang, Q.: A numerical simulation on the perforation of reinforced concrete targets. Int. J. Impact Eng. **32**, 173–187 (2005)
12. Nia, A.A., Zolfaghari, M., Mahmoudi, A.H., Nili, M., Khodarahmi, H.: Analysis of resistance of concrete target against penetration of eroding long rod projectile regarding flow field around the projectile tip. Int. J. Impact Eng. **57**, 36–42 (2013)

13. Chen, X.W., Li, X.L., Huang, F.L., Wu, H.J., Chen, Y.Z.: Normal perforation of reinforced concrete target by rigid projectile. Int. J. Impact Eng. **35**, 1119–1129 (2008)
14. Chen, X.W., Fan, S.C., Li, Q.M.: Oblique and normal perforation of concrete targets by a rigid projectile. Int. J. Impact Eng. **29**, 617–637 (2004)
15. Latif, I., Rahman, I.A., Ahmad-Zaidi, A.M.: Development of empirical formula prediction on critical impact energy for perforation phenomena on concrete structures [sic], J. Math. Res. **3** (2011)
16. Latif, I., Rahman, I.A., Ahmad-Zaidi, A.M., Latif, K., Hameed, A., Nagapan, S.: Analytical model for critical impact energy of spalling and penetration in concrete wall [sic]. Int. J. Adv. Appl. Sci. **1**, 53–64 (2012)
17. Latif, I., Rahman, I.A., Ahmad-Zaidi, A.M., Latif, K.: Critical impact energy for spalling, tunnelling and penetration of concrete slab impacted with hard projectile. KSCE J. Civ. Eng. **19**(1), 265–273 (2014)
18. Li, Q.M., Reid, S.R., Ahmad-Zaidi, A.M.: Critical impact energies for scabbing and perforation of concrete target. Nucl. Eng. Des. **236**, 1140–1148 (2006)
19. Bainbridge, P.: World Impact Data-S.R.D. Impact Database Version Pre 3i, CCSD/CIWP(88)107(P) (1988)
20. Meyer, C.S.: Development of brick and mortar material parameters for numerical simulations using the Holmquist-Johnson-Cook constitutive model for concrete. In: Proceedings of the 26th International Symposium on Ballistics, Miami (2012)
21. Meyer, C.S.: Modeling experiments of hypervelocity penetration of adobe by spheres and rods. Proc. Eng. **58**, 138–146 (2013)
22. Meyer, C.S.: Numerical exploration of the terminal effects of multiple penetrators perforating concrete. In: Proceedings of the 28th International Symposium on Ballistics, Atlanta (2014)
23. Meyer, C.S.: Kinetic energy required for perforating double reinforced concrete targets: a parametric numerical study considering impact velocity and penetrator presented area. In: 13th Hypervelocity Impact Symposium (2015)
24. McGlaun, J.M., Thompson, S.L., Elrick, M.G.: CTH: a three-dimensional shock wave physics code. Int. J. Impact Eng. **10**, 351–360 (1990)
25. Holmquist, T.J., Johnson, G.R., Cook, W.H.: A computational constitutive model for concrete subjected to large strains, high strain rates, and high pressures. In: 14th International Symposium on Ballistics, Quebec, pp. 591–600 (1993)
26. Williams, E.M., Akers, S.A., Reed, P.A.: Laboratory Characterization of SAM-35 Concrete, ERDC/GSL TR-06-15. U.S. Army Corps of Engineers, Engineer Research and Development Center, Vicksburg (2006)
27. RTC concrete data provided by S.A. Akers: U.S. Army Corps of Engineers Engineer Research and Development Center. Geotechnical and Structures Laboratory, Vicksburg (2011)
28. Timber, Masonry, and Urban Type Target Construction for Warhead Testing, ITOP 5-2-503, U.S. Army Developmental Test Command, Aberdeen Proving Ground (2003)
29. Mie, G.: Zur kinetischen Theorie der einatomigen Körper. Ann. Phys. **316**, 657–697 (1903)
30. Grüneisen, E.: Theorie des festen Zustandes einatomiger Elemente. Ann. Phys. **344**, 257–306 (1912)
31. Johnson, G.R., Cook, W.H.: A constitutive model and data for metals subjected to large strains, high strain rates and high temperatures. In: Proceedings of the 7th International Symposium on Ballistics, The Hague, pp. 541–547 (1983)
32. A615 steel data provided by S.J. Schraml: U.S. Army Research Laboratory, Aberdeen Proving Ground (2012)
33. Holmquist, T.J., Templeton, D.W., Bishnoi, K.D.: Constitutive modeling of aluminum nitride for large strain, high strain rate, and high pressure applications. Int. J. Impact Eng. **25**, 211–231 (2001)
34. Gray, G.T., Chen, S.R., Wright, W., Lopez, M.F.: Constitutive equations for annealed metals under compression at high strain rates and high temperatures, LA-12669-MS. Los Alamos National Laboratory, Los Alamos (1994)
35. Anderson, C.E., Walker, J.D.: An examination of long-rod penetration. Int. J. Impact Eng. **11**, 481–501 (1991)
36. Scheffler, D.R.: Modeling non-eroding perforation of an oblique aluminum target using the Eulerian CTH hydrocode. Int. J. Impact Eng. **32**, 461–472 (2006)
37. Silling, S.A.: Eulerian simulation of the perforation of auminum plates by nondeforming projectiles, SAND91-0344. Sandia National Laboratory, Albuquerque (1992)
38. Kmetyk, L.N., Yarrington, P.: CTH analyses of steel rod penetration into aluminum and concrete targets with comparisons to experimental data, SAND94-1498. Sandia National Laboratory, Albuquerque (1994)

Chapter 30
Identification of the Dynamic Tensile Behavior of Geomaterials Based on the Virtual Fields Method and a New Generation-Ultra-High-Speed Camera

D. Saletti and P. Forquin

Abstract Dynamic behavior of a granite rock was investigated by using the spalling test method. This technique, based on the use of a Hopkinson bar, allows applying a tensile loading at high strain-rates, from a few tens to two hundreds of 1/s, to geomaterials to characterize their dynamic tensile strength. However, the standard 'Novikov' processing method providing the spall strength is based on basic assumptions (linear-elastic behavior until the peak). In addition, the post-peak behavior and the kinetics of damage in the material remain unknown. The use of full-field measurement appears to be of great interest to improve the processing method and to obtain more information from the spalling tests.

A new generation ultra-high speed (UHS) camera (Kirana, Specialized Imaging) was used in association with a digital image correlation (DIC) technique to measure the displacement field. Image acquisition was performed at 1,000,000 fps with a resolution close to 800,000 pixels. Dynamic tensile strength was characterized by post-processing DIC measurements with the virtual fields method (VFM) as proposed by Pierron and Forquin (2012). The interest of using the Kirana camera allowing higher spatial resolution compared to previous model of UHS camera (HPV1 ultra-high speed camera is discussed in the present paper).

Keywords Spalling test • Digital image correlation • Virtual fields method • Geomaterials • Dynamic tensile strength

30.1 Introduction

The spalling technique is generally used to investigate the dynamic tensile strength of brittle geomaterials at strain rates ranging from a few tens of /s to about 200/s. The experimental set-up consists into creating a short compressive pulse in the specimen with a Hopkinson bar. This pulse is reflected into a tensile pulse at the free-end of the specimen. Then, the tensile failure of the sample can be analyzed [1–3]. In the literature, spalling tests have been used to study the Dynamic Increase Factors (DIFs: ratio of dynamic strength to quasi-static strength) of various brittle materials [3–6].

Various methods have been employed to post-process spalling tests. The first one consisted into measuring the distance crossed by the fragments in order to evaluate, with basic kinematic assumptions, their velocity of ejection and to determine the spalling strength [7]. The evolution of the measurement techniques in the last three decades increased the number of studies using the spalling test to analyze the dynamic tensile behavior of brittle materials and new techniques emerged from them. Among them, the Novikov's method prevails to identify the maximal tensile strength of the specimen during a spalling test [1, 3, 8]. This method is based on the measurement of the velocity profile on the rear face of the sample. However, it relies on the assumption of a linear-elastic behavior of the tested material until the stress-peak and provides only its spall strength. No information on the softening behavior that follows is available. Pierron and Forquin [9] recently used a full-field measurement technique based on the grid method [10] in the spalling of concrete. They obtained a displacement field at the surface of the specimen during the test. These data converted in acceleration fields, were post-processed with the Virtual Fields Method (VFM) in order to evaluate a stress field at the surface of the specimen, in the region captured by the Ultra-High-Speed (UHS) camera. This was the first use of a full-field measurement technique in a spalling test.

In this study, the authors decided to use the same approach for a granite rock specimen but the Digital Image Correlation (DIC) was used instead of the grid method. DIC is widely used nowadays and is quite easy to be set, in comparison with the grid method, by the application of a painted speckle. Up to now, it was quite challenging to use DIC for spalling test: the duration time of the test is around a hundred of microseconds and only UHS camera can capture satisfying image sequence,

D. Saletti (✉) • P. Forquin
University of Grenoble Alpes, 3SR, Grenoble 38000, France
e-mail: dominique.saletti@3sr-grenoble.fr

B. Song et al. (eds.), *Dynamic Behavior of Materials, Volume 1*,
Conference Proceedings of the Society for Experimental Mechanics Series, DOI 10.1007/978-3-319-22452-7_30

with recording frequency starting from 500,000 frames per second (fps) to few millions of fps. A main limitation of these cameras relies on the resolution available (80 kpixels for a Shimadzu HPV-1) and DIC measurement is strongly dependent of this parameter. In this study, the authors had the opportunity to use a new generation of UHS camera: the Kirana model from Specialized Imaging. This camera has a constant resolution of 924 pixels by 768 pixels (around 710 kpixels) at recording frequencies up to 5 Mfps. The goal of the present study is to analyze the feasibility of a DIC-VFM approach for spalling tests on granite rocks and, therefore, brittle geomaterials.

30.2 Experimental Technique and Image Processing

30.2.1 Sample

The materiel tested in this study is a Bohus granite and is characterized by a longitudinal wave speed C of 4400 m/s, a density of 2630 kg/m^3 and a Young modulus of 50.9 GPa. This material was already subjected to static tests (bending tests and quasi-oedometric compression tests) as well as Edge-On-Impact (EOI) experiments [11, 12]. The sample is cylindrical, 45 mm in diameter and 140 mm in the length. As it can be seen in the Fig. 30.1, a flat surface was realized along the specimen and a painted speckle was applied on it.

30.2.2 Spalling Test Technique and Optical Measurement

The spalling test set-up used in this study is composed of a 50 mm-long spherical-cap-ended projectile and a Hopkinson bar both with a diameter of 45 mm and made of a high-strength aluminum characterized by a longitudinal wave speed of 5090 m/s, a density of 2810 kg/m^3 and a Young's modulus of 72.8 GPa. In order to make a comparison with the DIC, a laser interferometer from Polytec enabling velocity measurements up to 20 m/s with a bandwidth of 1.5 MHz is used to measure the particle velocity at the free-end of the specimen [3].

A Kirana UHS camera, from Specialized Imaging, was used in this study. This device allows recording a sequence of 180 images up to five million frames per second with a constant resolution of 924 $\times$ 768 pixel^2. A frame rate of 1 Mfps was employed and the exposure time was set to 1 µs. The horizontal axis corresponds to the longitudinal axis of the specimen and the left-hand side of the image corresponds to the free-end of the specimen (Fig. 30.1). The length of the specimen capture by the camera is around 85 mm and the scale of the image is 0.094 mm/pixel.

30.2.3 Digital Image Correlation

The DIC method was applied in this study with the CorreliQ4 code. The principle of this software is given by Besnard et al. [13]. A region of interest (ROI) is defined on a reference image and a mesh grid is created with a user-defined element size. Each Q4 element of this mesh is also called a Zone of Interest (ZOI). The correlation computation consists of finding the displacement field to link a deformed image of sequence to the reference image. The strain field is computed on the surface of the specimen using the gradient of displacement fields. The size of the ZOI is a compromise between the resulting

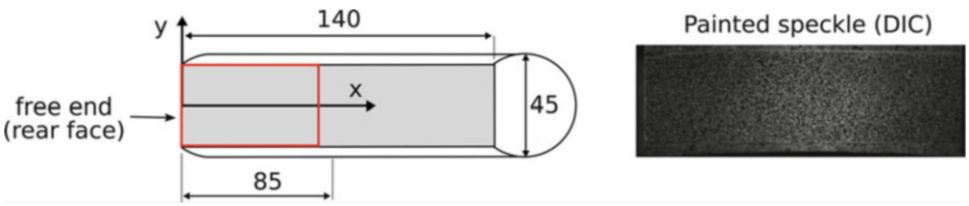

Fig. 30.1 Specimen dimensions (mm) and painted speckle applied

measurement uncertainties (ZOI size should be increased) and the heterogeneous nature of the expected displacement field (ZOI size should be decreased). For this study, measurement results with a ZOI size of 32 pixels are presented. Therefore, the created mesh contains 6 by 28 elements.

30.2.4 The Virtual Fields Method (VFM)

The VFM is based on the principle of the virtual work. In that case, and as described in [9], by defining a rigid body-like virtual field, the mean stress in any cross section Sx of coordinate x along the length of the sample captured by the camera can be calculated for each image of the sequence and is equal to the product of the density of the specimen with the length between Sx and the free-end of the specimen and the mean longitudinal acceleration along this length.

Therefore, an acceleration map has to be extract from the DIC measurements. It is realized by a double differentiation of the obtained displacement field. A temporal fitting is applied on this result with a second-order polynomial function over a sliding of 15 images in this case.

30.3 Results

30.3.1 Displacement Measurement

The particle velocity measured at the free end of the specimen with the laser interferometer was integrated to have a displacement. This displacement was compared with the one obtained with the DIC from the elements close to the rear-face of the sample. The comparison is presented on the Fig. 30.2. A maximum displacement of 0.45 mm was measured at the end of the image sequence. A maximum gap of 8 µm was found between DIC and laser displacement and can assess for the reliability of the displacement measurement performed with the digital image correlation.

A displacement field was measured on the surface of the specimen for all the image sequence. Figure 30.3 represents the field of axial displacement considering four distinct times: (1) at time 20 µs, in the early stage of the compression phase; (2) at time 30 µs, corresponding to the end of the compression phase before the unloading phase; (3) at time 60 µs, during the tension phase: displacement discontinuities can be observed, related to the apparition of fractures inside the specimen; (4) at time 75 µs, just after the tensile phase: displacement discontinuities due to tensile fracturing are increasing.

30.3.2 Strain and Stress Measurements

The strain field is computed at the surface of the specimen using the gradient of the displacement field. These strain fields can be used as multiple strain-gauge measurements. Figure 30.4 shows the strain history in the specimen at three different

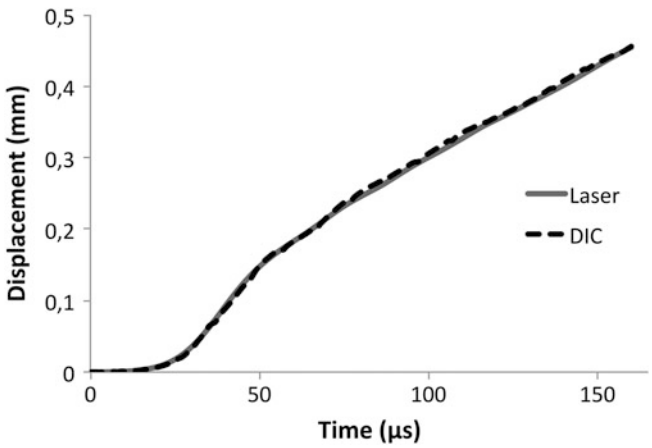

Fig. 30.2 Displacement ux at the free-end of the specimen. Comparison of the measurements obtained with a laser interferometer and the DIC method (32 px ZOI size)

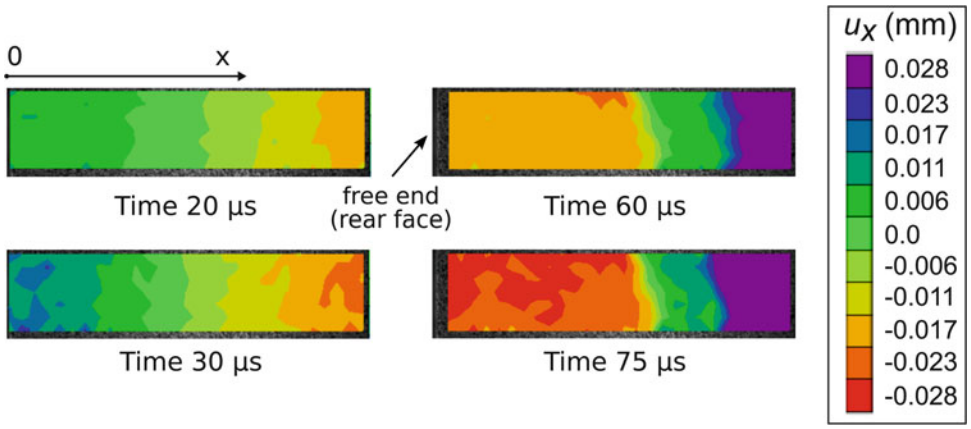

Fig. 30.3 Axial displacement field for four different stages without rigid body motion. 20 µs: beginning of compression phase. 30 µs: end of the compression phase. 60 µs: tension phase and apparition of displacement discontinuities in the specimen. 75 µs: just after the tensile phase, unloading of the specimen

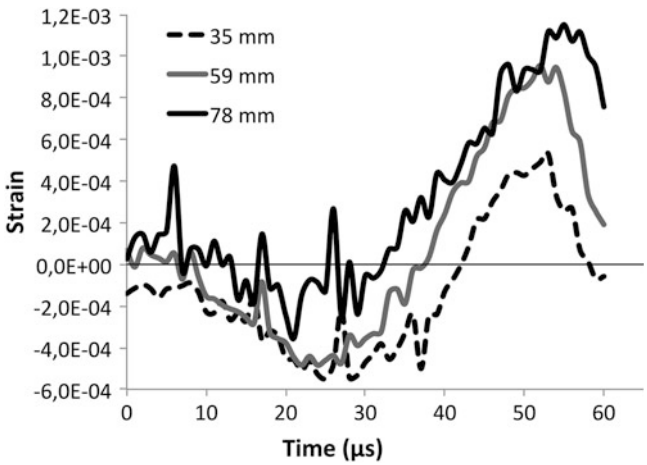

Fig. 30.4 Strain history at three locations in the specimen. The distance is expressed from the free-end of the sample

location: (1) at 35 mm from the free-end, on the left-side of the displacement discontinuities observed in Fig. 30.3; (2) at 59 mm, between the two discontinuities; and (3) at 78 mm from the free-end, on the right-side of the discontinuities. For the three curves, a compressive phase (time 15 µs to time 30 µs) and a tensile phase (beginning around time 40 µs) are noted (Fig. 30.4). One can observe that the 35 mm curve presents a vertical offset (initial value is not equal to zero) which may lead to think that tension come later on this part of the specimen, which is not the case. This effect is not found in the stress history curve (Fig. 30.5) and the authors chose to plot the strain values as they are, as this paper deals with the feasibility of DIC + VFM for spalling tests.

As it was previously mentioned, the displacement fields measured with the DIC was post-processed and used in the VFM to evaluate the stress history along the surface of the specimen contained in the observation window of the camera. As for the strain history, the stress history is presented in the Fig. 30.5 for the same three locations.

The maximum tensile stress obtained at each location is: (1) 25.1 MPa at 35 mm, (2) 26.9 MPa at 59 mm and (3) 29.1 mm at 78 mm. This last value is close to 29.2 MPa, the maximal measured stress on the whole stress field.

By combining stress and strain measurements, the mechanical response of the specimen is represented on Fig. 30.6 at the three proposed locations.

This is a first result and the gaps observed from the expected linear behavior in tension as in compression can be explained by the error in the measurement of the stress and of the strain. This effect is emphasized for the 78 mm curve in compression for which strain measurement is very noisy at this stage (Fig. 30.4).

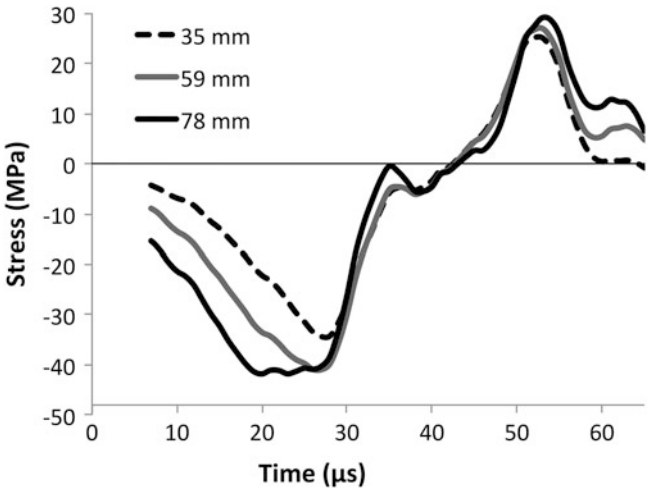

Fig. 30.5 Stress history at three locations in the specimen. The distance is expressed from the free-end of the sample

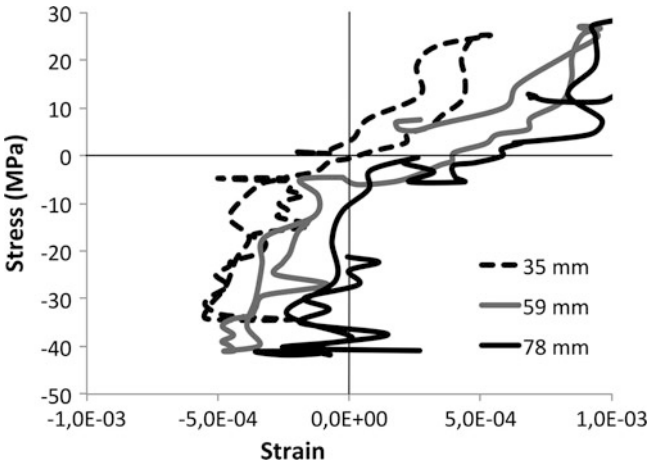

Fig. 30.6 Mechanical response of the sample at three locations. The distance is expressed form the free-end of the sample

30.4 Discussion and Conclusion

The tensile strength of Bohus granite was investigated by means of spalling experiments and by processing the experimental data with a new generation ultra-high speed (UHS) cameras (Kirana, Specialized Imaging) in association with a digital image correlation (DIC) technique to measure the displacement field. On the one hand, DIC measurements have been performed to deduce the axial displacement near the free-end of the sample and the level of axial strain at different locations regarding the free-end. On the other hand, the VFM processing method proposed by Pierron and Forquin [9] was used to calculate the change of stress in three cross-sections based on the measurements of acceleration obtained from the displacement fields. The obtained results allow plotting the stress-strain curves at the corresponding positions. Further study will have to focus on the sensibility of the DIC parameters (ZOI size, magnification of the image) and of the UHS camera ones (frame rate, exposure time, lightning).

References

1. Schuler, H., Mayrhofer, C., Thoma, K.: Spall experiments for the measurement of the tensile strength and fracture energy at high strain rates. Int. J. Impact Eng. **32**, 1635–1650 (2006)
2. Weerheijm, J., van Doormaal, J.C.A.M.: Tensile failure of concrete at high loading rates: new test data on strength and fracture energy from instrumented spalling test. Int. J. Impact Eng. **34**, 609–626 (2007)

3. Erzar, B., Forquin, P.: An experimental method to determine the tensile strength of concrete at high rates of strain. Exp. Mech. **50**, 941–955 (2010)
4. Klepaczko, J.R., Brara, A.: An experimental method for dynamic tensile testing of concrete by spalling. Int. J. Impact Eng. **25**, 387 (2001)
5. Erzar, B., Forquin, P.: Experiments and mesoscopic modelling of dynamic testing of concrete. Mech. Mater. **43**, 505–527 (2011)
6. Erzar, B., Forquin, P.: Analysis and modelling of the cohesion strength of concrete at high strain-rates. Int. J. Solids Struct. **51**, 2559 (2014)
7. Landon, J.W., Quinney, H.: Experiments with the pressure Hopkinson bar. Proc. R. Soc. Lond. A **103**, 622–643 (1923)
8. Novikov, S.A., Divnov, I.I., Ivanov, A.G.: The study of fracture of steel, aluminium and copper under explosive loading. Fizika Metallov i Metallovedeniye **21**, 608 (1966)
9. Pierron, F., Forquin, P.: Ultra high speed full-field deformation measurements on concrete spalling specimens and stiffness identification with the Virtual Fields Method. Strain **48**, 388 (2012)
10. Surrel, Y.: Moiré and grid methods: a signal-processing approach. In: Pryputniewicz R.J., Stupnicki J. (eds.) Interferometry '94: Photomechanics, p. 118. SPIE, Warsaw (1994)
11. Saadati, M., Forquin, P., Weddfelt, K., Larsson, P.-L., Hild, F.: Granite rock fragmentation at percussive drilling—experimental and numerical investigation. Int. J. Numer. Anal. Methods Geomech. **38**, 828–843 (2014)
12. Saadati, M., Forquin, P., Weddfelt, K., Larsson, P.-L., Hild, F.: A numerical study of the influence from pre-existing cracks on granite rock fragmentation at percussive drilling. Int. J. Numer. Anal. Methods Geomech. **39**, 558 (2015)
13. Besnard, G., Hild, F., Roux, S.: Finite-element displacement fields analysis from digital images: application to Portevin-le Chatelier bands. Exp. Mech. **46**, 89 (2006)

Chapter 31
Particle Size Reduction in Granular Materials During Rapid Penetration

Eduardo Suescun-Florez, Ivan L. Guzman, Stephan Bless, and Magued Iskander

Abstract Rapid penetration experiments using spherical projectiles at speeds up to 100 m/s were conducted in natural silica sand and in artificial sand comprised of crushed fused quartz. Material was recovered from the impact zone and subjected to size analysis and microscopic inspection. The fused quartz was much more susceptible to particle size reduction, particularly at lower velocities than natural sand. However, when the sand fractured, the particles were considerably smaller than those observed in fused quartz.

Keywords Penetration • Sand • Quartz • Crushing • Size analysis

31.1 Introduction

Penetration of granular materials is a topic of both engineering and scientific importance. Among the engineering applications, soil penetrometer probes [*e.g.* 1], military earth penetrators [*e.g.* 2], and locomotion in sandy environments [*e.g.* 3] are common examples. Scientific interest arises because theoretical treatments of penetration are dependent on constitutive behavior [4] including failure and porosity evolution. Thus characterization of penetration phenomena in granular materials can aid in the determination of low and high rate mechanical properties.

Dynamic penetration invokes modes of material response that are beyond the scope of conventional laboratory material testing. Chief among these is high deformation rates. The strain rate during penetration is of the order of U/D, where U is penetration rate and D is penetrator diameter, and for some penetrators this value can be well over 1000/s. Another aspect of dynamic penetration is the high pressure generated, which may contributes to particle breakage. During penetration the stress, $\boldsymbol{\sigma}$, in front of the penetrator is on the order M(dU/dt)/A, where M is the penetrator mass, and A is the cross-sectional area of the penetrator. Impact stresses not only depend on the strain rates but also on the transferred energy provided by the mass of the projectile. In the experiments reported in [5], for example, the stress levels were found to be above 100 MPa. At this stress crushing occurs in many laboratory tests on sand [6, 7]. High speed penetration, along with high impact stresses, through sand creates a channel of very fine white powder that has resulted from grain comminution, which has been reported by several investigators including Allen et al. [8–10].

When crushing takes place strain energy is dissipated forming new granular arrangement and surface areas. Since time is required to fracture grains and then rearrange the fragments, a relaxation time associated with these processes is also observed [11–13]. Laboratory studies have observed that there appears to be a distinct threshold penetration velocity above which grain comminution is greatly increased [14, 15]. Whether crushing aids or hinders penetration is not clear. On the one hand, crushing facilitates elimination of voids, creating free volume into which the penetrator can advance, and crushing is usually associated with reduction of shear resistance. On the other hand, both creation of new surface area and pressure-volume work associated with void collapse might help absorb the projectile kinetic energy.

In this study, two different types of granular particles were used in penetration experiments, and particles were collected to observe the presence, or not, of grain fracture and comminution. The occurrence of comminution was evaluated through microscopy as well as study of the change in grain size distribution in material penetrated by spherical projectiles.

E. Suescun-Florez • S. Bless (✉) • M. Iskander
Civil & Urban Engineering Department, New York University, New York, NY, USA
e-mail: sbless@nyu.edu

I.L. Guzman
Civil & Environmental Engineering Department, New Jersey Institute of Technology, Newark, NJ 07103, USA

B. Song et al. (eds.), *Dynamic Behavior of Materials, Volume 1*,
Conference Proceedings of the Society for Experimental Mechanics Series, DOI 10.1007/978-3-319-22452-7_31

31.2 Materials and Experimental Configuration

The current work was conducted on two different granular materials: Ottawa Sand and Fused Quartz. Ottawa sand was selected because it is used extensively for engineering research and application purposes. It is essentially pure silica, and sand grains are agglomerations of cemented quartz crystallites. Fused quartz is comprised of particles of amorphous quartz glass; particles are less rounded than sand, but otherwise provides similar mechanical characteristics to natural sand [16]. Fused quartz is also being used by the Geomechanics Research Group at New York University to make transparent soils that are currently used to model soil structure interaction non-intrusively by employing optical visualization techniques [17].

31.2.1 Target Preparation

Target models for the impact tests were prepared in 150 × 150 × 175 mm (width × depth × depth) transparent containers. Soil targets of dry Ottawa sand and dry fused quartz were tested.

The fused quartz was manufactured by Mintec Inc. In order to better observe the amount of particle breakage, an initial particle size distribution was narrowed somewhat. This was achieved by sieving the as-received material through a #20 sieve (0.853 mm) and a #60 sieve (0.251 mm). Particles retained in the #20 sieve and particles that passed the #60 sieve were eliminated from the soil mixture, thus creating a controlled fused quartz sample with very little fines. The resulting fused quartz gradation is thus termed FQ (−20 + 60). More information about fused quartz is available in [18]. The delivered Ottawa sand gradation used in this study has very little fines; thus a pre sieving process was not needed to eliminate small particles.

Targets were made by using a sand pluviator to rain both soils into the container. The sand pluviator serves to create a soil structure that mimics natural sedimentation at a controlled relative density of medium dense. This process guarantees that the desired relative density is achieved. Weight measurements of the container prior and after pluviation of soil along with the volume of the soil model were taken to check the relative density before the impacting phase.

Particle sizes are summarized in Table 31.1. The diameters corresponding to percentage finer by weight are presented as D_{60}, D_{50}, D_{30}, and D_{10} for 60 %, 50 %, 30 %, and 10 % finer by weight respectively. Two commonly used gradation parameters *Coefficient of Curvature* $\left[Cc = \frac{D_{30}{}^2}{D_{60} \times D_{10}}\right]$ and *Uniformity Coefficient* $\left[Cu = \frac{D_{60}}{D_{10}}\right]$ are also presented, along with The American Society of Testing of Materials (ASTM) *Unified Soil Classification System* (USCS) for the tested materials.

31.2.2 Projectiles and Projectile Accelerator (Gas-Gun)

The projectiles used in this study consisted of metal spheres with an approximate diameter of 10 mm (0.39 in). The projectile material was stainless steel (Type, 316 18 % chromium and 8 % nickel) having a density of 7600 kg/m^3, which yields mass to diameter ratios of 0.39 kg/m. None of the projectiles were plastically deformed by the impacts.

An electro-pneumatic projectile accelerator (air-gun), designed and constructed in the facilities of Civil Engineering Department at NYU-Poly [19], was used to propel the projectiles to speeds ranging from 60 to 100 m/s. The projectile accelerator consists of a 300 cm^3 stainless steel gas chamber that acts as a reservoir to store Helium under pressures of

Table 31.1 Particle size parameters of granular materials tested

		Gradation Parameters	
Physical property		FQ (−20 + 60)	Ottawa sand
Particle size (mm)	D_{60}	0.54	0.59
	D_{50}	0.49	0.56
	D_{30}	0.40	0.50
	D_{10}	0.28	0.45
Coefficient of curvature	C_c	1.1	0.9
Coefficient of uniformity	C_u (D_{60}/D_{10})	1.9	1.3
USCS classification	USCS	SP	SP

up to 800 psi. The gas chamber contains an electro-pneumatic ball valve that acts as the firing mechanism and releases compressed Helium into a 0.76 m (30 in) barrel. Helium was selected as the propellant gas to improve the accelerator's efficiency.

Projectile exit velocities were measured by using an optical speedometer. The optical speedometer uses a series of three photo gates separated by a known distance. As the projectile crosses the plane of the photo gate light the signal is interrupted and a time stamp is recorded. The time difference between the photo gates interruptions divided by the distance between the photo gates yields the velocity of the projectile. The series of three photo gates are able to take two independent velocity measurements as the projectile exits the end of the barrel. The average of the two velocity measurements was used for calculations. For safety, the projectile accelerator was activated remotely by the use of a solenoid trigger.

31.3 Breakage Analysis

31.3.1 Experimental Process

Once the model preparation was complete, specimens were retrieved prior to and after the penetration event by using a simple suction consisting of an Erlenmeyer flask, a rubber stopper with an orifice, and two hoses. One of the hoses was threaded through the rubber stopper. The rubber stopper was then inserted into the top of the flask and served as the suctioning device. The side hose barb was fitted with the second hose and connected to a vacuum source.

A specimen labeled as "control specimen" was collected with the suction device prior to the penetration event from the sides of the target container. After the penetration event the suction device was used to carefully collect a specimen, labeled as "sample", from the middle of the impact crater down to the top of the projectile when possible. Although sampling was carefully conducted, samples may have been affected by comminuted material traveling in the after flow along the trajectory of the projectile. After the impact, the top view of the impacted model where a crater full of pulverized fused quartz is typically clearly identifiable as shown in Fig. 31.1. The center of the impacted area is the section of most interest to retrieve the sample for post-impact analysis. However, soil ejecta may contribute to filling the crater and reducing the magnitude of observed breakage/comminution.

After each shot, control specimens and sample specimens were collected and subjected to a grain size analysis using a series of 3 in. diameter stainless steel sieves (#25, #40, #60, #80, #140, #200, #325 and #450) to create gradation curves. Additionally, both control and sample specimens were visually analyzed by using a Scanning Electron Microscope (SEM) and X-ray diffraction to visually assess the amount of particle breakage and the nature of particle breakage.

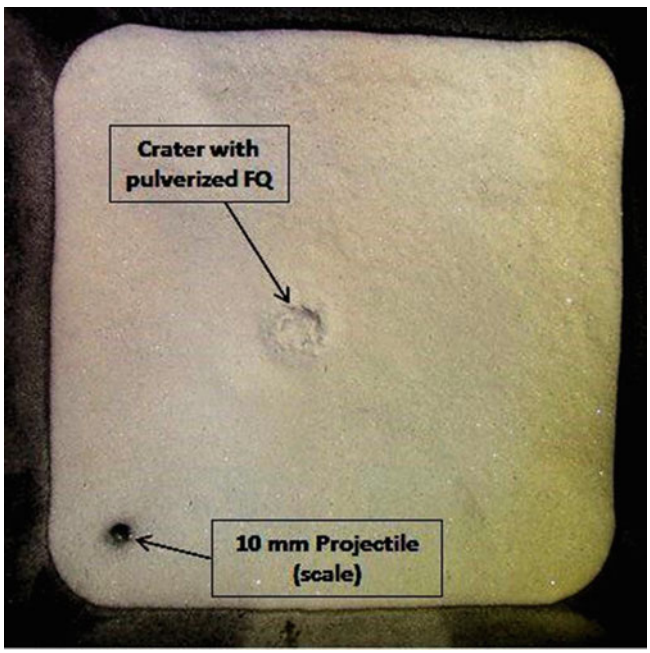

Fig. 31.1 Picture of closed crater after penetration event (*top view*)

31.3.2 Hardin's B-Factor Approach to Quantify Particle Breakage

Hardin [20] suggested a commonly used method for estimating the potential for breakage (Bp). The calculation is valid for granular soils with particles greater than 0.074 mm (silt soil), and it is computed as;

$$B_p = \int_0^1 b_p df$$

where b_p corresponds to the potential breakage for a given size fraction, df is a differential of "percent passing" divided by 100. B_p is equal to the area above the gradation curve, without including the part of the gradation curve that is beyond the biggest silt soil size (Fig. 31.2).

When a granular material, having certain breakage potential, is exposed to impact loading, the gradation curve will shift to the right indicating that some particles have been broken leading to the creation of new smaller ones. By comparing the two gradation curves: before and after impact event, the quantification of crushing can then be found as follows;

$$B_t = \int_0^1 \left(b_{po} - b_{pl}\right) df$$

where $\boldsymbol{b_{po}}$ is the original value of $\boldsymbol{B_p}$, and $\boldsymbol{B_{pl}}$ is the value after the crushing load. In other words, $\boldsymbol{B_t}$ is the difference between the areas above the gradation curve (excluding silty grain sizes) before and after impact load. This leads to the definition of relative breakage, $\boldsymbol{B_r}$, suggested by Hardin and commonly referred to as ***B-factor***;

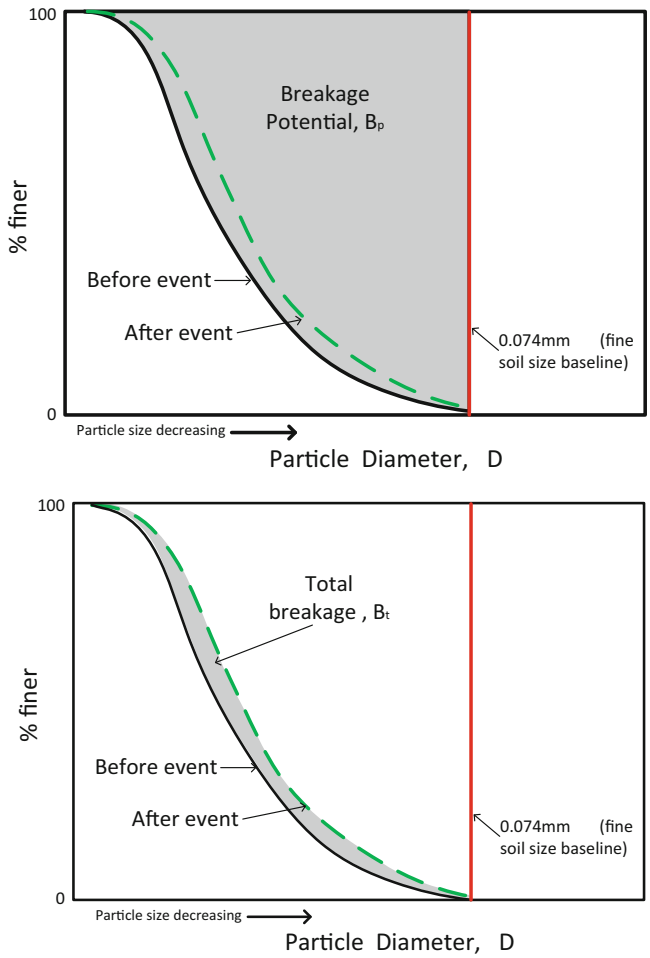

Fig. 31.2 Schematic diagram of definition of breakage potential, Bp, and total breakage, Bt

$$B_r = \frac{B_t}{B_p}$$

The B-factor is independent of particle size distribution when particle size distribution is the only variable. A B-factor of zero suggests no particle breakage is detected, whereas B-factor of unity indicates that all particles break to the smallest possible size within the analysis (0.074 mm).

31.3.3 Optical Analysis of Samples

A scanning electron microscope (SEM) was employed to qualitatively assess the amount and characteristics of particle breakage that occurred due to rapid penetration with a steel projectile. A Hitachi model S-3400 N scanning electron microscope (SEM) was employed which permitted observations of features as small as 10 μm. SEM specimens were randomly recovered from the sample bag leading to obtain representative material to be exposed to microscope analysis. In order to prepare the sample, first a black non-reflective double-sided adhesive tape was attached to the sample holder. Next, the sample holder was pushed against recovered samples, which attached themselves to the adhesive tape. Finally, the sample holder was inserted into the SEM chamber and images were taken at different magnifications.

31.3.4 X-Ray Analysis of Samples

X-ray diffraction measurements were conducted on Ottawa sand and fused quartz samples in order to (a) validate their crystal structure and (b) to investigate whether rapid impact of projectiles caused changes within their micro-structure. A Rigaku-Miniflex X-Ray Diffractometer was used which permitted irradiating the granular material with wavelengths of down to 1 Å and a range of diffraction angles from 10 to 80°. Samples were carefully prepared following the powder method [21] in which first, double sided black adhesive tape is attached to the bottom of the sample holder. Next, granular materials are carefully poured until the entire black surface of the tape is no longer visible. Next, a gentle pressure is applied on the granular sample to ensure full contact to the tape. Finally, the sample holder is placed in the X-ray diffractometer, and the sample is bombarded with X-rays. Sample placement results in a random arrangement of particles. Therefore, when X-rays bombard the particles, only some crystals will be correctly aligned to face the X-rays, and reflect them back. By altering the angle of the X-rays to sweep the entire trajectory the diffractometer record the X-ray reflections of the entire set of lattice planes. Peaks of reflection can be employed to identify the mineral composition of the sample because they are associated with specific lattice planes.

31.4 Breakage Analysis: Results and Discussion

It is difficult to control sampling errors in our experiments. This is because of infilling of the penetration channel after the shot, and because it is not certain what fraction of the particles that are collected actually interacted with the penetrator. With this in mind, optical and sieve analysis were conducted on the representative control specimen and all of the post-penetration samples for all of the tests conducted.

31.4.1 Ottawa Sand Crushing

The pre and post sieve analysis of Ottawa samples show that nearly no particle breakage occurred during penetration with a steel projectile at speeds of 60 and 100 m/s (Fig. 31.3 top). This observation was quantified by computing B-values for all of the specimens. The Ottawa sand specimens at 60 and 100 m/s showed B-values of approximately zero suggesting no particle breakage was identified during penetration.

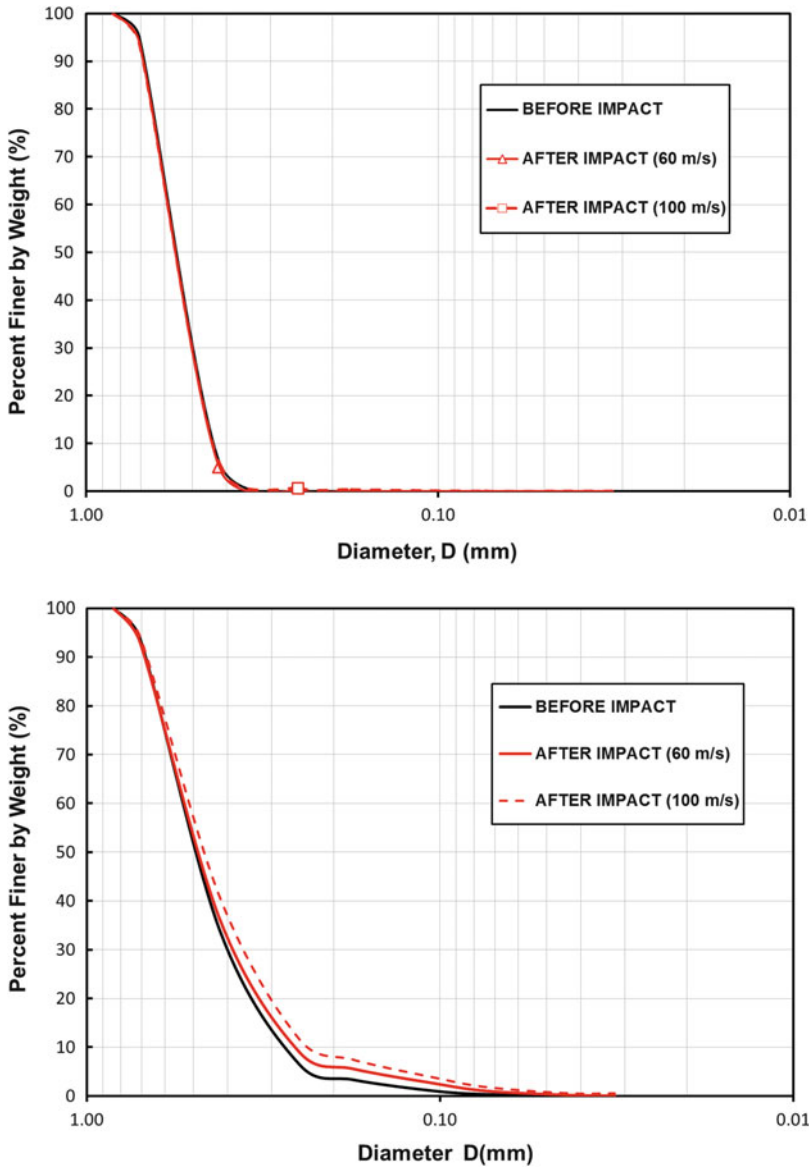

Fig. 31.3 Sieve analyses for qualitative description of particle breakage after rapid penetration into (*top*) Ottawa sand and (*bottom*) FQ (−20 + 60)

Images of Ottawa sand before and after penetration at speeds of 60 and 100 m/s are presented in Fig. 31.4. From the figure the roundness nature of the Ottawa sand in both scenarios is fully highlighted. Images show very little to negligible signs of breakage when velocity is 60 m/s. On the other hand, when the velocity is increased to 100 m/s there are trace amounts of very small grains that were not present in the original material, with a mean particle size of about 50 μm. The new smaller particles are more angular in shape. Bless et al. [22] in SEM photographs of Ottawa found that after impact at 300 m/s significant comminution into much smaller particles in the range of 5–50 μm is observed. Borg et al. [23] also reported significant comminution of sand at impact speeds exceeding about 100 m/s.

In conventional shear, it has been shown that particle breakage in granular media occurs when edges and asperities break into smaller particles which later continue to break into even smaller particles [6]. Although comminution was not directly observed in the current study, given the high stresses imposed during impact, one might speculate that particle size reduction in sand involves sudden comminution as seen by Bless et at. [10] in white sand trails.

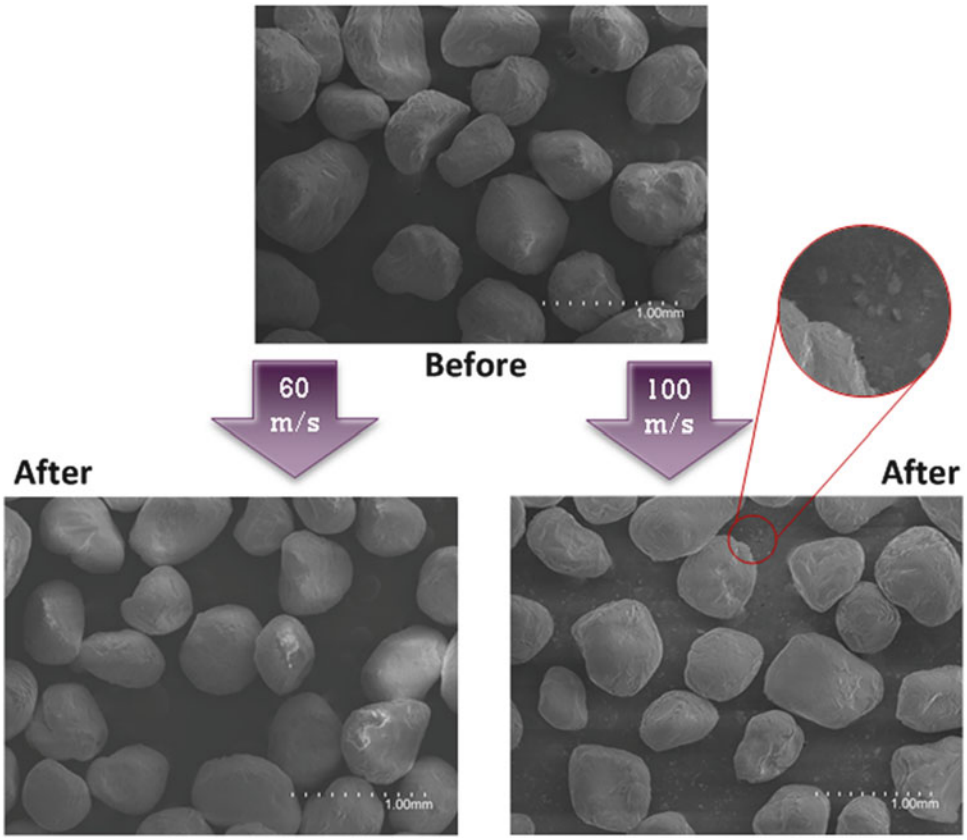

Fig. 31.4 Scanning electron images of Ottawa sand before penetration (*top*) and after penetration at 60 m/s (*bottom left*) and at 100 m/s (*bottom right*)

31.4.2 Fused Quartz Crushing

Gradation analysis was also performed in fused quartz before and after impact events, and it was observed that there is more particle crushing than in Ottawa sand at both velocities (Fig. 31.3 bottom). However, the extent of particle size reduction is less stark. When velocities of 60 m/s were applied, small amount of particle breakage was observed, while somewhat more particle breakage was visible after impact at 100 m/s. Following the pre-established experimental process B-values for fused quartz were also calculated. It was found that specimens yielded B-values of 0.022 and 0.066 for velocities of 60 and 100 m/s respectively, which suggest tangible breakage. In this study the B-values represent indicative numbers of the relative breakage among their respective velocities rather than established values to be used, for example, to validate constitutive models. B-values may vary since the sampling process does not identify the source of recovered material, which can be contaminated by ejecta. Definitive identification of the source of the sampled material requires the use of a real-time high resolution X-ray tomography, which is not available to us at this time.

SEM images of fused quartz before and after penetration with a steel projectile traveling at 60 and 100 m/s are presented in Fig. 31.5. From the images it can be seen that unlike Ottawa sand, the shape of fused quartz particles is mostly sub angular to angular. Also that fused quartz fractures at a speed of 60 m/s with fragmented particles that range in size between 50 and 500 μm. Furthermore, at impact speeds of 100 m/s, significant siz reduction is detected resulting in particles in the range of 50–100 μm. It can also be observed that the smaller fragmented particles are more angular in nature than their parents.

31.4.3 Effect of Grain Size Distribution and Mineralogy on Particle Breakage

The effect of grain size distribution on sand breakage during projectile penetration has been previously discussed [24]. It is believed that larger sand grains are more susceptible to breakage. This behavior is common in brittle materials and is normally attributed to the larger number of flaws in larger grains. However, there are other variables that may play important

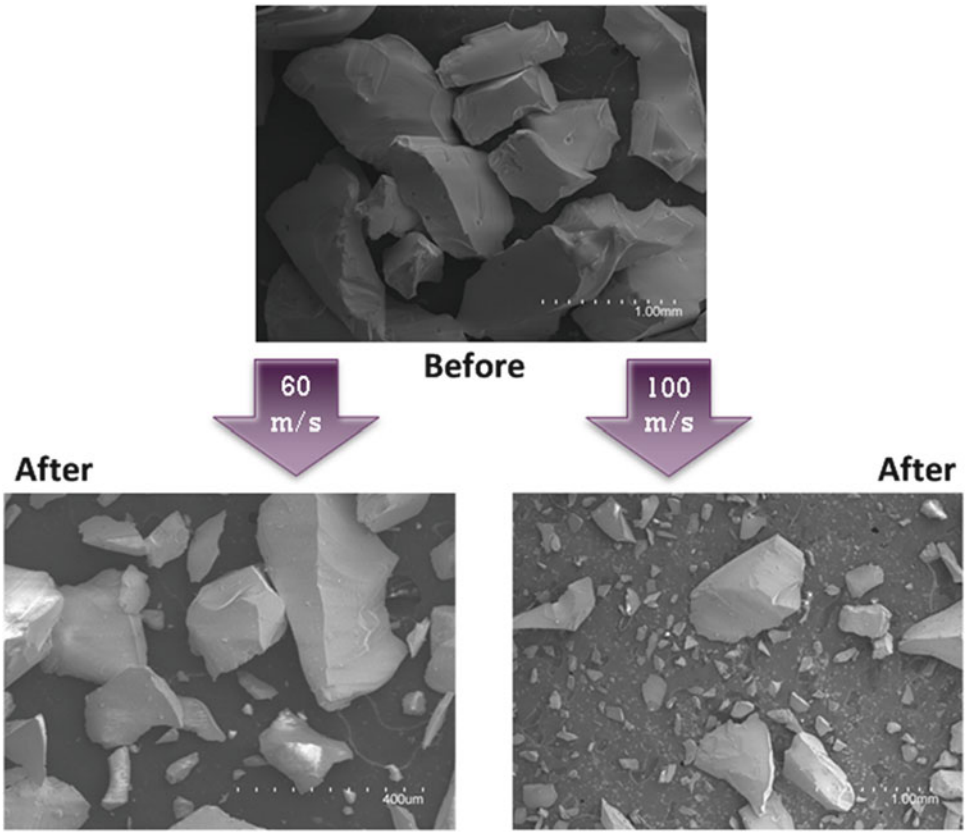

Fig. 31.5 Scanning electron images of FQ (−20 + 60) before penetration (*top*) and after penetration at 60 m/s (*bottom left*) and at 100 m/s (*bottom right*)

roles in breakage including grain size distribution, angularity, and mineralogy of the parent particle. In principal, well-graded materials have a higher coordination number (the number of contacts points per grain), since they are surrounded by smaller grains [25]. A higher coordination number produces a cushioning effect and reduces stress concentrations. This ends up providing greater confinement and prevention of stress localization, and mitigates breakage due to tensile failure [6, 26, 27]. The previous statement is true only when the applied load is uniformly distributed. Based on these results, it is reasonable to expect, that grain size distribution plays a role in the grain breakage phenomenon.

Mineralogical composition of grains may also contribute to the fracture vulnerability, since the sand contains trace amounts of aluminum oxide. The micro-analysis of the grain is then partially contributing to the skeleton strength. Silicon dioxide (SiO_2), the main component of the natural sand and Fused quartz, occurs in either a crystalline (Ottawa sand) or non-crystalline or "amorphous" (Fused quartz) form. Fracture of sand grains involves cracks that run on the boundaries between quartz crystals, and hence these cracks do not have an effect of the crystal structure itself. Fractures in fused quartz clearly run through the glass particles, but since the material is amorphous, there is no effect on the x-ray structure.

X-ray diffraction confirmed that the lattice parameters of both Ottawa sand and fused quartz were not affected by the impact. The series of reflections of different intensities at different values of 2θ allows the determination of individual crystals present in the granular samples. Since all reflections fall within the same angle limits and no shifting was observed during pre- and post-impact events it can be concluded that there were no changes in lattice parameters. Diffraction analysis also confirms the amorphous nature of fused quartz and that Ottawa sand possessed minor amounts of Iron, and titanium impurities.

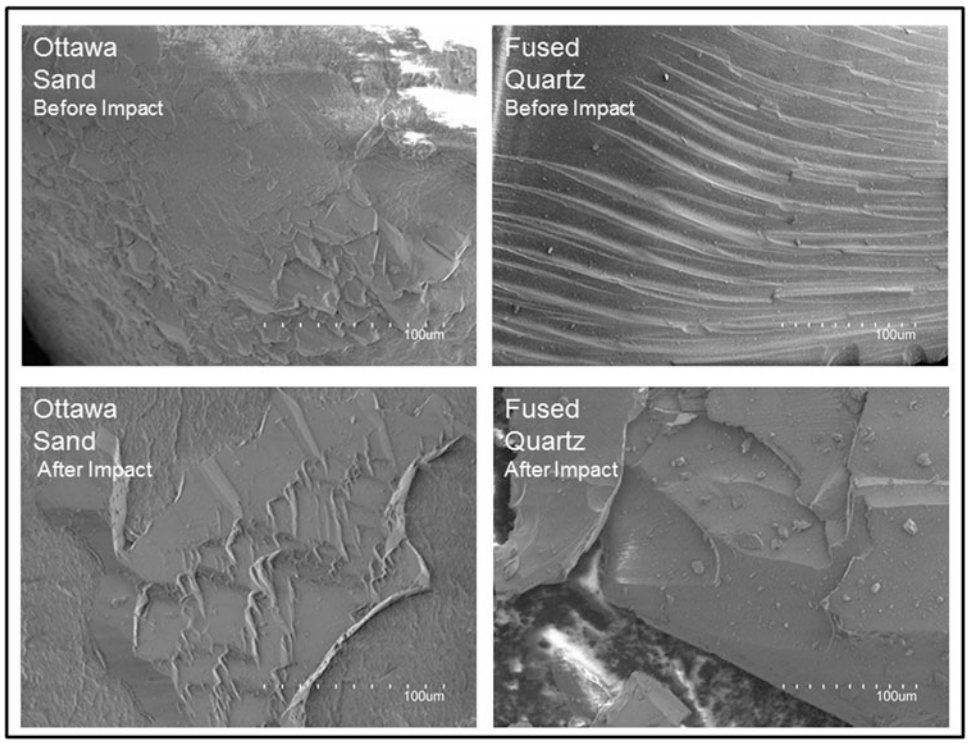

Fig. 31.6 Scanning Electron Images of the surface of Ottawa Sand and Fused Quartz particles before and after impact, at 100 m/s

31.4.4 Effect of Grain Morphology

Magnified images of grains' surfaces are provided in Fig. 31.6. Interestingly, the only indications of high speed fracture, hackle patterns, are observed on some of the as received fused quartz particles. These patterns probably indicate that this material is produced by rapid fracture of larger pieces of quartz glass. Otherwise, the usual indications of rapid fracture in brittle materials, mist-hackle transitions, are absent from these materials. This suggests that the fracture process is by activation of many preexisting flaws, not by initiation and bifurcation of a rapidly-running single fracture that begins at a largest flaw. One can argue that the fracture process is not really dynamic: The time for fracture is of the order particle diameter/fracture velocity. Fracture velocities in quartz glass are typically 1.5 mm/μs, so the time to fracture a typical particle is only 1/3 μs. In that time the projectile moves at most 30 μm, which is much less than a particle diameter. Therefore, the rate at which the load is applied is longer than the characteristic time required for a grain to fracture.

31.5 Conclusions

This work presents experimental data to illustrate particle breakage during penetration of two different granular materials: Ottawa sand and fused quartz. It was shown that quartz particles break at impact velocities of 60–100 m/s. However, the daughter particles are still an appreciable fraction of the size of their parents. Sand, on the other hand, only exhibits breakage at 100 m/s, and the daughter particles are much smaller than their parents. This suggests that when sand particles fail, they fail by disintegration. Modifications of material fabric caused by particle breaking should be taken into account when constitutive models are developed for penetration predictions.

Acknowledgment The authors gratefully acknowledge the support of the Defense Threat Reduction Agency (DTRA) of the United States of America, Grant No: HDTRA1-10-1-0049.

References

1. Dayal, U., Allen, J.H., Jones, J.M.: Use of an impact penetrometer for the evaluation of in-situ strength of marine sediments. Mar. Geotechnol. **1**(2), 73–89 (1975)
2. Backman, M.E., Goldsmith, W.: The mechanics of penetration of projectiles into targets. Int. J. Eng. Sci. **16**, 1–99 (1978)
3. Chen, C.L., Zhang, T., Goldman, D.L.: A terradynamics of legged locomotion on granular media. Science **22**, 1408–1412 (2012)
4. Forrestal, M.J., Luk, V.K.: Penetration into soil targets. Int. J. Impact Eng. **12**(3), 427–444 (1992)
5. Bless, S., Peden, B., Guzman, I.L., Omidvar, M., Iskander, M.: Poncelet coefficients of granular media. In: Society for Experimental Mechanics Proceedings of 2013 Annual Conference and Exposition on Experimental and Applied Mechanics, Lombard, 2–5 June 2013
6. McDowell, G.R., Bolton, M.D.: On the micromechanics of crushable aggregates. Geotechnique **48**, 667–679 (1998)
7. Luo, H., Cooper, W.L., Lu, H.: Effect of moisture on the compressive behavior of dense eglin sand under confinement at high strain rates. In: Proceedings of 2013 Annual Conference and Exposition on Experimental and Applied Mechanics, Lombard, 2–5 June 2013
8. Allen, W.A., Mayfield, E.B., Morrison, H.L.: Dynamics of a projectile penetrating sand. J. Appl. Phys. **28**, 370–376 (1957)
9. Allen, W.A., Mayfield, E.B., Morrison, H.L.: Dynamics of a projectile penetrating sand. J. Appl. Phys. **28**, 1331–1335 (1957)
10. Bless, S.J., Cooper, W., Watanbe, K.: Penetration of rigid rods into sand. In: International Symposium on Ballistics, Miami (2011)
11. Ben-Nun, O., Einav, I.: The role of self-organization during confined comminution of granular materials. Philos Trans A Math Phys Eng Sci. **368**(1910), 231–247 (2010)
12. Nguyen, G.D., Einav, I.: The energetics of cataclasis based on breakage mechanics. In: Mechanics, Structure and Evolution of Fault Zones. Pageoph Topical Volumes, pp. 1693–1724. Birkhäuser, Basel (2010)
13. Omidvar, M., Iskander, M., Bless, S.: Stress-strain behavior of sand at high strain rates. Int. J. Impact Eng. **49**, 192–213 (2012)
14. Bless, S.J.: Failure waves and their possible roles in determining penetration resistance of glass. Int. J. Appl. Ceram. Technol. **7**, 400–408 (2009)
15. Borg, J.P., Morrissey, M., Perich, C., Vogler, T., Chhabildas, L.: In situ velocity and stress characterization of a projectile penetrating a sand target: experimental measurements and continuum simulations. Int. J. Impact Eng. **51**, 23–35 (2013)
16. Guzman, I.L., Iskander, M.: Geotechnical properties of sucrose-saturated fused quartz for use in physical modeling. Geotech. Test. J. **36**, 8 (2013)
17. Iskander, M.: Modeling with Transparent Soils, Visualizing Soil Structure Interaction and Multi Phase Flow, Non-Intrusively, p. 329. Springer, New York (2010)
18. Guzman, I.L., Iskander, M., Suescun-Florez, E., Omidvar, M.: A transparent aqueous-saturated sand surrogate for use in physical modeling. Acta Geotech. **9**(2), 187–206 (2013)
19. Cave, A., Roslyakov, S., Iskander, M., Bless, S.: Design and performance of a laboratory pneumatic gun for soil ballistic applications. Experimental Techniques, Wiley, EXT-T-1050.R1 (2013)
20. Hardin, B.O.: Crushing of particles. J. Geotech. Eng. ASCE **111**, 1177–1192 (1985)
21. Cullity, B.D., Stock, S.R.: Elements of X-Ray Diffraction, 3rd edn, pp. 185–201. Pearson, Prentice Hall, Upper Saddle River (2001)
22. Bless, S.J., Berry, D.T., Pederson, B., Lawhorn, W.: Sand penetration by high speed projectiles. In: Proceedings of Shock Compression of Condensed Matter, pp. 1361–1364, (2009)
23. Borg, J., Van Vooren, A., Sandusky, H., Felts, J.: Sand penetration: a near nose investigation of a sand penetration event. In: Society for Experimental Mechanics Proceedings of 2013 Annual Conference and Exposition on Experimental and Applied Mechanics, Lombard, 2–5 June 2013
24. Omidvar, M., Iskander, M., & Bless, S.: Response of granular media to rapid penetration. Int. J. Impact Eng. **66**, 60–82 (2014)
25. Nakata, Y., Hyodo, M., Hyde, A., Kato, Y., Murata, H.: Microscopic particle crushing in sand subjected to high pressure one-dimensional compression. Soils Found. **41**(1), 69–82 (2001)
26. Cavarretta, I., Coop, M., O'Sullivan, C.: The influence of particle characteristics on the behavior of coarse grained soils. Geotechnique **60**(6), 413–423 (2010)
27. Altuhafi, F.N., Coop, M.R.: Changes to particle characteristics associated with the compression of sands. Geotechnique **61**(6), 459–471 (2011)

Chapter 32
Experimental Techniques to Characterize the Mechanical Behaviour of Ultra-High-Strength-Concrete Under Extreme Loading Conditions

P. Forquin and B. Lukic

Abstract In the present work, three experimental methods have been employed to characterize the dynamic tensile, shear and confined behavior of an UHSC (Ultra-High Strength Concrete) with and without steel fiber reinforcement. On the one hand, a dynamic testing method was developed to investigate the post-peak tensile behavior of UHSC. A Split-Hopkinson Pressure Bar (SHPB) device is used and the notched-concrete sample is glued in-between the input and output bar. A compressive pulse reflects as a tensile pulse leading to the breakage of the sample. In this case a strong influence of fibers is noted. On the other hand, two experimental methods are used to investigate the confined behavior of UHSC under shear and quasi-oedometric loading paths. In the quasi-oedometric compression test the concrete sample is inserted in a confining vessel and axially compressed. Hydrostatic pressure as high as 800 MPa are obtained and the hydrostatic and deviatoric behavior are deduced. The PTS (Punch-Trough-Shear test) provides lateral pressure of over 70 MPa in the sheared zone, high shear strain and leads to a mode II fracturing of the sample. Influence of fibers on the dynamic behavior of UHSC is discussed thanks to the previous experiments.

Keywords Split Hopkinson Pressure Bar • Ultra-high performance concrete • Hydrostatic pressure • Punch-Trough-Shear test

32.1 Introduction

For several years, defense organizations have been interested in the dynamic behavior of new concrete materials, e.g., Ultra-High Strength Concrete (UHSC) due to their exquisite material properties. Quasi-static mechanical properties of concrete have increased considerably over the last than 20 years [1]. In the middle of the 1990s, the use of superplastifiers, silica fumes and quartz grains led to production of UHSC concrete materials with a compressive strength of about 200 MPa [2], that were outstanding compared with that of ordinary concrete. Research programs that aim at evaluating ballistic performance of ultra-high strength concrete are currently under way. One of the goals is to improve the knowledge and modeling of damage mechanisms under impact [3]. In the present study, a UHSC similar to that of Ductal® concrete produced by Lafarge is investigated under different loading conditions. Besides its compressive strength (200 MPa), this UHSC is of interest to be produced on an industrial scale. Significant increase of flexural strength and ductility is obtained by adding fibers during the mixing process [4]. However, the potential effects of fiber content under extreme loading conditions such as impact of rigid projectile is yet to be thoroughly investigated. The present project aims at evaluating the influence of fibers under three different types of loadings: dynamic tensile loading, confined compression loading and dynamic shear loading. Indeed, during the impact of a rigid projectile against a concrete target severe damage modes are observed such as spalling on the front face, radial cracking in the whole target and, in case of the perforation, scabbing on the rear face [5]. Moreover, high confining pressures are observed in front of the projectile involving mechanisms such as micro-cracking and collapse of porosity [6]. Both confined and tensile behaviors are influencing the penetration resistance of the target [7]. Therefore, the constitutive model used in numerical simulations of a penetrating rigid projectile in a concrete target, should take into account the concrete confined behavior and the tensile resistance of concrete at high strain rates [8].

In the present work, three testing methods are used to investigate the behavior of an UHSC. Dynamic tensile test are performed with a Split Hopkinson Pressure Bar using cylindrical notched samples. Furthermore, the confined behavior of UHSC is investigated through quasi-oedometric compression tests. Finally, the shear behavior of UHSC is analyzed by employing a so called dynamic Punch-Trough-Shear testing technique. The principle of each experimental method and experimental results are presented in the following chapters.

P. Forquin (✉) • B. Lukic
3SR Laboratory, Grenoble Alpes University, Grenoble 38041, France
e-mail: pascal.forquin@3sr-grenoble.fr

B. Song et al. (eds.), *Dynamic Behavior of Materials, Volume 1*,
Conference Proceedings of the Society for Experimental Mechanics Series, DOI 10.1007/978-3-319-22452-7_32

32.2 Tested Material

32.2.1 Composition of UHSC

The material investigated is an Ultra High Strength Concrete (UHSC) whose mechanical properties and composition are gathered in Table 32.1. Although characterized as concrete, UHPC varies in composition compared to conventional concrete and is defined primarily by its material properties. In contrast to conventional concrete, apart from cement, sand and water, it contains finely crushed quartz grains and silica fume. The optimized granular mixture of UHPC, where the maximal grain size is approximately 0.6 mm (sand), and extremely low water to cementious material (cement and silica fumes) ratio allows casting a finely graded and highly homogeneous concrete matrix with outstanding mechanical properties. The use of superplasticizer in order to increase the workability is of great importance. In the present work, two sets of specimens have been considered for static and dynamic testing: one which contains 2 % volumetric ratio of short steel fibers (0.2 mm diameter and 7 mm in length) and the other without additional fiber reinforcement.

32.2.2 Mixing and Casting of UHSC and Concrete Samples

The specimens used in tensile testing, quasi-oedometric testing and in PTS experiments are notched or un-notched cylinders of respective diameter around 46 mm, 29 mm, and 100 mm and 60 mm, 40 mm and 30 mm in length. The specimens were cored out from large blocks ($270 \times 270 \times 170$ mm^3) more than 40 days after the mix was poured into watertight plywood molds. All the samples had been stored in water saturated by lime in order to avoid the dissolution of portlandite into water.

32.3 Dynamic Tensile Testing of UHSC

32.3.1 Principle of the Experimental Procedure

A Split Hopkinson Bar facility was developed in 3SR to perform the dynamic tensile experiments on notched samples. It is composed of an input bar 45 mm in diameter and 150 mm in length and an output bar of the same diameter and 120 mm in

Table 32.1 Material composition and mechanical properties of an ultra high strength concrete [3]

Composition		UHSC
Cement	[kg/m^3]	*730*
Silica fume	[kg/m^3]	*235*
Crushed quartz grains	[kg/m^3]	*220*
Sand	[kg/m^3]	*885*
Superplasticizer	[kg/m^3]	*10*
Water	[l/m^3]	*160*
Steel fibers	[vol. %]	*2 %*
W/(C + SF)		*0.17*
Mechanical properties		
Density	[kg/m^3]	*2396*
Young's modulus	[GPa]	55
Quasi-static compressive strength	[MPa]	200

length. Both input and output bars are made of the same high-strength aluminum alloy (Fig. 32.1). The UHSC cylindrical sample is a cylinder 60 mm in length and 46 mm in diameter. It is tapped on both sides to the input and output bar with a high strength (Pleximon) glue. Moreover, circular notch 5 mm in depth is performed into the sample to avoid unsticking of the sample at Hopkinson bar interface. The striker used for the dynamic experiments of the same diameter than Hopkinson bar is 480 mm in length. In addition, a small ring of lead is put in contact with the impacted end of the input bar to produce a pulse-shaper effect. It results in a longer rising time and lower level on loading rate in the sample that ensure a correct mechanical equilibrium of the tested sample. The compressive incident pulse travels through the input bar, is transmitted to the sample and to the output bar prior to reflect on the free-end of the output bar as a tensile pulse. This tensile pulse propagates back to the sample leading to its tensile failure.

The device used for the experiments is detailed in the Fig. 32.1. As instrumentation, three photodiodes are used for measuring the striker velocity prior to impact. Data of strain-gages glue on both input and output bars are amplified and

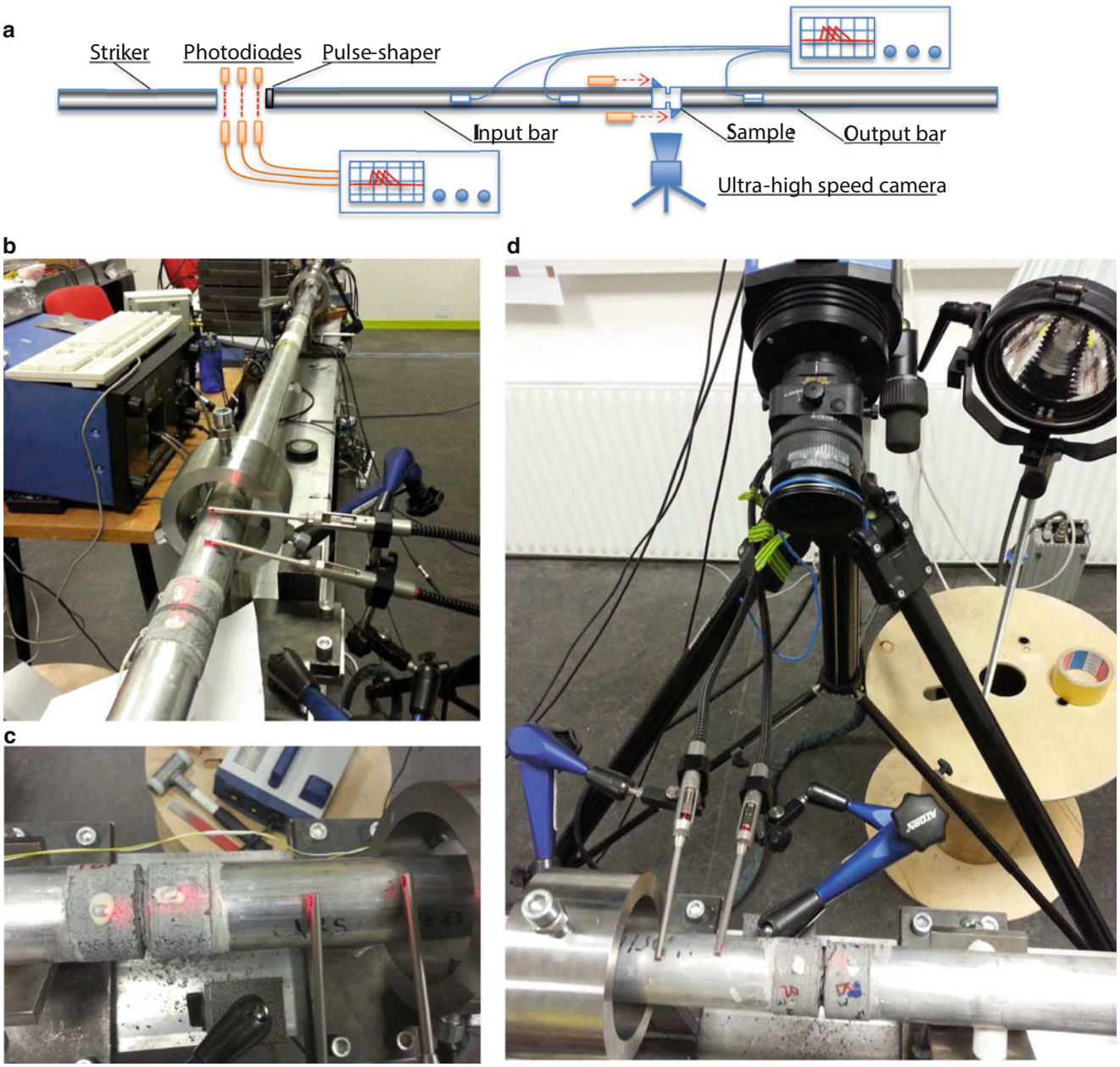

Fig. 32.1 Dynamic tensile test performed with a Split Hopkinson Bar device on notched samples (**a**) Principle of the experimental method, (**b–d**) Photos of the experimental device (3SR Lab.)

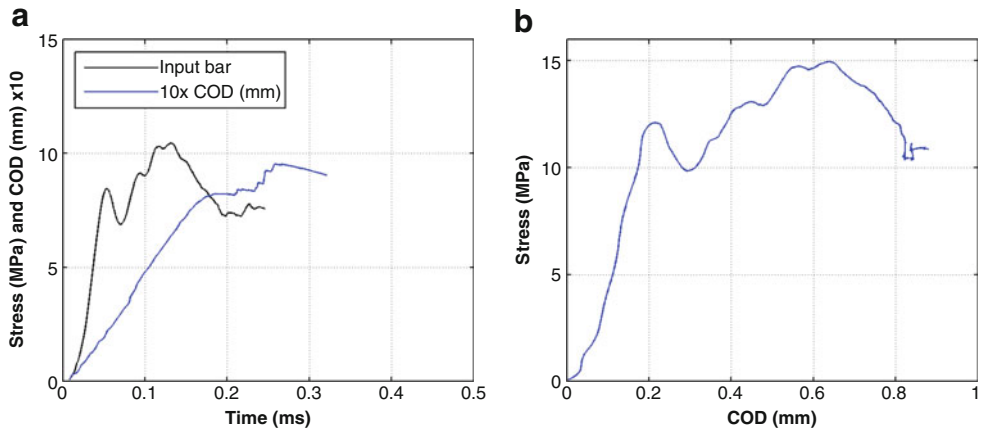

Fig. 32.2 (**a**) Crack opening displacement (COD) and stress as function of time (**b**) Stress as function of crack opening displacement

recorder through a data recorder before to be processed. These data allows measuring the input and output forces applied to the sample. Thus, the average stress in the notched area of the sample is deduced:

$$\sigma_{notch} = \frac{F_{input} + F_{output}}{2S_{notch}} \tag{32.1}$$

In addition, in the present study two devices have been used to measure the crack opening displacement (COD). One the one hand, laser interferometer is used to capture the displacement difference on both sides of the notch. On the other hand, a speckle is applied to the sample to perform full-fields measurement by means of an ultra-high speed camera (Shimadzu HPV1, resolution: 312 × 260 pixels, number of frames per second: up to 1 Mfps). Both methods provide very similar results.

32.3.2 Experimental Results

A set of experimental results obtained with a fibered UHSC is given in the Fig. 32.2. The mean stress in the notch zone and the COD are plotted as function of time in the Fig. 32.2a. A linear increase of COD is noted in the first 180 µs. This time interval is much larger than the round-trip time of wave in the sample (about 25 µs). A hardening-like behavior of UHSC is noted for COD below 0.6 mm according to Fig. 32.2b showing the stress in the ligament as function of the COD. Next, a decrease of stress is observed until unloading time (300 µs). Finally, the experiments demonstrate a good resisting and strain-hardening behavior of fiber reinforced UHSC to the contrary of un-reinforced UHSC.

32.4 Quasi-Oedometric Compression Tests Performed on UHSC

32.4.1 Principle of the Experimental Procedure

The Fig. 32.3 explains the procedure of the quasi-oedometric compression tests carried out as to further investigate the confined behavior of UHSC. The principles behind the method is explained in more detail [9, 10]. The cylindrical specimen (30 mm in diameter and 40 mm in height) is placed in a high-strength steel confinement vessel and the gap between the two is filled by a bi-component resin (Chrysor®). The steel confinement vessel is of 30 mm as inner diameter, 55 mm as outer diameter and 50 mm in height. The outer diameter was chosen as to obtain a sufficient stiffness of the vessel and a good sensibility of strains measurement on the outer surface of the vessel. As the deformation of the vessel is heterogeneous, the expansion is registered by the three hoop strain gauges attached around the external surface of the vessel, one at the level of the symmetry plane and the other two at a distance of 18 mm from this level. The confined sample is exposed to axial compression load applied by the Shenck hydraulic press (Fig. 32.3). Steel compression plugs are used to apply the axial load to the sample. Under compression, the specimen tends to expand under the effect of radial dilatancy and presses against the

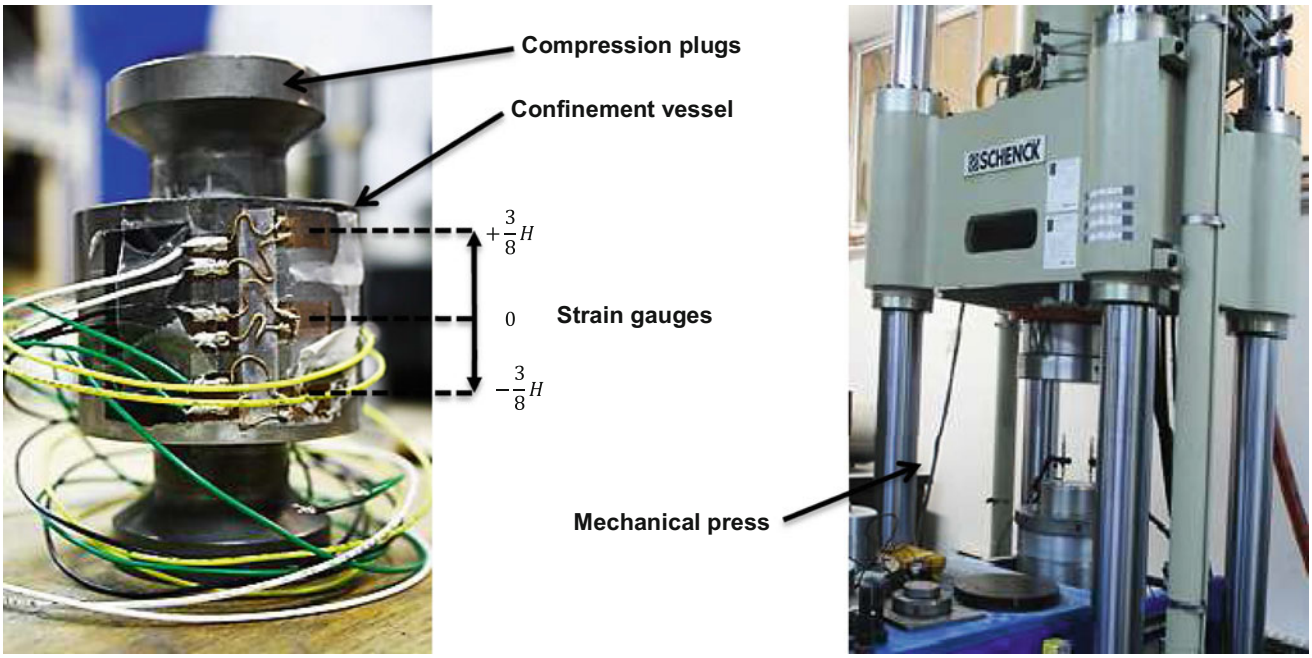

Fig. 32.3 Confining ring and plugs used for the quasi-oedometric compression test. Schenk press used for quasi-oedometric compression test

confinement vessel. In the course of the test, a rise of both axial and radial stress (in absolute value) is observed. The axial strain of the specimen is deduced from measuring the displacement of the compression plugs with two synchronized linear variable differential transformers (LVDTs). The maximal load reached in the confined compression was around 950 kN which was fairly close to the maximum machine capacity.

In order to evaluate the change of concrete strength, one must determine the lateral pressure exerted by the specimen against the inner wall of the vessel. The relationship between the radial stress, and the hoop strain was deduced by numerical simulations detailed in [11]. First, the nominal axial strain is calculated as the variation of specimen height using the data obtained from the LVDT measurements. Then, the average radial strain on the specimen is calculated taking into account of the 'barrel' deformation of the confinement vessel and using the measurement registered by the hoop strain gauges on the vessel outer surface. Finally, the average radial stress is obtained as:

$$\overline{\sigma}_{radial}(\overline{\varepsilon}_{axial}, \varepsilon_{\theta\theta}) = \left(1 - \frac{\overline{\varepsilon}_{axial}}{\varepsilon_{ref}}\right) f^a(\varepsilon_{\theta\theta}) + \left(\frac{\overline{\varepsilon}_{axial}}{\varepsilon_{ref}}\right) f^b(\varepsilon_{\theta\theta}) \tag{32.2}$$

Where the functions f^a, f^b are identified based on numerical simulations taking into account the different heights of the sample. Finally, since the average radial strain and stress in the specimen are known, one can deduce the deviatoric and the hydrostatic pressure as:

$$\begin{aligned} \overline{\sigma}_{deviatoric} &= |\overline{\sigma}_{axial} - \overline{\sigma}_{radial}| \\ P_{hydrostatic} &= -\frac{1}{3}(\overline{\sigma}_{axial} + 2\overline{\sigma}_{radial}) \end{aligned} \tag{32.3}$$

The presented processing of data was used to analyses the results of the quasi-oedometric tests carried out on UHSC which are presented below.

32.4.2 Experimental Results

The deviatoric and hydrostatic pressure curves obtained from two quasi-oedometric compression tests carried out on UHSC with and without fiber reinforcement are presented in the Fig. 32.4. When compared to common concrete, a notable rise of

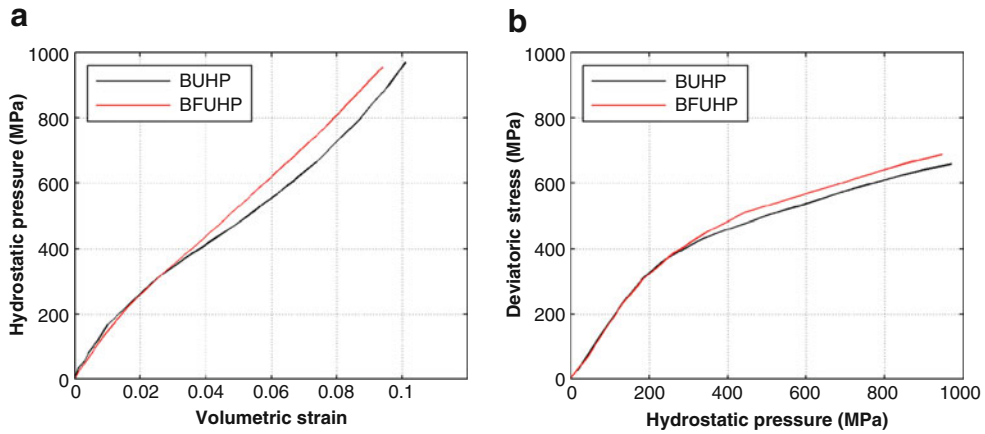

Fig. 32.4 Results of quasi-oedometric compression tests performed on UHSC with (BFUHP) and without fibers (BUHP). (**a**) Hydrostatic behavior, (**b**) deviatoric behavior

strength occurs with the hydrostatic pressure in both types of concrete mixtures. Nevertheless, it seems that the additional fiber content has a little effect on the concrete deviatoric behaviour, as both types of concrete exhibited similar compression strength of around 670 MPa under approximately the same value of hydrostatic pressure of 980 MPa. However, by closely observing the compaction curves, it can be noticed that for the same hydrostatic pressure of around 800 MPa sample with addition of short steel fibers exhibited a reduction on volumetric deformation compared to concrete without additional fiber content. This volumetric reduction may be contributed to the assumption that the addition of steel fibers has a positive effect on limiting a little the collapse of pores in the samples under high confinement.

32.5 Punch Through Shear Tests Performed on UHSC

32.5.1 Principle of the Experimental Procedure

Shear behavior of UHSC under dynamic loading conditions was characterized with the dynamic experimental set-up built in 3SR Laboratory and is presented in the Fig. 32.5 together with the sample geometry. It is based on a so called Punch-Through-Shear test geometry [12]. Recently, a similar technique has been employed to testing regular concrete [13]. The sample geometry is such that the inner diameter of the upper notch and outer diameter of the bottom notch coincide perfectly to form a straight cylindrical fracture surface. When axially displaced, the central part induces a pure mode II fracturing in the ligament. Furthermore, radial notches are performed in order to reduce the self-confinement of the sample peripheral part and it has been observed in experimental procedure that eight notches were sufficient. The sample is introduced into a well-instrumented aluminum confinement ring which purpose is to deduce the contact stress that originates from material dilatant behavior under shear deformation in the ligament. The sample is then subjected to a dynamic shear load using a modified Split Hopkinson Pressure Bar (SHPB). It is composed of a projectile, input bar and output tube all made out of the same high-strength aluminum alloy. The instrumented sample is placed in between the bar and the tube such that their axes perfectly align. The contact surface of the sample is treated with a plaster mixture in order to allow perfect impedance continuity during wave propagation. The inner diameter of the tube is large enough so it allows the axial displacement of the sample central part. The cylindrical Hopkinson bar and the tube are both instrumented with strain gauges located in their half-lengths which purpose is to measure the amplitude of waves in the input and output bars due to projectile impact. The striker impacts the input bar at high velocity (about 20 m/s) and generates an incident compressive pulse that propagates towards the sample. The rising time of the generated pulse is almost instantaneous and can cause unwanted inertial effects that may impair the mechanical equilibrium of the sample. Therefore a use of a lead pulse-shaper is necessary to increase the pulse rising time and to decrease the level of loading-rate in the sample. The processing procedure is the following. First, the mean radial stress in the shear zone is deduced from the contact pressure between the sample and the confining vessel:

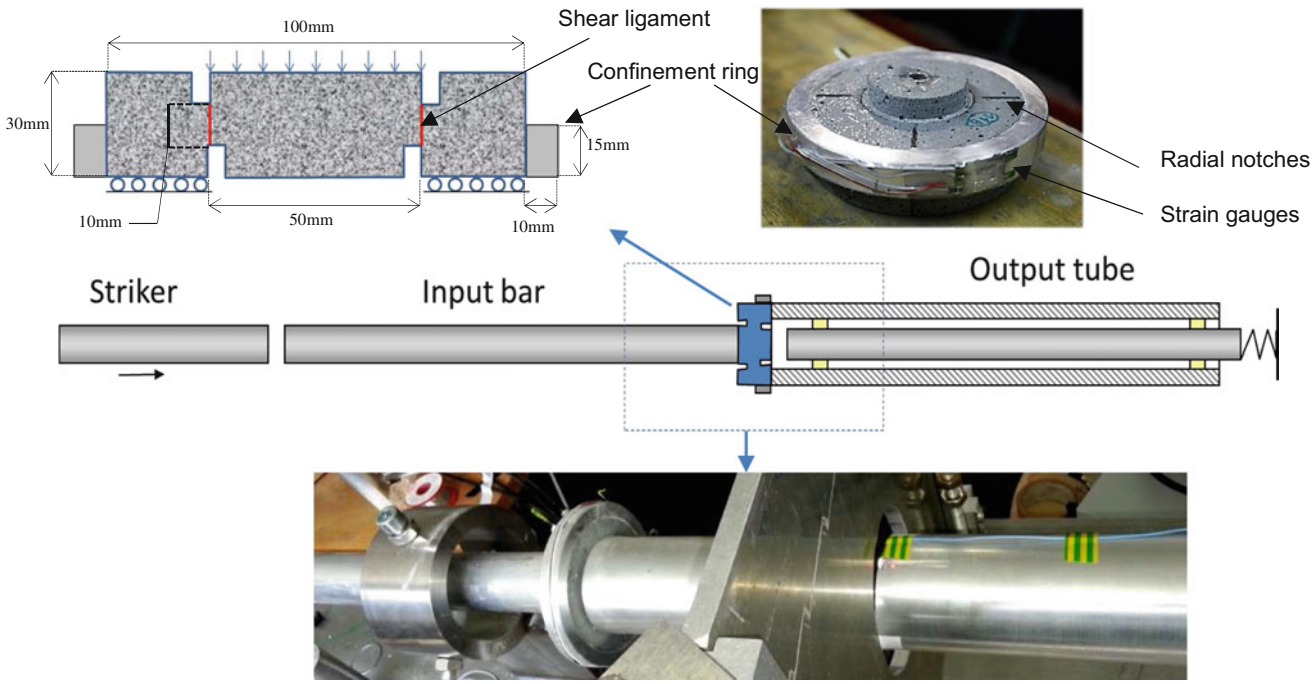

Fig. 32.5 Experimental device used in 3SR Laboratory to perform dynamic PTS tests and the sample geometry

$$\sigma_{shear} = \frac{F_{axial}}{S_{ligement}}, \tag{32.4}$$

Second, the strain gauge measurements on the input bar provide the incident and reflected waves so the input and output forces between the specimen and the Hopkinson bars are obtained as following:

$$\begin{aligned} F_{input} &= S_{input} E_{bar} \left(\varepsilon_{incident} - \varepsilon_{reflected}\right) \\ F_{output} &= S_{output} E_{bar} \left(\varepsilon_{transmited}\right) \end{aligned} \tag{32.5}$$

Finally, the shear stress in the ligament is deduced by averaging the input and output forces:

$$\sigma_{shear} = \frac{F_{input} + F_{output}}{2.S_{ligament}} \tag{32.6}$$

The axial displacement of the sample central part is obtained by integrating the particle velocities measured by the laser interferometer pointed out toward the middle of the output tube or deduced from strain gauge on the input bar.

$$V_{axial} = V_{reflected} + V_{incident} - V_{transmited} \tag{32.7}$$

This method was used to process the data obtained from the dynamic experiments performed on ultra-high strength concrete samples and the results are presented in the following section.

32.5.2 Experimental Results

A series of experiments have been carried out on an ultra-high strength concrete with and without addition of short steel fibers as to characterize the influence of steel fiber content on punching through shear strength. Projectile impact velocity was kept constant for all tested samples, exposing them to a high strain rate loading that ranged between 100 and 230 s^{-1}.

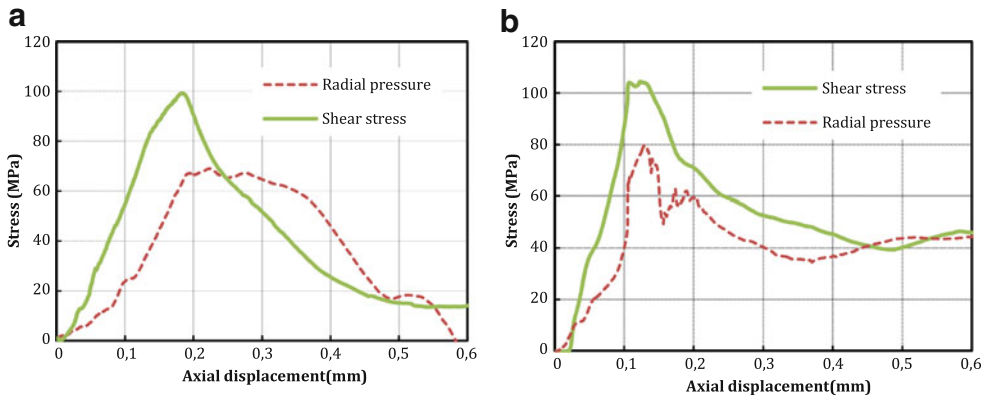

Fig. 32.6 Results of dynamic shear tests performed on *eight-notch* specimen (**a**) UHPC without additional fibers (**b**) UHPC with addition of 2 % volumetric addition of short steel fibers

The results of two dynamic tests performed are presented in the Fig. 32.6. The maximum shear stress reached in non-fiber reinforced sample was around 100 MPa with a corresponding radial stress at peak of about 65 MPa, while on the other hand the fibered sample exhibited a shear stress of 108 MPa with a corresponding radial stress at peak of about 75 MPa. It is clear that the values of maximal shear strength are fairly similar for both mixtures and therefore a poor effect of fiber content on the dynamic shear strength may be observed. However, when post-peak behavior is observed, a clear difference can be noticed between samples with and without additional fiber reinforcement. The fiber reinforced sample indicated a less brittle post peak response with higher residual shear strength. This may be explained with a higher residual radial stress registered in the ligament that is apparently a result of fiber crack bridging effect, where fibers are considered to prevent complete opening of tensile radial cracks.

32.6 Conclusion

In conclusion, the dynamic tensile, shear and confined behavior of an UHSC (Ultra-High Strength Concrete) with and without steel fiber reinforcement have been investigated through three experimental methods. A Split-Hopkinson Pressure Bar (SHPB) device is used with notched-concrete sample to analyze the post-peak tensile behavior of UHSC. In this case a strong influence of fibers is noted as the notched-concrete exhibits a strain-hardening behavior for COD up to 0.6 mm. Quasi-oedometric compression test performed on fibered and un-fibered UHSC concrete sample allow reaching hydrostatic pressure as high as 800 MPa. The measurements of radial and axial stresses provide the hydrostatic and deviatoric responses of the tested material. According to these experiments a very little influence of fibers reinforcements is noted. In the PTS (Punch-Trough-Shear test) experiments lateral pressure of over 50 MPa are applied to the sheared zone. High shear strains leads to a mode II fracturing of the sample. Again a weak influence of fibers is noted at the peak stress. Finally, strength enhancement is clearly observed in fibered UHSC when subjected to dynamic tensile loading. Under confined oedometric or shear loadings the influence of fibers remains at least limited.

Acknowledgments This research has been performed with the financial support of the Gramat Research Center (CEA-Gramat). We would like to thank Dr. Eric Buzaud (CEA-Gramat), Dr. Benjamin Erzar and Dr. Christophe Pontiroli (CEA-Gramat) for their sound technical and scientific advices. The support of LabEx Tec 21 (Investissements d'Avenir - grant agreement n°ANR-11-LABX-0030) is also gratefully acknowledged by the authors.

References

1. Malier, Y.: Les bétons à hautes performances, l'Ecole Nationale des Ponts et Chaussées, France (1992)
2. Richard, P., Cheyrezy, M.: Composition of reactive powder concretes. Cem. Concr. Res. **25**(7), 1501–1511 (1995)
3. Forquin, P., Hild, F.: Dynamic Fragmentation of an ultra-high strength concrete during edge-on impact tests. J. Eng. Mech. **4**(134), 302–315 (2008)

4. Bayard, O.: Approche multi-échelles du comportement mécanique des bétons à ultra hautes performances renforcés par des fibres courtes. Ph.D. dissertation, Ecole Normale Supérieure de Cachan, French (2003)
5. Li, Q.M., Reid, S.R., Wen, H.M., Telford, A.R.: Local impact effects of hard missiles on concrete targets. Int. J. Impact Eng. **32**(1–4), 224–284 (2005)
6. Forquin, P., Arias, A., Zaera, R.: Role of porosity in controlling the mechanical and impact behaviours of cement-based materials. Int. J. Impact Eng. **35**(3), 133–146 (2008)
7. Forquin, P., Sallier, L., Pontiroli, C.: A numerical study on the influence of free water content on the ballistic performances of plain concrete targets. Mech. Mater. **89**, 176–189 (2015)
8. Erzar, B., Forquin, P.: Experiments and mesoscopic modelling of dynamic testing of concrete. Mech. Mater. **43**, 505–527 (2011)
9. Forquin, P., Safa, K., Gary, G.: Influence of free water on the quasi-static and dynamic strength of concrete in confined compression tests. Cem. Concr. Res. **40**(2), 321–333 (2010)
10. Forquin, P., Arias, A., Zaera, R.: Relationship between mesostructure, mechanical behaviour and damage of cement composites under high-pressure confinement. Exp. Mech. **49**(5), 613–625 (2008)
11. Forquin, P., Arias, A., Zaera, R.: An experimental method of measuring the confined compression strength of geomaterials. Int. J. Solids Struct. **44**(13), 4291–4317 (2007)
12. Backers, T., Stephansson, O., Rybacki, E.: Rock fracture toughness testing in Mode II—punch-through shear test. Int. J. Rock Mech. Min. Sci. **39**(6), 755–769 (2002)
13. Forquin, P., Sallier, L.: A testing technique to characterise the shear behaviour of concrete at high strain-rates. In: Chalivendra, V., Song, B., Casem, D. (eds.) Dynamic Behaviour of Materials, vol. 1, pp. 531–536. Springer, New York (2013)

Chapter 33
Highly Stretchable Miniature Strain Sensor for Large Strain Measurement

Shurong Yao, Xu Nie, Xun Yu, Bo Song, and Jill Blecke

Abstract In this research, a new type of highly stretchable strain sensor was developed to measure large strains. The sensor was based on the piezo-resistive response of carbon nanotube (CNT)/polydimethylsiloxane (PDMS) composite thin films. The piezo-resistive response of CNT composite gives accurate strain measurement with high frequency response, while the ultra-soft PDMS matrix provides high flexibility and ductility for large strain measurement. Experimental results show that the CNT/PDMS sensor measures large strains (up to 8 %) with an excellent linearity and a fast frequency response. The new miniature strain sensor also exhibits much higher sensitivities than the conventional foil strain gages, as its gauge factor is 500 times of that of the conventional foil strain gages.

Keywords Large strain sensor • Ultra stretchable • CNT/PDMS composite thin film • Piezo-resistive response • Frequency response

33.1 Introduction

Strain, as one of the key mechanical parameters, needs to be precisely measured in engineering applications. Conventional foil strain gages that are based on the piezo-resistive effect of metals have been commonly used in both quasi-static and dynamic experiments to measure the specimen strain due to the high frequency and linearity response. However, the metal foil strain gages have a very limited measurable strain range, which limits the utilization of traditional sensors for large strain measurements. Digital image correlation (DIC) has been recently developed for the full-field strain measurement [1–3]. In this method, speckles are introduced on the surface of the specimen and a digital camera is used to capture the images of the speckles during the test. Strain can then be calculated by analyzing the movements of those speckles on the captured images. This non-contact method can measure relatively large strains. When DIC is applied for dynamic testing, it requires implementation of a high-speed camera with a high resolution to capture the dynamic images. Other challenges of the dynamic DIC technique are reliable patterning and lighting of the specimen. Some engineering circumstances where the camera and lighting are not easily installed also make the DIC not applicable. The resolution of dynamic DIC technique is limited by the frame rate of the camera and the total number of images that could be stored during a single test. Therefore, it is desirable to develop a new strain sensor with high flexibility and miniature size which can measure relatively large local deformation for an extensive range of engineering practice.

Recent studies in the field of stretchable electronics led to the development of stretchable strain sensors. Based on piezo-resistive response, Choong et al. [4] developed stretchable pressure sensors with conductive elastomeric composites. Canavese et al. [5] used piezo-resistive metal-polymer composites for the stretchable pressure sensor applications. Vatani et al. [6] developed a stretchable strain sensor [6]. In that research, carbon nanotube (CNT)/monofunctional acrylate monomers composite was encapsulated in stretchable Polyurethane (PU) rubber. The piezo-resistive property of the CNT composite yielded a linear response to strains up to 80 %. However, as the sensing element (CNT composite) has to be encapsulated in the bulky PU substrate, it cannot accurately measure the strain on the surface that is in contact with the specimen. In addition, it has been challenging to bond the PU to a metallic specimen. To overcome the limitations of these current strain measurement techniques, we developed a nano-composite-based ultra flexible thin film strain sensor which can be strongly bonded to the surface of metallic specimens for large strain measurement.

S. Yao • X. Nie • X. Yu (✉)
Department of Mechanical and Energy Engineering, University of North Texas, 1155 Union Circle #311098, Denton, TX 76203-5017, USA
e-mail: Xun.Yu@unt.edu

B. Song • J. Blecke
Sandia National Laboratories, Albuquerque, NM 87185, USA

B. Song et al. (eds.), *Dynamic Behavior of Materials, Volume 1*,
Conference Proceedings of the Society for Experimental Mechanics Series, DOI 10.1007/978-3-319-22452-7_33

33.2 Materials and Experiments Methods

33.2.1 Materials

The Polydimethylsiloxane (PDMS) and CNTs used in this study were Sylgard 184 by Dow Corning and single-walled CNTs provided by Timesnano, China, respectively. A primer (92-023, Dow Corning) was used to enhance the adhesion between PDMS and Aluminum (Al) substrate. The surfactant used for dispersing the CNTs was sodium dodecylbenzene sulfonate (NaDDBS) provided by Sigma-Aldrich Co., USA. In addition to CNTs, nickel microparticles with needle-like surface (Type 123, Inco Ltd., CA) was used to improve the compressive sensing performance,

33.2.2 Sensor Fabrication

Because of the high viscosity of PDMS, it is very difficult to uniformly disperse CNTs into PDMS matrix to make the composite. In this study, PDMS was firstly dissolved in Toluene to reduce its viscosity. CNTs were also separately dissolved in Toluene with the assistance of NaDDBS. The CNT solution was then added into the PDMS solution. With continuous magnetic stirring, Toluene was evaporated and, as a consequence, a uniformly mixed CNT/PDMS composite was produced. The ultra-stretchable CNT/PDMS sensors were then deposited on aluminum substrates. Prior to deposit, the aluminum substrates were cleaned with acetone and then coated with a thin layer of pure PDMS for electric insulation. After electrodes made of gold wires were attached on the top of the PDMS layer with silver epoxy, the CNT/PDMS composite thin film was coated over the gold wires and cured for about 12 h at 70 °C. As the last step, another layer of pure PDMS was coated on the top of the CNT/PDMS sensing composite for protection. Figure 33.1 shows a picture of a fabricated sensor on an aluminum specimen (the black square is the sensing area of approximately 2×2 mm^2) and a schematic of the cross-section of the sensor.

33.2.3 Measurement Method

The sensors were tested with a Shimadzu Universal Materials Testing Machine under quasi-static strain rate. The sensor outputs were directly compared with the extensometer (Epsilon 3442) signal attached to the specimen. The sensor was serially connected with a constant reference resistor, as shown in Fig. 33.2. The resistance of the sensor can be calculated with the following equation,

$$R_s = \frac{V_x}{V_R} \cdot R \tag{33.1}$$

where V_x and V_R are voltages applied to the sensor and the resistor, respectively; R is the resistance of the reference resistor. As CNT/PDMS composite is not only a resistive element but also a capacitive element, if a constant DC voltage is applied, it could charge the internal capacitance of the sensor and lead to electrical polarization which will drift the sensor

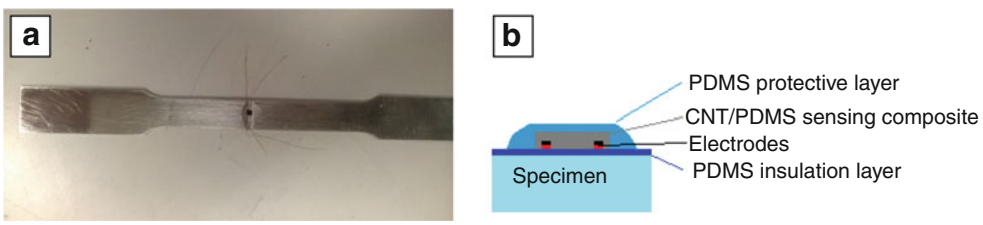

Fig. 33.1 A picture of fabricated sensor and sketch diagram of the cross-section of the sensor

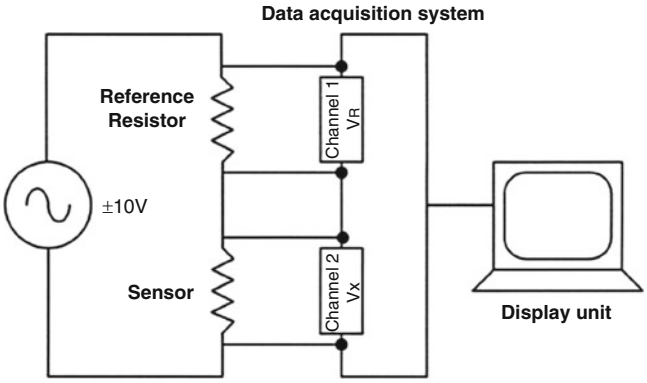

Fig. 33.2 Sensor output measurement system

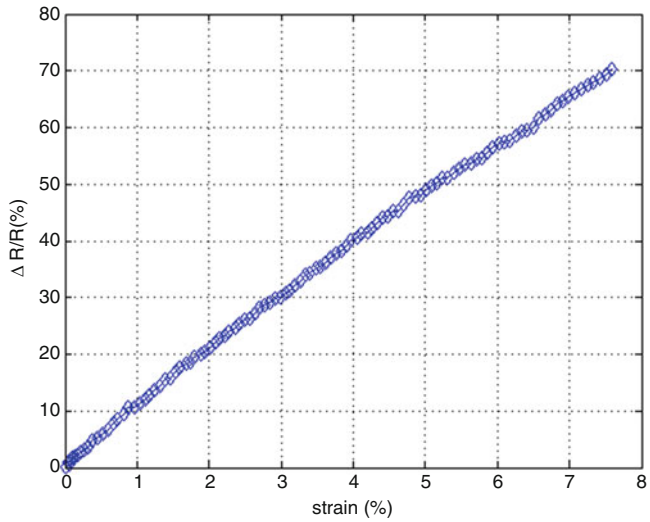

Fig. 33.3 20 %CNT/PDMS strain sensor outputs vs. extensometer strain measurement

measurement. Therefore, a 18 V, 60 Hz AC power supply was used as the power source of the circuit. The AC power can eliminate the polarization of capacitance. The voltage output on the sensor and the extensometer are measured by a dynamic data acquisition system (DT9837, Data Translation Inc) with a sampling rate of 1000 Hz.

33.3 Results and Discussions

Figure 33.3 shows the output (ΔR/R) of a CNT/PDMS strain sensor with 20 % CNTs versus the strain measurement with an extensometer. The CNT/PDMS sensor exhibits a wide range of linear response to strain up to about 8 % where the aluminum specimen failed in tension. This CNT/PDMS strain sensor also exhibits a very high sensitivity. The gauge factor $\left(\frac{\Delta R}{R.Strain}\right)$ of the CNT/PDMS sensor is about 1000, which is approximately 500 times higher than that of a conventional foil strain gage (typically around 2). The CNT/PDMS strain sensor was also tested under cyclic loads to examine its frequency response for potential vibration and dynamic strain measurements. Figure 33.4 shows the sensor response to cyclic loads. The results show that the sensor exhibits a nearly prompt response to external loading but a hysteretic response to unloading, which is possibly due to the nature of hysteresis of the polymer matrix. However, the hysteresis does not significantly affect the frequency and magnitude measurements of the cyclic loading, as evidenced by the consistency with the extensometer measurements.

To improve the compressive sensing response, micro-sized Nickel particles were added into the CNT/PDMS composites. Figure 33.5 shows the results of a sensor with 20 %CNT/25 %Ni/PDMS composite. The sensor shows quick and repeatable responses to loadings and some improved performance compared to CNT/PDMS composite, but the responses during the unloading stage still needs to be improved, especially at high frequency loads.

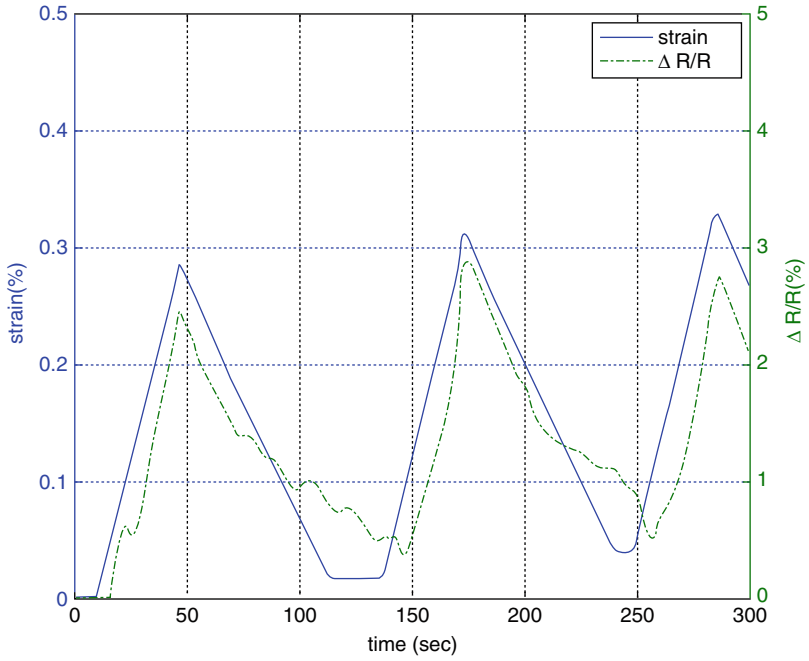

Fig. 33.4 The output of the 20 %CNT/PDMS strain sensor under cyclic loads

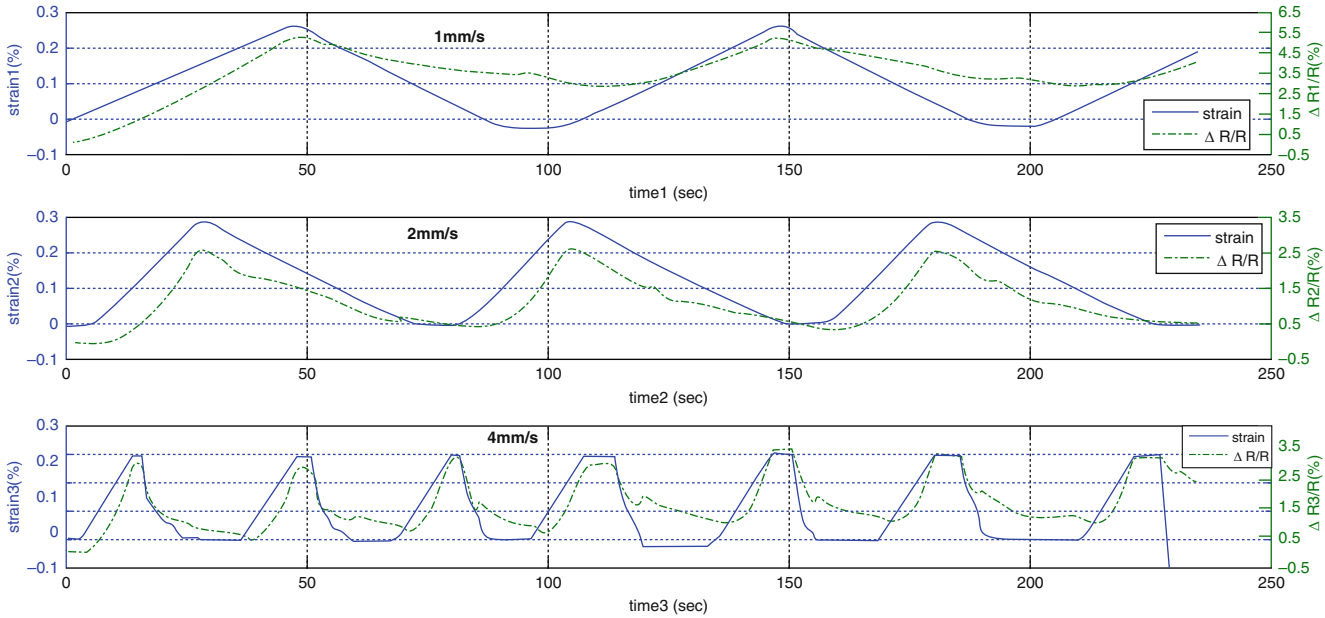

Fig. 33.5 Sensor outputs under different loading rates of cyclic loads

33.4 Conclusion

In this research, highly flexible CNT/PDMS composite stain sensors were designed, fabricated and tested. Experimental results show that the new sensors can measure strains up to 8 % with an excellent linearity and a fast frequency response. The new strain sensor also exhibits much higher sensitivities than the conventional foil strain gages. Although the unloading

performance of the CNT sensor still needs to be further improved, the developed sensor showed the potential for high-rate, large strain measurement applications.

Acknowledgments The authors thank the funding support from Sandia National Laboratories. Sandia National Laboratories is a multi-program laboratory managed and operated by Sandia Corporation, a wholly owned subsidiary of Lockheed Martin Corporation, for the U.S. Department of Energy's National Nuclear Security Administration under contract DE-AC04-94AL85000.

References

1. Chu, T.C., Ranson, W.F., Sutton, M.A.: Applications of digital-image-correlation techniques to experimental mechanics. Exp. Mech. **25**, 232–244 (1985)
2. Sutton, M.A., Mingqi, C., Peters, W.H., Chao, Y.J., McNeill, S.R.: Application of an optimized digital correlation method to planar deformation analysis. Image Vis. Comput. **4**, 143–150 (1986)
3. Tiwari, V., Sutton, M.A., McNeill, S.R., Xu, S., Deng, X., Fourney, W.L., Bretall, D.: Application of 3D image correlation for full-field transient plate deformation measurements during blast loading. Int. J. Impact Eng. **36**, 862–874 (2009)
4. Choong, C.-L., Shim, M.-B., Lee B.-S. et al.: Highly stretchable resistive pressure sensors using a conductive elastomeric composite on a micropyramid array. Adv. Mater. (2014). doi:10.1002/adma.201305182
5. Canavese, G., Stassi, S., Stralla, M., Bignardi, C., Pirri, C.F.: Stretchable and conformable metal-polymer piezoresistive hybrid system. Sensors Actuators A Phys. **186**, 191–197 (2012)
6. Vatani, M., Lu, Y., Lee, K.-S., Kim, H.-C., Choi, J.-W.: Direct-write stretchable sensors using single-walled carbon nanotube/polymer matrix. J. Electron. Packag. **135**, 011009 (5 pages), (2013)

Chapter 34
Clamping-Force Application for Kolsky Bar Tension Grips

Richard L. Rhorer

Abstract Dynamic testing using tension Kolsky bars presents a number of challenges, including the design of the grips to hold the specimen. Basic solid mechanics suggests that a grip can be designed such that the lateral clamping-force times the coefficient of friction exceeds the failure strength of the specimen. This approach is complicated by the specimen getting smaller—thereby releasing part of the clamping force—as it is stretched because of the Poisson strain. Therefore, a tension grip needs to apply an adequate lateral force plus it must have enough elastic recovery to maintain the force as the specimen shrinks. In applying the concept to a Kolsky bar, an impedance matched grip is ideal, which suggests a smaller grip body which requires a short clamping bolt. The effect of the bolt length on the clamping force is illustrated by analyzing a proposed design. Gripping of composites and polymer fibers for tension testing is especially challenging. The clamping force application for testing soft-material specimens using a Kolsky-bar grip is also discussed.

Keywords Kolsky bar testing • Dynamic material tests • Sheet-metal tension tests • Dynamic-test grip design • Acoustic impedance matching

34.1 Introduction

The Kolsky bar, also referred to as a split Hopkinson pressure bar (SHPB), is an extensively used device for dynamic material-property testing. There are many excellent references and papers describing the Kolsky bar and its applications; for example, the article by Professor Ramesh in the Handbook on Experimental Solid Mechanics provides a good introduction and a bibliography of relevant papers [1]. Originally the Kolsky bar was designed as a compression testing apparatus, but the basic idea and the simple operational theory also apply to tension testing. In the traditional compression Kolsky bar apparatus, a short cylindrical specimen is held between the two bars by sliding the bars together such that they touch the small specimen, and as the compression wave impacts the specimen from the incident bar the specimen is rapidly deformed. To apply the Kolsky bar concept to tension testing the specimen has to be firmly held by a gripping device to apply the tension load to the specimen.

The approach presented in this paper is a type of gripping system where a specimen is held tightly between two clamping surfaces where a high pressure is applied using a steel bolt. The clamping pressure needs to be high enough so that there is still adequate clamping force to prevent slipping, even as the specimen thins during the tension test. A simple analytical approach is presented here to quantify the magnitude of force needed to prevent slippage of the specimen.

In slow rate, or quasi-static testing, a specimen can be gripped by a clamping-block device and stretched in tension by a load frame. In general, the load frame approach is limited to maximum strain rates on the order of one per second ($\dot{\varepsilon} \approx 1\,\mathrm{s}^{-1}$), whereas the Kolsky bar apparatus is used in a higher strain rate range from approximately one hundred per second to as high as ten thousand per second ($\dot{\varepsilon} \approx 100\,\mathrm{s}^{-1}$ to $\dot{\varepsilon} \approx 10,000\,\mathrm{s}^{-1}$). Adapting a set of traditional load-frame grips to the end of a Kolsky bar is possible; however, any change in size, or material, in a Kolsky bar will cause the incident stress wave in the bar to be partially reflected. Therefore the ideal design of a gripping system should be "impedance matched" to the incident bar, allowing the undistorted stress pulse to be applied to the specimen.

R.L. Rhorer (✉)
Rhorer Precision Engineering LLC, 118 Summit Hall Road, Gaithersburg, MD 20877, USA
e-mail: rrhorer@rcn.com

B. Song et al. (eds.), *Dynamic Behavior of Materials, Volume 1*,
Conference Proceedings of the Society for Experimental Mechanics Series, DOI 10.1007/978-3-319-22452-7_34

34.2 Impedance Matching

A stress wave in a Kolsky bar, usually generated by a projectile impacting the end of the bar, propagates down the incident bar and impacts the specimen. In an analogue to an electrical wave in a conductor, the stress wave propagation is affected by any resistance or impedance change as the wave is conducted down the bar. For stress waves, or strain waves, in a metal bar the impedance is defined by: "The sonic, or sound, impedance is defined as the product of the medium density by its sound (or elastic) wave velocity." And, "...the impedances of the materials—ρC—product determine the amplitude of the transmitted and reflected pulses." Further, "When the cross-sectional area of a cylindrical bar is changed, one has a geometric impedance difference, although the intrinsic impedance of the material is unaltered." [2]

It is important when designing a grip system for a Kolsky bar to impedance match the grip to the bar so that the full wave pulse is transmitted to the sample and none of the wave is reflected back at the joint between the grip and the bar. The ideal situation would be to make the grip an integral part of the bar so that there is not a joint between the bar and the grip; however, this is often not practical. If the grip is made from the same material as the bar, and the cross-sectional area is the same at the joint, then the simple theory says the full wave would be transmitted through the joint to the sample. An ideal design for holding a sample in a tension Kolsky bar would look like that shown schematically in Fig. 34.1, where the material is the same all the way to the sample being tested, and there is no diameter change at the joint between the bar and the grip.

The transmitted and reflected wave amplitudes through a joint with less than perfect impedance match can be calculated by simple equations presented by Meyer [3]. When assuming the same material on both sides of the joint:

$$\sigma_T = \frac{2A_1}{A_1 + A_2}\sigma_I \tag{34.1}$$

$$\sigma_R = \frac{A_2 - A_1}{A_1 + A_2}\sigma_I \tag{34.2}$$

where σ_T and σ_R are the transmitted and reflected wave pulse with an incident wave σ_I. A_1 and A_2 are the cross-sectional areas of the bar upstream and downstream of the joint. These two equations make intuitive sense; for example if $A_1 = A_2$, then the transmitted wave magnitude is equal to the incident magnitude from (34.1), and the reflected wave magnitude is zero from (34.2).

When there is also a material difference at a joint, then the transmitted and reflected wave magnitudes can be expressed by:

$$\sigma_T = \frac{2A_1\rho_2 C_2}{A_1\rho_1 C_1 + A_2\rho_2 C_2} \tag{34.3}$$

$$\sigma_R = \frac{A_2\rho_2 C_2 - A_1\rho_1 C_1}{A_1\rho_1 C_1 + A_2\rho_2 C_2}\sigma_I \tag{34.4}$$

where ρ_1 and ρ_2 are the densities before and after the joint, and C_1 and C_2 are the corresponding wave speeds of the materials. (It is interesting that Professor Meyers states, when presenting these equations, the classic comment "The diligent student can easily show that—".)

The equations can be used to specify a correction factor to apply to the input stress wave when the grip is clearly not impedance matched to the bar. Such a case has been presented by Koh et al [4], where they have used a collet type grip to hold a yarn specimen. The cross-section of the grip is larger than their Kolsky bar, and they use an analytically derived factor based on equations similar to those presented above, which corrects the magnitude of the input pulse when carrying out the traditional calculations of stress-versus-strain Kolsky bar results.

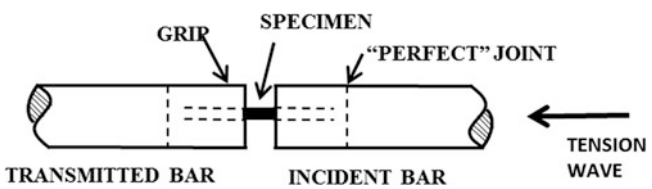

Fig. 34.1 Idealized tension grip model for testing a specimen in a Kolsky bar

The approach advocated in this present work is to design a grip system such that the joint between the bar and grip is close enough to being impedance matched that it is not necessary to include a correction factor in the final result calculations. Equations (34.1) or (34.2) can also be very useful when designing grips for Kolsky bars, or any type of joint in a Kolsky bar, because they can give a theoretical magnitude of the effect from mismatched diameters even if the material is the same. To design a joint such that the reflected pulse magnitude is less than 1 % of the input pulse, we need to make the areas match within about 2 %; for example, using a typical bar of 20 mm diameter, then the second side of the joint needs to be 20 mm plus-or-minus 0.2 mm diameter. This level of tolerance is well within typical manufacturing capabilities.

If a cylindrical grip is designed with a different material than the Kolsky bar, then the grip outer diameter could be adjusted to take in the effect of the ρC product change by using the expressions presented in (34.3) and (34.4).

34.3 Clamping Tension Specimens

The tension grip design presented here is to hold a thin specimen by applying a sufficient clamping force to perform a tension test, either quasi-static or dynamic. A typical thin specimen, with applied loading force, is shown in Fig. 34.2. When a tension force, P, is applied the axial strain in the sample is:

$$\varepsilon_{xx} = \frac{\sigma_{xx}}{E} \text{ or } \varepsilon_{xx} = \frac{P}{A_s E} \tag{34.5}$$

where E is the modulus of elasticity, assuming an isotropic material, and σ_{xx} is the stress in the axial direction of the specimen, and P is the axial load on the specimen of cross-sectional area of A_s. When the specimen is pulled there is also a strain in the z direction,

$$\varepsilon_{zz} = -\nu\varepsilon_{xx} \tag{34.6}$$

where ν is the Poisson's Ratio (about 0.3 for most metals). As the tension, P, is applied to the specimen the resulting cross-direction strain, ε_{zz}, causes the specimen to become thinner. This reduction, Δh, can be estimated by,

$$\Delta h = \varepsilon_{zz} h \tag{34.7}$$

from the definition of strain (change in length per unit length) where, h, is the specimen thickness as shown in Fig. 34.2. By combining (34.5), (34.6), and (34.7), the change in thickness of the sample due to the tension load is,

$$\Delta h = \frac{\nu P h}{A_s E}. \tag{34.8}$$

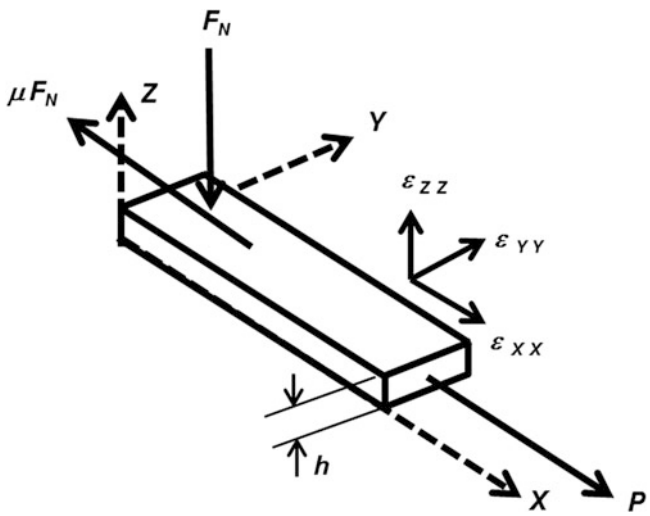

Fig. 34.2 Thin rectangular specimen in uniaxial tension

In a typical tension test the applied load is increased to cause failure of the specimen, or

$$P_{\max} = \sigma_{ult} A_s \tag{34.9}$$

where σ_{ult} is the uniaxial failure stress, or the maximum plastic flow stress, for the material of the specimen. The clamping force needs to be great enough so that the friction force on the specimen is greater than $P_{\max}$, or

$$F_N \geq \frac{P_{\max}}{\mu} \tag{34.10}$$

where μ is the coefficient of friction between the specimen and the clamp. The force needs to be initially greater than calculated by (34.10) because of any unloading of the clamp due to the shrinking of the specimen at the maximum applied load.

For a simple example using a steel test-specimen, (for example a piece of sheet metal), with a width of 10 mm and a thickness of 1 mm ($A_s = 1 \times 10^{-5}\text{m}^2$) and with steel properties assumed to be: $E = 200$ GPa, $\nu = 0.33$, $\sigma_{ult} = 500$ MPa. Then $P_{\max} = 5000\,\text{N}$ from (34.9) and the required clamping force would be higher, possibly $F_N \approx 25000\,\text{N}$, assuming a coefficient of friction, $\mu = 0.2$, in (34.10). The coefficient of friction might be increased by roughening of the clamping surfaces of the grip. The coefficient of friction is often difficult to measure, and so the actual clamping force may need to be determined by experiment; however, assuming a value and performing this calculation is valuable as a preliminary design and a "starting point" for experiments.

And, in this example the change in thickness of the specimen as it is stretched to failure can be estimated using (34.8):

$$\Delta h = \frac{(0.33)(5000\,\text{N})(0.001\,\text{m})}{\left(1 \times 10^{-5}\,\text{m}^2\right)\left(200 \times 10^{9}\,\text{Pa}\right)} = 8.25 \times 10^{-7}\text{m} \tag{34.11}$$

For this example, the change in thickness is small, less than one micrometer, and yet if there is not enough spring action in the bolt and clamping system, then the specimen could slip during the test as the specimen becomes thinner because the clamping force is partially reduced. This change in thickness would be greater for polymer specimens, and the calculation may be more challenging because the material may not be isotropic and would have a different modulus of elasticity in the cross-axis direction. Equation (34.8) will be helpful in investigating designs for grips to be used on polymers or composites, even though the estimates may not be precise.

34.4 Grip for Applying Tension Force

A straightforward design to apply the clamping force is shown in Fig. 34.3. One side of the clamp would be attached to the loading device, the ram in a load frame or the incident bar in the Kolsky bar apparatus, and a bolt is tightened to apply a normal force to squeeze the specimen.

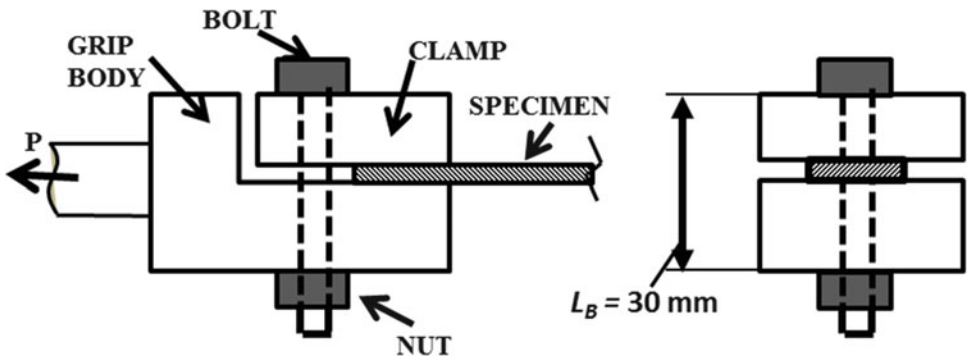

Fig. 34.3 Simple clamp for slow rate testing

The spring constant, force per change in length, of the bolt can be expressed as:

$$\frac{F_B}{\Delta L_B} = \frac{A_B E_B}{L_B} \tag{34.12}$$

where F_B is the force the bolt applies to the sample. The bolt's length changes by ΔL_B as it is tightened. The bolt properties are: modulus of elasticity E_B, cross-sectional area A_B, and the length of the bolt from the head to the nut is L_B. The deflection of the bolt becomes slightly less as the tension load is applied to the sample, which results in a slight decrease in the force.

The concept presented in this paper is to design the bolt such that the clamping force is adequate when the maximum tension force is applied (the failure load) to the specimen. In other words, the bolt needs to be stretched an additional amount initially to compensate for the shrinking of the specimen during the test. This can be expressed as,

$$\Delta L_B - \Delta h = \frac{F_N L_B}{A_B E_B} \tag{34.13}$$

where Δh can be calculated from (34.8) and F_N is specified by (34.10). By combining (34.12) and (34.13) and then rearranging the terms, the bolt force can be calculated as,

$$F_B = F_N + \frac{\Delta h A_B E_B}{L_B}. \tag{34.14}$$

By using (34.14) the total force to be applied to the specimen prior to the test can be estimated. The second term of the equation is the extra bolt force initially applied to ensure that there is still adequate friction force, F_N, even at the failure load, $P_{\max}$. An additional design check is necessary to ensure that the bolt is strong enough to handle the necessary load. The stress in the bolt is,

$$\sigma_B = \frac{F_B}{A_{B\sigma}} \tag{34.15}$$

where $A_{B\sigma}$ is the area of the bolt used to calculate the highest stress in the bolt, usually the area at the base of the threads. This stress area for a bolt can be obtained from the bolt supplier. For hardened steel bolts, the ultimate stress could be as high as 1200 MPa, but for design purposes a reasonable maximum would probably be about 800 MPa. (This is assuming we use a hardened steel bolt like a socket head cap screw—see bolt manufacturer specifications for verification.)

It is interesting that the size of the bolt is important when relying on the spring effect as in the clamping concept presented here. If a very large bolt is selected, thereby reducing the stress in the bolt, then the extra force term in (34.14) is larger. Ideally a very long bolt with as small a diameter as possible is the best design.

Using the example for the specimen presented previously (1 mm by 10 mm steel specimen), the clamping force, F_N, was calculated to be approximately 25,000 N using (34.10). With this load, a 3/8 in. steel bolt would be a reasonable design selection. If we use a 3/8-24 Unified National Fine (UNF) bolt the cross sectional area is $A_B = 7.10 \times 10^{-5}\text{m}^2$ (the stress area, $A_{B\sigma} = 5.67 \times 10^{-5}\text{m}^2$) and a length of 30 mm could be selected (the bolt stress is about 440 MPa, from (34.15), which is reasonable). The added load on the bolt to compensate for the cross-axis thickness change of the specimen can be calculated for this example by using the second term in (34.14):

$$\frac{\Delta h A_B E_B}{L_B} = \frac{\left(8.25 \times 10^{-7}\text{m}\right)\left(7.10 \times 10^{-5}\text{m}^2\right)\left(200 \times 10^{9}\text{Pa}\right)}{\left(3.00 \times 10^{-2}\text{m}\right)} = 390\,\text{N} \tag{34.16}$$

This load would be added to F_N, which was estimated by (34.10), to obtain the total load on the bolt at the start of a test. In this example, the added load is small, and only slightly increases the bolt stress (to about 448 MPa). In some cases, such as a very short bolt length, or a specimen with a low modulus resulting in a higher Δh, then the added bold stress could be a concern.

34.5 Kolsky Bar Clamp Design

If we design a clamp system for a Kolsky bar apparatus and attempt to impedance match the grip at the end of the Kolsky bar, we have additional design challenges. A possible design approach is shown in Fig. 34.4. By making the outer diameter of the grip body the same diameter as the Kolsky bar, and using the same material as the bar, the joint to the grip can be close to impedance matched.

The joint between the bar and the grip, shown schematically in Fig. 34.4, is a threaded joint designed such that the thread section nearly fills the void (that is, no excess drill depth) and the joint is sufficiently tightened for the tension wave to be transmitted without loosening the thread. This type of threaded joint, designed to very closely impedance match the bar and grip was discussed in our paper at ICEM16 [5].

The grip is designed to closely fit the specimen at assembly and have a slit back of the gripping area to allow enough flexibility in the clamping surface area to apply adequate load to the specimen. To avoid a step in the cross-sectional area, the outside of the grip section is designed to match the diameter of the Kolsky bar and the grip can be fabricated from the same material as the Kolsky bar (in the case of the NIST Tension Kolsky bar, the material would be a maraging steel). It makes a clean design to countersink the head of the cap screw and tap the lower part of the clamp. This makes the bolt short.

To design a grip based on the example presented above (testing a steel specimen 1 mm by 100 mm) the bolt diameter would need to be the same as specified before, but the length would now be considerably shorter.

To design a grip for the NIST Tension Kolsky bar (20 mm diameter bar), a reasonable active length of the bolt, L_B, would be about 4 mm. If we continue the example presented above, but using the shorter bolt length, then the load on the bolt is estimated by (34.14) to be:

$$F_B = 25,000\,\mathrm{N} + \frac{\left(8.25 \times 10^{-7}\mathrm{m}\right)\left(7.10 \times 10^{-5}\mathrm{m}^2\right)\left(200 \times 10^{9}\mathrm{Pa}\right)}{\left(4.00 \times 10^{-3}\mathrm{m}\right)} \tag{34.17}$$

$$F_B = 25,000\,\mathrm{N} + 2930\,\mathrm{N} = 27,930\,\mathrm{N}$$

The load on the bolt is higher for this Kolsky bar grip clamp than that required for the simple clamp block design that would be common in a quasi-static testing fixture. The increased load, about 2500 N, is due to the shorter bolt required to design an impedance matched clamp for the Kolsky bar application. The stress in the bolt for this example is close to 500 MPa (calculated with (34.15)), which is still reasonable for the hardened steel bolt suggested. However, the additional load on the bolt needs to be applied by an increased torque specified at assembly.

34.6 Dynamic Grips for Soft Materials

The example presented above is using a steel test specimen. Could we expect this type of grip to work for softer metals or even polymers? The basic equations presented are applicable, and theoretically a plastic or composite specimen could be clamped in a grip using the same basic design. However, there are practical considerations that need to be addressed.

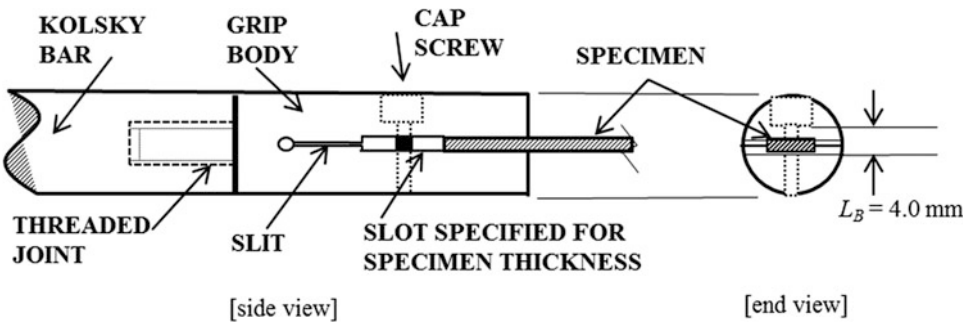

Fig. 34.4 Kolsky bar tension grip design

Even though the failure load, $P_{\max}$, for a polymer might be considerably less than a metal specimen of the same size, the coefficient of friction may be lower, the thinning due to cross-axis strain, ε_{zz}, may be greater and the material may be anisotropic, which would complicate the estimation of the strain effects.

Using the equations presented in this paper can be useful when designing a Kolsky experiment with a soft material. For example, if we propose a specimen of the same dimensions as that used in the previous examples (1 mm by 10 mm cross-section) with different material properties: $E = 2 \times 10^9$Pa, $\nu = 0.35$ and $\sigma_{ult} = 50$MPa (values similar to acrylics). If we assume a coefficient of friction $\mu = 0.1$, then we can calculate the maximum load and theoretical bolt load from (34.9) and (34.10) to be: $P_{\max} = 500$N, and $F_N = 5000$N. The thinning of the specimen can be estimated by using (34.8):

$$\Delta h = \frac{(0.35)(500\text{N})\left(1 \times 10^{-3}\text{m}\right)}{\left(1 \times 10^{-5}\text{m}^2\right)\left(2.0 \times 10^{9}\text{Pa}\right)} = 8.75 \times 10^{-6}\text{m}. \tag{34.18}$$

This thinning due to the Poisson strain is about ten times greater than we calculated for the steel specimen example. The bolt needs an increased elastic recovery for the clamp to work, which illustrates one of the challenges when gripping soft materials. The bolt load for this example can be estimated by using (34.14):

$$\begin{aligned} F_B &= 5000\text{N} + \frac{\left(8.75 \times 10^{-6}\text{m}\right)\left(7.10 \times 10^{-5}\text{m}^2\right)\left(200 \times 10^{9}\text{Pa}\right)}{\left(4.00 \times 10^{-3}\text{m}\right)} \\ F_B &= 5000\text{N} + 31,063\text{N} \approx 36,000\text{N}. \end{aligned} \tag{34.19}$$

The added force to provide the spring effect is obviously the largest component of the total bolt load. In this case the total stress in the bolt would be approximately 640 MPa, which is not too high for the bolt; however, there is a practical problem with loading the bolt this high—the specimen could yield and the necessary stretch of the bolt could not be applied.

The use of the same grip designed for a steel specimen may not work for a soft material like a polymer. It would be necessary to consider a very large tab-area on the specimen to provide a lower clamping stress on the end of the specimen, or adding more spring effect to the bolt. A small diameter bolt, or making the bolt very long, or adding some type of spring washers under the bolt could be evaluated and possibly make the grip function. Another approach is to add a thin layer between the specimen and the clamp surface. If this thin layer is made from a material with a modulus lower than the test specimen material it could provide an additional spring effect to the grip.

34.7 Conclusions

A clamping type grip, which can be impedance matched to a Kolsky bar, is theoretically possible. This paper has presented practical aspects that need to be considered in designing such a grip system. The equations presented can be used as a preliminary design approach; however, experimental refinement will be necessary before specifying final design parameters.

A clamping type grip for a Kolsky bar has several advantages: (a) the specimen design is simple and fabrication is inexpensive, (b) different materials, both metals and polymers, can be used with the same grips, (c) extremely short specimen lengths are possible, which are sometimes advantageous for high strain rate testing, (d) the boundary conditions at the ends of the specimen are similar to the conditions for compression Kolsky bar testing, and (e) when conductively heating the specimens for elevated temperature tests, the thermal boundary conditions are straightforward.

The clamping concept for holding tension specimens also presents a number of design challenges. The clamping bolt used in the proposed grip designs needs to be carefully specified. The initial tightening of the bolt, or pre-load, is very important and care must be exercised in specifying and applying adequate torque to the bolt. The fabrication of this type of grip needs to be precise in order to provide the impedance matching conditions and to insure consistent clamping forces.

The tension grip concept discussed in this paper could be adapted for testing cylindrical specimens such as wires or polymer yarns. A collet chuck system can be designed to “squeeze” a collar around a cylindrical specimen. Using equations similar to those presented here, a collet-grip with a spring effect can be designed to hold cylindrical specimens similar to the thin rectangular specimens discussed in the examples of this paper.

References

1. Ramesh, K.T.: Chapter 33: High rates and impact experiments. In: .Sharpe Jr., W.N. (ed.) Springer Handbook of Experimental Solid Mechanics, pp. 929–959. Springer, New York (2008)
2. Meyers, M.A.: Dynamic Behavior of Materials, pp. 48–58. Wiley, New York (1994)
3. Meyers, M.A.: Dynamic Behavior of Materials, p. 59. Wiley, New York (1994)
4. Koh, A.C.P., Shim, V.P.W., Tan, V.B.C.: Dynamic behavior of UHMWPE yarns and addressing impedance; mismatch effects of specimen clamps. Int. J. Impact Eng. **37**, 324–332 (2010)
5. Rhorer, R.L., Mates, S.P.: Design of threaded joints for Kolsky bars. In: *16th International Conference of Experimental Mechanics*, University of Cambridge, 7–11 July 2014

Chapter 35
An Improved Technique for Reducing the Load Ringing Phenomenon in Tensile Tests at High Strain Rates

J.B. Kwon, H. Huh, and C.N. Ahn

Abstract This paper describes the experimental procedure to reduce the load ringing phenomenon in dynamic tensile tests. Reduction and prevention of oscillations in the force signal is an important criterion in the selection of the test jigs. A slack adaptor type jig system has been newly developed for acceptable response at high strain rates. Dynamic tensile tests were conducted using a servo-hydraulic machine with high strength steel sheets at the strain rate of 200 s^{-1}. A piezo-electric load cell is used to measure the force. To confirm and determine the proportion of oscillations from bending effects on a specimen, two strain gauges are attached on the both sides of the gauge section for measurement of the difference in signals with deformation. A digital image correlation (DIC) method is employed to measure the strain during tensile tests. Experimental results show that the load ringing phenomenon in raw data of measured load signals has remarkably diminished with the slack adaptor jig newly developed at a strain rate of 200 s^{-1}.

Keywords Dynamic tensile tests • A servo-hydraulic system • A slack adaptor jig system • Load ringing phenomenon • High strain rate

35.1 Introduction

Tensile testing of sheet steels at high strain rates is becoming more important due to the need for the assessment of crashworthiness of car structures in the automotive industry. It is essential to obtain the dynamic material properties of sheet steels because auto body structures are likely to undergo high speed deformation during a crash event [1–3]. Stress–strain curves determined at the quasi-static state are not enough to describe the behavior of the structure under the dynamic load. Accurate numerical simulations of car-crash need stress–strain curves determined at high strain rates. There are many different types of testing techniques to obtain the material properties under dynamic conditions such as the servo-hydraulic system, the split Hopkinson (Kolsky) bar system and the drop weight system. Among these systems, the servo-hydraulic system can normally cover the strain rate range from 0.1 to 500 s^{-1}, while the split Hopkinson bar type system covers the strain rate range of 1000 s^{-1} or higher. So the servo-hydraulic system is suitable to characterize the mechanical behavior of steels under dynamic conditions for accurate crashworthiness analysis. The servo-hydraulic system for dynamic testing needs a special clamping method, load measurement system and strain measurement system due to different conditions from the quasi-static strain rate. These issues are critical to the quality of testing results, especially the load ringing which is the oscillation of acquired load signals.

This paper will present the experimental results of tensile tests using a servo-hydraulic machine on a high strength steel sheet, DP590, at a strain rate of 200 s^{-1}. To reduce the load ringing phenomenon in tensile tests at high strain rates, a new slack adaptor jig system has been carefully developed for smooth response during dynamic tensile tests. A piezo-electric load cell is used to measure the force signal. The direct measurement of strain at high strain rates is carried out with the use of a digital image correlation (DIC) method which is a non-contact optical measurement technique.

J.B. Kwon • H. Huh (✉)
School of Mechanical, Aerospace and Systems Engineering, Korea Advanced Institute of Science and Technology, Daeduk Science Town, Daejeon 305-701, South Korea
e-mail: hhuh@kaist.ac.kr

C.N. Ahn
Hyundai & Kia Corporate Research & Development Division, Hwaseong-Si, Republic of Korea

B. Song et al. (eds.), *Dynamic Behavior of Materials, Volume 1*,
Conference Proceedings of the Society for Experimental Mechanics Series, DOI 10.1007/978-3-319-22452-7_35

35.2 Development of a Slack Adaptor Jig System

For tensile testing on the quasi-static condition, a specimen is initially clamped at its both ends to the testing apparatus. However, for tensile testing at higher strain rates using servo-hydraulic systems, a special clamping system is necessary to grip a specimen instantly with the actuator when the stroke jig reaches the designated speed after the jig travels freely by some distance without loading the specimen. To satisfy this requirement, a slack adaptor type jig system has been newly developed. A schematic diagram of the slack adaptor is shown in Fig. 35.1a, b to describe the employment of the slack adaptor in a servo-hydraulic test machine, which is an in-house high-speed material testing machine (HSMTM) with a maximum stroke velocity of 7.8 m/s, a maximum load of 30 kN and a maximum displacement of 300 mm [4–7].

The slack adaptor was manufactured with titanium alloy grade 5 for light weight in order to reduce the impact force on the specimen. A sliding bar of a cylindrical rod has a conical shaped adaptor at its end, which has the contact angle of 60° between sliding bar adaptor and upper slack adaptor to relieve the impact force. The length of the sliding bar is determined as 150 mm to ensure a sufficient acceleration distance.

The dimensions of the test specimen in this paper are shown in Fig. 35.2 where the gauge length is 9.53 mm and the width of the gauge section is 3.18 mm. These dimensions were determined based on ASTM D638 type V [8, 9] and referred to recommendation of ISO/DIS 26203-2 [10] which guides a tensile testing method at high strain rates for metallic materials.

To assess any bending component on the specimen and check the alignment between the jig and the specimen, an ultrahigh-elongation strain gauge was applied on each side of the specimen gauge section. The strain was measured

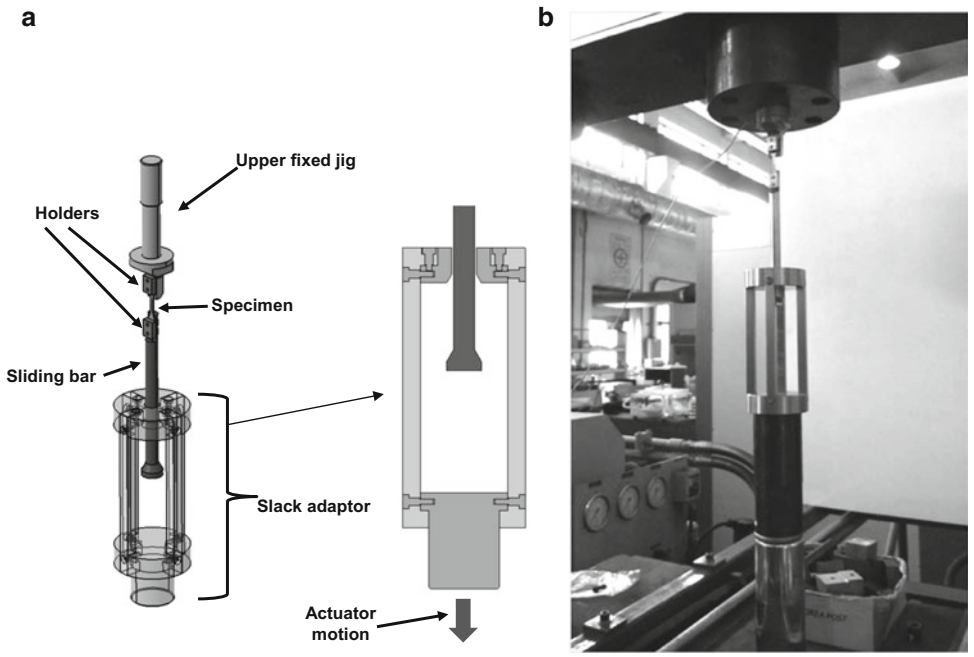

Fig. 35.1 Developed slack adaptor type jig system: (**a**) Schematic of slack adaptor; (**b**) employment of the slack adaptor in a servo-hydraulic test machine

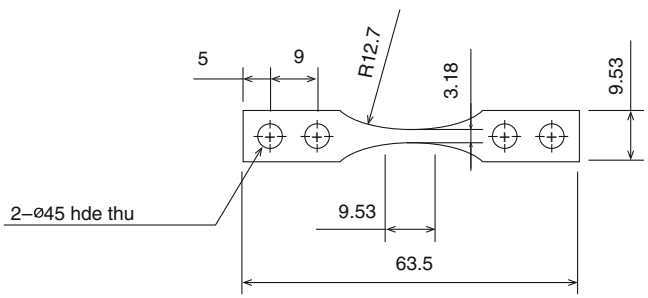

Fig. 35.2 Dimensions of a test specimen for slack adaptor jig [unit: mm]

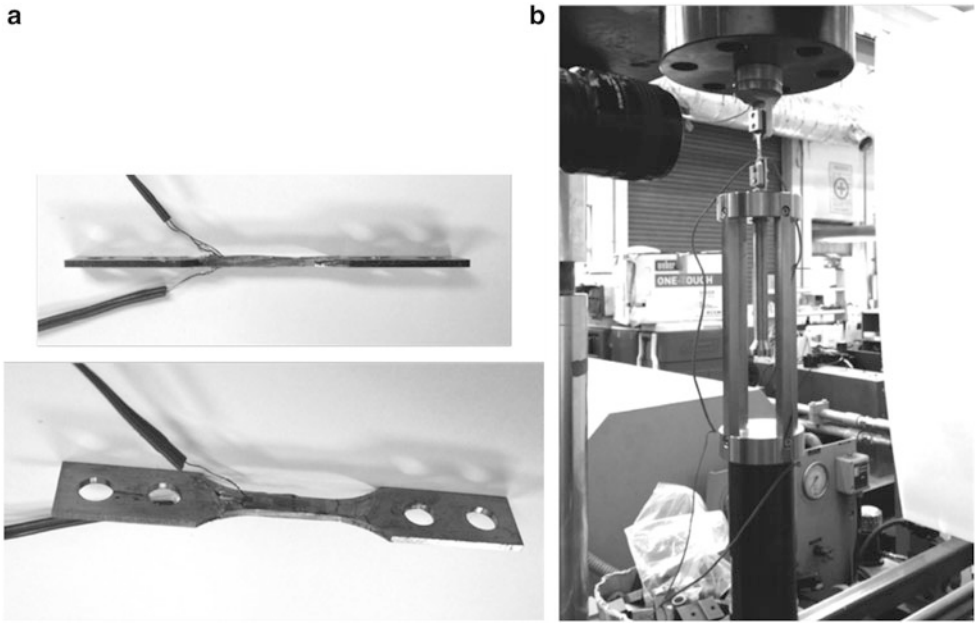

Fig. 35.3 Preparations for assessment of bending effects on the specimen: (**a**) attachment of strain gauge at specimens; (**b**) setting of the HSMTM and slack adaptor to assess the bending effects

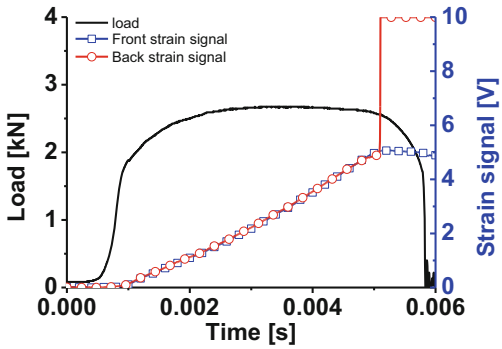

Fig. 35.4 Assessment of bending effects on the specimen by tensile test at strain rate of 100 s^{-1}

at both sides of the gauge section independently. Figure 35.3a shows how to attach the strain gauge on each side of the gauge section and Fig. 35.3b shows setting of the HSMTM and the slack adaptor to assess the bending effects during the tensile tests.

Figure 35.4 shows the comparison result of strain gauge signals between the front and the back of the specimen gauge section. The load data and the signals from the strain gauges were acquired simultaneously using the same DAQ board for synchronization. The tensile test was conducted at a strain rate of 100 s^{-1}. The signals from the strain gauges on the front and back side of the specimen gauge section are exactly the same, which ensures that there is no bending effect on the specimen. The peak value in signals at the back side of specimen is due to breakage of a strain gauge.

35.3 Tensile Tests Results Using Developed Slack Adaptor Jig at Strain Rate of 200 s^{-1}

Tensile tests of DP590 with the thickness of 1.2 t were carried out using the slack adaptor jig developed at a strain rate of 200 s^{-1}. The axial strain was measured by a DIC method from images acquired from the FASTCAM SA4 high speed camera. The alignment of a test specimen was checked using the high speed camera during specimen deformation. Captured digital images were recorded with a resolution of 256 × 976 pixels at a frame rate of 12,500 frames/sec. An AF Micro

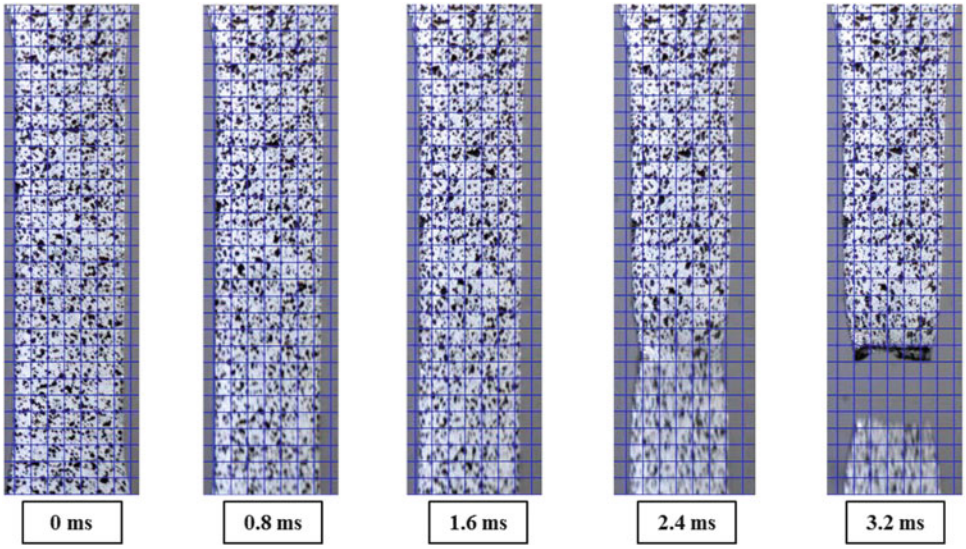

Fig. 35.5 Sequential deformed shapes of the specimen gauge section at a strain rate of 200 s^{-1}

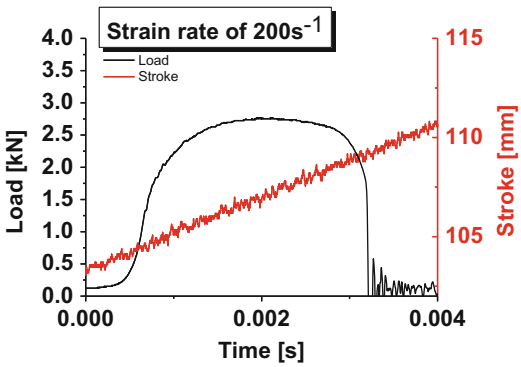

Fig. 35.6 The load curve and the displacement curve with respect to time for a steel sheet of SPFC590DP with a thickness of 1.2 t at a strain rate of 200 s^{-1}

Nikkor 60 mm F2.8D lens and a fiber optic light were used during tests to reduce temperature elevation. Sequential deformed shapes of the specimen gauge section at a strain rate of 200 s^{-1} are shown in Fig. 35.5. The slack adaptor developed ensures good alignment during tensile tests. The load–time curve at a strain rate of 200 s^{-1} is plotted as raw data in Fig. 35.6. The displacement of the actuator measured by an LVDT and the load data measured by a piezo-electric type load cell was synchronized with the same DAQ system. Tensile testing results often show oscillation in load signals due to the load ringing noise at strain rates higher than about 100 s^{-1} and the smoothing or filtering process is necessary for usable smooth data, especially to determine the yield stress [11–14]. In the figure, no load ringing phenomenon is observed in raw data at a strain rate of 200 s^{-1} and stress–strain curves were obtained more accurately using the slack adaptor developed than that in general cases [14].

35.4 Summary

A new slack adaptor was developed for the high speed material testing for sheet steels. The slack adaptor jig system proposed was prepared with titanium alloy for light weight and a conical shaped adaptor was employed to reduce the impact force on the specimen. In order to investigate the proportion of oscillations resulting from bending effects, two ultrahigh-elongation strain gauges were attached on the both side of the specimen gage length to measure each signal separately. It is noted that there are no bending effects on the specimen using the slack adaptor developed. Tensile tests at a strain rate of

200 s^{-1} were conducted with high strength steel sheet of DP590 with the thickness of 1.2 mm. It is also noted from experimental results that the slack adaptor developed remarkably reduces the load ringing in raw data of load signals. Consequently, the slack adaptor developed diminishes the load ringing phenomenon in the load data during dynamic tensile tests at a strain rates of 200 s^{-1} and improves the quality of the dynamic material properties of sheet steels.

References

1. Yoon, J.H., Huh, H., Kim, S.H., Kim, H.K., Park, S.H.: Comparative Crashworthiness Assessment of the ULSAB-AVC model with advance high strength steel and conventional steel. In: Proc. of IPC-13, pp. 724–747, Gyeongju, Korea (2005)
2. Huh, H., Lim, J.H., Song, J.H., Lee, K.S., Lee, Y.W., Han, S.S.: Crashworthiness assessment of side impact of an auto-body with 60TRIP steel for side members. Int. J. Automot. Technol. **4**(3), 149–156 (2003)
3. Mahadevan, K., Liang, P., Fekete, J.: Effect of strain rate in full vehicle frontal crash analysis. SAE Trans. **109**(6), 863–871 (2000)
4. Huh, H., Lim, J.H., Park, S.H.: High speed tensile test of steel sheets for stress-strain curve at the intermediate strain rate. Int. J. Automot. Technol. **10**(2), 195–204 (2009)
5. Huh, H., Jeong, S.H., Bahng, G.W., Che, K.S., Kim, C.G.: Standard uncertainty evaluation for dynamic tensile properties of auto-body steel-sheets. Exp. Mech. **24**, 943–956 (2014)
6. Huh, J., Huh, H., Lee, C.S.: Effect of strain rate on plastic anisotropy of advanced high strength steel sheets. Int. J. Plast. **44**, 23–46 (2013)
7. Ahn, K., Huh, H., Yoon, J.: Strain hardening model of pure titanium considering effects of deformation twinning. Met. Mater. Int. **19**(4), 749–758 (2013)
8. Hill, S.I.: Standardization of high strain rate test techniques for automotive plastics project. UDRI: Structural Test Group, UDR-TR-2004-00016 (2004)
9. Xiao, X.: Dynamic tensile testing of plastic materials. Poym. Testing **27**, 164–178 (2008)
10. ISO/DIS 26203-2: Metallic Materials–Tensile Testing Method at High Strain Rates–Part 2: Servo-Hydraulic and Other Test Systems (2009)
11. Leblanc, M.M., Lassila, D.H.: A hybrid technique for compression testing at intermediate strain rates. Exp. Tech. **20**(5), 21–24 (1996)
12. Zhu, D., Rajan, S.D., Mobasher, B., Peled, A., Mignolet, M.: Modal analysis of a servo-hydraulic high speed machine and its application to dynamic tensile testing at an intermediate strain rate. Exp. Mech. **51**(8), 1347–1363 (2011)
13. Huh, H., Lim, J.H., Park, S.H.: High speed tensile test of steel sheets for the stress-strain curve at the intermediate strain rate. Int. J. Autom. Technol. **10**(2), 195–204 (2009)
14. Bruce, D.M., Matlock, D.K., Speer, J.G., De, A.K.: Assessment of the Strain-Rate Dependent Tensile Properties of Automotive Sheet Steels. (No. 2004-01-0507), SAE Technical Paper (2004)

Chapter 36
Experimental and Numerical Analysis of Pressure Waves Propagation in a Viscoelastic Hopkinson Bar

M. Sasso, M.G. Antonelli, E. Mancini, M. Radoni, and D. Amodio

Abstract In this paper, the viscoelastic behaviour of PET is assessed in order to study the wave propagation in long SHPB made of polymeric materials.

First, an analytical formulation and a numerical FE model were set up and validated using viscoelastic parameters borrowed from literature. However, for a correct description of the attenuation factor and the complex wave number of the real PET material, the storage and loss moduli as functions of the frequency must be known. For this reason, DTMA tests have been conducted at different temperatures and frequency; the experimental curves have been shifted, extrapolating the storage and loss master functions up to 100 kHz, and used for identifying the stiffness and damping parameters of a generalized Maxwell model. Then, these parameters were implemented into the numerical model for simulating the wave propagation in long bars. The numerical results are compared with the real wave signals measured from experiments performed on a SHPB made of the same PET material.

Keywords SHPB • Viscoelasticity • DTMA • PET • FEM

36.1 Introduction

The Split Hopkinson Pressure Bar (SHPB) is an experimental technique for the determination of the constitutive behaviour of materials at high stain rates [1]. Specimen to be tested is placed between an input and an output long bars; the impact of a striker against the input bar, or a preload and a fast release of a part of it, generates a pressure wave travelling along the input bar with the sound speed of the bar material C_b; when the wave reaches the specimen, it is partially transmitted to the output bar and partially reflected back into the input bar. Specimen, made of a softer material [2, 3], undergoes large plastic deformation at high strain rate while the bars remain within the elastic limit. Classical formulae for experimental determination of the stress-strain curve of the specimen material are

$$\dot{\varepsilon}(t) = -2\frac{C_b}{L_s}\varepsilon_R(t) \quad \sigma(t) = E_b\frac{A_b}{A_s}\varepsilon_T(t) \tag{36.1}$$

where $\dot{\varepsilon}(t)$ is the strain rate, A_b and E_b are the bar cross-sectional area and elastic modulus, and where L_s and A_s represent the specimen original gauge length and cross-sectional area, respectively. ε_R and ε_T represent the reflected and transmitted strain pulses, typically measured by strain gauges glued on the bars.

Polymeric materials, as polyethylene terephthalate (PET) used in this work, show a mechanical viscoelastic behaviour significantly time-dependent; the shape of the waves along viscoelastic bars changes due to both attenuation (depending on material damping) and dispersion (depending on geometrical effects and material phase velocities) [4]; moreover, the transmitted force cannot be computed considering a constant E_b. Hence, the correct application of (36.1) requires to shift ε_R and ε_T, measured at a certain position in the bars, to evaluate the real loading history experimented by the sample and to adopt the hereditary integral formulation to compute the stress from the measured ε_T. For these reasons, on one hand it is important to study the wave propagation behaviour in viscoelastic materials; on the other, it is necessary to adopt a suitable model of the viscoelastic material.

M. Sasso (✉) • E. Mancini • M. Radoni • D. Amodio
DIISM, Università Politecnica delle Marche, Via Brecce Bianche, Ancona 60121, Italy
e-mail: m.sasso@univpm.it

M.G. Antonelli
DIIIE, Università degli Studi dell'Aquila, Via Giovanni Gronchi 18, L'Aquila 67100, Italy

B. Song et al. (eds.), *Dynamic Behavior of Materials, Volume 1*,
Conference Proceedings of the Society for Experimental Mechanics Series, DOI 10.1007/978-3-319-22452-7_36

Wave propagation in viscoelastic rods were investigated by many authors; several methods for correcting the effects of attenuation and dispersion were proposed. The basic equations for the determination of the stress–strain–strain rate relationship for the tested material can be found in [5]; a method, based on the spectral analysis of wave motion, was also developed for the correction of the dispersion and attenuation of viscoelastic waves. The specific problems encountered in the use of viscoelastic bars in the SHPB setup were analysed in [6].

Benatar et al. [7] used a simplified Pochhammer equation for low and intermediate loss viscoelastic materials and formulated corrections for geometric dispersion, phase velocity and attenuation. In [8, 9] a wave model for longitudinal waves was developed and a closed form solution of the attenuation coefficient and of the phase velocity was reached. Bacon [10] used a fully experimental approach to extract a transfer function of the bar in the frequency domain, automatically correcting both material and geometric dispersion in Hopkinson bar experiments.

Adopting a 1D wave propagation theory and utilizing strains at multiple locations on a long impacted bar, the complex moduli [11, 12] or the viscoelastic models parameters [13, 14] of a polymeric can be found. However, as highlighted in [15], a relevant scatter is observed in literature among the coefficients identified through the wave propagation experiments. Indeed, a large variance in parametric identification of complex modulus from propagation experiments is likely to be found [16].

The classical approach to the analytical modelling of the rheological behaviour of viscoelastic materials is represented by the family of the Standard Linear Solid models (SLS), which consists of a combination of linear springs and dashpots [17, 18]. Other approaches based on fractional calculus has also received considerable attention [19–21]. However, the former class of models is still the most adopted and will be used in the present work. The stress–strain relation for such SLS systems is commonly expressed in a differential form, and the derived time-domain material functions reduces to a series of decaying exponentials, referred to as Prony series. The Generalized Maxwell model, shown in Fig. 36.1, is the archetype of this approach.

The response to a generic strain history is given, as aforementioned, by the hereditary [22] integral of the relaxation modulus E multiplying the strain increments $\dot{\varepsilon}$:

$$\sigma(t) = \int_{-\infty}^{t} E(t-\tau)\dot{\varepsilon}(\tau)d\tau \tag{36.2}$$

where E is given by:

$$E(t) = E_0 + \sum_{k=1}^{n} E_i exp\left(-t\frac{E_i}{\eta_i}\right) \tag{36.3}$$

The parameters in (36.2) and (36.3) are usually extracted from relaxation tests, but this is mainly intended for long term phenomena. The analysis of dynamic phenomena can be suitably treated in the frequency domain exploiting the Alfred's correspondence principle [18, 23], introducing the concept of complex elastic modulus $E^* = E^{'}(\omega) + iE^{''}(\omega)$:

The determination of E' and E'', respectively the storage and loss moduli, as functions of frequency and temperature, can be efficiently worked out by Dynamic Thermal-Mechanical Analyses (DTMA) [24–26] coupled with the shifting technique and Time-Temperature Superposition Principle (TTSP) [27, 28]. In this ways it is possible to obtain master curves of the storage and loss moduli ranging from low to very high frequency at a given temperature, as done in [29–31].

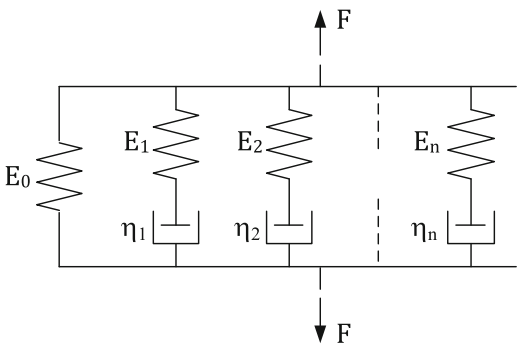

Fig. 36.1 Generalized Maxwell model

In this work, the numerical and experimental analysis of wave propagation in a PET Hopkinson Bar has been accompanied by DTMA tests on the bar material. Section 36.2 describes the implemented polymeric SHPB; in Sect. 36.3 the numerical FE model of SHPB and its validation procedure are described; Sect. 36.4 shows DTMA results on PET and the procedure to obtain stiffness and damping parameters of a seven parameters generalized Maxwell model; Sect. 36.5 describes experimental activity carried out with SHPB having a PET output bar and the comparison between experimental, analytical and numerical results, in order to study and to model the wave propagation.

36.2 SHPB Equipment

A new configuration of SHPB equipment was implemented in the present work: striker bar was substituted by a cylindrical pre-tensioned bar with a fixed end connected to the input bar; a linear actuator provides the displacement of the other end. An annealed steel sacrificial element (whose thickness is in the range $0.3 \div 0.7$ mm) is placed between the actuator and the pre-tensioned bar: during the resulting tensile load application, the failure of the sacrificial element occurs and provides a fast release of elastic energy, stored in the pre-tensioned bar, as a compressive pressure whose amplitude is equal to the half of the stress level of the pre-tensioned bar, at the moment of energy release, and the length is equal to the double of the pre-tensioned bar length.

Bar diameters are equal to 18 mm; lengths of the pre-tensioned, input and output bars are equal, respectively, to 3, 7.5 and 4 m. In order to satisfy a right alignment of bars and a weak friction, bars can slide inside a set of adjustable bearings in PTFE. Bearings are mounted on a structure made of a commercial double-T profile. An arrest system is placed at the opposite end, as regards the specimen placement, of the output bar. For each bar, a strain gauge is placed; wave signals are acquired by a NI PCI 6120 system managed by a customized software. Figure 36.2 shows the SPBH configuration.

In the present work, pre-tensioned and input bars are made of high strength steel; the study of wave propagation in viscoelastic material was performed analysing strain waves propagating along the output bar, realized in PET.

36.3 Validation of Numerical And Analytical Procedures

A 2D finite element (FE) model of SHPB, based on the axisymmetric geometry of bars, was realized by LS-Dyna numerical code to simulate the wave propagation in bars of viscoelastic material.

Four nodes SHELL elements were used. The connection between the pre-tensioned and the input bar was modelled by coincident nodes at bars interface; the displacement was applied to the free end of the pre-tensioned bar; to the fixed one a *rigidwall* constraint was applied. Mesh size of specimen is considerably lower than bars one in order to analyse, with a good accuracy, plastic strains of specimen. Only axial movements are allowed; contacts constrains were modelled as *automatic surface to surface contact*, based on the penalty stiffness algorithm. Barelling phenomenon of specimen was considered by a friction coefficient at specimen-bars interfaces. Figure 36.3 shows the FE model.

For later use of FE model, firstly validation of it was achieved and then it was evaluated its accuracy to simulate time-dependant stress-strain behaviour and to simulate strain waves propagation.

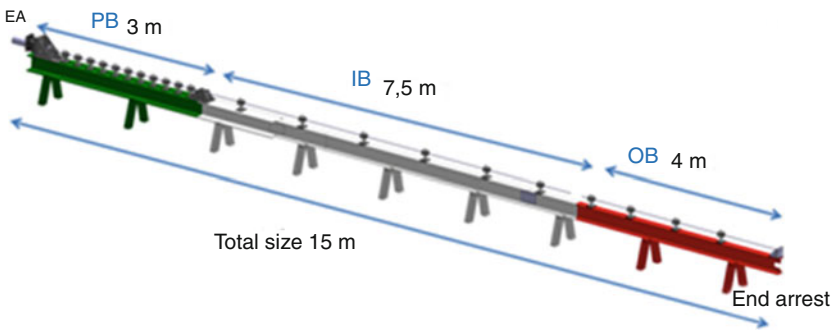

Fig. 36.2 The SHPB equipment

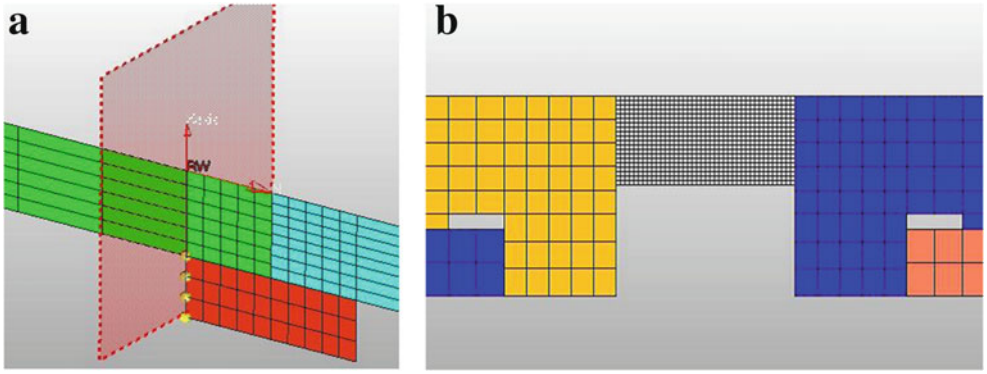

Fig. 36.3 FE model of SHPB: (**a**) pre-tensioned-input bars interface and the rigidwall constraint; (**b**) specimen placed between input and output bars

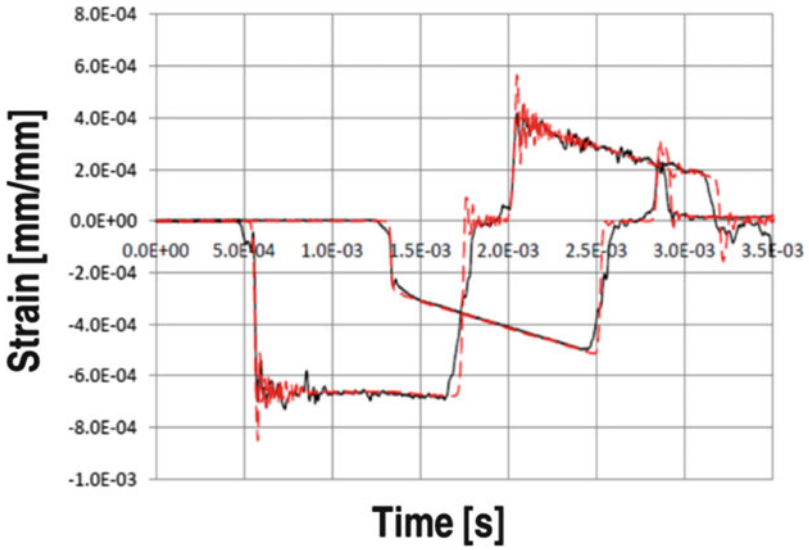

Fig. 36.4 Comparison between experimental (*black*) and numerical (*red*) results

FE model validation was carried out by comparison between numerical and experimental results, in terms of strain waves, on the basis of a compressive test of an Ergal specimen, whose material was modelled by the constitutive model of Jhonson-Cook (J-C), to take into account the effect of strain rate, and the state equation of Mie-Gruneisen (M-G), to define hydrostatic behaviour in terms of pressure inside the material, between high strength steel bars, whose materials were modelled as linear isotropic ($E = 200$ GPa; $\rho = 7800$ kg/m^3; $\nu = 0.3$). Diameter and height of specimen were equal to 8 mm. The same experimental ramp displacement of 4 mm in a time period equal to 0.05 s was applied, providing a pressure wave amplitude equal to 133.5 MPa, a wave length equal to 6 m and a wave velocity equal to 5063.7 m/s; specimen strain happens in 1.2 ms; average strain rate of the specimen was equal to $10^{2.5}$ s^{-1}.

As shown in Fig. 36.4, the good agreement between numerical and experimental results validated the FE model; the simulation of the viscoelastic SHPB required only the change of material model.

Indeed, in order to evaluate accuracy to simulate time-dependant stress-strain behaviour, viscoelastic FE model was built with the pre-tensioned bar in high strength steel and the input bar in polymeric material, with the same boundary conditions, contacts and loads previously described. Viscoelasticity was modelled by the general viscoelastic material formulation of LS-Dyna, based on a 3 parameters generalized Maxwell model, whose values were borrowed from literature [5]: $E_0 = 3.14$ GPa, $E_1 = 3.98$ GPa, $\eta_1 = 0.268$ MPa; moreover, $\rho = 1.2 \times 10^3$ kg/m^3 and $\nu = 0$.

Time-dependant behaviour of viscoelastic material in FE model is taken into account through linear viscoelasticity by the hereditary integral (36.2) where the time-dependant $E(t)$ is substituted by the relaxation function $g(t)$ expressed by a n-terms Prony series in terms of G_i shear moduli, β_i decay constants, K_i bulk relaxation moduli and β_{K_i} bulk decay constants. Table 36.1 reports imposed values of the above mentioned parameters.

Table 36.1 Values of viscoelasticity parameters in viscoelastic FE model

G_1 [MPa]	G_2 [MPa]	K_1 [MPa]	K_2 [MPa]	β_1 [s^{-1}]	β_2 [s^{-1}]	β_{K_1} [s^{-1}]	β_{K_2} [s^{-1}]
1570	1990	1046.667	1326.667	0	14850.74	0	14850.74

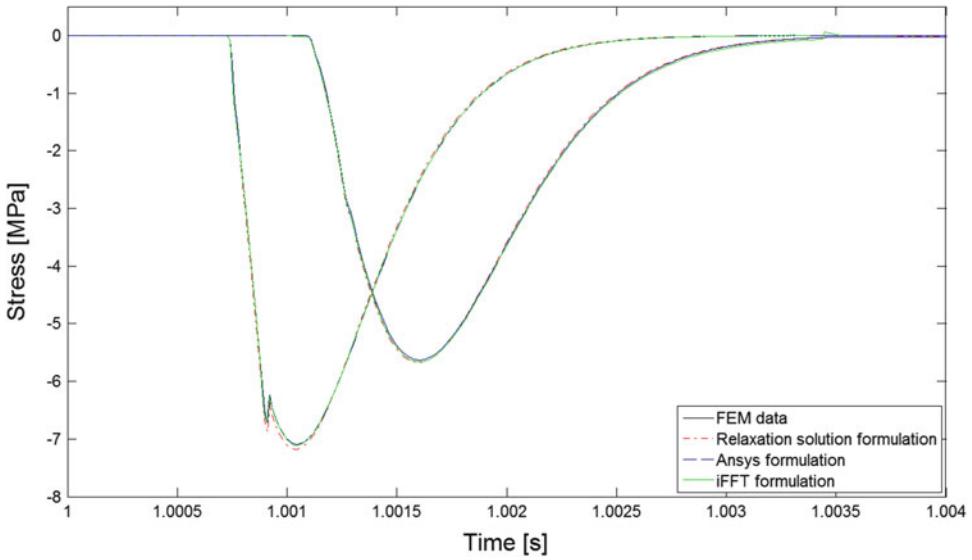

Fig. 36.5 Comparison between numerical and analytical stress values along the input bar at 1613.8 mm and 2503.4 mm from the pre-tensioned bar

Results, in terms of stress, of two calculation procedures in time domain and one in frequency domain were compared to results of the viscoelastic FE model, in order to validate the accuracy of time-dependent behaviour of it.

In the time domain, the hereditary integral (36.2) was solved:

- by the generalized relaxation solution $\sigma(t) = \varepsilon_0 E(t)$, where $E(t)$ is expressed as (36.3), referred to a 3 parameters generalized Maxwell model;
- by the integration scheme of (36.2), implemented by Ansys code and expressed as function of the stress asymptotic value added to a summatory whose each stress term operator is expressed by the recursive formula:

$$(s_i)_{n+1} = (s_i)_n \cdot e^{\left(-\frac{\Delta t}{\tau_i^G}\right)} + 2 \cdot \frac{E_1}{2(1+\nu)} \cdot \Delta\varepsilon \cdot e^{\left(-\frac{\Delta t}{2\tau_i^G}\right)} \tag{36.4}$$

where $\Delta\varepsilon = \varepsilon_{n+1} - \varepsilon_n$ is the difference between deviatoric parts of the strains of two consecutive iterative steps.

Stresses values were calculated on the basis of numerical strain waves computed at two different points of the input bar model, far from the free end in order to avoid overlaps of incident and reflected waves.

In the frequency domain, time-dependent behaviour was evaluated for a 3 parameters generalized Maxwell model, as:

$$\sigma(\omega) = \left[E_0 + \frac{\eta_1^2\omega^2 E_1}{\eta_1^2\omega^2 + E_1^2} + i\eta_1\omega\frac{E_1^2}{\eta_1^2\omega^2 + E_1^2}\right] \cdot \varepsilon(\omega) \tag{36.5}$$

In this approach, the previous two numerical strain waves were Fourier transformed (after opportune zero-padding) into the frequency domain; hence, stresses were computed by (36.5) to be subsequently anti-transformed into the time domain and then compared to the computed numerical stresses.

A good accuracy of the implemented FE model to simulate time-dependant behaviour of viscoelastic materials was achieved, as shown in Fig. 36.5 where numerical results are as expected by analytical formulations.

As final step, a new comparison procedure was applied with results, in terms of strain, obtained by the analytical formulation of the wave propagation theory in viscoelastic materials. For 1D propagation, in the frequency domain for only

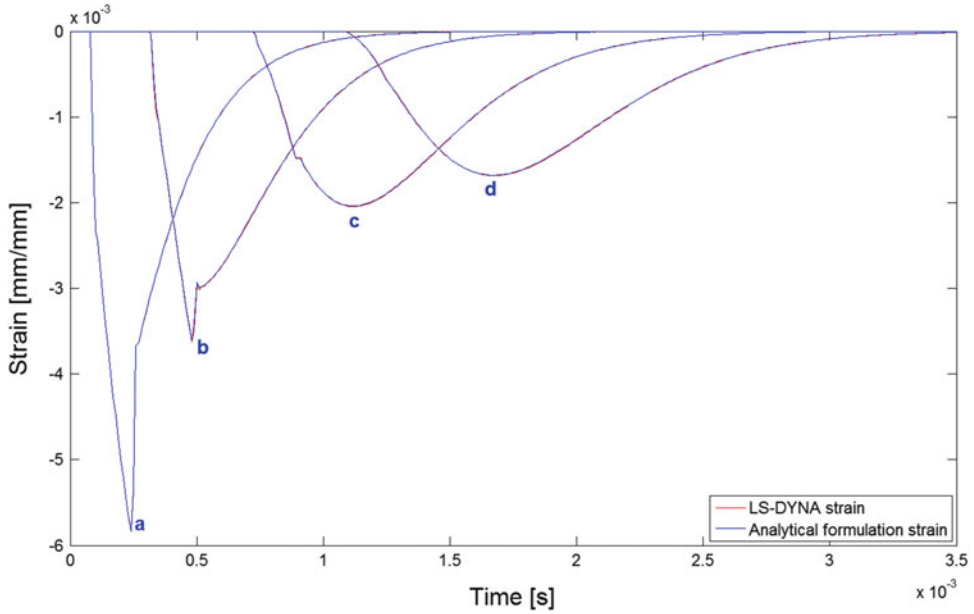

Fig. 36.6 Comparison between numerical and analytical strain waves along viscoelastic input bar at: (*a*) 208 mm; (*b*) 790.40 mm; (*c*) 1782.40 mm; (*d*) 2675.20 mm

forward waves, the strain at the position x can be computed as a function of the strain at a zero position and of material [5], according the following expression:

$$\widetilde{\varepsilon}(x,\omega) = -\widetilde{\varepsilon}(0,\omega) \cdot e^{-\gamma(\omega)x} \tag{36.6}$$

where $\widetilde{\varepsilon}(0,\omega)$ is the strain spectrum at zero position, $\gamma(\omega)$ is the propagation coefficient, function of the wave number k, responsible of the wave dispersion due to accumulation of phase displacement among the harmonics, and the attenuation factor α, responsible of the reduction of harmonic amplitudes, according to

$$\gamma(\omega) = \alpha(\omega) + ik(\omega) = \alpha(\omega) + i\frac{\omega}{C(\omega)} \tag{36.7}$$

where C indicates the phase velocity. Analytical expressions of k and α for a 3 parameters generalized Maxwell model can be found in [5].

Strain at zero position was the strain wave computed by FE model along the input bar at a distance equal to 208 mm from the pre-tensioned bar; after opportune zero-padding, it was Fourier transformed; strain waves in frequency domain were computed at four positions by (36.6) and then anti-transformed and compared with numerical strain waves at the same positions. An optimal correspondence furtherly validated the numerical model, as shown in Fig. 36.6, where numerical and analytical results are compared.

However, the correct description of real PET behaviour, in terms of attenuation and complex wave number, requires the knowledge of the storage and loss moduli, as functions of the frequency; for this reason, they were determined by DTMA tests and the application of TTSP, as described in the next session.

36.4 DTMA: Experimental Characterization of PET

DTMA is an experimental technique that obtain the properties of materials under several conditions of time (or frequency) and temperature, typically, measuring stress resultant by the application of a constant sinusoidal strain [24]. In viscoelastic materials, a phase retardation of an angle δ between stress and strain is recorded and implemented, together with the amplitude of stress and strain waves, to extract storage and loss moduli and $tan(\delta)$, according to the expressions:

Table 36.2 Best-fitting parameters of the generalized Maxwell model

E_0 [MPa]	E_1 [MPa]	E_2 [MPa]	E_3 [MPa]	η_1 [$MPa \cdot s$]	η_2 [MPa · s]	η_3 [MPa · s]
3393.7	1165.2	198.52	186.76	0.0014	0.1165	0.0071

$$E^{'} = E^{*} \cdot cos\delta \quad E^{''} = E^{*} \cdot sin\delta \quad \tan(\delta) = E^{''}/E^{'} \tag{36.8}$$

TTSP allows to estimate viscoelastic behaviour over a broad range of time or frequencies, within and over the range of experiments, by a horizontal shift of data obtained at several temperatures to a common reference temperature [18, 28, 27], in the form of a master curve. The horizontal shift, called shift factor a_T, is commonly evaluated by two approaches: the Williams-Landel-Ferry (WLF) equation, valid near and above the glass transition temperature, and the Arrhenius equation, valid for the secondary polymer transition; the Arrhenius equation is expressed as:

$$log a_T = \frac{E_a}{2.303R}\left(\frac{1}{T} - \frac{1}{T_0}\right) \tag{36.9}$$

where T is the measurement temperature, T_0 is the reference temperature, C_1 and C_2 are constants, usually assumed equal to 17.4 and 51.6 respectively, if T_0 is equal to the glass transition temperature [26, 27], E_a is the activation energy associated to the relaxation transition and R is the gas constant (8.314 J/mol °C) [18]. Experimental characterization of PET, whose density and transition temperature are, respectively, equal to 1380 kg/m^3 and 75 °C, was carried out by a NETZSCH DMA 242C system, in three-point bending deformation mode tests, in which the probe-edge applied a sinusoidal strain, with a constant amplitude equal to 120 μm.

Three specimens (50 mm × 10 mm × 3 mm) have been subjected to the same set of tests: four different values of frequency (0.1—1—10—50 Hz) while varying temperature in the range $-20 \div 20$ °C; heat-rate equal to 0.5 K/min.

Numerical determination of storage and loss moduli, in the frequency range $10^{-1} \div 10^{6}$ Hz, was applied to a material modelled by a 7 parameters generalized Maxwell model (1 spring and 3 Maxwell models) and carried out by minimization of the normalized error function f_e, expressed in the following form:

$$f_e = \sum_{i=1}^{n}\left(E_i^{'(exp)} - E_i^{'(num)}\right)^2 + \sum_{i=1}^{n}\left(E_i^{''(exp)} - E_i^{''(num)}\right)^2 \tag{36.10}$$

The best-fitting stiffness and damping parameters found by (36.10) are reported in Table 36.2.

36.5 Experimental Analysis of PET SHPB

The experimental analysis was carried out in order to study the real wave propagation behaviour of strain waves in SHPB made with output bar in PET; experimental results are useful to calibrate and then to validate an analytical model to be applied in the characterization of materials, with low impedance, as tool for numerical correction of dispersion and attenuation of experimental strain waves. In the setup described in Sect. 36.2, output bar was neared to input one, without specimen, in a compressive test. Two strain gauges were glued on it: the first was placed at 155 mm from the input bar and the second at the middle of the bar, to avoid overlaps at gauge position between the positive travelling incident wave and its reflection. Thickness of sacrificial element was equal to 0.3 mm, generating an incident pressure wave of 50 MPa amplitude, along the input bar. Experimental strain waves were compared to analytical strain waves computed by the application of the complex modulus $E^*(i\omega)$ [10, 15], as obtained by DTMA with the following expression:

$$\gamma^2(\omega) = -\frac{\rho\omega^2}{E^*(i\omega)} \tag{36.11}$$

Then, the Fourier transforms (after opportune zero-padding) of the incident and reflected signals at the position of the second strain gauges were computed by the application of equation (36.6) where $\widetilde{\varepsilon}(0,\omega)$ is the Fourier transform of the first strain gauge signal; then, they were anti-transformed to obtain analytical strain histories to be compared with experimental ones. Figure 36.7 shows the comparison between the experimental and the numerical strain histories.

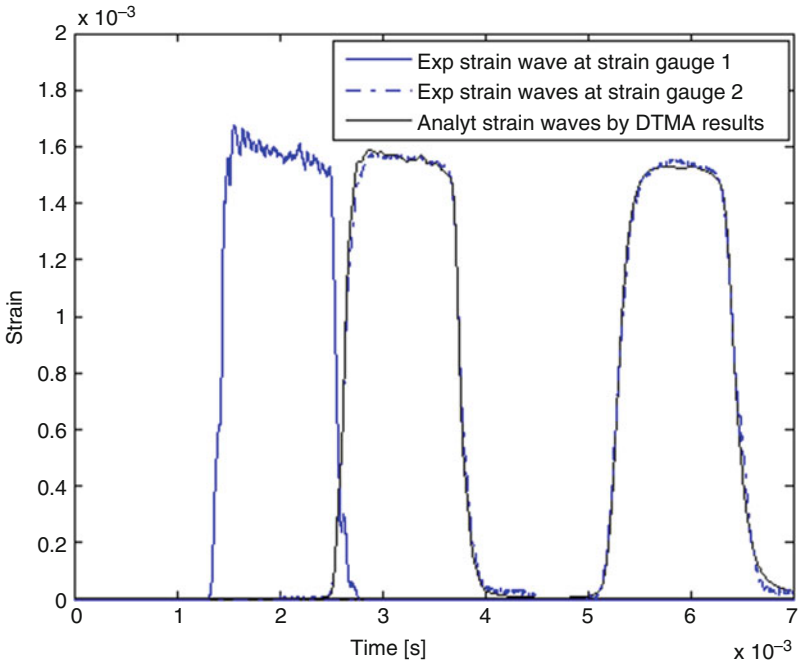

Fig. 36.7 Comparison of experimental and analytical strain histories

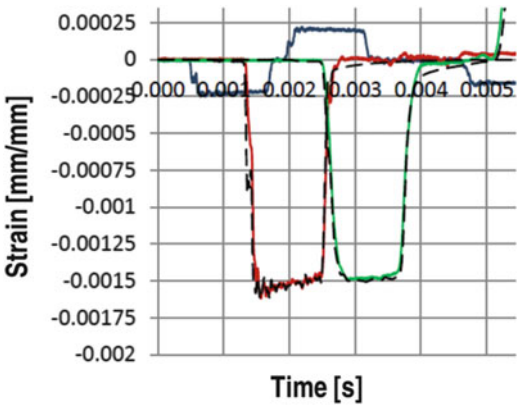

Fig. 36.8 Comparison between experimental and numerical results for a PET SHPB

It can be noted a satisfying correspondence as regards incident strain waves: analytical results of reflected strain wave show a good fitting with experimental ones. As consequence, the final viscoelastic FE model was built with the pre-tensioned and input bar in high strength steel and the output bar made in PET, modelled by the general viscoelastic material formulation of LS-Dyna, based on the 7 parameters values reported in Table 36.2. A displacement equal to 1.5 mm was applied to the pre-tensioned bar so to generate a pressure wave of 100 MPa amplitude.

Figure 36.8 shows comparison between experimental and numerical results. It can be concluded that the built FE model provides an optimal simulation of the correction of attenuation and dispersion of strain waves along a PET SHPB.

36.6 Conclusions

In a SHPB made with viscoelastic bars, the shape of the waves along the bars changes due to both attenuation and dispersion. On one hand, classical formulae of SHPB can't be applied; on the other, the knowledge of the attenuation factor and the complex wave number is necessarily required to shift reflected and transmitted waves for the evaluation of the real loading history experimented by the sample; moreover, the hereditary integral formulation allows to compute the stress from the measured transmitted wave. For these reasons, the present work was focussed to study the wave propagation along a PET

SHPB. In particular, a FE model was developed in order to simulate the attenuation and dispersion effect along bars in PET. Validation of the model was carried out by comparison with analytical models of the time-dependant behaviour of viscoelastic materials, in time and frequency domain, and of the 1D propagation theory, on the basis of data borrowed from literature. To take into account the real behaviour of PET, storage and loss master function were obtained by DTMA tests, at the reference temperature of 18.9 °C; at the same time, it was possible to obtain stiffness and damping parameters of a 7 generalized Maxwell model. These data were adopted to build the final viscoelastic FE model and to calculate the propagation coefficient, by analytical formulation. A good correspondence between experimental results and numerical and analytical results suggest to use the viscoelastic FE model and the analytical model, respectively, as a tool for the predictive evaluation of stress-strain curve of material at low impedance and as tool for correction of attenuation and dispersion of experimental strain waves acquired in a SHPB made of viscoelastic bars.

References

1. Song, B., Chen, W.: Split Hopkinson Kolsky Bar: Design, Testing and Applications. Springer, New York (2010)
2. Wang, L., Labibes, K., Azari, Z., Pluvinage, G.: Generalization of split Hopkinson bar technique to use viscoelastic bars. Int. J. Impact Eng. **15** (5), 669–686 (1994)
3. Cronin, D., Salisbury C., Horst, C.: High Rate Characterization of Low Impedance Materials Using a Polymeric Split Hopkinson Pressure Bar. In: Proceedings of SEM annual conference, St Louis (2006)
4. Kolsky, H.: Stress waves in solids. Dover, New York (1963)
5. Cheng, Z., Crandall, J., Pilkey, W.: Wave dispersion and attenuation in viscoelastic split Hopkinson pressure bar. Shock. Vib. **5**, 307–315 (1998)
6. Zhao, H., Gary, G., Klepaczko, J.: On the use of a viscoelastic split hopkinson pressure bar. Int. J. Impact Eng. **19**(4), 319–330 (1997)
7. Benatar, A., Rittel, D., Yarin, A.: Theoretical and experimental analysis of longitudinal wave propagation in cylindrical viscoelastic rods. J. Mech. Phys. Solids **51**, 1413–1431 (2003)
8. Ahonsi, B., Harrigan, J., Aleyaasin, M.: On the propagation coefficient of longitudinal stress waves in viscoelastic bars. Int. J. Impact Eng. **45**, 39–51 (2012)
9. Aleyaasin, M., Harrigan, J.: Wave dispersion and attenuation in viscoelastic polymeric bars: Analysing the effect of lateral inertia. Int. J. Mech. Sciences **52**, 754–757 (2010)
10. Bacon, C.: An Experimental Method for Considering Dispersion and Attenuation in a Viscoelastic Hopkinson Bar. Experimental Mechanics **38**(4), 242–249 (1998)
11. Lundberg, B., Blanc, R.: Determination of mechanical material properties from the two-point response of an impacted linearly viscoelastic rod specimen. J. Sound Vib. **126**, 97–108 (1988)
12. Blanc, R.: Transient wave propagation methods for determining the viscoelastic properties of solids. J. Appl. Mech. Trans. ASME **60**(3), 763–768 (1993)
13. Mousavi, S., Nicolas, D., Lundberg, B.: Identification of complex moduli and Poisson's ratio from measured strains on an impacted bar. J. Sound Vib. **277**, 971–986 (2004)
14. Mossberg, M.: Parametric identification of viscoelastic materials from time and frequency domain data. Inverse Prob. Eng. **9**, 37–41 (2001)
15. Butt, H., Xue, P.: Determination of the wave propagation coefficient of viscoelastic SHPB: significance for characterization of cellular materials. Int. J. Impact Eng. (2013). doi:10.1016/j.ijimpeng.2013.11.010
16. Rensfelt, A., Söderström, T.: Parametric identification of complex modulus. Automatica **47**, 813–818 (2011)
17. Tschoegl, N.: The Phenomenological Theory of Linear Viscoelastic Behavior. Springer, Berlin (1989)
18. Brinson, H., Brinson, L.: Polymer Engineering Science and Viscoelasticity—An Introduction. Springer, Berlin (2008)
19. Bagley, R., Torvik, P.: On the fractional calculus model of viscoelastic behavior. J. Rheol. **30**, 133–155 (1986)
20. Atanackovic, T., Stankovic, B.: Dynamics of viscoelastic rod of fractional derivative type. J. Appl. Math. Mech. **82**, 377–386 (2002)
21. Sasso, M., Palmieri, G., Amodio, D.: Application of fractional derivative models in linear viscoelastic problems. Mech. Time-Depend. Mater. **15**, 367–387 (2011)
22. Schapery, R.A.: On the characterization of nonlinear viscoelastic materials. Polym. Eng. Sci. **9**(4), 295–310 (1969)
23. Alfrey, T.: Nonhomogeneous stress in viscoelastic media. Q. J. Appl. Mat. **21**(113), 113–119 (1944)
24. Foreman, J.: Dynamic mechanical analysis of polymers. Am. Lab. **29**(1), 21–24 (1997)
25. Menard, K.: Dynamic Mechanical Analysis: A Practical Introduction. CRC Press, Boca Raton (1999)
26. Ferry, J.: Viscoelasic Properties of Polymers, 3rd edn. Wiley, New York (1980)
27. Williams, M., Landel, R., Ferry, J.: The temperature dependence of relaxation mechanisms in amorphous polymers and other glass-forming liquids. J. Am. Chem. Soc. **77**, 3701–3707 (1955)
28. Brostow, W., D'Souza, N., Kubat, J., Maksimov, R.: Creep and stress relaxation in a longitudinal polymer liquid crystal: Prediction of the temperature shift factor. J. Chem. Phys. **110**(19), 9706–9712 (1999)
29. Nair, T., Kumaran, M., Unnikrishnan, G., Pillai, V.: Dynamic mechanical analysis of ethylene–propylene–diene monomer rubber and styrene–butadiene rubber blends. J. Appl. Polym. Sci. **112**(1), 72–81 (2009)
30. Bhushan, B., Ma, T., Higashioji, T.: Tensile and dynamic mechanical properties of Improved ultrathin polymeric films. J. Appl. Polym. Sci. **83**(10), 2225–2244 (2002)
31. Daga, V.K., Wagner, N.J.: Linear viscoelastic master curves of neat and laponite-filled poly(ethylene oxide)-water solutions. Rheol. Acta **45**, 813–824 (2006)

Chapter 37
An Innovative Instrumented Projectile for Dynamic Testing and Material Characterization

Guojing Li, Dahsin Liu, and Dan Schleh

Abstract Measuring impact-induced contact force history is critically important to understanding the nature of impact events and the associated damage processes of materials/structures involved in the impact. In order to investigate the impact-induced contact force history involved in free impacts, such as ballistic impact and high-speed crash, this study developed an innovative instrumented projectile. Both instrumented projectiles with and without an innovative geometry were constructed, tested and compared. An independent optical method was also used to justify the measurements from the innovative instrumented projectile. Experimental results confirmed the effectiveness and accuracy of the innovative instrumented projectile in measuring impact-induced force history.

Keywords Instrumentation • Projectile • Dynamic testing • Material characterization

37.1 Background and Motivation

Drop-weight impact testers (DWIT) have been commonly used in laboratories for measuring force histories involved in low-velocity impact. The measurements from DWIT are usually based on a metallic cylinder mounted with a pair of electrical resistance strain gauges. When dropped onto a target specimen, the metallic cylinder experiences a length change which, in turn, causes a change of the electrical resistance in the strain gauges. The change of resistance can be converted into the impact force involved in the impact event with an external data acquisition and signal processing (DAQ&SP) system. The success of DWIT in measuring low-velocity impact force raises interest in using a similar concept to measure the forces involved in higher-velocity impacts, such as free projectile impacts and crash impacts. By taking advantage of the capability and efficiency of electrical resistance strain gauges in recording time-dependent strain histories, this study looks into building, testing and validating a resistance strain gauge based instrumented projectile (IP) for measuring impact-induced force history due to higher-velocity free impact.

37.2 Development of a Strain Gauge Based IP

When materials and structures are subjected to impact loading, complex strain wave propagation, rebounding and overlapping can take place in them, resulting in disfigurement of the initial impact-induced strain wave. Subsequent vibration and damage process can take place in the materials and structures involved in the impact event and further complicate the measurement of the impact-induced strain wave history and subsequent force history. Since the initial impact-induced strain wave bears the critical key to understanding the primary behavior of the materials and structures being impacted, it is of great interest to isolate the initial impact-induced strain wave from the complex wave combining impacting, reflecting and rebounding elements. This study is focused on identifying the initial wave segment measured by the electrical resistance strain gauges.

G. Li • D. Liu (✉) • D. Schleh
Composite Vehicle Research Center, Department of Mechanical Engineering, Michigan State University,
2727 Alliance Drive, Lansing 48910, Michigan
e-mail: liu@msu.edu

B. Song et al. (eds.), *Dynamic Behavior of Materials, Volume 1*,
Conference Proceedings of the Society for Experimental Mechanics Series, DOI 10.1007/978-3-319-22452-7_37

37.3 Experimental Setup

In this study, an aluminum projectile as shown in Fig. 37.1 was prepared. It consisted of a thick cylindrical neck and a hollow cylindrical body. They were joined by a special cylindrical shoulder. The nose had a length of 50 mm and diameter of 7 mm. The body was 85 mm long with an external diameter around 13.5 mm and a thickness of 1 mm. The external surface of the cylindrical neck of the projectile was equipped with a pair of electrical resistance strain gauges on the opposite sides while the cylindrical body housed a microprocessor and a battery, as shown in Fig. 37.1, to record the strain history during impact. Hence, the stand-alone IP is able to record the strain history which can later be downloaded onto an outside computer for calculation of forces involved in impact events. Figure 37.2 shows an experimental setup. It includes a gas gun barrel, a guiding tube, triggering elements and a long target bar. The measurement from the long target bar can be compared with that from the IP. If they match well, the ability of the IP to eliminate the wave rebounding can be confirmed.

37.4 IP Without a Specially Designed Shoulder

To begin with, an IP consisted of a tube with a regular cylindrical shoulder, i.e. without a specially designed shoulder, was prepared. A long solid bar of 3.5 m, similar to those commonly used in split Hopkinson's pressure bar (SHPB), was also installed with a pair of strain gauges and used as a target bar. Figure 37.3 shows the strain history recorded by both the long target bar and the IP without a specially designed shoulder when the latter was fired from the gas gun and impacted the long

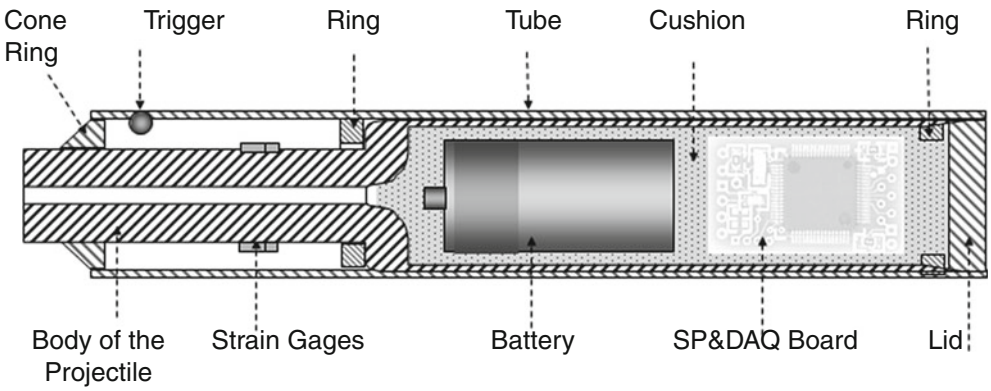

Fig. 37.1 An instrumented projectile

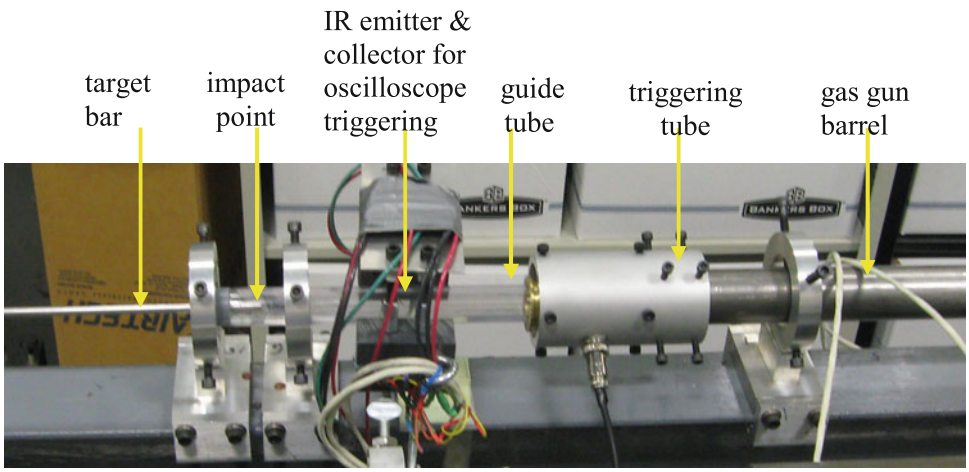

Fig. 37.2 Assembly of gas gun, triggering tube and target bar

target bar. The two measurements do not seem to have any correlation due to the multiple rebounding waves overlapped in the short IP. It should be pointed out that the wave recorded in the long target bar only included the initial impact-induced strain history. That is, there was no rebounding wave overlapped with the initial strain wave due to the length of the bar. However, the IP without a special geometry recorded the overlapped wave combining the initial impact-induced wave and subsequent reflected ones.

37.5 IP with a Specially Designed Shoulder

Since the initial impact-induced force history bears the most fundamental characteristics of an impact event, there is a need to isolate the initial impact-induced strain history from overlapping with the subsequent strain waves reflected from the ends of the short IP. In order to achieve such a goal, this study takes an optimization approach to achieve a special geometry for the shoulder of the IP via multiple trial-and-errors. Figure 37.1 shows an IP with an identical thick-walled cylindrical neck and an identical hollow cylindrical body as the IP without a special geometry. However, its specially designed shoulder is capable of eliminating the majority of rebounding waves. Similar microprocessor and battery used in the IP without a specially designed shoulder was also installed in it.

The IP with the specially designed shoulder was then used for impacting the same long bar used for the IP without a specially designed shoulder. Figure 37.4 shows that the force histories from the IP with the specially designed shoulder and the long bar are almost identical to each other. The capability of the special geometry in maintaining the initial impact-induced wave is thus confirmed. In other words, the IP with the specially designed shoulder was able to isolate the initial strain history and to prevent it from being distorted by the rebounding strain waves. This result demonstrates that the IP with a specially designed shoulder is equivalent to a long bar.

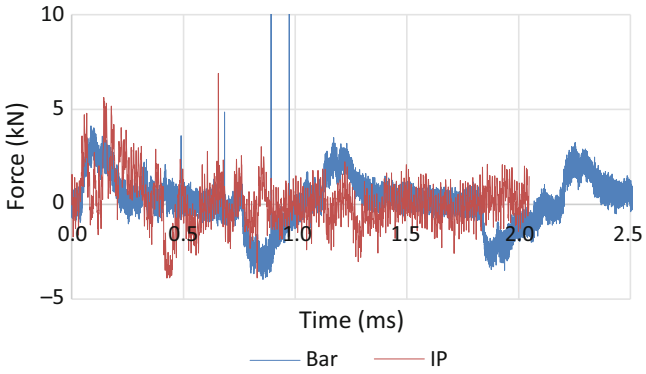

Fig. 37.3 Comparison of force histories between the results from an IP without a special geometry and that from a long bar

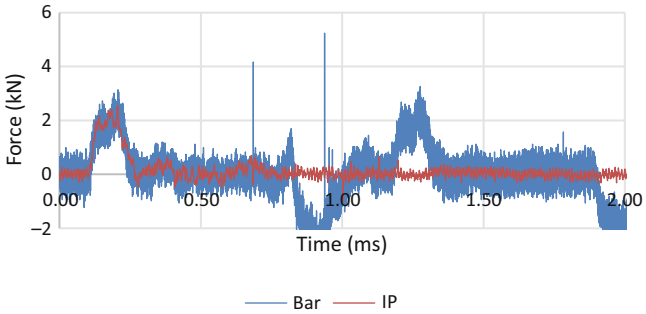

Fig. 37.4 Comparison of force histories between the results from an IP with a special geometry and that from a long bar

37.6 Validation of Force Measurement

To justify the force history measured by the innovative instrumented projectile, IP, a ballistic impact of the IP into a thin aluminum specimen was performed. The experiment included an IP impacting on one side of the specimen and measurement of the out-of-plane deformation on the other side with an optical method so-called fringe projection [2]. Figure 37.5 shows the top view of the experimental setup. The non-impacted surface of the specimen was painted white to increase optical contrast for dynamic measurements. A grating (lines with constant distance) was installed in front of the light source and shone onto the back surface of the painted aluminum specimen. When the projectile impacted the specimen, it caused deformation to the specimen, resulting in the distortion of the projected straight lines. Contours of the out-of-plane deformation of the specimen could then be identified from the comparison between the projected straight lines and the distorted lines. By taking the out-plane deformation twice, an acceleration history, and subsequently the force history of the projectile, can be obtained. Figure 37.6 show the comparison from the IP and the FP. They seem to agree quite well.

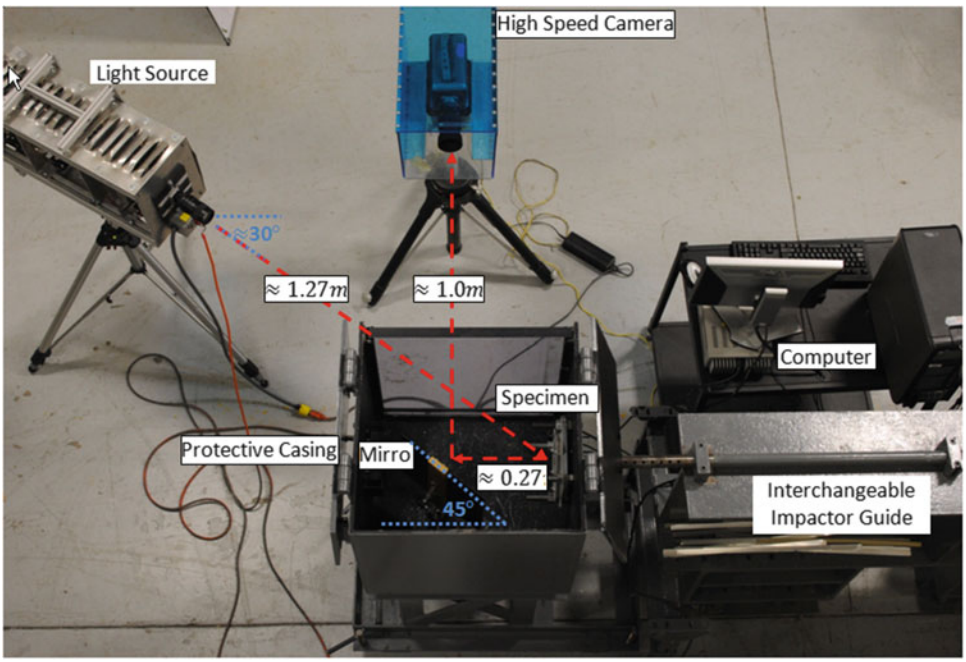

Fig. 37.5 Experimental setup of fringe projection technique

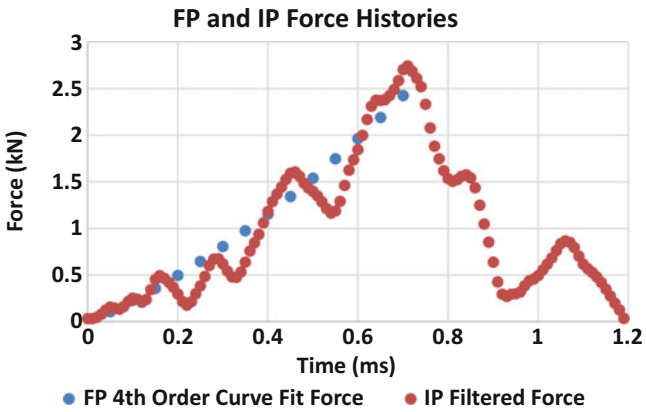

Fig. 37.6 Comparison between IP (instrumented projectile) and FP (fringe projection)

37.7 Conclusions

When a projectile hits a target, impact-induced waves can form in both the projectile and the target. If the projectile is short, there will be significant wave rebounding between the ends of the projectile, resulting in a very complex wave overlapping. This causes the initial characteristics of the impact-induced wave, which is critically important to understanding the impact-induced event in the structure, to be obscured. With a careful design, it is possible to isolate the initial impact-induced wave in the projectile. In this study, a projectile with a specially designed geometry is developed and shown to significantly reduce the reflection of the wave propagation from the end of the projectile. Hence, it can be used for measuring the initial wave propagation generated at the onset of impact.

Acknowledgements The authors wish to express their sincere appreciation to Army Research Laboratory for financial support and Liuman Technologies for the use of the instrumented projectile.